OAK RIDGE NATIONAL LABORATORY LIBRARIES
3 4456 0570483 2

CENTRAL RESEARCH LIBRARY

ORNL-5103

Cy 1

Mechanical Properties Test Data for Structural Materials Quarterly Progress Report for Period Ending October 31, 1974

[redacted]

OAK RIDGE NATIONAL LABORATORY
CENTRAL RESEARCH LIBRARY
DOCUMENT COLLECTION
LIBRARY LOAN COPY
DO NOT TRANSFER TO ANOTHER PERSON
If you wish someone else to see this document, send in name with document and the library will arrange a loan.
UCN-7969
(3 3-67)

OAK RIDGE NATIONAL LABORATORY
OPERATED BY UNION CARBIDE CORPORATION • FOR THE U.S. ATOMIC ENERGY COMMISSION

Printed in the United States of America. Available from
the U.S. Atomic Energy Commission, Technical Information Center
P.O. Box 62, Oak Ridge, Tennessee 37830
Price: Printed Copy $10.60 ; Microfiche $2.25

This report was prepared as an account of work sponsored by the United States Government. Neither the United States nor the United States Atomic Energy Commission, nor any of their employees, nor any of their contractors, subcontractors, or their employees, makes any warranty, express or implied, or assumes any legal liability or responsibility for the accuracy, completeness or usefulness of any information, apparatus, product or process disclosed, or represents that its use would not infringe privately owned rights.

ORNL-5103
UC-79b, -h, -k
(Liquid Metal Fast
Breeder Reactors)

Contract No. W-7405-eng-26

METALS AND CERAMICS DIVISION

MECHANICAL PROPERTIES TEST DATA FOR STRUCTURAL MATERIALS QUARTERLY PROGRESS REPORT FOR PERIOD ENDING OCTOBER 31, 1974

Aerojet Nuclear Company

Argonne National Laboratory

Hanford Engineering Development Laboratory

Naval Research Laboratory

Oak Ridge National Laboratory

Westinghouse Advanced Reactors Division

University of Cincinnati

University of California at Los Angeles

General Electric Company

Compiled by M. R. Hill

DECEMBER 1974

OAK RIDGE NATIONAL LABORATORY
Oak Ridge, Tennessee 37830
operated by
UNION CARBIDE CORPORATION
for the
U.S. ATOMIC ENERGY COMMISSION

FOREWORD

This is the fifth in a series of progress reports, the purpose of which is to record and distribute quarterly the collected results of all structural materials mechanical properties test programs sponsored by the Reactor Research and Development Division of the USAEC.

To be useful as resource documents, the reports in this series must be published and distributed in a timely manner to those in the reactor design and materials technology community who have a need of mechanical property test data for nuclear reactor and power plant applications. A test and material index is included to increase the effectiveness of the report.

Reports previously issued in this series are as follows: ORNL-4936, period ending October 31, 1973; ORNL-4948, period ending January 31, 1974; ORNL-4963, period ending April 30, 1974; and ORNL-4998, period ending July 31, 1974. The next quarterly report will be for the period ending January 31, 1975, and contributions are due at ORNL by February 15, 1975.

W. R. Martin
Metals and Ceramics Division
Oak Ridge National Laboratory

CONTENTS

SUMMARY ix

1. AEROJET NUCLEAR COMPANY 1

1.1 INTRODUCTION 1

1.2 FATIGUE TESTS ON CLADDING AND STRUCTURAL MATERIALS 2

1.2.1 Fatigue and Creep-Fatigue of Type 304 Stainless Steel Weldment Material Aged for 8000 Hours 2

1.3 INCONEL 718 MECHANICAL PROPERTY PROGRAM 5

2. ARGONNE NATIONAL LABORATORY 7

2.1 INTRODUCTION 7

2.2 FRACTURE AND FATIGUE STUDIES ON STAINLESS STEELS 7

2.2.1 Effect of Rising Mean Strain on the Fatigue Life of Type 304 Stainless Steel 7

2.3 SODIUM EFFECTS ON LFMBR MATERIALS 13

2.3.1 Influence of Sodium Environment on the Low-Cycle Fatigue Behavior of Austenitic Stainless Steels . . 13

2.4 REFERENCES 17

3. HANFORD ENGINEERING DEVELOPMENT LABORATORY 19

3.1 INTRODUCTION 19

3.2 LFMBR STRUCTURAL MATERIALS 19

3.2.1 FFTF/LMFBR Weld Materials Properties 19

3.2.1.1 Objective 19

3.2.1.2 Accomplishments and Status 19

3.2.1.3 Results 21

3.2.1.4 Discussion 29

3.2.1.5 Expected Achievements 32

3.2.2 LMFBR Structural Materials Evaluation 33

3.2.2.1 Objective 33

3.2.2.2 Accomplishments and Status 33

3.2.2.3 Results 33

3.2.2.4 Expected Achievements 41

3.3 MATERIALS SAFETY AND ENGINEERING 41

3.3.1 Subcritical Crack Growth 41

3.3.1.1 Objective 41

3.3.1.2 Accomplishments and Status 41

3.3.1.3 Expected Achievements 47

3.4 IRRADIATION DAMAGE TO REACTOR METALS 47

3.4.1 Application of the Life Fraction Rule to the Stress-Rupture Behavior of 20% C.W. Type 316 Stainless Steel 47

3.4.1.1 Objective 47

3.4.1.2 Accomplishments and Status 47

3.4.2 Low Temperature Creep of 20% Cold Worked Type 316 Stainless Steel 60

3.4.2.1 Objective 60

3.4.2.2 Accomplishments and Status 60

3.4.3 Thermal Creep in Pressurized Tubes of 20% Cold Worked Type 316 Stainless Steel 69

3.4.3.1 Objective 69

3.4.3.2 Scope of Work 69

3.4.3.3 Results 71

3.4.3.4 Evaluation of Results 84

3.4.3.5 Conclusions and/or Recommendations 98

3.4.3.6 Applications 98

3.4.3.7 Expected Achievements 98

3.5 REFERENCES 98

4. NAVAL RESEARCH LABORATORY 101

4.1 INTRODUCTION 101

4.2 EFFECT OF HOLD-TIME ON FATIGUE CRACK PROPAGATION IN THERMALLY AGED, ANNEALED AND 25% COLD-WORKED TYPE 304 STAINLESS STEEL 101

4.2.1 Background 101

4.2.2 Materials and Test Procedures 101

4.2.3 Results and Discussion 104

4.3 REFERENCES 107

5. OAK RIDGE NATIONAL LABORATORY 109

5.1 INTRODUCTION 109

5.2 MECHANICAL PROPERTIES AND BEHAVIOR FOR STRUCTURAL MATERIALS 109

5.2.1 Mechanical Property Characterization of Type 304 Stainless Steel Reference Heat 109

5.2.1.1 Creep and Rupture Properties of the 2-in. (51-mm) Plate of Reference Heat 109

5.2.1.2 Uniaxial Tensile Tests Following Periods of Creep 116

5.2.2 Heat-to-Heat Variation of Mechanical Properties of Types 304 and 316 Stainless Steel 119

5.2.2.1 Long-Term Creep Tests in Heat-to-Heat Variation Study of Type 304 Stainless Steel 119

5.2.2.2 Creep Data on Weak, Medium, and Strong Heats of Type 304 Stainless Steel 122

5.2.2.3 Effect of Aging on Tensile and Creeep Properties of Type 304 Stainless Steel . . 126

5.2.2.4 Heat-to-Heat Variation of Type 316 Stainless Steel 137

5.2.3 Materials Behavior in Support of Development and Evaluation of Failure Criteria for Materials . . . 148

5.2.4 Mechanical Property Characterization of Type 316 Stainless Steel Reference Heat 157

5.2.4.1 Procurement of Type 316 Stainless Steel Reference Heat 157

5.2.5 Structural Materials Information Center 158

5.2.6 Elastic Properties of Engineering Materials 161

5.2.6.1 Program Progress 162

5.2.6.2 Elastic Properties Determined by Dynamic Tests 164

5.2.7 Analytical Studies of Mechanical Properties Testing 167

5.2.7.1 Development of Finite Element Models for Crack Tip Analysis 167

5.2.7.2 Finite Element Analysis of Creep and Plasticity in Tensile Test Specimens . . . 169

5.3 MECHANICAL AND METALLURGICAL BEHAVIOR OF WELDMENTS FOR LMFBR 175

5.3.1 Analysis of Tensile Test Data for a Type 308 CRE Stainless Steel Pressure Vessel Weld at 0.004/min Strain Rate 175

5.3.2 Thermal Properties of CRE Type 308 Stainless Steel Weld Metal 183

5.3.3 Creep-Rupture Properties of GTA Type 16-8-2 Welds . 203

5.4 MECHANICAL PROPERTIES OF STEAM GENERATOR AND HEAT EXCHANGER MATERIALS 207

5.4.1 Tensile Properties of 2 1/4 Cr-1 Mo Steel 207

5.4.2 Effect of Sodium on the Mechanical Properties of 2 1/4 Cr-1 Mo Steel 219

5.4.3 Fatigue Behavior of 2 1/4 Cr-1 Mo Steel 220

5.4.4 Mechanical Properties Correlations of 2 1/4 Cr-1 Mo Steel for LMFBR Steam Generator 232

5.4.4.1 True Fracture Stress 232

5.4.4.2 Time to Tertiary Creep 233

5.4.4.3 Diamond Pyramid Hardness 234

5.4.4.4 Creep Equation for 2 1/4 Cr-1 Mo Steel . . 234

5.4.5 Mechanical Properties of Weld-Overlaid Forgings . . 236

5.5 HIGH TEMPERATURE DESIGN 241

5.5.1 Exploratory Studies in Support of Structural Design Methods 241

5.5.1.1 Creep Testing 241

5.5.1.2 Relaxation Testing 250

5.5.1.3 Creep-Plasticity Studies 258

5.5.1.4 Strain Cycling 260

5.5.2 Investigations of Creep Failure Under Uniaxial and Multiaxial Conditions 260

5.6 MECHANICAL PROPERTIES OF HTGR STEAM GENERATOR AND PRIMARY CIRCUIT MATERIALS 286

5.6.1 Materials 286

5.6.2 Tensile Testing 286

5.6.3 Environmental Creep Testing 287

5.6.4 Environmental Fatigue Testing 293

5.6.4.1 Subcritical Crack Growth 293

5.6.4.2 Fatigue Life Testing 296

5.7 REFERENCES 296

6. WESTINGHOUSE ADVANCED REACTORS DIVISION 303

6.1 INTRODUCTION 303

6.2 BASIC SPECIMEN TESTING 303

6.2.1 Uniaxially Loaded Specimen Models with Uniform Gage Section (304 SS, Heat 9T2796) 303

6.2.1.1 Test Piece Description 303
6.2.1.2 Current Results 303
6.2.2 Uniaxially Loaded Specimen Models with Nonuniform Gage Section 312
6.2.2.1 Test Piece Description 312
6.2.2.2 Current Results 312
6.2.3 Specimens with Welds (304 SS, Heat 9T2796) 312
6.2.3.1 Test Piece Description 312
6.2.3.2 Current Results 312
6.3 TUBULAR SPECIMEN TESTING 313
6.3.1 Test Piece Description 313
6.3.2 Test Results and Planning (304 SS, Heat 9T2796) . . 313
6.3.3 316 SS Tubular Testing 321
6.4 REFERENCES 321
7. UNIVERSITIES 323
7.1 UNIVERSITY OF CINCINNATI 323
7.1.1 Introduction 323
7.1.2 Experimental Program 323
7.1.2.1 Characterization of the Creep and Tensile Substructure of 304 Stainless Steel, Reference Heat 9T2796 324
7.1.2.2 Analysis of Relationships of Deformation Rate, Stress and Temperature for 304 Stainless Steel 326
7.1.2.3 Intragranular Deformation Behavior of AISI 304 Stainless Steel at Elevated Temperature 334
7.1.2.4 Deformation Substructure of Austenitic Stainless Steel from Low Cycle Fatigue at Elevated Temperature 340
7.1.2.5 Deformation Behavior and Substructure Characteristics of Several Nickel Based Alloys 341
7.1.3 References 342
7.2 UNIVERSITY OF CALIFORNIA, LOS ANGELES 343
7.2.1 Microstructure and High Temperature Deformation of Cr-Mo Steels for LMFBR Heat Exchanger 343
7.2.2 Introduction 343

7.2.3 Creep Properties of 2 1/4 Cr-1 Mo Steels 344

7.2.3.1 Alloy H (High Carbon) 347

7.2.3.2 Alloy I (Intermediate Carbon) 349

7.2.3.3 Alloy L (Low Carbon) 353

7.2.3.4 Alloy M (Medium Carbon) 356

7.2.4 Creep Studies in Lightly Cold-Worked Stainless Steels 356

7.2.5 The Effect of Case Carburization Fracture Mode of Type 316 Stainless Steel 357

7.2.5.1 Introduction 357

7.2.5.2 Experimental Procedures/Fractography . . . 358

7.2.6 Results 359

7.2.6.1 Mechanical Properties 359

7.2.6.2 Fracture Mode 359

7.2.7 References 370

8. GENERAL ELECTRIC COMPANY 373

INDEX 375

SUMMARY

1. AEROJET NUCLEAR COMPANY

Fatigue and creep-fatigue tests at 593°C (1100°F) of Type 304/308 FFTF weldment stainless steel are reported. Testing of specimens aged for 8000 hours at 593°C (1100°F) has begun and current data from these tests is compared with as-received material. The aged stainless steel consistently shows a longer cyclic life with both the base and weld metal. The base metal, however, shows a much more marked increase especially with hold times.

Work continues on efforts to improve the mechanical properties of Inconel Alloy 718 through modifications of conventional thermal treatments. Attempts to correlate varying mechanical properties in the solution-annealed condition with chemistry and microstructure were not entirely successful. Additional work, involving material of different processing history, is planned.

2. ARGONNE NATIONAL LABORATORY

A series of strain-controlled rising-mean-strain fatigue tests on Type 304 stainless steel at 593°C (1100°F) has been completed. The data indicate a decrease in fatigue life with an increase in mean strain at failure and also suggest that this effect is greater for 0.5% total strain-range tests than for 1% tests. The significance of these results with respect to ASME Code Case 1592 is discussed briefly. When the test data are plotted as fatigue damage fraction versus creep damage fraction, the points are found to fall below the predictions of the linear summation-of-damage rule. The saturated stress ranges for the rising-mean-strain tests were found to be slightly greater than for zero-mean-strain tests, but essentially no tendency toward a rising mean stress was observed.

Fatigue tests in sodium are being conducted to determine the effect of a sodium environment on the low-cycle fatigue behavior or Types 304 and 316 stainless steel in annealed, annealed and aged, and sodium-exposed conditions. The emphasis is placed on the effect of long-term (to 5000 hr) exposure of the materials to well-characterized sodium at temperatures between 550 and 700°C. Oxygen, carbon, and hydrogen concentrations in the sodium during specimen exposure are controlled at levels of interest for present-day LMFBR applications. The materials for this program are from the same heats as materials used in other testing programs (Type 304 -- Heat 9T2796; Type 316 -- Heat V87210). Test specimens with a 0.200-in.-dia by 0.500-in.-long gauge section are used in the present program. Preliminary results obtained for annealed Type 304 stainless steel at 600°C in sodium are compared with 593°C air data of Weeks et al.

3. HANFORD ENGINEERING DEVELOPMENT LABORATORY

Trend curves describing the temperature dependence of tensile properties have been formulated for several weld-deposited austenitic stainless steels and also for wrought Type 304. Ratios of elevated-temperature properties to room-temperature properties were fitted to polynomial expressions in temperature by regression analysis. Trend curves were established for 308/308L, CRE 308 and 16-8-2 as well as for all the weld metal data. The results showed that the degree of correlation between predicted and observed properties was dependent upon variations in weld process and parameters but that the ratio trend curve approach yielded a useful degree of correlation of the elevated-temperature properties even without considering all the complex features of the weld deposited materials.

The ductile-to-brittle transition of CLIRA meltdown cup materials, TZM and tungsten, irradiated to expected FTR goal fluences ($\sim 1 \times 10^{22}$ n/cm^2, E > 0.1 MeV) has been determined to remain below operating temperatures. The tungsten transition shifted from about 143°F to 445°F and the TZM, from -122°F to 293°F.

The effect of stress ratio and cyclic frequency on the fatigue-crack growth behavior of Inconel 718 was studied at 800°F and 1000°F. Stress ratio effects were accounted for by use of the "effective stress intensity factor" concept. Fatigue-crack growth rates increased with decreasing cyclic frequency at both test temperatures.

Tests were conducted to determine the stress-rupture behavior of 20% C.W. Type 316 stainless steel tubing subjected to variable loads and the results were analyzed in terms of the life fraction rule. It was determined that this rule can be used only with qualification. Results of thermal aging tests showed that at 1200°F there is no degradation in the stress-rupture behavior due to aging.

Thermal creep strains in 20% cold worked Type 316 stainless steel after 1000 hours under a stress of 20,000 psi are small at both 850°F (a strain of 120×10^{-6}) and 1000°F (a strain of 540×10^{-6}). A significant portion of the creep strain is recoverable during periods of unloading, with both the magnitude and time dependence of fractional strain recovery being insensitive to temperature. Creep response under unloading and reloading situations is consistent with a substantial anelastic component in the total deformation. Evidence of static thermal recovery during unload periods is observed at 1000°F, but not at 850°F.

Diametral and axial creep strains in pressurized tube specimens of 20% cold worked Type 316 stainless steel were measured over the temperature range from 825 to 1400°F for times to 2400 hours. Nominal stress levels for the tests were varied in increments of about 2500 psi over the range from 0 to 10,000 psi and in increments of about 5000 psi over the range from 10,000 to 60,000 psi.

4. NAVAL RESEARCH LABORATORY

The effect of fatigue-creep interaction was investigated at 1100°F (593°C) for solution annealed and 25% cold-worked Type 304 stainless steel previously thermally aged at 1100°F (593°C) for 5000 hr. Tension loads were held on the SEN fatigue specimens for times of 0.1 and 1.0 minutes each cycle to study the effect of hold time on the crack growth resistance of the steel. For the 25% cold-worked material, 0.1 and 1.0 minutes hold times increased initial crack growth rates by nearly factors of 3 and 5, respectively, over zero hold-time tests. By comparison, 0.1 and 1.0 minute hold-times increased the initial crack growth rate of the annealed material by only factors of approximately 2 and 1.5. It was found that, in the aged condition, the crack growth resistance of the annealed specimens was superior to that of cold-worked specimens. This behavior is in contrast with previous unaged results which showed that crack growth resistance was improved by cold working. Under the conditions of the present study, specimen life appears to be dependent on number of cycles rather than on time. This indicates that fatigue is the predominant mechanism of the fatigue-creep interaction for these results.

5. OAK RIDGE NATIONAL LABORATORY

Elevated-temperature creep testing of the ORNL reference heat of type 304 stainless steel is continuing. Some creep tests have exceeded a test time of 16,200 hr. One creep test has ruptured after 14,647 hr. The total elongation, reduction of area, and stable creep strain for this test have been compared with previously reported and published data. Additional data on creep tests and tensile tests following periods of creep are reported.

Ten long-term (50,000 hr) creep tests are in progress on nine different heats of type 304 stainless steel. One test had ruptured last quarter after 14,077 hr. Another test ruptured during this quarter after 22,622 hr. Times to rupture for 20 heats of type 304 stainless steel have been compared with each other and with the minimum expected value curve from Code Case 1592. Stable creep strain for the weak heat (187), the strong heat (845), and the reference heat have been compared for a test temperature of 593°C (1100°F). Creep data on weak, medium, and strong heats of type 304 stainless steel have been presented.

In continued aging studies on various heats of type 304 stainless steel, 16 blocks have been aged up to 10,000 hr. Creep data on aged specimens of the reference heat and heat 845 are presented. Aging increased both minimum creep rate and time to rupture for the reference heat and increased minimum creep rate and decreased time to rupture for heat 845. Loading strain for both steels decreased on aging, whereas strain in first-, second-, and third-stage creep increased. Time to rupture for both heats in unaged and aged conditions can be related to duration of second stage and time to onset of third stage.

Time to rupture has been related to minimum creep rate by the same expression for both unaged and aged conditions. Maximum effect on creep parameters was observed for the aging temperature of 649°C (1200°F). Aging has been shown to decrease uniform and total elongation in the tensile range and increase the same quantities in the creep range.

Elevated-temperature creep and tensile tests of seven heats of type 316 stainless steel in both unaged and aged conditions continued. Heat 686 is strong at both room and elevated temperatures. Creep curves on these specimens are unusual and have been explained on the basis of precipitation and its location. The precipitate observed in as-received materials has been shown not to dissolve on reannealing.

Effect of grain size on creep properties of heat 686 was investigated. Coarse-grained material showed a large increase in loading strain and a decrease in time to rupture. Aging of heat 686 showed effects similar to those observed for the reference heat and heat 845 of type 304 stainless steel.

Work is continuing on development of relevant material failure criteria. Parametric methods have been used to predict various "strain limits," with somewhat encouraging results. Analysis is continuing.

Some product forms of the reference heat of type 316 stainless steel have been delivered, and manufacture is nearing completion on others.

Input of mechanical properties data to the Data Storage and Retrieval System is continuing. The entire computerized data management system is continuing to expand and develop, providing increased user services. The Automatic Data Acquisition System for the creep laboratory is now in operation.

Experimental data gathered on the dynamic elastic constants of type 304 stainless steel (heat 346544) were analyzed, and the equations with estimated values of the elastic constants (E, G, and ν) as functions of temperature were determined. Correlations of the dynamic and static elastic constants for 2 1/4 Cr-1 Mo steel were prepared for the *Nuclear Systems Materials Handbook*.

Finite element methods are being used to enhance understanding of fracture mechanics and tensile testing. Special elements have been developed for crack tips to aid in crack propagation studies in weld metal and other anisotropic media. Analysis of the hourglass specimen and the cylindrical specimen show that the triaxiality in the hourglass is not large, that there is some nonuniformity in strain — which depends on taper — in the cylindrical specimen, and that the expected error in extensometry is less for the hourglass specimen that it is for the cylindrical specimen.

Tensile test data at 0.004/min strain rate on type 308 stainless steel weld metal with controlled residual elements (CRE) has been statistically evaluated to determine the significance of several independent variables on 16 characteristic tensile test measurements (yield strength, ultimate tensile strength, etc.). The independent variables included heat of base metal, welding electrode, test temperature, and location from which specimens were cut. Results are summarized.

Analysis of thermal transient strains in weld metal requires thermal transport and thermal expansion properties for weld metal and base metal. Measured values of these properties in the temperature range of interest for LMFBR applications show some apparently significant differences between base metal and weld metal. Anisotropy of these properties in weld metal was also explored experimentally.

Creep testing continues on 16-8-2 weld metal deposited in 1/2-in.-thick (13 mm) type 316 stainless steel plate. Welds made with Bechtel reference heat, Arcos 2367-R-16-8-2, a production filler metal for hot-leg FFTF primary containment piping, exhibit at least 30% elongation and at least 30% reduction of area at 649°C lasting to 3600 hr, but much of the strain occurs during tertiary creep. Tests at 482 and 593°C are in progress.

True-stress true-strain tensile data for 2 1/4 Cr-1 Mo steel has now been fit by the Holloman, Ludwik, Ludwigson, and Voce equations. By comparing the standard error of estimate, the Voce equation was concluded to be the best mathematical description of the data under most test conditions and the best single representation over the wide range of test conditions for which the data were fit. Transmission electron microscopy was used to characterize the precipitates present in 2 1/4 Cr-1 Mo steel that had been decarburized and aged by MSA Corp. for 26,500 hr at 566°C (1050°F).

Results obtained to date from both load- and strain-controlled fatigue testing of 2 1/4 Cr-1 Mo are reported. Test data are given for a single heat of material tested in strain control at room temperature, 315, 427, and 539°C (600, 800, and 1000°F). Extrapolations of the data are compared with the results of load-controlled tests. Information concerning the cyclic hardening and softening of this material in both load and strain control is also given.

Work is continuing to develop mechanical property correlations for 2 1/4 Cr-1 Mo steel for input to the *Nuclear Systems Materials Handbook*. Correlations have been developed for Bridgman-corrected true fracture stress, time to tertiary creep, and diamond pyramid hardness, with corresponding tolerance limits. Development of a creep strain mathematical model for 2 1/4 Cr-1 Mo steel has been completed.

Creep-rupture studies of the overlaid tubesheet forging at 593°C (1100°F) were summarized; tests were conducted on the forging, the overlay, and the forging adjacent to the overlay-forging fusion line. Tests at 482°C (900°F) are also reported.

Creep-rupture data accumulated on the 1-in. (25.4-mm) plate of the reference heat of type 304 stainless steel (heat 9T2796) are summarized, and the results from the fits of several time-temperature parameters to secondary creep rate, tertiary creep life, and rupture life data are presented. The ability of the time-temperature parameters to fit the data is impaired by a rather abrupt change in the creep-rupture behavior at temperatures between 621 and 704°C (1150 and 1300°F). An alternative model is developed; based on a power stress dependence, it incorporates the abrupt change in creep rate and rupture behavior.

Relaxation data to 100 hr were collected and used to construct "isochronous relaxation curves." These relate the relaxation strength to the initial applied strain for temperatures between 482 and 593°C (900 and 1100°F).

The procurement and tensile testing of HTGR structural alloys has continued, and subcritical crack growth rate studies (in steam) and environmental creep tests (in simulated gas-cooled reactor helium) have begun. Facility preparation for environmental testing — including the setup of an MTS for low-cycle fatigue — continues as a major task in this project.

6. WESTINGHOUSE ADVANCED REACTORS DIVISION

Creep testing of bar- and plate-type specimens was continued using material from the ORNL type 304 stainless steel reference heat (9T2796). Results were obtained from double-notched bar and eccentrically-loaded plate base material and three different types of welded specimens.

Creep testing of tubular specimens from the ORNL type 304 stainless steel reference heat (9T2796) continued, with four multiaxial tests completed. One of the specimens failed by rupture after 808 hr under an internal pressure of 2729 psi at 1100°F.

7. UNIVERSITIES

7.1 UNIVERSITY OF CINCINNATI

Characterization of creep and tensile substructures of type 304 stainless steel reference heat 9T2796 is continuing. Work has been completed on three creep rupture specimens and six tensile specimens. Preliminary results are consistent with previous TEM data, in that the subgrain size varies inversely with the applied stress according to σ^{-1} at low stress and σ^{-2} at the high stress levels.

A temperature compensated creep rate plot versus the hyperbolic sign of the applied stress suggests that both the tensile and creep data of the 304 stainless steel specimens tested over a temperature range of 538 to 816°C are in reasonable accord. The relationship is

$$Z = \dot{\varepsilon} \exp(Q/RT) = [\mathrm{Sinh}\ (\alpha\sigma/E)]^n$$

with the exponent n being equal to approximately seven. The effective strain rates varied by about ten orders of magnitude.

Detailed analysis of the intragranular elongation contribution to the total uniform strain has been measured on 304 stainless steel tested at 650°C at six different strain rates. The results are consistent with other related studies in that the grain boundary sliding component becomes more important as the strain rate decreases.

Work is continuing on the substructure evaluation of 304 and 316 stainless steel specimens which have been tested at elevated temperature in the low cycle fatigue mode with hold-times up to ten hours. New work is being initiated on some of the nickel base ternary alloys with particular emphasis on two heats containing 19 and 48 percent nickel and one binary alloy with 85 percent nickel. Each alloy has about 15 percent chromium. Procedures for thinning nickel base alloys for TEM evaluation and the characterization of the structure has been initiated on approximately seven different engineering alloys.

7.2 UNIVERSITY OF CALIFORNIA, LOS ANGELES

Step-load creep tests on 2 1/4 Cr-1 Mo steel in the normalized and tempered condition were completed at temperatures in the range of 850 to 1050°F, and the stress exponents are reported.

The influence of small amounts of cold work (0—10%) on the creep kinetics of austenitic stainless steels is being studied. Test conditions were selected for test and additional constant creep test capability was developed.

We are continuing our study on the ductile-brittle behavior of carbonized type 316 stainless steel. It now appears justifiable to attribute the primary cause of the observed transitions on fracture mode to the increase in local strain rate acting on the matrix at the tip of core cracks. This cause seems applicable when the failure of the carbon core is the controlling step in the fracture process.

8. GENERAL ELECTRIC COMPANY

(Will report next quarter.)

1. AEROJET NUCLEAR COMPANY

W. C. Francis

1.1 INTRODUCTION

Aerojet Nuclear Company is conducting mechanical properties investigations under two programs sponsored by the AEC Division of Reactor Research and Development. Program 06031, Fatigue Tests on Cladding and Structural Materials, involves experimental fatigue tests on stainless steel Types 304 and 316 as well as Type 304/308 weldments. These tests are intended to determine the influence of irradiation, cold work, heat treatment, heat-to-heat property variations, and temperature on fatigue behavior. Irradiated, thermal control, as-received, and annealed specimens are being tested at 427 to 700°C (800 to 1292°F). Current work on irradiated material is reported in the Semi-Annual Progress Report for the Irradiation Effects on Reactor Structural Materials Program compiled at HEDL. Unirradiated work currently involves low cycle fatigue and creep-fatigue tests of Type 304/308 weldment material with long time aging treatment and is reported in this document.

Program 06084, Inconel 718 Mechanical Property Program, has as its primary objective the acquisition of the necessary mechanical property data to permit safe, efficient use of this material in LMFBR service. The specific immediate application is for selected structural components of the Clinch River Breeder Reactor Project. Other reactor service applications which require high levels of mechanical properties at temperatures up to 649°C (1200°F) are also expected to make use of this material.

What have been considered standard heat treatments for Inconel 718 have not consistently yielded acceptable ductility values for the welded material. Current work involves scoping tests on material subjected to modified thermal treatments in an effort to optimize the heat treatment that will yield the best mechanical properties of both base and weld metal.

1.2 FATIGUE TESTS ON CLADDING AND STRUCTURAL MATERIALS - G. E. Korth and M. D. Harper

1.2.1 Fatigue and Creep-Fatigue of Type 304/308 Stainless Steel Weldment Material Aged for 8000 Hours

Base metal and weld metal specimens were cut from an as-welded block of Type 304 stainless steel welded with Type 308 weld wire and then aged in argon for 8000 hours at 593°C (1100°F). Details on the weldment material and previous testing on unaged stainless has been reported[1,2,3]. The aged specimens are currently being fatigue tested at 593°C (1100°F) with and without hold times to determine the effect of long time aging on the fatigue and creep-fatigue behavior of this material. Specimens were tested in air using strain control with a fully reversed ramp waveform and a strain rate of $4 \times 10^{-3} s^{-1}$. Results of current tests are reported in Table 1.1 where:

$\Delta\varepsilon_t$ = total strain range

$\Delta\varepsilon_p$ = plastic strain range at ∿1/2 cycle life

$\Delta\sigma$ = stress range

$\sigma_{t,max}$ = maximum tensile stress amplitude

$\sigma_{t,min}$ = tensile stress amplitude at the end of a hold time

N_f = number of cycles to failure

t_f = total time to fail

Only current test data is contained in Table 1.1 since most of the unaged tests have been previously reported[3]. Although the test matrix is not yet complete trends are starting to emerge. The data is plotted in Figure 1.1 and compared to unaged tests. The aged stainless

---

[1] C. R. Brinkman and G. E. Korth, "Heat-to-Heat Variations in the Fatigue and Creep-Fatigue Behavior of AISI Type 304 Stainless Steel, and the Fatigue Behavior of Type 308 Stainless Steel Weld Material," ANCR-1097, May, 1973.

[2] G. E. Korth and M/ D. Harper, "Mechanical Properties Quarterly Progress Report for Period ending Nov. 30, 1973, ORNL-4936 and Jan., 1974,ORNL-4948.

[3] G. E. Korth and M. D. Harper, "Semi-Annual Progress Report for the Irradiation Effects on Reactor Structural Materials Program for period ending Aug. 31, 1974, HEDL-TME-7451. (To be published in forthcoming ASTM-STP of Seventh Radiation Effects Symposium of Reactor Structural Materials held at Gatlinburg, Tenn., on June 11-13, 1974.

Table 1.1 Strain Fatigue Behavior of Type 304/308 Stainless Steel Weldments Tested[a] at 593°C (1100°F)

Specimen No.	Condition[b]	$\Delta\varepsilon_t$,%	$\Delta\varepsilon_p$,%	$\Delta\sigma$, @$N_f/2$ MPa	$\Delta\sigma$, @$N_f/2$ ksi	σ_t, @ $N_f/2$ MPa	σ_t, @ $N_f/2$ ksi	σ_t min, @ $N_f/2$ MPa	σ_t min, @ $N_f/2$ ksi	N_f	Time to Fail,h	Tensile Hold,h
BT-7	Base,2d-T	2.00	1.55	676.4	98.1	332.3	48.2	259.9	37.7	629	64.10	0.1
BT-8	Base,2d-T	1.98	1.54	648.8	94.1	319.2	46.3	273.0	39.6	807	10.17	0.01
BP-2	Base,2d-P	0.99	0.59	520.6	75.5	255.8	37.4	----	----	3,602	5.04	0
BP-67	Base,2a-P	1.01	0.58	581.9	84.4	286.8	41.6	----	----	2,558	3.58	0
BT-10	Base,2d-T	1.01	0.66	501.2	72.7	242.0	35.1	208.9	30.3	3,473	39.29	0.01
WP-3	Weld,2d-P-C	1.01	0.61	422.0	61.2	207.5	30.1	183.4	26.6	2,343	26.50	0.01
WT-3	Weld,2d-T-C	1.01	0.58	497.8	72.2	245.4	35.6	219.9	31.9	1,351	15.30	0.01
WF-3	Weld,2d-FL-C	1.01	0.66	569.5	82.6	280.6	40.7	249.6	36.2	1,028	11.63	0.01
WT-24	Weld,2d-T-S	1.01	0.62	528.8	76.7	258.6	37.5	217.9	31.6	1,212	121.80	0.1
BT-1	Base,2d-T	1.00	0.65	501.9	72.8	240.6	34.9	211.7	30.7	2,564	257.35	0.1
BT-31	Base,2a-T	1.00	0.65	590.9	85.7	283.4	41.1	257.2	37.3	790	80.19	0.1

[a]Triangular waveform with strain rate of $4 \times 10^{-3} s^{-1}$

[b]2=Base metal heat 600414
a=As welded condition
d=Aged 8000 hours at 593°C
T=Specimen taken transverse to weld seam
P=Specimen taken parallel to weld seam
FL=Transverse specimens across fusion line
S=Taken from section near surface of weldment
C=Taken from section near center of weldment

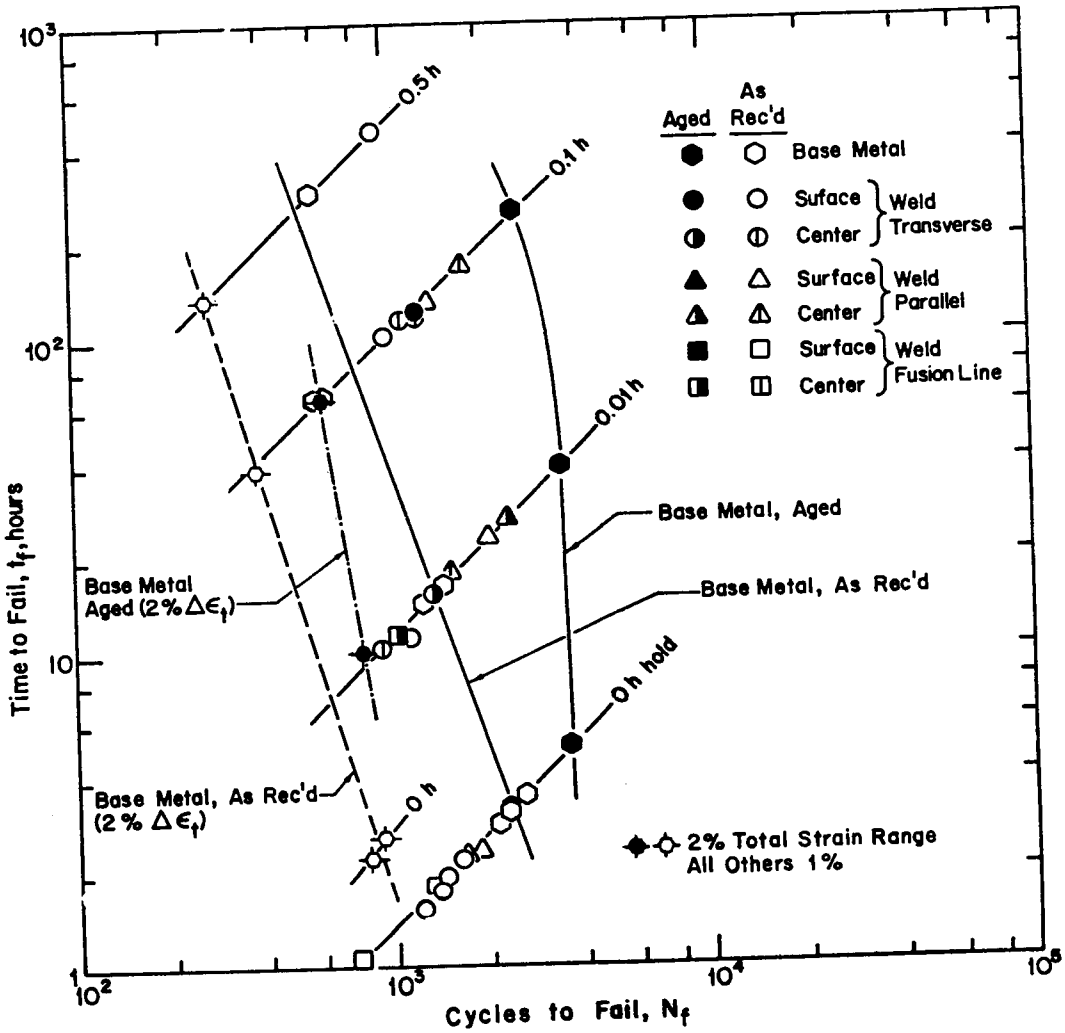

Figure 1.1 Time to fail vs cycles to fail plot for Type 304/308 weldment stainless steel showing creep-fatigue interaction in the as-received and aged conditions.

steel consistently shows a longer cyclic life with both the base metal and the weld metal. However the base metal shows a much more marked increase, especially when tensile hold times are incorporated into each cycle to introduce creep-fatigue interaction. At zero hold time the cyclic life of the aged base metal has increased over the as-received base metal by approximately 50%, but with 0.01 and 0.1 hour hold times the increase in cycles to fail is 250% and 430% respectively.

The stress range at half cycle life of the aged base and also the weld material is 10 to 15% lower than the as-received material for the same strain range. The weld metal could have undergone some stress relieving of residual weld stresses but the base metal should have experienced very little stress relief, if any, since it was in the mill anneal condition. Another indication that the base metal was not experiencing a stress relief came from 0.2% offset yield strength measurements obtained from the first quarter cycle of the tests. These measurements showed the yield strength of the aged stainless exhibited a slightly higher value than the as-received material. An average of three measurements of each type showed the aged and as-received yield strengths to be 174.4 mPa (25.3 ksi) and 151.5 mPa (22.0 ksi) respectively. Therefore the lower stabilized stress range of the aged specimens was probably not due to a stress relieving action of the 8000 hour age.

Preliminary optical metallography revealed no further clues as to the metallurgical change that had occurred during aging. In fact, it was somewhat surprising that the metallography didn't show quite extensive carbide precipitation. TEM is planned in the near future to see if precipitation occurred on a finer scale.

1.3 Inconel 718 Mechanical Property Program - D. D. Keiser, W. G. Reuter, G. R. Smolik, H. L. Brown

In the program to improve the mechanical properties of Inconel 718 via modified heat treatment, elevated temperature stress-rupture tests of fully-aged material continue. Data from elevated temperature tensile tests of solution-annealed material have varied

with material source and attempts to attribute the observed differences to chemistry and/or microstructure have not yet been successful. Redirected work will investigate additional material from one source, but with a different ingot production history, in an effort to establish the cause of the differences as either chemistry-related or process-related.

2. ARGONNE NATIONAL LABORATORY

R. W. Weeks

2.1 INTRODUCTION

Argonne National Laboratory (ANL) is conducting an extensive program to provide low-cycle, high-temperature fatigue data on Types 304 and 316 stainless steel in support of LMFBR component design, as outlined in a previous report.[1] The present report describes results obtained from rising-mean-strain fatigue tests on Type 304 stainless steel and also some early results from low-cycle fatigue tests conducted in flowing sodium.

2.2 FRACTURE AND FATIGUE STUDIES ON STAINLESS STEELS -- D. R. Diercks, C. F. Cheng, P. S. Maiya, and S. Majumdar

2.2.1 Effect of Rising Mean Strain on the Fatigue Life of Type 304 Stainless Steel -- D. R. Diercks

A series of strain-controlled rising-mean-strain fatigue tests on Type 304 stainless steel at 593°C (1100°F) has been completed. The tests were run at a constant cyclic strain rate of 4×10^{-3} sec^{-1} and total strain ranges of 0.5 and 1.0%. A rising mean true strain with a constant rate from 5×10^{-7} sec^{-1} to 8×10^{-6} sec^{-1} was simultaneously imposed. This loading resulted in tensile mean strains at failure of from 1.8 to 9.9%. The tests simulate a rather idealized ratchetting situation, and are intended to examine the adequacy of current design rules under conditions of rising mean strain.

Test data are given in Table 2.1, and a plot of fatigue damage fraction versus mean strain at failure is shown in Fig. 2.1. Despite the scatter present, these data indicate a decrease in fatigue life with an increase in mean strain at failure and also suggest that this effect is greater for the 0.5% total strain-range tests than for the 1% tests. Current design rules in ASME Code Case 1592[2] specify a limit of 1% on averaged strains through the thickness of a component, 2% on strains at the surface, and 5% on local strains at any point. Although a local ratchetting situation is difficult to imagine, Fig. 2.1 suggests, for

Table 2.1. Fatigue Data for Rising-mean-strain Tests on Type 304 Stainless Steel (Heat 9T2796) at 593°C (1100°F). The cyclic strain rate in all cases is 4×10^{-3} sec^{-1}.

Test No.	Total Strain Range, %	Plastic Strain Range, %	Stress Range at $N_f/2$, MPa	Rising-mean-strain Rate, sec^{-1}	Exper. Cycles to Failure, N_f	Exper. Time to Failure, min	Mean True Strain at Failure, %	Expected N_f for Zero Mean Strain	Expected Strain at Failure (No Cycling), %	Fatigue Damage Fraction	Creep Damage Fraction
628	0.501	0.258	371	5×10^{-7}	14,630	608.82	1.80	26,000	26	0.56	0.07
636	0.499	0.259	371	5×10^{-7}	16,648	692.70	2.07	26,000	26	0.64	0.08
619	0.504	0.243	397	1.2×10^{-6}	17,369	722.69	5.16	26,000	31	0.67	0.17
623	0.501	0.232	409	4×10^{-6}	9,667	402.22	9.87	26,000	38	0.37	0.26
625	1.004	0.653	534	2×10^{-6}	2,825	235.01	2.80	3,700	34	0.76	0.08
630	0.997	0.654	521	2×10^{-6}	3,733	310.90	3.73	3,700	34	1.01	0.11
613	0.986	0.643	521	4×10^{-6}	2,938	244.52	5.93	3,700	38	0.79	0.16
622	1.005	0.657	530	8×10^{-6}	2,255	187.62	9.42	3,700	42	0.61	0.22

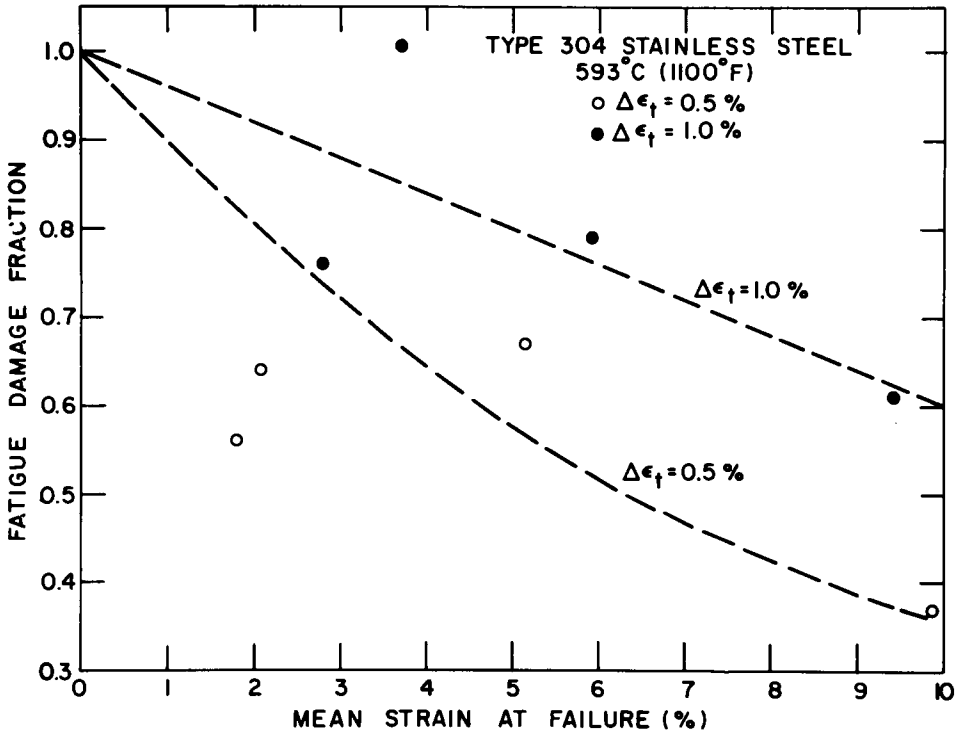

Fig. 2.1. Plot of Fatigue Damage Fraction vs Mean Strain at Failure for Rising-mean-strain Fatigue Tests.

such a case, that a 5% limit on mean strain may be rather liberal. In general, a ratchetting strain may be expected to be controlled by the Code Case limit of 1% on averaged strains through the thickness, and Fig. 2.1 indicates only a nominal reduction of fatigue life at this strain.

The data of Fig. 2.1 and Table 2.1 may be replotted as the fatigue damage fraction versus creep damage fraction and thus be compared with the predictions of the linear summation-of-damage rule. However, a procedure must first be adopted for the calculation of the creep damage fraction. The creep damage fraction was therefore defined as the ratio of the mean true axial strain accumulated at failure to the true axial strain to failure (or tensile ductility) for pure tensile loading. The latter quantity is strongly dependent on strain rate at 593°C (1100°F), as may be seen in Fig. 2.2, for the heat of material under consideration here. The strain rate plotted in Fig. 2.2 is taken to be the minimum creep rate for the ORNL creep data,[3] the engineering strain rate for the ORNL constant crosshead speed tensile data,[4] and the true axial strain rate for the Diercks and Burke[5] tensile data.

The use of strain-to-failure values from Fig. 2.2 to calculate creep damage resulted in the fatigue damage versus creep damage plot of Fig. 2.3. All but one of the points fall below the linear summation-of-damage rule, indicating that the rising mean strain is more detrimental to cyclic life than would be expected on a linear summation basis. Furthermore, the departure from the linear summation curve appears to be greater for the 0.5% strain-range data than for the 1% strain-range data.

Finally, it is interesting to note that the saturated stress ranges for the rising-mean-strain tests appear to be ∿10% greater than for zero-mean-strain tests with the same strain rate and total strain range. However, the stress range remains essentially symmetric about zero stress throughout the test, with little or no tendency toward a rising mean stress.

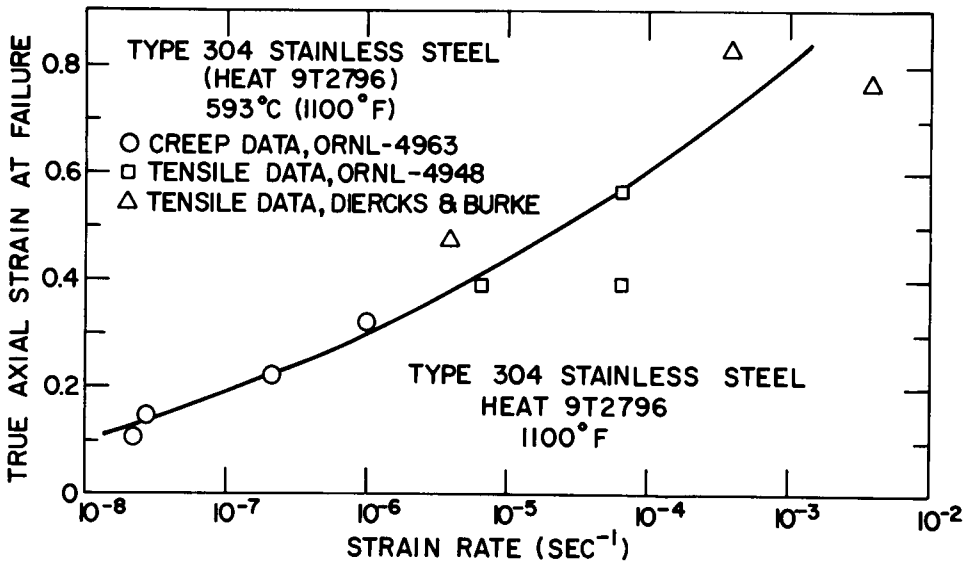

Fig. 2.2. True Axial Strain to Failure (Tensile Ductility) as a Function of Strain Rate for Type 304 Stainless Steel (Heat 9T2796) at 593°C (1100°F).

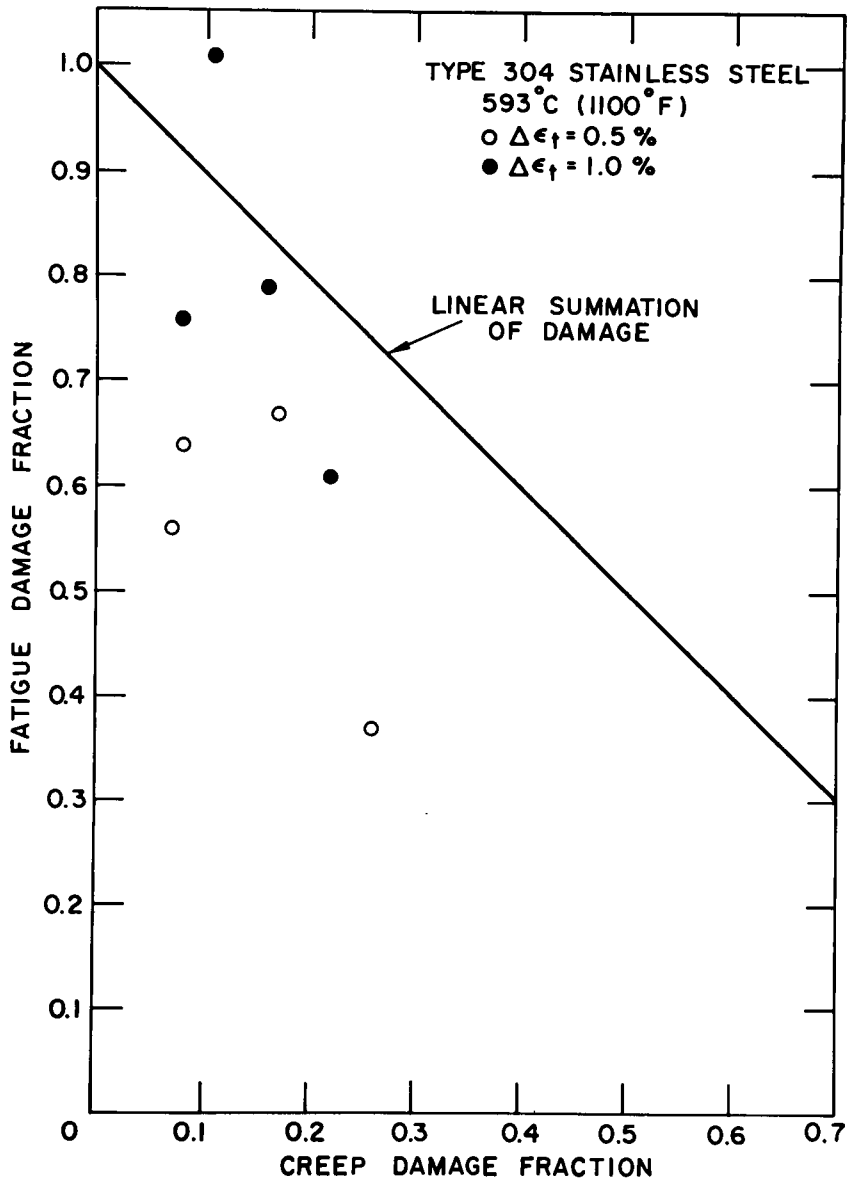

Fig. 2.3. Fatigue Damage Fraction vs Creep Damage Fraction for Rising-mean-strain Fatigue Tests.

2.3 SODIUM EFFECTS ON LMFBR MATERIALS -- T. F. Kassner

2.3.1 Influence of Sodium Environment on the Low-cycle Fatigue Behavior of Austenitic Stainless Steels -- D. L. Smith, K. Natesan, J. Y. N. Wang, and G. J. Zeman

Fatigue tests in sodium are being conducted to determine the effect of a sodium environment on the low-cycle fatigue behavior of Types 304 and 316 stainless steel in annealed, annealed and aged, and sodium-exposed conditions. The emphasis is placed on the effect of long-term (to 5000 hr) exposure of the materials to well-characterized sodium at temperatures between 550 and 700°C. Oxygen, carbon, and hydrogen concentrations in the sodium during specimen exposure are controlled at levels of interest for present-day LMFBR applications. The materials for this program are from the same heats as materials used in other testing programs (Type 304 -- Heat 9T2796; Type 316 -- Heat V87210). The compositions of these materials are given in the previous quarterly report.[6] Threaded test specimens with a 0.200-in.-dia by 0.500-in.-long gauge section have been machined from 0.625-in.-dia rod. The transition region from the gauge section to a 0.545-in.-dia shoulder is machined on a 1.000-in. radius.

Two facilities for fatigue testing in sodium (FFTS) have been installed in the sodium technology laboratory. Each facility consists of an MTS low-cycle closed-loop fatigue machine with an associated sodium loop. Figure 2.4 is a schematic diagram of an FFTS. The sodium loop provides a well-characterized sodium environment for fatigue testing at temperatures to 750°C. A capability for monitoring and controlling the oxygen, carbon, and hydrogen concentrations in sodium exists on each loop.

Specially designed fatigue machines and fixtures were required to facilitate the insertion and removal of the test specimens from the sodium environment. Since direct measurement of the specimen strain in the sodium was not considered feasible, the tests are conducted in a stroke control mode, using a standard resistive-type extensometer, located as shown in Fig. 2.4. The extensometer measures the sum of the strains in the fixture, the specimen gauge section, and the transition

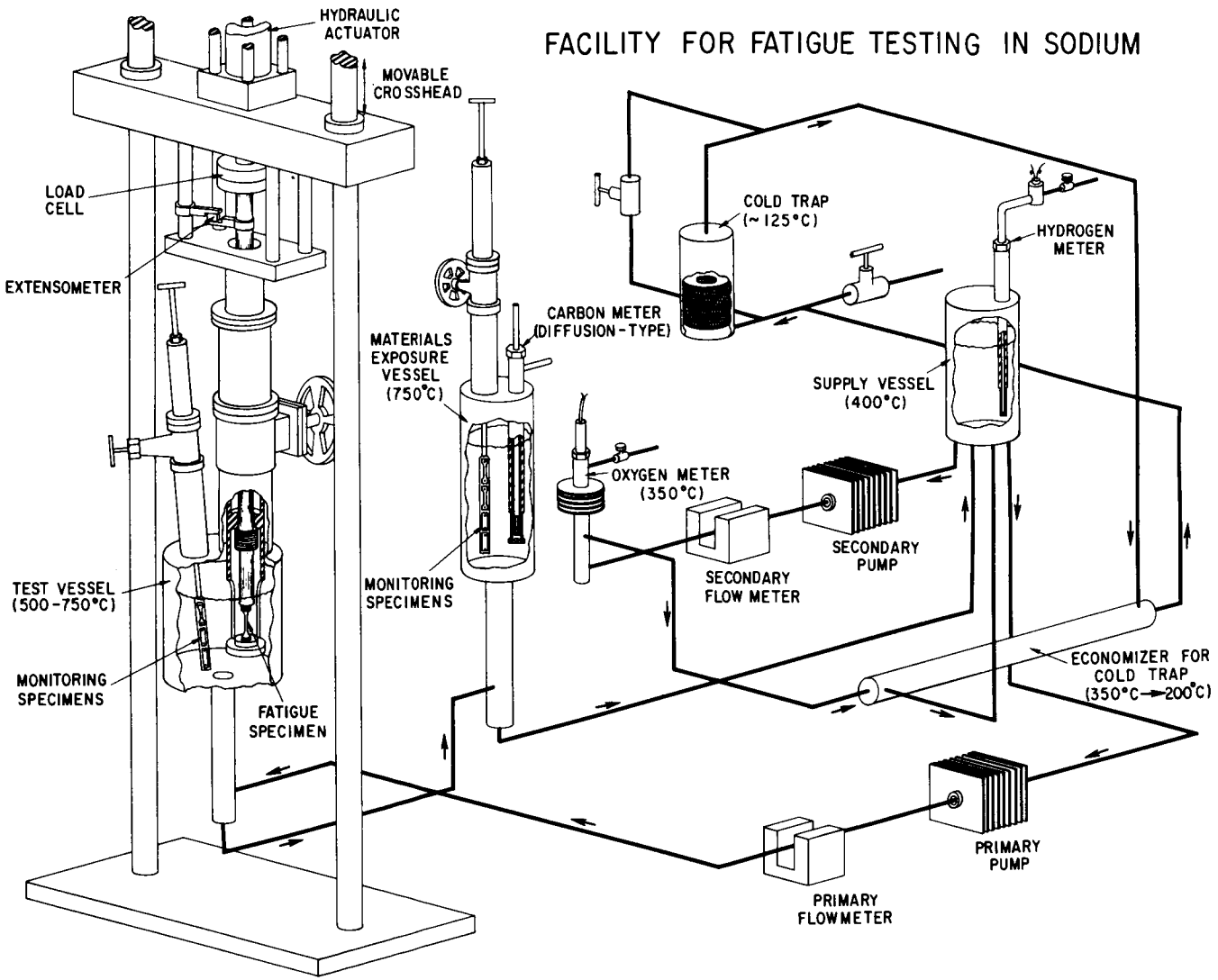

Fig. 2.4. Schematic Diagram of Facility for Fatigue Testing in Sodium (FFTS).

region of the specimen. To determine the amount of strain in the gauge section of a test specimen, hourglass specimens with an identical geometry, except for the gauge section, are used as a reference or blank from which the amount of strain in the fixture and transition region of the specimen is determined. The measured strain obtained with an hourglass specimen is subtracted from the measured strain of a test specimen under identical loading conditions to determine the total strain in the gauge section of the test specimen. Similarly, the desired plastic strain in the test specimen can be derived from hysteresis curves for test specimens and calibration curves for the hourglass specimens. The accuracy of the above procedure has been determined in air at room temperature by comparing these results with those obtained from an extensometer placed directly on the gauge section of a test specimen. Satisfactory agreement was obtained under these conditions.

A second procedure has also been used to verify the validity of fatigue results obtained with these systems. Several specimens have been tested in air at both room and elevated temperatures for comparison with published results of other investigators on similar material. Results obtained at 593°C (1100°F) from the present investigation were slightly lower than the lifetimes obtained by Weeks et al.[7] with hourglass-type samples. However, part of the discrepancy has been attributed to higher-than-nominal strains produced during the first few cycles, as a result of the stroke control mode of operation. The present test procedure involves incremental increases in the stroke for the first 10 to 20 cycles to permit some work hardening of the sample to occur before the desired strain is reached, thereby preventing the initial overstraining that occurred in the specimens when the nominal stroke was reached on the first cycle.

Preliminary tests have been conducted in sodium at 600°C. Satisfactory operation, which included insertion of the specimen and fixture into the sodium, fatigue testing, and removal of the fixture from the sodium vessel, was achieved. An important aspect of the FFTS was to minimize the turn-around time for specimen testing. During routine

operation, one specimen can be tested every other day (for each FFTS), assuming a normal 8-hr work day and a test lasting ∿ 6 hr.

In the first series of in-sodium tests, as-received Type 304 stainless steel specimens in the annealed condition have been fatigue tested in 600°C sodium that contained 0.8 ppm oxygen and 0.3 ppm carbon. The fatigue tests were conducted at a strain rate of 4×10^{-3} sec^{-1} with a fully reversed triangular waveform under the stroke control mode discussed above. Figure 2.5 is a plot of fatigue lifetimes as a function of total strain range. The point at 2.61% strain range is questionable because of the slight buckling observed in the specimen after test.

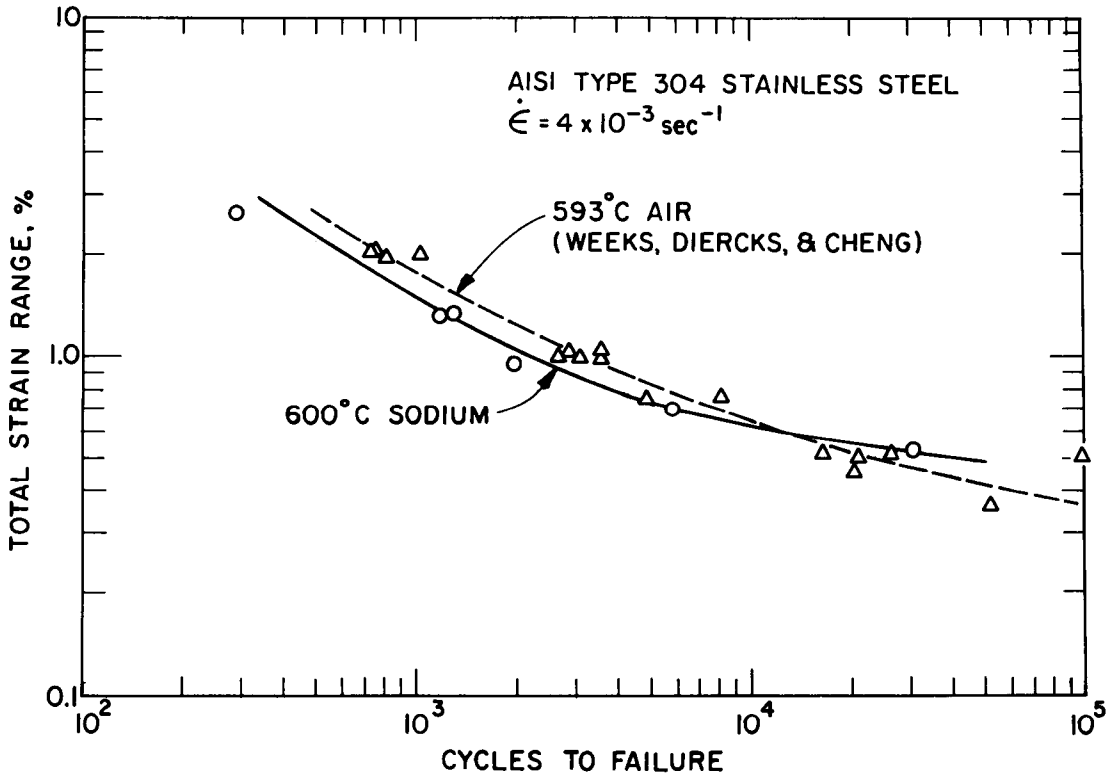

Fig. 2.5. Plot of Total Strain Range vs Cycles to Failure for Stainless Steel Tested in Sodium and Air Environments.

Air data from Weeks et al.[7] obtained at 593°C (1100°F) with hourglass specimens, from the same heat of Type 304 stainless steel, are shown for comparison. Except for the lowest strain-range measurement, the fatigue lifetimes obtained from the in-sodium tests are lower than the air data (neglecting the small temperature differences). The in-sodium results in Fig. 2.5 will be used as baseline data for comparison with fatigue lifetimes that are presently being obtained on samples which have received long-term exposure to sodium. The major effect of the long-term sodium exposure is expected to be caused by varying carbon profiles produced in the test specimens.

2.4 REFERENCES

1. Mechanical Properties Test Data for Structural Materials Quarterly Progress Report for Period Ending October 31, 1973, Oak Ridge National Laboratory, ORNL-4936, pp. 15-33.

2. Case 1592 of the ASME Boiler and Pressure Vessel Code, Appendix T, pp. 387-388.

3. Mechanical Properties Test Data for Structural Materials Quarterly Progress Report for Period Ending April 30, 1974, Oak Ridge National Laboratory, ORNL-4963, p. 69.

4. Mechanical Properties Test Data for Structural Materials Quarterly Progress Report for Period Ending January 31, 1974, Oak Ridge National Laboratory, ORNL-4948, pp. 183-187.

5. D. R. Diercks and W. F. Burke, "Elevated-temperature True Stress-True Strain Tensile Behavior of AISI Type 304 Stainless Steel," Symp. on Elevated Temperature Properties of Austenitic Stainless Steels, ASME, New York (1974), pp. 19-30.

6. Mechanical Properties Test Data for Structural Materials Quarterly Progress Report for Period Ending July 31, 1974, Oak Ridge National Laboratory, ORNL-4998, p. 37.

7. R. W. Weeks, D. R. Diercks, and C. F. Cheng, "ANL Low-cycle Fatigue Studies -- Program, Results, and Analysis," Argonne National Laboratory, ANL-8009 (November 1973).

3. HANFORD ENGINEERING DEVELOPMENT LABORATORY

T. T. Claudson

3.1 INTRODUCTION

The objectives of the structural materials investigation conducted at the Hanford Engineering Development Laboratory are to provide control data for the in-reactor and postirradiation tests and to provide direct and timely assistance to FFTF and Demonstration plant structural design and analysis programs. The HEDL efforts involve evaluation of mechanical properties at high strain rates, creep testing and analysis, fatigue crack growth, and tensile tests of such materials as FFTF weldments, vessel and piping, core support structures, reflectors as well as duct and cladding. Those test results and analyses appropriate to the "Structural Materials Quarterly Report" will be reported herein; however those investigations associated with irradiation effects per se will continue to be reported in the "Irradiation Damage to Reactor Structural Materials" Quarterly Report published at HEDL.

3.2 LMFBR STRUCTURAL MATERIALS - T. T. Claudson and H. H. Yoshikawa

3.2.1 FFTF/LMFBR Weld Materials Properties

3.2.1.1 Objective

The objective of this program is to describe the effects of elevated temperatures and fast reactor environments on the mechanical properties of structural base and weld materials for FFTF/LMFBR applications.

3.2.1.2 Accomplishments and Status

Current design rules[1] for nuclear systems operating at temperatures above 800°F provide for use of the wrought base metal mechanical properties in welded structures but restrict the allowable deformation in the weld region to one-half that permitted for the base metal. Since these rules are based on wrought base materials data, they do not directly account for

property variations in and near weldments. The deformation restriction in welds arises from the general knowledge that weld-deposited austenitic stainless steels are often less ductile than the wrought products. Sufficient experimental weld metal property data need to be generated before differences can be treated explicitly and quantitatively.

In view of these general requirements for weld property data, this report presents property trend curves based upon the results of conventional tensile tests conducted over the range from room temperature to 1200°F. The data treatment technique parallels that used by Smith[2] for several austenitic stainless steels and involves establishing ratios of the tensile properties at a given temperature to those at room temperature and then fitting the ratio values to a polynomial expression in temperature.

The ratio trend curves established by Smith for the yield and tensile strength of wrought Type 304 are used directly for comparison with the curves developed here for weld-deposited materials. In addition, since Smith addressed only strength considerations, the present work included formulation of trend curves for total elongation and reduction of area for wrought 304. Data for these curves were taken largely from the same source *(ASTM DS5S1)*[3] used by Smith[2]; however, no attempt was made to assure one-to-one correspondence with the data used by Smith for the yield and tensile strength treatments. A few test results from a well-characterized heat (A1 Ht. No. 55697) of 304 (3/8 inch diameter rod) were also included.

Detailed descriptions of the weldments, materials and specimens are given elsewhere[4] along with the experimental data used in this analysis. For evaluation purposes the data were arbitrarily divided into three groups according to filler metal composition: 308/308L Group; CRE 308 Group (CRE denotes controlled residual elements -- B, P and Ti), and 16-8-2 (Cr-Ni-Mo) Group. A fourth group designated All-Weld includes all of the data from the three groups above plus data from a 316 weld.

The procedures for establishing the behavioral trend curves began simply by computing the ratio values for all of the elevated temperature test results. These ratio values were then fitted by a computer program to a polynomial of the form:

$$R_p = A_o + A_1T + A_2T^2 + \ldots\ldots A_iT^n$$

by the least squares regression method. The program provided values of the coefficients and the standard error of the estimate of R_p. Since the ratio value at room temperature is defined as unity, a number of such values were input in order to force the curve to unity at 75°F. Adequacy of the fit was judged on the basis of a combination of minimizing the value of the standard error of the estimate of R_p (S_y) and subjective visual examination of the resulting curves.

3.2.1.3 Results

3.2.1.3.1 Room Temperature Properties. A summary of the room-temperature properties is given in Table 3.1. The maximum and minimum values are based upon observed values and not upon any statistical evaluation. Because the 308/308L group contains property values for both as-welded and heat treated materials it is divided into two parts: as-welded only and all-308/308L-group data. It can thus be seen that the various heat treatments reduced the mean value by 10% and yielded a minimum value nearly 10 ksi lower than that of the as-welded-only portion.

3.2.1.3.2 Wrought Type 304 Evaluation. The yield and tensile strength curves for the Type 304 are those of Smith[2] and those for total elongation (ε_T) and reduction of area (RA) were developed in the present work. The analysis of the wrought Type 304 ductility is summarized in Table 3.2 along with the results of Smith's analysis of the strength. Two ε_T ratio values are given at each temperature because of an anomolous, but distinct separation of the data into two populations.

The reduction of area evaluation (Table 3.2) extends only to a temperature of 1100°F because there were considerably fewer data available at higher temperatures and because the existing data indicate a very sharp reduction between 1100 and 1200°F. This had the effect of introducing a substantial difference between the regression curve and the data in the region near the apparent discontinuity.

Table 3.1. Room Temperature Property Summary

Data Group	Value	σ_y	σ_u	ε_u	ε_T	RA	No. of Tests
308/308L (As-Welded Only)	Mean	55.7	84.2	31.6	39.3	64.0	12
	Std. Dev.*	8.3	5.5	6.5	7.0	8.4	
	Min.	45.2	76.1	22.3	31.1	46	
	Max.	70.7	92.7	41.0	54.0	77	
(All 308/308L Data)	Mean	50.1	83.8	35.7	41.7	59.7	24
	Std. Dev.*	9.7	5.5	7.9	7.5	9.1	
	Min.	35.5	75.5	22.3	31.1	40	
	Max.	70.7	92.7	49.3	54.2	77	
CRE 308	Mean	66.8	92.2	33.1	37.3	60.5	4
	Std. Dev.*	7.5	3.8	1.7	3.6	6.0	
	Min.	58.1	88.4	30.6	32.6	53	
	Max.	76.2	97.1	34.2	40.9	67	
16-8-2	Mean	49.2	90.0	44.0	48.3	50.3	3
	Std. Dev.*	8.6	4.1	7.9	9.0	15.7	
	Min.	45.9	85.4	38.2	42.9	38	
	Max.	61.6	93.3	53.0	58.7	68	
All Welds	Mean	52.8	85.5	36.1	41.7	58.9	31
	Std. Dev.*	10.8	6.0	7.7	7.5	9.6	
	Min.	35.5	75.5	22.3	31.1	38	
	Max.	76.2	97.1	53.0	58.7	77	

*Std. Dev. = $[\sum_i (x_i-\bar{x})^2/n-1]^{1/2}$ where x_i = property values, $\bar{x}$ = arithmetic mean value, and n = sample size or number of tests.

Table 3.2. Least Squares Polynomial Regression Analysis Results
(Property Ratios vs. Test Temperature)

Property	S_y*	Temperature, °F 100	200	300	400	500	600	700	800	900	1000	1100	1200
308/308L													
σ_y	.0846	.982	.919	.870	.831	.800	.773	.747	.718	.682	.637	.580	.506
σ_u	.0540	.973	.886	.832	.802	.788	.779	.767	.744	.699	.624	.511	.349
ϵ_T	.1355	.968	.851	.755	.679	.624	.590	.575	.582	.608	.656	.723	.812
ϵ_u	.1220	.942	.762	.652	.598	.582	.590	.606	.614	.600	.547	.440	.263
RA	.1287	.988	.940	.900	.869	.848	.835	.831	.836	.850	.874	.906	.947
CRE 308													
σ_y	.0492	.981	.918	.865	.821	.784	.751	.722	.695	.668	.638	.606	.568
σ_u	.0174	.970	.876	.811	.770	.745	.730	.718	.702	.676	.632	.564	.464
ϵ_T	.0876	.952	.802	.700	.638	.606	.597	.602	.611	.617	.610	.581	.522
ϵ_u	.1060	.938	.743	.627	.572	.560	.575	.598	.612	.601	.545	.428	.233
RA	.0922	.994	.982	.963	.940	.918	.901	.892	.896	.917	.958	1.020	1.120
16-8-2													
σ_y	.0843	.992	.949	.906	.864	.822	.782	.742	.703	.664	.626	.589	.553
σ_u	.0372	.971	.877	.813	.773	.751	.740	.734	.727	.711	.682	.632	.556
ϵ_T	.0816	.954	.800	.685	.604	.552	.523	.512	.516	.527	.542	.556	.562
ϵ_u	.0774	.944	.758	.627	.543	.495	.475	.473	.482	.490	.491	.473	.429
RA	.1414	1.022	1.077	1.117	1.144	1.156	1.154	1.138	1.109	1.065	1.006	.934	.848
ALL-WELD													
σ_y	.0780	.983	.926	.878	.838	.804	.773	.744	.714	.683	.648	.608	.560
σ_u	.0542	.973	.894	.839	.804	.782	.766	.751	.730	.697	.647	.572	.466
ϵ_T	.1310	.954	.804	.697	.626	.586	.571	.574	.588	.609	.630	.644	.646
ϵ_u	.1342	.943	.765	.652	.590	.567	.568	.581	.593	.589	.557	.484	.355
RA	.1518	.996	.963	.936	.915	.900	.892	.889	.893	.903	.919	.942	.970
WROUGHT 304													
σ_y	-----	.96	.83	.75	.69	.65	.61	.59	.56	.54	.52	.49	.47
σ_u	-----	.97	.86	.80	.78	.77	.77	.77	.76	.74	.70	.63	.55
ϵ_T	.036/.048	.975/.960	.880/.820	.790/.700	.735/.635	.710/.610	.710/.610	.730/.610	.745/.610	.740/.605	.700/.595	.635/.565	.550/.540
RA	.043	.994	.968	.945	.927	.910	.895	.882	.875	.867	.865	.860	.857

$*S_y = [\Sigma (d^2)/n]^{1/2}$ where d = deviation of actual values from curve, and
n = sample (number of data).

3.2.1.3.3 Weld Metal Evaluation. The results of the weld metal property analysis are also summarized in Table 3.2 The values listed were taken from the regression curves at 100°F intervals.

The yield strength ratio curves (Fig. 3.1) for the weld materials data groups are quite similar in form and magnitude despite the variations in materials, welding procedures, material conditions, and data-sample size. For this ratio, the all-weld trend curve could be used without introducing differences of more than 10% in the ratio values even at 1200°F. In all cases, the weld-deposited austenitic stainless steels appear to maintain a higher fraction of their room-temperature strengths at elevated temperatures than does the wrought Type 304 in these short-term tests.

The ultimate tensile strength ratio trend curves for the weld metal data groups are basically similar in both shape and magnitude (Fig. 3.2) up to 1000°F, but appear to diverge at higher temperatures. Below 1000°F, the all weld curve could be used without introducing differences of more than 5%. At higher temperatures however, the curves for the 308/308L and CRE 308 materials decrease more rapidly than does the curve for 16-8-2 materials and adoption of the all weld trend curve leads to differences in ratio values as large as 33%. This maximum difference occurs at 1200°F where there were no data for the 308/308L group and the ratio value represents a 100°F extrapolation of the polynomial expression.

The uniform elongation values used in this study are those engineering strain values which correspond to the point of maximum load on the stress-strain curves (Fig. 3.3). The ratio trend curves shown in Fig. 3.4 do not include curves for the 304 because uniform elongation data source used *(ASTM DS5S1)*. In all the weld data groups, the trend curves exhibit a minimum and a maximum. This behavior could be the result of the mathematical curve-fitting method rather than a real physical phenomenon, particularly in view of the limited data at low temperatures. Uniform elongation trend curves are essentially identical for the 308/308L and CRE 308 groups, but the curve for 16-8-2 material is significantly lower. In this case, the all-weld trend curve introduces rather large differences (i.e., up to 50%) in ratio values for the 308-type groups at 1200°F and significant differences (i.e., up to 23%) in ratio values for the 16-8-2 material throughout much of the temperature range.

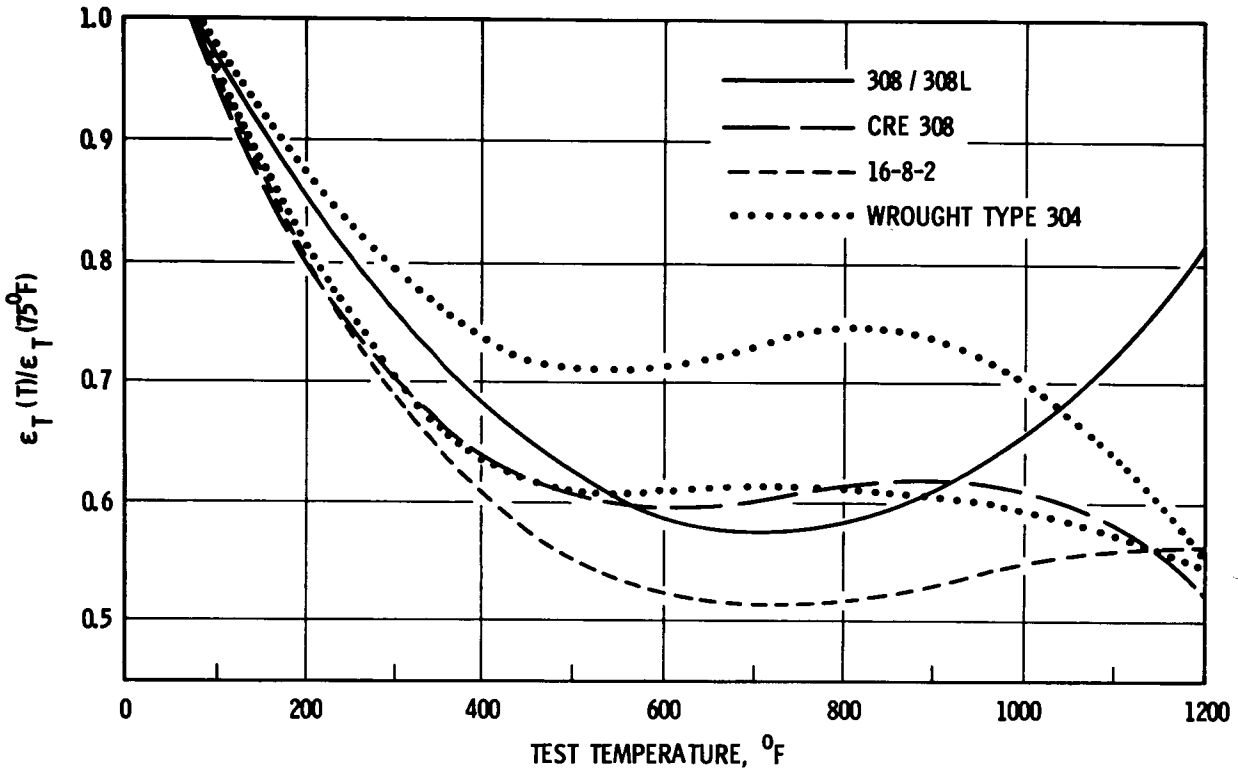

Figure 3.4. Total Elongation Ratio Trend Curves for Weld-Deposited Stainless Steels and Wrought Type 304.

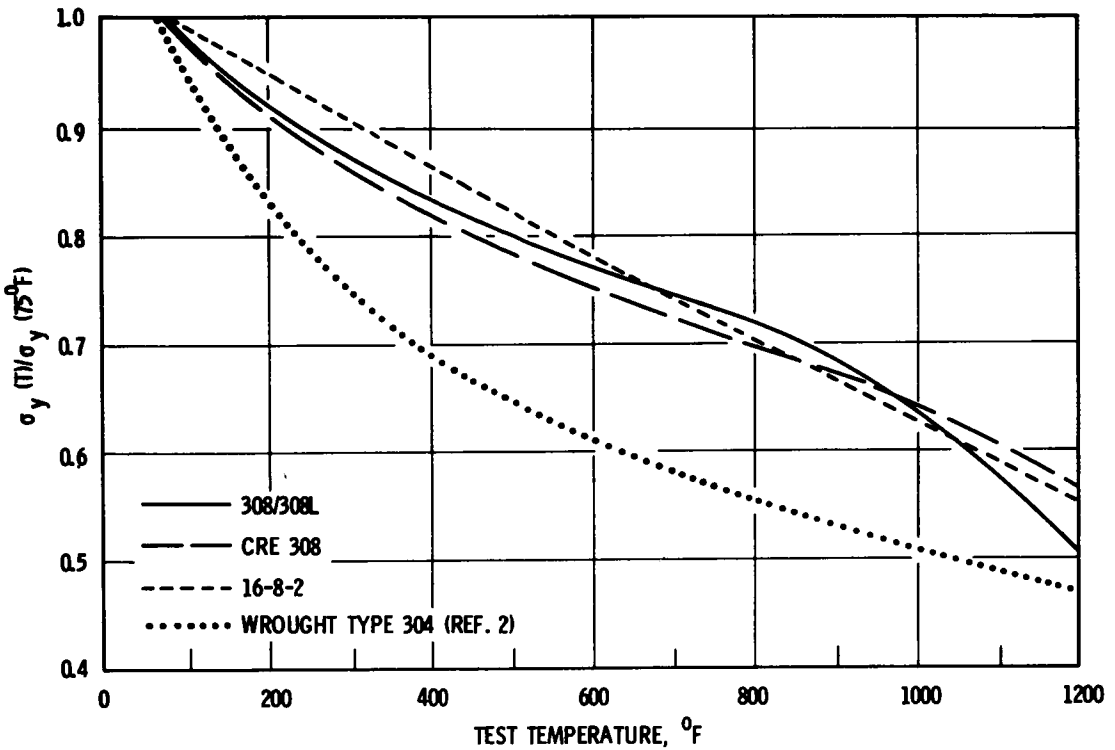

Figure 3.1. Yield Strength Ratio Trend Curves for Weld-Deposited Stainless Steels and Wrought Type 304.

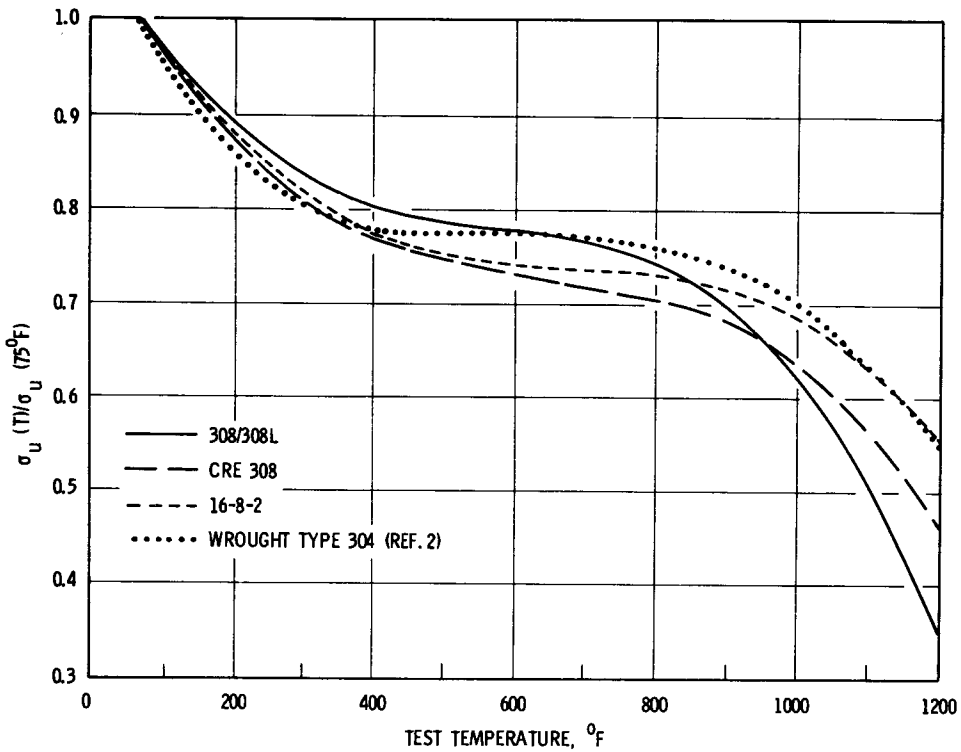

Figure 3.2. Tensile Strength Ratio Trend Curves for Weld-Deposited Stainless Steels and Wrought Type 304.

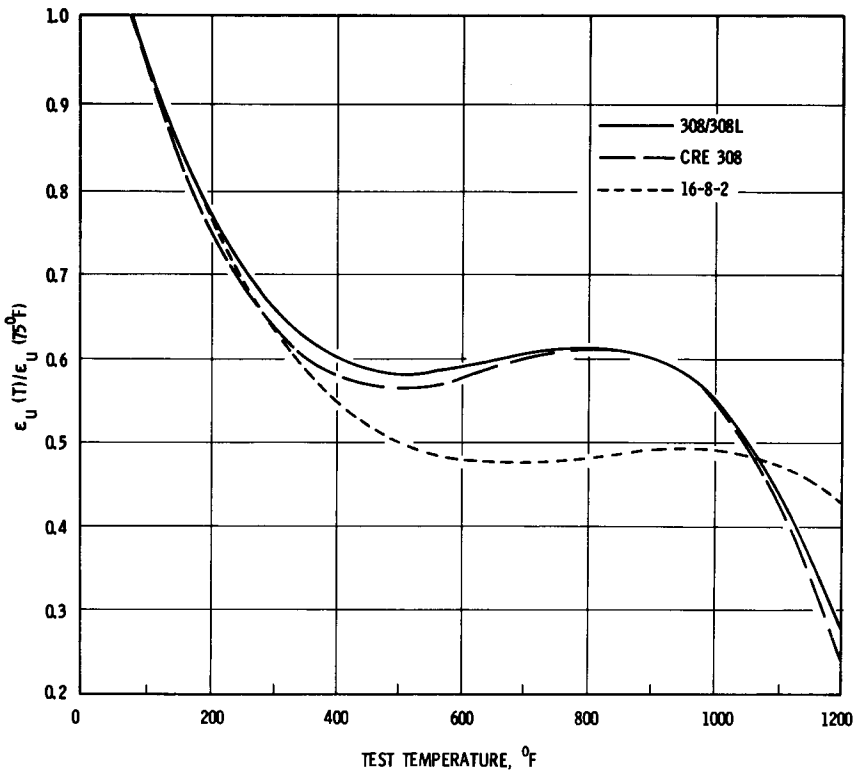

Figure 3.3. Uniform Elongation Ratio Trend Curves for Weld-Deposited Stainless Steels.

Trend curves for total elongation are quite similar for the 308/308L and CRE 308 materials up to 900°F (Fig. 3.4). At higher temperatures, the curves for these groups diverge markedly. Again, the trend curve for 16-8-2 material is lower than the other two over the range from 600 to 1000°F. As a result, the all-weld trend curve leads to potentially significant differences in ratio values, but these differences are generally smaller than for the case of uniform elongation. In general, the weld materials trend curves compare favorably with the lower wrought 304 curve. Over the entire temperature range, there is remarable similarity between the curves for the CRE 308 and the lower wrought 304 group, with the largest difference of 3.5% occurring at 1200°F. At and below 1000°F, there is also little difference (6.8% maximum) between the all-weld and the lower wrought 304 curves although the difference reaches nearly 20% at 1200°F largely because of the effect of including the 308/308L data.

Reduction of area trend curves for the 308/308L and CRE 308 groups are only slightly different, and are in reasonable agreement with the 304 curve up to 800°F (Fig. 3.5). At higher temperatures, however, the two weld metal curves increase significantly, while the 304 curve does not. The 16-8-2 group trend curve lies significantly higher than those of the other welds, but the scatter in the ratio values was quite large for this material and the shape of the resulting trend curve may not be realistic. Differences between the all-weld trend curve and the individual group curves are not large (i.e., generally less than 7%) for the 308/308L and CRE 308 materials, but are more significant (i.e., up to 23%) for the 16-8-2 group.

3.2.1.4 Discussion

The trend curve analysis shows differences among the three weld groups in the ultimate tensile strength and the ductility parameters. The 308/308L and CRE 308 materials exhibit basically similar trend curves for all parameters, which is not unexpected since the compositional differences between these groups are primarily in the minor elements. It is quite possible that the differences which are indicated for these groups stem in part from the inclusion of a greater range of welding parameters and material conditions in the data sample for the 308/308L material.

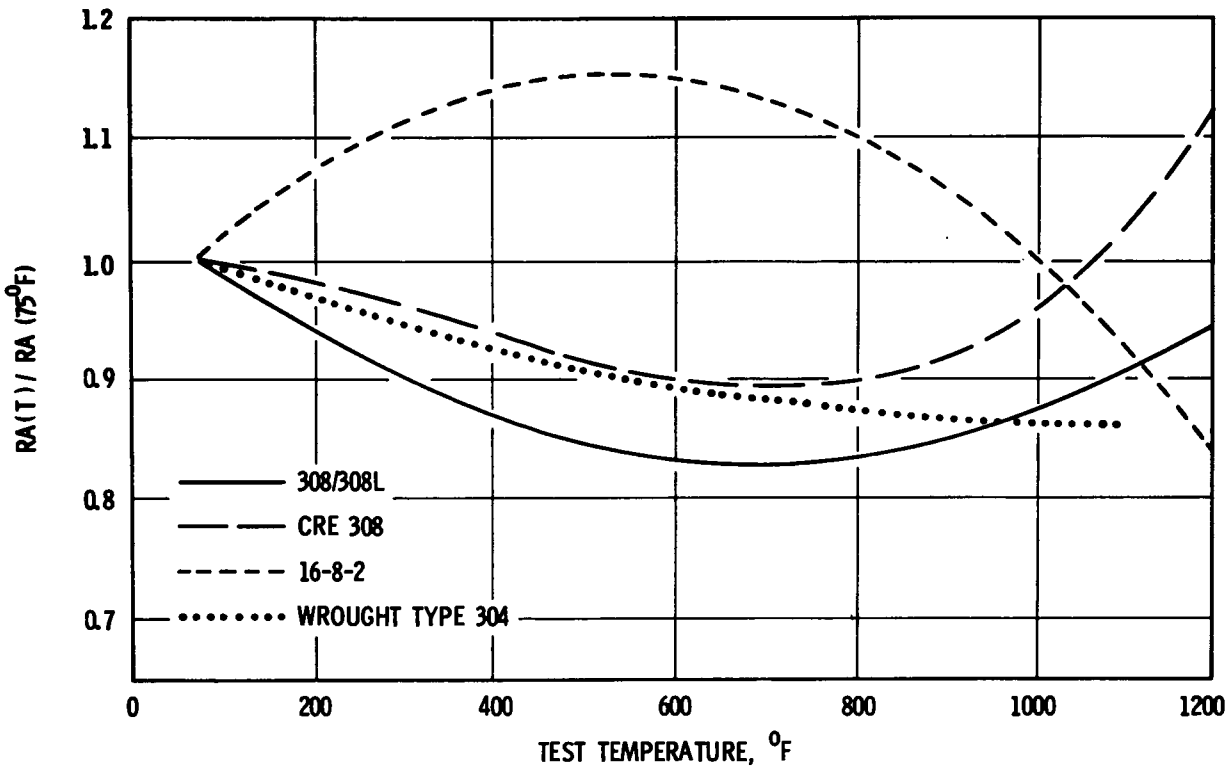

Figure 3.5. Reduction of Area Ratio Trend Curves for Weld-Deposited Stainless Steels and Wrought Type 304.

Differences between the 308-type groups and the 16-8-2 group are somewhat more pronounced, but once again variations in welding parameters may contribute to the apparent differences, particularly in view of the smaller sample size for the 16-8-2 group. The good agreement among the yield strength ratio trend curves suggests that perhaps the effect of temperature on the early stages of plastic deformation is quite similar for weld-deposited austenitic stainless steels in general, with recognizable differences between various welds arising at larger deformations associated with instability and fracture.

The most prominent difference between ductility parameter trend curves for weld materials and wrought 304 is the increase in ratio values for total elongation (308/308L group) and reduction of area (308/308L group and CRE 308 group) at temperatures above 800°F. Type 304 stainless steel frequently exhibits a decrease in fracture ductility (particularly reduction of area) at temperatures above about 1100°F accompanying the onset of intergranular fracture. However, the possibility that the increases in weld ductility ratios over the range from 800 to 1200°F are associated with a suppression of intergranular failure has not been clearly demonstrated.

The interpretation and utilization of the property ratio trend curves should be made with a recognition of the variability or scatter in the experimental data. One measure of data variability is the standard error of the estimate of the property ratio trend curve, S_y. The statistical quantity, S_y, relates to the regression curve in a manner which is exactly analogous to the relationship of the standard deviation to the arithmetic mean of a data sample. As such, S_y is a measure of the dispersion, variability or scatter about the line of regression.

Values of S_y given in Table 3.2 clearly show that less variation is observed in the strength parameters than in the ductility parameters. Also, the S_y values for ultimate strength ratio curves are consistently lower than values for yield strength curves, indicating greater variation in the latter trend curves. Comparing total elongation and reduction of area trend curves for weld materials with those for wrought 304 (Table 3.2), substantially higher S_y values are obtained for welds, reflecting a greater variability in the ductility parameter for these materials. Although results for S_y were not reported by Smith[2] for yield and ultimate tensile

strength trend curves for 304, we might also expect lower S_y values and less variability for the wrought product than for welds.

Data variability can be viewed in a somewhat different light by examining the accuracy with which the trend curve approach correlates the absolute property values. To do this, we selected the trend curves for the 308/308L group and the CRE 308 group, and for each data set computed elevated temperature property values using the ratio values and the measured room temperature properties. These predicted property values were then compared with experimentally observed values. For the CRE 308 group, the correlation is good for both yield strength and ultimate tensile strength, predicted values falling in general within ± 4000 psi of measured values. Comparison of predicted and measured total elongation values showed rather large variations; predicted values generally falling within ± 7.5% (on an absolute basis) of measured elongation values. For the 308/308L group, predicted yield strength values generally fell within ± 8,000 psi of measured values, while predicted ultimate tensile strengths were within about ± 6,000 psi of experimental results. In the case of total elongation, predicted values are within about ± 10% (on an absolute basis) of measured values.

It is significant that the CRE 308 group produced the lowest overall S_y values and showed the closest agreement between measured and predicted properties. This is the only group in the study which represents a single material (CRE 308) and a single weld process (SMA) with fairly similar welding parameters. The degree of departure from a perfect correlation was substantially greater for all 308/308L properties than for the CRE 308. While this result is not surprising in view of the greater variation in weld process and parameters, it serves to emphasize the difficulties associated with establishing broadly applicable weld metal property specifications and thus points to a need for additional work in this area. Nevertheless, the present work indicates that the property ratio trend curve approach provides a useful degree of correlation of the elevated-temperature properties of an important group of materials.

3.2.1.5 Expected Achievements

The tensile property analysis presented here completes this phase of

study conducted under the LMFBR Structural Materials Program, although as additional new data are generated, the curves will be updated. Current program goals include a behavioral description of the creep properties of weld deposited austenitic stainless steels, however, near term emphasis will be placed on analysis of postirradiation data taken from materials irradiated in the FTR Component Materials Irradiation Experiment and on extending irradiation effects studies to reference and candidate materials for the CRBR demonstration plant.

3.2.2 LMFBR Structural Materials Evaluation

3.2.2.1 Objective

The objective of this program is to determine the mechanical properties of LMFBR component structural materials for their anticipated service conditions. Results are for use in design confirmation and operations support of FFTF, and for materials selection and application in future LMFBRs.

3.2.2.2 Accomplishments and Status

The elevated temperature tensile properties of unirradiated and irradiated tungsten and TZM, meltdown cup materials for the Closed-Loop In-Reactor Assemblies (CLIRA), have been determined. Irradiation conditions were representative of those expected in the FTR and testing was performed at temperatures from room temperature to 1700°F and strain rates from 3×10^{-5} to 1 in/in/sec. Results from those tests are presented herein.

Specimen irradiations were performed in Row II of EBR-II in subassembly X-195. Neutron exposures for the specimens ranged from 0.37 to 1×10^{22} n/cm^2 ($E > 0.1$ MeV) and the irradiation temperatures ranged from ∿700 to 730°F. All specimens were irradiated in EBR-II coolant (weeper capsules) in order to maintain the desired irradiation temperatures.

3.2.2.3 Results

Unirradiated test results on tungsten and TZM are listed in Table 3.3 and summarized in Figures 3.6 and 3.7. In Figure 3.6, the yield strength of tungsten is plotted versus the rate-temperature parameter ($T \ln A/\dot{\varepsilon}$) developed by Bennett and Sinclair[5]. Correlation of the test data with this

Table 3.3. Tensile Properties of Unirradiated Tungsten and TZM

Test Material	Test Temp.-°F	$\dot{\varepsilon}$ Sec.-1	Strength - Ksi Yield	Strength - Ksi Ultimate	Total Elongation-%	Reduction of Area-%
Tungsten	72	3×10^{-4}	195.0	195.0	0	0
	150		191.5	191.5	0.3	0
	350		136.8	136.8	15.5	54.5
	500		134.0	134.0	24.8	56.6
	625		93.6	93.6	19.6	74.6
	800		94.7	94.7	11.8	74.4
	1200		84.7	84.7	9.8	82.8
	1700		66.4	66.4	10.1	93.4
	350	3×10^{-2}	177.2	177.2	13.0	49.6
	1200		83.2	83.2	10.4	77.9
	1700		67.6	67.6	11.5	91.8
	600	1.0	151.4	151.4	15.0	71.2
	800		136.9	136.9	17.4	73.0
	1200		98.1	98.1	17.1	80.3
	1700		73.4	73.4	12.7	27.0
TZM	72	3×10^{-4}	91.7	91.9	18.0	31.1
	450		66.0	75.4	15.0	77.2
	800		61.6	67.9	15.7	91.8
	1200		60.5	66.4	12.7	91.8
	1700		55.9	59.9	14.2	91.8
	72	3×10^{-2}	115.2	115.2	5.6	16.4
	350		74.7	84.5	18.8	69.9
	560		63.9	73.5	18.9	85.2
	800		61.2	69.7	18.6	89.3
	1200		55.7	62.5	14.4	89.3
	1700		54.1	60.6	12.7	90.2
	72	1.0	144.3	144.3	2.7	0.6
	350		89.7	90.9	20.8	8.0
	800		67.1	75.0	17.5	7.1
	1200		56.9	65.0	15.6	4.7

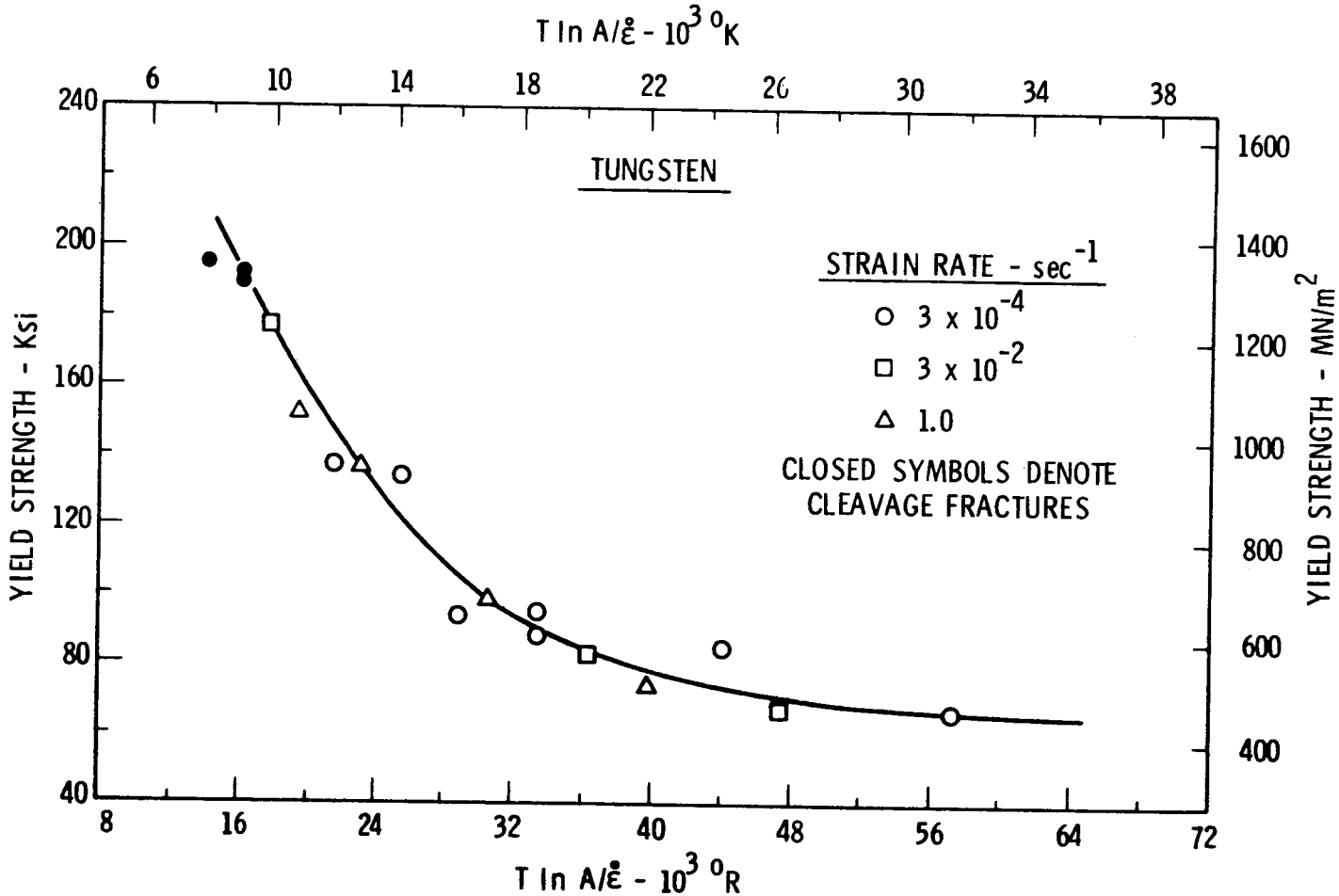

Figure 3.6. Rate-Temperature Parameter Representation of the Yield Strength of Tungsten.

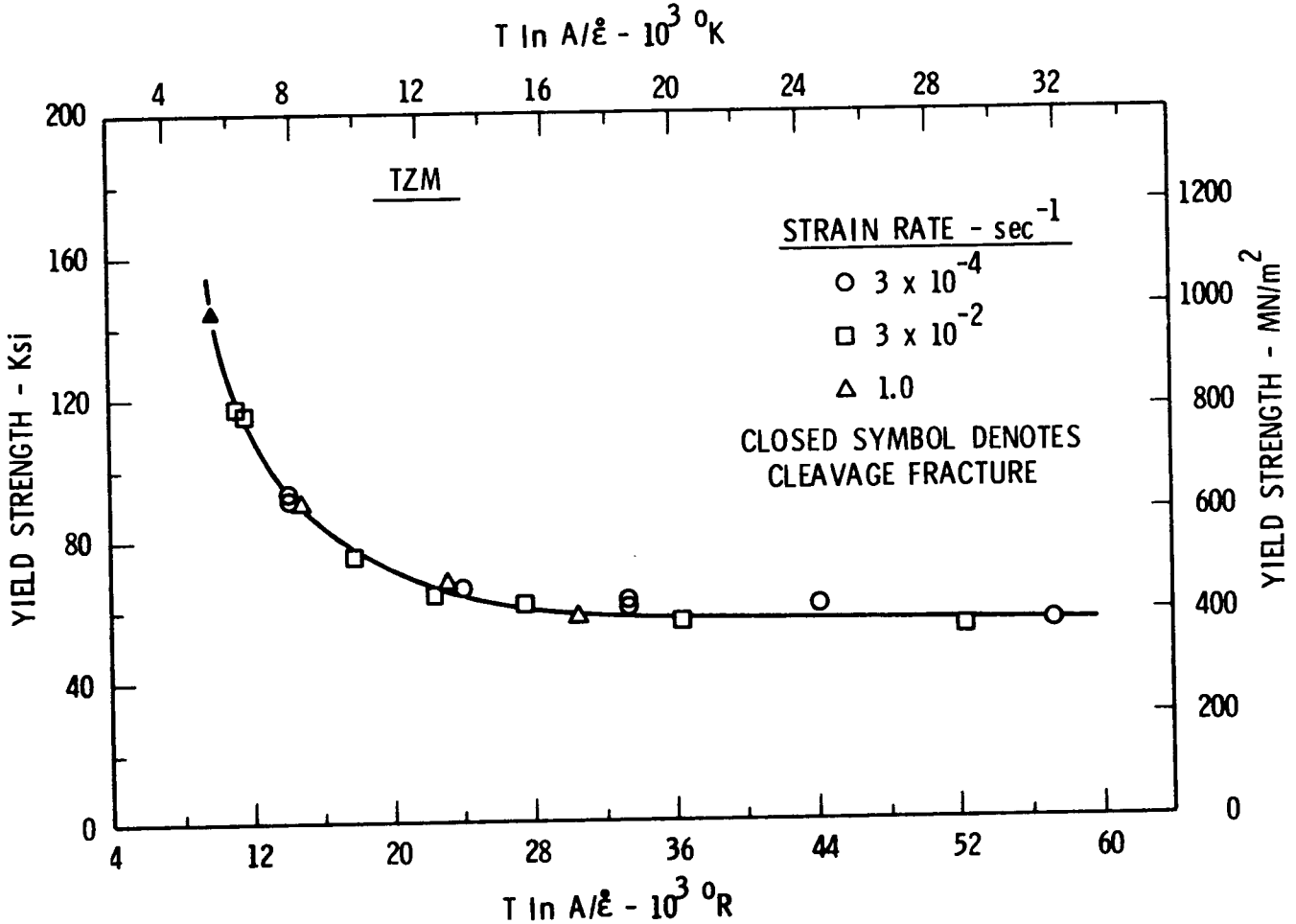

Figure 3.7. Rate-Temperature Parameter Representation of the Yield Strength of TZM.

parameter provides a means to ascertain temperature and strain rate effects on mechanical properties as well as a means to determine the ductile-to-brittle transition temperature of the test material. The yield strength decreases rapidly with increasing rate-temperature values and is most sensitive to test temperature and strain rate at low parameter values ($T \ln A/\dot{\varepsilon} < 30 \times 10^3$ °R). At parameter values of $\sim 16 \times 10^3$ °R cleavage fractures were observed. Using this parameter value and assuming that a conventional tensile test is performed at a strain rate of $\sim 3 \times 10^{-4}$ sec^{-1} (0.02 $in{:}in^{-1}$) the ductile-to-brittle transition temperature for the subject material is calculated to be ∿143°F (62°C).

Similarly, the yield strength data for TZM can be correlated with the rate-temperature parameter (Figure 3.7). Data for TZM reveals that cleavage fractures occur at parameter values of $\sim 10 \times 10^3$ °R. This parameter value corresponds to a ductile-to-brittle transition temperature of ∿-122°F (-86°C).

To characterize effects of neutron irradiation on the tensile properties and the ductile-to-brittle transition temperatures of tungsten and TZM a series of tests at various temperatures and strain rates were performed on irradiated material. Results from these tests are listed in Table 3.4 and illustrated in Figures 3.8 and 3.9. In Figure 3.8 the yield strength of irradiated and unirradiated tungsten is plotted versus the rate-temperature parameter. At the lower parameter values ($< 44 \times 10^3$ °R) the yield strength of irradiated material is significantly higher than that of the unirradiated material and the strength increases rapidly with decreasing parameter values. At high parameter values ($> 44 \times 10^3$ °R) the yield strength of irradiated material converges with that of the unirradiated material. This convergence is believed to result from irradiation damage annealing at these higher test temperatures (1200-1600°F) and low test rates. No fluence effect on yield strength was observed. In the irradiated material cleavage fractures were observed at a parameter value of $\sim 24 \times 10^3$ °R and the corresponding ductile-to-brittle transition temperature was 445°F (229°C). For unirradiated material the transition temperature was ∿143°F (62°C), therefore, neutron irradiation to a fluence of 1×10^{22} n/cm^2 ($E > 0.1$ MeV) increased the ductile-to-brittle transition temperature by about 300°F (149°C).

Table 3.4. Tensile Properties of Irradiated Tungsten and TZM

Material	Irradiation Conditions		Test Conditions		Strength - Ksi		Total Elon-gation-%	Reduction of Area-%
	Fluence-n/cm^2(E 0.1 MeV)	Temp.°F	Temp.-°F	$\dot{\varepsilon}$-Sec^{-1}	Yield	Ultimate		
Tungsten	4.8×10^{21}	700	800	3×10^{-4}	169.1	169.1	5.2	33.3
			1200		118.7	118.7	6.4	77.1
			1400		90.2	105.6	8.5	89.3
			800	3×10^{-2}	165.4	165.4	2.0	34.9
			1200		135.4	135.4	8.8	76.4
	1.0×10^{22}	720	450	3×10^{-4}	197.6	197.6	0.8	0.8
			800		152.7	152.7	7.2	65.6
			1200		112.3	112.3	6.2	75.6
			800	3×10^{-2}	178.7	178.7	3.8	4.1
			1200		133.6	133.6	8.7	75.6
TZM	3.7×10^{21}	700	800	3×10^{-4}	115.4	115.4	8.4	87.7
			1000		123.2	123.2	9.0	88.5
			1200		106.1	106.1	7.8	86.9
			450	3×10^{-2}	141.1	141.1	0	0
			800		120.3	120.3	8.3	81.3
	1×10^{22}	730	800	3×10^{-4}	135.4	135.4	7.6	86.1
			1200		107.0	107.0	7.6	86.1
			450	3×10^{-2}	132.7	132.7	5.2	46.7
			800		118.4	118.4	2.0	1.6

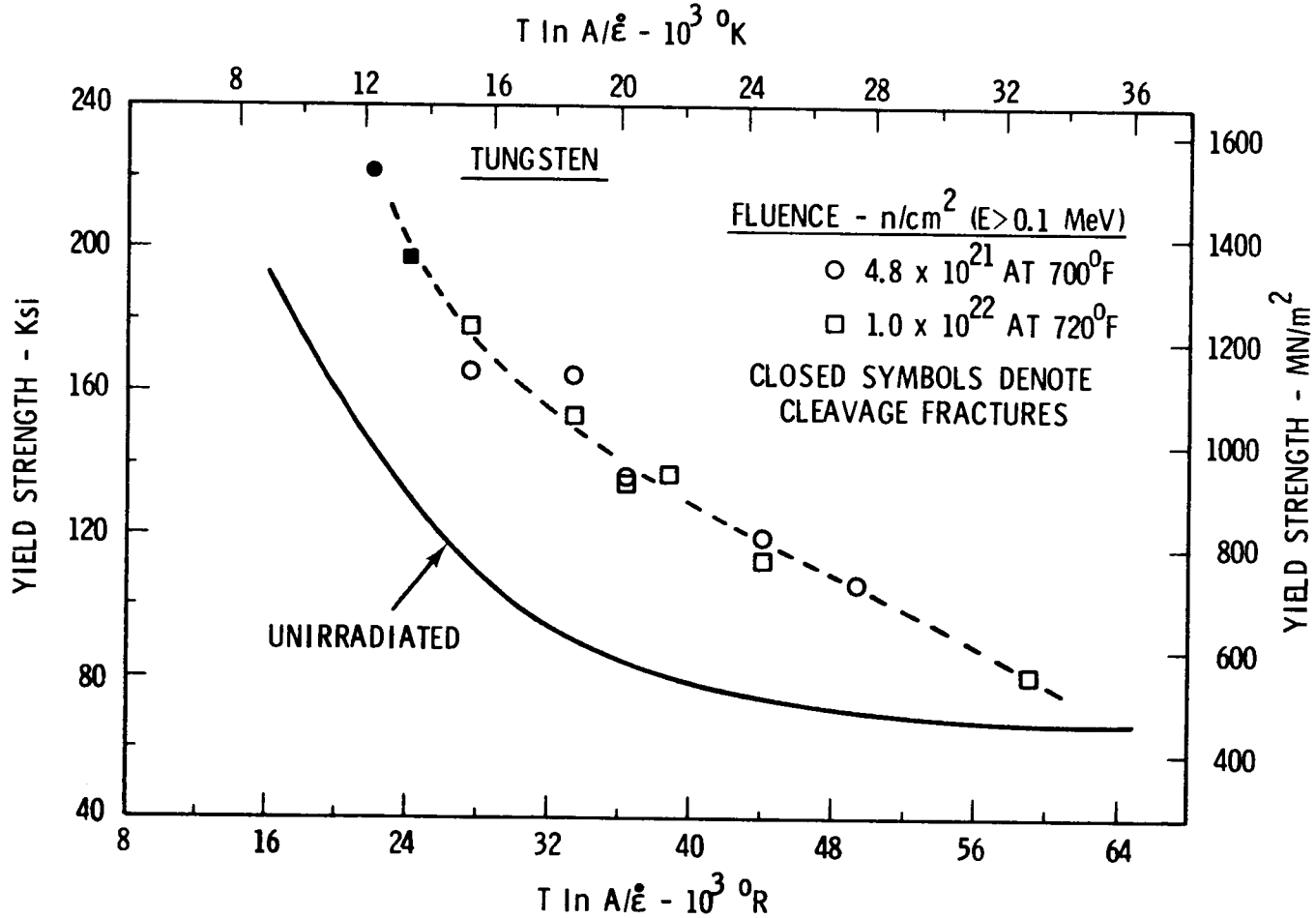

Figure 3.8. Rate-Temperature Parameter Representation of the Yield Strength of Irradiated Tungsten.

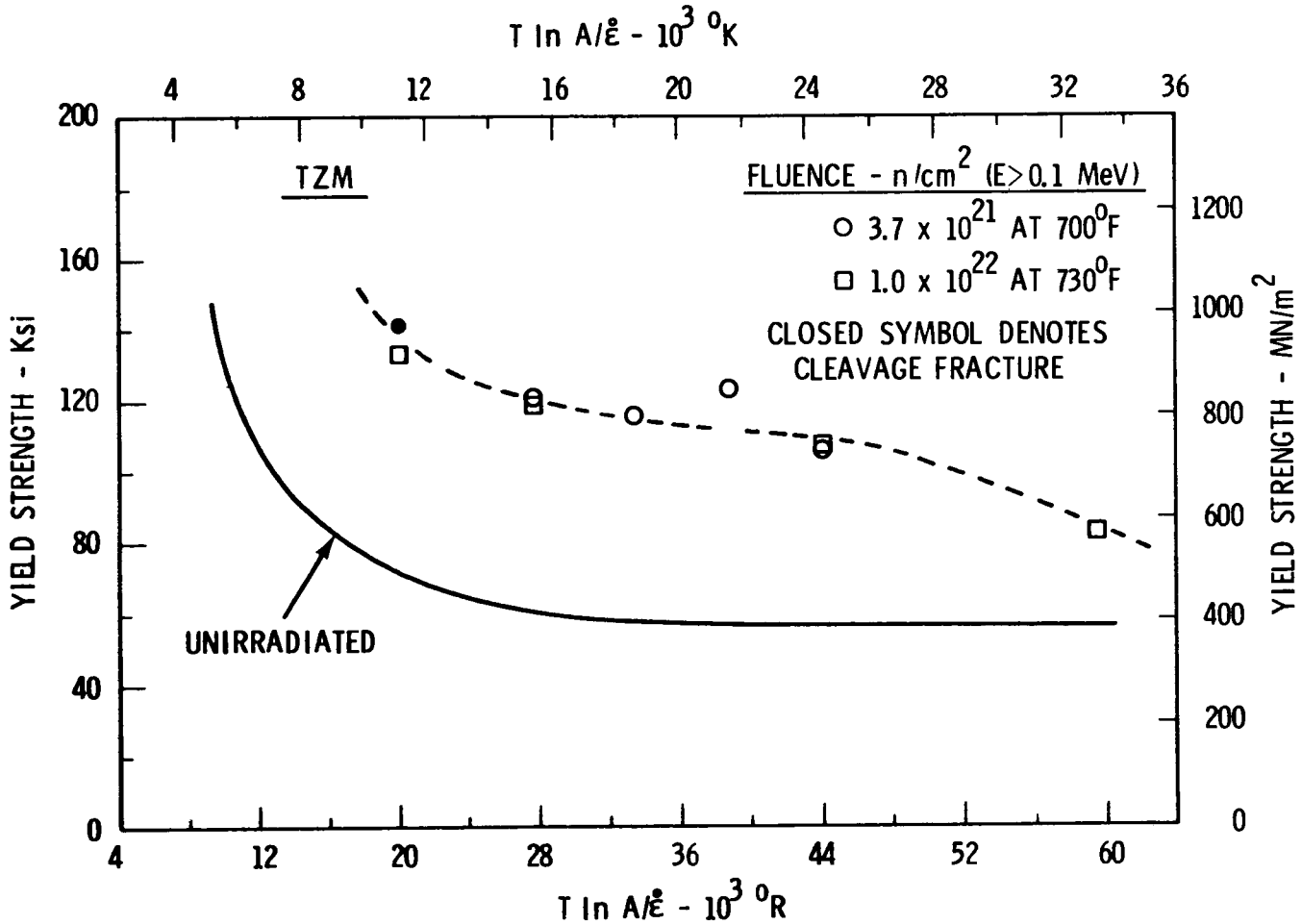

Figure 3.9. Rate-Temperature Parameter Representation of the Yield Strength of Irradiated TZM.

The effect of neutron irradiation on the yield strength of TZM is very similar to that for tungsten (Figure 3.9). Neutron irradiation to a fluence of 1×10^{22} n/cm^2 (E > 0.1 MeV) resulted in a ductile-to-brittle transition temperature of ∿293°F (145°C). The unirradiated transition temperature was -122°F (-86°C), therefore, the increase due to neutron irradiation was 415°F (213°C). Of significance is the fact that the ductile-to-brittle transition temperatures of both irradiated tungsten and TZM (at CLIRA neutron exposures) are well below the anticipated operating temperatures for the CLIRA meltdown cups (∿800°F).

3.2.2.4 Expected Achievements

The effect of strain rate and temperature on the tensile properties of unirradiated and irradiated A-286 will be completed during the next reporting period. These data will be used in analysis of several FTR bolting applications.

3.3 MATERIALS SAFETY AND ENGINEERING - T. T. Claudson and H. H. Yoshikawa

3.3.1 Subcritical Crack Growth

3.3.1.1 Objective

The objectives of this study are to determine the subcritical crack growth properties of FFTF/CRBRP structural materials for various operating environments and to perform fatigue failure analyses for structural components as required.

3.3.1.2 Accomplishments and Status

Linear-elastic fracture mechanics techniques were used to characterize the effects of cyclic frequency and stress ratio on fatigue-crack propagation behavior of precipitation heat-treated Inconel 718 at 800°F and 1000°F. The effect of frequency was examined over the range 4 < f < 400 cpm, and stress ratios ranged between 0.05 < R < 0.50.

The material used in this study was from the same heat (Huntington Heat No. 52C9EK) employed by Aerojet Nuclear Company in the preparation of

the ASME Code Case on Inconel 718 for AEC/RRD. The material had received the following precipitation heat-treatment: Annealed 1/2 hour at 1750°F, air cooled. Aged 8 hours at 1325°F, furnace cooled to 1150°F and held for a total aging time of 18 hours, air cooled. The fatigue tests were all conducted in an air environment.

The effect of cyclic frequency in an air environment at 800°F and 1000°F is shown in Figures 3.10 and 3.11, respectively. It will be noted that, at a given value of ΔK, fatigue-crack growth rates increase with decreasing frequency at both test temperatures. This is in qualitative agreement with tests conducted in a 1000°F air environment of ΔK, fatigue-crack growth rates increase with decreasing frequency at both test temperatures. This is in qualitative agreement with tests conducted in a 1000°F air environment on annealed Type 304[6], annealed Type 316[7], and 20% cold-worked Type 316[8] stainless steels.

Previous work[9] has shown that the stress intensity factor range ($\Delta K = K_{max} - K_{min}$) does not provide an adequate description of crack growth behavior over a wide range of stress ratios ($R - K_{min}/K_{max}$). The "effective stress intensity factor" ($K_{eff} = K_{max}[1-R]^m$) provides a much better correlation of crack growth rates over a wide range of R-values, and is therefore more useful in structural analyses[10]. The effect of stress ratio was determined at 800°F and 1000°F and the results are shown in Figures 3.12 and 3.13, respectively, plotted in terms of the effective stress intensity factor. The exponent "m" (see above) is empirically determined in order to obtain the best correlation of the data over the range of stress ratios tested. For precipitation heat-treated Inconel 718, the values of m at 800°F and 1000°F are 0.5 and 0.6, respectively.

Some previous testing on precipitation heat-treated Inconel 718 has been done at 1000°F using a different heat of material (Haynes heat no. 2180-9-9104). Comparing the results for specimen no. 156 (Figure 3.11) with the results for heat 2180-9-9104 tested at the same temperature, cyclic frequency and stress ratio[11] indicates very good correlation between the two heats. This implies that heat-to-heat differences may be minimal, a conclusion also reached for annealed Types 304 and 316 stainless steels[7].

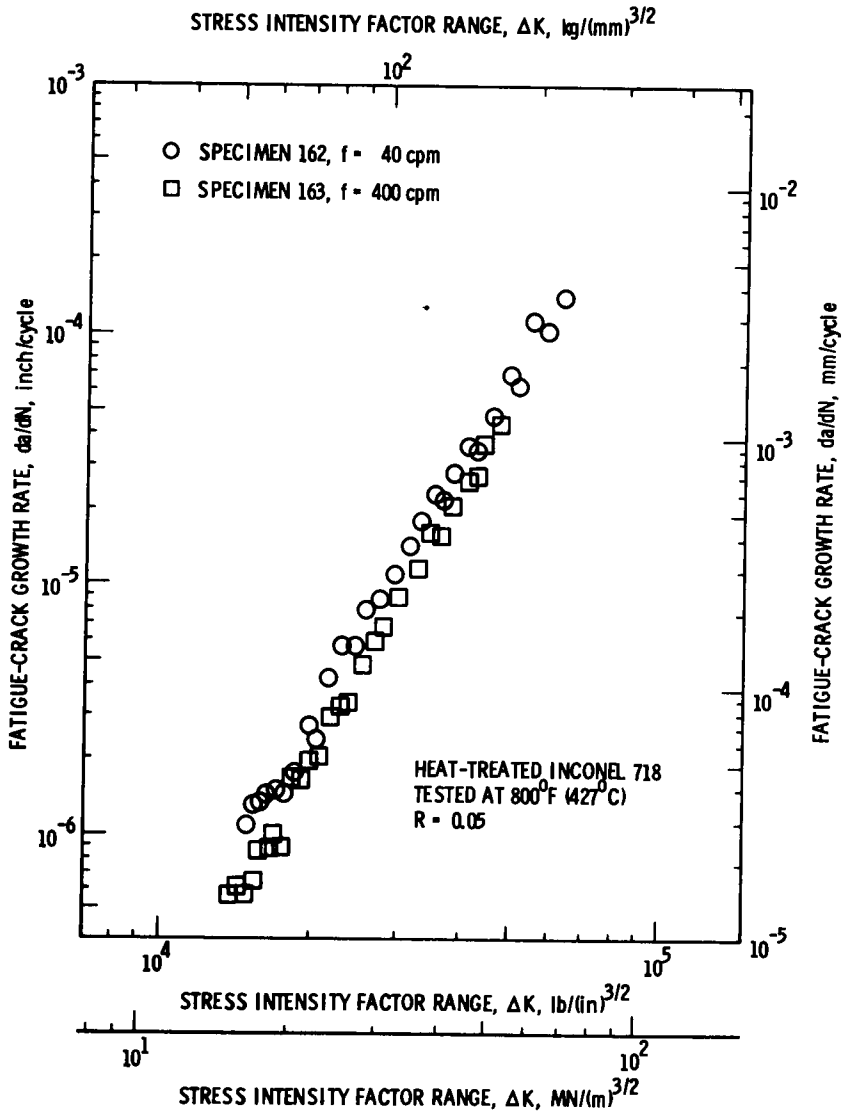

Figure 3.10. Effect of Frequency upon the Fatigue-Crack Growth Behavior of Heat-Treated Inconel 718 in 800°F Air.

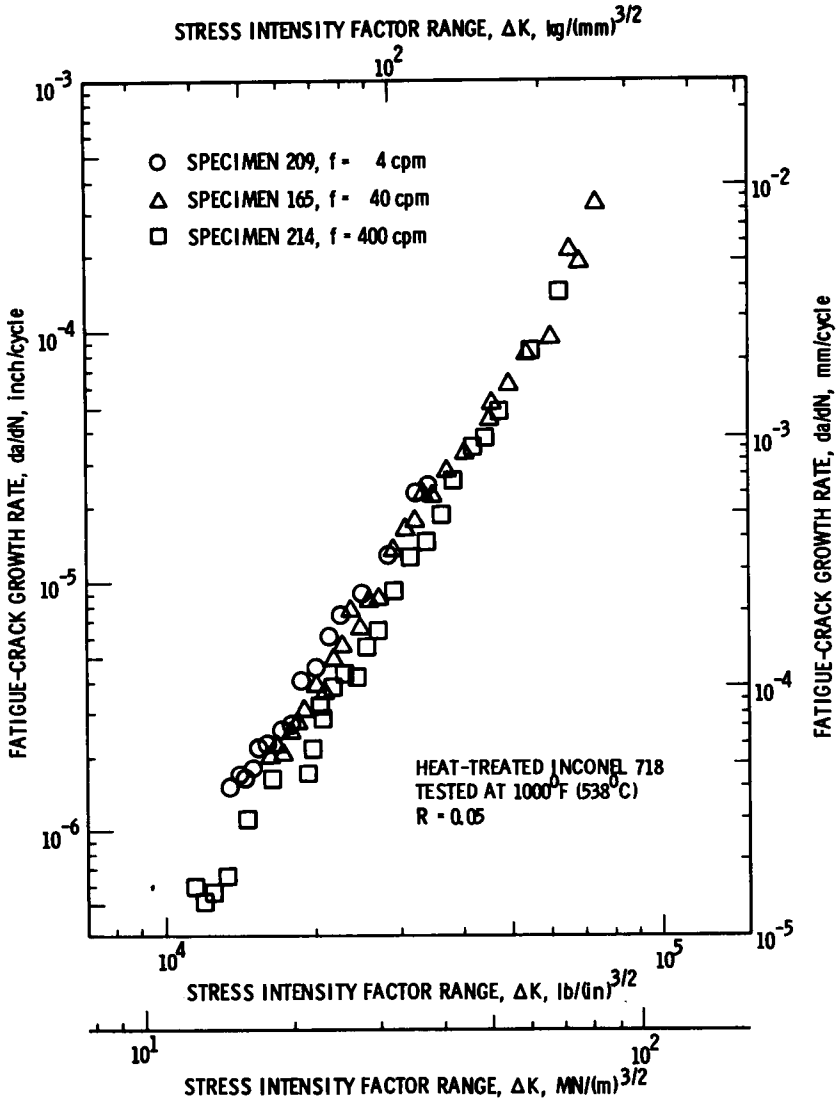

Figure 3.11. Effect of Frequency upon the Fatigue-Crack Growth Behavior of Heat-Treated Inconel 718 in 1000°F Air.

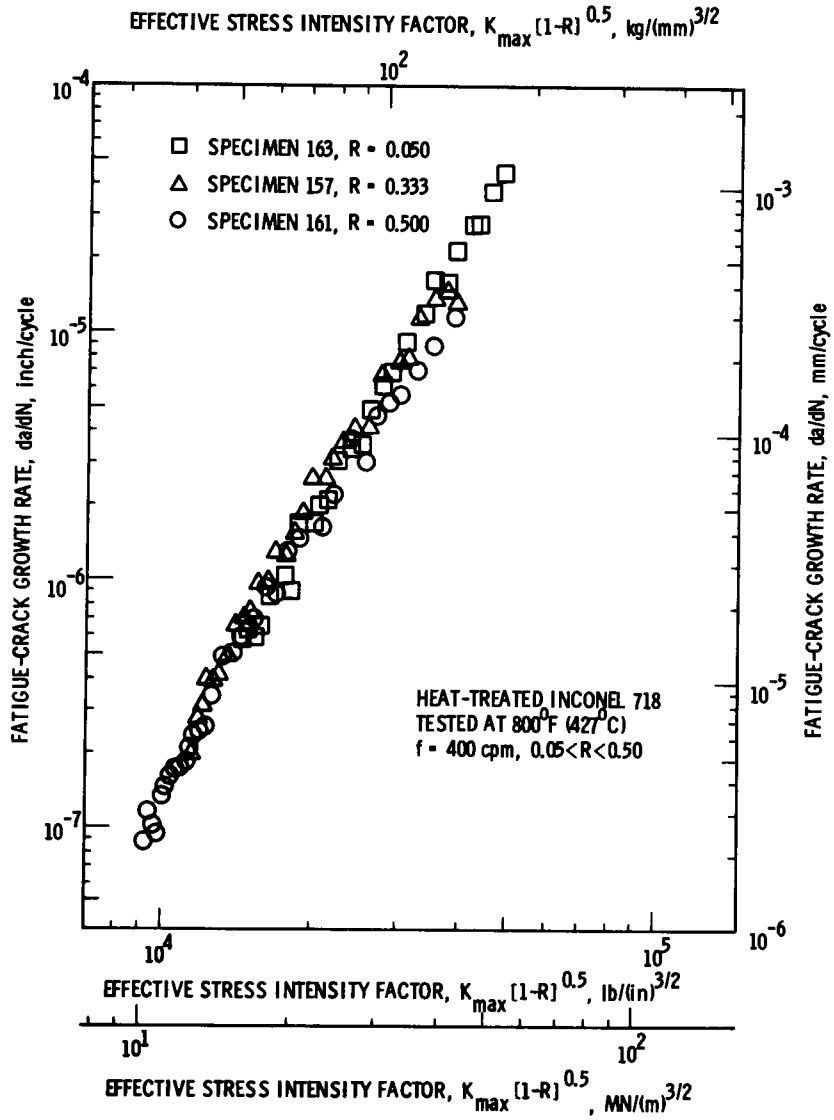

Figure 3.12. Crack Growth Behavior of Heat-Treated Inconel 718 at 800°F Expressed as a Function of the Effective Stress Intensity Factor.

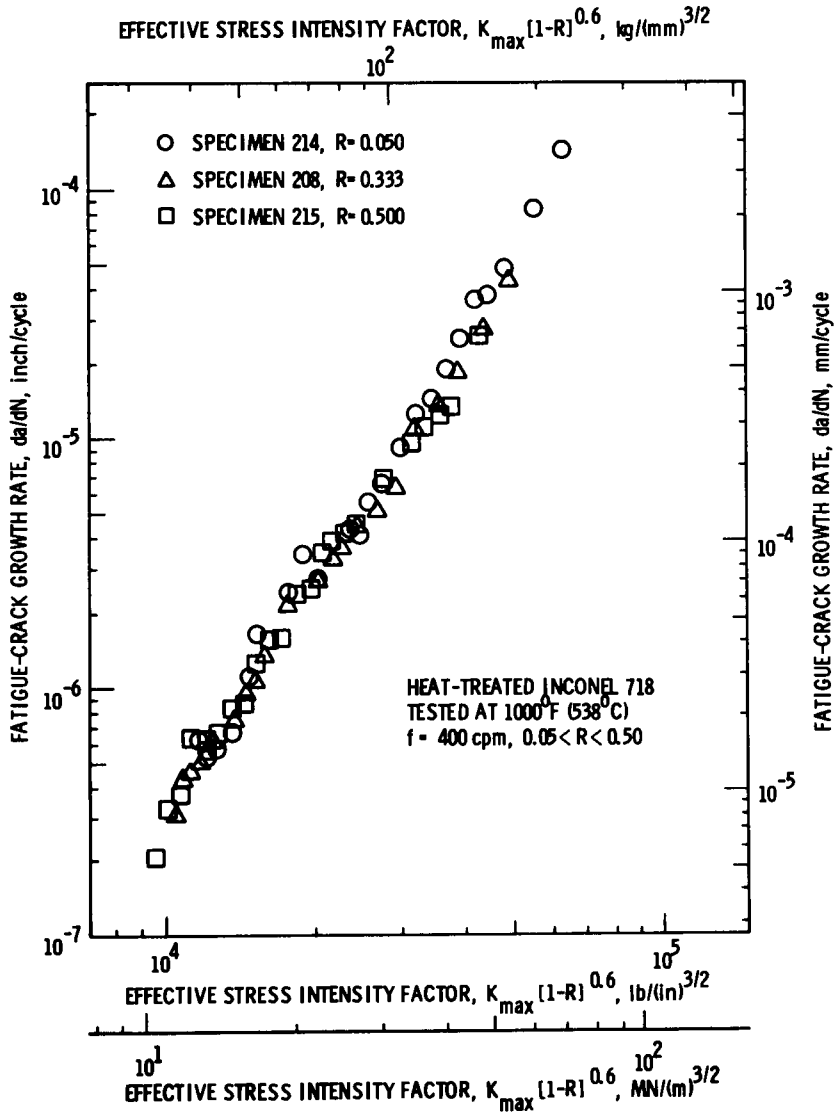

Figure 3.13. Crack Growth Behavior of Heat-Treated Inconel 718 at 1000°F Expressed as a Function of the Effective Stress Intensity Factor.

3.3.1.3 Expected Achievements

The work described is part of a larger effort to determine the effects of temperature, cyclic frequency, stress ratio, heat-treatment, neutron irradiation and sodium environment upon the crack growth behavior of Inconel 718. The survey tests on effects of the sodium environment will be completed during the next reporting period. Work on the other parameters is continuing.

3.4 IRRADIATION DAMAGE TO REACTOR METALS - T. T. Claudson and J. J. Holmes

3.4.1 Application of the Life Fraction Rule to the Stress-Rupture Behavior of 20% C.W. Type 316 Stainless Steel

3.4.1.1 Objective

The purpose of this work is to determine the stress-rupture behavior of 20% C.W. Type 316 stainless steel under variable stress history. This information supports the design and analysis of FTR fuel pin cladding.

3.4.1.2 Accomplishments and Status

3.4.1.2.1 Scope of Work. Results[12] of stress-rupture tests on 20% C.W. Type 316 stainless steel conducted at 1200°F under variable stress conditions exhibited a reasonable correlation with the life fraction rule. Further testing has been recently conducted for the purpose of resolving the few anomalous data points of the previous work. These additional tests were conducted to evaluate: (a) the effect of thermal aging, and (b) the rupture life at 60,000 psi hoop stress as affected by prior creep at various lower stress levels.

All tests were conducted on tubular samples of N-3 lot prototypic cladding. Three-inch long samples of 0.230 inch O.D., 0.015 inch wall thickness, were loaded by internal pressurization at 1200°F. The samples were heated to 1200°F in approximately two hours and were held at temperature only 10-15 minutes before pressurization.

3.4.1.2.2 Experimental Results. Table 3.5 summarizes the results of the 1200°F stress-rupture tests. Two tests were conducted at 60,000 psi to add more data at this stress for statistical purposes. Three tests were conducted for evaluation of aging effects and seven tests were conducted under multiple stress history. These seven tests were conducted at nominal stresses of 37.5, 45, 50 and 55 ksi were a subsequent increase to 60 ksi. The uniform diametral strain values represent the average maximum strain away from the rupture site.

3.4.1.2.3 Evaluation of Results. The values of the mean rupture life, t_r, at 1200°F for various stresses, were obtained by fitting an equation to selected data of Blackburn[12], Paxton[13], along with the present results. These data are shown in Figure 3.14 as a log-log plot of time to rupture as a function of hoop stress. The equation obtained for these data is:

$$\log t_r = 5432.89 - 3507.11 (\log \sigma) + 756.83 (\log \sigma)^2 - 54.5826 (\log \sigma)^3 \quad (1)$$

where t_r is hours and σ in psi. The coefficient of determination for this equation is 0.994 and the standard error of estimate of $\log t_r$ is 0.0988. All baseline rupture lives for the present analysis were obtained from this equation.

A portion of the reduction in the observed total life fraction data for some of the tests in Reference 12 was attributed to a thermal aging effect. The present results do not substantiate this conjecture. Table 3.6 summarizes the results of the aging tests. Rupture times for unaged material were obtained from Equation (1). The 40.8 hour aged specimen tested at 60 ksi is from Reference 12. Within the predicted scatter based on the standard error of estimate, the results do not exhibit an effect due to thermal aging. Although it has been shown by Paxton and Holmes[14] that recovery is occurring during these time periods, these present results do not show that recovery has an effect on the stress-rupture properties. Paxton and Holmes showed that the combination of stress and temperature did not significantly enhance recovery at 1200°F.

Application of a so-called life fraction rule was first applied by Robinson[15] who proposed that:

$$\sum_i = \frac{t_i}{t_{ri}} = 1 \quad (2)$$

Table 3.5. Test Results

Test No.	Hoop Stress, psi	Time, hr.	Hoop Stress, psi	Time to Rupture, hr.	Uniform Diametral Failure Strain, %
N3-SR-115	0	0	60,000	1.03	---
N3-SR-116	0	0	60,000	0.867	4.0
N3-SR-122	0	22.2	60,000	1.00	3.0
N3-SR-123	0	77	60,000	1.30	2.5
N3-SR-112	0	40	55,000	3.30	3.7
N3-SR-117	45,000	7.7	60,000	0.183	4.0
N3-SR-118	50,000	2.5	60,000	0.428	4.4
N3-SR-119	55,000	0.8	60,000	0.673	5.1
N3-SR-120	37,500	20	60,000	0.40	2.9
N3-SR-121	37,500	60.2	60,000	0.183	3.4
N3-SR-113	37,500	80	60,000	0.050	4.3
N3-SR-114	37,500	100	60,000	0.017	4.1

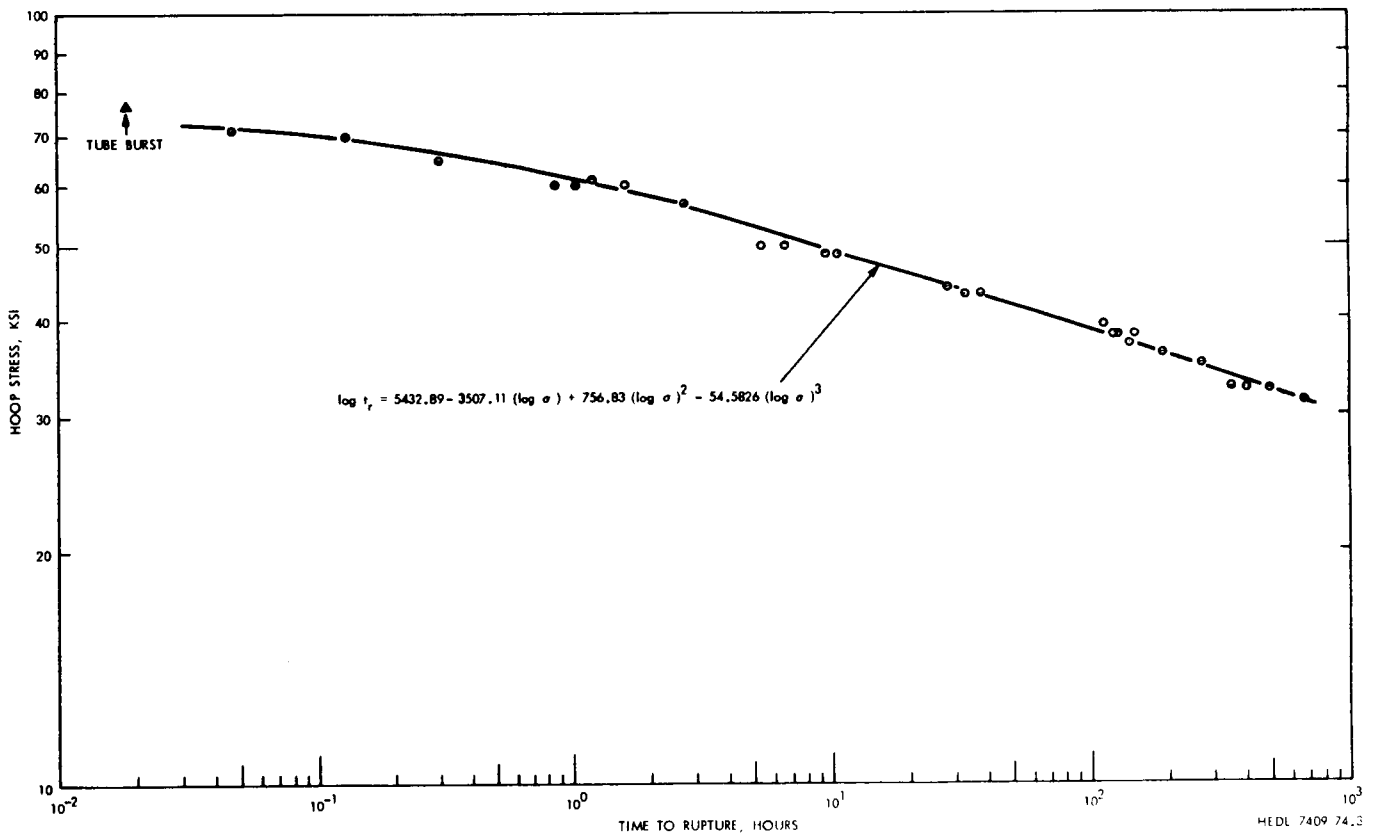

Figure 3.14. Stress-Rupture Properties of 20% Cold Worked Type 316 Stainless Steel at 1200°F.

Table 3.6. Effect of Thermal Aging on Rupture Life

Age Time, Hr.	Hoop Stress, Ksi	Time to Rupture, Hr.
0	60.0	1.06 (0.84-1.33)
22.2	60.0	1.0
40.8	60.0	0.8
77.0	60.0	1.3
0	55.0	3.06 (2.44-3.85)
40.0	55.0	3.3

Note: Times to rupture for 0 hour age are predicted results with minimum and maximum times, in parenthesis, obtained from the standard error of estimate on log t_r.

where t_i is the period of time spent at a particular stress and temperature, and t_{ri} is the rupture time corresponding to that stress and temperature. This expression has also been called the linear cumulative damage rule. Table 3.7 presents the calculated life fractions for the present tests. Included in Table 3.7 are two tests from Reference 12. If Equation (2) is valid then a plot of column 3 in Table 3.7 versus column 6 should yield a straight line. This data is plotted as life fraction at the lower stress versus life fraction at the higher stress in Figure 3.15. Included in the figure are the results from the multicycle tests for 37.5/50 ksi from Reference 12. The life fractions for these tests were also computed with the use of Equation (1). It is immediately evident from Figure 3.15 that most of the tests exhibit a large negative deviation from the life fraction rule. The tests showing the greatest deviation are those involving single changes in stress coupled with a large differential in stress.

One possible reason for the deviation arises from the actual test procedure. Namely, the tests were conducted for a fixed pressure and not a fixed stress. The test summary from Table 3.7 shows that the second stress in every case was 60 ksi, and this stress was based on the original dimensions of the tube. Since the tubes are deforming during the application of the first stress, the diameters are increasing and when the second condition was attained the hoop stress was actually greater than 60 ksi since the tests were pressurized to the value based on the original dimensions. An attempt was made to estimate the actual hoop stress for the second condition shown in Table 3.7.

Calculation of the actual diameters requires a knowledge of the diametral creep rate and an equation for the stress as a function of strain. Creep rates were obtained by fitting a polynominal equation to selected data from References 12 and 13 along with some of the data given in Table 3.5. The creep equation is given by:

$$\log \dot{\varepsilon} = -307.753 + 122.954 (\log \sigma) - 12.236 (\log \sigma)^2 \qquad (3)$$

where $\dot{\varepsilon}$ is the average diametral creep rate (%/hr) at 1200°F and σ is the hoop stress (psi). Figure 3.16 shows the creep data as a function of stress for a temperature of 1200°F. Equation (3) was used to obtain strains for the various tests.

Table 3.7. Life Fraction Data

σ_1, ksi	Time, Hr.	Life Fraction	σ_2, ksi	Time to Rupture, Hr.	Life Fraction
37.5	20	0.160	60	0.4	0.378
37.5	40	0.320	60	0.1	0.094
37.5	40	0.320	60	0.33	0.312
37.5	60.2	0.481	60	0.183	0.173
37.5	80	0.640	60	0.05	0.047
37.5	100	0.800	60	0.0167	0.016
45	7.7	0.329	60	0.183	0.173
50	2.5	0.295	60	0.428	0.404
55	0.8	0.262	60	0.673	0.636

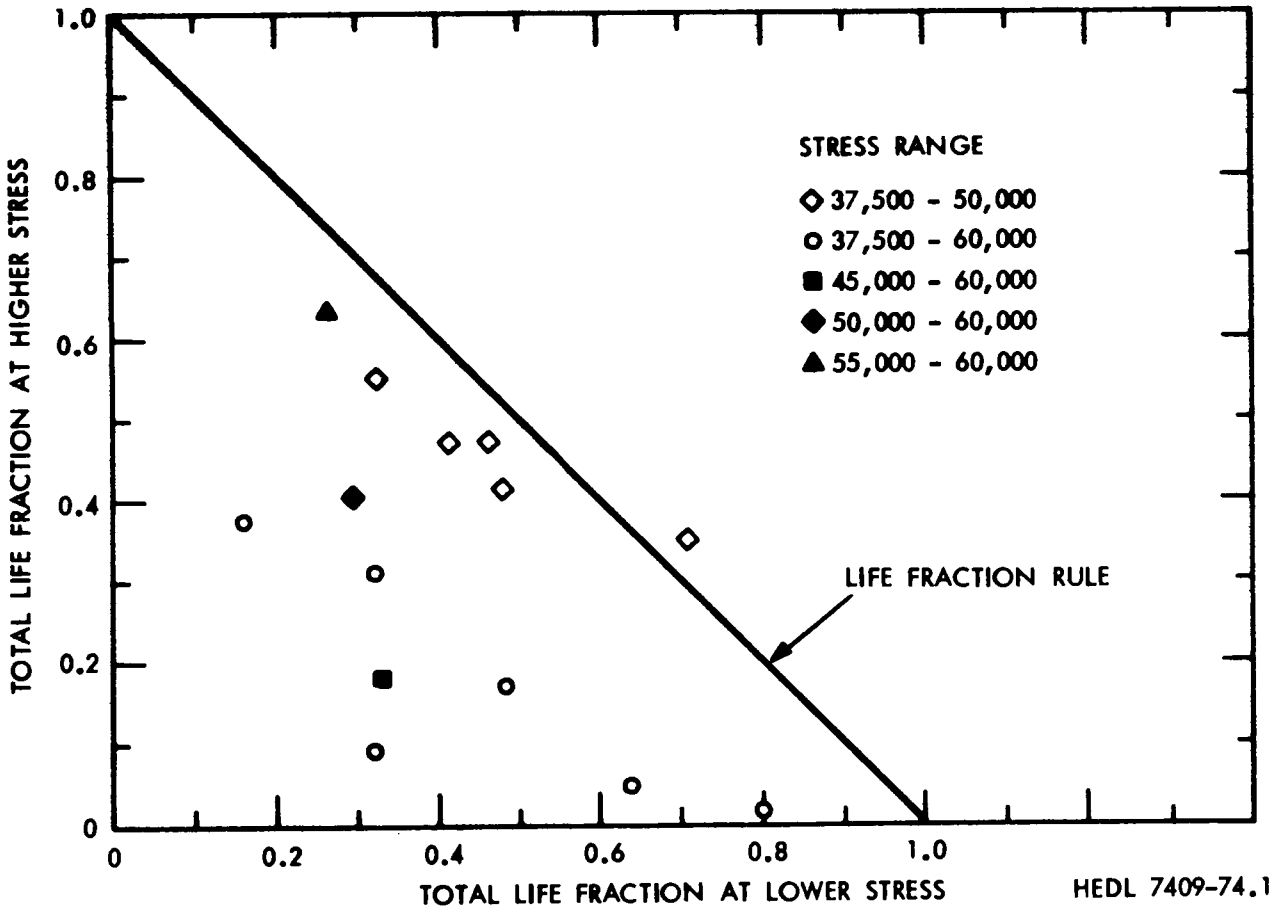

Figure 3.15. Comparison of 1200°F Stress-Rupture Data with Life Fraction Rule.

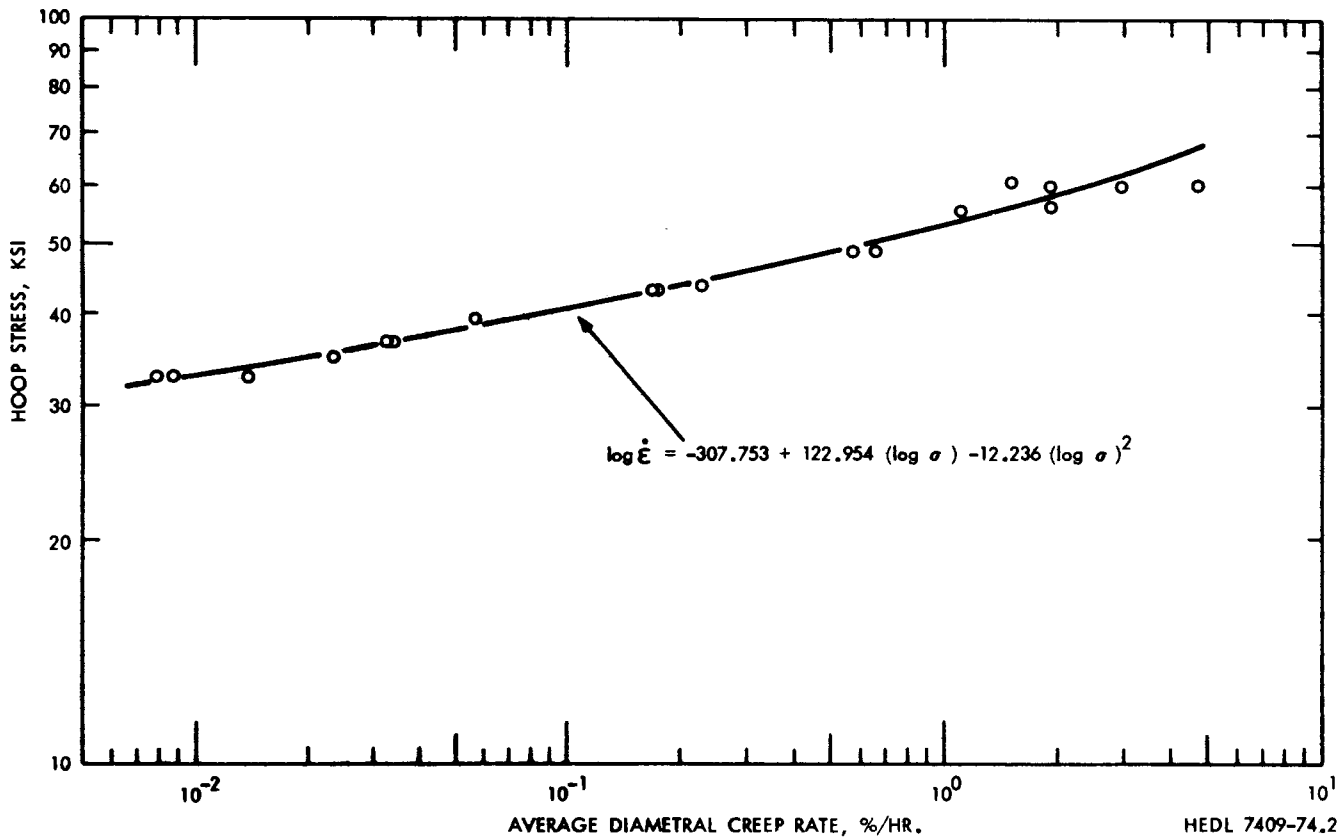

Figure 3.16. Creep Data for 20% Cold Worked Type 316 Stainless Steel at 1200°F.

Stresses were obtained from Equation (6) of Yaggee and Li[16]. When this equation is solved for stress in a biaxial stress state the following result is obtained:

$$\sigma = \frac{P\ r_o}{t_o\ e^{-2\varepsilon}} \tag{4}$$

where P is the internal pressure in psi, r_o is the original midwall radius in inches, t_o is the original wall thickness in inches and ε is the diametral strain. Results of the strain calculations are summarized in Table 3.8. These calculations show the stress in the second portion of the test was greater than 60 ksi in each case. Also, the calculated total strains agree reasonably well with the post-test measured strains. Using the stresses in column 5 of Table 3.8 and Equation (1), new values of life fraction were calculated. Also the expected variance in life fraction was calculated using the standard error of estimate in log t_r. These life fraction values are listed in Table 3.9. Comparison of column 7 in Table 3.9 with column 6 in Table 3.7 shows that the life fraction values have slightly increased, although column 9 in Table 3.9 still shows an overall negative deviation from the life fraction rule. The expected range in the life fraction in column 10 shows that the maximum values do provide better fit with the life fraction rule. Thus, incorporating the effect of the increase in diameter tends to improve the correlation.

This procedure, however, conflicts with some of the earlier stress change tests given in Reference 12. If the change in diameters are calculated for the 37.5/50 ksi series of tests, the calculated total strain values are greater than the measured values and some of the life fraction values are increased to values up to about 2. This observation should be obvious since this test series had already provided a good correlation without any correction. Proper definition of the tube diameters as a function of time will be possible after the results of current HEDL work on creep of pressurized tubes is completed.

A recent paper by Abo El Ata and Finnie[17] reviewed the validity of various creep damage rules. Their review presented a number of observations which help to qualify the data presented in Figure 3.15. They showed that life fractions calculated by Equation (2) for a number of structural

Table 3.8. Diametral Strain Analysis

First Hoop Stress, ksi	Time,hr	Strain Rate,%/hr	Strain, %	Second Hoop Stress, ksi	Time to Rupture,hr	Strain Rate,%/hr	Strain,%	Total Strain,%	Measured Strain,%
37.5	20	0.044	0.88	60.82	0.4	2.62	1.05	1.93	2.9
37.5	40	0.044	1.76	61.94	0.1	2.91	0.29	2.05	2.8
37.5	40	0.044	1.76	61.94	0.33	2.91	0.96	2.72	3.8
37.5	60.2	0.044	2.65	63.07	0.183	3.22	0.59	3.24	3.4
37.5	80	0.044	3.52	64.17	0.05	3.53	0.18	3.70	4.3
37.5	100	0.044	4.40	65.29	0.0167	3.87	0.06	4.46	4.1
45.0	7.7	0.274	2.11	62.39	0.183	3.03	0.55	2.66	4.0
50.0	2.5	0.675	1.69	61.85	0.428	2.88	1.23	2.92	4.4
55.0	0.8	1.366	1.09	61.09	0.673	2.69	1.81	2.90	5.1

Table 3.9. Life Fraction Summary Based on R sults Given in Table 3.8

σ_1,ksi	t_1,hr	L_{F1}	Range of L_{F1}	σ_2,ksi	t_2, hr	L_{F2}	Range of L_{F2}	ΣL_F	Range of ΣL_F
37.5	20	0.160	0.127-0.201	60.82	0.4	0.451	0.359-0.566	0.611	0.486-0.767
37.5	40	0.320	0.255-0.402	61.94	0.1	0.145	0.115-0.182	0.465	0.370-0.584
37.5	40	0.320	0.255-0.402	61.94	0.33	0.478	0.381-0.600	0.798	0.636-1.002
37.5	60.2	0.481	0.384-0.605	63.07	0.183	0.341	0.272-0.429	0.822	0.656-1.034
37.5	80	0.640	0.510-0.803	64.17	0.05	0.120	0.095-0.150	0.760	0.605-0.953
37.5	100	0.800	0.637-1.004	65.29	0.0167	0.052	0.041-0.065	0.852	0.678-1.069
45.0	7.7	0.329	0.262-0.414	62.39	0.183	0.293	0.233-0.367	0.622	0.495-0.781
50.0	2.5	0.295	0.235-0.370	61.85	0.428	0.606	0.483-0.762	0.901	0.718-1.132
55.0	0.8	0.262	0.208-0.328	61.09	0.673	0.808	0.643-1.014	1.070	0.851-1.342

alloys ranged from 0.36 to 2.08 for temperatures in the region of 900 to 1500°F. Several limitations to the life fraction rule were discussed. The main points are: (a) the life fraction rule predicts life adequately under conditions involving small changes in stress and temperatures, and multiple excursions; (b) conditions involving appreciable changes in test conditions or a single excursion show poor agreement with the rule; (c) the life fraction rule is useful only if the loads are high enough to produce significant plastic deformation; and (d) the rule is applicable if the temperature is low enough and exposure to it is short enough to minimize the effect of solid state reactions. One other observation discussed by Abo El Ata and Finnie was that initial high stress creep under some conditions increases rupture life significantly. This observation was substantiated by the results of Blackburn[12]. The data given in Figure 3.15 are entirely consistent with the restrictions listed above. That is, all the tests showing a large deviation from the life fraction rule involved large changes in stress and consisted of only a single excursion. The data exhibiting a good correlation involved small changes in stress or were for multiple excursions.

A number of tests involving a tube burst after prior creep were also conducted by Blackburn[12]. Tube burst tests are essentially very short time stress rupture tests. Tube burst data of Paxton[13] were corrected for equivalent stress-rupture times by the procedure developed in Reference 18. The average of nine tests for N-lot material is shown as the tube burst data point in Figure 3.14. It can be seen that this point is in close agreement with the stress rupture data. The life fractions for the creep plus tube burst tests from Reference 12 were all less than 0.8. This is consistent with the earlier discussion in that poor agreement would be expected for tests involving a large change in stress with a single excursion.

3.4.1.2.4 Conclusions. Results of the present investigation coupled with those of Blackburn[12] have shown that the life fraction rule may be used under certain conditions. The life fraction rule predicts life adequately under conditions involving small changes in stress and temperature and for multiple excursions. Thermal aging does not affect the stress rupture properties of 20% C.W. Type 316 stainless steel at 1200°F.

3.4.2 Low Temperature Creep of 20% Cold Worked Type 316 Stainless Steel

3.4.2.1 Objective

The objectives of this work are: (1) to accurately measure thermal creep in 20% cold worked Type 316 stainless steel, and (2) to further demonsrate the application of microwave extensometers for high precision creep strain measurements.

3.4.2.2 Accomplishments and Status

3.4.2.2.1 Scope of Work. A creep test on 20% cold worked Type 316 stainless steel at 850°F was continued using a high precision microwave extensometer to measure strain. The first 1030 hours of the test were conducted at a stress of 20,000 psi, and the experimental details and results were reported previously[19]. During the subsequent 960 hours, the specimen was subjected to the following stress changes: (1) unload to 220 psi at 1030 hours, (2) reload to 20,000 psi at 1320 hours, (3) partially unload to 9110 psi at 1655 hours, and (4) unload to 220 psi at 1990 hours. All load changes were made by rapidly removing or adding weights to the load pan.

After the final unloading, the test temperature was increased to 1000°F in 7 hours, and then held constant for 40 hours. The specimen was then loaded in increments of about 2,000 psi to a total stress of 20,000 psi within about 8 minutes. After maintaining this stress for 960 hours, the specimen was unloaded to 220 psi for a period of 240 hours, and was then reloaded to 20,000 psi at a total elapsed time of 1200 hours.

3.4.2.2.2 Results. Elastic deformation was observed on loading at both 850°F and 1000°F, as shown in Figure 3.17. The experimental values of Young's modulus (24.5×10^6 psi at 850°F and 23.2×10^6 psi at 1000°F) are in good agreement with the results of Garafalo et al[20].

Complete results of creep strain measurements at both temperatures are presented in Figures 3.18 and 3.19. Since the elastic extensions and contractions accompanying stress changes were much larger than the time-dependent deformation, these strain contributions were subtracted out and are tabulated separately in the figures. These elastic strain measurements

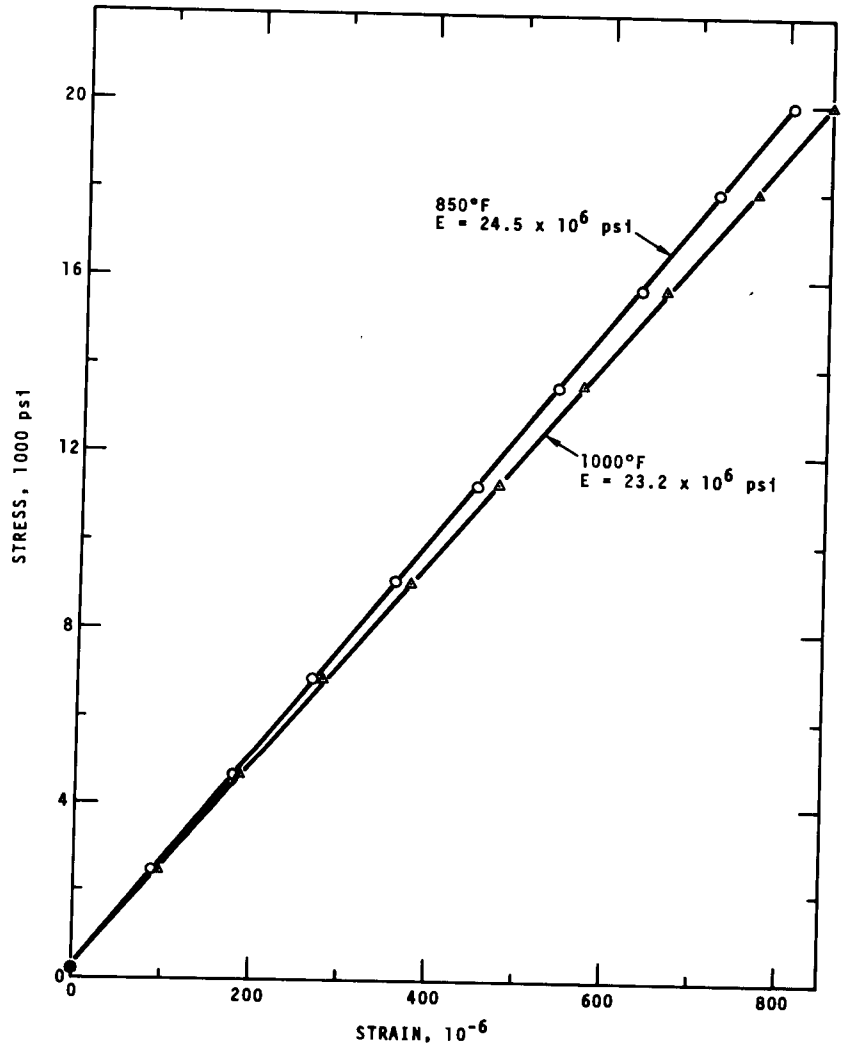

Figure 3.17. Elastic Loading Curves for 20% Cold Worked Type 316 Stainless Steel at 850°F and 1000°F.

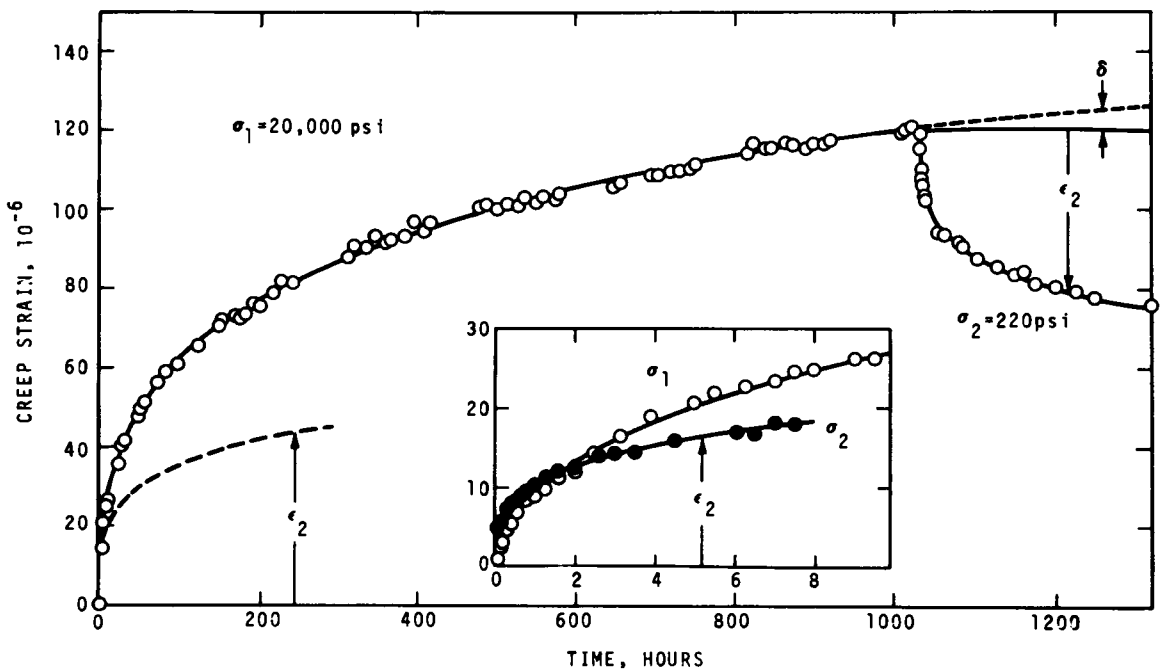

Figure 3.18a. Creep Curve for Initial Loading and Full Unloading of 20% Cold Worked Type 316 Stainless Steel at 850°F.

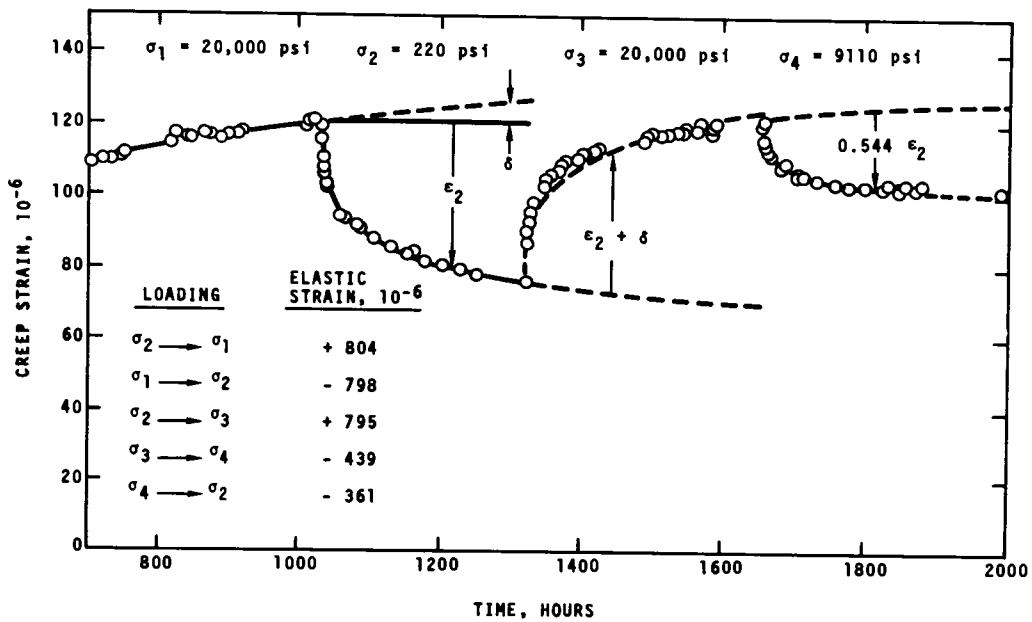

Figure 3.18b. Creep Curve for Full Unloading, Reloading, and Partial Unloading of 20% Cold Worked Type 316 Stainless Steel at 850°F.

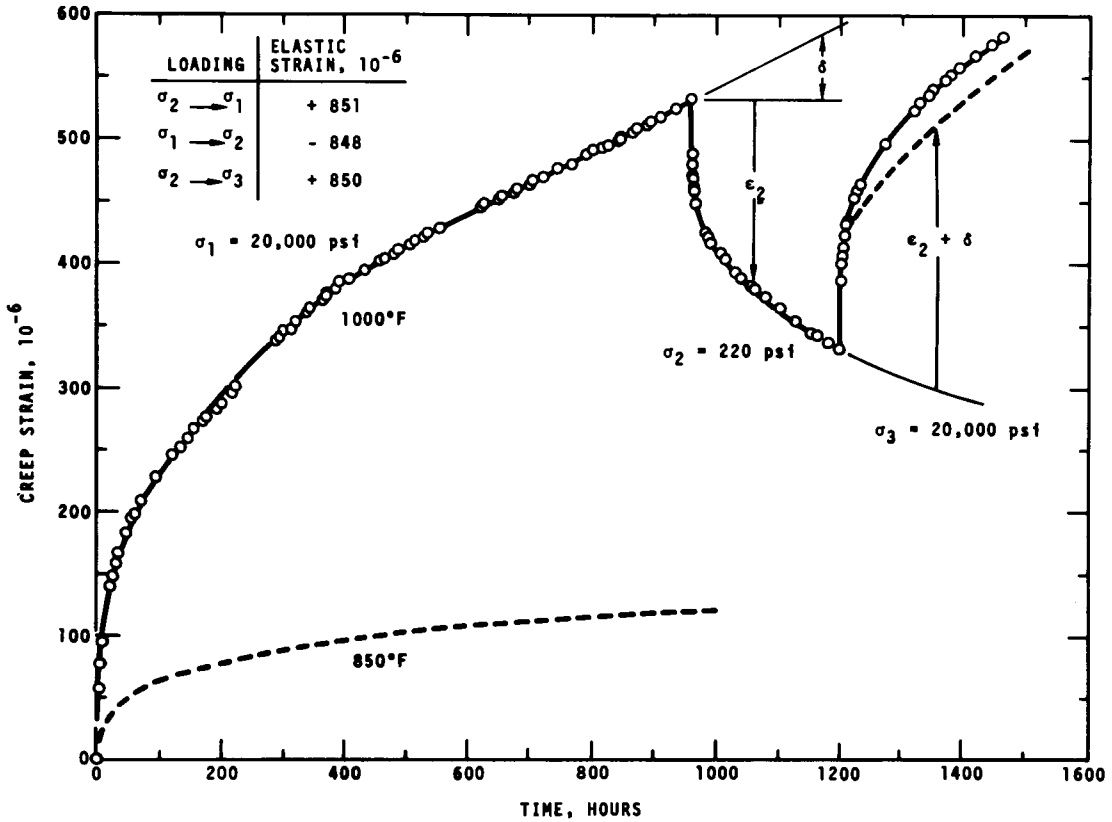

Figure 3.19. Creep Curve for Loading, Full Unloading, and Reloading of 20% Cold Worked Type 316 Stainless Steel at 1000°F.

agree to within about 1%.

The creep strain at 850°F after initial loading is very small, reaching a value of 120 x 10^{-6} in 1030 hours. At 1000°F, the initial creep strain is significantly larger than that observed at the lower temperature, but the strain value of 533 x 10^{-6} at 960 hours is still quite small on an absolute basis. A substantial portion of the forward creep strain at both temperatures is recoverable upon unloading, as shown in Figures 3.18 and 3.19. In Figure 3.20, we have plotted the ratio of the recovery strain (ε_2 in Figures 3.18 and 3.19) to the maximum creep strain against the recovery time. This strain ratio is simply the fractional recovery of the forward creep strain, and the results in Figure 3.20 show that about 37% of the creep strain is recovered during the off-load periods at each temperature, with creep recovery still proceeding at a slow rate. The creep recovery behavior at the two temperatures is very similar when expressed as fractional strain recovery, as seen in Figure 3.20. This result shows that the relative importance of creep recovery is quite insensitive to temperature over the range investigated, and also that the time dependence of creep recovery does not depend strongly on temperature. This creep recovery is apparently a manifestation of anelastic behavior, as discussed in a later section.

On reloading following creep recovery, strain accrues rapidly at both 850 and 1000°F. Partial unloading at 850°F then results in strain recovery again; the magnitude of strain recovery is smaller than for full unloading and is consistent with a linear stress dependence, as expected for anelasticity.

3.4.2.2.3 Evaluation of Results. The initial creep curve at 850°F up to the time of the first unloading represents the behavior of a virgin specimen of the 20% cold worked material. However, we might expect that the initial portion of the 1000°F curve could be influenced by the prior deformation and thermal history at 850°F. After the final full unloading at 850°F some creep recovery occurred during heat to and holding at 1000°F, but this recovery strain rate reached a low value (i.e. $< 1 \times 10^{-6}$ per hr.) prior to initial loading at 1000°F. Thus, the final unrecoverable creep strain at 850°F was even less than the 100 x 10^{-6} indicated in Figure 3.18.

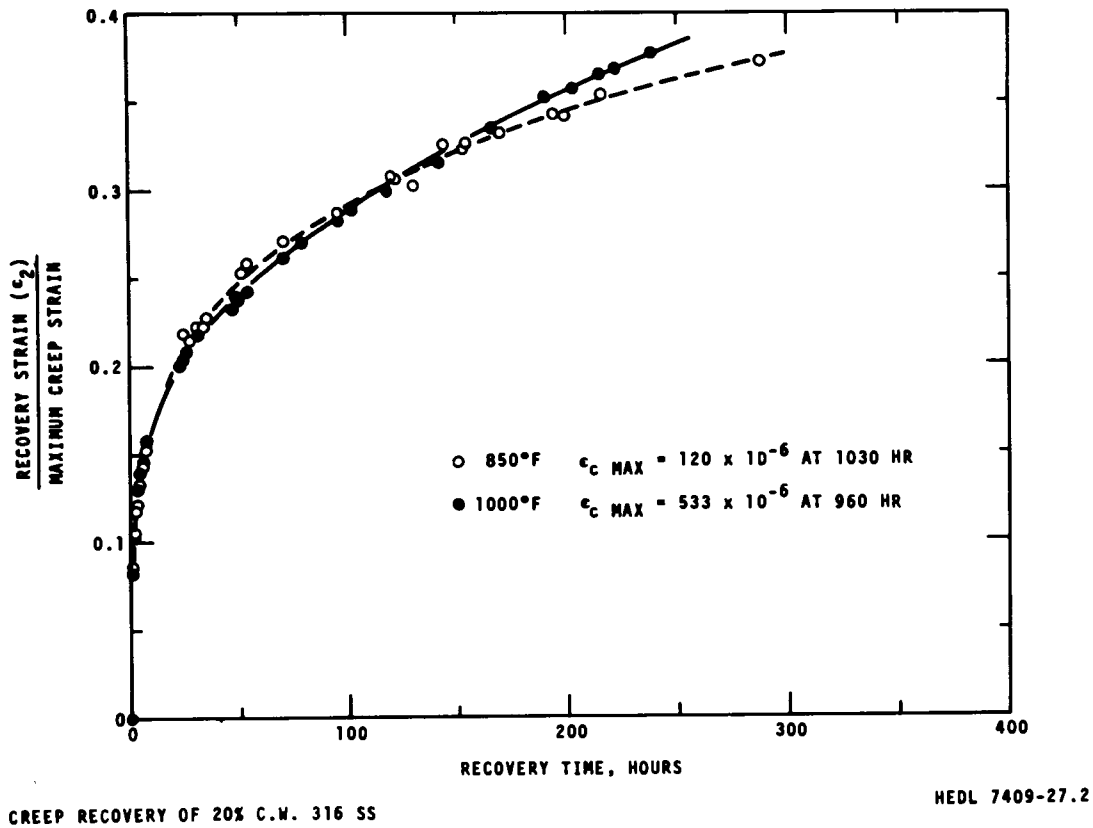

Figure 3.20. Fractional Creep Recovery in 20% Cold Worked Type 316 Stainless Steel at 850°F and 1000°F.

This deformation is probably too small to significantly affect the response at 1000°F, particularly in view of the large deformation introduced in fabrication. Later in this section, we present evidence that static thermal recovery effects are small at 850°F, so the prior thermal history is also unlikely to produce important changes in the subsequent creep response at 1000°F. We therefore conclude that the reported creep curve is representative of the response expected from a virgin specimen at 1000°F.

Time-dependent strain recovery following unloading is a characteristic of anelastic deformation, and we will examine the present results in terms of a spring and dashpot model of anelasticity. The time dependence of the recovery strain, ε_2, does not fit a simple spring and dashpot element using a single relaxation time, but rather than attempt an analytical formulation based on a spectrum of relaxation times, we will employ simple graphical construction based on the requirements of a simple spring and dashpot model. As a starting point, we will assume that ε_2 represents the basic anelastic deformation. This assumption implies that during the initial forward creep deformation, the anelastic contribution reached its limiting value before 1030 hours, and the anelastic component of forward creep is congruent with the recovery strain, ε_2. This assumption is not exactly correct, since the initial recovery strain rate is somewhat higher than the initial total forward creep rate (i.e. the sum of plastic and anelastic creep rates) as shown in the inset of Figure 3.18. This same behavior was also observed at 1000°F. Nevertheless, we will retain this assumption to examine the subsequent reloading and partial unloading behavior.

The predicted behavior after reloading is given by the graphical construction in Figures 3.18 and 3.19. The quantity δ is the incremental plastic strain accrued beyond the initial time on load. At 850°F, agreement between the experimental data and the predicted response, while not exact, is reasonable (Figure 3.18). The results show no indication of significant static thermal recovery during the prior unload period, which would lead to enhanced plastic creep strain on reloading.[21,22] However, at 1000°F, the experimental data show more strain after reloading than predicted by the construction in Figure 3.19. This behavior is evidence for a small amount of thermal recovery during the unload period.

Predicted response during the partial unload at 850°F using a linear stress dependence is also compared with experimental data in Figure 3.18. Here the extrapolation of the prior reloading curve is based on the experimental data, rather than on the predicted reloading behavior. This procedure minimizes accumulation of errors from the uncertainty in further graphical extrapolation of the initial loading and unloading curves. It was assumed that plastic creep strain is negligible at the reduced stress. Agreement between experimental results and prediction is excellent.

The present results are therefore consistent with a significant anelastic contribution to the total strain at both 850 and 1000°F and with some thermal recovery at 1000°F following stress reductions or unloadings.

3.4.2.2.4 Conclusions and/or Recommendations. The present study leads to following conclusions:

1. Thermal creep strains in 20% cold worked Type 316 stainless steel at 20,000 psi are small at both 850 and 1000°F, reaching values of 120×10^{-6} and 540×10^{-6}, respectively, in 1000 hours.
2. A significant fraction of the creep strain is recoverable during periods of unloading. The fraction of strain recovered and the time dependence of strain recovery are insensitive to temperature.
3. Creep response under unloading and reloading situations is consistent with the presence of a substantial anelastic component in the total deformation.
4. Some static thermal recovery during unload periods of 240 hours occurs at 1000°F, but not at 850°F.

3.4.2.2.5 Applications. The observation of significant creep recovery is potentially important, since this behavioral feature is not specifically incorporated into current materials descriptions of 20% cold worked Type 316 stainless steel. Since the forward creep strains measured here are quite small, it seems unlikely that the inclusion of creep recovery would have a major impact on design or performance analysis of components at temperatures up to 1000°F. However, the present observation that fractional creep strain recovery is insensitive to temperature points to potentially larger creep strains and recovery strains at higher temperatures, in which

case the inclusion of creep recovery effects could affect predicted component behavior.

3.4.3 Thermal Creep in Pressurized Tubes of 20% Cold Worked Type 316 Stainless Steel

3.4.3.1 Objective

The purpose of this work is to determine the thermal creep deformation of pressurized tubes of 20% cold worked Type 316 stainless steel. Results of these experiments will be compared with companion in-reactor tests to define the irradiation creep component of in-reactor deformation.

3.4.3.2 Scope of Work

Creep strains in pressurized tube samples of 20% cold worked Type 316 stainless steel were measured over the temperature range from 825 to 1400°F for times to 2400 hours. Nominal stress levels for these tests varied in increments of about 2500 psi over the range from 0 to 10,000 psi and in increments of about 5000 psi over the range from 10,000 psi to 60,000 psi. Diameter and length measurements were made to define both diametral and axial creep strains.

Specimens were fabricated from prototypic FTR cladding (Lot N-2), which is 0.230 inch outside diameter by 0.015 inch wall thickness tubing. A one-inch length was selected for the present specimens, since the strain measurement and rupture life studies conducted by Venard[23] showed that a 4:1 length to diameter ratio was adequate for such studies. End plugs, one of which contains a fill tube, were electron beam welded to the tube specimen. A fiducial mark was scribed in the edge of one end cap to provide an orientation index for subsequent diameter and length measurements.

Specimens were pressurized with welding grade helium. Pressure was adjusted by introducing helium until a calibrated Heise gage indicated the desired fill pressure. Fill pressures were measured to an accuracy of one percent. After obtaining the desired fill pressure, the fill tube was mechanically cold sealed, disconnected from the pressure source, and sealed with a TIG weld. All specimens were visually inspected for weld defects and helium leak tested at a leak rate of 1×10^{-8} standard cc/sec. Measurement

of the helium volume emitted after puncturing selected pressurized specimens verified that the desired pressure was obtained in completed samples.

Ceramic kiln type furnaces were used for isothermal exposure of the pressurized tubes. Specimens were stacked in a stainless steel pipe which was evacuated and filled with helium to a pressure of two atmospheres. During heating the helium was periodically vented until a steady state pressure of two atmospheres absolute was achieved at the test temperature. Specimens were stacked over an eight-inch length for which temperature was controlled to within ± 5°F of the nominal test temperature. Heating time ranged from 23 minutes for the 1400°F furnace to 45 minutes for the 825°F furnace. Exposure times are measured after specimens reach the test temperature.

The pressure at the test temperature was computed using the ideal gas law with compensation for thermal expansion of the specimen, and is given by:

$$\Delta P = \frac{P(72°F) + 14.56}{\frac{532}{(T+460)}\left[1 + 3\times10^{-5}\ (T-72)\right]} - 29.56$$

where ΔP is the difference between internal and external pressure in psi, T is the temperature in °F, P(72°F) is the gauge fill pressure at ambient temperature in psig. Stresses were computed based on the thin-wall approximation using the midwall diameter (0.215 inch) and are given by:

$$\sigma_\theta = 7.17\ \Delta P$$

$$\sigma_z = 3.585\ \Delta P$$

$$\sigma_r = 0$$

where σ_θ, σ_z, σ_r are the circumferential (hoop), axial, and radial stresses, respectively.

The diameter and length of each specimen was measured at ambient temperature after pressurization and periodically after selected elevated temperature exposures using highly accurate equipment specially developed for this purpose. Differential LVDT probes were used to contact the specimen at diametrically opposing positions. These diameter measurements were made at five locations spaced 0.2 inches apart along the specimen length,

and at 0. 90, 180 and 270° rotations with respect to the index mark for each axial position. The specimen was held in a flat bottom chuck at each end and rotated and translated on precision ball bearings with a remotely operated stepping motor. The LVDT deflections were indicated on a digital voltmeter and manually recorded to the nearest 10^{-5} inch. A class X dowel pin standard was measured before and after each group of five specimens. The differential amplifier was set to zero with this standard dowel pin and the readings taken were the difference in diameter between the standard and each specimen. Diameter measurements showed uniform straining at all five locations for strain levels less than 0.5%. At larger strains, measurements at the three center locations indicated uniform strain, with less strain measured at the end positions. All strain measurements reported here are based on the average of the twelve readings from the center three positions.

For length measurements, the bottom of the specimen rests on a hardened edge and the top is contacted with an LVDT. Measurements were referenced to a standard specimen which was used to set the zero on the amplifier. Each specimen was measured at four locations in 90° intervals around the circumference of the tube. Axial strains were computed from the average of the four length measurements on each specimen.

3.4.3.3 Results

Length measurements of the pressurized tube specimens generally yielded axial strain values within the range ± 0.04%, with some values as large as ± 0.06%, over the first 100 hours of test. After 2410 hours, the total range of axial strain values was ± 0.08%. We detected no systematic dependence of axial strain results on either stress or time, so axial strain is taken to be zero within the above limits.

Diametral strain values determined at the outside diameter of the tubes were converted to diametral strain values at midwall by applying a conservation of volume calculation with zero axial strain. For the tube size used here, measured outside diameter strains were multiplied by 1.15 to obtain midwall hoop strains. The experimental results are presented in Table 3.10 in terms of midwall hoop stress and strain.

For each temperature/time combination, plots of hoop strain against hoop stress were constructed graphically by visually judging the best

Table 3.10. Creep Strain Results for 20% Cold Worked Type 316 Stainless Steel Pressurized Tubes

Hoop Stress, 1000 psi	Hoop Strain, 10^{-6}									
	0.5 hr.	1 hr.	2 hr.	5 hr.	10 hr.	30 hr.	100 hr.	300 hr.	900 hr.	2410 hr.
825°F										
0	-196	-213	- 41	-316	-350	-179	0	-259	-370	-162
0	-138	-150	226	-216	-250	- 29	- 16	-113	-280	225
0.1	- 95	125	-238	-179	- 95	233, -75	421, 242	345	308	141
1.1	25	25	-162	-150	-159	113	304, 79	-121	54	113
2.6	- 49	- 62	-150	-105	- 16	75	221, 87	-150	8	175
5.1	- 8	- 79	-175	- 41	100	171	292, 279	-225	87	154
7.6	-113	- 17	-220	-183	79	129	221, -21	- 95	- 41	146
15.1	-345	-391	-465	-416	-159	162	41, -280	-233	- 75	-229
20.0	- 79	-109	- 67	-175	- 83	470, -25	-46, 75	33	121	75
25.0	-129	-162	46	-205	21	413, 49	-46, 141	75	67	196
30.0	-100	-100	265	- 95	71	346, 958	196, 313	300	621	388
35.0	- 8	- 37	235	1004	267	359	-29, 221	616	175	380
40.0	- 75	- 75	328	- 71	300	945, 904	300, 225	271	208	383
44.9	- 33	-113	-51	-183	92	780, 196	116	334	288	67
49.9	-129	-179	-229	-221	-283	416, 108	29, 283	313	5	-71
54.9	49	- 13	- 81	-125	71	250	400, 450	225	229	221
59.9	5	5	- 60	-129	92	125, 262	171, 262	33	133	254
1000°F										
0	-179	62	154	-238	-370	142	59	- 41	-213	16
0	-192	-183	- 16	-221	-200	383	8	- 59	-250	-121
1.2	-150	-183	- 59	-208	753	129	259, 208	87	- 25	25
2.7	-154	-159	67	-192	834	138	337, 183	41	79	296
5.1	-138	-154	-154	-121	-179	54	192, 79	100	171	- 29
7.6	33	- 29	-124	- 59	13	254	54	62	8	162
15.1	-105	- 92	-121	- 83	- 79	167	116	- 49	141	450
20.0	- 67	- 87	- 79	- 49	46	500	183	200	958	570
25.0	-105	-108	- 13	- 41	41	446	221	121	746	688
30.0	0	- 46	- 46	- 92	46	658	337	233	804	1075

Table 3.10. Creep Strain Results for 20% Cold Worked Type 316 Stainless Steel Pressurized Tubes (Cont'd)

Hoop Stress 1000 psi	Hoop Strain $^{-6}$ 0.5 hr.	1 hr.	2 hr.	5 hr.	10 hr.	30 hr.	100 hr.	300 hr.	900 hr.	2410 hr.
1000°F (continued)										
35.0	5	25	95	- 79	105	737	321	205	780	1229
40.0	-16	- 5	129	- 41	38	729, 537	362	262	721	1792
44.9	38	5	76	- 59	62	721	350	367	1209	2721
49.9	75	13	159	5	141	238	546	480	1317	3817
54.9	79	71	296	100, 362	242	954	716	583	1684	5479, 5434
61.6	283	83	262	167, 526	271	937	871	825	2604	11405, 11379
1100°F										
0	-121	-192	146	-216	-83	142	33	-41	-280	- 16
0	-205	-184	13	-159	-242	133	-16	-16	-113	-105
0.4	-105	-154	-159	-129	-108	138	146	150	187	-187
1.2	-87	-141	- 41	167	250	108	62	283	275	-213
2.7	-133	-187	-225	-121	-221	-108	213	426	246	- 46
5.3	- 54	- 87	13	33	-141	238	267	462	416	167
7.7	- 92	-125	- 67	29	- 59	382	271	442	483	308
10.1	- 75	- 67	162	71	113	362	459	783	316	546
15.1	421	8	154	259	79	842, 546	762	909	537	850
20.0	54	21	83	67	129	575	879	1045	791	1188
25.1	-192	-171	- 38	- 95	- 13	624	1101	1520	1283	1692
30.0	16	71	146	71	342	1083	1638	2217	2200	2713
35.0	0	138	300	225	429	1266	1924	2567	3067	3383
40.0	87	262	400	346	567	1609	2395	3558	4783	5679
1200°F										
0	-288	- 83	-226	-150	-304	5, 375	67	-16	21	-238
0	-246	-208	250	38	-213	325	-38	-75	-205	38
0.4	-141	- 59	-146	-196	-105	-175	121	141	116	54
1.2	- 75	- 5	-100	-138	- 92	383	113	167	100	146
2.9	- 5	62	- 21	- 62	141	200	221	308	550	388

Table 3.10. Creep Strain Results for 20% Cold Worked Type 316 Stainless Steel Pressurized Tubes (Cont'd)

Hoop Stress 1000 psi	Hoop Strain 10^{-6} 0.5 hr.	1 hr.	2 hr.	5 hr.	10 hr.	30 hr.	100 hr.	300 hr.	900 hr.	2410 hr.
1200°F (continued)										
5.4	125	150	225	146	271	725	521	537	646	729
7.7	- 25	- 67	- 46	462	667	1075	788	1121	662	825
10.2	238	337	288	346	325	1576	867	1442	991	1379
15.1	308	462	470	721	646	1804	1266	1850	1533	2017
20.1	516	762	837	1446	1150	2788	2000	2108	2875	3979
25.1	780	1045	1112	1684	1796	2788	3409	3358	5346	9367
30.1	929	1217	1400	1921	2362	3571	4321	4787	7059	21042
34.9	1217	1687	2054	2829	3499	6158	7408	10800	12833	31633
1400°F										
0	-179	-288	-380	-425	-326	259, 38	- 46	-200	-229	- 29
0	-342	-337	-425	-417	-404	-179	- 67	-113	- 13	- 67
0.5	-121	-129	-208	5	-146	742	25	5	334	100
1.5	- 8	- 46	13	150	442	624	213	362	775	1158
3.0	154	254	138	342	1101	1158	654	783	1576	3842
5.4	167	250	233	437	1071	1704	1042	1237	2813	21596
7.7	562	654	842	1021	1400	2416	2684	4779	33996	54009
10.2	942	1045	1266	1512	2004	4165	5916	19679	38484	39038
15.2	1471	1804	2184	2870	3804	6929	26167	43829	43287	-----

smoooth curve fit through the experimental data. Figure 3.21 illustrates the construction of a portion of these isochronous strain-stress plots for the 2410-hour data. The experimental results in Figure 3.21 show less scatter than numerous other data sets, but rarely was there significant ambiguity in establishing a well-defined smooth curve through the data (for other examples see Figures 3.35-3.40). In constructing the strain-stress plots, the curves were allowed to intercept the strain axis at non-zero values. These intercept strains, ε_o, were generally in the range ± 0.02%, which is considered to be within the measurement uncertainty. By way of comparison, the experimental strain values for unstressed tubes were generally in the range ± 0.03%, and showed no systematic dependence on time or temperature. We then consider that, if ε is the strain value read from the strain-stress plot at a stress σ, the creep strain, ε_c, is given by:

$$\varepsilon_c = \varepsilon - \varepsilon_o$$

where ε_o is taken from the same curve as ε, and may be either positive or negative.

The strain-stress curves so constructed are shown in Figures 3.22-3.28 where the experimental data points are omitted for the sake of clarity. In developing these curves, when the experimental data scatter permitted some latitude in the exact positioning of a curve, the construction was made to provide good consistency within the family of curves corresponding to various time values. The constant temperature curves are generally well-ordered, showing greater strains with increasing time, with the most notable exception being the 30-hour, 100-hour and 300-hour curves at 1000°F (Figure 3.23). A consideration of the results in terms of strain-time behavior presented below suggests that the 30-hour and 300-hour curves may be in error. The strain-stress curves are also well-ordered with respect to temperature. At 825°F (Figure 3.22), the indicated creep strains are probably within the measurement uncertainty and are therefore not precisely defined. At the other temperatures, the curves reflect progressively larger creep strains as temperature increases.

Throughout the temperature range, the experimental results show essentially a linear relation between stress and strain over a substantial portion of the strain-stress curves. At very short times, the linear stress

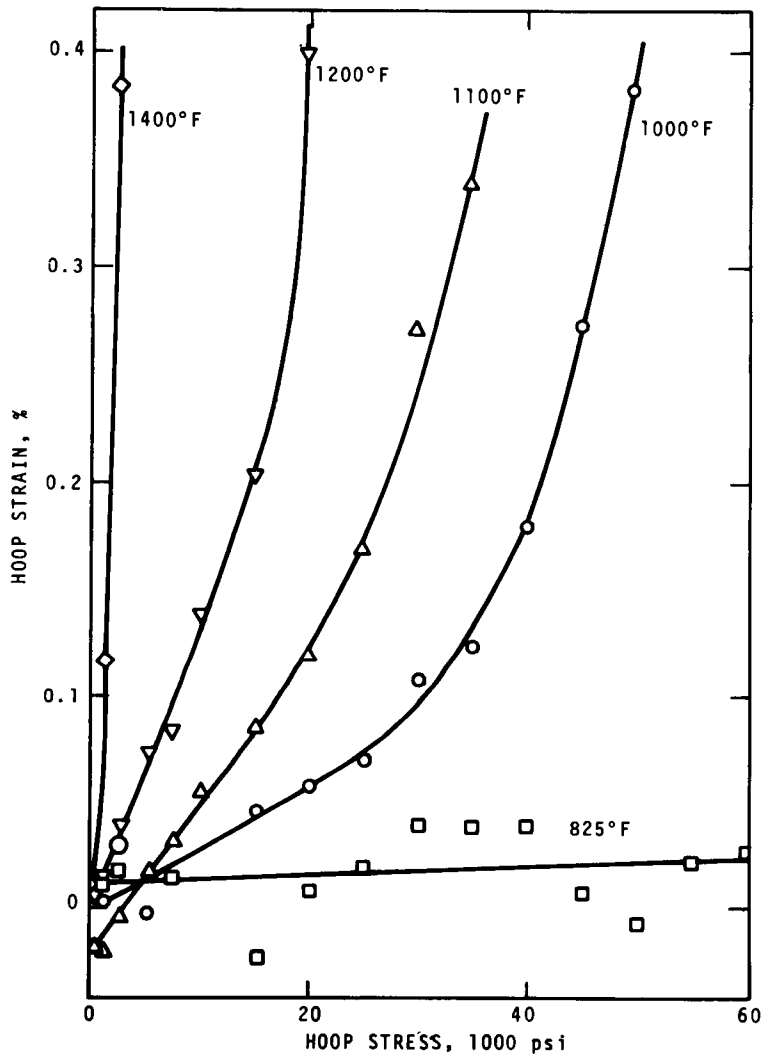

Figure 3.21. Illustration of Construction of Isochronous Strain-Stress Curves for 2410-hour Data.

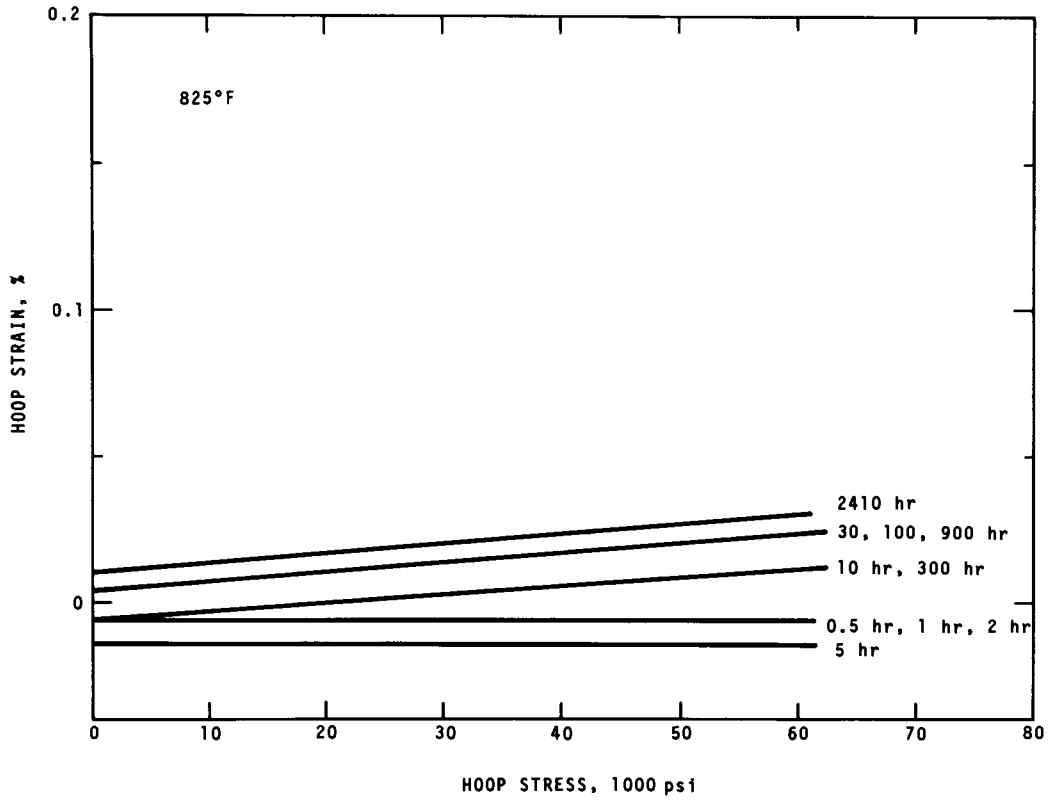

Figure 3.22. Isochronous Strain-Stress Curves for 20% Cold Worked Type 316 Stainless Steel at 825°F.

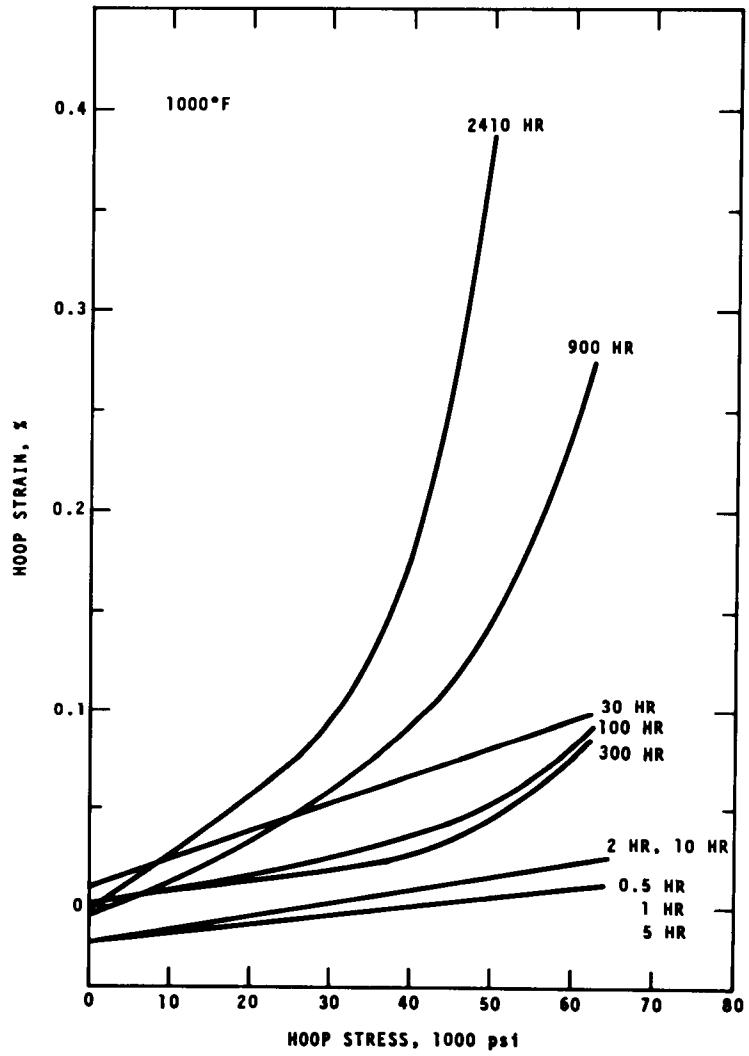

CREEP STRAIN IN 20% C.W. 316 SS TUBES AT 1000°F HEDL 7409-27.13

Figure 3.23. Isochronous Strain-Stress Curves for 20% Cold Worked Type 316 Stainless Steel at 1000°F.

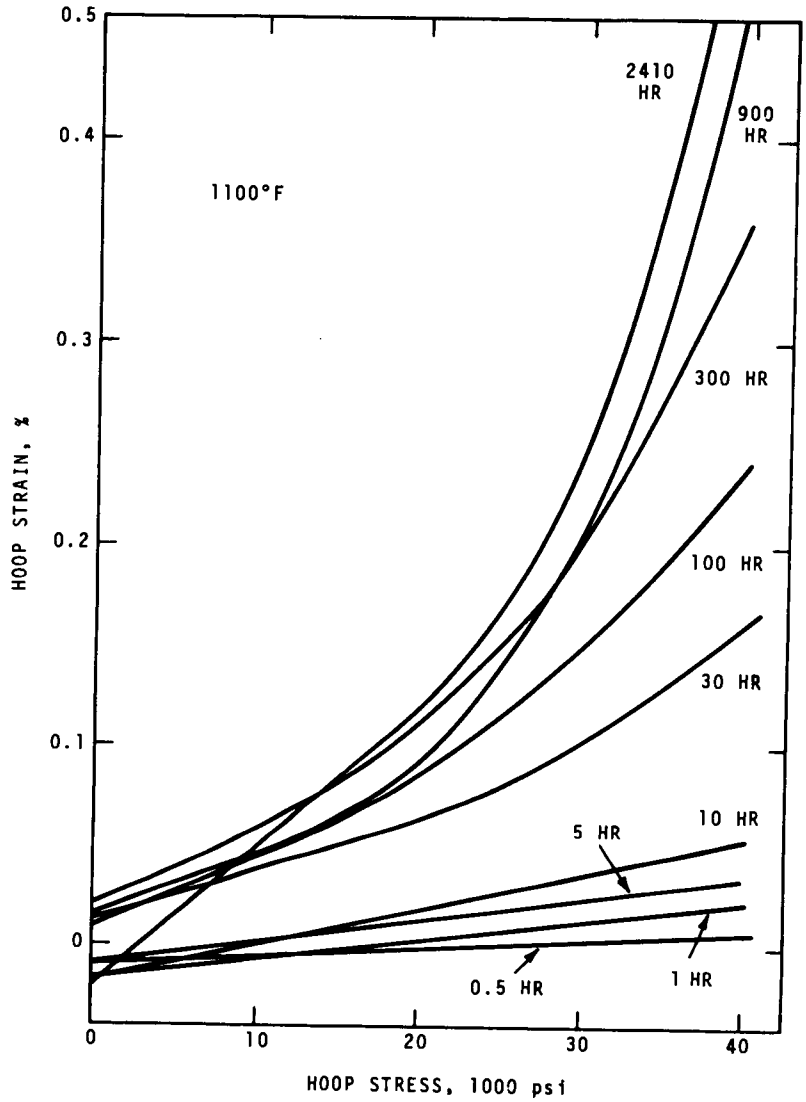

Figure 3.24. Isochronous Strain-Stress Curves for 20% Cold Worked Type 316 Stainless Steel at 1100°F.

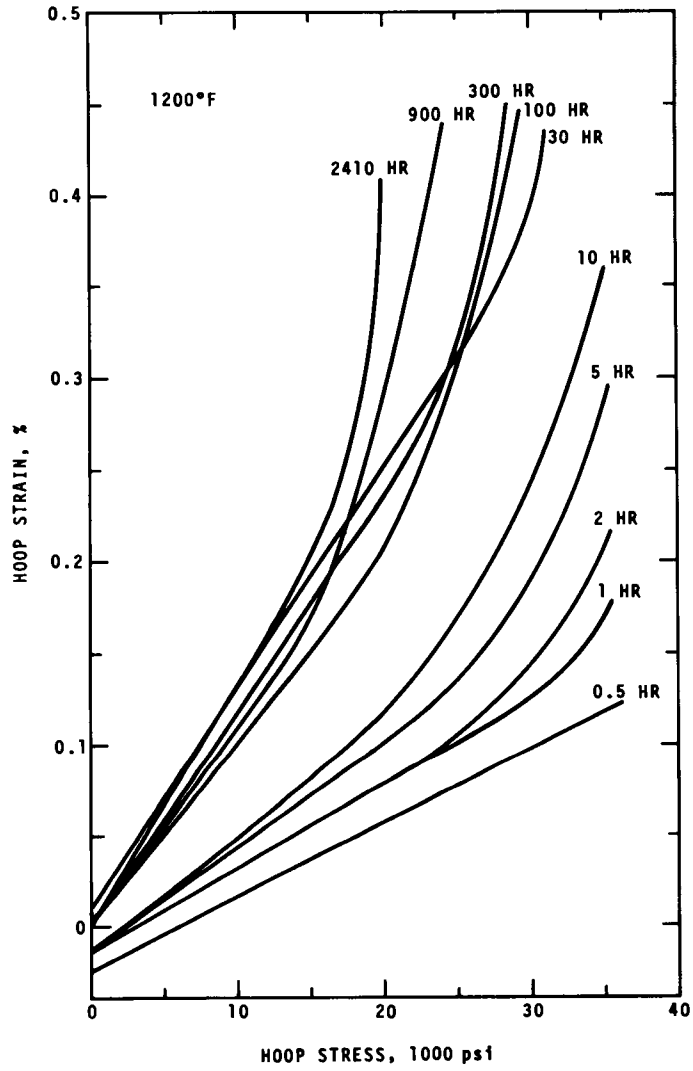

CREEP STRAIN IN 20% C.W. 316 SS TUBES AT 1200°F HEDL 7409-27.12

Figure 3.25. Isochronous Strain-Stress Curves for 20% Cold Worked Type 316 Stainless Steel at 1200°F.

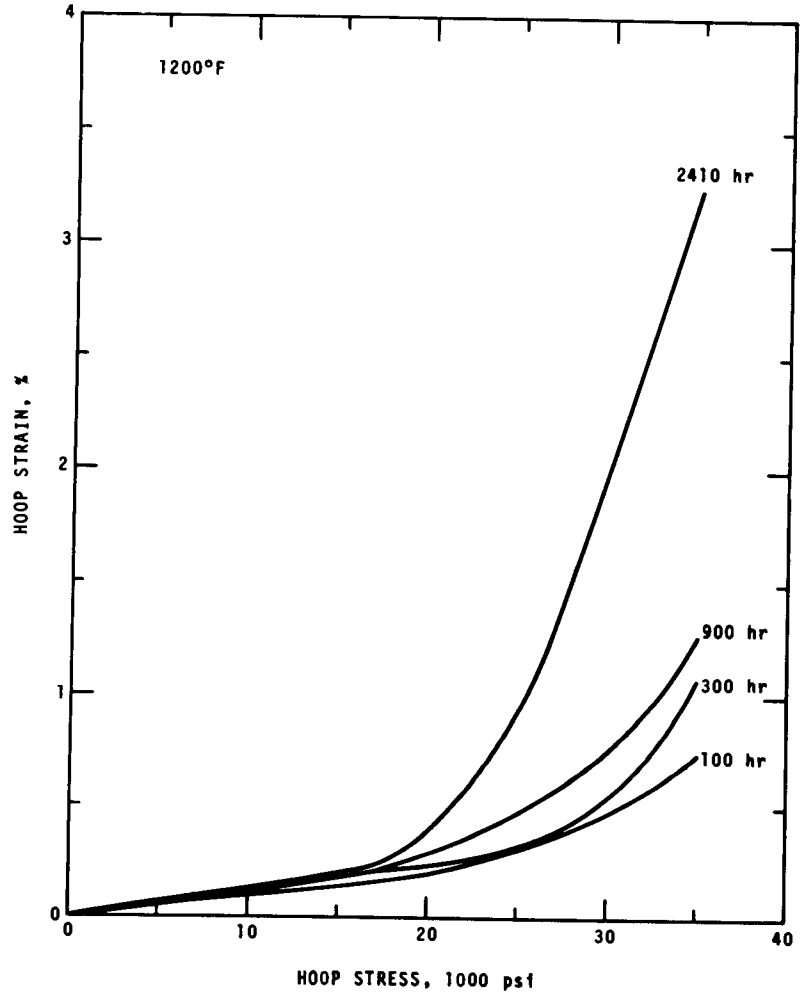

Figure 3.26. Isochronous Strain-Stress Curves for 20% Cold Worked Type 316 Stainless Steel at 1200°F.

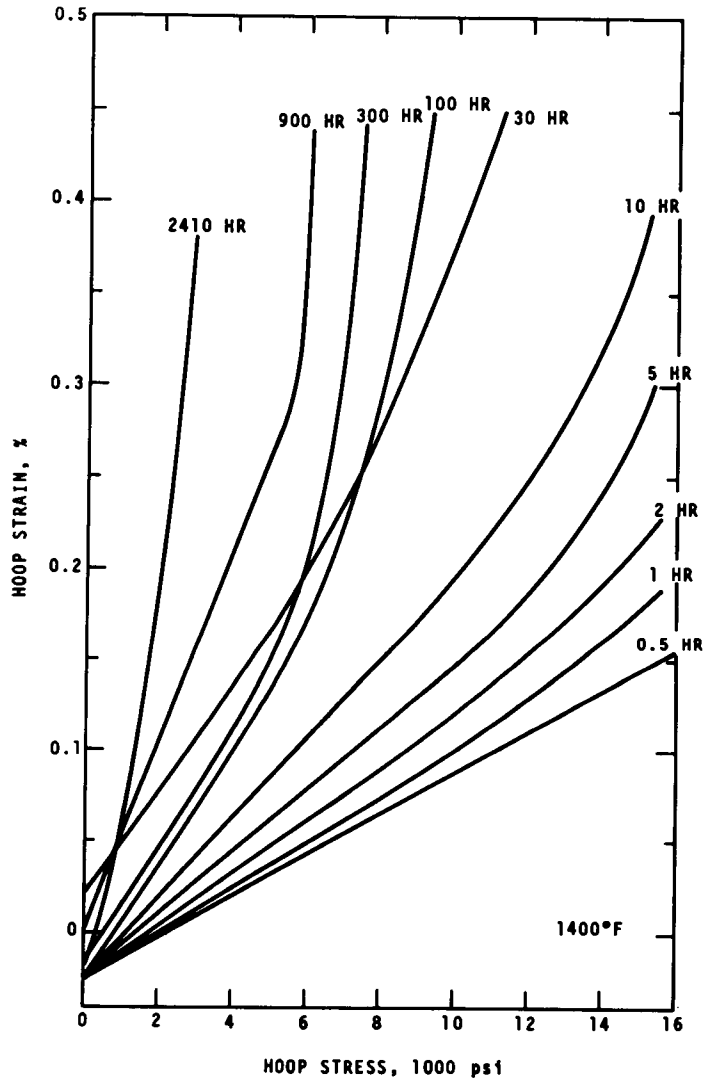

CREEP STRAIN IN 20% C.W. 316 SS TUBES AT 1400°F HEDL 7409-27.11

Figure 3.27. Isochronous Strain-Stress Curves for 20% Cold Worked Type 316 Stainless Steel at 1400°F.

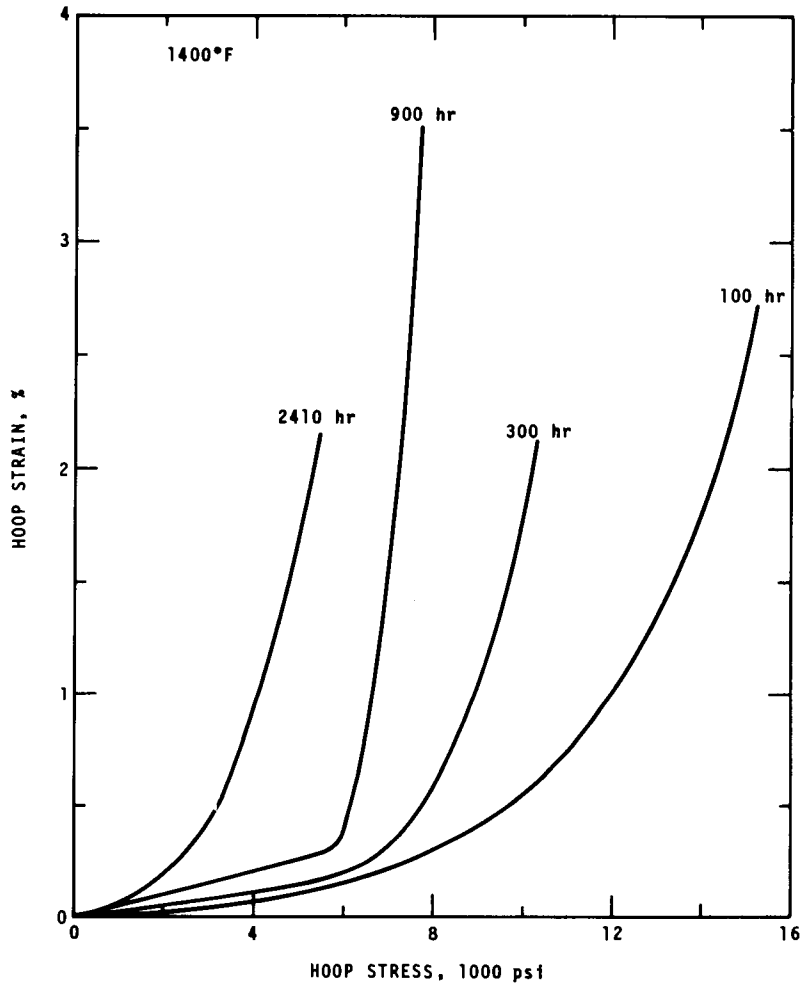

Figure 3.28. Isochronous Strain-Stress Curves for 20% Cold Worked Type 316 Stainless Steel at 1400°F.

dependence encompasses almost the entire stress range at each temperature, but at longer times there is a gradual decrease in the stress range for linear behavior with a stronger stress dependence appearing in the high stress range. Nevertheless, the linear stress dependence is still clearly evident in the 2410-hour results at temperatures of 1200°F and below (Figure 3.21).

Curves of creep strain, ε_c, against time for fixed stress levels were constructed by cross-plotting the results in the isochronous strain-stress plots. These curves, plotted in full logrithmic coordinates, are shown in Figures 3.29-3.32. In constructing these curves, we found that the best overall consistency was obtained by ignoring the 30-hour and 300-hour results at 1000°F, the 30-hour results at 1200°F, and the 900-hour results at 1000°F, but an explanation for possible error in these data sets is unclear. Figures 3.29-3.32, of course, again exhibit well-ordered families of curves, with strain increasing with both stress and temperature.

Three of the high stress tests at 1400°F ruptured during the first 2410 hours of testing. The strain-time data for these tests are shown in Figure 3.33, where the indicated graphical construction appears to provide a reasonable estimate of rupture time. These results are compared to other stress rupture data[24] on the same tubing material obtained at constant pressure (i.e., the specimen is connected to a large reservoir of pressurized gas) in Figure 3.34. Data from the present sealed tube tests indicate somewhat shorter rupture life and lower failure ductilities than results from the constant pressure tests. However, at 1200°F the current results indicate longer rupture times than observed in the constant pressure data (Figure 3.34).

3.4.3.4 Evaluation of Results

In presenting the experimental results, we have considered that the strain measurements reflect only time-dependent creep strain, and that they contain no plastic strain contribution from initial loading. Paxton reported proportional elastic limit stresses in uniaxial tension for the same tubing material used in this study. When his results are converted to hoop stresses using the effective stress correlation, the resulting values are higher than the experimental stresses employed here, indicating plastic

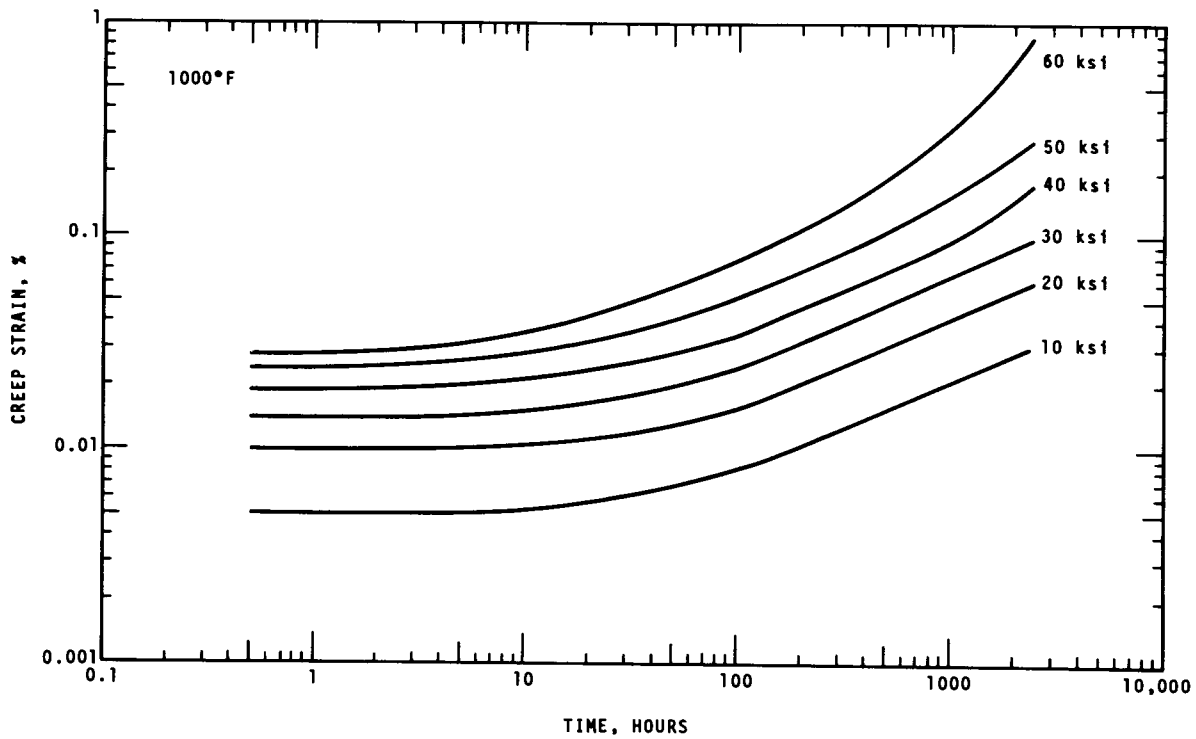

Figure 3.29. Creep Strain-Time Curves for 20% Cold Worked Type 316 Stainless Steel at 1000°F.

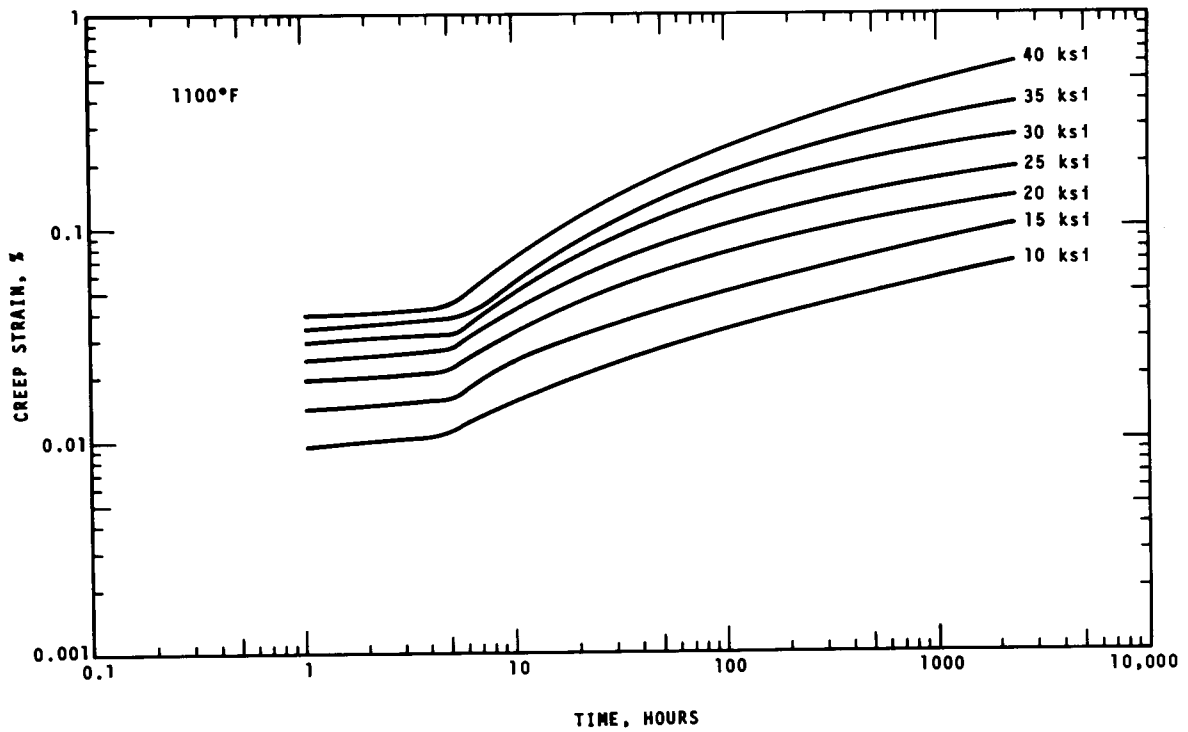

Figure 3.30. Creep Strain-Time Curves for 20% Cold Worked Type 316 Stainless Steel at 1100°F.

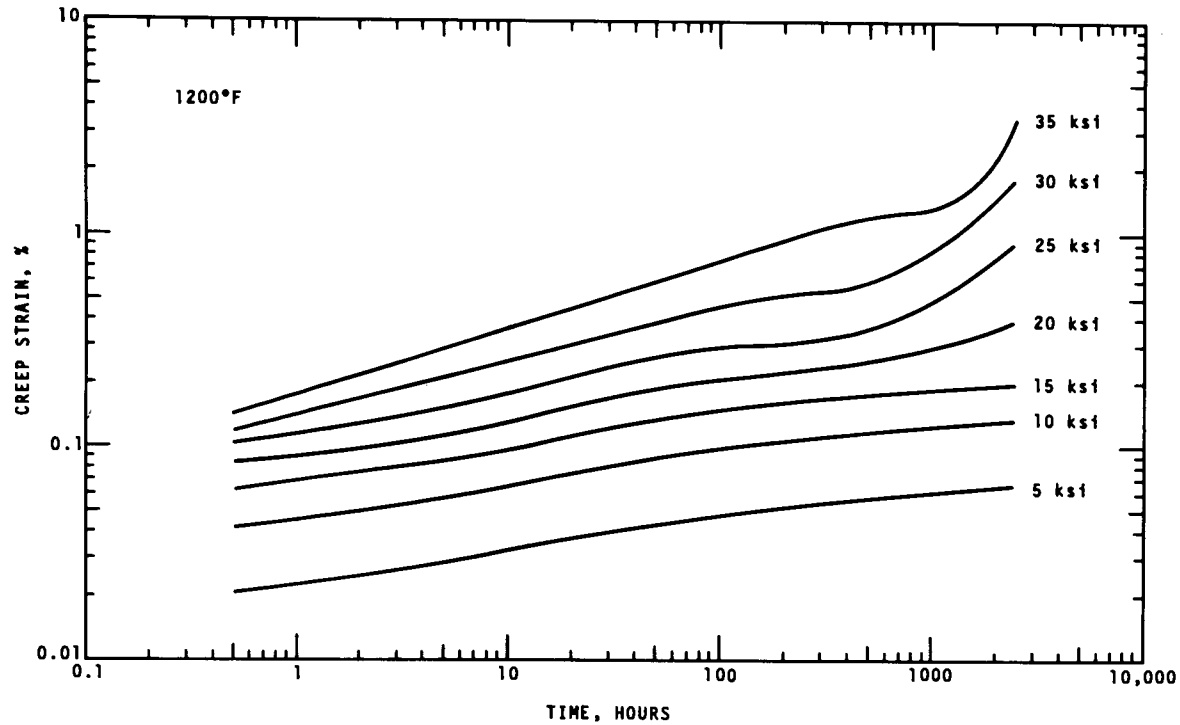

Figure 3.31. Creep Strain-Time Curves for 20% Cold Worked Type 316 Stainless Steel at 1200°F.

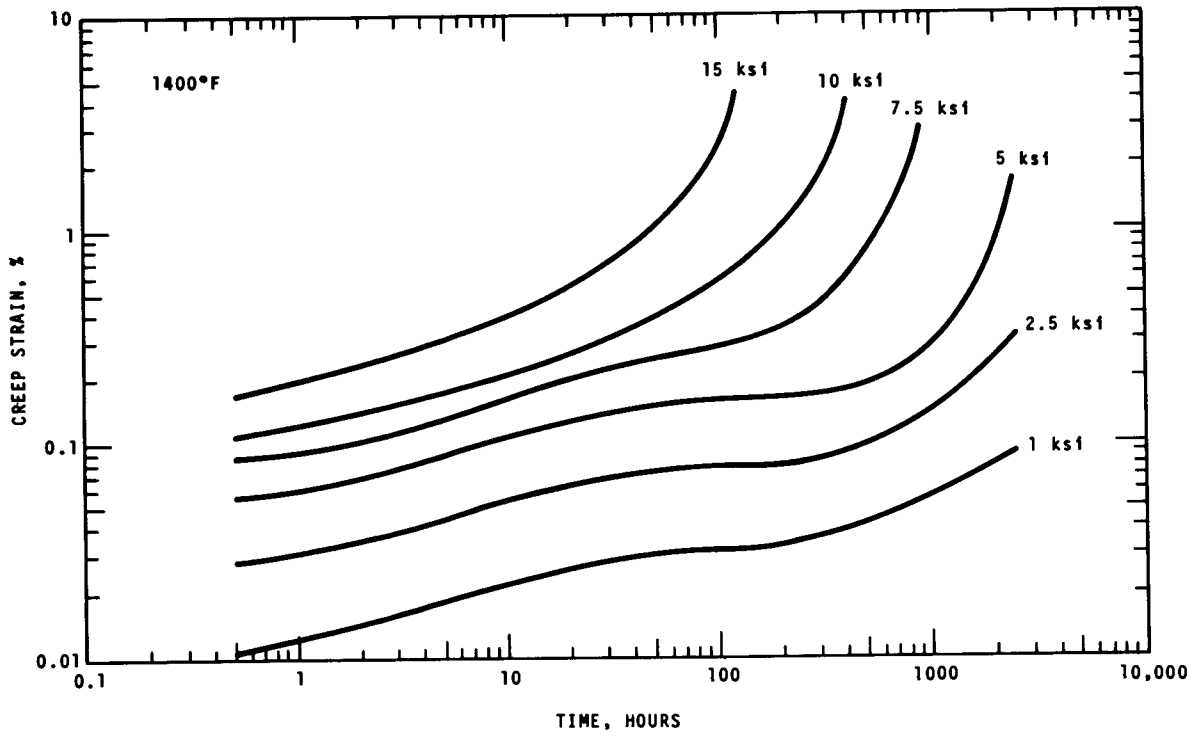

Figure 3.32. Creep Strain-Time Curves for 20% Cold Worked Type 316 Stainless Steel at 1400°F.

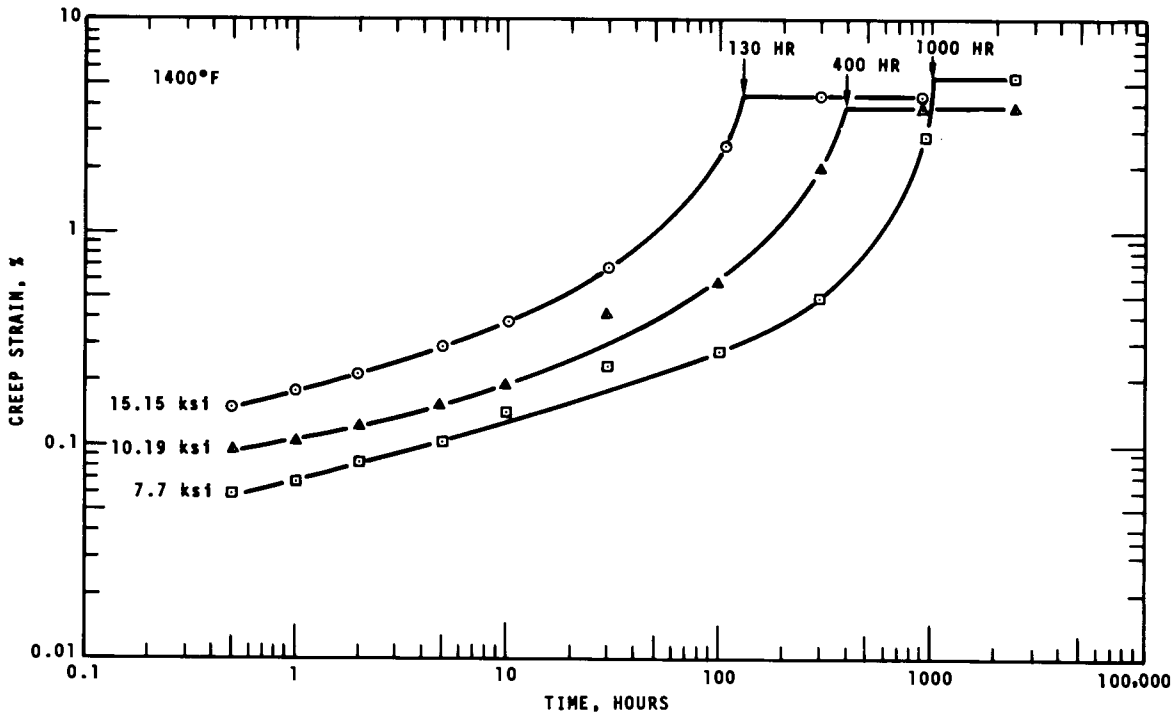

Figure 3.33. Estimation of Rupture Time from Strain-Time Data for 20% Cold-Worked Type 316 Stainless Steel at 1400°F.

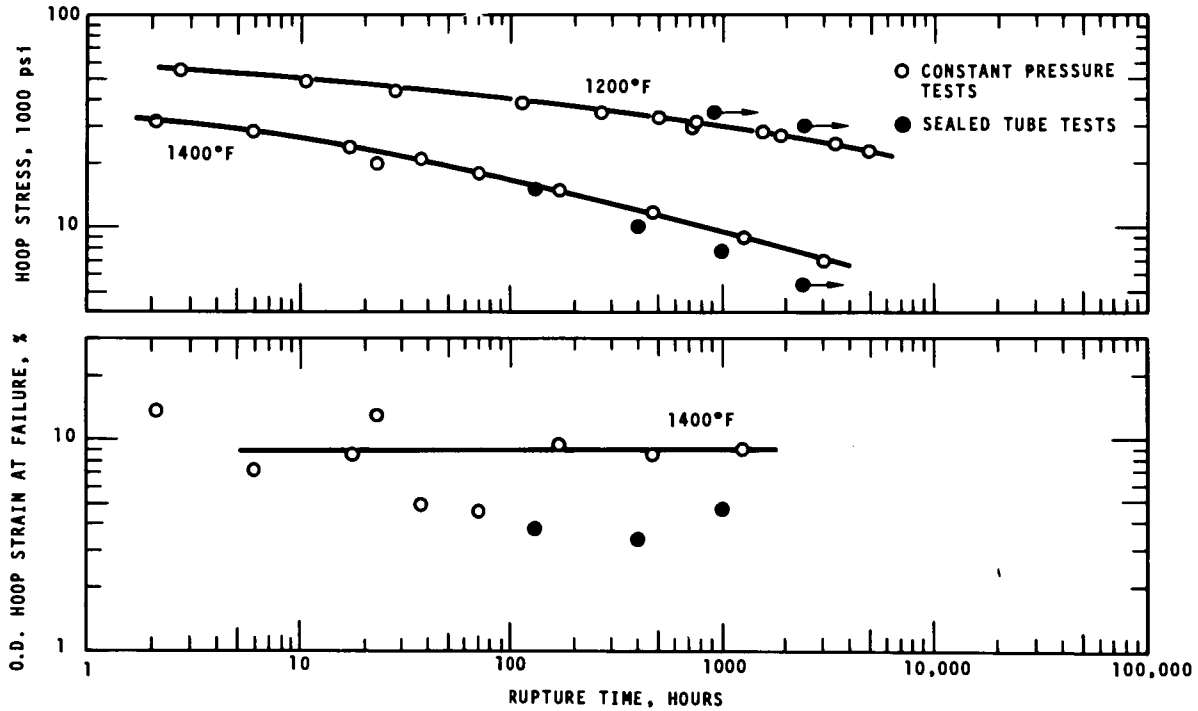

Figure 3.34. Comparison of Constant Pressure and Sealed Tube Rupture Data for 20% Cold Worked Type 316 Stainless Steel.

loading strain is not to be expected. In addition, we find no evidence in the experimental results which is indicative of significant loading strains at the high stresses. We therefore conclude that the present results do properly represent time-dependent creep strain in the absence of plastic loading strains.

One unexpected result revealed by the present study is the linear stress dependence of creep strain in the low stress range. The stress dependence of creep rate is classically considered to be much stronger than linear except at very high temperatures, so a strong stress dependence of creep strain at constant time should be expected. At the present time, we do not have an explanation for the linear stress dependence.

We have compared the present results with the predictions of creep equations reported by Lovell[25]. These creep equations were formulated from results of uniaxial creep rupture tests, and a large portion of the experimental data used in deriving the equations was obtained on the same tubing material employed in the present study. Specific comparison of our data with creep equation predictions are presented in Figures 3.35-340, where creep equations results were converted to hoop stress and hoop strain on the basis of effective stress and strain calculations. In general, the creep equations tend to overpredict the present results, particularly at high stresses. Nevertheless, the essential features of the experimental data are well-represented by the creep equation formulation, and some modification of the stress and temperature dependencies in the creep equations would undoubtedly result in improved numerical agreement between the data and predictions.

Some preliminary study was directed to formulating new analytical creep equations based on the present data. Our initial evaluation indicates that a basic analytical form of the type:

$$\varepsilon = \sigma\,[A + B \ln t] + K\sigma^{n}\, t^{m}$$

may provide a good fit to the experimental data. Future work will be directed to formulating descriptions of the time and temperature dependence of K and the temperature dependence of A, B and n.

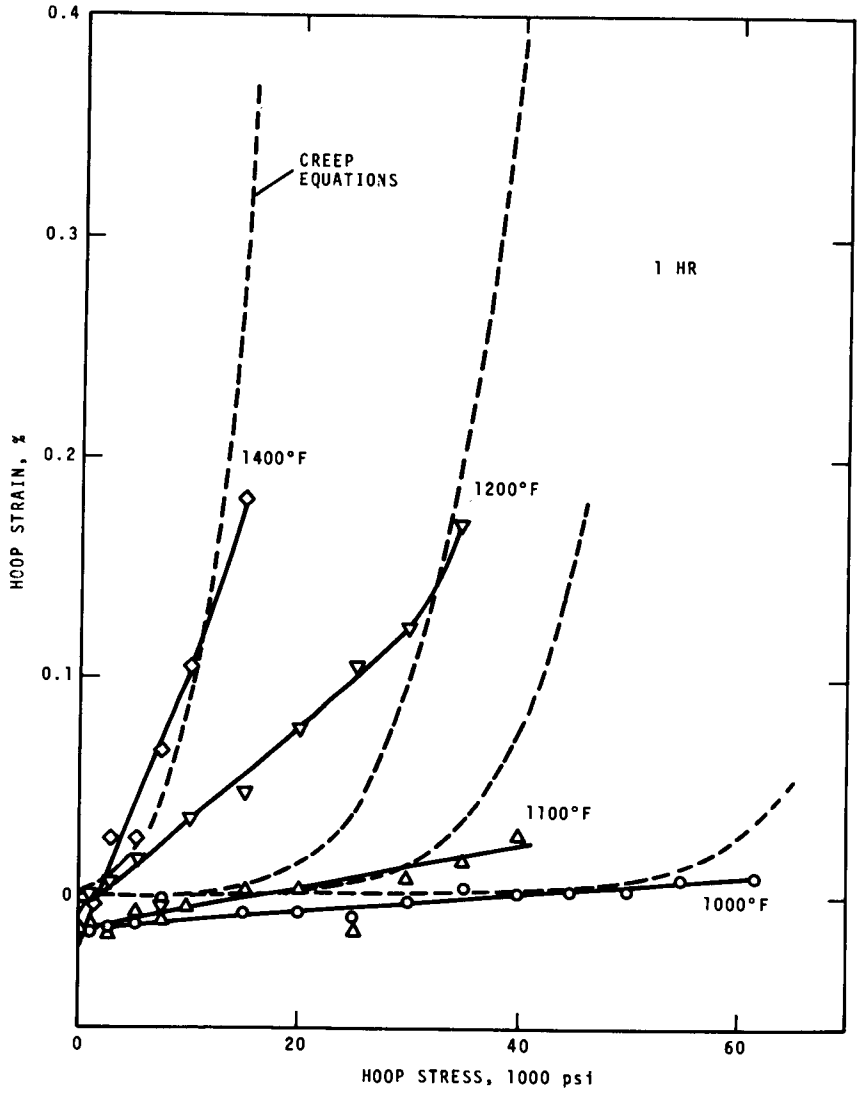

Figure 3.35. Comparison of One-Hour Strain-Stress Curves with Prediction of Lovell's Creep Equation.

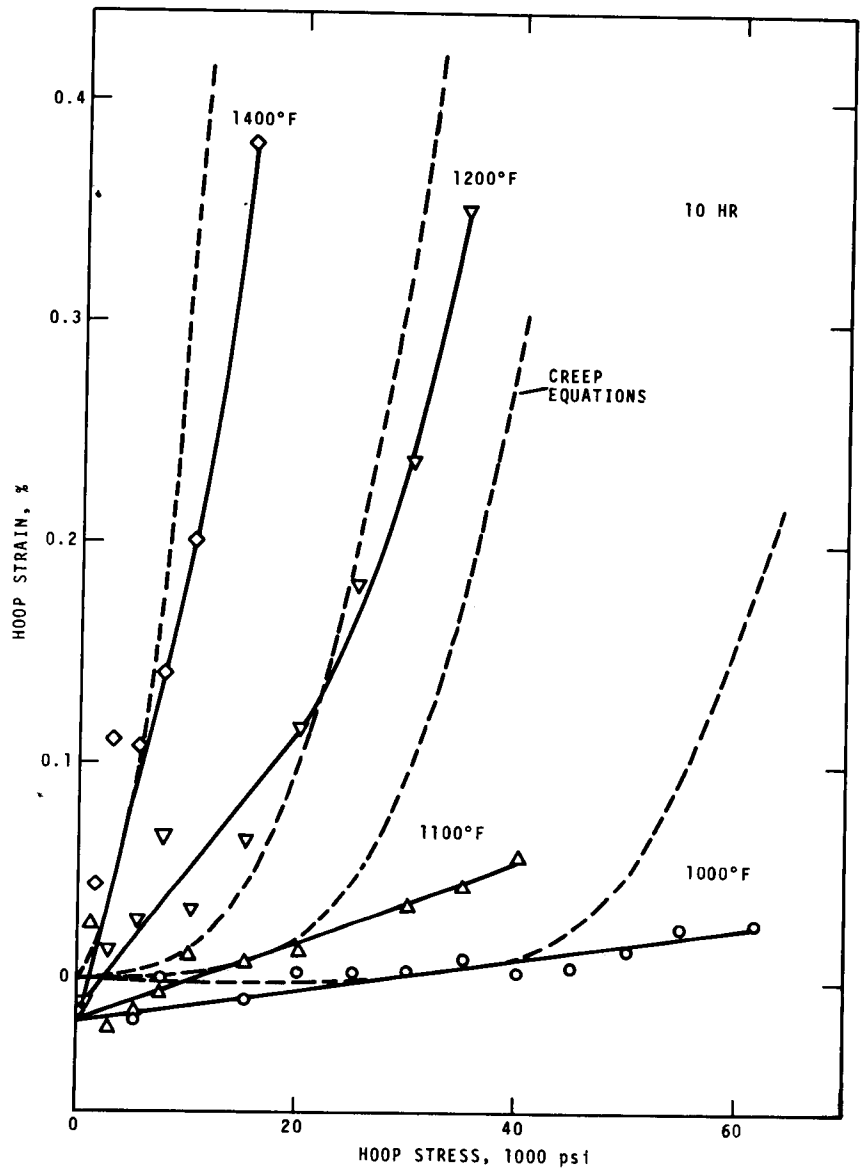

Figure 3.36. Comparison of 10-Hour Strain-Stress Curves with Prediction of Lovell's Creep Equations.

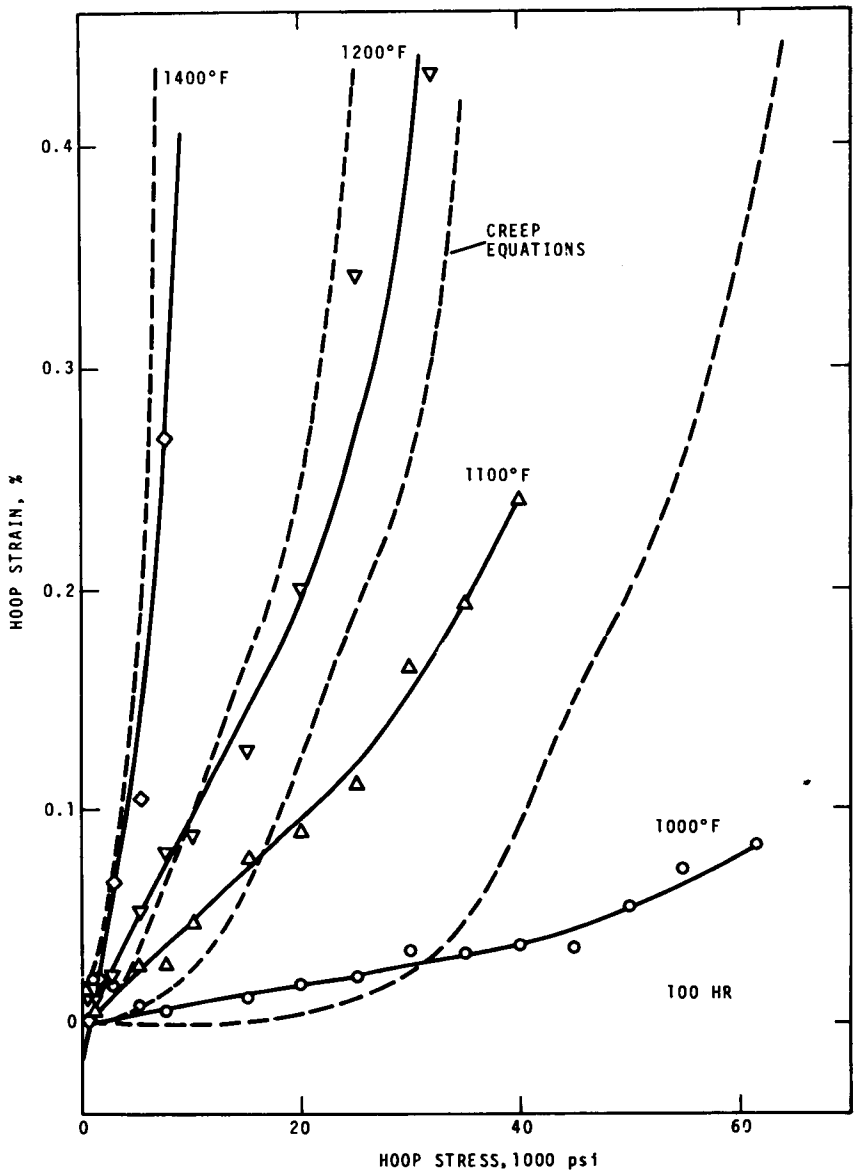

Figure 3.37. Comparison of 100-Hour Strain-Stress Curves with Prediction of Lovell's Creep Equation.

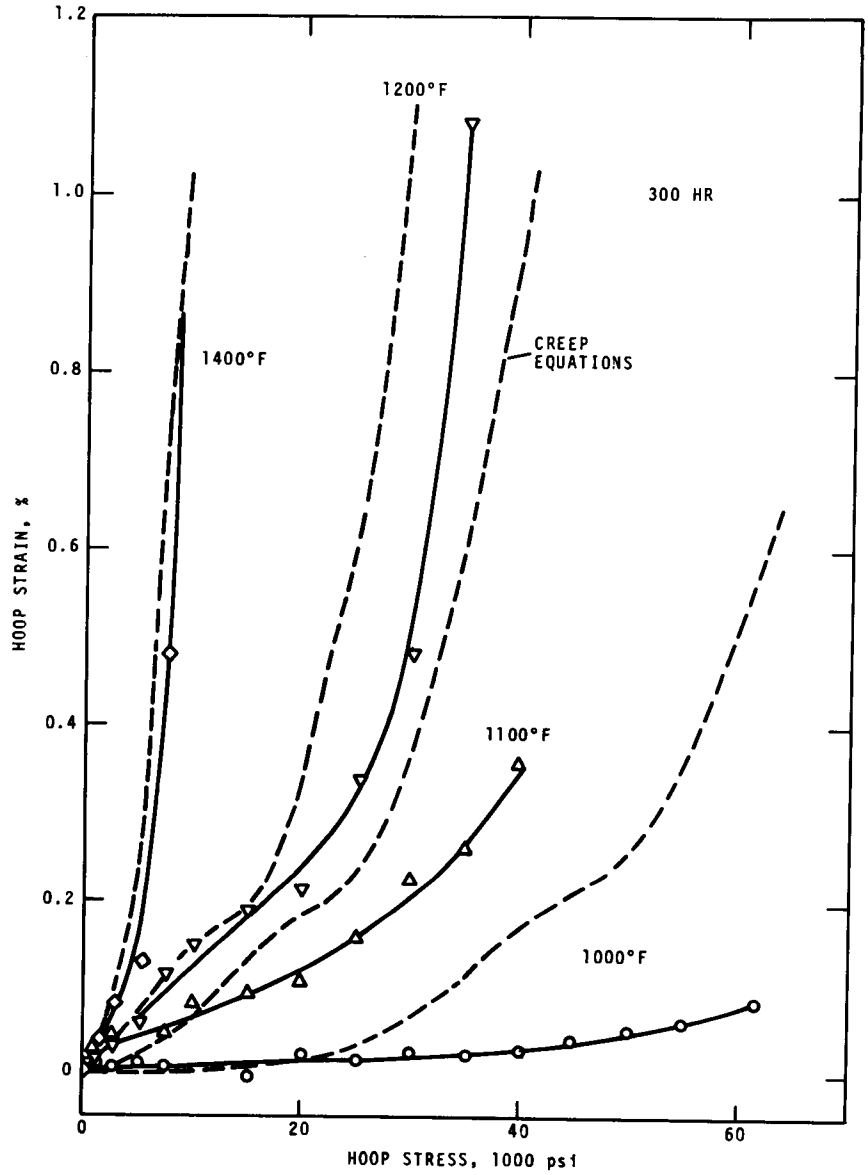

3.38. Comparison of 300-Hour Strain-Stress Curves with Prediction of Lovell's Creep Equations.

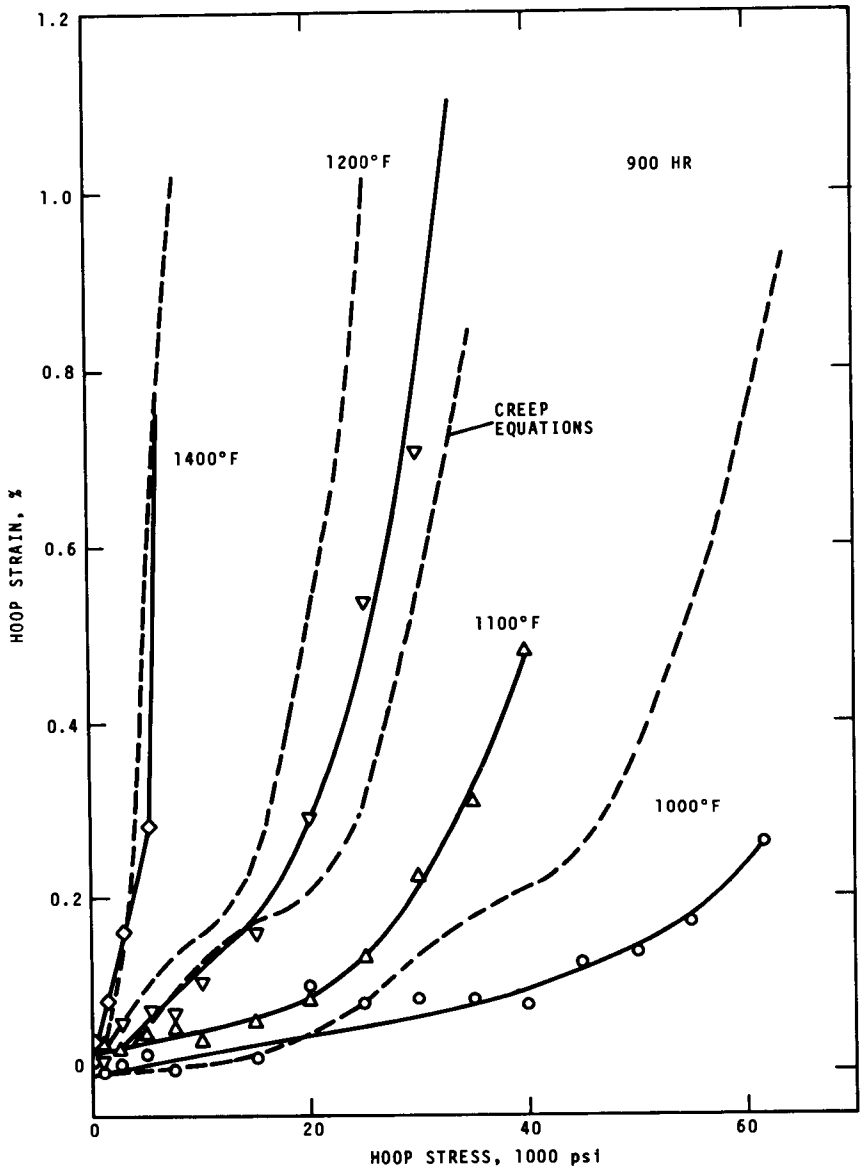

Figure 3.39. Comparison of 900-Hour Strain-Stress Curves with Prediction of Lovell's Creep Equation.

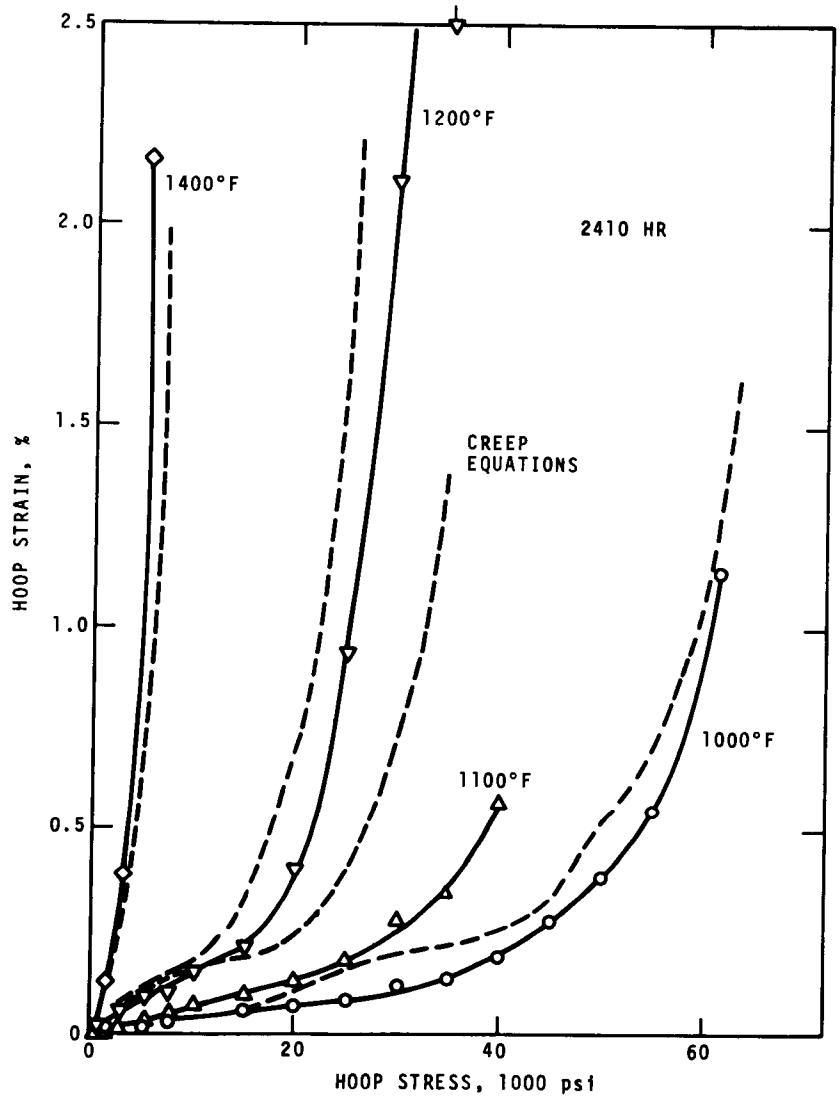

Figure 3.40. Comparison of 2410-Hour Strain-Stress Curves with Prediction of Lovell's Creep Equation.

3.4.3.5 Conclusions and/or Recommendations

Results of the present investigation demonstrate that the measurement of sealed pressurized tube specimens is a valid and useful method of establishing the creep deformation behavior of materials over a wide range of stress, temperature and time parameters.

3.4.3.6 Applications

The thermal creep results obtained here are currently being compared with data from similar tests conducted in EBR-II to assess the irradiation creep component of in-reactor deformation.

3.4.3.7 Expected Achievements

The tests described here are continuing, and the next series of results are expected within about four months.

3.5 REFERENCES

1. *Case 1331-7, Interpretations of ASME Boiler and Pressure Vessel Code,* American Society of Mechanical Engineers, New York, 1972.
2. G. V. Smith, *An Evaluation of the Yield, Tensile, Creep and Rupture Strengths of Wrought 304, 316, 321 and 347 Stainless Steels at Elevated Temperatures, ASTM Data Series 5S2,* American Society for Testing and Materials, Philadelphia, Pennsylvania (1969).
3. W. F. Simmons and J. A. Van Echo, *The Elevated-Temperature Properties of Stainless Steels, ASTM Data Series 5S1,* American Society for Testing and Materials, Philadelphia, Pennsylvania (1965).
4. A. L. Ward, "Austenitic Stainless Steel Weld Materials, A Data Compilation and Review, *HEDL-TME 74-25,* May 1974.
5. P. E. Bennett and G. M. Sinclair, "Parameter Representation of Low Temperature Yield Behavior of Body-Centered-Cubic Transition Metals," *J. Basic Eng.,* Vol. 88, No. 2, June 1966.
6. L. A. James, "The Effect of Frequency Upon the Fatigue-Crack Growth of Type 304 Stainless Steel at 1000°F", *Stress Analysis and Growth of Cracks, ASTM STP-513,* pp. 218-299, 1972.
7. L. A. James, "Fatigue-Crack Propagation Behavior of FTR Outlet Piping Material at 1000°F", *Report HEDL-TME 74-48,* July 1974.

8. L. A. James, "Fatigue-Crack Growth in 20% Cold Worked Type 316 Stainless Steel at Elevated Temperatures", *Nuclear Technology*, Vol. 16, No. 1, pp. 316-322, 1972.

9. L. A. James, "The Effect of Stress Ratio on the Elevated Temperature Fatigue-Crack Propagation of Type 304 Stainless Steel", *Nuclear Technology*, Vol. 14, No. 2, pp. 163-170, 1972.

10. L. A. James, "Estimation of Crack Extension in a Piping Elbow Using Fracture Mechanics Techniques", *Journal of Pressure Vessel Technology, Trans. ASME*, (in press).

11. L. A. James, "The Effect of Temperature Upon the Fatigue-Crack Growth Behavior of Two Nickel-Base Alloys", *Journal of Engineering Materials and Technology, Trans. ASME*, Vol. 95, No. 4, pp. 254-256, 1973.

12. L. D. Blackburn, "Stress-Rupture of 20% Cold-Worked Type 316 Stainless Steel Under Variable Stress Histories," *HEDL Quarterly Technical Report, October-December 1973, Vol. 1, HEDL-TME 73-6.*

13. M. M. Paxton, "Mechanical Properties of Annealed and Cold Worked Type 316 Stainless Steel Fast Reactor Seamless Tubing," *Report HEDL-TME 74-11.*

14. M. M. Paxton and J. J. Holmes, "Recovery and Recrystallization of Prototypic FTR Fuel Cladding--20% C.W. 316 Stainless Steel Tubing," *Report HEDL-TME 71-126.*

15. E. L. Robinson, "Effect of Temperature Variation on the Creep Strength of Steels," *Trans. ASME*, Vol. 60, 1938, pp. 253-259.

16. F. L. Yaggee and Che-Yu Li, "Failure Mechanisms for Internally Pressurized Thin-Wall Tubes and Their Relationship to Fuel-Element Failure Criteria," *Report ANL-7805.*

17. M. M. Abo El Ata and I. Finnie, "A Study of Creep Damage Rules," *Jrnl. of Basic Engr., ASME*, September 1972, pp. 533-543.

18. J. L. Straalsund, R. L. Fish and G. D. Johnson, "Correlation of Transient Test Data With Conventional Mechanical Properties Data", *Nuclear Technology*, to be published.

19. L. D. Blackburn, R. W. Barker and T. K. Billeter, "Low Temperature Creep of 20% Cold Worked Type 316 STainless Steel," *HEDL Quarterly Technical Report--April, May, June 1974, Vol. 1, HEDL-TME 74-2.*

20. F. Garofalo, P. R. Malenoch and G. V. Smith, "The Influence of Temperature on the Elastic Constants of Some Commercial Steels," *Symposium on Determination of Elastic Constants, ASTM STP 129,* American Society for Testing and Materials, Philadelphia, Pennsylvania, 1952, p. 10.

21. D. K. Matlock, W. C. Harrigan, Jr., and W. D. Nix, "On the Importance of Including Recovery in Phenomenological Theories of Plastic Flow in Metals," *Acta Metallurgica, 20* (1972) 661.

22. T. B. Gibbons, J. S. Herd, L. N. McCartney and D. McLean, "Creep Under Varying Load," *Metal Science Journal, 7* (1973) 196.

23. J. T. Venard, "Stress-Rupture Properties of Type 304 Stainless Steel Tubing, *Report ORNL-TM 535,* 1963.

24. M. M. Paxton, R. L. Knecht and T. T. Claudson in *Quarterly Progress Report Irradiation Effects on Reactor Structural Materials, May, June, July 1971, HEDL-TME 71-116,* edited by T. T. Claudson, September 1971, p. HEDL-6.

25. A. J. Lovell, "Creep of 20% C.W. Type 316 Stainless Steel," *Report HEDL-TME 73-65,* October 1973.

4. NAVAL RESEARCH LABORATORY

L. E. Steele

4.1 INTRODUCTION - L. E. Steele

The research program of the NRL, Engineering Materials Division, Thermostructural Materials Branch, includes the study of the behavior of structural materials useful in reactor construction. This report is developed using such data to support the USAEC objective of compiling structural materials properties data for the use in national reactor development programs. The NRL program is sponsored by the Office of Naval Research, the U. S. Atomic Energy Commission, and the U. S. Army Engineer Power Group. The unirradiated materials properties data contributed here include those developed in the course of research for these sponsors in the areas of high temperature materials, radiation damage, and fracture mechanics.

4.2 EFFECT OF HOLD-TIME ON FATIGUE CRACK PROPAGATION IN THERMALLY AGED, ANNEALED AND 25% COLD-WORKED TYPE 304 STAINLESS STEEL - H. H. Smith, D. J. Michel and H. E. Watson

4.2.1 Background

The fatigue crack growth resistance of austenitic stainless steels (SS) is presently being investigated for structural applications at high temperature. The purpose of this work is to determine the effect of high-temperature time-dependent processes such as thermal aging and creep on the fatigue crack growth resistance of these alloys. It is also intended to correlate crack growth behavior with microstructural changes produced by extended elevated temperature exposure.

In a recent report[1], it was shown that prior thermal aging at high temperature altered the fatigue properties of Type 304 SS. As a continuation of that study this report presents results of the combined effect of cyclic (fatigue) and static (creep) loading on crack growth rates in thermally aged Type 304 SS.

4.2.2 Materials and Test Procedures

The effect of the fatigue-creep interaction was investigated at 1100°F (593°C) for solution annealed and 25% cold-worked Type 304 SS

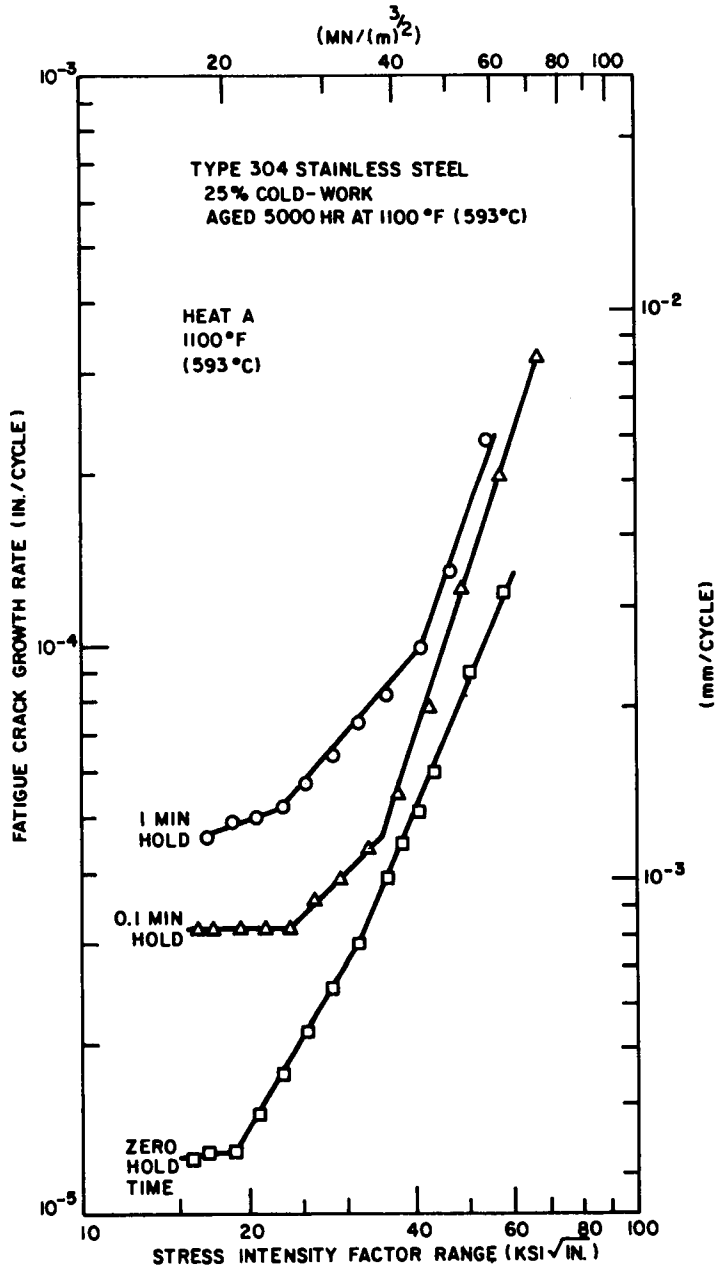

Fig. 4.1 - Effect of hold-time on fatigue crack growth rates in 25% cold-worked and thermally aged Type 304 stainless steel as a function of the stress intensity factor range.

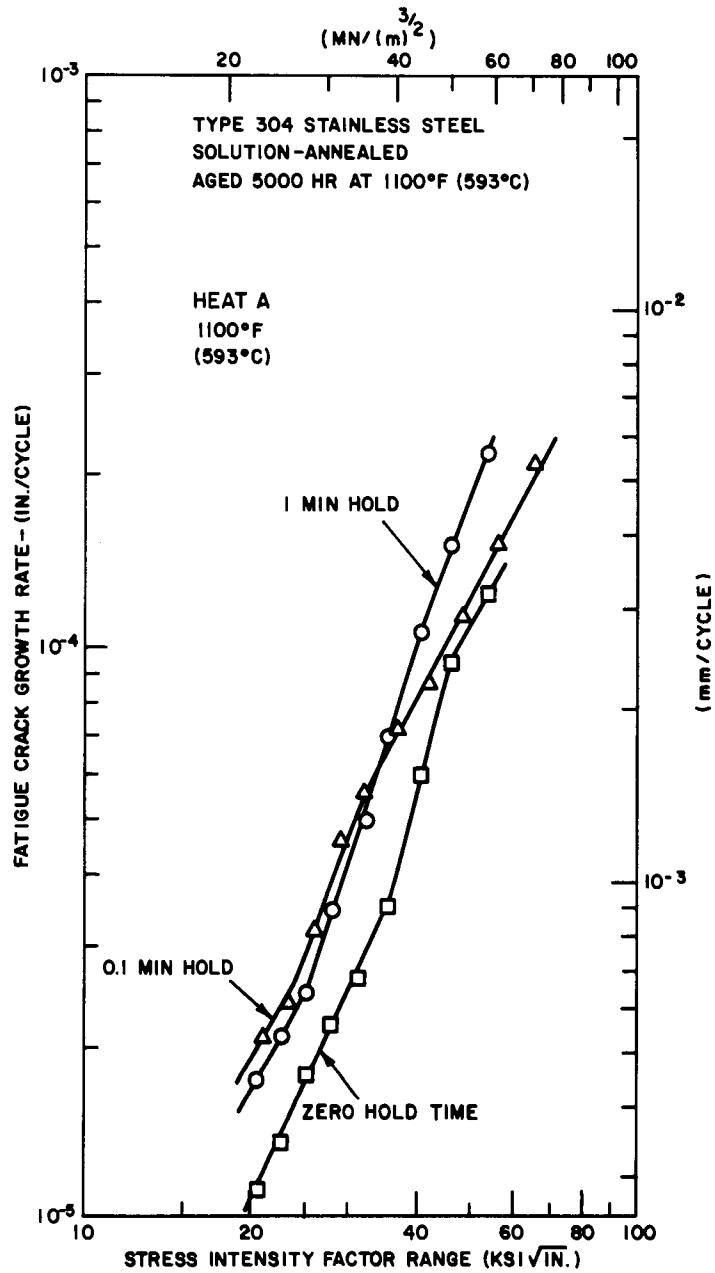

Fig. 4.2 - Effect of hold-time on fatigue crack growth rates in solution annealed and thermally aged Type 304 stainless steel as a function of the stress intensity factor range.

thermally aged at 1100°F (593°C) for 5000 hours. The chemical composition of the material, the specimen design, and the general test procedures have been previously reported[2]. Briefly, single-edge-notched cantilever specimens were cycled under zero-to-tension loading in a saw-tooth mode to a constant maximum load. To study the fatigue-creep interaction, tension loads were imposed on the test specimen during each cycle by holding the load at the maximum value for times of 0.1 and 1.0 minutes before returning to zero load. The loading and unloading rates remained constant for all hold times.

4.2.3 Results and Discussion

The experimental data were analyzed to yield crack growth rate, da/dN, as a function of the stress intensity factor range, ΔK. For the 25% cold-worked, thermally aged Type 304 SS tested at 1100°F (593°C), Fig. 4.1 indicates that a 0.1 minute hold-time increased the initial crack growth rate by nearly a factor of three when compared to the zero hold-time results. The crack growth rates for these two test conditions become convergent toward the midrange of stress intensity factor values, followed by a divergence at higher values of ΔK. Increasing the hold-time to 1 minute resulted in nearly a factor of five increase in initial crack growth rate when compared to the zero hold-time test results. However, at higher values of ΔK, the crack growth rates of the 0.1 and 1 minute hold-time tests become quite similar. Thus, the results in Fig. 4.1 clearly indicate that crack growth rate at 1100°F (593°C) is increased with increasing periods of static loading on a per cycle basis in 25% cold-worked and thermally aged, Type 304 SS. This behavior is not considered to be related to a strain rate effect since the loading rate and the mean cyclic stress was constant for all tests regardless of hold-time.

Figure 4.2 summarizes the results for the effects of hold-time on fatigue crack growth rate in solution annealed, thermally aged Type 304 SS tested at 1100°F (593°C). From Fig. 4.2, it is seen that a 1 minute hold-time increased the crack growth rate by nearly a factor of two over that for the zero hold-time tests for all values of ΔK. However, a different behavior is seen for the 0.1 minute hold-time results. The

data show a slightly higher crack growth rate for the 0.1 minute hold-time specimen when compared with the 1 minute hold-time results for low values of ΔK and a lower crack growth rate for higher ΔK values.

A comparison of the results on the basis of crack extension per unit time (da/dt vs ΔK) shows that the 1 minute hold-time specimens exhibited a markedly lower crack growth behavior than the respective 0.1 minute hold-time specimens. This is contrary to what would be expected if creep provided the dominant contribution to the crack growth process. In that case, the results would show a dependence of crack growth on total time at load rather than on the number of cycles. Since the time dependence was not observed, this strongly suggests that the cyclic rather than the static portion of the present tests produced the majority of the crack growth.

The results given in Figs. 4.1 and 4.2 indicate that the crack growth rates at equivalent hold-times and ΔK values are higher for the cold-worked specimens than for the annealed specimens. These higher crack growth rates for the cold-worked specimens are also reflected in the decreased fatigue lives of these specimens as opposed to the aged, annealed specimens. This fatigue life decrease is particularly large for the 1 minute hold-time tests where the fatigue life of the aged, cold-worked specimens is nearly one-half that of the aged, annealed specimens. This behavior is in contrast with the results from zero hold-time tests on unaged Type 304 SS at lower temperatures where the crack growth rates for cold-worked specimens were equal to or lower than those for annealed specimens.

Comparison of the present results with those from previous hold-time tests[3] conducted using unaged solution annealed Type 304 SS at 1100°F (593°C) shows that thermal aging has decreased the crack growth rate for the 0, 0.1, and 1 minute hold-time tests by nearly a factor of two at all except the higher ΔK values where the growth rates were nearly the same. Other work[4] has shown that thermal aging at 1000°F (538°C) and 1200°F (649°C) reduces the fatigue crack growth rate in solution annealed Type 304 SS tested at 1000°F (538°C) where no hold-time was considered. However, one hold-time test conducted during that study[4] suggested that thermal aging does not affect crack growth behavior in contrast to the

substantial effect observed in the present study.

Since no hold-time results are presently available for unaged 25% cold-worked Type 304 SS, a direct comparison with the present hold-time results for thermally aged material are not possible. However, comparison with hold-time results for 20% cold-worked Type 316 SS[5] suggests that thermal aging may decrease the crack growth rate, especially for hold-times of 0.1 and 1.0 minute.

In the absence of studies which provide detailed microstructural evidence, it is not possible to determine which mechanism is responsible for the observed crack growth behavior for the solution annealed and cold-worked, thermally aged specimens. Certainly, precipitate formation during aging has contributed to the present results. In addition, hardness measurements indicate that aging has also produced bulk softing in both material conditions. For the annealed SS, hardness at the crack tip appears to be a function of the number of cycles suggesting that the material is either work hardening or stress induced precipitation is taking place during cycling. No such relationship of hardness to number of cycles was observed for the cold-worked steel.

The fatigue specimens from this study are presently being examined metallographically to determine the relationship between the observed crack growth behavior and precipitate formation. As for the effect of hold time, fractographic studies of the specimens will be performed to see if there is a tendency for the mode of fracture to change with increasing hold times as observed by others[4] under different conditions. These results will be presented in a future report.

4.3 REFERENCES

1. D. J. Michel, H. H. Smith, and H. E. Watson, "Fatigue Crack Growth in Thermally-Aged Types 304 and 316 Stainless Steel Plate," in Mechanical Properties Test Data for Structural Materials, Quarterly Progress Report for period ending July 31, 1974, ORNL-4998, Oak Ridge National Laboratory, Oak Ridge, Tennessee, September 1974, pp. 103-110.
2. P. Shahinian, H. E. Watson, and H. H. Smith, "Effect of Neutron Irradiation on Fatigue Crack Propagation in Types 304 and 316 Stainless Steel at High Temperature," NRL Report 7446, Naval Research Laboratory, July 21, 1972.
3. P. Shahinian, Naval Research Laboratory, unpublished results (1973).
4. L. A. James, "Effect of Thermal Aging Upon the Fatigue Crack Propagation of Austenitic Stainless Steels," HEDL-SA-636, submitted for publication 1973; also HEDL-TME-73-25, Hanford Engineering Development Laboratory, March 1973.
5. P. Shahinian, "Effect of Hold-Time on Fatigue Crack Propagation in 20% Cold-Worked Stainless Steel," in Irradiation Effects on Reactor Structural Materials, QPR, 1 Feb-30 Apr 1973, NRL Memorandum Report 2595, Naval Research Laboratory, May 15, 1973, p. 1-3; also HEDL-TME-47, Hanford Engineering Development Laboratory, June 1973.

5. OAK RIDGE NATIONAL LABORATORY

W. R. Martin

5.1 INTRODUCTION

The ORNL mechanical properties effort comprises several programs. The program Mechanical Properties and Behavior for Structural Materials deals with materials of general applicability to the LMFBR program. Other programs are concerned with the mechanical properties of weldments in LMFBR components, the specific materials of interest for LMFBR steam generators, collection and correlation of mechanical data needed for design of high-temperature LMFBR systems, and materials for the primary circuit and steam generators of HTGR systems.

5.2 MECHANICAL PROPERTIES AND BEHAVIOR FOR STRUCTURAL MATERIALS — C. R. Brinkman

The objective of this program is to collect mechanical property data and material behavior for LMFBR structural and component materials. Included in the scope of this effort are the following: (1) basic tensile, creep, creep-rupture, and relaxation base-line data that are directly applicable to design criteria and methods for types 304 and 316 stainless steel reference heats and cyclic stress-strain tests performed with emphasis on loading and history effects, (2) find the variations in properties for several heats of types 304 and 316 stainless steel to allow establishment of minimum and average values of specific properties and the equation parameters required for design purposes. This work will include determination of property variation of samples from different mill products within a given heat of stainless steel.

5.2.1 Mechanical Property Characterization of Type 304 Stainless Steel Reference Heat — V. K. Sikka, E. Lee, and E. B. Patton

5.2.1.1 Creep and Rupture Properties of the 2-in. (51-mm) Plate of Reference Heat

Several creep tests on 2-in. (51-mm) plate of reference heat of type 304 stainless steel (9T2796) continued. The test times and creep

strains for all tests have been updated and are summarized in Table 5.1. Three creep tests have exceeded test times over 16,200 hr, and two other tests have exceeded 14,200 hr. All creep tests are progressing smoothly and will be continued during the next quarter.

One test at 593°C (1100°F) and 16 ksi (110 MPa) ruptured recently after 14,647 hr. The creep curve for this test is shown in Fig. 5.1. The strain at rupture for this test was 5.84%, the reduction of area at rupture 5.51%, and the creep strain 3.55%. Time to the onset of third stage and strain at that point were 14,200 hr and 2.075%, respectively.

Time to rupture for this test has been plotted in Fig. 5.2 along with previously reported[1] data, and it can be noted that the new data point falls on the previously drawn line through short-time tests. The stress-rupture plots in Fig. 5.2 have been compared with minimum value curves from Code Case 1592. The stress-rupture curves through ORNL data show divergence at longer test times from the minimum value curves from Code Case 1592. The Code values were conservative with respect to lifetime at all temperatures.

Minimum creep rate and time to rupture for the test in Fig. 5.1 were used to calculate the previously defined[1] stable creep strain ($e_s = t_r\dot{\varepsilon}_m$). The stable creep strain was 0.98% and has been plotted in Fig. 5.3. It can be noted that the stable creep strain for this test compared well with the line calculated from the equation

$$e_s = \dot{\varepsilon}_m t_r = C t_r^{-k} \quad . \tag{1}$$

Values of constants C and k have been reported previously.[1] The stable creep strain data on the longest ruptured creep test for the reference heat are compared with HEDL data[2] in Fig. 5.4. It is interesting to note that the stable creep strain decreases very sharply at 593°C (1100°F) with increasing time to rupture and has already reached a value approximating 1% (0.98%) at about 20,000 hr. It will be interesting to see what happens at a test time even greater than 14,647 hr, for which data will probably become available in the next reporting period.

Table 5.1. Creep Tests on Type 304 Stainless Steel Reference Heat 9T2796 2-in.-thick (51-mm) Plate[a]

Test	Temperature		Stress		Time in Test	Strain, %		Ratio of Creep Stress to Yield Stress[b]	Comments[c]
	(°C)	(°F)	ksi	MPa	(hr)	Loading	Creep		
11595	427	800	20.0	138	11,436	2.67	0.05989	1.57	
12368	427	800	18.0	124	8,411	1.91	0.00967	1.42	
12472	427	800	16.0	110	7,543	1.17	0.05178	1.26	
12570	427	800	14.9	97	7,215	0.83	0.03544	1.10	
11569	482	900	20.0	138	11,561	3.27	0.1082	1.70	
12375	482	900	18.0	124	8,338	2.40	0.032	1.53	
11675	482	900	16.0	110	2,451	1.48	0.032	1.36	Discontinued
11693	482	900	14.0	97	2,202	0.92	0.14	1.19	Discontinued
11830	482	900	12.0	83	1,682	0.35	0.04	1.02	Discontinued
13152	482	900	10.0	69	5,395	0.089	0.08467	0.85	
13020	482	900	10.0	69	6,080	0.085	0.03056	0.85	
10489	538	1000	20.0	138	16,450	3.80	0.593	1.80	
12250	538	1000	18.0	124	8,915	2.62	0.2663	1.62	
11625	538	1000	16.0	110	11,315	1.79	0.2173	1.44	
10491	538	1000	14.0	97	16,470	1.16	0.0391	1.26	
12444	538	1000	14.0	97	7,886	1.18	0.18789	1.26	
12445	538	1000	14.0	97	4,498	1.17	0.090	1.26	Discontinued
11568	538	1000	12.0	83	11,560	0.53	0.0819	1.08	
11626	538	1000	10.0	69	11,316	0.071	0.09267	0.90	
11641	538	1000	8.0	55	3,170	0.040	0.027	0.72	Discontinued
10853	593	1100	18.0	124	4,547	2.84	5.94	1.65	Ruptured
10852	593	1100	16.0	110	14,647	2.29	3.55	1.47	Ruptured
13947	593	1100	16.0	110	1,218	2.13	0.675	1.47	
10554	593	1100	14.0	97	8,710	1.40	0.65	1.28	Discontinued

Table 5.1. (Continued)

Test	Temperature (°C)	Temperature (°F)	Stress ksi	Stress MPa	Time in Test (hr)	Strain, % Loading	Strain, % Creep	Ratio of Creep Stress to Yield Stress[b]	Comments[c]
11596	593	1100	12.0	83	11,412	0.52	0.4039	1.10	
10490	593	1100	10.0	69	16,445	0.22	0.3983	0.92	
13710	593	1100	10.0	69	2,010	0.096	0.156	0.92	Discontinued
14163	593	1100	10.0	69	405	0.228	0.041	0.92	
11227	593	1100	8.0	55	6,103	0.041	0.080	0.73	Discontinued
12459	593	1100	5.0	34	7,630	0.024	0.08756	0.46	
10855	649	1200	16.0	110	304	2.41	12.0	1.57	Ruptured
10854	649	1200	14.0	97	761	1.60	13.0	1.37	Ruptured
11563	649	1200	12.0	83	2,674	0.59	13.4	1.18	Ruptured
11226	649	1200	10.0	69	7,278	0.18	7.0	0.98	Ruptured
10851	649	1200	8.0	55	14,625	0.044	1.5183	0.78	
12255	649	1200	5.0	34	992	0.030	0.08	0.49	Discontinued
12443	649	1200	5.0	34	7,585	0.024	0.11889	0.49	
12460	649	1200	3.0	21	7,601	0.020	0.1910	0.29	
10856	704	1300	10.0	69	568	0.067	15.6	0.90	Ruptured
11562	704	1300	10.0	69	653	0.12	22.5	0.90	Ruptured
11222	704	1300	8.0	55	2,760	0.031	16.4	0.72	Ruptured
12254	704	1300	5.0	34	8,780	0.030	1.35	0.45	
12461	704	1300	3.0	21	7,600	0.018	0.26756	0.27	
12462	704	1300	2.0	14	7,560	0.010	0.2104	0.18	

[a]Annealed 0.5 hr at 1093°C before testing. All tests loaded at a strain rate of 0.004/min.

[b]Yield stresses used in this ratio were 12,700 psi (88 MPa) at 427°C (800°F), 11,800 psi (81 MPa) at 482°C (900°F), 11,100 psi (77 MPa) at 538°C (1000°F), 10,900 psi (75 MPa) at 593°C (1100°F), 10,200 psi (70 MPa) at 649°C (1200°F), 11,100 psi (77 MPa) at 704°C (1300°F).

[c]Unless otherwise noted, tests in progress.

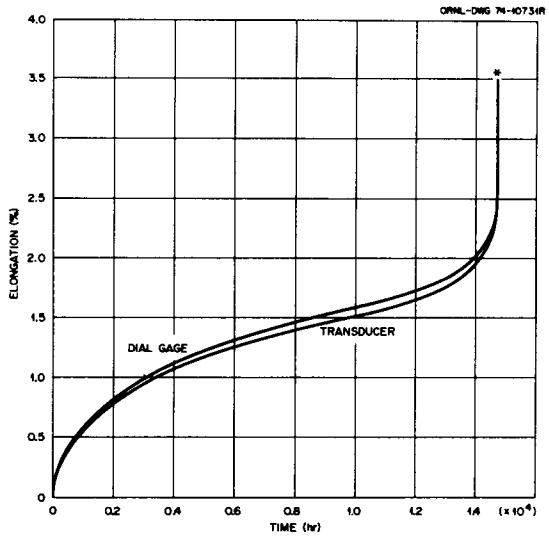

Fig. 5.1. Creep Curve for Reference Heat 2-in. (51-mm) Plate of Type 304 Stainless Steel, Tested at 593°C (1100°F) and 16 ksi (110 MPa).

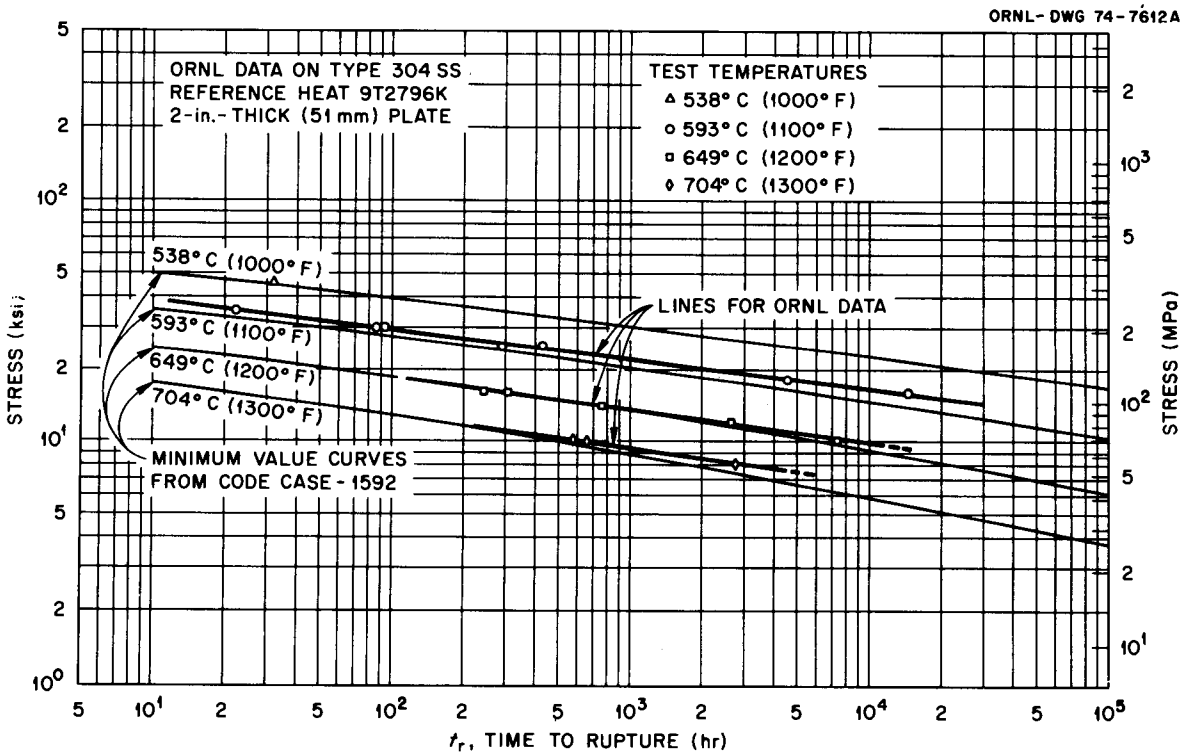

Fig. 5.2. Stress Versus Time to Rupture for Reference Heat 9T2796K of Type 304 Stainless Steel, Compared with Code Case 1592 Minimum Values.

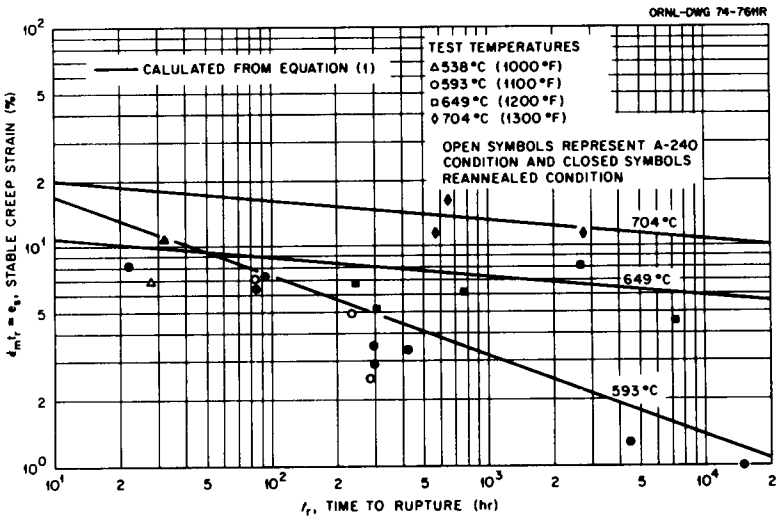

Fig. 5.3. Stable Creep Strain Versus Time to Rupture for Reference Heat 9T2796K 2-in. (51-mm) Plate of Type 304 Stainless Steel.

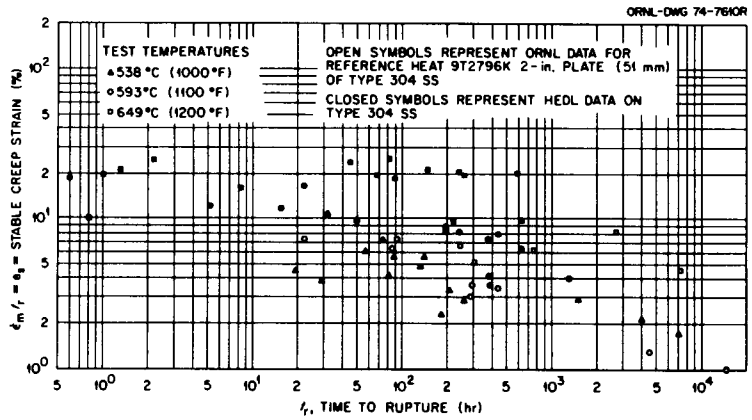

Fig. 5.4. Stable Creep Strain Versus Time to Rupture; Comparison Between ORNL and HEDL Data.

In the earlier report[1] total elongation at rupture and reduction of area were compared with results published by Kirsch.[3] During this quarter, a 14,647-hr test value has become available on the reference heat and one at 22,622 hr on heat 187 of type 304 stainless steel. Both tests are the longest time tests available for their respective heats and probably longer than those published by Kirsch. We have compared our total elongation and reduction of area of both these heats with data by Kirsch and ORNL in Fig. 5.5. It is to be noted that the ORNL long-term data for a test temperature of 593°C (1100°F) compares fairly well with results of Kirsch.

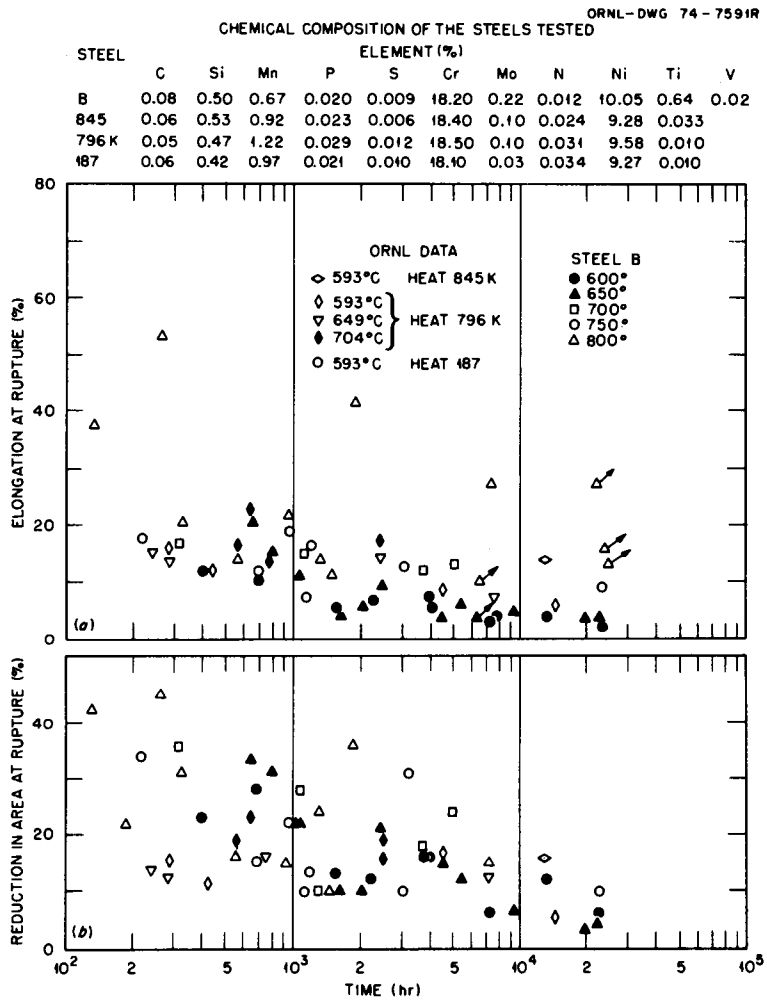

Fig. 5.5. Ductility of Reference Heat of Type 304 Stainless Steel Compared with Data Reported by Kirsch, *Joint Intern. Conf. Creep*, The Institute of Mechanical Engineers, London, 1963, pp. 1-81–1-89.

Work will continue in this area and more results will be plotted as they become available.

5.2.1.2 Uniaxial Tensile Tests Following Periods of Creep

Eight more creep tests were completed from the test matrix and are represented by closed symbols in Table 5.2. The creep data on discontinued specimens are presented in Table 5.3. Tensile data on the specimens with and without creep prestrain are listed in Table 5.4. Data at present are not sufficient for any meaningful analysis. Similar testing will continue during next quarter.

Table 5.2. Uniaxial Tensile Tests Following Periods of Creep on Reference Heat of Type 304 Stainless Steel

ORNL-DWG 74-7614R

STRESS ksi (MPa)	TEMPERATURE °C (°F)			
	482 (900)	538 (1000)	593 (1100)	649 (1200)
5 (34)			○ △ □ ◊	○ △ □ ◊
7 (48)		○ △ □ ◊	○ △ □ ◊	○ △ □ ◊
10 (69)	○ △ □ ◊	○ △ □ ◊	○ △ □ ◆	○ △ □ ◊
-10 (-69)	○ △ □ ◊	○ △ □ ◊	○ △ □ ◊	○ △ □ ◊
12 (83)	○ △ □ ◊	○ △ □ ◊	○ △ □ ◊	● △ □ ◆
12 (83)	▽	▽	▽	
16 (110)	○ △ □ ◊	○ △ □ ◊	○ △ ■ ◊	● ▲ ◘ ◆
16 (110)	▽	▽	▽	
20 (138)	○ ▲ □ ◊	● △ □ ◊	● ▲ □ ◊	
20 (138)	▽	▽	▽	

SYMBOLS ARE FOR DIFFERENT CREEP TEST PERIODS

○= 100, △= 500, = 2000, ◊= 10,000 hr.

▽= TEST DURATIONS ESTABLISHED WHEN THE TOTAL STRAINS AT THE END OF CREEP PERIODS ARE EQUAL TO THOSE FOR THE 10 ksi TESTS AT THE SAME TEMPERATURE AND WITH A 10,000 hr CREEP PERIOD.

CLOSED SYMBOL REPRESENTS A COMPLETED CREEP TEST. HALF CLOSED SYMBOL REPRESENTS TEST, THAT WILL RUPTURE OR HAVE RUPTURED BEFORE DISCONTINUING PERIOD.

Table 5.3. Creep Data on the Reference Heat 9T2796K[a] of Type 304 Stainless Steel Before Tensile Test

Test	Temperature		Stress		Duration (hr)	Strain, %		Creep State
	(°C)	(°F)	(ksi)	(MPa)		Creep	Total	
11693[b]	482	900	14	97	2690.0	0.14	1.06	2
11675[b]	482	900	16	110	2451.0	0.032	1.51	2
12445[b]	538	1000	14	97	4498.0	0.09	1.26	1
13996	538	1000	20	138	97.5	0.056	4.43	2
13710[b]	593	1100	10	69	2009.6	0.06	0.156	2
13755	593	1100	20	138	100.0	0.536	4.24	2
13946	593	1100	20	138	99.4	0.545	4.17	2
13853	593	1100	20	138	500.0	1.20	4.92	2
13951	649	1200	12	83	98.6	0.59	1.528	2
13824	649	1200	16	110	102.2	2.80	5.11	2
13764[c]	649	1200	16	110	244.9	14.53	16.95	Rupture

[a]Annealed for 0.5 hr at 1093°C (2000°F) before testing.

[b]Specimens taken from the center of 2-in. plate. All other specimens were from the bottom level of the plate.

[c]Test was intended to be discontinued after 500 hr.

Table 5.4. Tensile Properties on Reference Heat 9T2796K[a] of Type 304 Stainless Steel After Creep Tests

Tensile Test	Creep Test	Temperature		Proportional Limit		Strength, ksi(Mpa)		Elongation, %		Reduction of Area (%)
		(°C)	(°F)	(ksi)	(MPa)	0.2% Yield	Ultimate Tensile	Uniform	Total	
13978		482	900	6.5	45	11.8(81)			42.2	66.8
11798[b]		482	900	6.1	42	12.2(84)	55.8(385)	46.4	51.5	71.4
13701	11693	482	900	7.2	50	15.8(109)	57.3(395)	38.0	40.7	63.2
13702	11675	482	900	12.4	85	21.9(151)	55.8(385)	33.8	39.5	67.9
13979		538	1000	7.3	50	10.6(73)	51.9(358)	37.6	42.5	63.6
12163[b]		593	1100			9.46(65)	47.2(325)	37.8	39.1	66.3
13980		593	1100	5.89	41	10.2(70)			43.4	67.8
13983	13710	593	1100	4.4	30	14.3(99)	46.8(323)	34.1	40.1	61.9
13982	13946	593	1100	13.9	96	22.3(154)	49.0(338)	30.6	34.0	53.2
13984	13853	593	1100	19.3	133	24.5(169)	47.5(328)	20.2	22.5	42.4
13981		649	1200	4.5	31	9.5(66)	39.4(272)	32.4	41.5	47.2
14149	13951	649	1200	13.0	90	16.0(110)	40.1(276)	31.0	40.3	42.5
13869	13824	649	1200	19.5	134	21.1(145)	39.8(274)	20.2	25.8	35.0
14150[c]	13996	649	1200	14.9	103	19.9(137)	40.8(281)	27.2	36.9	37.3

[a]Annealed for 0.5 hr at 1093°C (2000°F) before creep and tensile testing.

[b]Specimen gage length-to-diameter ratio = 5 for these specimens. All other specimens have a gage length-to-diameter ratio = 9.

[c]Prior creep temperature was 538°C (1000°F) rather than the tensile temperature 649°C (1200°F).

5.2.2 Heat-to-Heat Variation of Mechanical Properties of Types 304 and 316 Stainless Steel — V. K. Sikka, E. Lee, and E. B. Patton

5.2.2.1 Long-Term Creep Tests in Heat-to-Heat Variation Study of Type 304 Stainless Steel

Ten long-term creep tests are in progress on several heats of type 304 stainless steel at 593°C (1100°F). One test on heat 845 ruptured previously after 14,077 hr. One test on heat 187 ruptured during this quarter after 22,622 hr. The creep curve for this test is shown in Fig. 5.6. The time to third stage (0.2% offset) in this test was 17,500 hr, and the creep strain at that time was 2.93%. The rupture strain (including loading strain) was 9.97%, whereas creep strain (inelastic) to rupture was 9.50%. The reduction of area at rupture was 8.8%. The stable creep strain (defined by $e_s = t_r\dot{\varepsilon}_m$) was 2.18%.

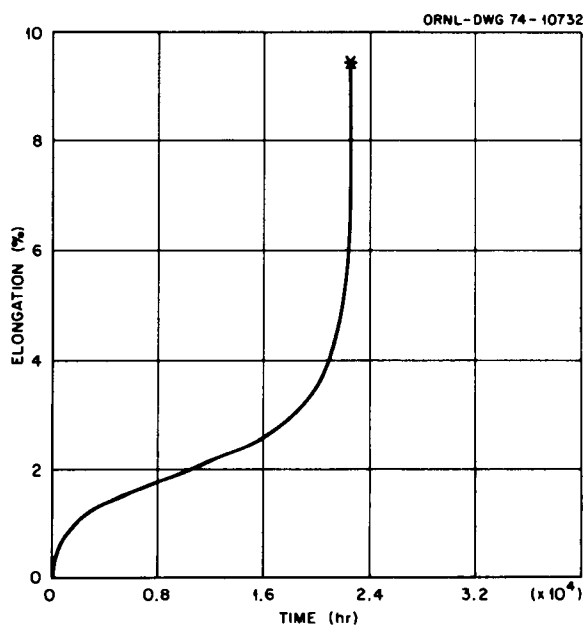

Fig. 5.6. Creep Curve for Heat 187 in As-Received Condition Tested at 593°C (1100°F) and a Stress of 17 ksi (117 MPa).

Minimum creep rate and time to rupture for the long-term test at 593°C (1100°F) are plotted in Fig. 5.7 along with short-term data for both as-received and reannealed conditions. Time to rupture data at

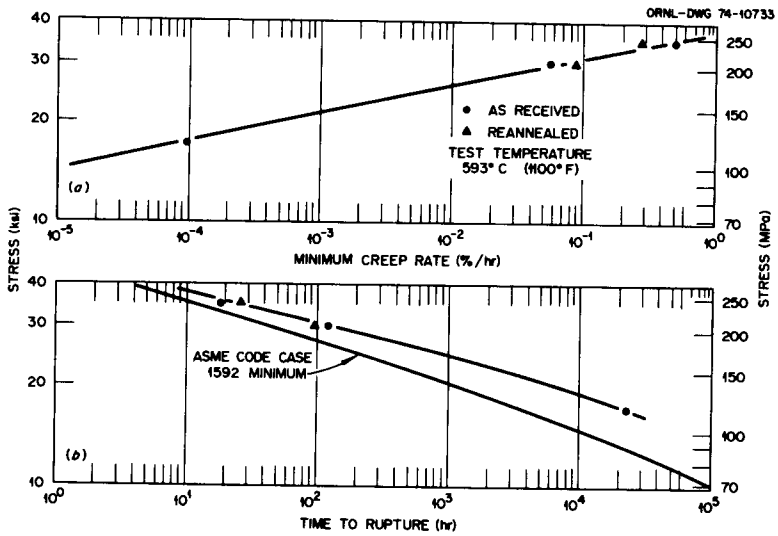

Fig. 5.7. Stress Versus Minimum Creep Rate and Time to Rupture for Heat 187 in Both As-Received and Reannealed Conditions.

593°C (1100°F) on heat 187 for the reannealed condition are compared with the reference heat, 18 other heats, and the Code 1592 minimum value curve in Fig. 5.8. Similar comparison for the time to rupture in the as-received condition is made in Fig. 5.9. In both reannealed and as-received conditions, heat 187 is the weakest at a test temperature of 593°C (1100°F) compared with other heats, and it compares well with the reference heat (796) and heat 807. One test on heat 845, in the as-received condition, has the longest time to rupture, 14,077 hr, and it has been plotted along with short time data in Fig. 5.9. It can be noted that heat 845 is significantly stronger at 593°C (1100°F) than heat 187. For example, creep-rupture strengths for heats 845 and 187 are respectively 30.5 and 24.5 ksi (210 and 169 MPa) at 1000 hr and 25.5 and 18.8 ksi (176 and 130 MPa) at 10,000 hr.

Total elongation and reduction of area at rupture for the longest time test on heat 187 have been compared in the previous section with data on heat 845, on reference heat, and published by Kirsch.[3] The stable creep strain has been calculated for heats 187, 845, and the reference heat of type 304 stainless steel and compared in Fig. 5.10. It is to be noted that the stable creep strain for all three heats at all test temperatures decreases with the increasing test time and has reached a

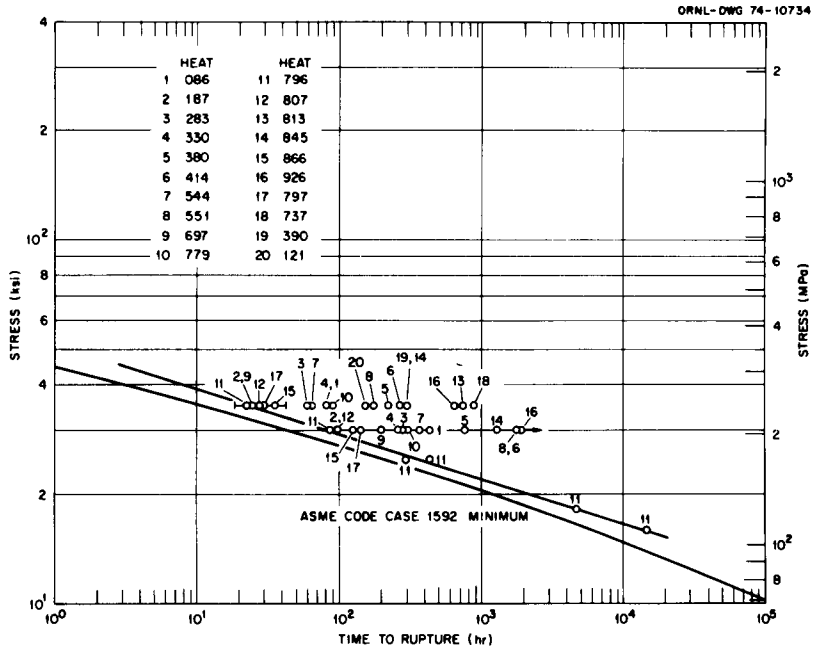

Fig. 5.8. Comparison of Time to Rupture at a Test Temperature of 593°C (1100°F) for Various Heats of Type 304 Stainless Steel in the Reannealed Condition.

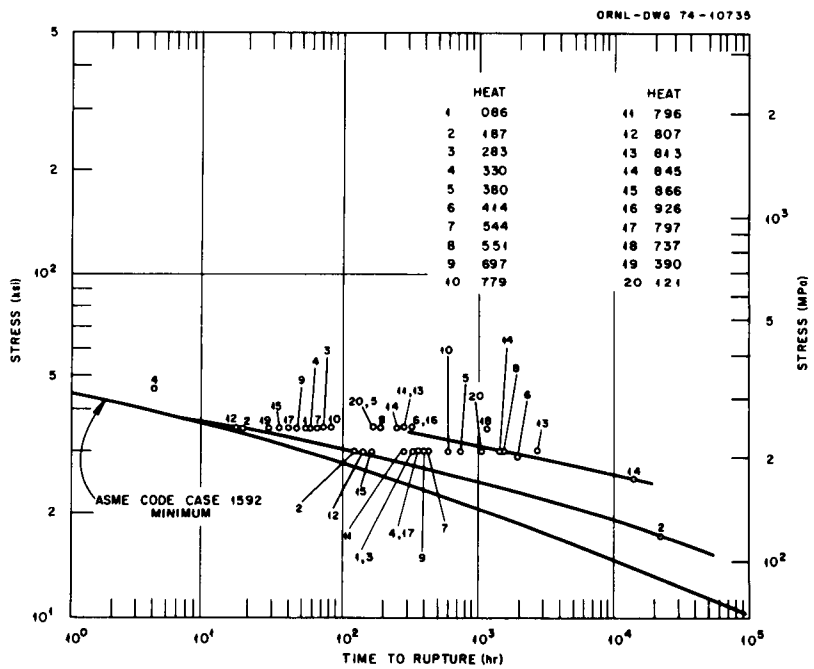

Fig. 5.9. Comparison of Time to Rupture at a Test Temperature of 593°C (1100°F) for Various Heats of Type 304 Stainless Steel in the As-Received Condition.

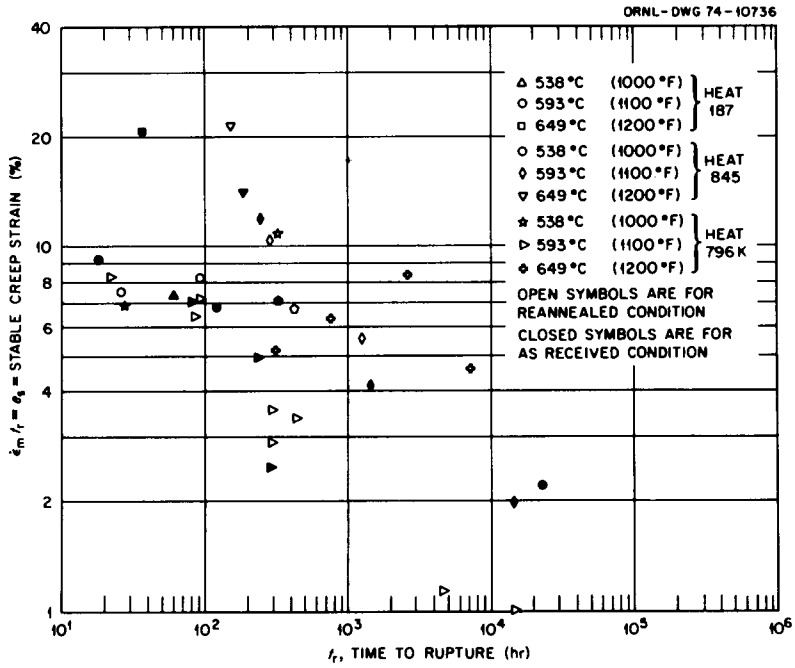

Fig. 5.10. Stable Creep Strain Versus Time to Rupture for Various Heats of Type 304 Stainless Steel.

minimum value of approximately 1% for the reference heat at a test time of 14,647 hr. The wide variation in creep strengths for various heats of type 304 stainless steel shown in Figs. 5.8 and 5.9 are being studied in terms of chemical analysis and grain size variation between the various heats and will be published as a separate report.

The other eight long-term creep tests are still in progress, and their present status is shown in Table 5.5. One of the creep tests has reached a test time of 25,860 hr and is continuing. The creep curves on these long-term tests will be updated during next quarter.

5.2.2.2 Creep Data on Weak, Medium, and Strong Heats of Type 304 Stainless Steel

Three heats out of 20 heats of type 304 stainless steel, weak, medium, and strong, were selected for detailed creep testing including long-term tests. Creep data on these heats are summarized in Table 5.6. Several long-term tests are in progress, and data will be presented during the forthcoming reports.

Table 5.5. Status of Several Long-Term Creep Tests of Type 304 Stainless Steel at 593°C (1100°F)

Test	Heat	Condition[a]	Stress, (ksi)	Stress, (MPa)	Test Time[b] (hr)	Strain, % Loading	Strain, % Creep	Minimum Creep Rate (%/hr)	Time to Rupture (hr)
10396	60551	A 479	25.0	172	17,030	1.81	4.450	1.4×10^{-4}	
10395	346845	A 240	25.0	172	Ruptured	1.37	11.35	1.4×10^{-4}	14,077
9499	300380	Reannealed	17.0	117	23,225	0.72	0.941	~0	
9483	600414	Reannealed	17.0	117	23,300	1.49	0.932	1.1×10^{-5}	
9464	337330	A 240	17.0	117	23,560	−0.20	0.997	5.5×10^{-6}	
9446	9T2796	A 479	17.0	117	23,562	0.13	1.317	2.1×10^{-5}	
9443	337187	A 240	17.0	117	Ruptured	0.47	10.18	9.7×10^{-5}	22,622
9371	55697	A 479	17.0	117	23,760	0.62	4.279	1.4×10^{-4}	
9221	600414	A 240	17.0	117	25,695	0.18	0.725	1.0×10^{-5}	
9508	346544	A 240	17.0	117	21,128	0.22	2.590	3.5×10^{-5}	

[a]As received per indicated specification or reannealed 0.5 hr at 1065°C (1950°F).

[b]Unless otherwise noted tests are in progress.

Table 5.6. Creep Data on the Weak (807), Medium (544), and Strong (845) Heats of Type 304 Stainless Steel

Test	Temperature (°C)	Temperature (°F)	Stress (ksi)	Stress (MPa)	Time (hr)	Strain, % Loading	Strain, % Creep	Minimum Creep Rate (% hr^{-1})	Comments
					807, A 240[a]				
12600	538	1000	46	317	62.3	16.38	27.1	0.226	Ruptured
9788	593	1100	35	241	16.8	8.60	30.1	1.100	Ruptured
9815	593	1100	30	207	143.2	4.85	36.8	0.150	Ruptured
12571	649	1200	25	172	43.5	1.70	64.6	0.700	Ruptured
					807, Reannealed[b]				
12606	538	1000	46	317	44.2	11.1	36.9	0.410	Ruptured
12774	538	1000	25	172	842.0	4.1	0.8	7.7×10^{-4}	Discontinued
10397	593	1100	35	241	35.8	13.8	40.2	0.70	Ruptured
10485	593	1100	35	241	18.1	12.3	37.9	0.97	Ruptured
11914	593	1100	30	207	96.4	7.69	39.0	0.16	Ruptured
14042	593	1100	16	110	592	0.938	1.004	c	In progress
13150	593	1100	10	69	4744	0.068	0.256	c	In progress
13157	593	1100	10	69	4716	0.078	0.366	c	In progress
13160	593	1100	10	69	4529	0.060	0.344	c	In progress
12601	649	1200	25	172	26.8	4.90	54.2	1.60	Ruptured
					544, A 240[a]				
12922	538	1000	46	317	120.1	11.9	24.0	0.066	Ruptured
9535	593	1100	35	241	66.3	7.4	17.1	0.190	Ruptured
9547	593	1100	30	207	431.0	4.6	16.1	0.170	Ruptured
9508	593	1100	17	117					In progress
9675	649	1200	25	172	45.6	2.3	47.0	0.590	Ruptured

Table 5.6. (Continued)

Test	Temperature (°C)	Temperature (°F)	Stress (ksi)	Stress (MPa)	Time (hr)	Strain, % Loading	Strain, % Creep	Minimum Creep Rate (% hr^{-1})	Comments
					544, Reannealed[b]				
12927	538	1000	46	317	139.3	14.7	11.8	0.054	Ruptured
10155	593	1100	35	241	62.1	8.6	17.2	0.190	Ruptured
11923	593	1100	30	207	356.1	5.84	17.8	0.022	Ruptured
13149	593	1100	10	69	5033.6	0.053	0.122	2.44×10^{-5}	Discontinued
13159	593	1100	10	69	4843	0.059	0.168	c	In progress
12668	649	1200	25	172	44.5	3.90	33.5	0.460	Ruptured
					845, A 240[a]				
12943	538	1000	46	317	334.9	11.30	16.40	0.021	Ruptured
9804	593	1100	35	241	247.7	6.92	28.0	0.048	Ruptured
9817	593	1100	30	207	1459.6	3.54	26.1	2.9×10^{-3}	Ruptured
10395	593	1100	25	172	14077.0	1.40	11.40	1.6×10^{-4}	Ruptured
12605	649	1200	25	172	186.1	0.44	52.90	0.075	Ruptured
					845, Reannealed[b]				
13040	538	1000	46	317	420.3	16.7	10.7	0.016	Ruptured
9874	593	1100	35	241	287.0	9.57	19.8	0.035	Ruptured
10463	593	1100	30	207	1275.4	7.20	28.8	4.40×10^{-3}	Ruptured
13158	593	1100	10	69	4970.8	0.068	0.068	5.8×10^{-6}	Discontinued
13151	593	1100	10	69	4671	0.051	0.071	c	In progress
12667	649	1200	25	172	152.3	4.17	49.6	0.141	Ruptured

[a]A 240 represents specimen in as-received condition, containing forming, straightening, and machining stresses.

[b]Reannealed condition represents annealing specimen for 0.5 hr at 1065°C (1950°F).

[c]Second stage not yet reached.

5.2.2.3 Effect of Aging on Tensile and Creep Properties of Type 304 Stainless Steel

The investigation on influence of aging on the mechanical properties of various heats of type 304 stainless steel continued. The program involves nine heats and various combinations of time and temperature. The scope of the aging program is shown in Fig. 5.11(a). Sixteen more blocks of several different heats of type 304 stainless steel aged for 10,000 hr were removed from the furnaces. The present status of the aging program is shown in Fig. 5.11(b). All aged blocks are being

(a)

X-22807
600414
300380
9T2796K
R22926
346845
8043813
346544
3121

Aging Program

Time (hr)	Temperature (°F)
1,000	900
2,000	1100
4,000	1200
10,000	

(1) Microstructure
(2) Tensile Properties, RT, 1100°F
(3) Creep Behavior at
1100°F – 30 ksi (100 to 2000 hr)
1100°F – 17 ksi (Disc. 2000 hr)
1200°F – 14 ksi (Disc. 2000 hr)
900°F – 20 ksi (Disc. 2000 hr)

(b)

ORNL-DWG 73-11407R4

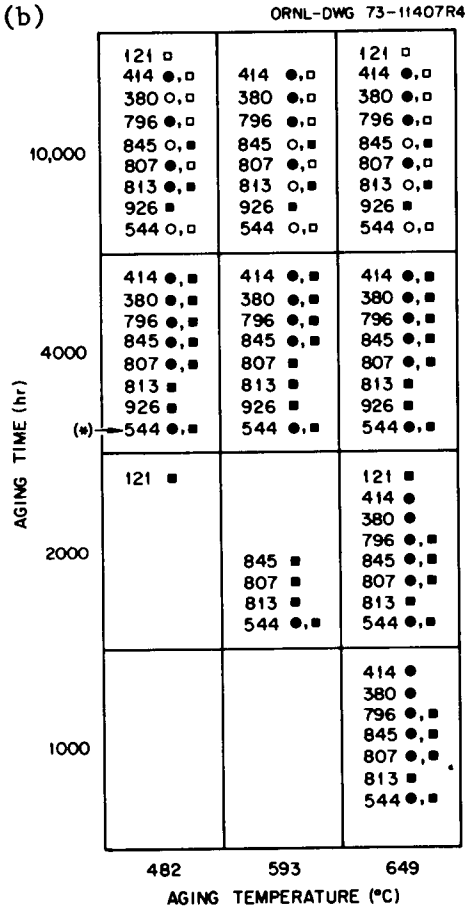

○ ANNEALED 0.5 hr AT 1065°C PRIOR TO AGING
□ AGED IN AS-RECEIVED CONDITION
OPEN SYMBOLS – AGING IN PROGRESS
CLOSED SYMBOLS – COMPLETED
* REACHED 5000 hr INSTEAD OF 4000 hr.

Fig. 5.11. Aging Program for Type 304 Stainless Steel. (a) Scope. (b) Status.

machined into specimens, and they will be tested during the next quarter. Some of the blocks have been left in the furnaces to age 50,000 hr.

A large number of aged specimens of several heats of type 304 stainless steel have been tensile tested at both room temperature and 593°C (1100°F). The effect of aging treatment on tensile properties has been reported.[4,5] The effect of aging on creep properties of the reference heat and heat 845 will now be discussed.

Creep properties of these heats of type 304 stainless steel at 593°C (1100°F) and 30 ksi (207 MPa), for both unaged and aged condition, are listed in Tables 5.7 and 5.8. The following are some general comments:

1. Both minimum creep rate and time to rupture increase on aging for the reference heat, whereas minimum creep rate increases with decrease in time to rupture for heat 845. Changes in minimum creep rate and time to rupture are small for an aging temperature of 482°C (900°F), but increase with increasing aging time and temperature.

2. Loading strain decreases on aging for both heats.

3. Strain in all stages of creep (1st, 2nd, and 3rd) increases on aging for both heats. Thereby, total elongation at rupture and reduction of area also increase on aging for both heats.

4. Duration of second- and third-stage creep increases on aging for the reference heat but decreases for heat 845.

5. The creep curve for heat 845 changes on aging in such a way as to keep percent strain in third stage $[100(\varepsilon_{cs} - \varepsilon_2)/\varepsilon_{cs}^{\cdot}]$ and percent time in third stage $[100(t_r - t_2)/t_r]$ essentially constant. For the reference heat the same quantities increase on aging.

The effects of aging on minimum creep rate and time to rupture in both as-received and reannealed conditions for the reference heat and heat 845 are plotted as bar charts in Figs. 5.12 and 5.13. Bar charts for strain to third stage (0.2% offset) and rupture elongation are shown in Figs. 5.14 and 5.15. It is interesting to note that rupture elongation for the reference heat increases from 19% in the as-received condition to 65% in the aged condition. Similarly for the reannealed condition it goes from 20 to 55%. For heat 845 it increases from 30% in the as-received condition to 73% and from 36% in the reannealed condition to 67% in the aged condition.

Table 5.7. Creep[a] Properties of Aged Reference Heat of Type 304 Stainless Steel

Treatment			Strain, %							Time, hr				Minimum Creep Rate (%/hr)	Rupture Strain ε_f (%)	Reduction of Area RA (%)	Duration, hr		Time Ratio, %		Strain Ratio, %	
Time (hr)	Temperature (°C)	Temperature (°F)	Loading ε_L	End of Primary ε_1	End of Secondary Actual, ε_2	End of Secondary 0.2% Offset, ε_{ss}	Creep Strain ε_{cs}	$\varepsilon_2 - \varepsilon_1$	$\varepsilon_{cs} - \varepsilon_2$	End of Primary t_1	End of Secondary Actual, t_2	End of Secondary 0.2% Offset, t_{ss}	Rupture t_r				Third Stage $t_r - t_2$	Second Stage $t_2 - t_1$	$\frac{t_2 - t_1}{t_r}$	$\frac{t_r - t_2}{t_r}$	$\frac{\varepsilon_2 - \varepsilon_1}{\varepsilon_{cs}}$	$\frac{\varepsilon_{cs} - \varepsilon_2}{\varepsilon_{cs}}$
As-Received Condition																						
			6.74	1.80	6.00	6.80	12.38	4.20	5.58	10.25	66.5	73.5	84.4	7.70×10^{-2}	19.12	24.47	17.9	56.25	66.6	21.2	33.93	45.07
4000	482	900	6.23	3.00	7.90	9.20	18.81	4.90	10.91	17.00	59.0	68.0	82.6	1.2×10^{-1}	25.04	26.81	23.6	42.00	50.8	28.6	26.05	58.00
4000	593	1100	5.46	0.10	5.40	6.10	12.92	5.30	7.52	0.00	42.5	47.0	54.4	1.26×10^{-1}	18.38	22.25	11.9	42.50	78.1	21.9	41.02	58.20
1000	649	1200	2.92	3.13	14.25	17.00	40.56	11.12	26.31	16.5	100.0	120.0	188.2	1.3×10^{-1}	43.48	50.53	88.2	83.50	44.4	46.9	27.42	64.87
2000	649	1200	3.88	1.75	16.50	19.50	62.05	14.75	45.55	5.0	92.5	109.0	186.9	1.7×10^{-1}	65.94	65.29	94.4	87.50	46.8	50.5	23.77	73.41
4000	649	1200	3.37	2.50	17.50	19.50	56.48	15.00	38.98	10.0	95.0	105.0	170.1	1.7×10^{-1}	59.85	63.50	75.1	85.00	49.9	26.5	26.56	69.01
0.5 hr at 1093°C (2000°F), Reannealed Condition																						
			9.87	1.70	5.70	6.70	10.23	4.00	4.53	11.5	65.5	75.3	86.8	7.4×10^{-2}	20.10	20.18	21.3	54.00	62.2	24.5	39.1	44.3
			10.41	2.20	6.20	7.20	11.40	4.00	5.20	16.0	66.0	76.5	92.8	7.8×10^{-2}	21.81	19.97	26.8	50.00	53.9	28.9	35.1	45.6
4000	482	900	7.90	3.00	10.00	11.38	24.85	7.00	14.85	20.0	85.0	96.0	122.2	1.2×10^{-1}	32.75	27.4	37.2	65.00	53.2	30.4	28.2	59.8
4000	593	1100	8.63	4.63	11.25	13.00	24.10	6.62	12.85	33.0	111.5	129.0	160.9	8.38×10^{-2}	32.73	29.5	49.4	78.50	48.8	30.7	27.5	53.3
1000	649	1200	5.80	3.50	16.25	18.25	37.18	12.75	20.93	11.5	90.0	100.0	146.3	1.60×10^{-1}	42.98	45.2	53.3	78.50	53.7	36.4	34.30	56.3
2000	649	1200	6.52	3.50	12.88	15.50	37.68	9.38	24.80	13.5	57.5	68.0	129.7	2.1×10^{-1}	44.2	43.38	72.2	44.00	33.9	55.7	24.9	65.8
4000	649	1200	2.52	2.50	10.50	14.00	52.18	8.00	41.68	12.0	66.5	85.0	186.9	1.5×10^{-1}	54.7	46.30	120.4	54.50	64.1	64.4	15.3	79.9

[a]All creep tests were performed at a stress of 30 ksi (207 MPa) and a test temperature of 593°C (1100°F).

Table 5.8. Creep Properties of Aged Heat 845 of Type 304 Stainless Steel at 593°C (1100°F) and 30 ksi (207 MPa)

Treatment			Strain, %							Time, hr														
Time (hr)	Temperature (°C)	Temperature (°F)	Loading ε_L	End of Primary ε_1	End of Secondary: Actual, ε_2	End of Secondary: 0.2% Offset, ε_{ss}	Creep Strain ε_{cs}	$\varepsilon_2 - \varepsilon_1$	$\varepsilon_{cs} - \varepsilon_2$	End of Primary t_1	End of Secondary: Actual, t_2	End of Secondary: 0.2% Offset, t_{ss}	Rupture t_r	Minimum Creep Rate (%/hr)	Rupture Strain ε_f (%)	Reduction of Area RA (%)	Duration, hr: Third Stage $t_r - t_2$	Duration, hr: Second Stage $t_2 - t_1$	Time Ratio, %: $t_2 - t_1$ / t_r	Time Ratio, %: $t_r - t_2$ / t_r	Strain Ratio, %: $\varepsilon_2 - \varepsilon_1$ / ε_{cs}	Strain Ratio, %: $\varepsilon_{cs} - \varepsilon_2$ / ε_{cs}
										As-Received Condition														
			3.54	2.00	3.50	4.00	26.10	1.50	22.60	180	660	760	1460	2.9×10^{-3}	29.6	32.3	800	480	32.9	54.8	5.747	86.6
4000	482	900	2.32	2.25	4.75	5.40	39.90	2.50	35.15	100	480	550	1059	6.3×10^{-3}	42.2	37.4	579	380	35.9	54.7	6.266	88.1
10000	482	900	4.26	2.50	4.13	5.00	30.62	1.63	26.49	115	365	470	951	6.28×10^{-3}	34.9	37.7	586	250	26.3	61.6	5.323	86.5
2000	593	1100	3.67	2.00	5.75	6.50	43.60	3.75	37.85	80	430	480	1205	1.03×10^{-2}	47.2	51.8	775	350	29.0	64.3	8.601	86.8
4000	593	1100	3.24	3.50	8.25	10.50	45.69	4.75	37.44	82.5	250	330	763	2.7×10^{-2}	48.9	54.3	513	167.5	22.0	67.2	10.352	81.9
1000	649	1200	2.62	2.00	10.10	12.00	53.74	8.10	43.64	35.0	245	275	582	3.80×10^{-2}	56.4	77.6	337	210.0	36.1	57.9	15.070	81.2
2000	649	1200	2.25	4.00	16.50	16.70	59.82	12.50	43.32	37.5	225	230	442	6.60×10^{-2}	62.0	59.1	217	187.5	42.4	49.1	20.895	72.4
4000	649	1200	1.50	3.00	12.50	15.00	61.95	9.50	49.45	40.0	242.5	295	600	4.70×10^{-2}	63.5	78.3	357.5	202.5	33.8	59.6	15.335	71.8
10000	649	1200	2.22	3.00	14.00	16.00	69.74	11.00	55.74	16.25	110	125	259	1.18×10^{-1}	72.0	75.7	149.0	93.75	36.2	57.5	15.773	80.0
										0.5 hr at 1065°C (1950°F), Reannealed Condition														
			7.20	2.0	3.75	4.25	28.8	1.75	25.05	240	630	700	1275											
4000	482	900	5.15	2.75	5.75	7.00	32.5	3.00	26.75	125	475	565	859	4.40×10^{-3}	36.0	40.0	645	390.0	30.6	50.6	6.076	87.0
4000	593	1100	5.35	4.00	8.00	8.75	31.49	4.00	23.49	150	470	475	849	8.5×10^{-3}	37.6	41.4	384	350.0	40.7	44.7	9.231	82.3
1000	649	1200	4.03	5.25	11.75	12.50	37.97	6.50	22.22	165	580	625	1051	1.30×10^{-2}	36.8	43.70	379	320.0	37.7	44.6	12.702	74.6
2000	649	1200	3.52	2.50	16.00	18.00	52.67	13.50	36.67	17.5	175	195	307	1.50×10^{-2}	42.0	44.50	471	415.0	39.5	44.8	17.119	58.5
4000	649	1200	3.34	3.00	12.50	15.00	63.43	9.50	50.93	26.25	150	175	360	8.7×10^{-2}	56.20	54.91	132	157.5	51.3	43.0	25.631	61.6
														7.70×10^{-2}	66.80	68.40	160	123.8	34.4	44.4	14.980	80.3

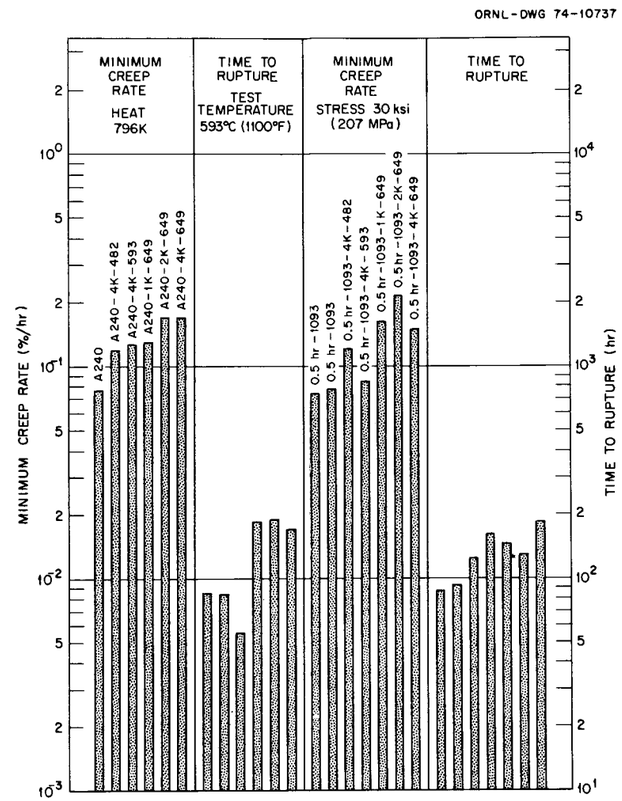

Fig. 5.12. Effect of Aging on Minimum Creep Rate and Time to Rupture at a Test Temperature of 593°C (1100°F) and a Stress of 30 ksi (207 MPa) for Heat 9T2796K in Both As-Received and Reannealed Conditions.

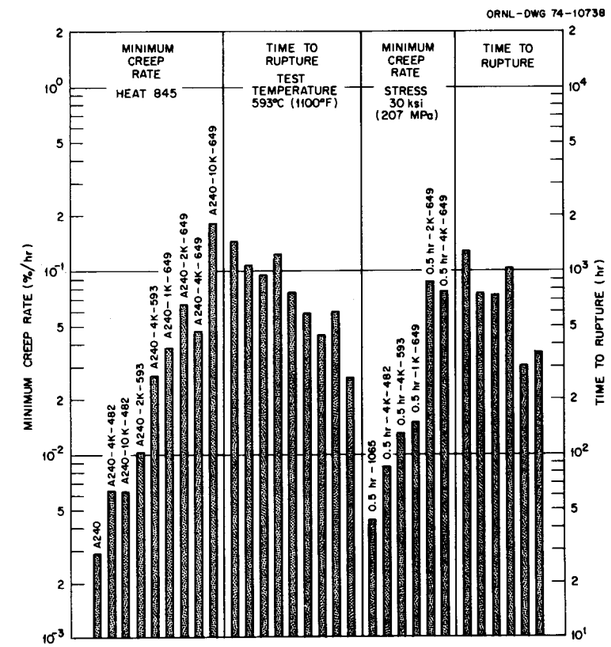

Fig. 5.13. Effect of Aging on Minimum Creep Rate and Time to Rupture at a Test Temperature of 593°C (1100°F) and a Stress of 30 ksi (207 MPa) for Heat 346845 Aged in Both As-Received and Reannealed Conditions.

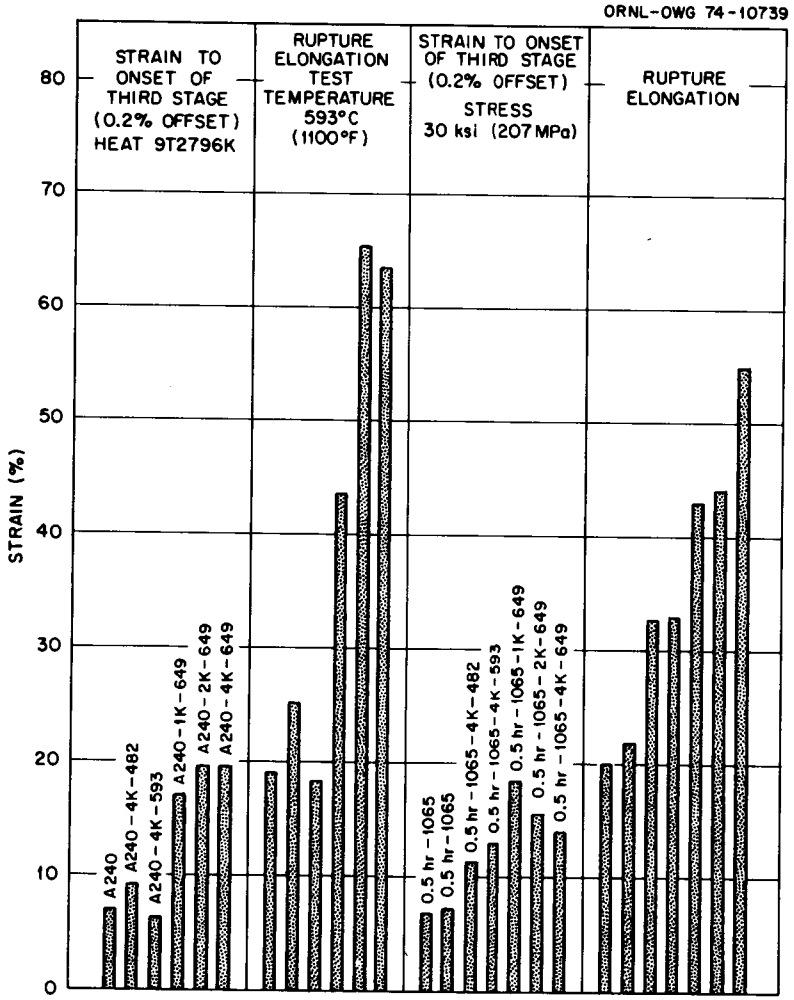

Fig. 5.14. Effect of Aging on Strain to Third Stage and Rupture Elongation at a Test Temperature of 593°C (1100°F) and a Stress of 30 ksi (207 MPa) for Heat 9T2796K Aged in Both As-Received and Reannealed Conditions.

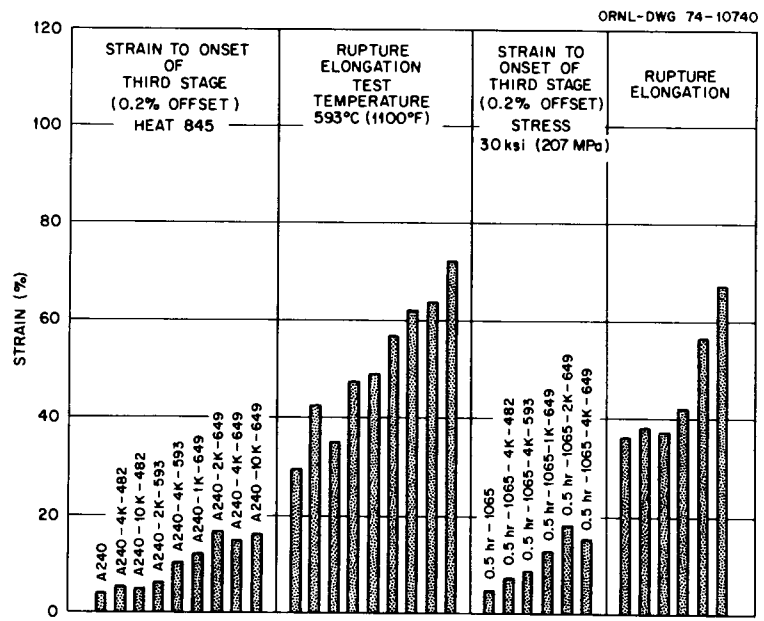

Fig. 5.15. Effect of Aging on Strain to Third Stage and Rupture Elongation at a Test Temperature of 593°C (1100°F) and a Stress of 30 ksi (207 MPa) for Heat 346845 Aged in Both As-Received and Reannealed Conditions.

Garofalo et al.[6] showed that the time to rupture, t_r, can be related to the duration of the second stage, $t_2 - t_1$, by the relationship

$$t_r = A(t_2 - t_1)^{\alpha} , \tag{2}$$

where A and α are constants.

Time to rupture for both unaged and aged conditions for both reference heat and heat 845 in as-received and reannealed conditions is plotted as a function of $t_2 - t_1$ in Fig. 5.16. It can be noted that the data for the reference heat and heat 845 can be represented by Eq. (2) for

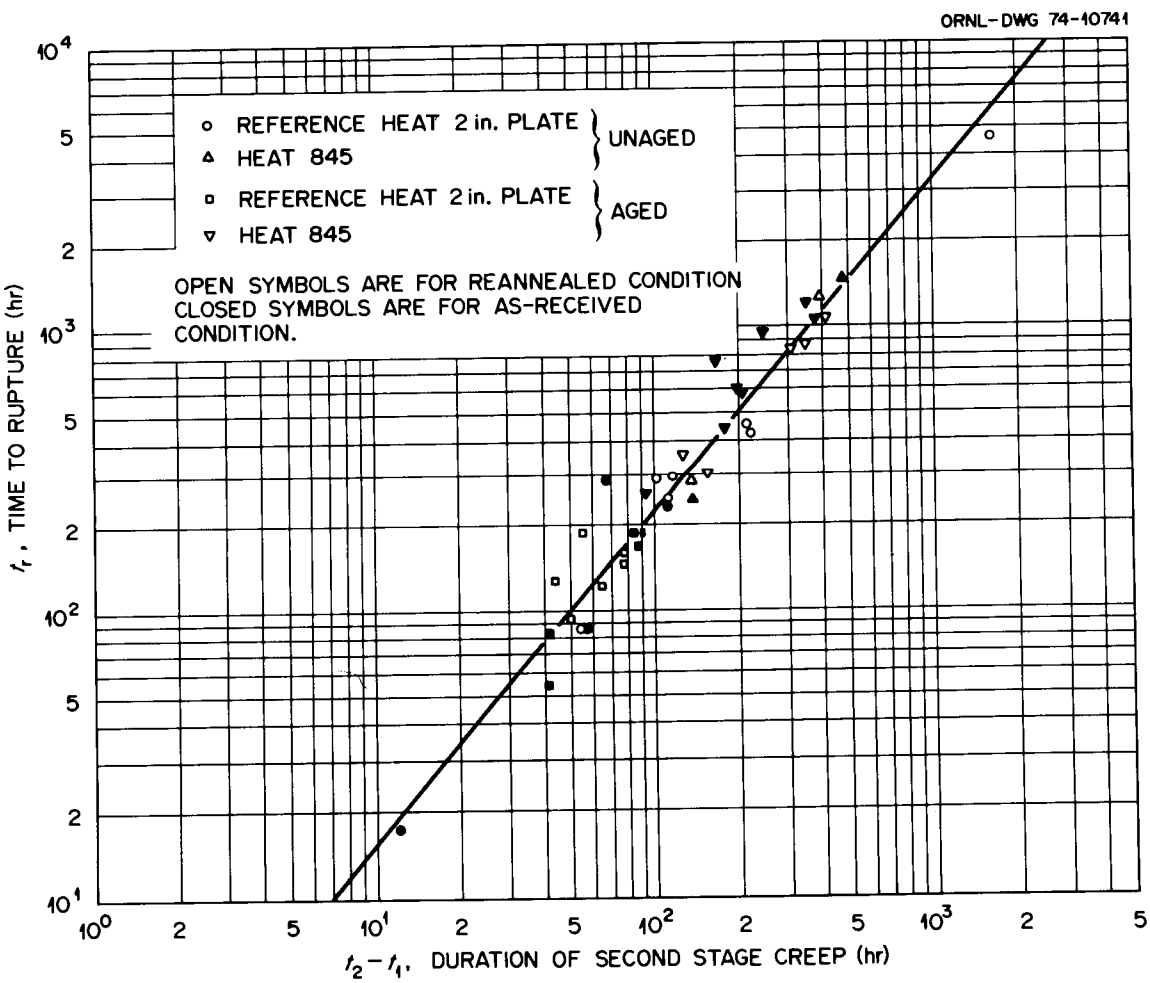

Fig. 5.16. Plot of Time to Rupture Against Duration of Second-Stage Creep for the Reference Heat and Heat 845 of Type 304 Stainless Steel Tested at 593°C (1100°F) for Both Unaged and Aged Conditions.

both unaged and aged conditions. The values of constants α and A were calculated to be 1.17 and 1.03, respectively, as compared with 0.98 and 1.81 reported by Garofalo et al.[6] for type 316 stainless steel tested at 593°C (1100°F).

Garofalo et al.[6] also observed an empirical relationship between time to rupture and the end of the second-creep stage. The relation was:

$$t_r = Bt_2^{\beta} , \tag{3}$$

where β and B are constants.

Time to rupture for unaged and aged conditions for both the reference heat and heat 845 in as-received and reannealed conditions is plotted as a function of t_2 in Fig. 5.17. It is worth noting that the data for the reference heat and heat 845 can be represented by Eq. (3) for both unaged and aged conditions. The values of β and B were calculated to be 1.162 and 0.827, respectively. Values of β and B are comparable with constants

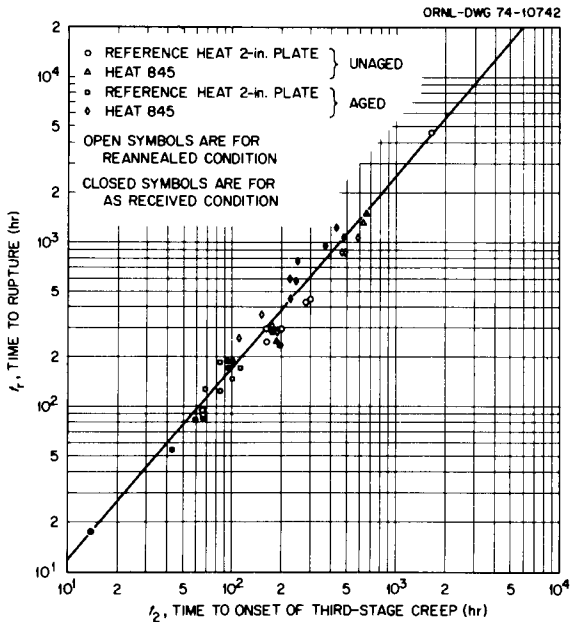

Fig. 5.17. Plot of Time to Rupture Against Time to Onset of Third-Stage Creep for the Reference Heat and Heat 845 of Type 304 Stainless Steel Tested at a Temperature of 593°C (1100°F) for Both Unaged and Aged Conditions.

α and A calculated from Eq. (2). Values of β and B reported by Garofalo[6] for type 316 stainless steel were 0.98 and 1.48, respectively. Although values of α,A and β,B from Eqs. (2) and (3) did not compare with those reported by Garofalo et al., aging did not have any effect on the equations. Furthermore, the reference heat is a weak heat, whereas heat 845 is a strong heat, and both could be combined in Eqs. (2) and (3). The most important result of Eq. (3) is from the design point of view because t_2, which represents the useful life during creep (time after which creep rate increases rapidly), appears to be independent of the type of heat, pretreatment (as-received or reannealed condition), and aging treatment. From Eq. (3), t_2 for a test temperature of 593°C (1100°F) can be expressed as:

$$t_2 = t_r^{1/\beta}/B = 1.21 t_r^{0.86} \ . \tag{4}$$

Thus, knowing time to rupture, one could determine the useful life in creep from Eq. (4). More work is needed in this area. During next quarter, we shall try to plot the data for all 20 heats and then determine the average line with upper and lower limits.

It is common to relate time to rupture with minimum creep rate by an equation of the type:

$$t_r = C\dot{\varepsilon}_m^{-\gamma} \ . \tag{5}$$

We attempted to determine the effect of aging on Eq. (5). Thus, time to rupture and minimum creep rate for both unaged and aged conditions were plotted in Fig. 5.18. For the reference heat in the unaged condition the value of γ was 0.75. For heat 845, γ for the unaged condition was 0.67. As seen in Fig. 5.18, aging shifts the line to the right but leaves the value of γ constant at 0.67. Although there are limited data for the reference heat, a line parallel to the unaged condition has also been drawn for it based on the data on heat 845. For both reference heat and heat 845, data points fall closer to the unaged line for aging at 482°C (900°F), lie between unaged and aged lines for aging at 593°C (1100°F),

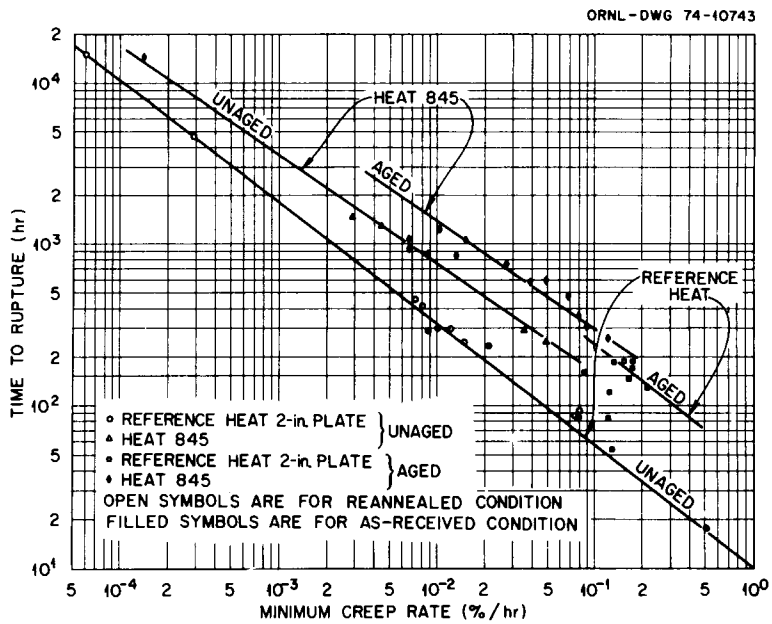

Fig. 5.18. Time to Rupture Versus Minimum Creep Rate for Reference Heat and Heat 845 of Type 304 Stainless Steel, Tested at 593°C (1100°F), for Both Unaged and Aged Conditions.

and lie on a separate line for aging at 649°C (1200°F). In other words, the effect of aging on minimum creep rate and time to rupture is maximum for an aging temperature of 649°C (1200°F).

In Fig. 5.19, we have plotted, for the reference heat of type 304 stainless steel, uniform elongation during tensile tests and strain to third stage (0.2% offset) including loading strain as a function of strain rate or minimum creep rate. Figure 5.20 shows a similar plot for total elongation (elongation at rupture). For the unaged condition, decreasing strain rate (i.e., in going from tensile to the creep range) decreases uniform elongation, strain to third stage, and total elongation. Aging tends to decrease the uniform elongation in the tensile range, whereas it increases the strain to third stage in the creep range. Similarly, aging decreases total elongation during tensile testing, but increases it in creep. The decrease in uniform elongation in the tensile range is quite significant and increases with the increasing aging time and temperature. The maximum increase in strain to third stage for the aged condition is about 7%, but such an increase is very large when one recognizes that it is only 17% for the annealed condition. Furthermore,

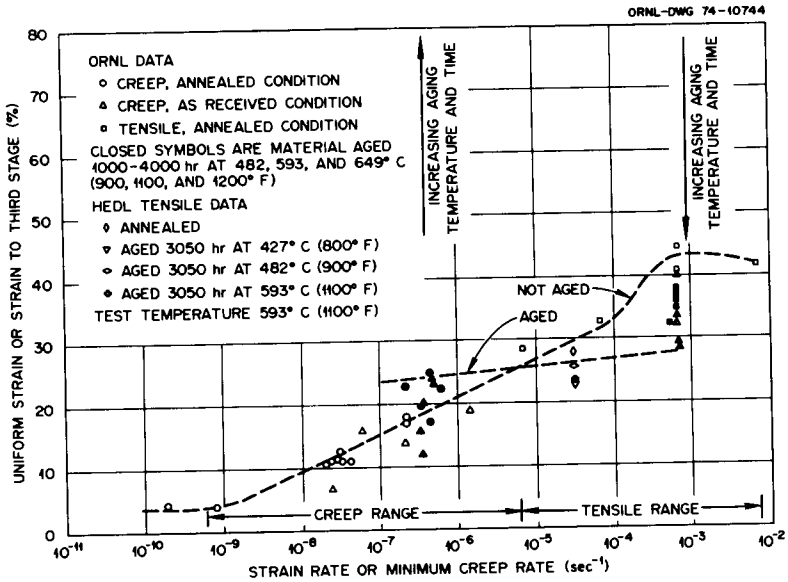

Fig. 5.19. Effect of Thermal Aging on Uniform Elongation During Creep and Tensile Testing of Reference Heat (9T2796K) of Type 304 Stainless Steel. Strain in third stage is 0.2% offset from onset of third state.

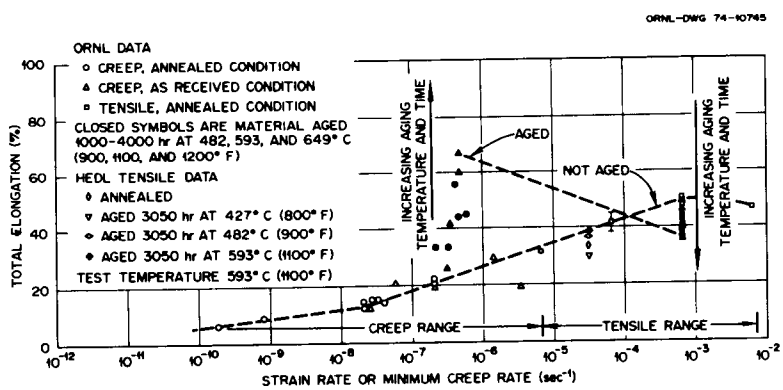

Fig. 5.20. Effect of Thermal Aging on Total Elongation During Creep and Tensile Testing of Reference Heat (9T2796K) of Type 304 Stainless Steel.

the increase in strain to third stage also increases with increasing aging time and temperature. Total elongation in the creep range for the aged condition increases from 22 to 67%, whereas in the tensile range it decreases from 50 to 36%. The increase in total elongation in the creep range and the decrease in tensile range increase with increasing aging time and temperature. HEDL[7] tensile data for the annealed and aged condition have also been plotted on Figs. 5.19 and 5.20 and show similar trends as observed in the ORNL data.

Garofalo et al.[6,8] investigated the effect of pretreatment at 816°C (1500°F) for 24 hr before creep testing at 593°C (1100°F) under stresses in the range 32 to 42 ksi (221–290 MPa). Consistent with present results, the line for time to rupture versus minimum creep rate was shifted to the right by pretreatment at 816°C (1500°F) for 24 hr. Garofalo et al. also found no systematic change in minimum creep rate, but pretreatment increased secondary creep strain. The time to rupture and total elongation also increased. It is interesting to note that in contrast with results of Garofalo et al. ORNL data show that aging increases the time to rupture for the reference heat but decreases it for heat 845.

Garofalo et al.[6,8] indicated that for the annealed material a carbide precipitate of small, closely spaced particles is formed at the test temperature of 593°C (1100°F). No grain-boundary migration is possible under these conditions; the elongation at rupture is low and the fracture is totally intergranular. Aging at 816°C (1500°F) for 24 hr spheroidized the precipitate at grain boundaries and gave rise to some grain-boundary migration. They did not observe any cracks associated with carbide particles and attributed the lack of cracks to high adherence between matrix and particles. It was also suggested that some grain-boundary migration associated with coarse particles suppresses crack formation and thereby increases the time to rupture.

Metallographic examination and transmission electron microscopy will be performed during next quarter to explain the results presented above.

5.2.2.4 Heat-to-Heat Variation of Type 316 Stainless Steel

Heat 686 is the strongest in both tensile and creep of the seven wrought heats of type 316 stainless steel being studied at ORNL. The

chemical analysis of this heat is shown in Table 5.9. Tensile properties of heat 686 for both as-received and reannealed condition are listed in Table 5.10. Tensile results show that heat 686 is extremely strong at all temperatures in both as-received and reannealed conditions. Creep data have been obtained on this heat at several stresses but only one test temperature, 593°C (1100°F); these data are listed in Table 5.11. The creep curves for heat 686, tested at 593°C (1100°F) and a stress of 40 ksi (276 MPa), in both as-received and reannealed conditions, are shown in Figs. 5.21 and 5.22. Note that these tests have gone to test times of 3185 and 3162 hr, respectively, and have still not ruptured. Furthermore, neither creep curve is typical. For the as-received condition, extremely small strain is observed for test time of 375 hr, and then it increases rapidly. For the reannealed condition, the strain is small for a test time of 350 hr, and then it increases rapidly. The increasing strain part of the curve for both cases shows similarity to a typical third stage, but is exceptional in the sense that it shows a downward curvature. Such a curvature implies decreasing rate with increasing time and thus could also be considered similar to a primary creep stage. The minimum creep rate in Table 5.11 has been calculated from the flat portion of the creep curve equation up to test times of 375 and 350 hr in Figs. 5.21 and 5.22, respectively.

To explain the creep curves observed in Figs. 5.21 and 5.22, we used metallographic and transmission electron microscopic examination of the specimens in as-received, reannealed, and creep-tested conditions. Typical optical micrographs for heat 686 in as-received and reannealed conditions are shown in Fig. 5.23. The average grain intercept for both conditions is about 8 μm. Transmission electron micrographs for both conditions are shown in Fig. 5.24. The electron micrograph in Fig. 5.24(a) shows a relatively low dislocation density, but extensive precipitation can be observed within the grain. Grain boundaries appear relatively free of precipitate. The electron micrograph for the reannealed condition, Fig. 5.24(b), also shows a low dislocation density, grain boundries free of precipitate, and the grain interior containing precipitate. Precipitate distribution within the grain is shown in Fig. 5.24(c). It can be noted

Table 5.9. Chemical Analysis of Heat 327686[a] of Type 316 Stainless Steel

Chemical Element	Content, %		
	Vendor Analysis	ORNL I	ORNL II
C	0.056	0.053	
N		0.079	
P	0.02	0.023	
B		0.001	0.001
O		0.0066	
H		0.0005	
Ni	13.0	13.3	
Mn	1.70	1.60	
Cr	17.50	17.20	
Si	0.55	0.55	
Mo		2.20	
S	0.009	0.007	
Ti		0.037	
Cu		0.130	
Co		0.030	
Pb		0.0007	
Nb		0.15	0.050
Sn		<0.01	
Ta		<0.001	
V			0.040
W			0.150
Al			0.015

[a]Vendor — Allegheny Ludlum, product form — 1/2-in. plate (12.7 mm). As received grain size ~ASTM 10 (~8 μm).

Table 5.10. Tensile Properties of Heat 327686 of Type 316 Stainless Steel[a]

Test Temperature (°C)	Test Temperature (°F)	Stress, ksi (MPa) Yield	Stress, ksi (MPa) Ultimate Tensile	Strain (%) Uniform	Strain (%) Total	Reduction of Area (%)
		A 240, As Received				
25	75	53.4(367.5)	100.3(691.5)	38.8	57.0	69.0
427	800	32.3(222.7)	81.3(560.5)	35.2	43.6	59.1
593	1100	30.2(208.0)	75.0(517.0)	35.2	46.5	59.5
649	1200	29.7(204.8)	64.8(447.0)	32.0	46.0	62.8
		0.5 hr - 1065°C(1950°F) Reannealed				
25	75	52.2(359.9)	98.5(679.1)	39.8	57.0	70.7
25	75	53.3(367.5)	100.5(692.9)	38.8	58.0	70.2
427	800	32.6(224.8)	79.6(548.8)	44.6	45.0	59.5
593	1100	28.8(198.6)	72.6(500.6)	38.4	48.8	60.5
649	1200	28.0(193.0)	62.3(429.5)	36.0	54.3	60.2

[a]All tests were performed at a strain rate of 0.040/min on specimens cut along the rolling direction of the plate.

Table 5.11. Creep Properties of Heat 327686 of Type 316 Stainless Steel[a]

Stress (ksi)	Stress (MPa)	Time to Rupture (hr)	Minimum Creep Rate (%/hr)	Strain, % Loading	Strain, % Creep	Reduction of Area (%)
			A-240, As Received			
50	345	531.4	1.11×10^{-3}	5.2	6.9	12.7
40	276	3186.4[b]	5.0×10^{-5}	2.5	3.7	5.4
35	241	5260.2[b]		0.88	3.2	3.4
			0.5 hr - 1065°C, Air Cool, Reannealed			
40	276	3161.9[b]	6.4×10^{-4}	2.9	6.9	7.7
35	241	1007.4[b]		1.88	0.9	2.5
			0.5 hr - 1200°C, Water Quench, Reannealed[c]			
40	276	1122.5	1.58×10^{-4}	9.60	1.98	12.5
			0.5 hr - 1350°C, Air Cool, Reannealed[d]			
40	276	84.8	1.08×10^{-3}	23.13	7.22	29.61
			0.5 hr - 1065°C, 4000 hr - 593°C, Aged			
50	345	219.3	7.42×10^{-2}	5.37	36.2	50.79
			0.5 hr - 1065°C, 4000 hr - 593°C, Aged			
50	345	158.4	1.36×10^{-1}	4.05	42.5	58.78

[a]All tests were performed on specimens cut along the rolling direction of the plate.

[b]Discontinued before rupture.

[c]This treatment produced a grain size of 68 μm.

[d]This treatment produced a grain size of 250 μm.

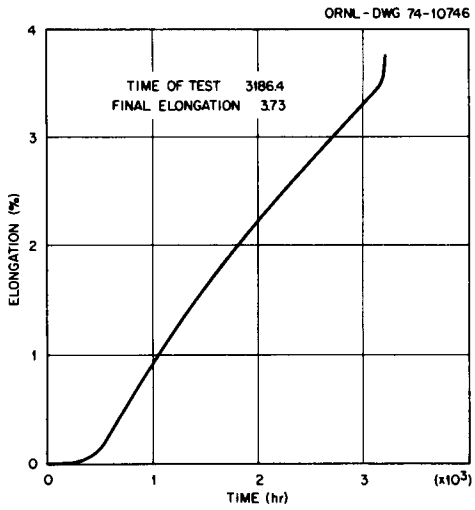

Fig. 5.21. Creep Curve for Heat 686 in As-Received Condition, Tested at 593°C (1100°F) and 40 ksi (276 MPa).

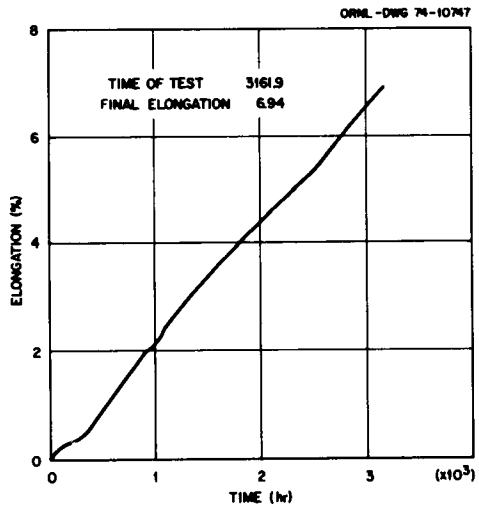

Fig. 5.22. Creep Curve for Heat 686 in Reannealed Condition (0.5 hr at 1065°C), Tested at 593°C (1100°F) and 40 ksi (276 MPa).

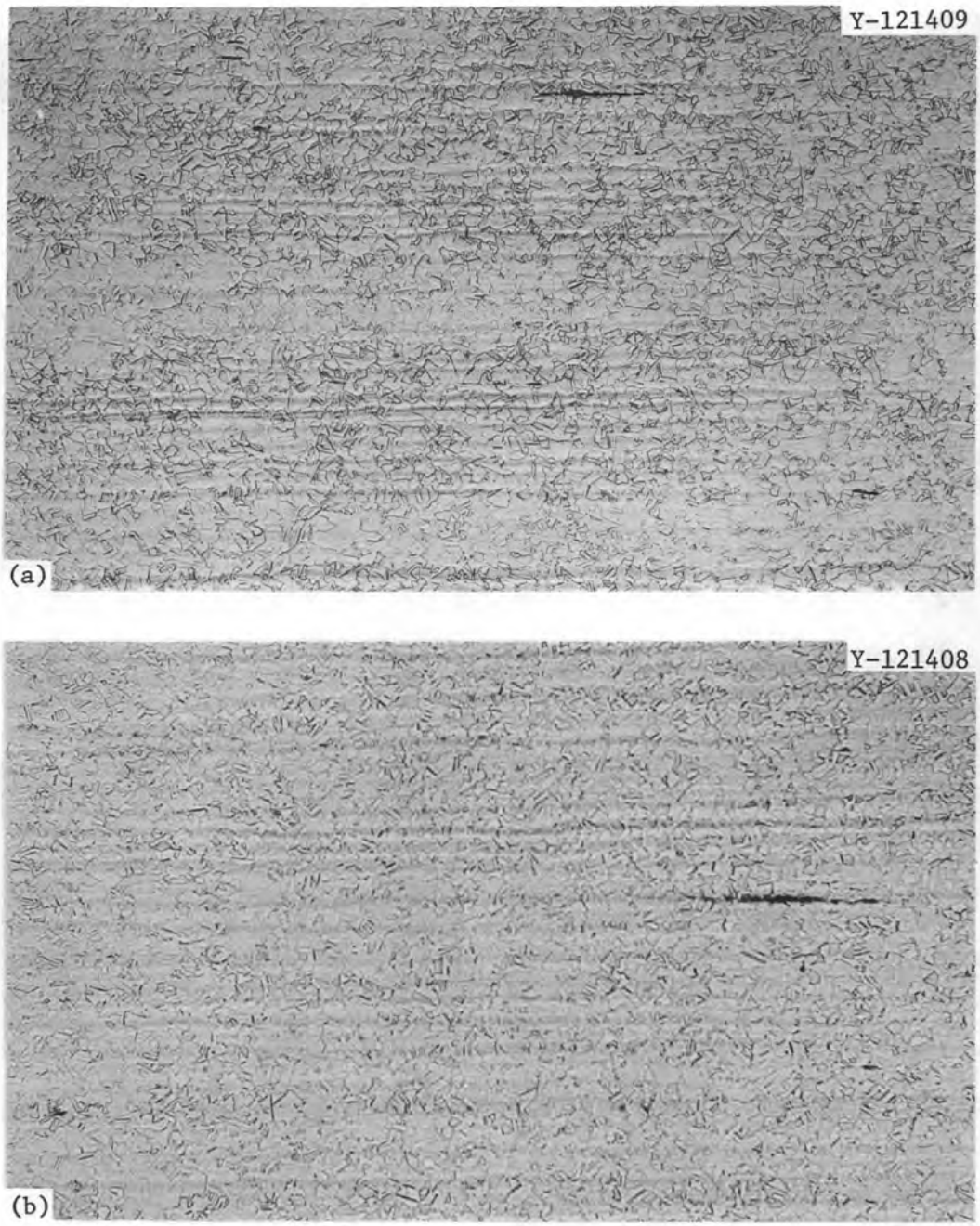

Fig. 5.23. Microstructure of Heat 686 of Type 316 Stainless Steel Steel. 100×. (a) In as-received conditions. (b) In reannealed condition.

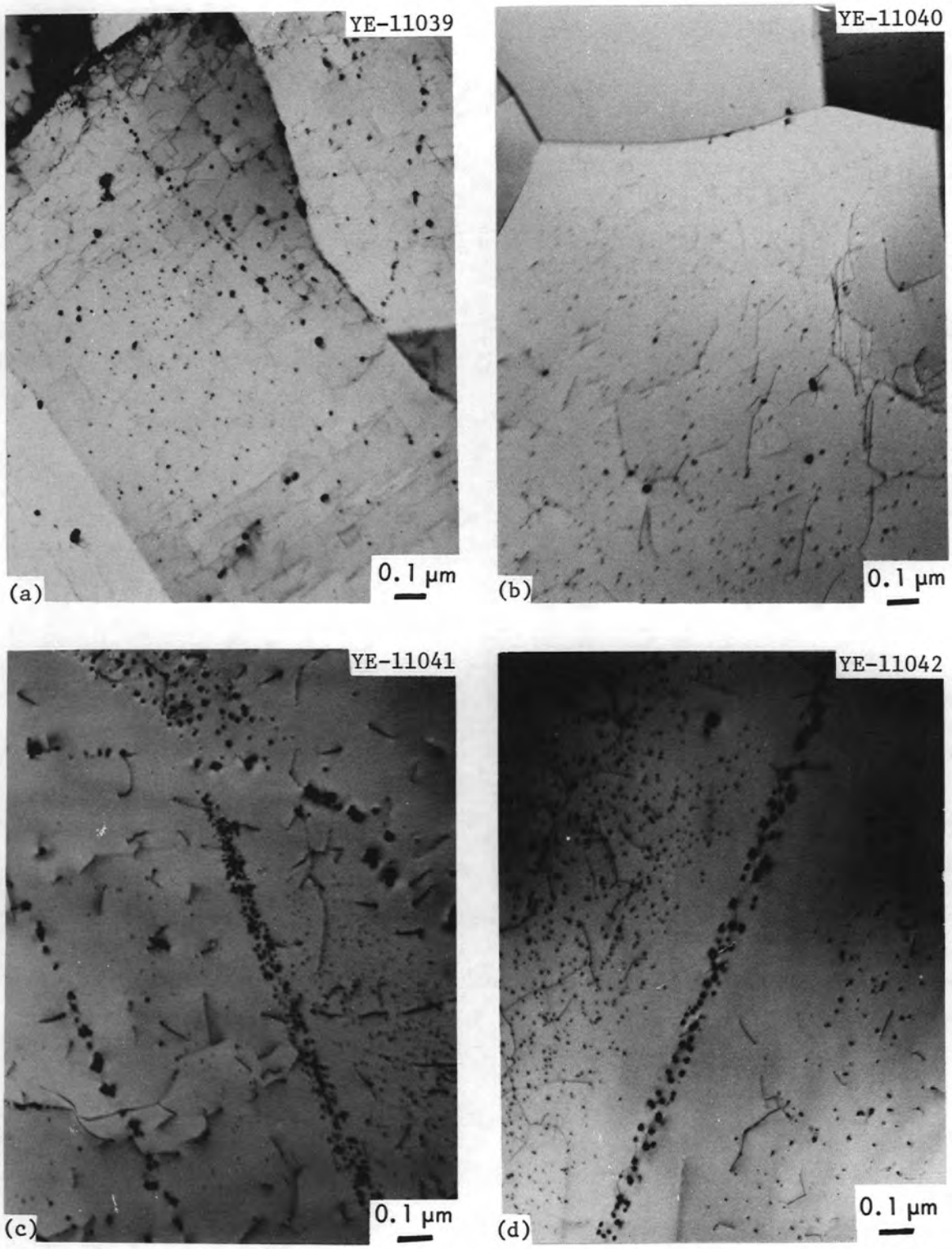

Fig. 5.24. Electron Micrographs of Heat 686 of Type 316 Stainless Steel. (a) As-received condition. (b) Grain boundaries, (c) precipitate bands, and (d) denuding around the precipitate band in the reannealed condition.

that certain regions of the grain area contain a uniform distribution of precipitate particles separated by precipitate bands. A selected area containing precipitate bands is shown in Fig. 5.24(d), and it can be noted that the regions surrounding the precipitate band are denuded of precipitate. Regions next to the denuded zone show a very uniform distribution of almost the same size precipitate particles.

The reannealed specimen, creep tested at 593°C (1100°F) and 40 ksi (276 MPa) and discontinued after 3160 hr, was cut in the middle of the reduced section and examined by transmission electron microscopy. Typical electron micrographs are shown in Fig. 5.25. Figure 5.25(a) shows that, as opposed to the as-received and reannealed conditions, grain boundaries are filled with massive precipitate particles. The grain interiors are relatively free. The micrograph in Fig. 5.25(b) shows that in some grains, which contain no precipitate, a dislocation cell structure formed. In other grains, where precipitate was present, no dislocation cell structure was observed [Fig. 5.25(c)].

Precipitate was extracted from both the buttonhead and the reduced section of the creep specimen. The extracted precipitate was approximately 0.80 wt % for both unstressed and stressed regions. Prominent peaks for $M_{23}C_6$ were identified in the extracted precipitate by x-ray diffraction,

Since no obvious nucleation sites are observed for the banded precipitate structure in Fig. 5.24(d), we can assume that such a structure results from the nucleation of carbide particles at nonuniformly distributed alloying elements. The nucleated precipitate then grows at the expense of chromium and carbon from the surrounding region. Such a growth mechanism of precipitate in the banded region would leave areas low in chromium and carbon concentrations in its vicinity and thus make the region near it denuded of any precipitate. A uniform distribution of precipitate in the areas away from the banded region can then be associated with homogeneous nucleation.

The observation of no difference in precipitate concentration between the unstressed and stressed regions of the crept specimen and the precipitate being at the grain boundaries in the crept specimen rather than in the unstressed region show that the precipitate transfers from the

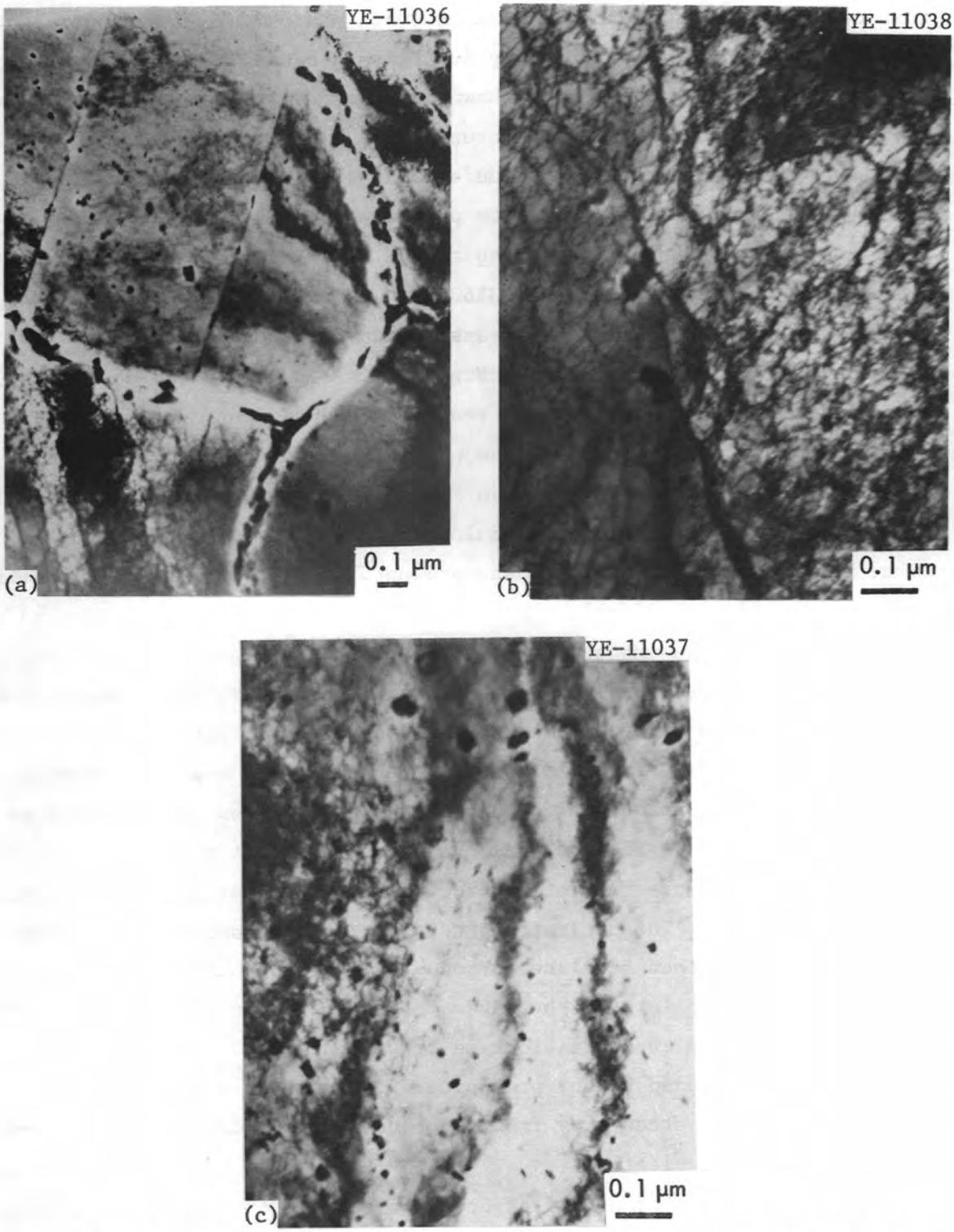

Fig. 5.25. Electron Micrograph for Heat 686 of Type 316 Stainless Steel, Creep Tested at 593°C (1100°F) and 40 ksi (276 MPa) for 3160 hr. (a) Grain boundary precipitate. (b) Dislocation cell structure. (c) Precipitate within grain interior.

grain interior to the grain boundary during the creep test. If such an explanation is possible, then the test time at which the creep rate increases in Figs. 5.21 and 5.22 could be associated with the time taken for the precipitate transfer from grain interior to grain boundaries. The fast creep rate can then result from grain deformation at a stress of 40 ksi (276 MPa) relative to the grain boundaries. More work is continuing in this area.

Attempts were made to change the grain size by different annealing treatments (Table 5.11) than used conventionally. The creep tests were performed on coarse-grained specimens at 593°C (1100°F) and 40 ksi (276 MPa). The creep data in Table 5.11 show a sharp decrease in time to rupture with increase in grain size. Furthermore, the loading strain increased very sharply with increasing grain size. Loading strain is plotted against square root of grain diameter in Fig. 5.26.

The effect of aging on the creep data for heat 686 is also included in Table 5.11. Aging has the following effects on creep properties of heat 686 of type 316 stainless steel:

1. Minimum creep rate increases and rupture life decreases.
2. Loading strain decreases.
3. Total elongation and reduction of area show large increases.

Work in this area will continue on heat 686 and six other heats of type 316 stainless steel during the next quarter.

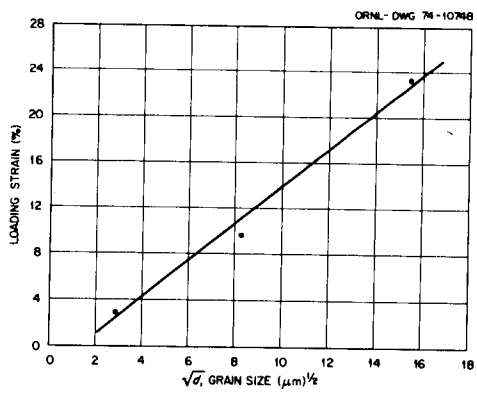

Fig. 5.26. Loading Strain Versus Square Root of Grain Size for Heat 686, Creep Tested at 593°C (1100°F) and 40 ksi (276 MPa).

5.2.3 Materials Behavior in Support of Development and Evaluation of Failure Criteria for Materials — M. K. Booker

Failure of materials may be predicted by use of several criteria. Creep rupture, in particular, depends on several factors. Stress and temperature are, of course, the most obvious variables to consider in the prediction of creep rupture. Thus, a natural criterion for failure might be the stress that would cause rupture in a given amount of time. Conversely, the rupture life at a given temperature and stress might be a useful criterion. The strain that can be endured to failure at a given temperature could be another criterion to use, but this concept of failure prediction is the least developed at this time. Various possible quantities to use as a "strain limit" and the advantages to using strain as a failure criterion have been previously described.[9,10]

Inherent scatter and inconsistencies in ductility data make direct correlation and extrapolation of such data difficult. Still it is desirable to be able to predict at least an approximation to the strain that can be endured under various conditions. A parametric method for estimating total rupture elongation has been described by Goldhoff.[11]

Basically, the Goldhoff method consists of correlating both rupture time and average creep rate,[12] and then fitting the subsequently obtained parameters to stress, using a simple polynomial fit. Thus, one would get two equations:

$$\text{(rupture time)}\ \sigma = a_0 + a_1 P + a_2 P^2 \ldots, \tag{6}$$

$$\text{(average creep rate)}\ \sigma = b_0 + b_1 P_1 + b_2 P_1^2 \ldots . \tag{7}$$

Choosing a rupture life and temperature, one can calculate the rupture life parameter, and thus the stress corresponding to the given conditions. Using the stress, one can solve Eq. (7) for the creep rate parameter, and thus the creep rate. Knowing rupture time and average creep rate, it is then a simple matter to calculate the total rupture elongation.

However, there are drawbacks to the use of total elongation as a failure criterion.[13] Perhaps a more relevant criterion would be the

creep strain to the onset of tertiary creep, ε_3, or the product of rupture life and minimum creep rate, $\dot{\varepsilon}_m t_r = e_s$. ORNL data[14] for e_s were reported previously. The data for the 2-in. plate form of the reference heat of type 304 stainless steel are being analyzed by parametric methods similar to those outlined above.

As a preliminary to the actual analysis, the isothermal creep-rupture data were converted to iso-stress data by conventional cross-plotting techniques.[15] The constants involved in many standard time-temperature parameters can then be calculated from these iso-stress curves. However, these values will be generally inferior to computer-optimized values. The main benefit of the iso-stress curves is to enable one to compare the data with the assumptions behind the parameters, since it is upon the appearance of these iso-stress curves that most of the parameters depend.[16] Although the assumptions of none of the parameters are fit exactly, both the Orr-Sherby-Dorn[17] and Manson-Succop[18] parameters agree reasonably well with the data.

For comparison, the data were also analyzed by the "graphical optimization procedure" of Woodford.[19] Again, the Orr-Sherby-Dorn and Manson-Succop parameters fit well, while others fit poorly.

Having determined which parameters are most consistent with physical reality, the data were then analyzed by a computer program[20] designed to calculate rupture time and minimum creep rate parameters, and then to calculate ductilities by the method of Goldhoff. However, the ductility value now being calculated is e_s, not rupture elongation. Also, the method used to calculate the parameters[21] automatically yields equations of the type

$$\text{(rupture time) } P = a_0 + a_1 \log \sigma + a_2(\log \sigma)^2 + a_3(\log \sigma)^3 \ , \quad (8)$$

$$\text{(minimum creep rate) } P_1 = b_0 + b_1 \log \sigma + b_2(\log \sigma)^2 + b_3(\log \sigma)^3 \ . \quad (9)$$

Therefore, these equations were used in place of Eqs. (6) and (7) with subsequent changes in technique. Note that this form, expressing P as a function of stress, rather than vice-versa, is a more natural one

mathematically. Analysis was also done for strain to third-stage creep, using time to tertiary creep and average creep rate to tertiary creep, defined by

$$\dot{\varepsilon}_{3\,(\text{average})} = \frac{\text{creep strain to tertiary creep}}{\text{time to tertiary creep}} \,. \qquad (10)$$

Onset of tertiary creep was defined by the 0.2% offset method.

Stress-rupture isothermals calculated from the optimized Manson-Succop parameter are compared with the actual experimental data in Fig. 5.27. Orr-Sherby-Dorn results were similar. Table 5.12 summarizes the results of calculation of the stress-rupture parameters by the various means employed. As can be seen, the comparison of calculated and experimental values is good, and the extrapolated values are at least reasonable. The rupture data are also currently being analyzed by the minimum committment method[15] using a computer program supplied by Ensign and Manson,[22] but results from this analysis are still in the preliminary stage.

These results can also be presented in terms of rupture strengths. Table 5.13 shows the 1000-, 10,000-, and 100,000-hr rupture strengths as calculated from the above analysis.

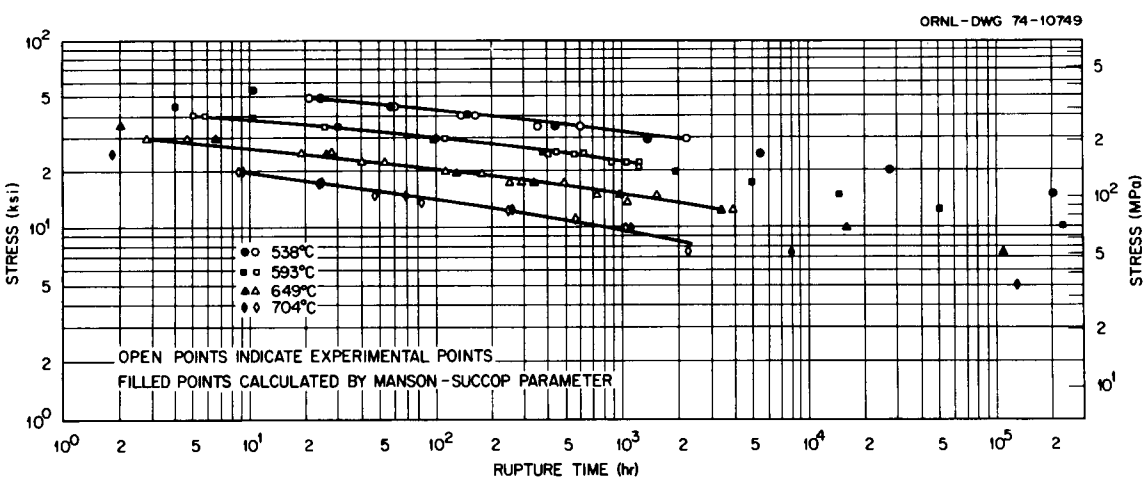

Fig. 5.27. Stress-Rupture Isothermals for Type 304 Stainless Steel, Heat 9T2796, 1-in. Plate.

Table 5.12. Stress-Rupture Parameters for Type 304 Stainless Steel Heat 9T2796 1-in. Plate

Definition of Parameters:

Manson-Succop $P = \log t_r + DT$,

Orr-Sherby-Dorn $P = \log t_r - Q/T$,

where t_r is rupture time in hours and T is the Kelvin temperature

Values of Temperature Coefficients:

Coefficient	Value for Each Fitting Method			ΣR^2, Optimized[b]
	Graphical	GOP[a]	Optimized	
D	0.02286	0.02195	0.020937	1.6359
Q	17,890	17,880	18,739	0.77846

Optimized Equations:

$$\text{M-S: } \log t_r + 0.020937T = 109.06 - 51.068 \log \sigma + 11.198 (\log \sigma)^2 - 0.94455 (\log \sigma)^3$$

$$\text{O-S-D: } \log t_r - 18{,}739/T = 204.08 - 155.06 \log \sigma + 37.755 (\log \sigma)^2 - 3.1904 (\log \sigma)^3$$

where σ = stress in psi.

[a]GOP = Graphical optimization procedure.
[b]ΣR^2 = Sum of squared residuals for $\log t_r$.

Figure 5.28 shows calculated minimum creep rate isothermals as compared with the experimental data. Table 5.14 and Figs. 5.29 and 5.30 show the results of the optimized calculations for time to tertiary creep and average creep rate to tertiary creep.

Using these results, the corresponding strain limits e_s and ε_3 may be calculated for given temperature and time values, as in the Goldhoff analysis. An even simpler approach would be to specify temperature and stress, and then to calculate the corresponding creep rate and time, and thus strain value, since then one could avoid

Table 5.13. Rupture Strengths for Type 304 Stainless Steel Heat 9T2796 1-in. Plate

Temperature		Rupture Time	Rupture Stress			
			Manson-Succop		Orr-Sherby-Dorn	
(°C)	(°F)	(hr)	(ksi)	(MPa)	(ksi)	(MPa)
538	1000	1,000	31.31	215.9	33.54	230.2
538	1000	10,000	23.00	158.6	25.79	177.8
538	1000	100,000	16.66	114.9	19.11	131.8
593	1100	1,000	21.92	151.1	22.53	155.3
593	1100	10,000	15.85	109.3	16.39	113.0
593	1100	100,000	11.36	78.3	11.51	79.4
649	1200	1,000	14.97	103.2	14.72	101.6
649	1200	10,000	10.72	73.9	10.24	70.6
649	1200	100,000	7.64	52.7	7.04	48.5
704	1300	1,000	10.18	70.2	9.70	66.9
704	1300	10,000	7.26	50.1	6.68	46.0
704	1300	100,000	5.20	35.8	4.69	32.3

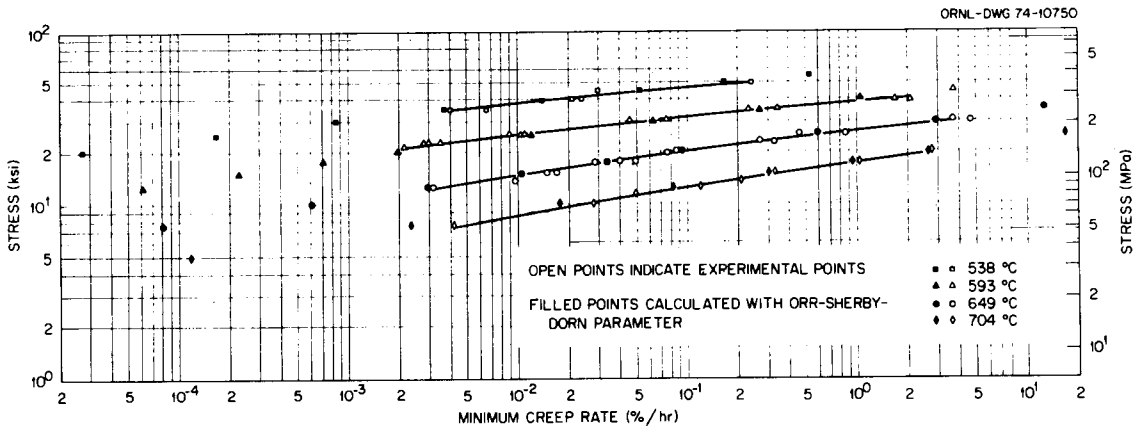

Fig. 5.28. Minimum Creep Rate Isothermals for Type 304 Stainless Steel, Heat 9T2796, 1-in. Plate.

Table 5.14. Time to Tertiary Creep Parameters for Type 304 Stainless Steel Heat 9T2796 1-in. Plate

Definition of Parameters:

Manson-Succop $P = \log t_3 + DP$,

Orr-Sherby-Dorn $P = \log t_3 - Q/T$,

where t_3 is the time in hours to tertiary creep and T is the Kelvin temperature.

Values of Temperature Coefficients, computer optimized

$D = 0.020898$; $\Sigma R^2 = 3.3078^a$

$Q = 18{,}711$; $\Sigma R^2 = 1.9527^a$

Optimized Equations:

$$\text{M-S: } \log t_3 + 0.020898T = 251.46 - 148.53 \log \sigma + 33.248 (\log \sigma)^2 - 2.5957 (\log \sigma)^3$$

$$\text{O-S-D: } \log t_3 - 18{,}711/T = 317.65 - 231.95 \log \sigma + 54.948 (\log \sigma)^2 - 4.4616 (\log \sigma)^3$$

where σ = stress in psi.

[a]Sum of squared residuals for $\log t_3$.

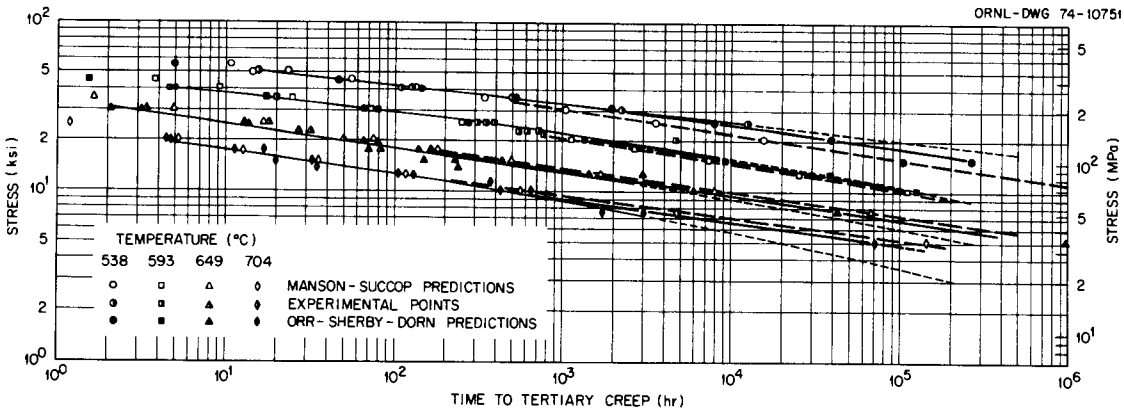

Fig. 5.29. Time to Tertiary Creep Isothermals for Type 304 Stainless Steel, Heat 9T2796, 1-in. Plate.

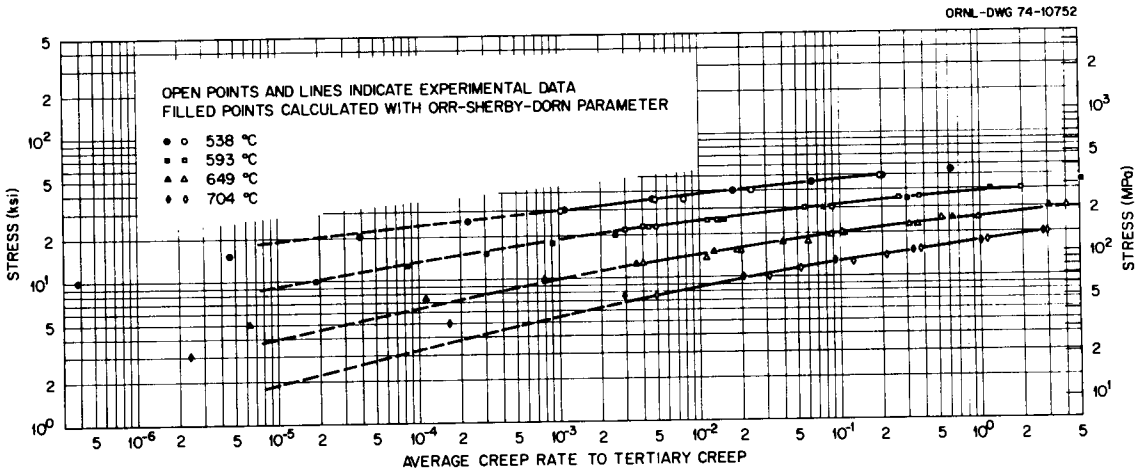

Fig. 5.30. Average Creep Rate to Tertiary Creep Isothermals for Type 304 Stainless Steel, Heat 9T2796, 1-in. Plate.

solving a cubic equation like (8) or (9) for stress. Results of the calculations for e_s and ε_3 are shown in Figs. 5.31 through 5.34.

The scatter in the actual experimental values of e_s and ε_3 make close correlation impossible. However, some conclusions can be drawn from the results. First, the results of the calculations for e_s seem more reasonable and consistent than those for ε_3. This could be due to the fact that the quanitities used to calculate e_s ($\dot{\varepsilon}_m$ and t_r) are measured with more accuracy than the onset of tertiary creep values. Thus, the increase in strain to tertiary creep at long times (low stresses) for 649 and 704°C (1200 and 1300°F) is probably not a real effect. However, the calculated e_s values show a definite increase with stress and temperature, and a definite decrease with time, especially at 593°C (1100°F) and above. Thus, the theory that e_s is constant for a wide variety of creep conditions[13] is not supported by this analysis. It must be remembered, however, that, because of data scatter, these correlations represent approximations only. Still, when used with caution, such methods show promise for use in development of ductility estimates for design use. Effects of complex stress and strain histories cannot, however, be clearly predicted without actual test data at such conditions. Tests of this type are included in present programs.

It should be noted that the parametric methods reported here are basically similar to the method first mentioned by Smith,[12] except that

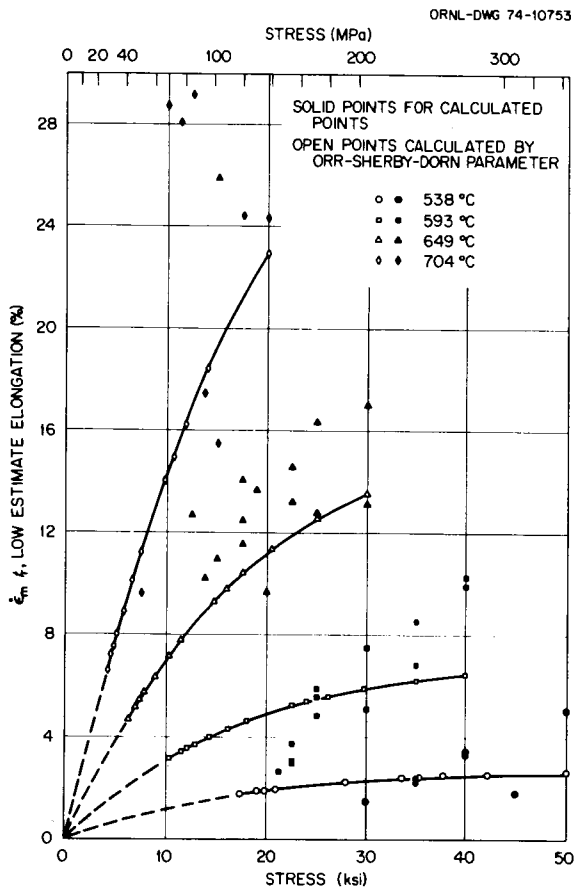

Fig. 5.31. Calculated Ductility Versus Stress for Type 304 Stainless Steel, Heat 9T2796, 1-in. Plate.

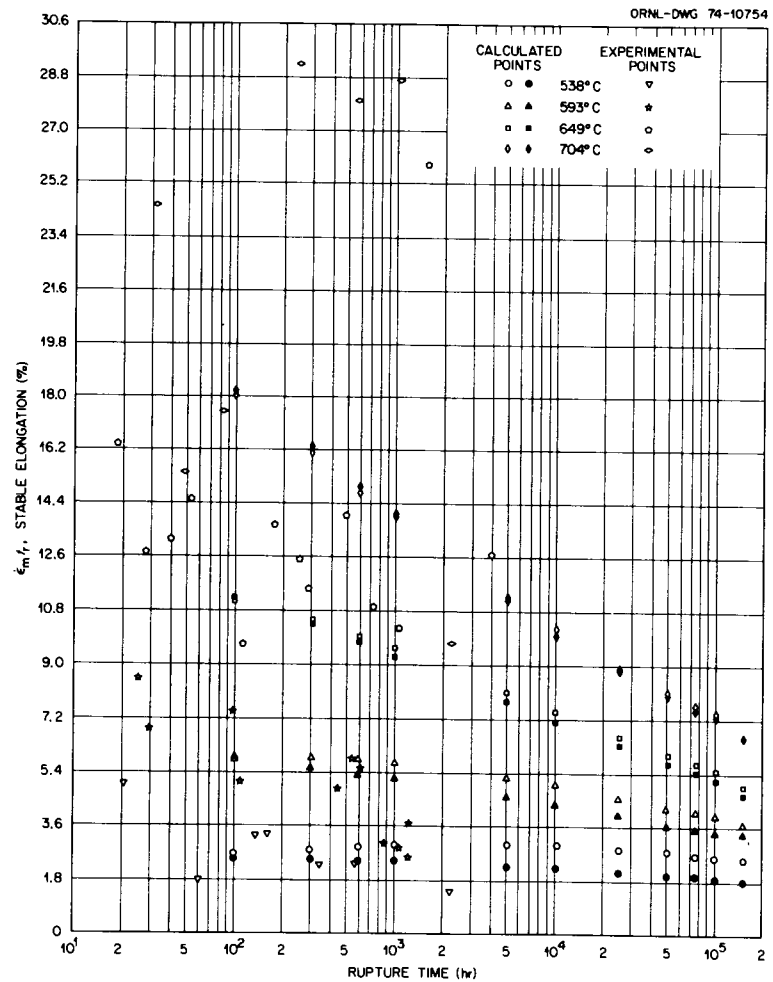

Fig. 5.32. Ductility Calculations for Type 304 Stainless Steel, Heat 9T2796, 1-in. Plate.

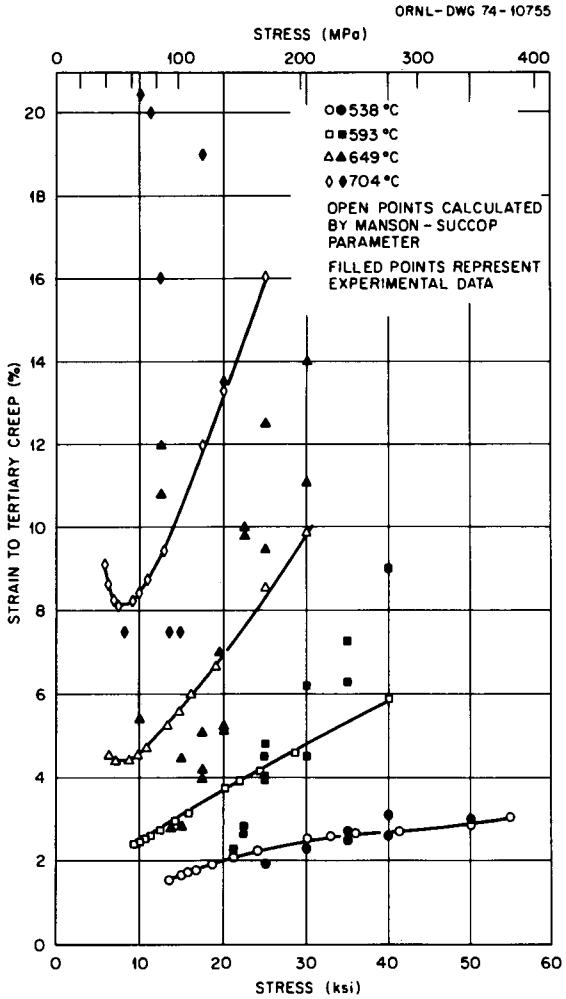

Fig. 5.33. Strain to Tertiary Creep Versus Stress for Type 304 Stainless Steel, Heat 9T2796, 1-in. Plate.

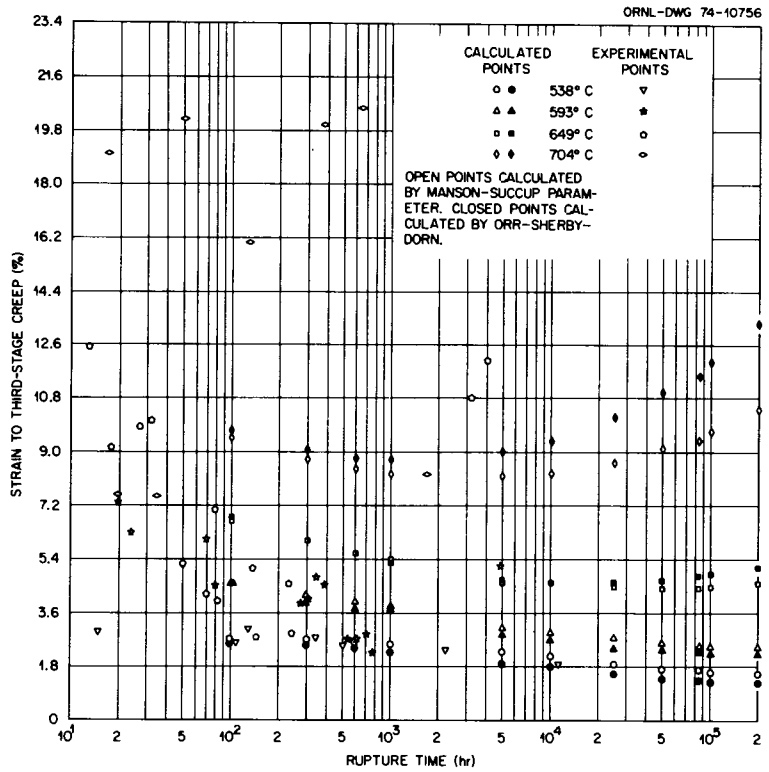

Fig. 5.34. Ductility Calculations for Type 304 Stainless Steel, Heat 9T2796, 1-in. Plate.

the extrapolation techniques used are considerably more sophisticated, and far more information on failure preduction is obtained. Results on the 1-in. plate of the reference heat obtained by the Smith method (Fig. 5.35) have been somewhat inferior to the parametric results.

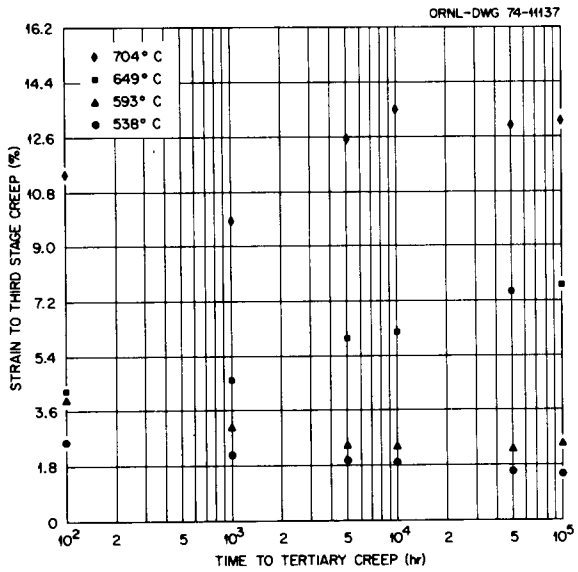

Fig. 5.35. Strain to Third-Stage Creep of Type 304 Stainless Steel, Heat 9T2796, 1-in. Plate, Calculated by Smith's Graphical Method.

Correlations of the quantities ε_3 and e_s are continuing, as are those for other quantities. Analysis of other product forms of the reference heat, and for different heats of type 304 stainless steel may provide new insights. Other methods of calculation are also being examined, but these examinations are still preliminary.

5.2.4 Mechanical Property Characterization of Type 316 Stainless Steel Reference Heat

5.2.4.1 Procurement of Type 316 Stainless Steel Reference Heat — R. J. Beaver

All plate items except the 2-in. (51-mm) plate have been received. It and all sheet items have been inspected and will be received early in October. Manufacturing of all bar items has been completed, and the bars were shipped to CONAM for inspection on September 23. Delivery at ORNL

is expected in October. Manufacturing of pipe items by the U.S. Steel Elwood City plant has progressed through all hot-piercing operations. Delivery is anticipated by late November.

Five pieces of forgings made at Republic Steel have been delivered to Carlton Forge, the Rollmet subcontractor for producing forged rings. Delivery of these forged rings for manufacturing into the 16- and 28-in.-diam (406- and 711-mm-) pipe by Rollmet is scheduled for late November. The Rollmet quality assurance plan and associated quality verification procedures have been received, and review of these procedures began in late September. The two forgings remaining on this order have been hot worked at Republic Steel.

5.2.5 Structural Materials Information Center — M. K. Booker and C. O. Stevens

The computerized mechanical properties data management system at ORNL is continuing to expand and develop. The results from over 2100 tensile, creep, impact, slow-bend, and relaxation tests are now stored in the Data Storage and Retrieval System. A data form for the input of the fatigue test results (Fig. 5.36) has been developed, and input of fatigue data is now beginning.

To make DSRS information fully useful, it is necessary to preserve uniformity and standardization in methods of determining the quantities to be stored in the system. To assure such uniformity, only tests conducted at ORNL have been input in the past, since full information and documentation on these tests is readily available. Also, a manual on standard methods of measurement of quantities to be input to DSRS is being developed, and a draft version is currently in the final stages of preparation. Work is also continuing on the development of a comprehensive system users' guide.

Unfortunately, the large amount of mechanical properties data currently available in the literature is greatly lacking in such standardization and documentation. Still, for many purposes, such data can be extremely useful; and often they are the only data available. The study of mechanical properties can require massive amounts of data, which cannot be easily handled or interpreted manually. Clearly, some sort of

MECHANICAL PROPERTIES DATA STORAGE FORM
FATIGUE

Test Number < > Specimen Number <NØ> Type of Test <TY>

Institution/Program/Date/Engineer/Technician <IP> ; ;

Temperature <TE> ; (°C) Irradiation Data:

Environment <EN> Experiment No. <EX>

Material <MA> Irradiation Temp. <IT> (°C)

Heat Number <HN> Fluence <FL> (N/cm²)

Alloy Base <AB> Reactor and Position <RP>

Heat Treatment <HT>

Specimen Description <SD>

Comments <CM>

Mode of Control	<LM>		Stress Range at: (cycles)	<SS>		
Strain Range	<ED>	(%)	(→1)		;	(psi)
Mean Strain	<ET>	(%)	(→2)		;	(psi)
Wave Form	<WF>		(→10)		;	(psi)
Hold Mode	<HM>		(→100)		;	(psi)
Hold Time	<TI>	(hrs)	(→1000)		;	(psi)
Ramp Strain Rate	<SR>	(%/sec)	(→Nf/2)		;	(psi)
Frequency	<FQ>	(Hz)	Cycles to Failure	<CF>		
Elastic Modulus	<YM>	(psi)	Time to Failure	<RT>	;	(hrs)
0.02% Offset Yield Stress	<YO>	(psi)	Maximum Tensile Stress at Nf/2	<TS>	;	(psi)
0.2% Offset Yield Stress	<Y2>	(psi)	Maximum Compressive Stress at Nf/2	<MC>	;	(psi)
Initial Stress Amplitude	<AS>	(psi)	Elastic Strain Range at Nf/2	<EL>	;	(%)
Initial Strain Amplitude	<NS>	(%)	Plastic Strain Range at Nf/2	<EP>	;	(%)
Saturation Stress Range	<ST>	(psi)	Cycles to First Decrease in Stress Range	<CD>		
Number Cycles at Saturation	<CS>		Cycles to 5% Reduction in Stress Range	<C5>		
Saturation Maximum Stress Amplitude	<MS>	(psi)				
Saturation Stress Amplitude at 0.1 Hold Time	<SH>	(psi)				
Saturation Minimum Stress Amplitude	<MN>	(psi)				

TX-4666 (8-74)

Fig. 5.36. Fatigue Data Storage Form.

computerization is necessary. Therefore, DSRS is now being expanded to include data from the literature and other outside sources. However, to preserve the uniformity in the ORNL data, these new data will be stored in a completely separate data base. Therefore, the information in one data base will be complete and standardized. The other data base will provide greater volume and variety of information, with some sacrifice in reliability. Still, though, these data will be as reliable as those available in the literature, and having these data stored in the system where they can easily be accessed for plotting, correlation, and comparison will make the data much more useful.

Expansion of services to system users is also continuing. A new computer program, TENSIS, has been developed to aid in the analysis of tensile test data. TENSIS accepts load-extension points from the Instron and extensometer charts of a test, then calculates the corresponding engineering stress-strain values. TENSIS then calculates the relevant DSRS identifiers (yield strength, tensile strength, uniform elongation, etc.). Output consists of a printed table of data and punched cards for input to DSRS. Also, the program is now being modified to provide graphical output, including calculation and plotting of true-stress true-strain curves on linear and log-log coordinates.

Another significant addition to the computerized data management system is the Automatic Data Acquisition System (ADAS). It is now in operation, with final checks being made on the efficiency of the system. Under ADAS, creep data are taken by a completely automated, computer-controlled system, with no human interaction. Thus, data points can be obtained more often with greater accuracy than previously possible.

The heart of ADAS is a PDP-8/E computer, including an additional 24K of Fabritek core. The computer is interfaced to a Digitrend 210. At the present time, the computer can accommodate 12 Digitrends, with 100 channels per Digitrend, although only one Digitrend is operating in the current initial phase. Through another interface, the Digitrend is linked to the creep frames. (Normally, each Digitrend is interfaced to 22 creep frames.) During each scan, the time, left and right linear variable differential transformer (LVDT) readings, load cell reading,

and temperature are read for each creep frame and recorded on magnetic tape. Also, extra channels are provided for special tests. Each scan and subsequent recording takes about 1 min per Digitrend, and scans are commenced every 6 min. If the computer should fail, the Digitrend would print out the data every 10 min. If a total power failure should occur, the clock converts automatically to battery power and continues to run. Then, when the power returns, the proper time is then still in the system.

The various tasks performed by ADAS are regulated by a real-time executive program. In the next phase, time-sharing will be incorporated to allow the computer to be used on various projects other than data taking. Additional developments, such as cathode ray tube (CRT) display and hard copy plots are also envisioned.

Development of the Structural Materials Information Center (SMIC) has continued. The new main computer program has been checked for efficiency, with minor problems being corrected. Computational subroutines have been modified, and the current demonstration data base has been updated.

5.2.6 Elastic Properties of Engineering Materials — J. P. Hammond

Precise measurements show that the elastic stress-strain relationships for metals are not perfectly linear and become progressively more nonlinear as strain increases. At the higher levels of strain, measurements reveal evidence of incipient plastic behavior, with strain a function of instantaneous stress, time, temperature, and prior strain history. As a consequence, discrepancies sometimes occur between elastic constants determined at different strain levels and rates of strain and between constants established by the dynamic (sonic) and static (monotonic tensile) methods. Data on dynamic properties are scant, and test variables for static data frequently are not reported.

The purpose of this program is to develop expected values of the elastic constants [Young's and shear moduli (E, G) and Poisson's ratio (ν)] of engineering materials of interest over useful ranges of temperature. Additionally, proportional and elastic limits (P.L., E.L.) will be examined. High-resolution static and dynamic methods of test will

be used, and test parameters will be varied through appropriate ranges to establish their influence. The findings will be correlated for engineering design use.

5.2.6.1 Program Progress

During the last quarter a correlation was prepared of the elastic constants (E, G, and ν) of 2 1/4 Cr-1 Mo steel as determined by the static and dynamic methods for the *Nuclear Systems Materials Handbook*. Expected values for static constants were estimated from data in the literature, whereas our recently developed values[23] for the dynamic constants were used. The elastic moduli characteristically decreased with increasing temperature, with the static values falling somewhat below the dynamic at all temperatures. The static values dropped off more markedly than the dynamic at temperatures above about 425°C (800°F). This inflection in the static curves was attributed to creep. Expected values of Poisson's ratio fell between 0.25 and 0.30 from room temperature to 650 or 760°C (1200 or 1400°F) irrespective of whether they were based on static or dynamic measurements.

Components for a laser diffraction microstrain measuring apparatus were ordered from Diffracto Ltd. This unit will be used to calibrate the micro stress-strain plotting apparatus being developed with resistance strain gages as sensors. Delivery of 16 weldable resistance strain gages each for 2 1/4 Cr-1 Mo steel and type 304 stainless steel is expected in six weeks.

Test specimens planned for the dynamic elastic properties studies are listed in Table 5.15. All materials for which heat numbers are shown in the table have been received and are largely processed. Heat 9T2796 of the type 304 stainless steel (Codes 1 through 4) will be used to examine directionality of elastic constants within the plate form. Heats 346845, 346544, and X22807 (Codes 5–7) are type 304 stainless steel with high, low, and medium creep strengths, and these will be used to examine heat-to-heat variations in elastic constants at room temperature. Variations in elastic constants at elevated temperatures will be assessed by comparing results for heats 9T2796, 346544, and 60551

Table 5.15. Specimens for Dynamic Elastic Properties Study

Code	Material					Orientation of Specimen Axis[a]	Specimen Condition[b]	
	Alloy	Dimension (in.)	Dimension (mm)	Form	Heat		Blocks for Room Temperature	Wire for Elevated Temperature
9	2 1/4 Cr-1 Mo	1	25	Plate	20017	‖ RD	Annealed	Annealed, CT, AT
17	9 Cr-1 Mo	0.5	13	Plate	316381-1A	‖ RD	Annealed	Annealed
15	Incoloy 800H	1	25	Plate	HH6758A	‖ RD	SA, MA	SA, MA
1	Type 304 SS	1	25	Plate	9T2796	‖ RD	SA, MA	SA, CT, AT
2	Type 304 SS	1	25	Plate	9T2796	In plane, 45° to RD	SA, MA	
3	Type 304 SS	1	25	Plate	9T2796	In plane, ⊥ RD	SA, MA	
4	Type 304 SS	1	25	Plate	9T2796	⊥ plane	SA, MA	
5	Type 304 SS	2.75	70	Plate	346845	‖ RD	SA, MA	
6	Type 304 SS	2	51	Plate	346544	‖ RD	SA, MA	SA
7	Type 304 SS	2.5	64	Plate	X22807	‖ RD	SA, MA	
8	Type 304 SS	3	76	Bar	60551	‖ RD	SA, MA	SA
10	Type 308 SS	FFTF Weld			CE-75	‖ WD	SA, as welded	SA, as welded
13	Type 316 SS	1	25	Plate		‖ RD	SA, 20% CR	SA, 20% CR
16	Hastelloy X	0.75	19	Rod	2600-0-2735	‖ RD	SA, MA	SA, MA
11	Inconel 718	0.75	19	Plate	2180-2-9247	‖ RD	Age hardened	Age hardened
12	Inconel 718	Weld deposit			2180-2-9247	‖ WD		Age hardened
19	Hastelloy N	1	25	Plate		‖ RD	SA, MA	SA
18	Inconel 617	1	25	Plate		‖ RD	SA, MA	SA

[a]RD = rolling direction; WD = welding direction.

[b]CT = treated to give cold-worked fiber texture; AT = treated to give recrystallized fiber texture; SA = solution annealed; MA = mill annealed; CR = cold reduced.

(Codes 1, 6, and 8). The effects of preferred crystallographic orientation of grain structure will be examined for the 2 1/4 Cr-1 Mo steel (Code 9) and type 304 stainless steel heat 9T2796 (Code 1).

5.2.6.2 Elastic Properties Determined by Dynamic Tests — J. P. Hammond and M. W. Moyer*

A mathematical analysis of the experimental elastic constant data forthcoming from the first of several heats of type 304 stainless steel examined in connection with a heat-to-heat variations effect study (Code 6, Table 5.15) was completed. The procedures used to determine elastic constants from sound velocity measurements and the subsequent treatment of the resulting data to establish equations of properties as a function of temperature were given previously.[23,24]

Cubic polynomials representing E, G, and ν of solution-annealed type 304 stainless steel heat 346544 as a function of temperature are given below with standard deviations of the constants, while graphical models of the equations are presented in Figs. 5.37, 5.38, and 5.39.

Young's Modulus:

$$E(T) = E(T_0)[1 + A_E(T - T_0) + B_E(T - T_0)^2 + C_E(T - T_0)^3] ,$$

where

T = temperature in °F,

T_0 = (75°F),

$E(T_0) = 29.23 \times 10^6$ psi,

$A_E = -2.47 \times 10^{-4} \pm 0.05 \times 10^{-4}$,

$B_E = -3 \times 10^{-8} \pm 1 \times 10^{-8}$, and

$C_E = 2.7 \times 10^{-11} \pm 0.8 \times 10^{-11}$.

---

*Laboratory Development, Y-12.

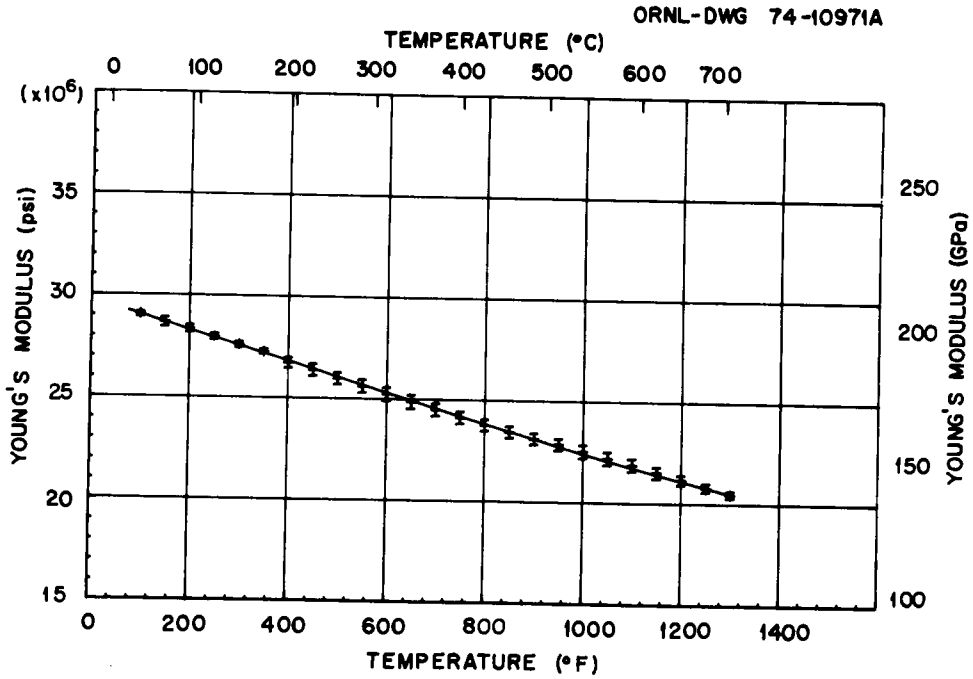

Fig. 5.37. Young's Modulus (E) of Type 304 Stainless Steel, Heat 346544.

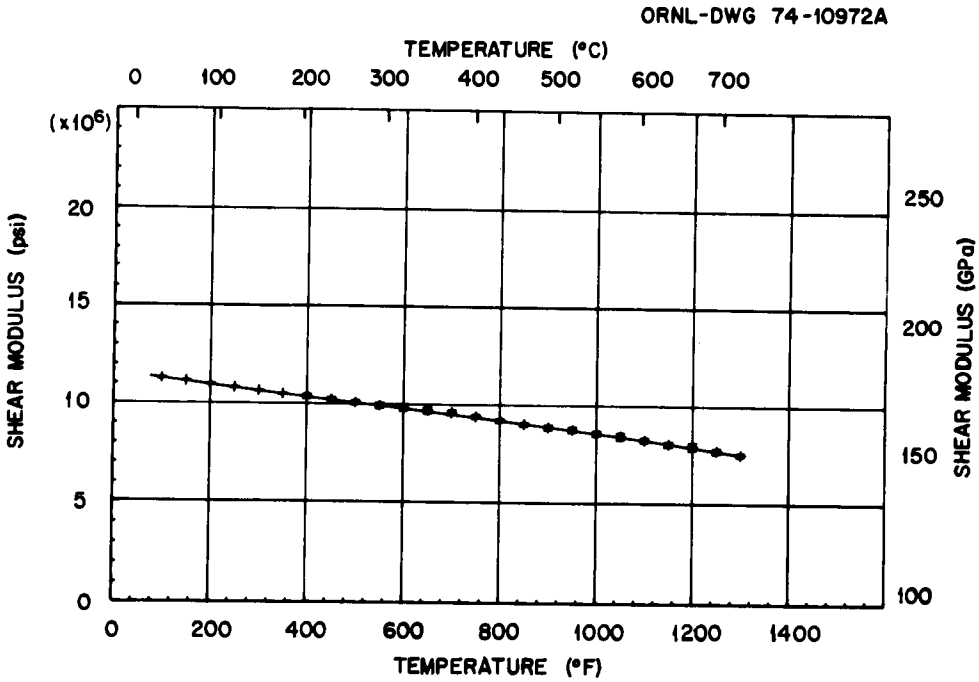

Fig. 5.38. Shear Modulus (G) of Type 304 Stainless Steel, Heat 346544.

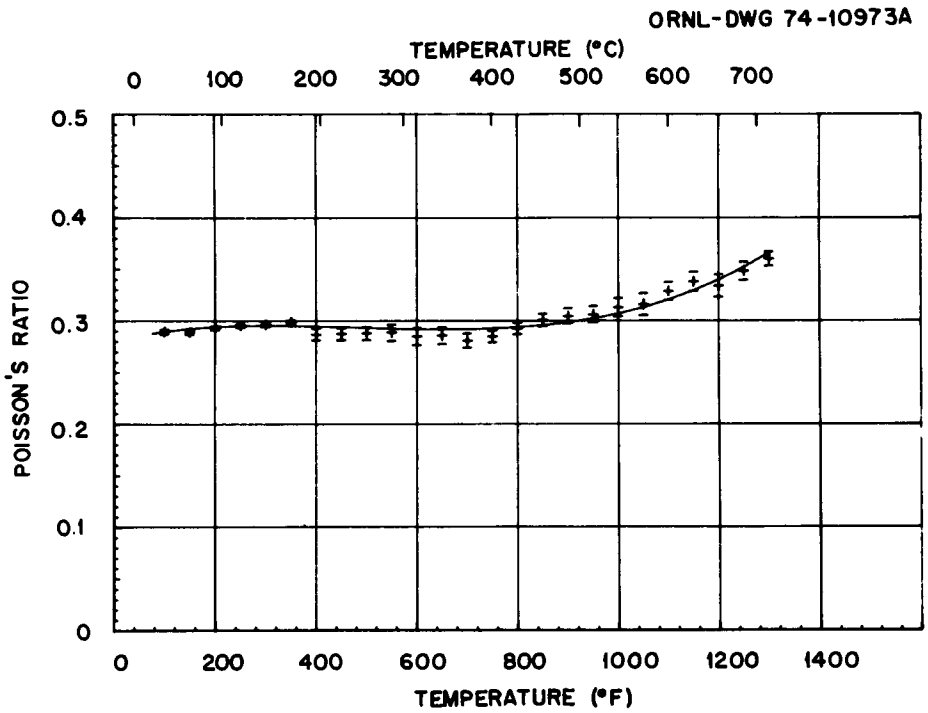

Fig. 5.39. Poisson's Ratio (ν) of Type 304 Stainless Steel, Heat 346544.

Shear Modulus:

$$G(T) = G(T_0)[1 + A_G(T - T_0) + B_G(T - T_0)^2 + C_G(T - T_0)^3] ,$$

where

$$G(T_0) = 11.35 \times 10^6 \text{ psi},$$
$$A_G = -2.86 \times 10^{-4} \pm 0.03 \times 10^{-4},$$
$$B_G = 7 \times 10^{-8} \pm 1 \times 10^{-8},$$
$$C_G = -4.8 \times 10^{-11} \pm 0.7 \times 10^{-11}.$$

Poisson's Ratio:

$$\nu(T) = A_\nu + B_\nu T + C_\nu T^2 + D_\nu T^3 ,$$

where

$$A_\nu = 0.281 \pm 0.004,$$
$$B_\nu = 1.1 \times 10^{-4} \pm 0.2 \times 10^{-4},$$
$$C_\nu = -2.5 \times 10^{-7} \pm 0.5 \times 10^{-7}, \text{ and}$$
$$D_\nu = 1.7 \times 10^{-10} \pm 0.2 \times 10^{-10}.$$

The residual mean squares associated with each elastic property for 25 observations are E, 0.10; G, 0.12; ν, 1.00.

The graphs of the dynamic Young's and shear moduli for this type 304 stainless steel show a nearly linear relationship with temperature (Figs. 5.37 and 5.38). The Poisson's ratio (Fig. 5.39) appears to be constant around 0.29 up to about 425°C (800°F) and then deflects upward to a value of about 0.36 at 704°C (1300°F).

Similar information is being processed for heats 9T2796 and 60551 to enable heat-to-heat comparisons of dynamic elastic constants of type 304 stainless steel.

5.2.7 Analytical Studies of Mechanical Properties Testing — B. R. Dewey*

5.2.7.1 Development of Finite Element Models for Crack Tip Analysis — J. E. Akin* and B. R. Dewey*

A series of reports dealing with needed improvements for application of finite element analysis to fracture mechanics has been prepared. These implementations in finite element analysis will primarily be used to aid crack-growth study in weldments, but will also be useful in all fracture mechanics calculations. It is well known that finite-element solutions for the stress intensity factor, for the strain energy release rate, for the J-integral, or for other such parameters are needed when boundary conditions, loading, or material properties are not tractible for closed-form solution. Three topics have been treated:

---

*Subcontractor from Department of Engineering Science and Mechanics, University of Tennessee, Knoxville, Tennessee.

5.2.7.1.1 Generation of Crack Tip Elements. A procedure is given for generating conforming crack tip elements from standard conforming elements. Two new elements are introduced. The technique is based on the use of elements defined by numerically integrated shape functions. The direct evaluation of element stress intensity factors is investigated and special quadrature rules are suggested for triangular elements.

5.2.7.1.2 Generalization of the J-Integral. A three-dimensional integral is defined and shown to reduce to the J-integral, which is commonly utilized in two-dimensional fracture mechanics. This new integral may suggest a new approach for computational methods in three-dimensional fracture mechanics.

5.2.7.1.3 Addition of Crack Tip Elements to a Finite Element Analysis Code. An existing finite element code (Wilson Code) has found wide use in elastic stress analysis of both isotropic and orthotropic materials. The two input elements are the quadrilateral and the triangular elements, which have linear displacements. Near the crack tip, the high strain gradient requires smaller elements, and hence, a large number of them. Not only is it more economical, but also it extends the range of problems that can be treated if a special element is used to bound the crack tip. Thus, such a special element, which can be as large as a standard element, has been developed to accurately model the $\sqrt{r}$ variation in displacements near the crack tip. In turn, this gives a $1/\sqrt{r}$ variation in stresses, whereas the stresses in the standard element are constant.

The special elements are triangular. For these elements the crack tip is defined to occur at the first node number listed for the element. The stresses output for these elements are the average stresses obtained by integrating the stresses over the volume of the element and then dividing by the volume.

The automatic evaluation of K_I and K_{II} for orthotropic materials with a material axis parallel to the crack direction has been formulated but not yet implemented into the code.

5.2.7.2 Finite Element Analysis of Creep and Plasticity in Tensile Test Specimens — B. R. Dewey*

Difficulty has long been recognized in producing a perfectly uniform uniaxial stress state for the measurement of mechanical properties. The well-known St. Venant principle, which intimates that stresses become uniform in regions sufficiently removed from discontinuities, has dictated the traditional use of the long-gage-length cylindrical tensile specimen. As test conditions such as elevated temperature, cyclic loading, large strains, and limitations of equipment, material, and space have been imposed, test specimen geometries have been modified.

Two typical but different specimen geometries finding wide use in the present high-temperature properties work are an hourglass (or zero-gage-length) specimen and a cylindrical specimen. The displacements, strains, and stresses in these two specimens have been studied in detail.

Particularly attractive features of the hourglass specimens include resistance to buckling when loaded in compression, ease of heating since only a small part of the specimen needs to be at uniform temperature, simplified data acquisition by use of diametral measurements for calculation of both radial and axial strains, and economy of material since the specimen is shorter for a given diameter. Balanced against these advantages is the triaxial stress state at the neck of the of the hourglass, which occurs as expected from St. Venant principle.

In contrast, the cylindrical specimen does provide pure uniaxial stress in the region removed from the transition fillets. Axial strain is assumed to be computed directly from the change in the gage length. On the other hand, the cylindrical specimen buckles under less compressive stress, requires a well-designed heating system to give uniform temperature over the gage length, has some triaxiality in the transition fillets, and poses some special problems in extensometry. High-temperature, large-strain testing requirements have forced the attachment of the extensometer on the shoulders instead of directly on the gage section; the material between the attachment points departs considerably from a state of pure uniaxial stress. In order to assure that rupture

---

*Subcontractor from the University of Tennessee.

occurs near mid-specimen, a slight taper has been found necessary, which in turn would produce a slight departure from uniform uniaxial stress.

As more and more high-temperature mechanical properties data are accumulated and compared, the question arises as to what causes the apparent differences in properties reported for the same material. Stress analysis provides a partial answer to the question.

With experimental stress analysis, limited information can be deduced from the outside looking in. Strain gage work at high temperature leads to advanced instrumentation problems, provides limited information on the strain state at the surface, and is relatively expensive considering the amount of data returned. Multiple extensometers have been used to help recognize bending and "bad" data. Other experimental observations have been made, such as comparing results from cylindrical specimens of two different gage lengths or comparing data from cylindrical and hour-glass specimens. Grid works and diametral measurements also have been used to study the strain distribution in the specimen.

Recent developments in finite element stress analysis for plasticity and creep permit a much more economical study of strain and stress distributions and of the extensometry of the specimens. The CREEP-PLAST Code[25] developed by ORNL for high-temperature design of axisymmetric and plane structures is particularly well suited for the study of mechanical properties test specimens. The features of CREEP-PLAST that are utilized here include an incremental plasticity solution, which uses the tangent stiffness approach, a bilinear representation of the stress-strain curve, an equation-of-state creep formulation easily usable for type 304 stainless steel and 2 1/4 Cr-1 Mo steel, ability to specify increments in loading or displacement on selected groups of nodal points, and a restart procedure that permits running a large number of increments with intermediate examinations of the solution.

In the results computed for this study with CREEP-PLAST is such a volume of data that only some representative conclusions can be presented here.

5.2.7.2.1 Hourglass Specimen. One concern with the hourglass specimen is the triaxiality of the stress state because of the neck — the same phenomenon as studied by Bridgman[26] with certain simplifying assumptions. Our results have shown that triaxiality at the neck is not particularly a problem. Figure 5.40 shows a summary of solutions for two hourglass configurations; R is the profile radius, and D is the diameter of the minimum section. The principal differences between the present work and Bridgman's work are that strain hardening is now included, and that the assumption that the radial and hoop components of the stress tensor are equal is not now required. As can be seen from Fig. 5.40, as plasticity progresses, the location of maximum triaxiality changes, and does not necessarily occur at the center of the specimen.

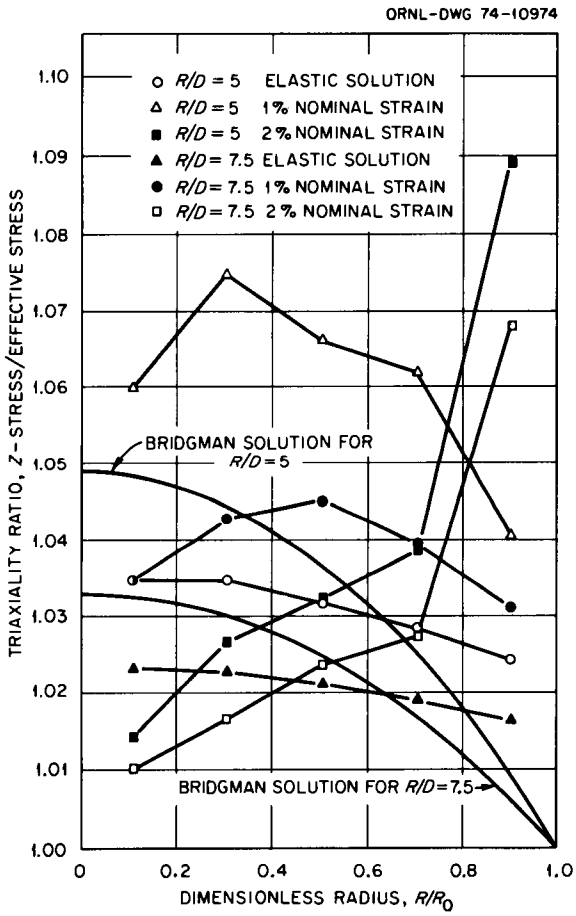

Fig. 5.40. Triaxiality in Hourglass Tensile Specimens.

Another concern is the use of diametral extensometry. An equation for the average strain ε_z can be developed from elementary principles and can be stated as

$$\varepsilon_z = (4P/\pi E d^2)(1 - \nu_e/\nu_p) - (1/\nu_p)\ \ln(d/d_0)\ , \qquad (11)$$

where P is the axial load, E is the modulus of elasticity, ν_e and ν_p are the elastic and plastic Poisson's ratios, and d and d_0 are the instantaneous and original diameters. The strain computed from Eq. (11) is plotted as the abscissa in Fig. 5.41, with the error in this strain plotted as the ordinate. The error is based on the mean strain computed from finite element analysis. Since the error appears to be generally less than 1%, the use of diametral extensometry *for monotonic loading* seems to be quite valid.

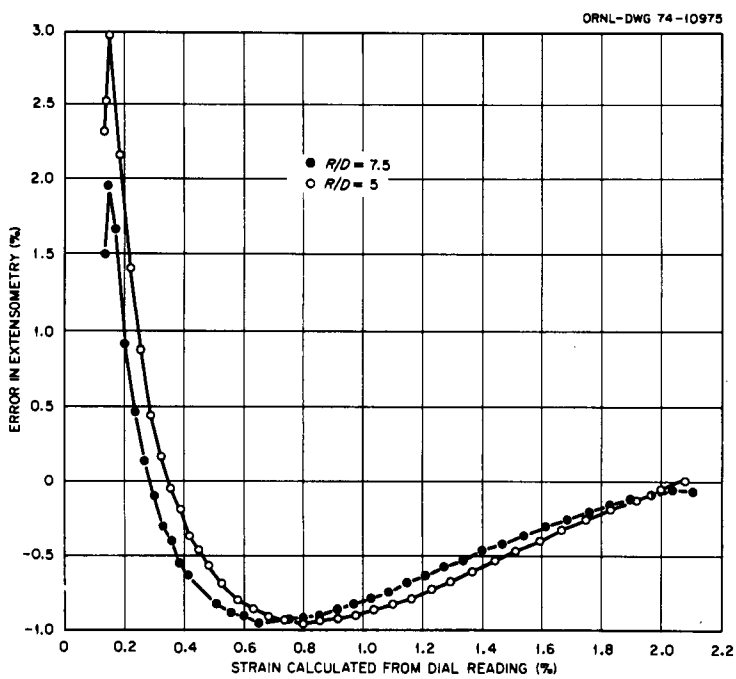

Fig. 5.41. Error in Diametral Extensometry.

5.2.7.2.2 Cylindrical Specimen. Standard ORNL cylindrical test specimens with a 1.25-in. (32-mm) gage length and 0.25-in. (6.4-mm)

diameter with and without a slight taper were selected for analysis. A standard creep and strain-hardening model of type 304 stainless steel was used in the CREEP-PLAST code.

Tapering the specimen reduces the propensity for fracture near the fillet radii. As shown in Fig. 5.42, the normalized axial strain does indeed peak away from the center of a nontapered specimen. Also, it may be observed that an essentially uniform elastic strain in the gage section becomes nonuniform under conditions of creep and plasticity. This is due to the reinforcing effect of the fillet radii; this effect apparently goes back about one diameter from the radius. The assumption that far less inelastic strain occurs in the region of the radius has been used in converting dial indicator readings from the extensometer to axial strain.

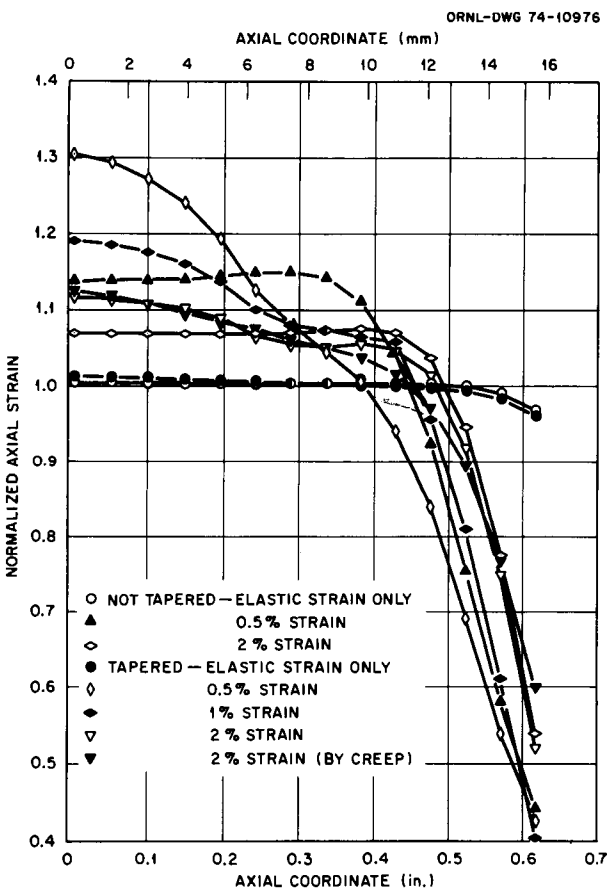

Fig. 5.42. Normalized Axial Strain Profiles in Cylindrical Specimens.

The efficacy of placing the extensometer on grooves on the specimen shoulders is summarized in Fig. 5.43 for a particular case of creep. Here, a very large extensometry error is observed at small strains. This large error is due to the elastic deformation in the fillet radii. As inelastic deformation progresses, the proportional decrease of additional strain in the fillet radii tends to balance the increased strain in the central part of the gage section; thus, as seen in Fig. 5.43, the extensometry error for creep at 2% strain is about 5%.

In view of the computed results, specimen profiles should be carefully controlled. Since strain distribution and extensometry are such strong functions of profile, this appears to be a major factor in scatter of creep data.

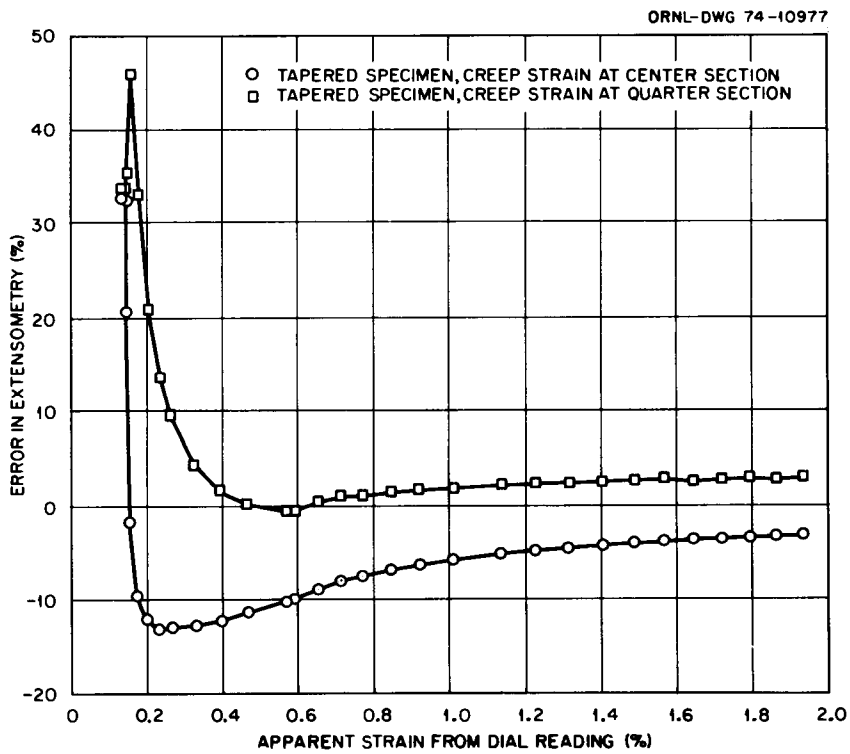

Fig. 5.43. Strain Measurement Errors Due to Deformation Outside the Gage Section.

5.3 MECHANICAL AND METALLURGICAL BEHAVIOR OF WELDMENTS FOR LMFBR — P. Patriarca, G. M. Slaughter, W. R. Martin, and C. R. Brinkman

5.3.1 Analysis of Tensile Test Data for a Type 308 CRE Stainless Steel Pressure Vessel Weld at 0.004/min Strain Rate — C. K. Bayne* and R. T. King

Tensile data for longitudinal all-weld-metal specimens from the FFTF vessel test welds have been reported previously.[27,28] The method of specimen preparation and testing methods have also been described.[29,30] The chemical compositions of the welds and base metal have also been given previously.[30]

This report is a statistical analysis of the tensile data at a constant strain rate of 0.004/min. A statistical analysis on the complete set of data would be difficult if not meaningless because of the highly unbalanced nature of the data. Although the set of data restricted to the constant strain rate of 0.004/min is also unbalanced, a statistical analysis that gives meaningful results can be performed.

Sixteen measurements or dependent variables were made on each tensile specimen. The measurements were made at different levels of four controlled, or independent variables.

The independent variables and their levels are:

$H_i \equiv$ Heat of type 304 stainless steel. $i = 1,2$.

$R_j \equiv$ Welding Rod. $j = 1,2$; where R_1 is type 308 CRE stainless steel electrode and R_2 is standard type 308 stainless steel electrode.

$T_k \equiv$ Temperature at which the dependent variables are measured, $k = 1,2,3$; where $T_1 = 75°F$, $T_2 = 900°F$, and $T_3 = 1100°F$.

$L_l \equiv$ Location from which the specimens are cut, $l = 1,2,3$; where L_1 = Location nearest the surface, L_2 = location in the mid-section, and L_3 = location in the middle.

For different heat and rod combinations, m repeated measurements are made, where $m = 1,\ldots,n_{ij}$; $n_{11} = 4$, $n_{12} = 1$, $n_{21} = 2$, and $n_{22} = 0$. From this subsampling, we see the data are not only unbalanced but also contain no observations for the $H_2 \times R_2$ combination, a situation that was dictated by the shortage of weld test plates, which had been divided between ORNL, ANL, and ANC at the start of the test program.

---

*Mathematics Research Staff.

The 16 measurements made for different combinations of the dependent variables are: (1) ultimate strength (engineering value), (2) ultimate strength (true value), (3) fracture strength (engineering value), (4) fracture strength (true value), (5) uniform strain (engineering value), (6) uniform strain (true value), (7) total strain (engineering value), (8) total strain (true value), (9) reduction of area (%), (10) ratio of maximum to minimum diametral strain at fracture, (11) ratio of maximum to minimum diametral strain away from fracture, (12) elastic limit measured by an averaging extensometer, (13) 0.2% offset yield stress measured by an averaging extensometer, (14) apparent elastic limit from the Instron chart, (15) 0.2% offset yield stress (engineering value), and (16) 0.2% offset yield stress (true value).

For each of the dependent variables, the following questions are asked:

1. Do the two different heats of base metal contribute significantly to the variation in the dependent variables?
2. Do the two different kinds of rods, CRE and conventional, contribute significantly to the variation in the dependent variables?
3. Are the different temperatures a significant factor?
4. Are the different specimen locations a significant factor?

To answer the four questions that are posed, an analysis of variance (ANOVA) model, which includes all the independent variables and their possible interactions, is used to describe the variation in each of the dependent variables. If the mth observed value of a dependent variable in the ith heat, jth rod, kth temperature, and lth location is represented by Y_{ijklm}, the ANOVA model is:

$$Y_{ijklm} = u + H_i + R_j + T_k + L_l + (HT)_{ik} + (HL)_{il} + (RT)_{jk}$$

$$+ (RL)_{jl} + (TL)_{kl} + (HTL)_{ikl} + (RTL)_{jkl} + \varepsilon_{ijklm} , \qquad \text{(model 1)}$$

where

$$i = 1,2;\ j = 1,2;\ k = 1,2,3;\ l = 1,2,3;\ \text{and}\ m = 1,\ldots,n_{ij},\ \text{with}\ n_{11}$$

$$= 4;\ n_{12} = 1;\ n_{21} = 2\ \text{and}\ n_{22} = 0 .$$

The error terms ε_{ijklm} are assumed to be independent and identically distributed as a normal distribution with mean zero and a constant variance. The term u is an overall general mean. Model 1 does not contain any terms involving heat and rod interaction because there are no observations for the $H_2 \times R_2$ combination (i.e., $n_{22} = 0$). Since model 1 does have missing observations and is unbalanced, another ANOVA model that does not contain the independent variable H was proposed to see if it would be as appropriate as model 1. Without the heat terms, the second ANOVA model that is used to describe the variation in each dependent variable is:

$$Y_{ijklm} = u + R_j + T_k + L_l + (RT)_{jk} + (RL)_{jl}$$

$$+ (TL)_{kl} + (RTL)_{jkl} + \varepsilon_{jklm} , \qquad \text{(model 2)}$$

where

$$j = 1,2;\ k = 1,2,3;\ l = 1,2,3;\ m = 1,\ldots,n_j, \text{ with}$$

$$n_1 = 6 \text{ and } n_2 = 1 .$$

The testing of significance of the independent variables R, T, and L depends on which ANOVA model is chosen. To alleviate this dependence on the model, the significance level for testing model 2 versus model 1 is chosen larger (i.e., 20% or greater) than the usual 5 or 10% levels. For each of the 16 dependent variables model 1 is not significantly better than model 2 in describing the variation in the dependent variables. This test also shows that variation due to using two different heats of steel is negligible for this experiment. Therefore, model 2 is an appropriate model to test the independent variable terms R, T, and L. The subsampling in model 2 is proportional; therefore, the sums of squares for model 2 can be found by using the usual formulas for proportional analysis of variance.[31] Table 5.16 gives the significant (S) and nonsignificant (NS) terms in model 2 for each of the dependent variables, for a 5% significance level.

Table 5.16. Significant (S) and Nonsignificant (NS) Independent Variables (5% Significance Level)

Dependent Variables[a]	Significance of Independent Variables						
	Rod *R*	Temp. *T*	Loc. *L*	Temp. × Loc. (*TL*)	Temp. × Rod (*TR*)	Loc. × Rod (*LR*)	Temp. × Rod × Loc. (*TLR*)
Ultimate strength (E)	S	S	S	S	S	NS	NS
Ultimate strength (T)	NS	S	S	NS	S	NS	NS
Fracture strength (E)	NS	S	S	NS	NS	NS	NS
Fracture strength (T)	NS	S	NS	S	NS	NS	NS
Uniform strain (E)	NS	S	S	NS	NS	NS	NS
Uniform strain (T)	NS	S	S	NS	NS	NS	NS
Total strain (E)	NS	S	S	NS	NS	NS	NS
Total strain (T)	NS	S	S	NS	NS	NS	NS
Reduction of Area	NS	S	S	NS	NS	NS	NS
Max/Min diametral strain (At)	NS	S	NS	S	NS	NS	NS
Max/Min diametral strain (Away)	NS	S	NS	NS	NS	NS	NS
Elastic limit by extensometer	NS	S	S	S	NS	NS	NS
0.2% offset yield strength by extensometer	S	S	S	S	NS	NS	NS
Apparent elastic limit	S	S	S	S	NS	NS	NS
0.2% offset yield stress (E)	S	S	S	S	NS	NS	NS
0.2% offset yield stress (T)	S	S	S	S	NS	NS	NS

[a](E) = engineering value, (T) = true value, (At) = at fracture, and (Away) = away from fracture.

Both the three-factor interaction (*TLR*) and the two-factor interaction (*LR*) are not significant for all dependent variables. The temperature by rod interaction (*TR*) is only significant for the engineering and true value measurements of ultimate strength. For the remaining 14 dependent variables, the (*TR*) interaction is not significant. The most important two-factor interaction is the temperature by location interaction (*TL*), which is nonzero for half the dependent variables.

A significant two-factor interaction is a measure of the failure of one factor to have the same response at each level of the second factor. Testing interactions may also be interpreted as testing the linearity of the factors in the model.

The only main effect that is significant for all dependent variables is temperature. The temperature effect also accounts for the largest variation of the dependent variables. The location effect is significant for all but three dependent variables; the true value of fracture strength, the ratio of maximum to minimum diametral strain at fracture, and the ratio of maximum to minimum diametral strain away from fracture.

For the significant temperature and location main effects, Tukey's w-procedure[31] is used to tell which of the three temperatures or locations can be considered different at the 5% significance level. The results for the temperature effects are given in Table 5.17 and for the location effects in Table 5.18. The dependent variables are classified in the tables according to how their main-effect means are ordered from largest to smallest. Those temperatures or locations that are underlined are *not* considered significantly different. The values of the temperature and location means are given in Table 5.19.

From Table 5.19 the means for the rod effect may also be compared. For the five dependent variables for which the rod effect is significant, the type 308 CRE stainless steel electrode (i.e., Rod 1) always has a higher mean value than the standard type 308 stainless steel electrode (i.e., Rod 2).

Table 5.17. Tukey's w-Procedure for Difference in Temperature Effects (5% Significance Level)

Dependent Variable[a]	Order of Temperature Means from Largest to Smallest[b]		
Ultimate strength (E)	1	2	3
Ultimate strength (T)	1	2	3
Fracture strength (E)	1	2	3
Fracture strength (T)	1	2	3
Uniform strain (E)	1	2	3
Uniform strain (T)	1	2	3
Max/Min diametral strain (At)	1	2	3
Elastic limit by extensometer	1	2	3
0.2% offset yield strength by extensometer	1	2	3
Apparent elastic limit	1	2	3
0.2% offset yield stress (E)	1	2	3
0.2% offset yield stress (T)	1	2	3
Total strain (T)	3	2	1
Reduction of area	3	2	1
Total strain (E)	1	3	2
Max/Min diametral strain (Away)	2	3	1

[a](E) = engineering value, (T) = true value, (At) = at fracture, (Away) = away from fracture.

[b]Underlined pairs of locations are *not* considered significantly different. Where two pairs are underlined for the same dependent variable, the extremes are significantly different. but the adjacent values are not.

Table 5.18. Tukey's w-Procedure for Difference in Location Effects (5% Significance Level)

Dependent Variable[a]	Order of Location Means from Largest to Smallest[b]		
Uniform strain (E)	1	2	3
Uniform strain (T)	1	2	3
Ultimate strength (E)	3	2	1
Elastic limit by extensometer	3	2	1
0.2% offset yield strength by extensometer	3	2	1
Apparent elastic limit	3	2	1
0.2% offset yield stress (E)	3	2	1
0.2% offset yield stress (T)	3	2	1
Ultimate strength (T)	1	3	2
Total strain (E)	1	3	2
Total strain (T)	1	3	2
Reduction of area	1	3	2
Fracture strength (E)	2	3	1

[a](E) = engineering value, (T) = true value.

[b]Underlined pairs of locations are *not* considered significantly different. Where two pairs are underlined for the same dependent variable, the extremes are significantly different, but the adjacent values are not.

Table 5.19. Means for Rods, Temperatures, and Locations

Dependent Variables[a]	Rods		Means for Temperatures			Means for Locations			Overall Mean	Standard Deviation[b]
	1	2	1	2	3	1	2	3		
Ultimate strength (E)	67.18	64.76	88.58	64.56	47.36	65.27	66.87	68.36	66.83	2.17
Ultimate strength (T)	86.80	84.63	124.74	79.92	54.80	89.05	84.91	85.50	86.49	4.16
Fracture strength (E)	57.40	56.03	84.54	53.06	34.01	55.49	58.45	57.67	57.20	3.87
Fracture strength (T)	110.82	106.07	150.01	105.87	74.55	111.96	104.51	113.95	110.14	15.32
Uniform strain (E)	27.06	27.43	41.70	23.79	15.85	33.64	24.60	23.10	27.11	3.80
Uniform strain (T)	0.23	0.24	0.35	0.21	0.15	0.29	0.22	0.20	0.23	0.03
Total strain (E)	36.23	37.43	46.31	30.76	32.12	42.96	32.93	33.30	36.40	5.12
Total strain (T)	0.68	0.66	0.56	0.69	0.79	0.73	0.61	0.69	0.67	0.15
Reduction of area	48.36	47.62	41.99	48.99	53.80	50.93	44.50	49.34	48.26	7.66
Max/Min diametral strain (At)	1.56	1.43	1.81	1.49	1.32	1.54	1.62	1.46	1.54	0.23
Max/Min diametral strain (Away)	2.52	2.42	2.29	2.79	2.45	2.66	2.50	2.36	2.51	0.56
Elastic limit by extensometer	27.40	26.53	34.99	24.89	21.96	21.47	30.13	30.23	27.28	4.21
0.2% offset yield strength by extensometer	45.06	43.36	57.69	41.20	35.57	37.66	46.85	49.95	44.82	2.01
Apparent elastic limit	37.13	35.03	48.47	33.01	29.01	30.55	39.04	40.90	36.83	2.88
0.2% offset yield stress (E)	45.48	43.37	57.61	41.94	35.97	38.28	47.10	50.15	45.18	1.85
0.2% offset yield stress (T)	45.59	43.48	57.79	42.03	36.05	38.35	47.22	50.30	45.29	1.82

[a](E) = engineering value, (T) = true value, (At) = at fracture, (Away) = away from fracture.

[b]The square root of the mean square error for the ANOVA Model.

5.3.2 Thermal Properties of CRE Type 308 Stainless Steel Weld Metal — J. D. Lore,* H. L. Richards,* and R. T. King

Structural design of LMFBR systems presents difficult design considerations not encountered in LWRs or in many other high-temperature nuclear systems. Components that are fabricated of type 304 or 316 stainless steel in current LMFBR designs not only operate at high temperatures where there is a significant reduction in elastic strength, but because of the good heat transfer characteristics of the sodium coolant and the large operating temperature differences across the reactor core, changes in reactor power can cause rapid temperature changes and severe thermal stresses in structures that are in contact with the coolant. Under these conditions (1) structural materials tend to creep and deform plastically under load, (2) large strains may concentrate in critical regions such as structural discontinuities, and (3) the repeated cycling of temperature at high temperature, as will occur during the normal 30-year lifetime of an LMFBR, can lead to progressive deformation and failure through inelastic behavior mechanisms such as ratchetting and creep fatigue.

A program is in progress to evaluate the mechanical properties of test welds that are prototypic longitudinal seam and girth welds of the FFTF vessel.[30,32] However, understanding the response of this weldment to thermal stresses required that the thermal properties of the base metal and weld metal be known as well as the mechanical properties. We have, therefore, measured the thermal expansion, thermal diffusivity, specific heat, and thermal conductivity *in vacuo* for these stainless steel weldments. These properties were measured for both the austenitic base metal and the partially ferritic weld metal to evaluate the differences in the composition and structure of the base metal and weld metal. The austenitic base metal was[30] all from Carlson Heat 300380. Specific heat samples were prepared[30] from a test weld made with electrode batch 6, while all other test samples were prepared[30] from a test weld made from electrode batch 11. These welds are identical for all practical purposes.

The test program was also designed to provide preliminary information on the effect of the known local anisotropy of the structure of the weld

---

*Y-12 Plant, Oak Ridge.

metal on the thermal expansion, thermal diffusivity, and thermal conductivity coefficients. This aim was satisfied by measuring these properties in three orthogonal directions within the weld. A typical weld section is shown in Fig. 5.44, with the assigned *X*, *Y*, and *Z* test measurement directions. The *X* orientation represents the weld pass direction, *Y* is the weld width, and *Z* is the weld depth. The *X* orientation is actually in a direction precisely perpendicular to the plane of the weld (plane of the photograph). Specimens were fabricated for linear thermal expansion measurements of the base material and for the *X*, *Y*, and *Z* weld directions.

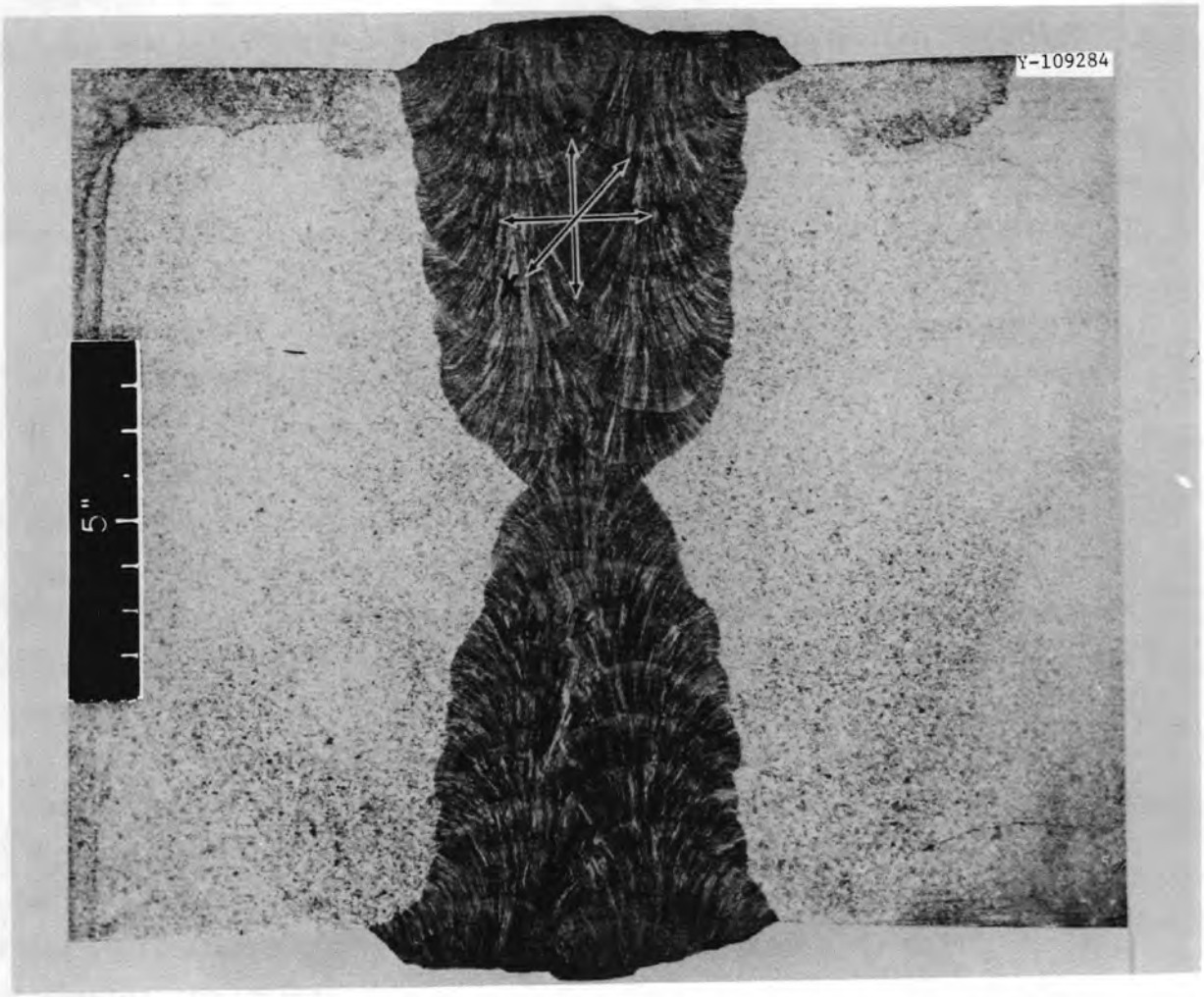

Fig. 5.44. Typical Type 304 Stainless Steel Weldment (FF9-S3).

The disk-shaped specimens for thermal diffusivity and specific heat measurements were 12.7 mm in diameter by 2.5 mm thick. The thermal expansion specimens were 5 mm in diameter by 127 mm long, except for the *Y* and *Z* specimens, which were only as long as the weld metal permitted. The specimens were centered in the weld cross section at a distance of 17.5 mm from the plate surface. These specimens clearly include a sufficient range of substructural orientations that the results are not those that would be obtained in the solidification direction and two orthonormal principal directions of anisotropy, but they may be used as indicators of anisotropy for the thermal expansion coefficient and heat conduction properties.

The linear thermal expansion, $\Delta\ell/\ell_0$, was measured with a high-temperature quartz push-rod automatic dilatometer. Tests were performed between 25 and 750°C in a vacuum of less than 1.33×10^{-4} Pa at a heating and cooling rate of 2°C/min. The measured expansion data had been corrected by previous calibration of the system using NBS-SRM copper. Results are compiled in Tables 5.20 through 5.24 and are illustrated in Fig. 5.45. The base metal data are compared with values from the *LMFBR Materials Handbook* in Fig. 5.46. Also, as a reproducibility check, the *Y* direction sample was rerun and showed little variation. Both the heating and cooling data were combined and reduced by least squares analysis to compute polynomial functions of temperature for $\Delta\ell/\ell_0$. The polynomial functions are:

(1) Base Material

$$10^6\ \Delta\ell/\ell_0 = -440.7 + 16.95T + 3.058 \times 10^{-3}T^2\ , \qquad (12)$$

(2) *X*-Direction

$$10^6\ \Delta\ell/\ell_0 = -419.6 + 16.61T + 2.850 \times 10^{-3}T^2\ , \qquad (13)$$

(3) *Y*-Direction

$$10^6\ \Delta\ell/\ell_0 = -462.6 + 17.72T + 3.787 \times 10^{-3}T^2\ , \qquad (14)$$

Table 5.20. Linear Thermal Expansion of Type 304 Stainless Steel Base Material

Temperature (°C)	$\Delta\ell/\ell_0$			$\alpha_{instant}$ ($°C^{-1}$)
	Measured	Computed[a]	Difference	
25	0	0.15×10^{-4}	0.15×10^{-4}	17.11×10^{-6}
41	2.36×10^{-4}	2.595	−0.235	17.20
54	4.10	4.837	−0.737	17.28
70	6.44	7.611	−1.17	17.38
108	12.99	14.26	−1.27	17.61
161	22.19	23.68	−1.49	17.94
234	36.11	36.94	−0.83	18.39
308	49.96	50.71	−0.75	18.84
383	64.72	65.01	−0.29	19.30
456	78.89	79.26	−0.37	19.74
528	92.53	93.63	−1.1	20.18
599	107.3	108.1	−0.8	20.62
670	122.2	122.9	−0.7	21.05
740	137.7	137.8	−0.1	21.48
756	141.8	141.2	0.6	21.58
745	139.3	138.9	0.4	21.51
732	136.2	136.1	0.2	21.43
693	128.0	127.8	0.2	21.19
625	113.6	113.5	0.1	20.78
554	99.09	98.90	0.19	20.34
485	85.26	85.01	0.25	19.92
415	71.72	71.22	0.50	19.49
343	58.09	57.34	0.75	19.05
276	45.63	44.72	0.91	18.64
209	33.78	32.36	1.42	18.23
148	23.11	21.35	1.76	17.86
112	16.35	14.97	1.38	17.64
103	14.50	13.38	1.12	17.58

[a]From $10^6\Delta\ell/\ell_0 = -440.7 + 16.95T + 3.058 \times 10^{-3}T^2$, $\sigma = 90$.

Table 5.21. Linear Thermal Expansion of Type 308 CRE Stainless Steel in Weld Pass, *X* Direction

Temperature (°C)	$\Delta\ell/\ell_0$			$\alpha_{instant}$ ($°C^{-1}$)
	Measured	Computed[a]	Difference	
25	0×10^{-4}	-0.025×10^{-4}	0.025×10^{-4}	16.75×10^{-6}
43	3.25	3.000	0.250	16.86
54	4.87	4.858	0.012	16.92
69	7.22	7.402	−0.182	17.01
107	13.57	13.91	−0.34	17.22
151	21.08	21.54	−0.46	17.47
195	28.74	29.28	−0.54	17.72
258	40.41	40.56	−0.15	18.08
320	52.17	51.88	0.29	18.44
393	65.75	65.49	0.26	18.85
464	79.16	79.02	0.14	19.26
534	92.48	92.64	−0.16	19.66
604	106.3	106.5	−0.2	20.06
672	119.3	120.3	−1.0	20.44
740	134.4	134.3	0.1	20.83
730	133.4	132.3	1.1	20.77
717	129.5	129.6	−0.1	20.70
691	123.9	124.2	−0.3	20.55
624	110.6	110.6	0.0	20.17
555	96.71	96.78	−0.07	19.78
487	83.25	83.47	−0.22	19.39
419	70.28	70.41	−0.13	19.00
350	57.73	57.44	0.29	18.61
282	45.33	44.92	0.41	18.22
217	33.55	33.20	0.35	17.85
154	22.55	22.06	0.49	17.49
112	14.96	14.77	0.19	17.25
97	11.98	12.19	0.21	17.17

[a]From $10^6\ \Delta\ell/\ell_0 = -419.6 + 16.61T + 2.851 \times 10^{-3}T^2$, $\sigma = 40$.

Table 5.22. Linear Thermal Expansion of Type 308 CRE Stainless Steel in Weld Width, Y Direction

Temperature (°C)	$\Delta\ell/\ell_0$			$\alpha_{instant}$ ($°C^{-1}$)
	Measured	Computed[a]	Difference	
25	0×10^{-4}	-0.1732×10^{-4}	0.1732×10^{-4}	17.91×10^{-6}
36	1.62	1.801	−0.181	17.99
49	4.00	4.146	−0.146	18.09
65	7.04	7.050	−0.010	18.21
82	10.51	10.16	0.35	18.34
104	14.43	14.21	0.21	18.51
125	18.32	18.11	0.22	18.66
147	22.19	22.24	−0.05	18.83
219	35.84	35.99	−0.15	19.38
293	49.88	50.54	−0.66	19.94
365	64.91	65.09	−0.18	20.48
438	79.71	80.24	−0.53	21.04
508	94.08	95.15	−1.07	21.57
577	109.0	110.2	−1.2	22.09
645	124.0	125.4	−1.4	22.60
713	140.1	141.0	−0.9	23.12
743	147.2	147.9	−0.7	23.35
726	144.9	144.0	0.9	23.22
674	133.6	132.0	1.6	22.82
608	118.6	117.1	1.5	22.32
540	102.9	102.1	0.8	21.81
472	87.81	87.44	0.37	21.29
403	73.41	72.93	0.48	20.77
332	58.72	58.37	0.35	20.23
265	45.40	44.99	0.41	19.73
202	33.00	32.71	0.29	19.25
132	19.67	19.42	0.25	18.72
101	12.79	13.66	0.87	18.48

[a]From $10^6\ \Delta\ell/\ell_0 = -462.6 + 17.72T + 3.787 \times 10^{-3}T^2$, $\sigma = 77$.

Table 5.23. Linear Thermal Expansion of Type 308 CRE Stainless Steel in Weld Width, *Y* Direction, Rerun

Temperature (°C)	$\Delta\ell/\ell_0$			$\alpha_{instant}$ ($°C^{-1}$)
	Measured	Computed[a]	Difference	
25	0.00×10^{-4}	0.094×10^{-4}	-0.094×10^{-4}	17.52×10^{-6}
36	2.08	2.027	0.053	17.62
50	4.55	4.503	0.047	17.75
73	8.43	8.611	−0.018	17.97
94	11.98	12.40	−0.042	18.17
147	21.05	22.16	−1.11	18.66
219	33.43	35.84	−2.41	19.34
292	48.86	50.21	−1.35	20.02
366	63.93	65.29	−1.35	20.72
437	78.47	80.23	−1.76	21.38
508	93.41	95.65	−2.24	22.05
577	108.7	111.1	−2.4	22.70
646	124.8	127.0	−2.2	23.35
714	141.7	143.1	−1.3	23.98
742	150.2	149.8	0.4	24.25
730	147.8	146.9	0.9	24.13
679	136.5	134.7	1.8	23.66
612	120.9	119.1	1.8	23.03
544	105.2	103.7	1.6	22.39
475	89.98	88.43	1.55	21.74
406	75.57	73.65	1.92	21.09
338	61.47	59.52	1.95	20.46
271	48.07	46.03	2.04	19.83
206	34.92	33.34	1.58	19.22
136	21.29	20.12	1.17	18.56
105	14.58	14.41	0.17	18.27

[a]From $10^6\ \Delta\ell/\ell_0 = -425.6 + 17.28T + 4.692 \times 10^{-3}T^2$, $\sigma = 160$.

Table 5.24. Linear Thermal Expansion of Type 308 CRE Stainless Steel in Weld Width, Z Direction

Temperature (°C)	$\Delta\ell/\ell_0$			$\alpha_{instant}$ ($°C^{-1}$)
	Measured	Computed[a]	Difference	
25	0.00×10^{-4}	-0.926×10^{-4}	0.926×10^{-4}	16.62×10^{-6}
44	2.91	2.243	0.667	16.73
76	7.55	7.627	−0.077	16.92
116	14.34	14.44	−0.10	17.16
158	21.68	21.70	−0.23	17.41
200	29.40	29.07	0.33	17.66
254	39.06	38.69	0.37	17.98
326	52.77	51.79	0.98	18.41
399	66.53	65.38	1.1	18.84
470	80.02	78.91	1.11	19.26
541	93.17	92.73	0.4	19.68
609	106.7	106.3	0.4	20.09
678	119.7	120.3	−0.5	20.50
745	134.2	134.1	0.1	20.89
728	130.9	130.6	0.4	20.79
637	111.4	111.9	−0.5	20.25
568	97.38	98.07	−0.69	19.84
500	83.90	84.71	−0.81	19.44
431	70.92	71.44	−0.52	19.03
362	58.10	58.45	−0.35	18.62
294	45.53	45.93	−0.40	18.22
228	33.61	34.04	−0.43	17.82
165	22.44	22.92	−0.48	17.45
120	14.33	15.13	−0.80	17.18
104	11.22	12.39	−1.17	17.09

[a]From $10^6\ \Delta\ell/\ell_0 = -506.2 + 16.47T + 2.968 \times 10^{-3}T^2$, $\sigma = 68$.

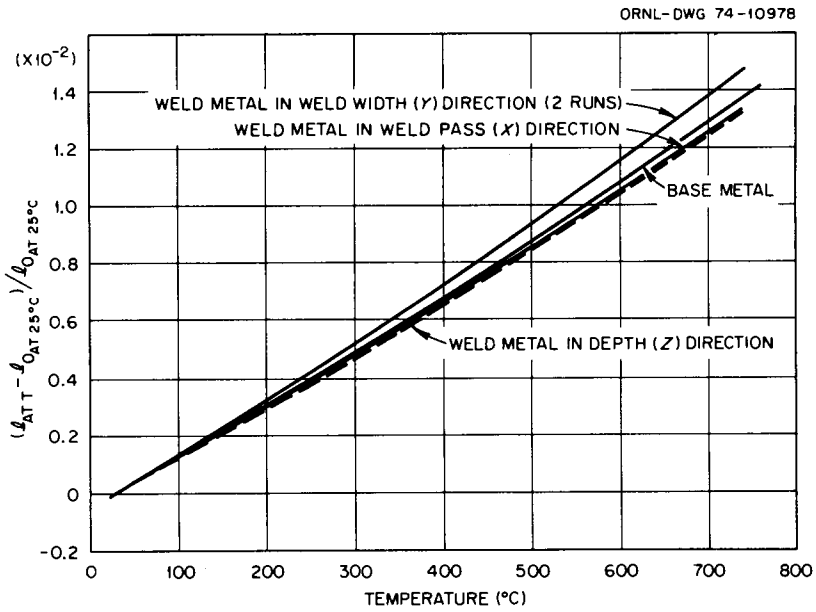

Fig. 5.45. Thermal Expansion of Type 308 Stainless Steel Weld in Type 304 Stainless Steel Base Metal.

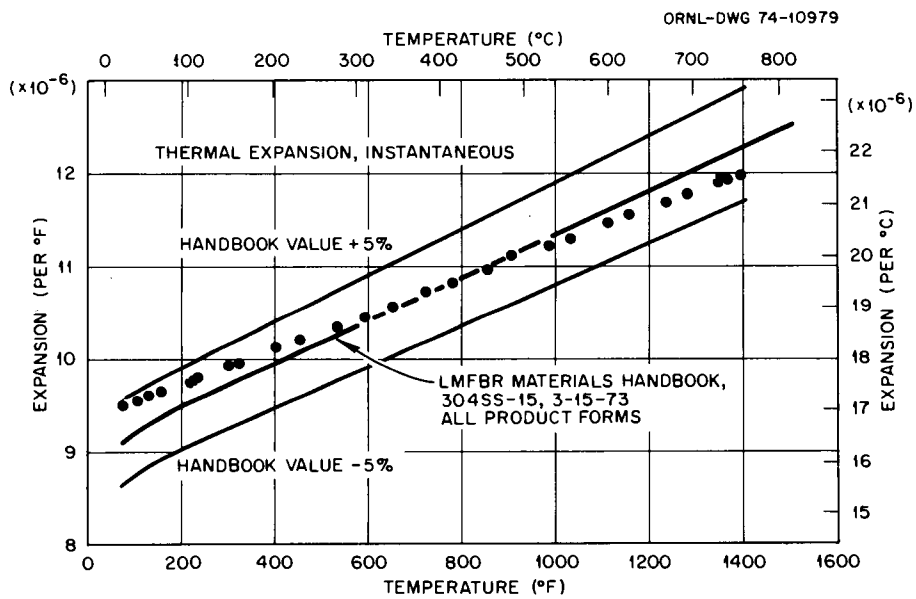

Fig. 5.46. Comparison of Instantaneous Linear Thermal Expansion Coefficient for Carlson Heat 300–380 Type 304 Stainless Steel with *Liquid Metal Fast Breeder Reactor Handbook* Values, HEDL-TME-71-32, p. 304 SS-15 Dated March 15, 1973.

(4) Z-Direction

$$10^6\ \Delta\ell/\ell_0 = -506.2 + 16.47T + 2.968 \times 10^{-3}T^2\ , \qquad (15)$$

where

$\Delta\ell$ is the change in length,

ℓ_0 is the length at 25°C, and

T is the temperature in degrees Celsius.

The linear coefficients of expansion $\bar{\varepsilon}$ between 25°C and the indicated temperatures are given in Table 5.25 and are defined as

$$\bar{\varepsilon} = \frac{(\Delta\ell/\ell_0)_T - (\Delta\ell/\ell_0)_{25}}{T - 25}\ . \qquad (16)$$

Table 5.25. Linear Coefficients of Thermal Expansion of Type 304 Stainless Steel Base Material and Weld Metal

Temperature Range (°C)	Linear Coefficient of Expansion,[a] $\bar{\varepsilon}$ °C^{-1}				
	Weld Metal in Direction Indicated				Base Metal
	X	Y[b]	Y[b]	Z	
25–100	16.93	17.96	17.99	15.61	17.13
25–200	17.24	18.47	18.39	16.61	17.55
25–300	17.53	18.89	18.84	17.10	17.89
25–400	17.81	19.28	19.30	17.48	18.21
25–500	18.10	19.67	19.76	17.83	18.52
25–600	18.39	20.06	20.23	18.16	18.84
25–700	18.67	20.44	20.70	18.48	19.14

[a]All values × 10^{-6}.

[b]Duplicate experiments.

Specific heat data were obtained with a differential scanning calorimeter (DSC). This method involves determining the energy, expressed as a peak height amplitude, required to heat a material at a given rate over a small temperature interval, usually 15°C. By correlating this value with one obtained from a calorimetric standard such as α-Al_2O_3 under identical test conditions, the heat capacity, C_p (cal g^{-1} $°C^{-1}$), of an unknown (x) material is as follows:

$$C_{p,x} = \frac{A_x W_{std}}{A_{std} W_x} C_{pstd} , \tag{17}$$

where

A is a dimensionless relative amplitude representative of a voltage differential, and

W is the mass (g) of the sample.

Specific heat results for the base material and the weld section, as given in Table 5.26, were indistinguishable and were, therefore, aggregated for regression analyses and illustrated as a linear function of temperature in Fig. 5.47. Base and weld metal results agreed to within ±1%, which is the stated accuracy and reproducibility of the DSC.

Thermal diffusivity measurements were made *in vacuo* (1.3 Pa) by the laser-flash method, which consists of measuring the back-face temperature transient of a thin disk (127 mm diam × 25 mm thick) after absorption of a short-duration (∿1 msec), high-energy-density (∿5 J/cm^2) pulse on the front face. An intrinsic Chromel vs Alumel thermojunction butted against the back face served as the temperature sensor. This experimental setup provided temperature excursions of 4 to 5°C, with half-rise times ($t_{1/2}$) ranging from 0.180 to 0.325 sec. The thermal diffusivity, α, calculated from half-rise times and sample thickness, d (cm), under ideal thermophysical conditions may be represented as

$$\alpha = 0.139 d^2 / t_{1/2} \cdot \tag{18}$$

Table 5.26. Specific Heat of Type 308 CRE Stainless Steel Weld Metal and Type 304 Stainless Steel Base Material Areas

Temperature (°C)	Specific Heat,[a] C_p, cal g^{-1} $°C^{-1}$		
	Measured	Computed[b]	Difference
35	0.1140	0.1154	−0.0014
65	0.1166	0.1170	−0.0004
100	0.1195	0.1188	0.0007
150	0.1210	0.1214	−0.0004
200	0.1248	0.1240	0.0008
300	0.1307	0.1293	0.0014
400	0.1344	0.1345	−0.0001
500	0.1390	0.1398	−0.0008
600	0.1447	0.1450	−0.0003
700	0.1504	0.1502	0.0002
35	0.1140	0.1154	−0.0014
65	0.1166	0.1170	−0.0004
100	0.1195	0.1188	0.0007
150	0.1213	0.1214	−0.0001
200	0.1256	0.1240	0.0016
300	0.1299	0.1293	0.0006
400	0.1347	0.1345	0.0008
500	0.1396	0.1398	−0.0002
600	0.1447	0.1450	−0.0003
700	0.1498	0.1502	−0.0004

[a]To convert to J g^{-1} k^{-1}, multiply by 4.184.

[b]From $C_p = 0.1136 + 5.241 \times 10^{-5}T$, $\sigma = 8.1 \times 10^{-4}$.

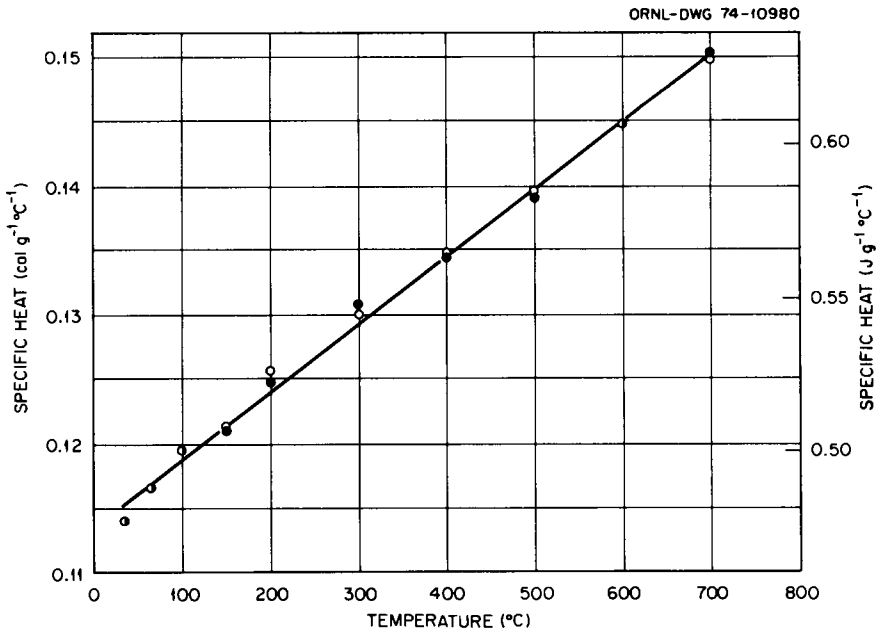

Fig. 5.47. Specific Heat of Type 304 Stainless Steel Base Metal.

The thermal diffusivity, α (cm^2/sec), and thermal conductivity, k, bear a direct relationship through the specific heat, C_p, and density, $\rho(g/cm^3)$:

$$k(T) = \alpha(T)\rho(T)C_p(T) \quad . \tag{19}$$

The thermal conductivity as a function of temperature over the interval 25 to 1000°C was computed by the above general equation. Measured values of α, typically variant to ±0.7% relative to the mean of four observations at a given temperature, are compiled in Tables 5.27 through 5.30 and are displayed in Figs. 5.48 through 5.52. Alpha and C_p values were separately grouped and statistically reduced to mathematical expressions to combine for determination of k values computed with Eq. (19) and for construction of the temperature functions illustrated in Fig. 5.53. Confidence intervals are defined for the directly determined diffusivities as functions of temperature in Figs. 5.48 through 5.51 by dashed lines. This interval around the computed mean regression line represents the limits within which the mean value for an infinite number of measurements can be expected to be found with a 90% probability. The adoption of linear $\alpha(T)$ trend lines shown in Figs. 5.48 through 5.52 was somewhat arbitrary in

Table 5.27. Thermal Diffusivity and Thermal Conductivity of Type 304 Stainless Steel Base Metal

Average Temperature (°C)	Thermal Diffusivity (cm^2/sec)		Calculated Thermal Conductivity ($W\ m^{-1}\ °C^{-1}$)
	Measured[a]	Calculated[b]	
25		3.38×10^{-2}	12.8
26	3.40×10^{-2}	3.38	
100		3.53	13.8
114	3.64	3.56	
154	3.58	3.63	
191	3.92	3.71	
200		3.72	15.2
229	3.76	3.78	
262	4.01	3.85	
300		3.92	16.7
322	3.88	3.97	
350	4.18	4.02	
395	4.00	4.11	
400		4.12	18.3
430	4.24	4.18	
479	4.18	4.28	
500		4.32	19.9
505	4.40	4.33	
549	4.29	4.42	
583	4.40	4.48	
600		4.52	21.6
631	4.33	4.58	
663	4.54	4.64	
697	4.36	4.71	
700		4.72	23.4
734	4.75	4.78	
769	4.47	4.85	
800		4.92	25.2
801	5.28	4.92	
843	4.88	5.00	
877	5.37	5.07	
900		5.11	27.1
925	5.35	5.16	
958	5.44	5.23	
1000		5.31	29.1

[a]Average of four observations.

[b]Computed by regression analysis: $\alpha_{comp} = 3.33 \times 10^{-2} + 1.98 \times 10^{-5} T$

Table 5.28. Thermal Diffusivity and Thermal Conductivity of Type 308 Stainless Steel Weld Metal in the *X* Direction

Average Temperature (°C)	Thermal Diffusivity (cm^2/sec)		Calculated Thermal Conductivity ($W\ m^{-1}\ °C^{-1}$)
	Measured[a]	Calculated[b]	
25	3.01×10^{-2}	3.01×10^{-2}	11.40
25		3.01	
25	3.20	3.01	
100	3.00	3.12	
100		3.12	12.2
114	3.07	3.14	
171	3.14	3.23	
191	3.20	3.26	
200		3.28	13.4
242	3.34	3.34	
274	3.38	3.40	
300		3.43	14.6
318	3.47	3.46	
350	3.51	3.51	
392	3.58	3.58	
400		3.59	15.9
434	3.67	3.64	
480	3.78	3.72	
500		3.75	17.3
510	3.73	3.76	
551	3.88	3.83	
589	3.87	3.89	
600		3.90	18.7
614	3.93	3.92	
663	4.09	4.00	
696	4.13	4.05	
700		4.06	20.1
737	4.13	4.12	
767	4.18	4.16	
800		4.21	21.6
807	4.25	4.22	
854	4.28	4.30	
885	4.44	4.35	
900		4.37	23.2
932	4.34	4.42	
964	4.29	4.47	
1000		4.53	24.8

[a]Average of four observations.

[b]Computed by regression analysis: $\alpha_{comp} = 2.97 \times 10^{-2} + 1.56 \times 10^{-5} T$

Table 5.29. Thermal Diffusivity and Thermal Conductivity of Type 308 Stainless Steel Weld Metal in the *Y* Direction

Average Temperature (°C)	Thermal Diffusivity (cm^2/sec)		Calculated Thermal Conductivity ($W\ m^{-1}\ °C^{-1}$)
	Measured[a]	Calculated[b]	
24	3.38×10^{-2}	3.32×10^{-2}	12.6
25		3.32	
92	3.51	3.43	
100		3.44	13.5
125	3.42	3.48	
167	3.88	3.55	
193	3.60	3.59	
200		3.60	14.8
245	3.68	3.68	
272	3.71	3.72	
300		3.77	16.1
320	3.76	3.80	
358	3.84	3.86	
400		3.93	17.4
401	3.90	3.93	
434	3.80	3.99	
478	4.06	4.06	
500		4.09	18.9
517	3.85	4.12	
557	4.12	4.19	
591	4.08	4.24	
600		4.26	20.4
626	4.42	4.30	
662	4.32	4.36	
694	4.42	4.41	
700		4.42	21.9
730	4.38	4.47	
767	4.54	4.53	
800		4.58	23.5
804	4.47	4.59	
841	4.85	4.65	
874	4.62	4.70	
900		4.75	25.2
920	5.20	4.78	
954	4.78	4.83	
1000		4.91	26.9

[a]Average of four observations.

[b]Computed by regression analysis: $\alpha_{comp} = 3.28 \times 10^{-2} + 1.63 \times 10^{-5} T$.

Table 5.30. Thermal Diffusivity and Thermal Conductivity of Type 308 Stainless Steel Weld Metal in the Z Direction

Average Temperature (°C)	Thermal Diffusivity (cm^2/sec)		Calculated Thermal Conductivity ($W\ m^{-1}\ °C^{-1}$)
	Measured[a]	Calculated[b]	
24	3.41×10^{-2}	3.26×10^{-2}	12.4
25		3.26	
81	3.44	3.34	
100		3.36	13.2
122	3.27	3.39	
153	3.41	3.43	
200		3.49	14.3
202	3.50	3.49	
247	3.57	3.55	
281	3.47	3.59	
300		3.61	15.4
319	3.54	3.64	
366	3.74	3.70	
395	3.65	3.73	
400		3.74	16.6
440	3.82	3.79	
482	3.81	3.84	
500		3.86	17.8
520	3.92	3.89	
561	3.90	3.94	
595	4.09	3.98	
600		3.99	19.1
635	4.00	4.03	
664	4.21	4.07	
700		4.12	20.4
706	4.08	4.12	
735	4.02	4.16	
772	4.16	4.21	
800		4.24	21.8
812	4.28	4.26	
845	4.30	4.30	
880	4.38	4.34	
900		4.37	23.2
915	4.40	4.39	
974	4.52	4.46	
1000		4.49	24.6

[a]Average of four observations.

[b]Computed by regression analysis: $\alpha_{comp} = 3.23 \times 10^{-2} + 1.26 \times 10^{-5} T$.

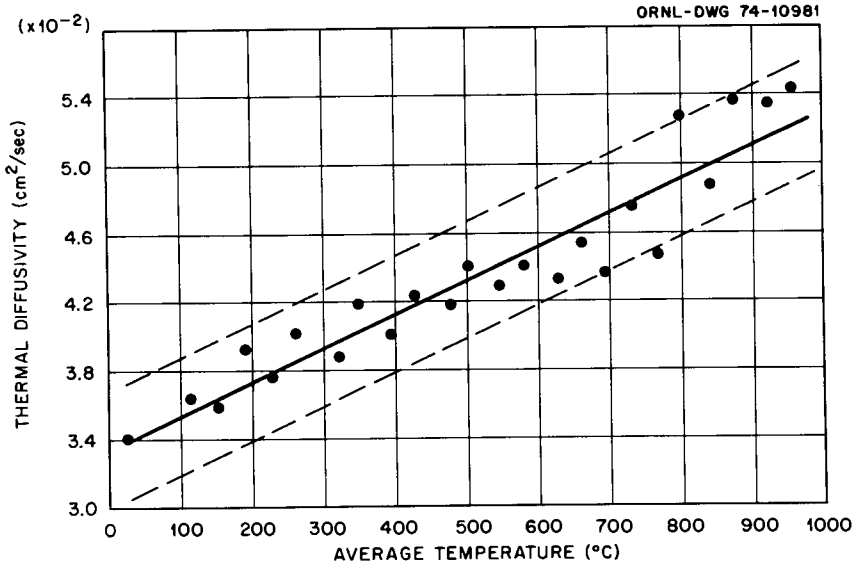

Fig. 5.48. Thermal Diffusivity of Type 304 Stainless Steel Base Metal

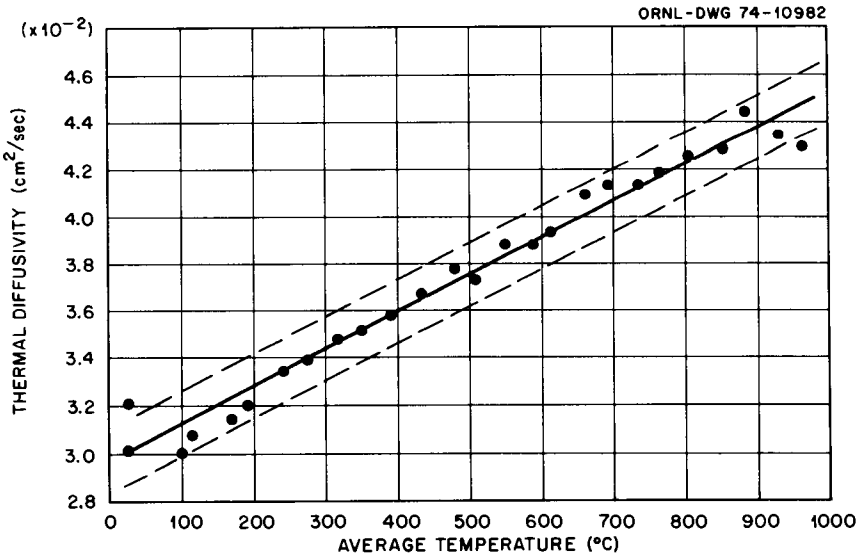

Fig. 5.49. Thermal Diffusivity of Type 308 Stainless Steel Weldment Measured in the Weld Pass (*X*) Direction.

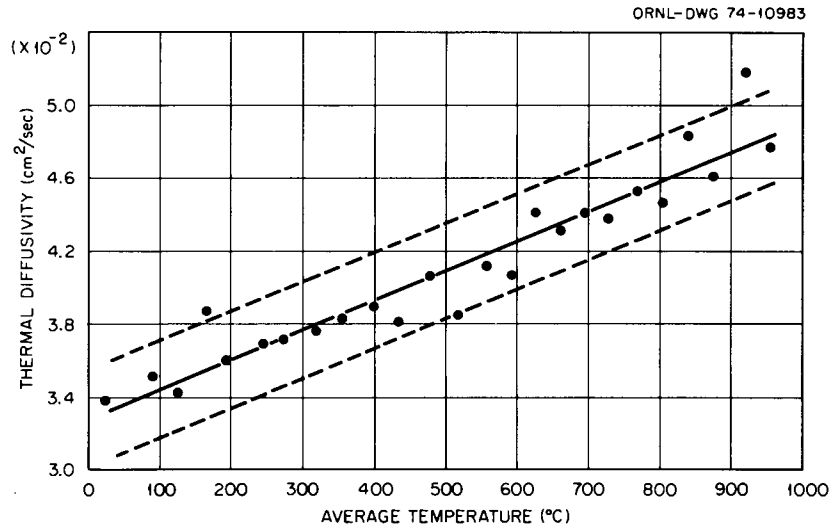

Fig. 5.50. Thermal Diffusivity of Type 308 Stainless Steel Weldment Measured in the Weld Width (*Y*) Direction.

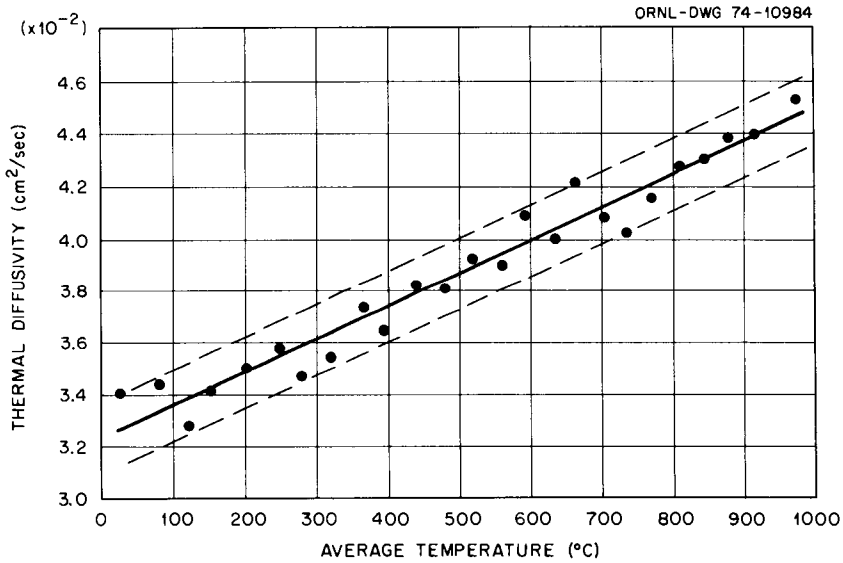

Fig. 5.51. Thermal Diffusivity of Type 308 Stainless Steel Weldment Measured in the Weld Depth (*Z*) Direction.

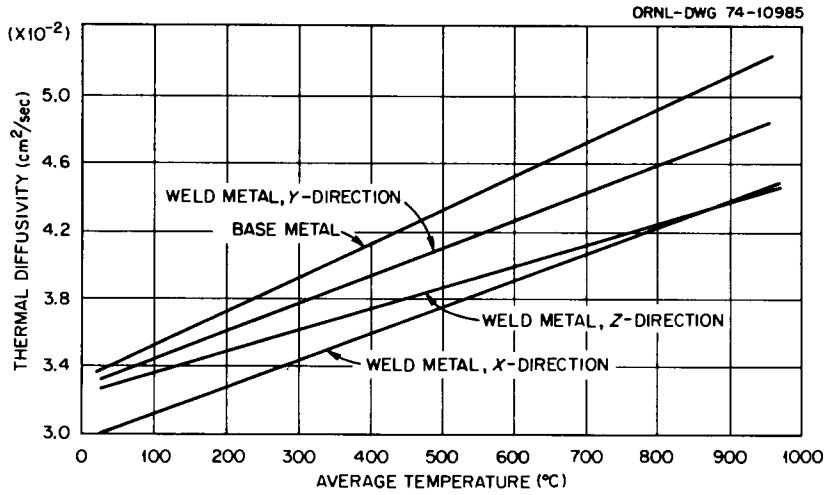

Fig. 5.52. Comparison of Thermal Diffusivity Trends for Base Metal and the *X*- *Y*- and *Z*-Weld Directions.

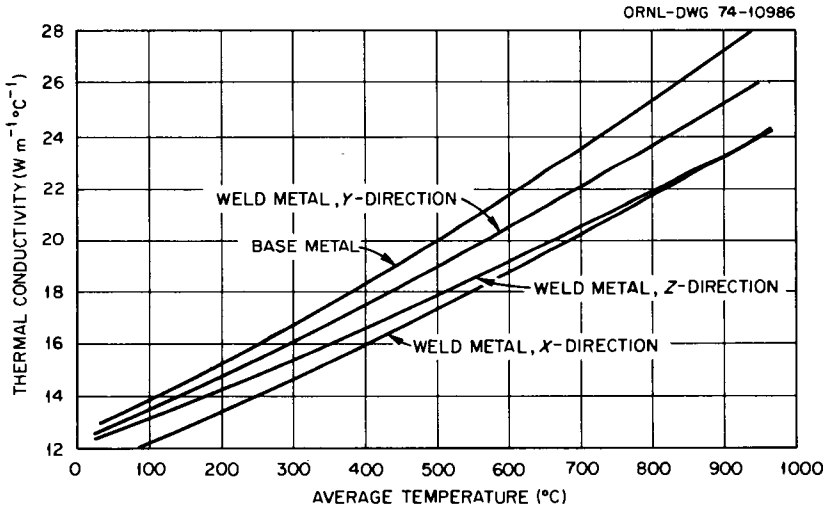

Fig 5.53. Comparison of Thermal Conductivity Trends for Base Metal and the *X*- *Y*- and *Z*-Weld Directions.

light of the data scatter, which is indicative of material nonhomogeneity between duplicate test specimens (differentiated symbolically) and/or experimental error. Base metal α values do agree with the Thermophysical Properties Research Center's provisional mean reference data for type 304 austenitic stainless steel to within ±5% over the interval 25 to 1000°C. The linear $\alpha(T)$ models to correlate with the experimental findings about as well as polynomials of order three or lower, according to covariance analyses. Further, the $\alpha(T) \times C_p(T)$ product, representing the coupling of two linear functions, becomes a polynomial of the second degree, which is consistent with the earlier results for a vacuum-arc-remelted type 304L stainless steel, as determined by the steady-state axial-rod technique.

Figure 5.53 illustrates the trends of thermal conductivity with increasing temperature for the base and weld metals. The base metal trend line conductivities were from 6 to 15% higher than the mean weld material values for the X, Y, and Z measurement directions. The range of X, Y, and Z values at a given temperature was about 9%. At 500°C, k for the base material was about 11% greater than the mean k value for the weld material. At and above this temperature, after accounting for the average weld 90% confidence limit bandwidth of about ±6%, the larger magnitude of base material k values (±10%, 90% confidence limit) commences to have some significance.

5.3.3 Creep-Rupture Properties of GTA Type 16-8-2 Welds — R. T. King, G. M. Goodwin, and E. Bolling

Two 16-8-2 welds (V-114 and V-115) were made in 12.7-mm-thick type 316 stainless steel plate by the GTA process, with 0.32-mm-diam electrodes from the Bechtel reference heat Arcos-2367-R-16-8-2. This lot of electrodes was used in the fabrication of the type 316 stainless steel sodium piping of the FFTF. The test welds may be regarded as simulated manual pipe welds, until actual prototype pipe welds are delivered to ORNL for testing.

We have previously reported data for other 16-8-2 weld deposits.[33] The specimens described here were buttonhead specimens with 28.6-mm-long by 3.2-mm-diam all-weld-metal gage sections. The methods used to perform the creep tests were the same as those reported previously.[33]

One specimen was tested at 482°C (900°F) (not yet failed), one specimen was tested at 593°C (1100°F) (not yet failed), and three specimens were tested to rupture at 649°C (1200°F). The times to various characteristic points of the creep curves are given in Table 5.31, while the corresponding strains are given in Table 5.32. The rupture times are plotted against the Larson-Miller parameter and compared with the range of values expected for type 316 stainless steel base metal in Fig. 5.54.[33,34]

The rupture times for these longitudinal all-weld-metal specimens lie well within the range of values expected for type 316 stainless steel base metal. The total elongations and reductions of area are relatively high, even for failure after 3600 hr at 649°C, conditions for which type 308 stainless steel weld metal frequently exhibits low ductility and fails along austenite-sigma phase boundaries.[35] Metallographic examination of these failed specimens is in progress.

However, the creep strain at the onset of tertiary creep at 649°C decreases with decreasing stress, and the creep strain at the onset of tertiary creep is approximately 1.5% for the 152-MPa test. This observation leads to concern that under long-time, steady load conditions at high temperature, the 16-8-2 weld metal may enter third-stage creep after almost no creep strain.

Table 5.31. Creep-Time Data for Type 16-8-2 Weld Metal at 649°C (1200°F)

Welds	Temperature		Stress		Time, hr, to Various Events						
	(°C)	(°F)	(ksi)	(MPa)	End First Stage	End Second Stage	0.2% Offset Third Stage	Fracture	0.5% Creep Strain	1% Creep Strain	2% Creep Strain
V-115-2	649	1200	22.0	152	50	2125	2275	3602.1			2625
V-115-1	649	1200	25.0	172	10	225	283	513			250
V-115-3	649	1200	28.0	193	1	35	42	107.1			12
V-114-1	593	1100	30.0	207	>5000	>5000	>5000	>5000	~0	25	375
V-114-2	482	900	55.0	482	>6380	>6380	>6380	>6380	~5600	>5600	>5600

Table 5.32. Creep Deformation Data for Type 16-8-2 Weld Metal, Welds V-114 to V-115

Welds	Temperature		Stress		Load in Strain	Strain, %				Reduction of Area (%)	Minimum Creep Rate (%/hr)
	(°C)	(°F)	(ksi)	(MPa)		First Stage	First and Second Stage	0.2% Offset Third Stage	Total at Failure		
V-115-2	649	1200	22.0	152	0.25	0.27	1.0	1.5	40.1	36.7	0.00047
V-115-1	649	1200	25.0	172	0.25	0.25	1.35	2.3	30.1	30.0	0.005
V-115-3	649	1200	28.0	193	0.5	0.25	4.5	6.2	55.0	35.5	0.121
V-114-1	593	1100	30.0	207	0.85	>2.3			>4.25		
V-114-2	482	900	55.0	379	9.30	>0.67			>10.0		

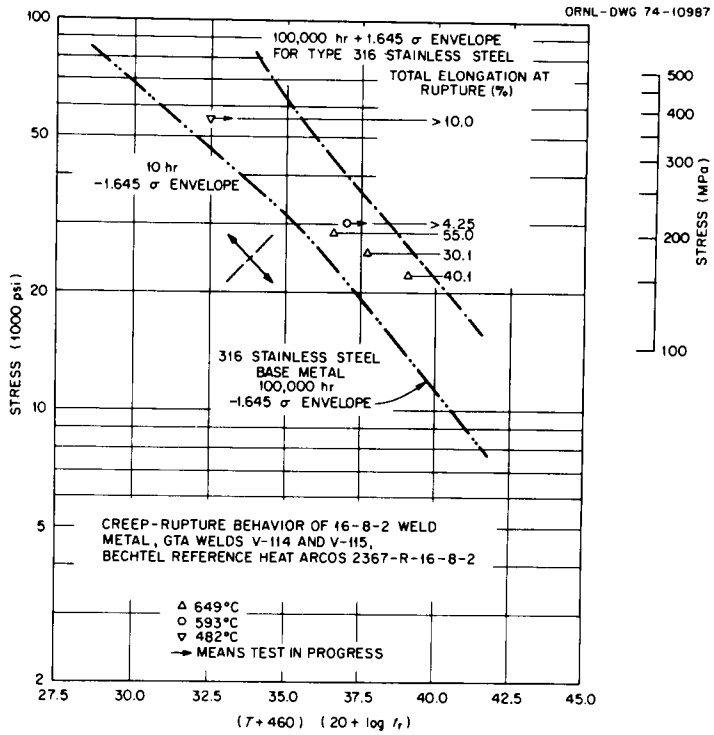

Fig. 5.54. Creep-Rupture Behavior of Type 16-8-2 Weld Metal, GTA Welds V-114 and V-115, Bechtel Reference Heat Arcos 2367-R-16-8-2.

5.4 MECHANICAL PROPERTIES OF STEAM GENERATOR AND HEAT EXCHANGER MATERIALS — C. R. Brinkman

Extensive mechanical properties studies are under way on 2 1/4 Cr-1 Mo low-alloy steel. These include tensile, creep, fatigue, and heat-to-heat variations. A number of correlations, with their tolerance limits, have also been made for inclusion in the *Nuclear Systems Materials Handbook*. A small study is also under way to determine the properties of weld-overlaid stainless steel for intermediate heat exchanger applications.

5.4.1 Tensile Properties of 2 1/4 Cr-1 Mo Steel — R. L. Klueh

We previously fit the true-stress true-plastic-strain data for a series of tensile tests[36] to the Holloman equation,[37]

$$\sigma = A_1 \varepsilon_p^{n_1} , \qquad (20)$$

and the Ludwik equation[38]

$$\sigma = A_2\varepsilon_p^{n_2} + B_2 \ , \tag{21}$$

where σ is the true stress, ε_p is the true plastic strain, and A_1, A_2, B_2, n_1, and n_2 are empirical constants. The Holloman equation gave the lowest standard error of estimate. The tests, which were fit from the 0.2% offset yield strength to the ultimate tensile strength, covered the range 25 to 593°C (75–1100°F) and strain rates of 0.4, 0.04, 0.004, and 0.0004/min.

During the last quarter we fit these same data to the Ludwigson[39] equation, which is written as

$$\sigma = A_3\varepsilon_p^{n_3} + \exp(B_3 + C_3\varepsilon_p) \ , \tag{22}$$

and the Voce[40] equation, which is written as

$$\sigma = A_4 \exp(C_4\varepsilon_p) + B_4 \ , \tag{23}$$

where A_3, B_3, n_3, m_3, A_4, B_4, and C_4 are empirical constants. Voce found Eq. (23) to have a rational basis and originally wrote it as

$$\sigma = (\sigma_0 - \sigma_\infty) \exp(-\varepsilon_p/k) + \sigma_\infty \ , \tag{24}$$

where σ_0, σ_∞, and k are constants. According to Voce,[40] σ_0 is "the initial or threshold stress at which homogeneous plastic deformation begins to be appreciable and corresponds roughly with the 0.1% proof stress." Voce termed σ_∞ "the final constant stress, the attainment of which at indefinitely large strains appears to be characteristic of homogeneous deformation."

The results for the Ludwigson and Voce equations are given in Tables 5.33 and 5.34, respectively. Also given in these tables are the residual sums of squares and the standard errors of estimate for each equation. The standard error of estimate for the curves with eight data points (the number of points fit) is given by

Table 5.33. Constants for Fitting the Tensile Curves for Annealed 2 1/4 Cr-1 Mo Steel to the Empirical Ludwigson Equation

Temperature (°C)	Temperature (°F)	A_3 ksi(MPa)	n_3	B_3	C_3	RSS[a] (ksi^2)	SE[b] (ksi)
		Strain Rate — 0.4/min					
25	77	169.4(1168)	0.424	3.228	−2.619	13.911	1.865
204	400	134.9(930)	0.358	2.835	−3.400	9.753	1.562
371	700	148.3(1022)	0.272	1.813	−5.460	5.521	1.175
454	800	133.6(921)	0.249	1.029	−5.837	8.022	1.416
510	950	125.4(865)	0.274	2.119	−5.630	4.445	1.054
538	1000	127.6(880)	0.307	2.575	−5.033	6.542	1.279
566	1050	102.5(707)	0.284	2.486	−5.284	3.383	0.920
593	1100	104.3(719)	0.339	2.907	−4.827	2.260	0.752
		Strain Rate — 0.04/min					
25	77	153.8(1060)	0.352	3.011	−3.171	8.451	1.454
93	200	142.3(981)	0.354	2.847	−3.222	9.354	1.529
204	400	135.6(935)	0.338	2.720	−3.723	8.788	1.482
316	600	140.4(968)	0.284	2.288	−5.033	2.897	0.851
371	700	153.9(1061)	0.294	2.344	−5.086	7.312	1.352
454	850	152.7(1053)	0.293	2.307	−5.234	9.920	1.575
510	950	133.5(920)	0.277	2.228	−5.296	8.682	1.473
538	1000	121.4(837)	0.275	2.348	−5.688	4.911	1.108
566	1050	106.0(731)	0.278	2.528	−6.177	2.193	0.740
593	1100	83.9(578)	0.338	3.164	−4.780	0.079	0.140
		Strain Rate — 0.004/min					
25	77	177.0(1220)	0.475	3.286	−2.153	17.590	2.097
204	400	139.5(962)	0.325	2.776	−3.939	6.859	1.309
371	700	151.2(1042)	0.277	1.931	−4.910	11.25	1.677
454	850	164.0(1130)	0.357	2.793	−4.109	10.56	1.625
510	950	130.0(896)	0.315	2.603	−5.260	5.646	1.188
538	1000	96.6(666)	0.264	2.446	−6.421	2.115	0.727
566	1050	89.8(619)	0.203	1.881	−78.14	0.723	0.425
593	1100	62.5(431)	0.315	2.932	−6.29	0.120	0.174
		Strain Rate −0.0004/min					
371	700	168.5(1162)	0.311	2.053	−4.046	13.41	1.831
454	850	142.8(985)	0.297	2.442	−4.795	10.94	1.653
510	950	100.2(691)	0.279	2.627	−7.414	2.783	0.834
566	1050	84.5(583)	0.429	3.067	−12.49	0.041	0.101

[a]Residual sum of squares.

[b]Standard error of estimate.

Table 5.34. Constants for Fitting the Tensile Curves for Annealed 2 1/4 Cr-1 Mo Steel to the Empirical Voce Equation

Temperature (°C)	Temperature (°F)	A_4 ksi(MPa)	B_4 ksi(MPa)	C_4	RSS[a] (ksi^2)	SE[b] (ksi)
		Strain Rate — 0.4/min				
25	77	−53.3(−367)	89.7(618)	−22.1	0.410	0.286
204	400	−43.0(−296)	73.7(508)	−27.0	0.547	0.331
371	700	−48.5(−334)	80.5(555)	−35.7	4.034	0.898
454	800	−45.9(−316)	75.8(523)	−35.2	3.243	0.805
510	950	−38.9(−268)	68.6(473)	−38.2	1.852	0.609
538	1000	−37.8(−260)	68.2(470)	−38.2	0.515	0.321
566	1050	−30.5(−210)	58.6(404)	−39.3	1.235	0.497
593	1100	−26.8(−185)	56.3(388)	−41.1	0.587	0.342
		Strain Rate — 0.04/min				
25	77	−50.6(−350)	87.7(605)	−24.9	2.572	0.717
93	200	−46.4(−320)	78.9(544)	−25.6	0.857	0.414
204	400	−43.3(−299)	74.1(511)	−29.2	0.879	0.419
316	600	−44.9(−310)	77.5(534)	−34.7	5.603	1.059
371	700	−49.4(−341)	83.0(572)	−34.5	3.662	0.856
454	850	−47.8(−330)	80.7(556)	−37.0	1.092	0.467
510	950	−42.0(−290)	73.7(508)	−37.5	1.492	0.546
538	1000	−36.6(−252)	67.6(466)	−40.0	1.145	0.479
566	1050	−29.6(−204)	59.4(410)	−44.5	1.131	0.476
593	1100	−18.2(−125)	51.0(352)	−48.1	1.151	0.480
		Strain Rate — 0.004/min				
25	77	−54.8(−378)	90.2(622)	−18.5	1.607	0.567
204	400	−44.2(−305)	77.9(537)	−29.8	1.667	0.578
371	700	−51.2(−353)	83.8(578)	−32.9	2.655	0.729
454	850	−48.6(−335)	80.9(558)	−33.0	2.382	0.690
510	950	−36.7(−253)	66.9(461)	−40.1	0.308	0.248
538	1000	−27.2(−188)	55.9(385)	−45.5	1.081	0.465
566	1050	−22.6(−156)	51.9(358)	−51.9	5.054	1.005
593	1100	−12.2(−84)	38.5(265)	−62.4	0.340	0.261
		Strain Rate — 0.0004/min				
371	700	−57.8(−399)	89.0(614)	−28.9	3.665	0.856
454	850	−45.2(−312)	77.8(536)	−35.1	1.109	0.471
510	950	−25.7(−177)	54.8(378)	−55.2	0.463	0.304
566	1050	−86.4(−596)	34.3(236)	−88.0	0.283	0.238

[a]Residual sum of squares.

[b]Standard error of estimate.

$$SE = \sqrt{RSS/(8 - n_f)} \ , \tag{25}$$

where RSS is the residual sum of squares and n_f is the number of degrees of freedom, which is 2, 4, and 3 for Eqs. (20), (22), and (23), respectively.

In Table 5.35 the standard errors of estimate for Eqs. (20), (22), and (23) are compared for each test. Overall, the Voce equation gives the lowest standard error of estimate. The exceptions were at the highest test temperatures, and even then the difference between the standard error of estimate for the Voce equation and the equation that showed the best fit was quite small.

The reason for the superior fit of the Voce equation can be seen in Fig. 5.55, where log σ is shown as a function of log ε_p. If Eq. (20) is to describe the behavior, these curves should be straight lines. Obviously, at the lowest temperatures there is significant deviation, with curvature apparent at both high and low strains. Only at the highest temperatures, where the Holloman equation gave a better fit than the Voce equation, can an essentially straight line be drawn. Since the Ludwigson equation often gave the best fit at the highest temperatures (Table 5.35), the curves must deviate slightly from a straight line at the low strains.

In a simple rank test (Table 5.35), the Voce equation is obviously the best representation over the entire range of experimental test variables. However, by such a test the two-parameter Holloman equation is found superior to the four-parameter Ludwigson equation. As seen in Table 5.35, the Holloman equation consistently ranks second. Only at room temperature is the Holloman equation ranked third behind the Ludwigson equation. In veiw of these results, only the Holloman and Voce equations are being further investigated. Although the Voce equation provides the best fit, the behavior of the Holloman equation was further examined because it contains one less constant that needs to be evaluated.

Figures 5.56 and 5.57 show the constants of the Holloman equation as functions of temperature. Both A_1 and n_1 have shapes similar to those for the ultimate tensile strength,[36] are multivalued functions of temperature, and depend on the strain rate at high temperatures. Since A_1 locates the height of the curve on the stress axis, while n_1 specifies

Table 5.35. A Comparison of the Standard Error of Estimate for the Holloman, Ludwigson, and Voce Equations

Temperature		Standard Error of Estimate, ksi		
(°C)	(°F)	Holloman	Ludwigson	Voce
		Strain Rate — 0.4/min		
25	77	2.416(3)[a]	1.865(2)[a]	0.286(1)[a]
204	400	1.561(2)	1.562(3)	0.331(1)
371	700	0.980(2)	1.175(3)	0.898(1)
454	800	1.161(2)	1.416(3)	0.805(1)
510	950	0.894(2)	1.054(3)	0.609(1)
538	1000	1.134(2)	1.279(3)	0.321(1)
566	1050	0.821(2)	0.920(3)	0.497(1)
593	1100	0.780(3)	0.752(2)	0.342(1)
		Strain Rate — 0.04/min		
25	77	1.552(3)	1.454(2)	0.717(1)
93	200	1.521(2)	1.529(3)	0.414(1)
204	400	1.409(2)	1.482(3)	0.419(1)
316	600	0.757(1)	0.851(2)	1.059(3)
371	700	1.170(2)	1.352(3)	0.856(1)
454	850	1.336(2)	1.575(3)	0.467(1)
510	950	1.240(2)	1.473(3)	0.546(1)
538	1000	0.951(2)	1.108(3)	0.479(1)
566	1050	0.666(2)	0.740(3)	0.476(1)
593	1100	0.240(2)	0.140(1)	0.480(3)
		Strain Rate — 0.004/min		
25	77	2.818(3)	2.097(2)	0.567(1)
204	400	1.243(2)	1.309(3)	0.578(1)
371	700	1.396(2)	1.677(3)	0.729(1)
454	850	1.560(2)	1.625(3)	0.690(1)
510	950	1.054(2)	1.188(3)	0.248(1)
538	1000	0.650(2)	0.727(3)	0.465(1)
566	1050	0.715(2)	0.425(1)	1.005(3)
593	1100	0.233(2)	0.174(1)	0.261(3)
		Strain Rate — 0.0004/min		
371	700	1.545(2)	1.831(3)	0.856(1)
454	850	1.422(2)	1.653(3)	0.471(1)
510	950	0.753(2)	0.834(3)	0.304(1)
566	1050	0.103(2)	0.101(1)	0.238(3)

[a]Number in parentheses is the rank, i.e., 1 indicates the equation that gave the best fit (least standard error of estimate), etc.

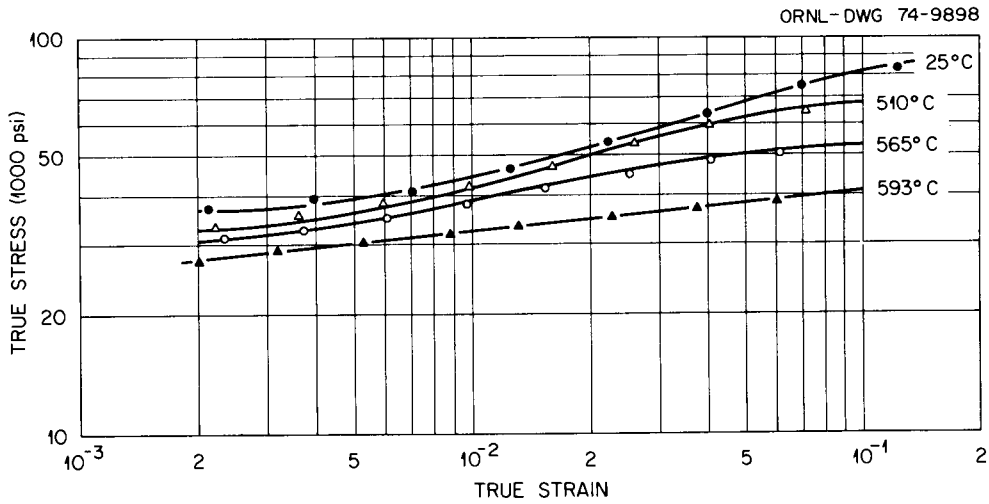

Fig. 5.55. Logarithmic Plot of True Stress Against True Strain for Selected Tests at 0.004/min. Note how the curvature increases as the temperature is decreased

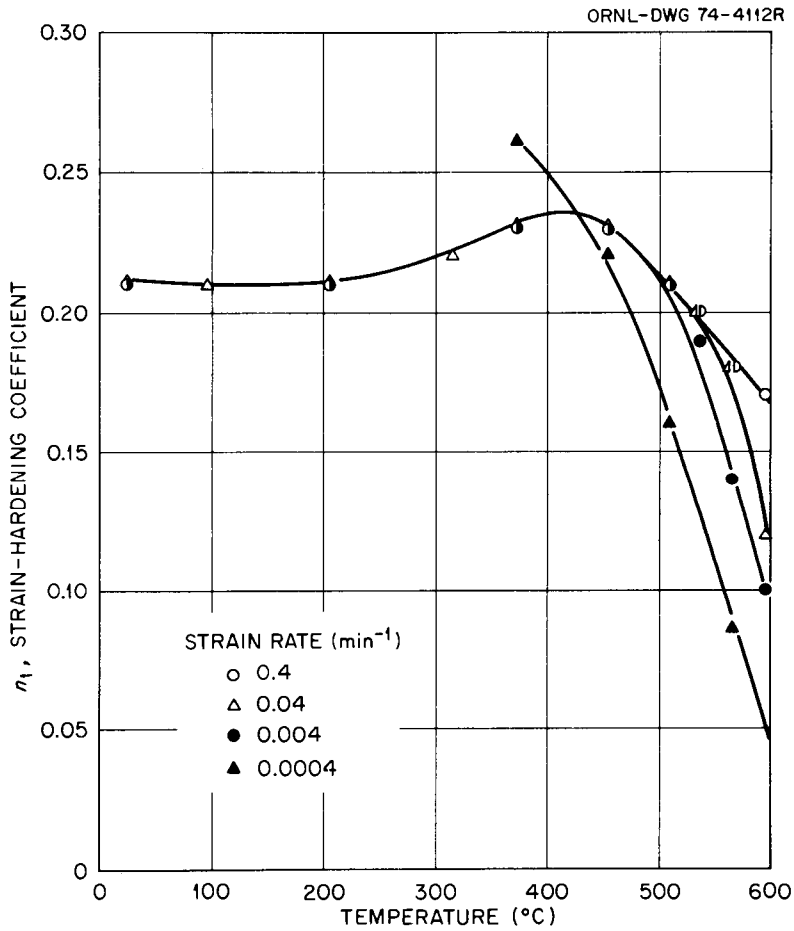

Fig. 5.56. Strain-Hardening Coefficient for the Holloman Equation as a Function of Temperature and Strain Rate for Annealed 2 1/4 Cr-1 Mo Steel.

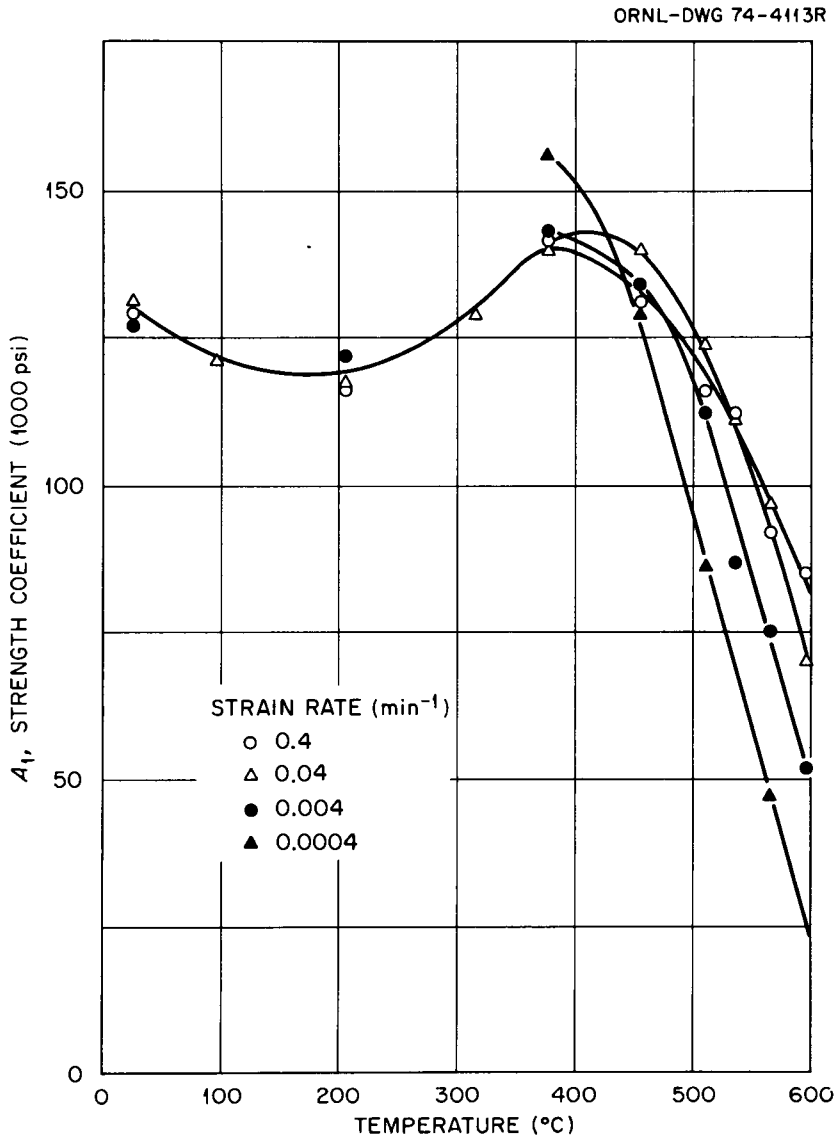

Fig. 5.57. Strength Coefficient for the Holloman Equation as a Function of Temperature and Strain Rate for Annealed 2 1/4 Cr-1 Mo Steel.

the shape, we would expect A_1 to depend on strength. Figure 5.58 shows A_1 as a function of the ultimate tensile strength, and it is seen that a linear relationship results, such that

$$A_1 = 2.36\tau - 34.8 \ , \tag{26}$$

where τ is the engineering ultimate tensile strength; both τ and A_1 are in ksi. As seen in Fig. 5.57, temperature and strain rate affect A_1 only through its effect on the ultimate tensile strength.

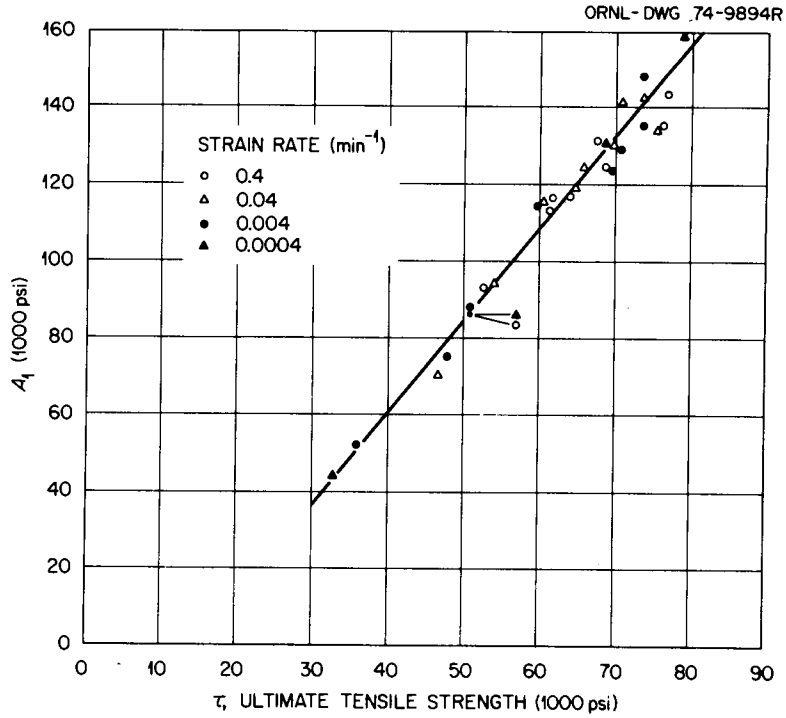

Fig. 5.58. The Variation of A_1 of the Holloman Equation with Engineering Ultimate Tensile Strength. 1000 psi = 6.895 MPa.

In Figs. 5.59, 5.60, and 5.61 A_4, B_4, and C_4 are shown as functions of temperature. All three constants show a dependence on strain rate and are multivalued functions of temperature. Since A_4 and B_4 define the magnitude of the stress, it is not unreasonable to expect a relationship between these constants and strength. In Figs. 5.62 and 5.63 A_4 and B_4 are shown as functions of ultimate tensile strength, and a linear relationship is apparent. The curves shown are given by

$$A_4 = 1.059\tau + 27.49 \ , \tag{27}$$

and

$$B_4 = 1.231\tau - 6.954 \ , \tag{28}$$

where A_4, B_4, and τ are in ksi (1000 psi). Note that one relationship fits all temperatures and strain rates (linear relationships were also found with the yield strength). Hence, if the ultimate tensile strength is known, both A_4 and B_4 — and thus, σ_0 and σ_∞ — can be determined.

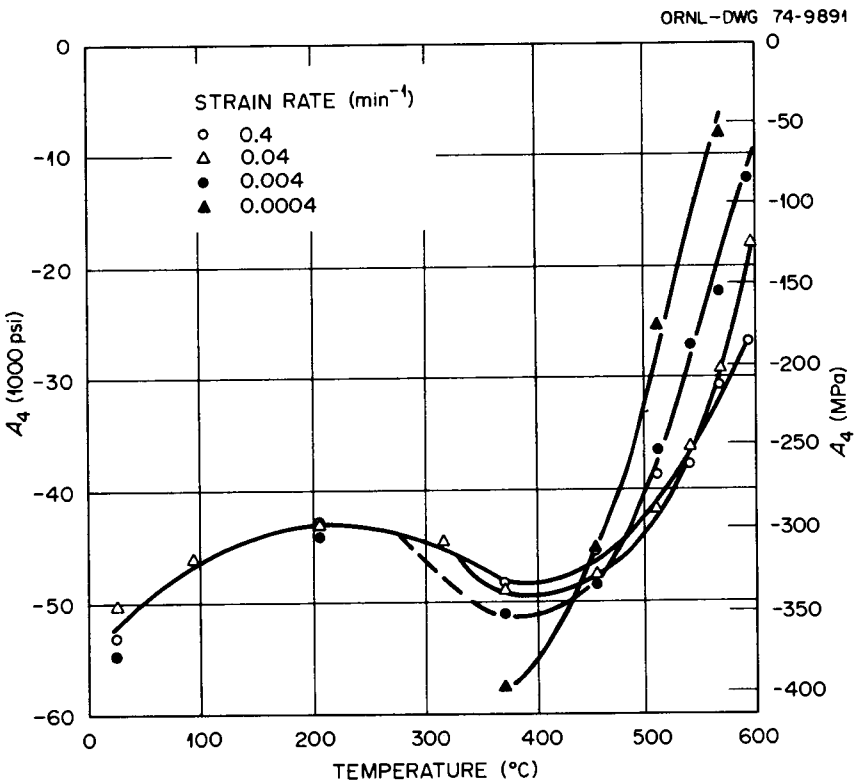

Fig. 5.59. The Variation of A_4 of the Voce Equation with Temperature and Strain Rate.

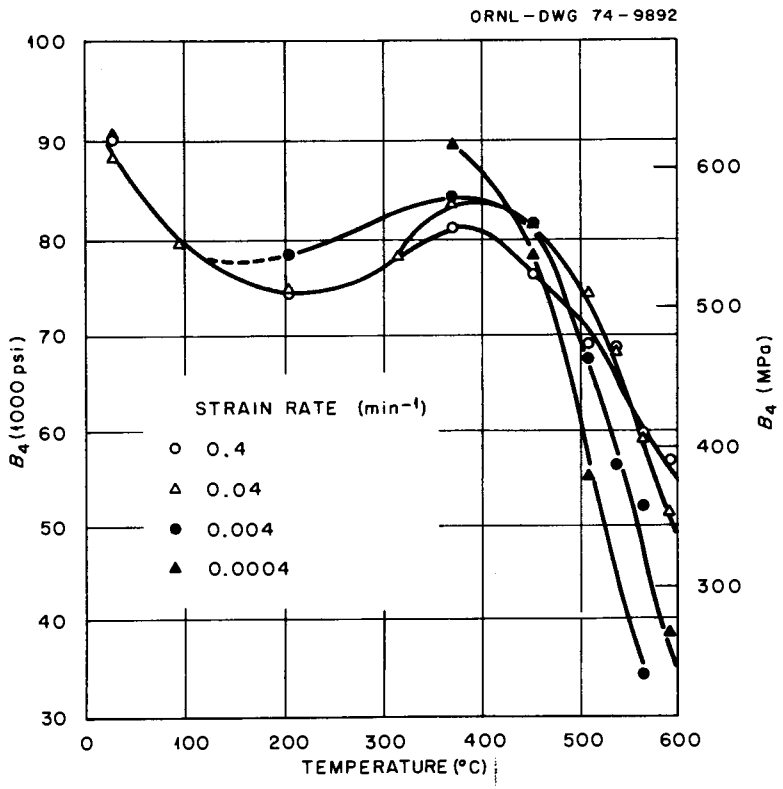

Fig. 5.60. The Variation of B_4 of the Voce Equation with Temperature and Strain Rate.

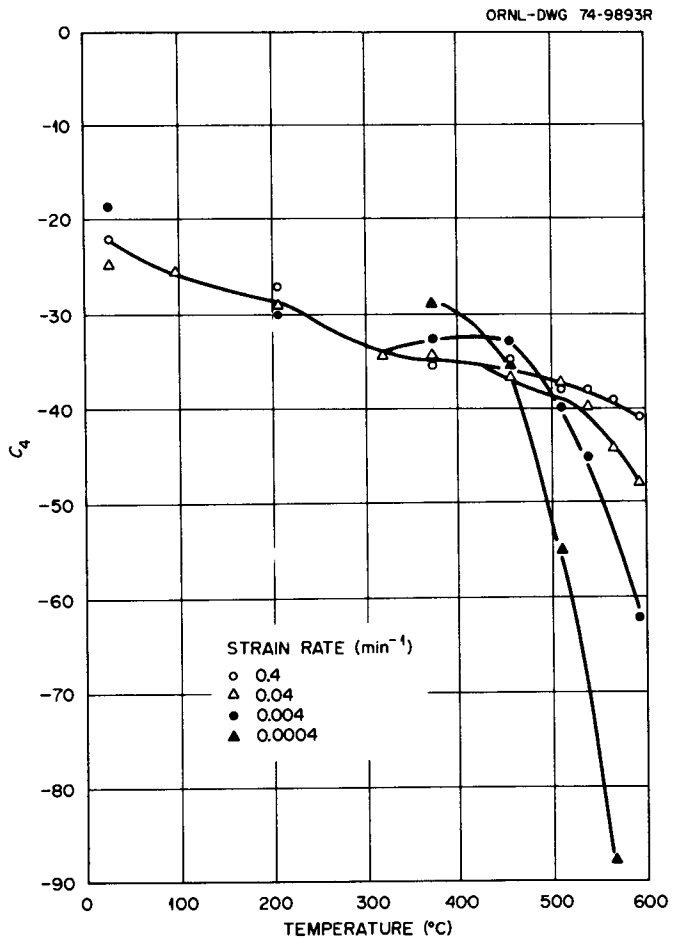

Fig. 5.61. The Variation of C_4 of the Voce Equation with Temperature and Strain Rate.

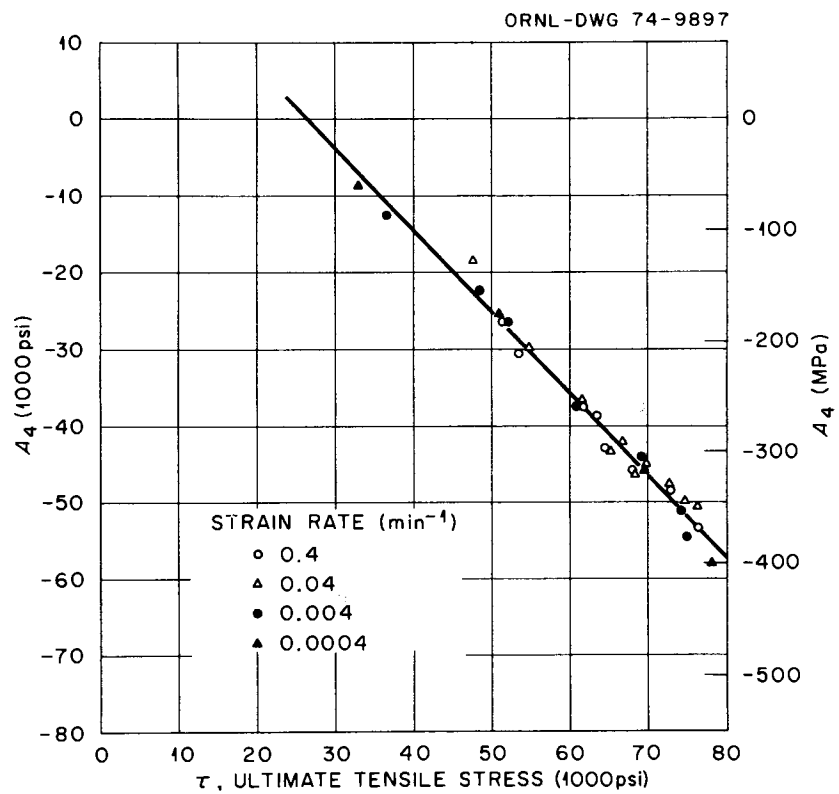

Fig. 5.62. The Variation of A_4 of the Voce Equation with Engineering Ultimate Tensile Strength.

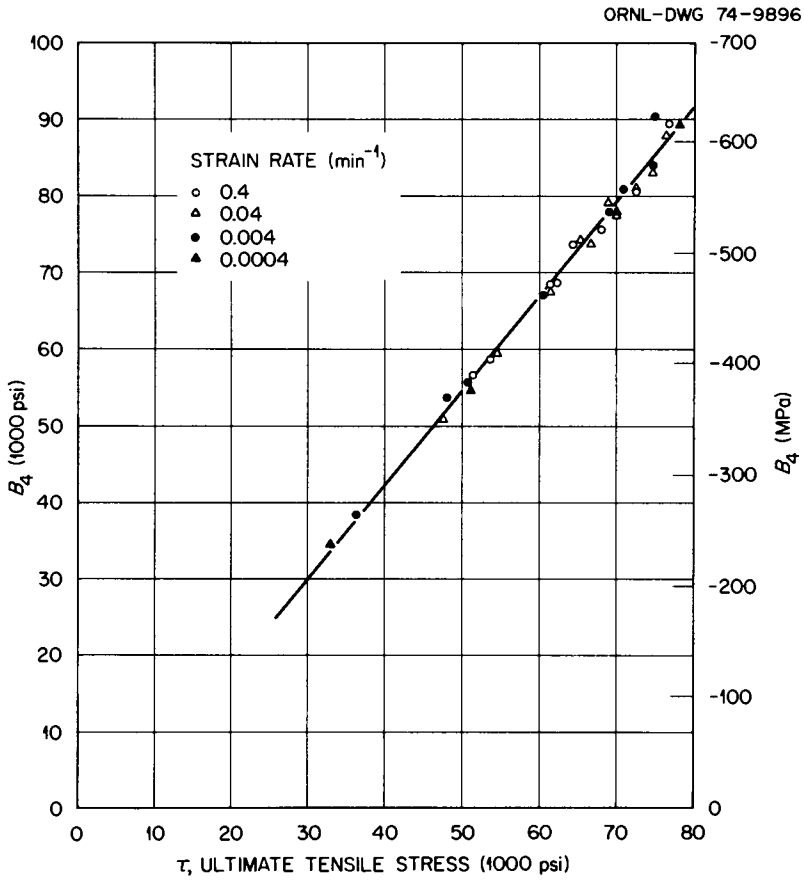

Fig. 5.63. The Variation of B_4 of the Voce Equation with Engineering Ultimate Tensile Strength.

In Fig. 5.64 $B = \sigma_\infty$ is shown as a function of k, the negative reciprocal of C_4 [see Eq. (24)]. Of interest is the fact that up to $k \cong 0.035$, σ_∞ appears to be a linear function of k. Then, at $k > 0.035$, the relationship becomes much more complicated. When these two regimes are examined relative to temperature and strain rate, the region that deviated from the apparent linear behavior occurs at the lowest temperatures. The room-temperature tests are those with the highest k values (upper right-hand corner of Fig. 5.64). As temperature increases, k decreases, while σ_∞ first decreases, goes through a local minimum followed by a local maximum, and then decreases, apparently linearly. The linear relationship, which is followed for all strain rates, covers the range 300 to 600°C — the region where strain rate has its major effect on A_4, B_4, and C_4. It is below 300°C, where deformation was found to be relatively independent of strain rate, that the deviation occurs.

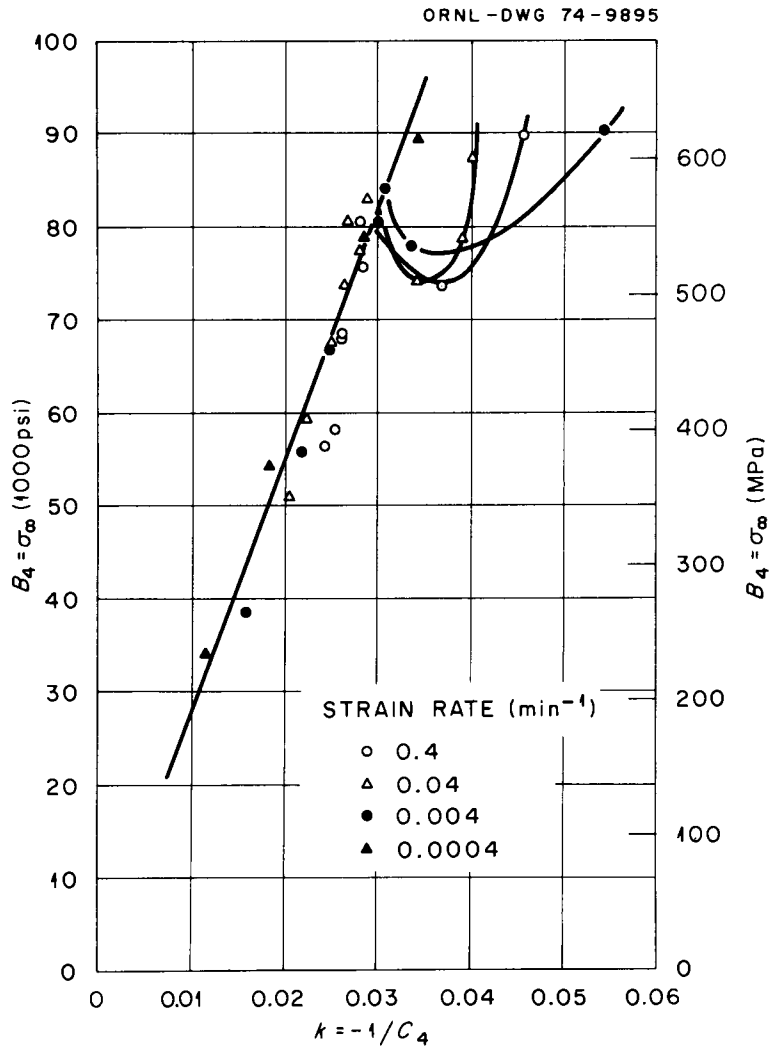

Fig. 5.64. The Variation of $B_4 = \sigma_\infty$ with $k = -1/C_4$.

5.4.2 Effect of Sodium on the Mechanical Properties of 2 1/4 Cr-1 Mo Steel — R. L. Klueh

Last quarter[41] we reported on the optical microscopy of 2 1/4 Cr-1 Mo steel specimens that had been decarburized in sodium for 26,500 hr at 566°C (1050°F) and others that had been aged in helium for the same time at 566°C. We have now examined these specimens by transmission electron microscopy.

Figure 5.65 shows the microstructure of the specimen "annealed" to simulate the before-test material and shows considerable precipitate. The parallel platelets are similar in morphology to Mo_2C observed in annealed 2 1/4 Cr-1 Mo steel.[42,43] The larger particles scattered through the microstructure are probably $M_{23}C_6$ or M_3C.

Y-126318

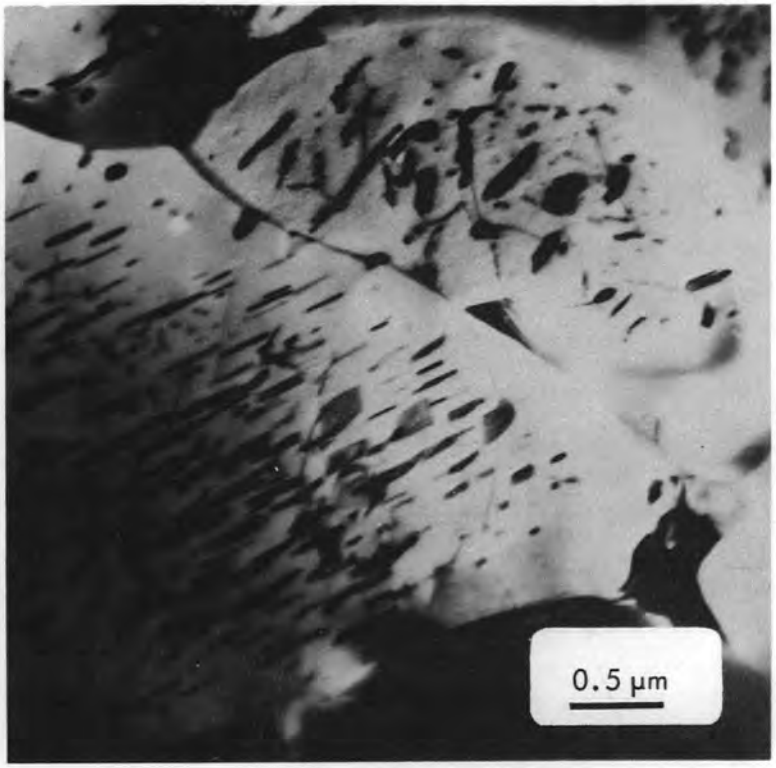

Fig. 5.65. Microstructure of Annealed 2 1/4 Cr-1 Mo Steel Heat Treated to Simulate the MSA Starting Material.

Figure 5.66 shows a typical area of the specimen that had been aged in helium for 26,500 hr. This specimen contained large globular carbide particles scattered through the matrix. Although not shown in Fig. 5.66, the grain boundaries of this specimen were heavily outlined with precipitate. A similar grain boundary precipitate was found in the specimens decarburized by sodium and is shown in Fig. 5.67. In the sodium-exposed specimen, there appeared to be much less matrix precipitate, as expected, since this material contained less carbon.

5.4.3 Fatigue Behavior of 2 1/4 Cr-1 Mo Steel — C. R. Brinkman, J. P. Strizak, and C. O. Stevens

Fatigue testing of 2 1/4 Cr-1 Mo steel is currently under way at several temperatures in order to define material behavior under cyclic loading conditions and to establish the data base for design-oriented correlations. The following types of tests are either under way or planned:

Fig. 5.66. Microstructure of 2 1/4 Cr-1 Mo Steel Aged in Helium for 26,500 hr.

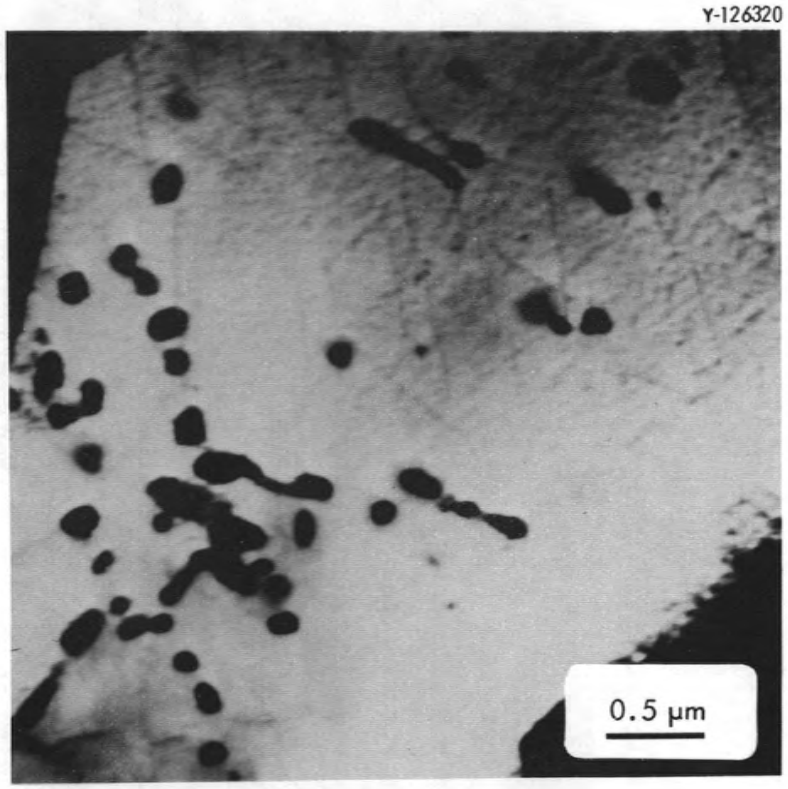

Fig. 5.67. Microstructure of 2 1/4 Cr-1 Mo Steel Decarburized by Sodium in a Stainless Steel Retort for 26,500 hr.

Low-cycle fatigue	Combined mode
High-cycle fatigue	Mixed mode
Fatigue, strain rate sensitivity	Mean strain fatigue
Creep fatigue tests	Fatigue of weld metal and weldments
Short term	Notched fatigue
Long term	Stable crack growth
Tensile tests	Combined push-pull axial and torsion
Constant strain rate to failure	Aging and test environment
Cyclic stress-strain curve	
Interrupted fatigue	
Block or multiple-step fatigue	

Currently, strain and load as well as stable (subcritical) crack growth tests are under way at temperatures from room to 538°C (1000°F). The test environment is air for the strain- and load-controlled tests and both air and steam for the stable crack growth tests. Material presently being used in these tests comes from a commerical 1-in.-thick (25.4 mm) Croloy plate with an average carbon content of 0.135%. Specimens were prepared from material in either the annealed or isothermally annealed condition. The isothermal annealing treatment consisted of the following: austenitize at 927 ± 14°C (1700 ± 25°F) for 1 hr and cool at a maximum rate of 85°C/hr (150°F/hr) to an isothermal transformation temperature of 705 ± 12°C (1300 ± 25°F). The plate was then held at this temperature for 2 hr and cooled to room temperature at a rate not to exceed 5°C/min (10°F/min). Tensile properties for this heat obtained from tests conducted at several crosshead speeds are given in Fig. 5.68.

Hourglass-shaped specimens (0.25 in. or 6.4 mm in diameter) were prepared for both the load- and strain-controlled tests from the plate material, with the major axis of the specimen parallel to the rolling direction of the plate. Tests were conducted by workers at both Mar-Test Inc. and BMI-Columbus.

Results of the strain- and load-controlled tests are plotted as elastic, plastic, and total strain range versus cycles to failure in Figs. 5.69 through 5.71. In Fig. 5.69 the results are plotted for strain-controlled tests conducted at both room temperature and 315°C (600°F).

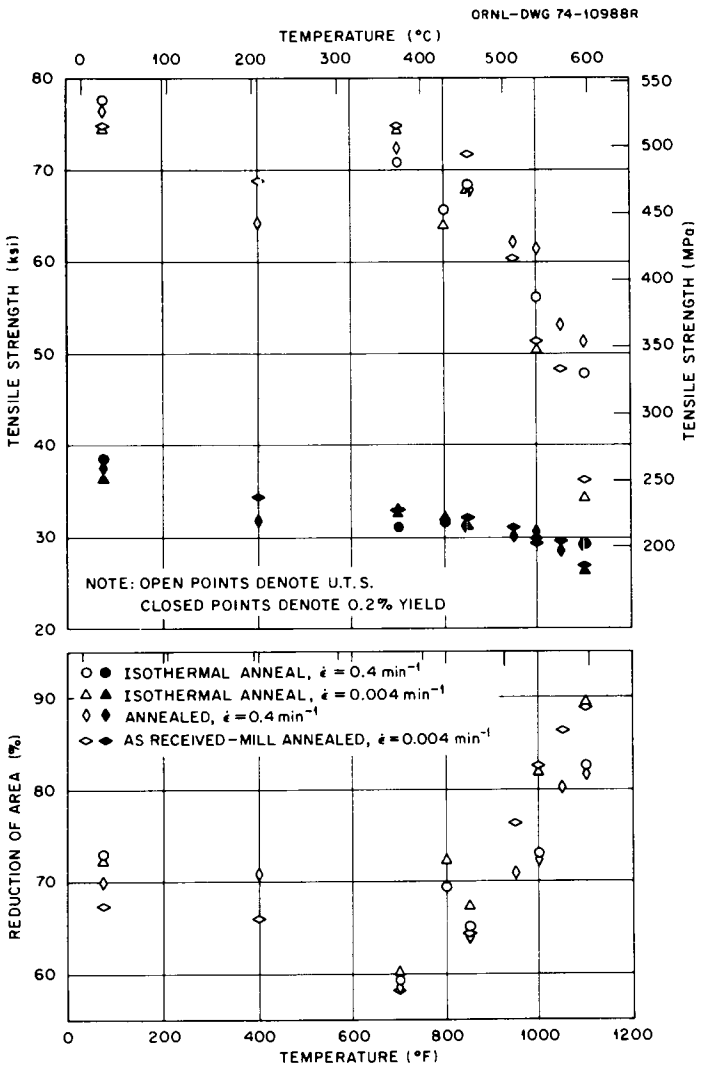

Fig. 5.68. Tensile Properties of Annealed 2 1/4 Cr-1 Mo Steel.

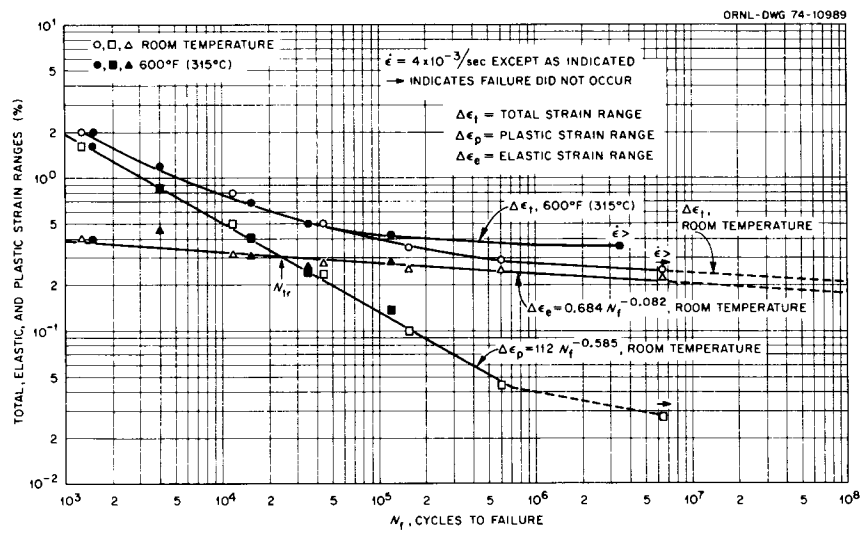

Fig. 5.69. Total, Elastic, and Plastic Strain Range Versus Cycles to Failure for Isothermally Annealed 2 1/4 Cr-1 Mo Steel at Room Temperature and 315°C (600°F), Showing Transition Fatigue Life, N_{tr}. Total strain range data points marked $\dot{\varepsilon}$> were obtained from tests started in strain control at the indicated strain rate, but were changed to load control and a higher strain rate after several hundred thousand cycles and an indication of load stability.

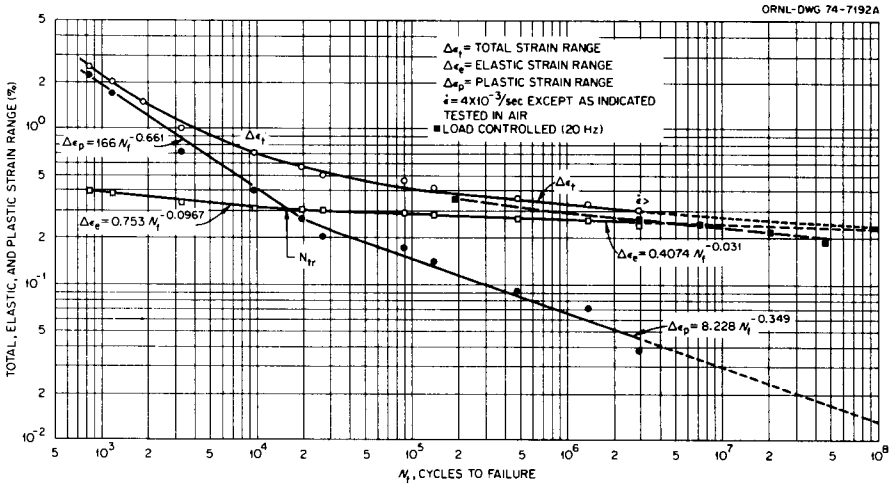

Fig. 5.70. Total, Elastic, and Plastic Strain Range Versus Cycles to Failure for Isothermally Annealed 2 1/4 Cr-1 Mo Steel at 427°C (800°F), Showing Transition Fatigue Life, N_{tr}. Extrapolations of data obtained from tests conducted in strain control are compared with data obtained from tests conducted in load control. In tests marked $\dot{\varepsilon}$>, strain rate increased after load stability was obtained.

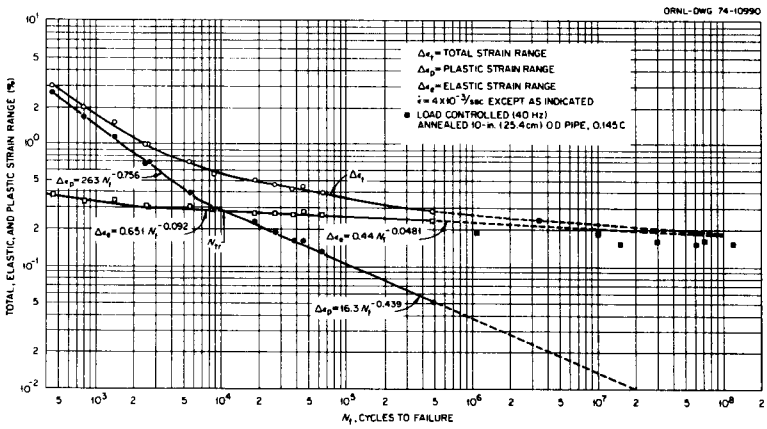

Fig. 5.71. Total, Elastic, and Plastic Strain Range Versus Cycles to Failure for Isothermally Annealed 2 1/4 Cr-1 Mo Steel at 539°C (1000°F), Showing Transition Fatigue Life, N_{tr}. Extrapolations, $\Delta\varepsilon_t$, of data obtained from strain-controlled tests are compared with data obtained from high-cycle load-controlled tests.

Data for both the elastic and plastic components of strain show linearity when plotted on log-log coordinates; hence, the room-temperature data were best-fit with simple power-law equations by least squares analysis. Extrapolation of the elastic and plastic best-fit lines, followed by summation, permitted a reasonable extrapolation of the total strain range for the room-temperature data out to 10^8 cycles to failure. Comparing the 315°C (600°F) fatigue data, obtained from limited tests, with the room-temperature data shows that little difference in fatigue life occurs in this temperature range within the low-cycle region. At cyclic lives exceeding approximately 60,000 cycles, however, there is a strong indication that the fatigue life of this material at 315°C (600°F) exceeds that of the material at room temperature.

In Fig. 5.70 the results are plotted from both strain- and load-controlled tests conducted at 427°C (800°F). However, as reported previously,[44] distinct breaks occurred in the otherwise linear (log-log) plots of elastic and plastic strain range versus cycles to failure, resulting in bilinear (log-log) data plots. The data were fitted and the total strain range was extrapolated similarly to the room-temperature data. The results of the load-controlled tests shown over the range of 1.87×10^5 to 1.45×10^7 cycles to failure were not considered in the extrapolation of the strain-controlled data. An estimate of the stabilized strains achieved for the load-controlled tests, which was used to compare the load-controlled cyclic lives with the strain-controlled lives, was obtained from the cyclic stress-strain curves included with this report. Alternatively, excellent agreement was found when the strains obtained from the cyclic stress-strain curve were compared with the appropriate values of stress divided by the appropriate dynamic Young's modulus. The single exception, however, was the test conducted at a stress level that resulted in failure at about 187,500 cycles, in which case the strain was taken from the cyclic stress-strain curve for this material. As shown in Fig. 5.70, the results of the load-controlled tests are not necessarily consistent with results or extrapolated results of the strain-controlled tests, even out in the ultrahigh-cycle range (i.e. $>10^7$ cycles), where the strain is nearly all elastic. There are several possible explanations

for this behavior, which can be enumerated as follows: (1) cyclic hardening followed by softening of the material, which while occurring primarily during the first part of a given test may complicate the strain history of a given test conducted in load control; (2) some ratchetting of the load-controlled specimen may occur, resulting in a nonzero mean load spectrum; (3) normal scatter in the data within the high-cycle region, resulting from subtle differences in surface finish, residual stress levels, etc.; and (4) subtle differences in experimental technique since the load-controlled tests, with the single exception of the test that failed at approximately 187,500 cycles, were conducted in a different laboratory than the strain-controlled tests.

Results of both the load- and strain-controlled tests obtained at 539°C (1000°F) are compared in Fig. 5.71. The load-controlled data were obtained by Brookhaven National Laboratory[45] on a different heat of Croloy (0.145% C in the annealed condition). An extrapolation of the data on total strain range versus cycles to failure, giving an indication of expected failure to 10^8 cycles, was similarly constructed from the elastic and plastic strain range values. Again the result of the load-controlled tests fall below the extrapolated curve for the strain-controlled test data.

A composite plot of total strain range versus cycles to failure is given in Fig. 5.72. This figure compares lines drawn through the strain-controlled test data points and associated extrapolations given in Figs. 5.69 through 5.71. In the low-cycle region, increasing the temperature beyond 315–371°C (600–700°F) results in a decrease in fatigue life at this strain rate. However, in the high-cycle region there is an indication of crossover, with material showing superior resistance to fatigue in the 427 to 539°C (800–1000°F) range than at room temperature.

Stress and plastic strain range developed during strain-controlled testing of this material are plotted for representative tests conducted in the low- and high-cycle regions at room temperature and 427°C (800°F) Figures 5.73 and 5.74 show that this material undergoes cyclic hardening at room temperature and either attains stability or continues to work harden throughout the test duration, depending upon the strain range.

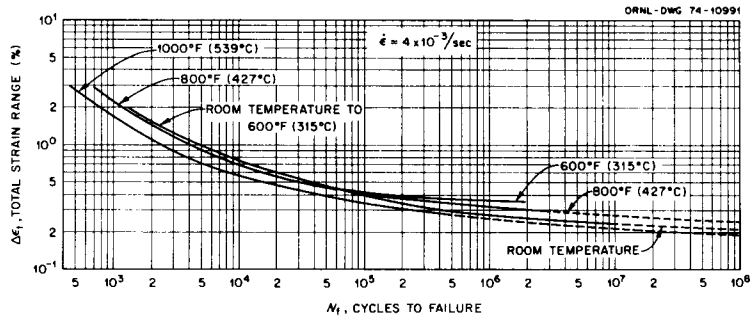

Fig. 5.72. Comparison of Best-Fit Curves for Total Strain Range as a Function of Cycles to Failure for a Single Heat of 2 1/4 Cr-1 Mo Steel in the Isothermally Annealed Condition. All testing was conducted in strain control. Dashed lines are extrapolations.

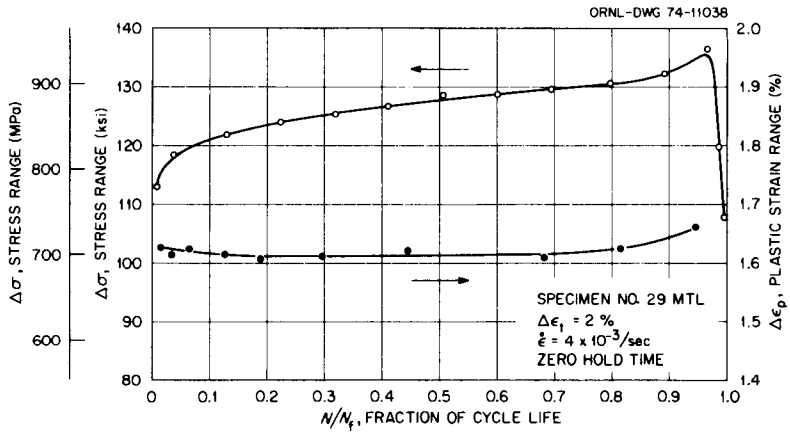

Fig. 5.73. Typical Stress and Plastic Strain Ranges as Functions of Fraction of Cyclic Life for Isothermally Annealed 2 1/4 Cr-1 Mo Steel at Room Temperature. Low-cycle range.

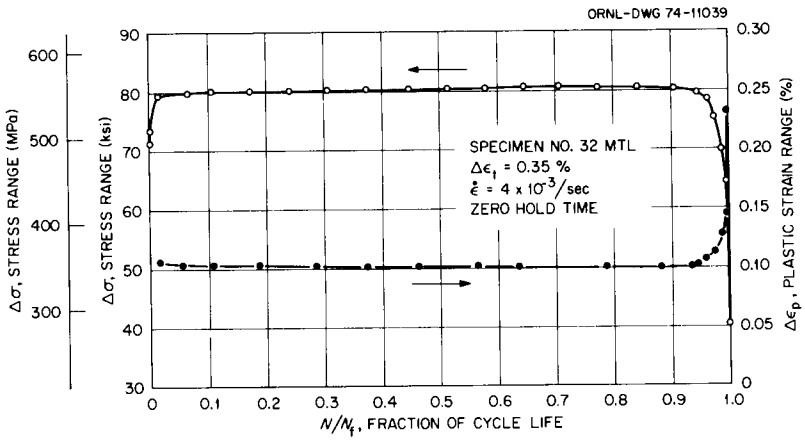

Fig. 5.74. Typical Stress and Plastic Strain Ranges as Functions of Fraction of Cyclic Life for Isothermally Annealed 2 1/4 Cr-1 Mo Steel at Room Temperature. High-cycle range.

At temperatures above about 427°C (800°F) this material cyclically hardens in the low-cycle range, Fig. 5.75, achieving some degree of stability, but cyclically hardens followed by some strain softening, as shown in Fig. 5.76, in the low-cycle region. Similar behavior was previously[44] reported at 538°C (1000°F), and the test results to date at 315°C (600°F) are inconclusive in this regard. This behavior accounts for the bilinear relationship in the elastic and plastic lines drawn in Figs. 5.70 and 5.71. Cyclic hardening followed by some softening can also be demonstrated

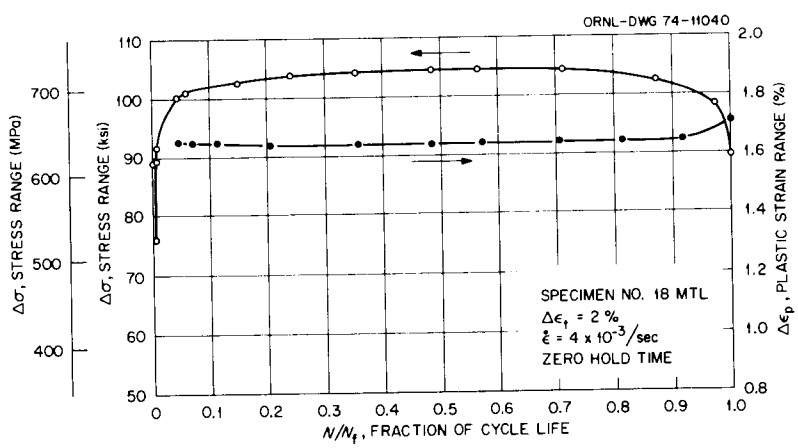

Fig. 5.75. Stress and Plastic Strain Ranges as Functions of Fraction of Cyclic Life for Isothermally Annealed 2 1/4 Cr-1 Mo Steel at 427°C (800°F). Low-cycle range.

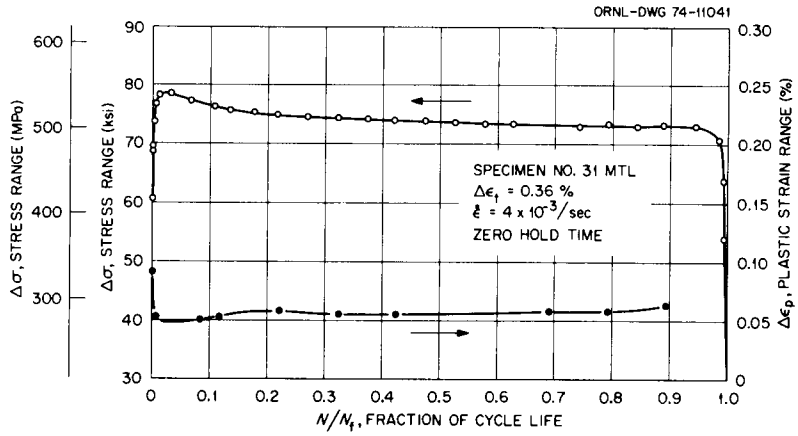

Fig. 5.76. Typical Stress and Plastic Strain Ranges as Functions of Fraction of Cyclic Life for Isothermally Annealed 2 1/4 Cr-1 Mo Steel at 427°C (800°F). High-cycle range.

to occur in load control at low strain ranges, as shown in Fig. 5.77. The strain range, showing upper and lower bounds and how they changed relative to the initial zero strain, is plotted as a function of number

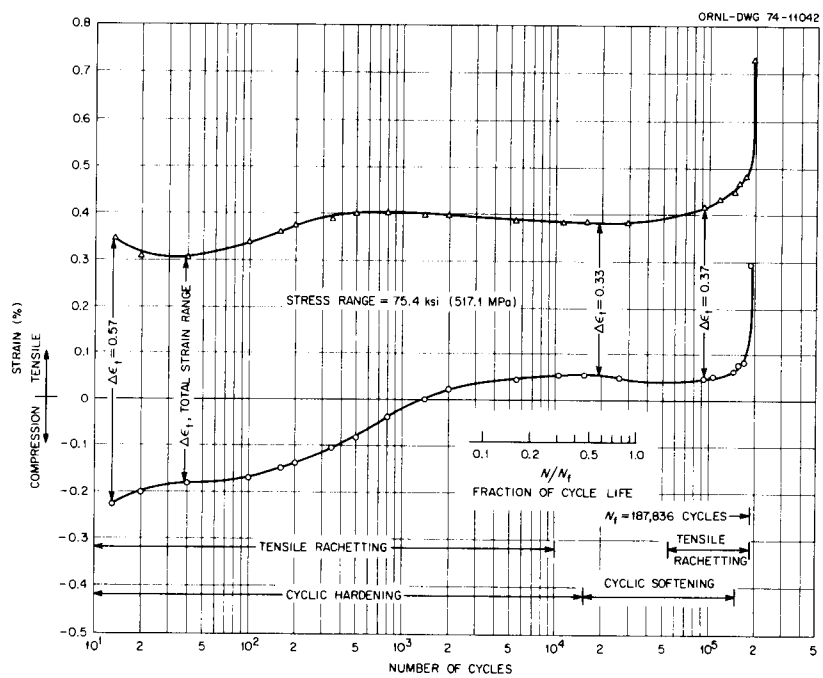

Fig. 5.77. Total Strain Range Developed as a Function of Cycles for Specimen 37MTL Fatigued in Load Control to Failure at 427°C (800°F). Various approximate regions of cyclic softening, hardening, and ratchetting are also shown.

of cycles in Fig. 5.77. In addition to cyclic hardening and softening the specimen also underwent ratchetting, developing a mean tensile strain. The strain range developed during stability, which occurred during a large fraction of the specimen lifetime, is plotted in Fig. 5.77, and it agrees well with the strain range calculated from the cyclic stress-strain curve.

Because of the cyclic softening displayed by this material in the upper temperature region, the cyclic stress-strain curves reported previously[44] were plotted again and compared with appropriate portions of the monotonic tensile stress-strain curves in Figs. 5.78 through 5.80. When softening was known to occur, Figs. 5.79 and 5.80, the near-stabilized data points were replaced by brackets indicating the range of stress developed during that particular test.

Stable (subcritical) crack growth testing of this material in both air and steam is continuing, and results will be reported in the next report.

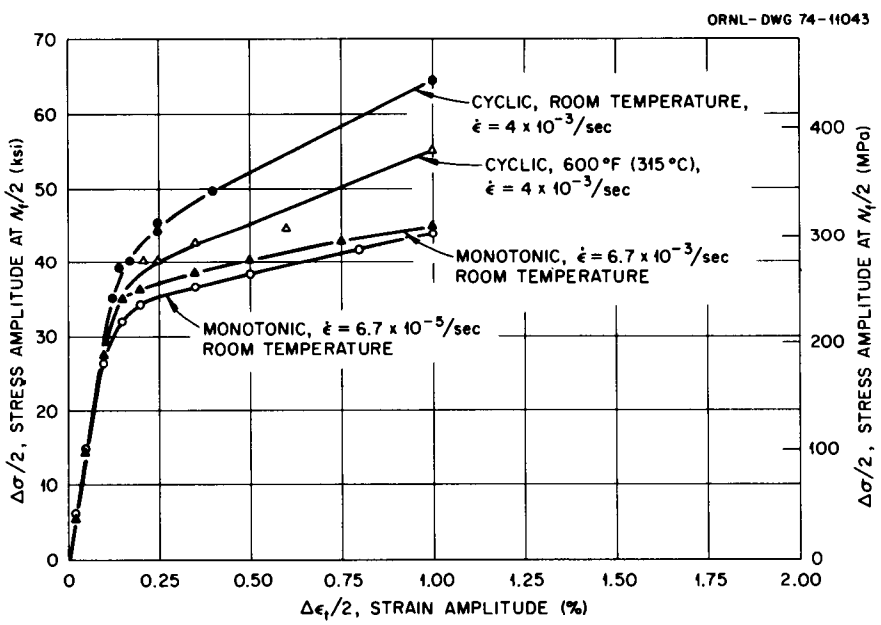

Fig. 5.78. Comparison of the Cyclic and Monotonic Stress-Strain Curves for Isothermally Annealed 2 1/4 Cr-1 Mo Steel at Room Temperature and 315°C (600°F).

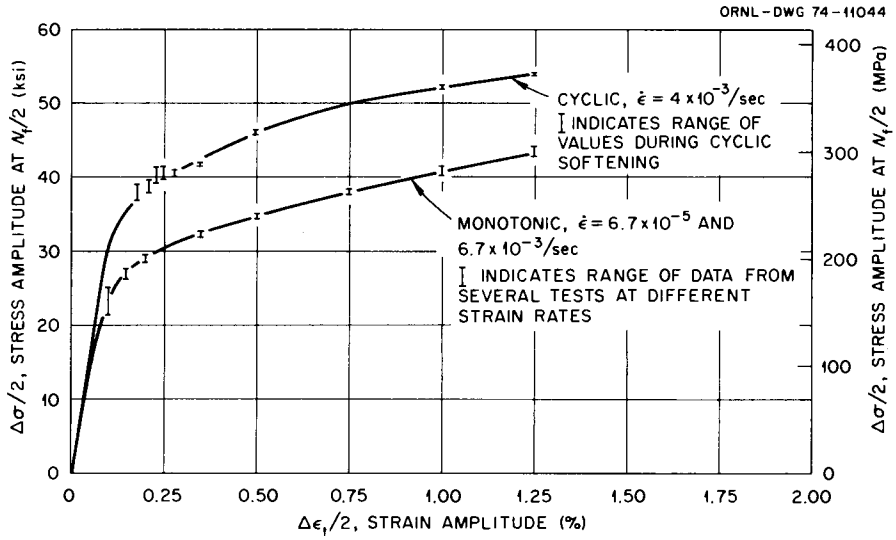

Fig. 5.79. Comparison of the Cyclic and Monotonic Stress-Strain Curves for Isothermally Annealed 2 1/4 Cr-1 Mo Steel at 427°C (800°F). Specimens for the monotonic tensile tests were taken from the plate material with their major axes both parallel and transverse to the rolling direction.

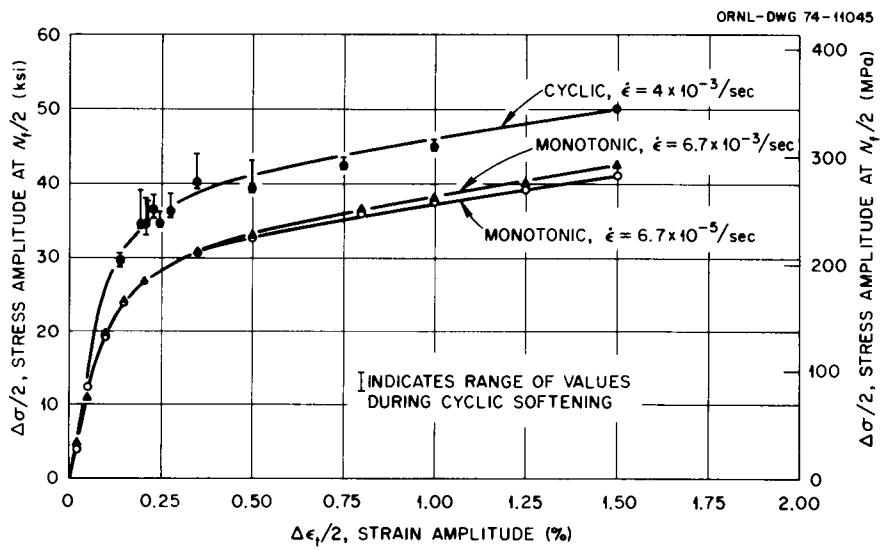

Fig. 5.80. Comparison of the Cyclic and Monotonic Stress-Strain Curves for Isothermally Annealed 2 1/4 Cr-1 Mo Steel at 539°C (1000°F).

5.4.4 Mechanical Properties Correlations of 2 1/4 Cr-1 Mo Steel for LMFBR Steam Generator — M. K. Booker and T. L. Hebble*

Mechanical property correlations for annealed 2 1/4 Cr-1 Mo steel are continuing, with the purpose of providing input to the *Nuclear Systems Materials Handbook* (NSMH). Correlations and corresponding tolerance limits have been developed for true fracture stress, time to tertiary creep, and diamond pyramid hardness.

Fracture stress data are seldom reported in the literature; therefore, most of the data (130 of 146 points) used in the correlation of fracture stress properties were obtained from the ORNL Data Storage and Retrieval System.[46] Time to tertiary creep data came primarily from information supplied by Babcock and Wilcox, although data from Combustion Engineering and ORNL were also used. Again, data in the literature were sparse, but a total of 155 tests was collected. Hardness data were obtained from the literature and from ORNL tests, though most had to be converted from other hardness scales. Correlations and tolerance limits have been developed in both English and SI units, but only the models in English (engineering) units will be presented here.

5.4.4.1 True Fracture Stress

Before developing models to describe the variation of true fracture stress with temperature, the data were corrected for triaxiality of stresses during necking. This factor was accounted for by use of the Bridgman correction factor, as calculated by the method of Nunes.[47] Then, the temperature dependence of this Bridgman-corrected true fracture stress was found to be adequately described by a simple cubic polynomial:

$$\widehat{FS} = 202 - 0.605T + 0.00127T^2 - 7.69 \times 10^{-7}T^3 ,$$

where $\widehat{FS}$ = expected value of Bridgman-corrected true fracture stress (ksi),
T = temperature (°F).

---

*Mathematics Research Staff.

The expected curve and tolerance limits are compared with the actual data in Fig. 5.81. This model is applicable to annealed plate, tube, and pipe, meeting specifications SA-387-D, SA-213-T22, and SA-335-P22 for ultimate tensile strength, yield strength, and chromium, molybdenum, and carbon contents, and for temperature ranging from 25 to 593°C (77 to 1100°F).

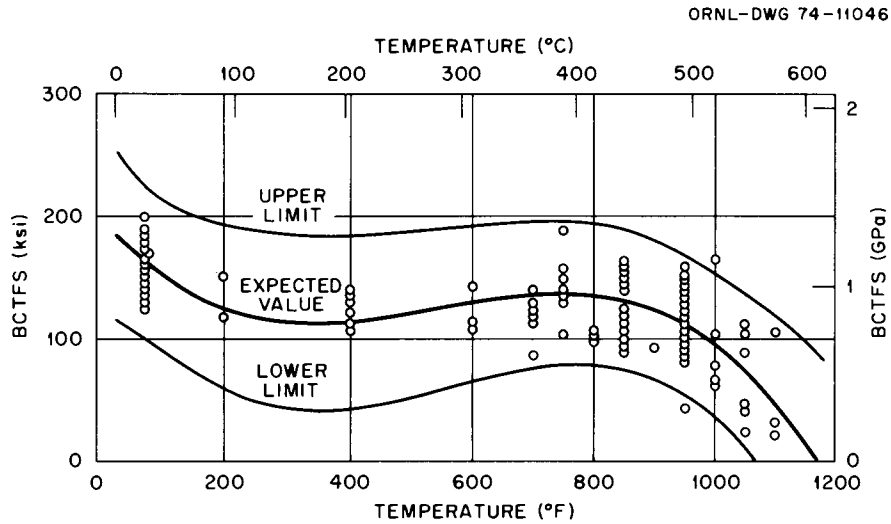

Fig. 5.81. Tolerance Limits (λ = 0.95, P = 0.90) About Expected Value of Bridgman-Corrected True Fracture Stress (BCTFS).

5.4.4.2 Time to Tertiary Creep

Times to tertiary creep, while displaying considerable scatter, may be described by a model of the form

$$\widehat{\log t_t} = 12.4 - 5.10 \times 10^{-3}T + 1.07 \log \sigma - 9.88 \times 10^{-7}T^2(\log \sigma)^2 ,$$

where $\widehat{\log t_t}$ = expected value of the logarithm of time to tertiary creep,

σ = creep stress (ksi),

T = test temperature (°F + 460).

Data were available from 454 to 677°C (850–1250°F), and while extrapolations to 371°C (700°F) appear to be reasonable and consistent, any extrapolation should be done with caution. Arbitrary limits on applicable stresses and times to tertiary creep have been set to define the region in which the model predicts reasonable results. For example, time values beyond

$\log t_t = 4.5$ should not be used. We are developing a model that overcomes these limitations. This model is applicable to annealed plate, tube, pipe, bar, and rod, meeting specifications SA-387-D, SA-213-T22, and SA-369-P22 for ultimate tensile strength, yield strength, and chromium, molybdenum, and carbon contents.

Better correlation could be obtained if additional factors, such as carbon content, were taken into account. Also, there is evidence[48] that room-temperature ultimate tensile strength might be a factor.

5.4.4.3 Diamond Pyramid Hardness

The ratio of room-temperature ultimate tensile strength to diamond pyramid hardness has been found to be relatively constant for a variety of heat treatments, carbon contents, and product forms, as might be expected from previous results.[49,50] The correlation coefficient between these two properties has been found to be 0.98, with the mean value of the ratio between the two being 482. Using this result and the previously reported[48] result for ultimate tensile strength, it is a simple matter to calculate room-temperature DPH for annealed material. Thus

$$\widehat{DPH} = \widehat{UTS}/482 ,$$

where $\widehat{DPH}$ = expected value of room-temperature diamond pyramid hardness,
$\widehat{UTS}$ = expected value of room-temperature ultimate tensile strength (ksi).

Lack of elevated-temperature hardness data makes it impossible to ascertain whether the UTS/DPH ratio remains constant at temperatures other than room temperature.

5.4.4.4 Creep Equation for 2 1/4 Cr-1 Mo Steel — D. O. Hobson and T. L. Hebble*

Development of a creep strain correlation for 2 1/4 Cr-1 Mo steel has been completed. The model is based on a small but high-quality

*Mathematics Research Staff.

set of creep curves obtained from work done by Klueh at ORNL and Combustion Engineering at Chattanooga and from selected curves furnished by Babcock & Wilcox. The model is for annealed material with room-temperature ultimate tensile strengths between 70 and 75 ksi (483 and 517 MPa) and temperatures between 427 and 593°C (800 and 1100°F). Although a need exists for extrapolability to 371°C (700°F), the fit of the mathematical model to the data is such that extrapolation of values of two of the coefficients is difficult. Therefore the 427°C (800°F) values are used for the lower temperature.

The model is a rational polynomial of the form

$$\varepsilon_c = t/(A + Bt) + Ct \ , \tag{29}$$

where ε_c = creep strain, %,
t = time, hr,

and A, B, and C = stress- and temperature-dependent coefficients. The coefficient C is the minimum creep rate, %/hr.

A total of 37 curves was individually fitted by the model, and the resulting coefficient values were examined as functions of temperature and stress. The resulting correlations are shown below.

$$\log A = 12.26 - 3.348 \times 10^{-6}T^2 + 9.353 \times 10^{-4}\sigma^2 - 1.167 \times 10^{-4}T\sigma \ , \tag{30}$$

$$\log B = -25.19 + 8.682 \times 10^{-2}T - 3.368 \times 10^{-5}T^2 - 1.152(\log \sigma)^2 \ , \tag{31}$$

$$\log C = -30.04 + 1.516 \times 10^{-2}T + 2.001 \times 10^{-3}T(\log \sigma)^2 \ , \tag{32}$$

where T = temperature in °R (°F + 460),
σ = stress, ksi.

The correlations given above are from a data base with test times of 5000 hr or less — that is, all tests were well into secondary creep before 5000 hr. It is recognized that lives in excess of 100,000 hr

are needed for steam generator materials and that extrapolations of this order are necessary. It is also recognized that the data base for the creep equations model is small, but it is the only base available with data of high enough precision within each test. The room-temperature ultimate tensile strength range (70–75 ksi, 483–517 MPa) used was too narrow to attempt to correlate into the equation.

Calculations made with the creep strain model agreed well with the original creep curves. It is recognized that the present model is very much the product of its data base and that comparisons with other creep data may show less agreement.

5.4.5 Mechanical Properties of Weld-Overlaid Forgings — R. L. Klueh

In previous quarterly reports,[51,52] we reported on the creep-rupture behavior of the type 304 stainless steel forging that had been overlaid with type 308 stainless steel weld metal. Forging specimens were tested in the axial, radial, and tangential orientations,[51] and specimens from the overlay and from the forging immediately adjacent to the fusion line were tested in the radial and tangential orientations.[52] These tests were at 593°C (1100°F), and in Fig. 5.82(a) the creep-rupture curves for forging, overlay weld metal, and forging adjacent to the fusion line are compared. The forging adjacent to the fusion line is slightly stronger than the unaffected forging and considerably stronger than the weld metal. When these results are compared with those given by Smith[53] in his compilation of properties on wrought type 304 stainless steel, it is found that both the unaffected forging and forging adjacent to the fusion line fall just above the maximum of Smith's scatter band. A comparison of creep rates [Fig. 5.82(b)] shows that the rates for the forging adjacent to the fusion line are slightly less than those of the unaffected forging, and both are considerably below those for the overlay.

In Fig. 5.83 the elongation and reduction of area are shown as functions of rupture life. The curves shown are meant only to represent the trend of the data, (these are visual fits). For the weld metal, separate curves were required for the radial and tangential specimens, whereas the ductility of the specimens from the two forging locations

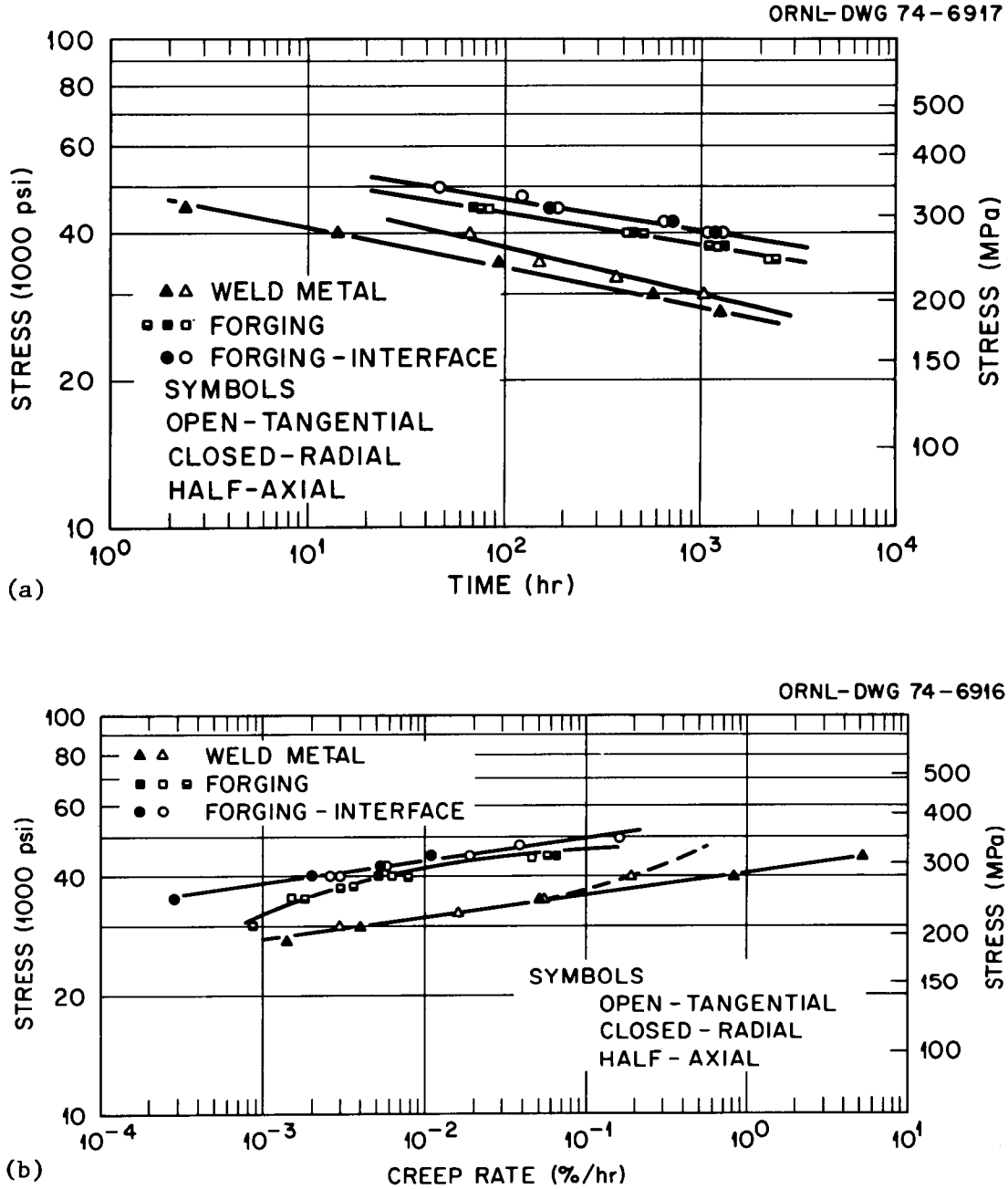

Fig. 5.82. A Comparison of the Creep-Rupture Properties of the Type 304 Stainless Steel Forging, Type 308 Stainless Steel Weld Metal, and Type 304 Stainless Steel Forging Adjacent to the Overlay-Forging Fusion Line. (a) Rupture life. (b) Minimum creep rate.

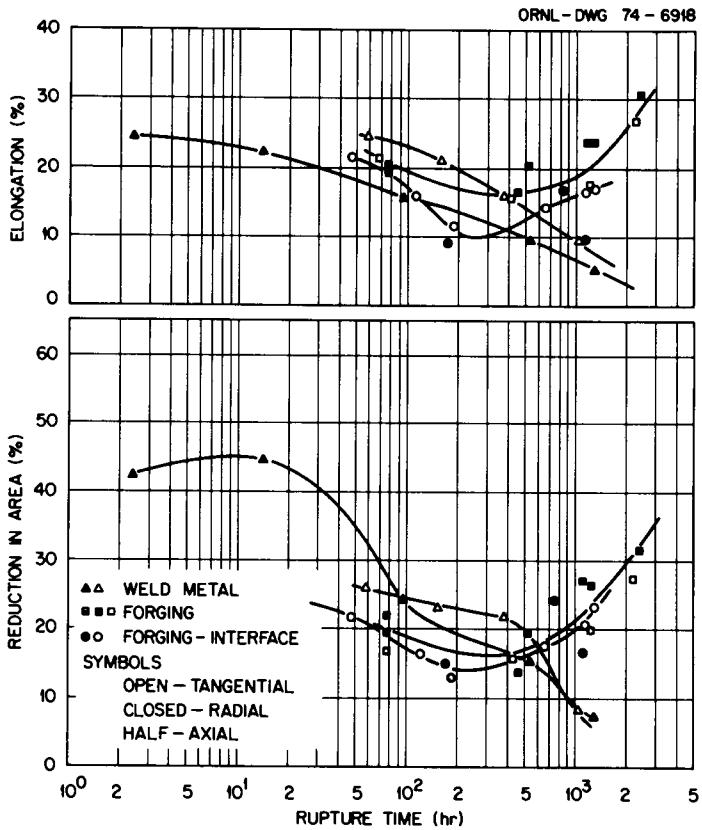

Fig. 5.83. Comparison of the Ductilities of the Type 304 Stainless Steel Forging, Type 308 Stainless Steel Weld Metal, and Type 304 Stainless Steel Forging Adjacent to the Overlay-Forging Fusion Line.

was independent of orientation. The ductility of the weld metal — both radial and tangential orientations — decreased with rupture life (decreasing stress) and appeared to approach a single curve at long times. Forging from both locations displayed a minimum in ductility with increasing rupture life.

When the fractured specimens were examined, both types of forging specimens exhibited fractures that were quite flat (i.e., without a neck). On the external surface of the gage section cracks were visible, indicating that grain boundaries may have been involved. In all cases, deformation appeared to be isotropic. The weld metal specimens, however, formed a neck at the higher stresses (short rupture times) and displayed two types of anisotropic deformation: (1) the cross section deformed to an ellipse rather than a circle, and (2) the specimens had a "knobby" appearance

(i.e., usually more than one point on the gage section appeared to be in the process of neck formation). As noted in the tensile tests,[54] the radial specimens were the most anisotropic. As the rupture life increased, the amount of neck formation decreased, and cracks perpendicular to the gage length appeared on the external surface.

In addition to specimens taken from overlay, forging, and forging adjacent to the fusion line, we also tested axial composite specimens that were taken from across the interface and contained both weld metal and forging in the gage section. The results of these tests are shown in Table 5.36. When these results are compared with those shown in Fig. 5.83, we find that the creep-rupture behavior of these specimens falls just above those for the tangential weld metal specimens.

Table 5.36. Creep-Rupture Properties of Composite Type 304 and 308 Stainless Steel Specimens at 593°C (1100°F)

Stress		Rupture Life (hr)	Elongation (%)	Reduction of Area (%)	Minimum Creep Rate (%/hr)
(ksi)	(MPa)				
40	276	66.3	12.4	37.3	0.0533
35	241	333.1	16.1	44.6	0.0085
32	221	571.1	16.5	44.8	0.00111
30	207	a			

[a]Test in progress.

We have conducted a series of tests at 482°C (900°F), and the results are given in Table 5.37. We limited our testing at this temperature because the stress required to cause rupture is quite large, leading to considerable plastic deformation before a stress is reached that would cause rupture in a reasonable time period (i.e., most of the deformation occurs on loading).

We are now conducting creep-rupture tests at 538°C (1000°F). With these studies, along with those at 482 and 593°C, we should be able to

Table 5.37. Creep-Rupture Properties of Overlaid Tubesheet Forging at 482°C (900°F)

Specimen Orientation	Stress (ksi)	Stress (MPa)	Rupture Life (hr)	Elongation (%)	Reduction of Area (%)	Minimum Creep Rate (%/hr)
			Type 308 Stainless Steel Overlay			
Radial	60	414	1257.0	19.3	18.7	0.001
Radial	61	421	744.3	21.0		0.0016
Radial	62.5	431	499.1	23.1	27.5	0.0021
Tangential	62.5	431	339.0	27.3	25.9	0.0025
			Type 304 Stainless Steel Forging			
Radial	64	441	1164.7	32.9		0.00035
Tangential	64	441	2161.5	30.9		0.00015
Axial	60	414	2542.3	31.1	25.8	0.0002
Axial	64	441	1540.3		33.0	0.00025
Axial	65	448	a	47.9	65.8	
			Type 304 Stainless Steel Forging at Interface			
Radial	62	427	1342.0	20.6		0.00034
Radial	64	441	574.0	24.8	23.9	0.00056
Tangential	64	441	1096.0	31.5		0.00029

[a]Ruptured on loading.

document the creep-rupture behavior of the tubesheet in the vicinity of the highest temperature of the intermediate heat exchanger of the FFTF (∿560°C or 1040°F).

5.5 HIGH TEMPERATURE DESIGN — W. L. Greenstreet,* J. M. Corum,* and C. E. Pugh*

5.5.1 Exploratory Studies in Support of Structural Design Methods — R. W. Swindeman

5.5.1.1 Creep Testing

Creep-rupture test data accumulated on the 1-in. (25.4-mm) plate product form of the reference heat of type 304 stainless steel (heat 9T2796), are summarized in Table 5.38. Except for four aged specimens, all specimens were tested in the reannealed condition (0.5 hr at 1093°C). The data are currently being evaluated in preparation for a final report dealing with the creep-rupture behavior. Efforts are under way to develop representations covering a broad range of temperatures, stresses, and times. Several approaches are being taken, as mentioned previously,[55] and one of the most straightforward of these concerns the use of time-temperature parameters. Four such parameters are as follows:

Orr-Sherby-Dorn:[17] $$P_D = \frac{C_D}{T} + \log t \ , \tag{33}$$

Larson-Miller:[56] $$P_{LM} = T(C_{LM} + \log t) \ , \tag{34}$$

Manson-Haferd:[57] $$P_{MH} = \frac{(\log t - \log t_a)}{(T - T_a)} \ , \tag{35}$$

and

Manson-Succop:[18] $$P_{MS} = C_{MS} + \log t \ , \tag{36}$$

where T is absolute temperature (K), t is time or reciprocal rate, and C_D, C_{LM}, (t_a, T_a), and C_{MS} are parametric constants defined by Eqs. (33),

*Reactor Division.

Table 5.38. Summary of Creep-Rupture Data for Type 304 Stainless Steel Heat 9T2796 1-in. (25.4-mm) Plate

Specimen	Temperature (°C)	Temperature (°F)	Stress (ksi)	Stress (MPa)	Status	Time, hr: to 1st Stage[a]	Time, hr: to 2nd Stage[a]	Time, hr: Total	Strain, %: Plastic Loading	Strain, %: Transient Creep	Strain, %: 1st Stage[a]	Strain, %: 2nd Stage[a]	Strain, %: Rupture	Reduction of Area (%)	Minimum Creep Rate (%/hr)	Test
RP 289	482	900	55.0	379	Ruptured		450.0	668.0	28.5			0.75	40	34	1.50×10^{-3}	13802
RP 172	482	900	50.0	345	Ruptured		675.0	884.8	20.8	0.05		0.44	25	23	2.80×10^{-4}	12286
RP 288	482	900	45.0	310	In test			1500.0	15.2						1.33×10^{-4}	13874
RP 119	538	1000	50.0	345	Ruptured	4.2	15.5	21.0	24.4	−0.85	0.30	3.0	36	43	0.240	9881
RP 6	538	1000	45.0	310	Ruptured	0.0		60.1	18.6	0.0	0.0		29	28	0.030	8863
RP 8	538	1000	40.0	275	Ruptured	0.0	130.0	162.8	14.3	0.1	0.0	3.1	22	22	0.021	8898
RP 168	538	1000	40.0	275	Ruptured	0.0	110.0	139.7	13.5	−0.16	0.0	2.6	21	31	0.024	12221
RP 9	538	1000	35.0	241	Ruptured	50.0	510.0	594.8	11.0	0.3	0.3	2.5	18		4.00×10^{-3}	8902
RP 251	538	1000	35.0	241	Ruptured	30.0	345.0	350.4	11.6	0.35	0.35	2.7	18	28	6.50×10^{-3}	12819
RP 129	538	1000	30.0	207	Ruptured	230.0	2219.0	2219.0	7.75	0.61	0.55	2.3	12	15	6.50×10^{-4}	11324
RP 24	538	1000	30.0	207	Discontinued	170.0		1171.0	8.3	0.51	0.4				6.30×10^{-4}	8938
RP 78	538	1000	25.0	172	Discontinued	600.0	11540.0	11540.0	5.5	0.55	0.41	1.94			1.00×10^{-4}	9389
RP 320	566	1051	25.0	172	Ruptured	130.0	1730.0	2054.0	5.2	0.80	0.75	2.95	13	10	1.20×10^{-3}	13825
RP 120	593	1100	40.0	275	Ruptured	0.3	4.7	4.9	15.5	−0.7	−0.1	9.0	31	33	2.10	9891
RP 163	593	1100	40.0	275	Ruptured	0.6		5.8	16.0	0.0	0.9		33	31	1.70	12155
RP 4	593	1100	35.0	241	Ruptured	0.0	20.0	25.1	11.7	0.2	0.0	7.3	27	36	0.340	8857
RP 86	593	1100	35.0	241	Ruptured	3.0	24.0	29.6	9.2	0.6	1.1	6.3	20	27	0.230	9603
RP 5	593	1100	30.0	207	Ruptured	5.0	80.0	110.8	8.3	0.85	0.6	4.5	19		0.046	8862
RP 166	593	1100	30.0	207	Ruptured	5.0	70.0	98.5	7.3	0.65	0.8	6.2	21	26	0.076	12191
RP 7	593	1100	25.0	172	Ruptured	40.0	280.0	440.1	5.8	0.70	1.1	3.9	16		0.0110	8897
RP 43	593	1100	25.0	172	Ruptured	35.0	390.0	619.2	4.5	0.95	1.50	4.5	16	18	9.00×10^{-3}	11319
RP 155	593	1100	25.0	172	Ruptured	30.0	350.0	552.9	5.0	0.95	1.00	4.8	15	18	0.0106	11190
RP 54	593	1100	25.0	172	Discontinued	25.0	310.0	402.5	5.5	0.70	0.75	4.0			0.0100	9183
RP 32	593	1100	22.5	155	Ruptured	25.0	550.0	878.1	4.6	0.60	0.45	2.7	15	11	3.50×10^{-3}	9036
RP 162	593	1100	22.5	155	Ruptured	40.0	620.0	1247.0	4.4	0.60	0.50	2.7	14	17	3.00×10^{-3}	12189
RP 239	593	1100	22.5	155	Ruptured	40.0	720.0	1063.0	4.3	0.61	0.55	2.85	16	13	2.80×10^{-3}	13032
RP 258	593	1100	21.25	147	Ruptured	80.0	770.0	1230.0	4.0	0.57	0.65	2.3	10	10	2.14×10^{-3}	13351
RP 58	593	1100	20.0	138	Discontinued	1600.0	4700.0	5060.0	2.8	1.95	2.95	5.15			6.50×10^{-4}	9067
RP 40	593	1100	17.5	121	Discontinued			5131.0	2.8	>1.29					$<1.80 \times 10^{-4}$	9037
RP 213	593	1100	17.5	121	In test	>2500.0		8000.0	2.3	>1.40	>1.40				$<7.00 \times 10^{-5}$	12447
RP 262	621	1150	30.0	207	Ruptured	3.0	13.5	21.0	7.8	1.20	2.50	8.00	26	25	0.590	13439
RP 263	621	1150	25.0	172	Ruptured	10.0	81.0	119.1	5.0	1.1	1.8	7.2	21	20	0.0725	13442
RP 276	621	1150	20.0	138	Ruptured	12.0	260.0	649.5	3.2	0.65	0.75	3.1	18	18	7.65×10^{-3}	13456
RP 266	621	1150	15.0	103	In test	>1400.0		3000.0	1.31	>2.0	>3.0				$<8.50 \times 10^{-4}$	13708
RP 121	649	1200	30.0	207	Ruptured	0.35	2.1	2.8	8.20	1.1	2.5	11.1	29	35	4.70	9892
RP 167	649	1200	30.0	207	Ruptured	0.75	3.4	4.6		1.1	2.3	14.0	27	37	3.70	12206
RP 1	649	1200	25.0	172	Ruptured	2.0	18.0	27.7	5.50	0.95	1.7	9.5	25	30	0.460	8826
RP 171	649	1200	25.0	172	Ruptured	1.0	13.0	18.8		1.30	2.1	12.5	32	34	0.870	12253
RP 122	649	1200	22.5	155	Ruptured	2.2	27.0	40.0	4.50	0.90	1.5	9.8	25	30	0.330	9895
RP 210	649	1200	22.5	155	Ruptured	3.0	32.0	53.8	4.40	0.70	1.5	10.0	28	26	0.270	12410
RP 2	649	1200	20.0	138	Ruptured	2.0	50.0	111.2	3.30	0.60	0.5	5.2	25	29	0.087	8828
RP 139	649	1200	19.5	134	Ruptured	2.5	80.0	177.9	3.00	0.55	0.5	7.0	27	29	0.077	11708
RP 85	649	1200	17.5	121	Ruptured	2.0	70.0	250.0	2.40	0.53	0.4	4.2	27	30	0.050	9586
RP 157	649	1200	17.5	121	Ruptured	3.0	83.0	288.2	2.20	0.60	0.5	4.0	27	30	0.040	11828
RP 272	649	1200	17.5	121	Ruptured	3.0	140.0	484.7	2.1	0.54	0.45	5.10	32	26	0.029	13365
RP 3	649	1200	15.0	103	Ruptured	1.0	150.0	730.0	1.35	0.30	0.1	2.8	21		0.0150	8832
RP 153	649	1200	15.0	103	Ruptured	1.0	230.0	1524.0	1.30	0.40	0.2	4.5	45	40	0.0170	11349
RP 260	649	1200	13.75	94.8	Ruptured	0.4	240.0	1053.0	1.2	0.25	0.05	2.80	23	20	9.70×10^{-3}	12829
RP 273	649	1200	13.75	94.8	Discontinued	2.0		257.8	1.1	0.25	0.10				8.00×10^{-3}	13540
RP 87	649	1200	12.5	86.2	Ruptured	1130.0	3000.0	3960.0	0.82	2.30	5.6	12.0	22	29	3.20×10^{-3}	9660
RPT247	649	1200	12.5	86.2	Discontinued	500.0	2220.0	2500.0	0.88	0.85	4.0	10.8			4.35×10^{-3}	13319
RP 144	649	1200	10.0	68.9	Discontinued	1500.0	8000.0	8082.0	0.15	1.30	1.8	5.4			5.00×10^{-4}	11069
RP 126	649	1200	7.5	51.7	Discontinued	400.0		10000.0	0.005	0.30	0.11				3.50×10^{-5}	10172
RP 298	704	1300	25.0	172	Ruptured	0.09	0.80	1.55	5.30	2.0	3.0	15.0	45	34	15.70	14239
RP 123	704	1300	20.00	138	Ruptured	0.2	4.5	8.7	3.6	0.70	1.0	13.5	38	42	2.80	9907
RP 124	704	1300	17.50	121	Ruptured	0.5	17.0	23.3	2.53	0.70	1.0	19.0	40	41	1.05	9908
RP 299	704	1300	17.0	117	Ruptured	0.5	8.5	22.1	2.70	0.80	1.0	7.5	33	29	0.800	14232
RP 27	704	1300	15.00	103	Ruptured	0.3	20.0	46.9	1.80	0.40	0.3	7.5	27		0.330	8965

Table 5.38. (Continued)

Specimen	Temperature (°C)	Temperature (°F)	Stress (ksi)	Stress (MPa)	Status	Time, hr to 1st Stage[a]	Time, hr to 2nd Stage[a]	Time, hr Total	Strain, % Plastic Loading	Strain, % Transient Creep	Strain, % 1st Stage[a]	Strain, % 2nd Stage[a]	Strain, % Rupture	Reduction of Area (%)	Minimum Creep Rate (%/hr)	Test
RP 297	704	1300	15.0	103	Ruptured	1.5	26.0	70.1	1.45	0.85	1.0	9.5	39	30	0.320	14245
RPT248	704	1300	13.75	94.8	Ruptured	0.1	35.0	83.1	1.10	0.42	0.25	7.50	30	28	0.210	13321
RP 102	704	1300	12.50	86.2	Ruptured	0.1	130.0	244.4	0.65	0.25	0.1	16.0	47	42	0.120	9611
RP 295	704	1300	12.5	86.2	Ruptured	0.2	90.0	170.5	0.66	0.25	0.1	12.5	38	26	0.132	14293
RPT 12	704	1300	11.25	77.6	Ruptured	50.0	375.0	562.7	0.41	0.60	3.2	20.0	42	39	0.050	12563
RP 160	704	1300	10.00	68.9	Ruptured	130.0	650.0	1027.0	0.20	1.50	5.0	20.5	40	37	0.028	11908
RP 255	704	1300	7.5	51.7	Ruptured	335.0	1710.0	2296.0	0.07	0.80	2.00	8.20	14	12	4.20×10^{-3}	12607
RP 109	760	1400	20.0	138.0	Ruptured	0.00	0.5	0.75	4.20	0.00	0.0	21.0	45	38	42.0	9970
RP 110	760	1400	17.5	121.0	Ruptured	0.08	1.25	2.1	2.60	0.60	1.0	19.0	45	36	14.5	9975
RP 118	760	1400	15.0	103.0	Ruptured	0.10	2.50	5.3	1.90	0.50	0.70	14.0	44	37	5.20	9912
RPT245	760	1400	12.5	86.1	Ruptured	0.2	8.5	16.1	0.50	0.40	0.50	13.30	32	36	1.50	13318
RP 83	760	1400	12.5	86.1	Ruptured	0.25	12.5	19.9	0.62	0.50	0.65	18.5	42	37	1.43	9542
RP 250	760	1400	10.0	68.9	Ruptured	5.0	42.0	61.4	0.20	0.60	2.10	15.70	30	27	0.355	13307
RP 30	760	1400	10.0	68.9	Ruptured	0.30	30.0	45.7	0.25	0.30	0.20	13.5	26		0.430	8971
RP 211	760	1400	8.5	58.6	Ruptured	11.0	120.0	195.9	0.05	1.25	2.50	19.0	38	38	0.140	12424
RP 84	760	1400	7.5	51.7	Ruptured	130.0	500.0	697.7	0.0	3.46	9.0	26.0	47	39	0.044	9550
RP 111	816	1500	12.5	86.1	Ruptured	0.05	1.25	2.1	0.85	0.6	0.8	17.0	49	44	14.3	10074
RP 81	816	1500	10.0	68.9	Ruptured	0.22	5.0	8.4	0.17	0.6	1.1	19.0	53	25	3.60	9539
RP 80	816	1500	7.5	51.7	Ruptured	10.0	50.0	77.7	0.0	2.0	5.5	21.3	42	40	0.380	9531
RP 214	816	1500	5.0	34.5	Ruptured	200.0	530.0	731.2	0.0	4.0	10.8	23.0	36	30	0.035	12451

[a]0.2% offset.

(34), (35), and (36), respectively. We used a least squares method suggested by Manson and Mendelson,[21] in which a polynomial involving log stress, $P(\log S)$, is used to represent the stress dependence of the parameter. This allows the parametric constants to be optimized for all stresses simultaneously. We chose the cubic form for the polynomial:

$$P(\log S) = a_0 + a_1(\log S) + a_2(\log S)^2 + a_3(\log S)^3 , \qquad (37)$$

where values for a_i are calculated along with the parametric constants. The results of this analysis for the secondary creep rate data are summarized in Table 5.39 and plotted along with the data in Fig. 5.84. The Orr-Sherby-Dorn parameter was slightly better than the others, but none were able to represent the low-stress data at 593°C very well.

The fit of the parametric relations to tertiary creep life data are summarized in Table 5.39 and Fig. 5.85. Again, the Orr-Sherby-Dorn parameter provides a slightly better fit to the data. Inspection of the data in Fig. 5.85 relative to the isothermal trends developed from the parametric fits reveals that a fairly large discrepancy occurs in the vicinity of 15,000 psi (103 MPa) at 649°C. Less obvious discrepancies

Table 5.39. Summary of Results from Time-Temperature-Parameter Fits to Type 304 Stainless Steel (Heat 9T2796) Creep-Rupture Data

Type of Data[a]	Parameter[b]	Value for Constant[c]	Value for Parameter at Indicated Stress					Standard[d] Deviation (log hr^{-1})
			50 ksi, 345 MPa	40 ksi, 276 MPa	30 ksi, 207 MPa	20 ksi, 138 MPa	10 ksi, 68.9 MPa	
$\dot{\varepsilon}_s, S$	O-S-D	−24788	−29.725	−28.645	−27.394	−25.846	−23.557	0.20
$\dot{\varepsilon}_s, S$	L-M	25.313	21354	22079	23001	24293	26542	0.25
$\dot{\varepsilon}_s, S$	M-H	10.470 598.0	−0.045652	−0.040099	−0.034445	−0.028770	−0.022894	0.22
$\dot{\varepsilon}_s, S$	M-S	−0.027686	−23.653	−24.351	−25.882	−26.631	−29.013	0.35
t_3, S	O-S-D	−18711	−21.907	−20.903	−19.790	−18.472	−16.516	0.18
t_3, S	L-M	18.168	15747	16472	17322	18430	20376	0.20
t_3, S	M-H	12.885 413.6	−0.029280	−0.026937	−0.024426	−0.021656	−0.018151	0.20
t_3, S	M-S	−0.020898	−18.318	−19.065	−19.959	−21.140	−23.171	0.23
t_R, S	O-S-D	−18829	−21.930	−20.928	−19.773	−18.359	−16.334	0.13
t_R, S	L-M	18.224	15928	16608	17480	18699	20759	0.15
t_R, S	M-H	11.640 477.7	−0.031076	−0.028043	−0.024841	−0.021426	−0.017512	0.12
t_R, S	M-S	−0.021052	−18.592	−19.299	−20.215	−21.505	−23.649	0.19
$\dot{\varepsilon}_s, \sigma$	O-S-D	−22687	−26.571	−25.656	−24.612	−23.320	−21.248	0.18
t_3, σ	O-S-D	−17641	−19.824	−19.091	−18.233	−17.122	−15.197	0.22
t_R, σ	O-S-D	−17621	−19.732	−18.970	−18.047	−16.836	−14.904	0.15
$\dot{\varepsilon}_s, \sigma/M$	B-A-S	−21179						0.18
$t_3, \sigma/M$	B-A-S	−15629						0.20
$t_R, \sigma/M$	B-A-S	−16230						0.15

[a] $\dot{\varepsilon}_s$ = creep rate; S = engineering stress; t_3 = time to tertiary; t_R = time to rupture; σ = true stress; M = dynamic modulus.

[b] O-S-D = Orr-Sherby-Dorn; L-M = Larson-Miller; M-H = Manson-Haferd; M-S = Manson-Succop; B-A-S = Barrett-Ardell-Sherby.

[c] First value for M-H = log t_a, second value = T_a.

[d] 72 data for $\dot{\varepsilon}_s$, 63 data for t_3, 60 data for t_R.

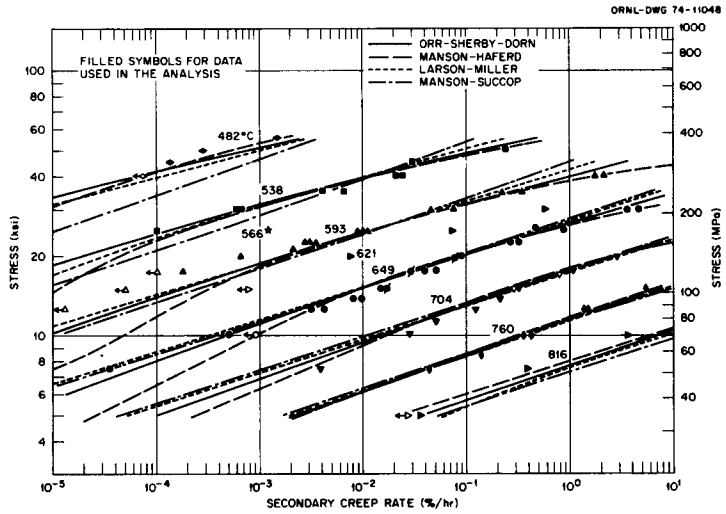

Fig. 5.84. Comparison of the Fit of Four Parametric Models to Secondary Creep Rate Data for Type 304 Stainless Steel (25.4-mm Plate from Heat 9T2796). Crossed symbols at 649°C represent results from specimens aged 4 days before testing.

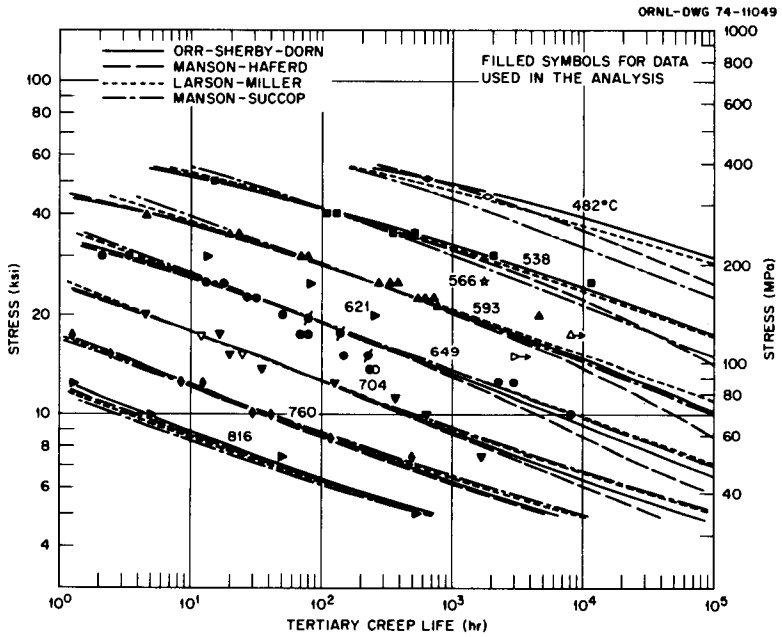

Fig. 5.85. Comparison of the Fit of Four Parametric Models to Tertiary Creep Life Data for Type 304 Stainless Steel (25.4-mm Plate from Heat 9T2796). Crossed symbols at 649°C represent results from specimens aged 4 days before testing.

also occur near 21,000 psi (145 MPa) at 593°C and 15,000 psi (103 MPa) at 704°C. The deviations of the data from the trend lines at these temperatures appear to be real and are probably associated with metallurgically instability. All parameters predicted tertiary creep lives that were too short for low stresses at 593°C.

The results from the parametric fit to rupture data are included in Table 5.39 and compared with actual data in Fig. 5.86. The Manson-Haferd parameter fit the data slightly better than the Orr-Sherby-Dorn parameter. Again, all the parameters predicted rupture lives that were too short relative to the data at 593°C.

Moteff and co-workers[58] have pointed out that correlations based on modulus-compensated true stresses might be more meaningful than representations based on engineering stress data. This could be very important for reannealed type 304 stainless steel, since large plastic loading strains are introduced at lower testing temperatures and, hence, the true stresses are greatly increased. The data in Table 5.39 were adjusted to

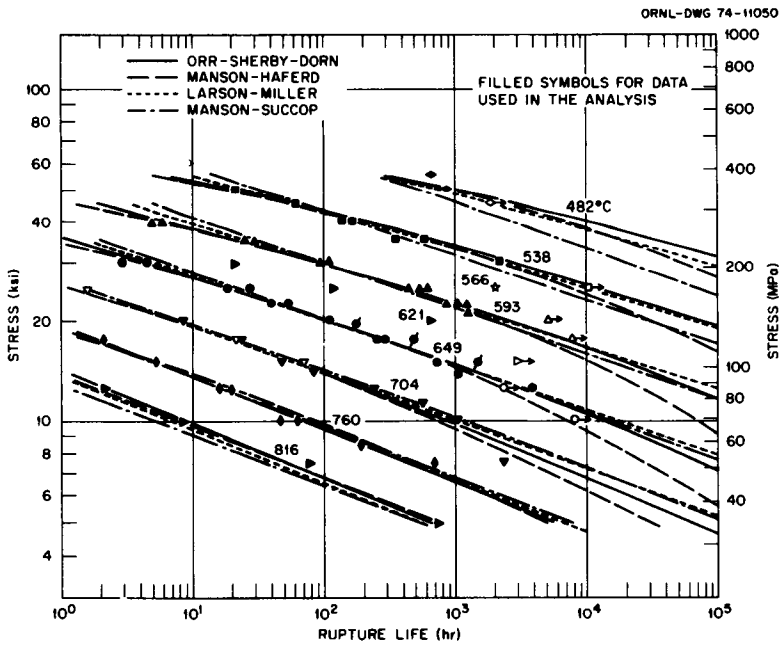

Fig. 5.86. Comparison of the Fit of Four Parametric Models to Rupture Life Data for Type 304 Stainless Steel (25.4-mm Plate from Heat 9T2796). Crossed symbols at 649°C represent results from specimens aged 4 days before testing.

true stresses by multiplying the engineering stresses by $(1 + \varepsilon_{inf})$, where ε_{inf} is the total inelastic strain at the inflection point of the creep curve. These data were modulus compensated by use of data reported by McCoy, Moyer, and Dews[24] for heat 9T2796. The resulting data set was used to obtain a least squares fit to the Barrett-Ardell-Sherby[59] parameter, assuming that a single diffusion process controls the secondary creep rate and rupture processes. A cubic polynomial in the logarithm of true stress similar to Eq. (37) was assumed to represent the stress dependence. The results obtained by fitting the parameter to secondary creep rate, tertiary creep life, and rupture life are summarized in Table 5.39 and plotted against the data in Figs. 5.87, 5.88, and 5.89. The use of modulus-compensated true stresses produces about the same fit as the more conventional approaches when dealing with secondary creep rate and rupture data. The discrepancies in the tertiary creep data at 593, 649, and 704°C (1100, 1200, and 1300°F) are exaggerated, however.

The parameter master curves for rupture life are shown plotted in Fig. 5.90. For three of the parameters, Larson-Miller, Manson-Succop, and Barrett-Ardell-Sherby, the master curves are straight lines when log S or log σ/M is plotted against the parameter value. This implies

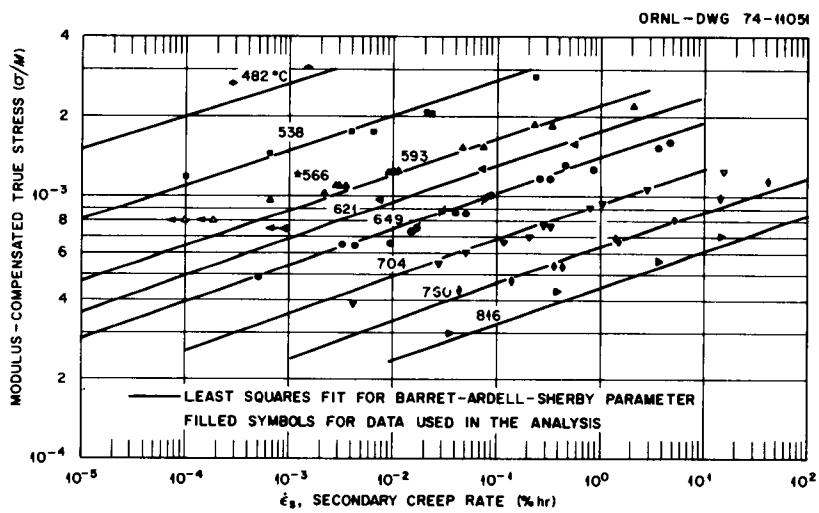

Fig. 5.87. The fit of the Barrett-Ardell-Sherby Parameter to Secondary Creep Rate Data for Type 304 Stainless Steel (25.4-mm Plate from Heat 9T2796). Crossed symbols at 649°C represent results from specimens aged 4 days before testing.

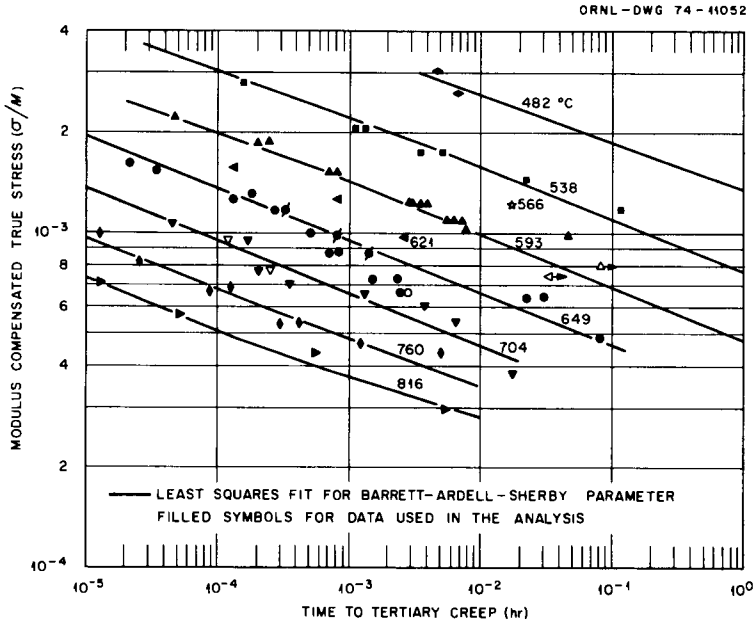

Fig. 5.88. The Fit of the Barrett-Ardell-Sherby Parameter to Tertiary Creep Life Data for Type 304 Stainless Steel (25.4-mm Plate from Heat 9T2796). Crossed symbols at 649°C represent results from specimens aged 4 days before testing.

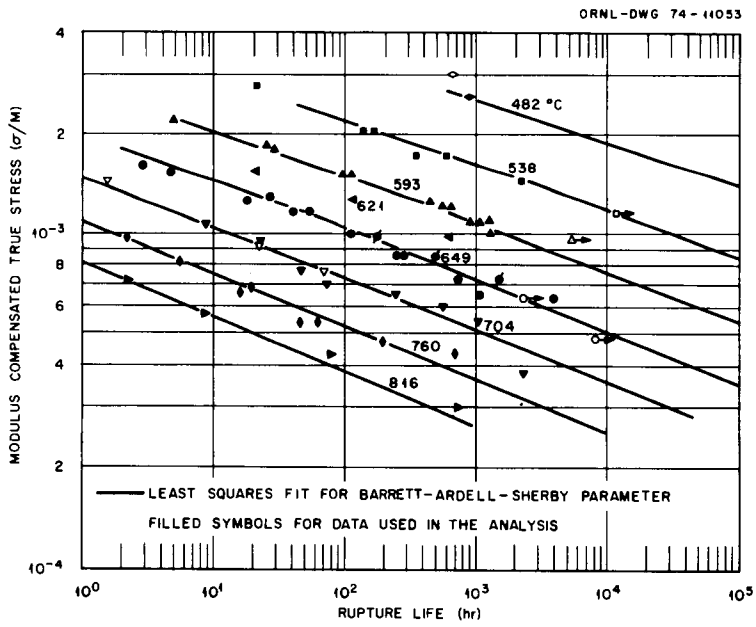

Fig. 5.89. The Fit of the Barrett-Ardell-Sherby Parameter to Rupture Life Data for Type 304 Stainless Steel (25.4-mm Plate from Heat 9T2796). Crossed symbols at 649°C represent results from specimens aged 4 days before testing.

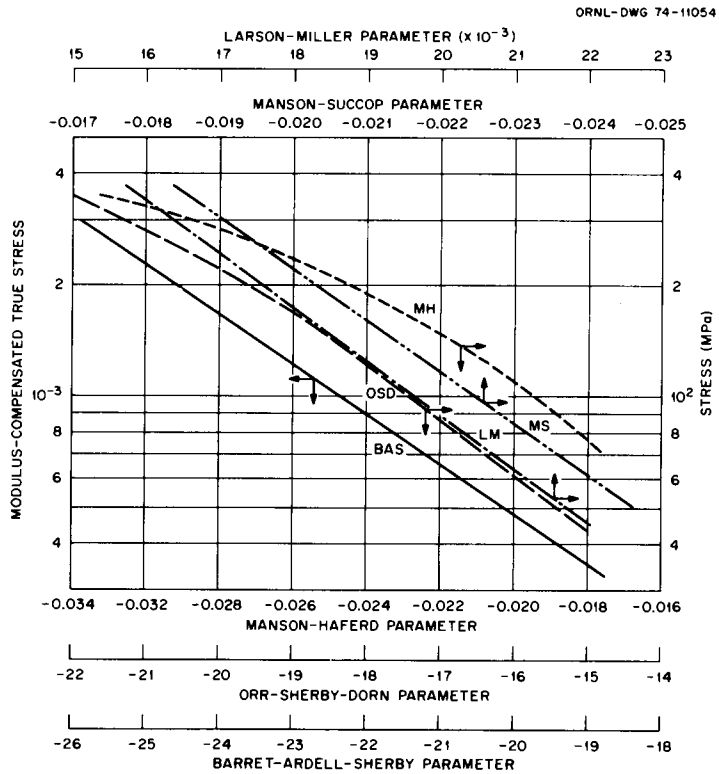

Fig. 5.90. Master Curves for Five Parameters Representing the Creep-Rupture Behavior of Type 304 Stainless Steel (25.4-mm Plate from Heat 9T2796).

that the cubic polynomial, Eq. (37), can be replaced by a logarithm form of the power law.

The parametric approaches, essentially, are based on a method of temperature compensating the time or rate for data at constant stress. A somewhat different approach can be taken in which the isothermal data are represented by means of the power law and attempts then made to determine the temperature dependence of the equation constants. The following results represent an update of previously reported information. We write the power law as:

$$\dot{\varepsilon} = (S/A)^n \ , \tag{38}$$

where $\dot{\varepsilon}$ is secondary creep rate or reciprocal time, S is engineering stress, and A and n are temperature-dependent constants. The results for fits to secondary creep rates, tertiary creep lives, and rupture

lives are given in Table 5.40 and plotted in Figs. 5.91 and 5.92. It is clear in Fig. 5.92 that the A values can be represented quite simply by the equation:

$$A = A^{c} e^{-\alpha(T - T^{c})} , \tag{39}$$

where values for A^{c}, α, and T^{c} are given in Table 5.41. The temperature dependence of the n value is quite complicated. For secondary creep rate and rupture life, however, the n values appear to be constant at low temperature and high temperature and to change abruptly between 621 and 677°C (1150–1250°F). Assuming this, the following representation was developed for the n values:

$$n = n^{c} - \Delta n \left\{ 1 - \exp - \left[\Theta \left(\frac{1}{T^{c}} - \frac{1}{T} \right) \right]^{\beta} \right\} , \tag{40}$$

where values for the five constants are given in Table 5.41. The fits of the models to creep rate and rupture data are shown in Figs. 5.93 and 5.94. The models do not fit the data at 482°C but appear to be an improvement over the parametric approaches at other temperatures.

The A and n values for modulus-compensated true stresses were also determined and are reported in Table 5.42.

5.5.1.2 Relaxation Testing

Data obtained from about 50 relaxation tests[60,63] on type 304 stainless steel were accumulated and used to construct "isochronous relaxation curves." Temperatures cover 482 to 593°C (900–1100°F) and times to 100 hr. Data obtained on reannealed material were adjusted to reflect "true" stresses by multiplying the starting stresses by $(1 + \varepsilon)$, where ε is the loading strain. The starting stresses were then located on a true-stress true-strain plot thought to be representative of an average heat of type 304 stainless steel in the mill-annealed condition.

Table 5.40. Temperature Dependence of the Constants in the Power Law Representing Creep-Rupture of Type 304 Stainless Steel (Heat 9T2796)

Temperature		Creep Rate			Tertiary Creep			Rupture		
		A		*n*	*A*		*n*	*A*		*n*
(°C)	(°F)	(ksi)	(MPa)		(ksi)	(MPa)		(ksi)	(MPa)	
538	1000	56.1	386	11.4	65.9	454	9.65	70.6	487	8.86
593	1100	38.6	266	10.7	49.4	341	8.46	49.9	344	8.82
621	1150	31.7	218	10.7	44.0	304	7.22	43.4	299	8.43
649	1200	26.1	180	7.79	35.4	244	6.83	36.8	254	7.68
704	1300	17.4	120	6.57	24.3	168	7.21	26.8	185	7.05
760	1400	11.7	80.4	6.73	17.7	122	6.70	19.2	133	6.54
816	1500	8.39	57.9	6.65	13.0	89.3	6.70	14.1	9.73	6.48

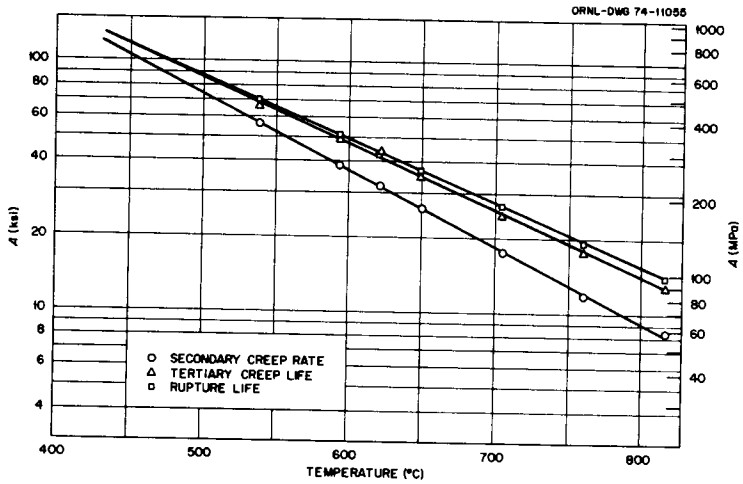

Fig. 5.91. Dependence of the Constant A in the Power Law on Temperature for Type 304 Stainless Steel (25.4-mm Plate from Heat 9T2796).

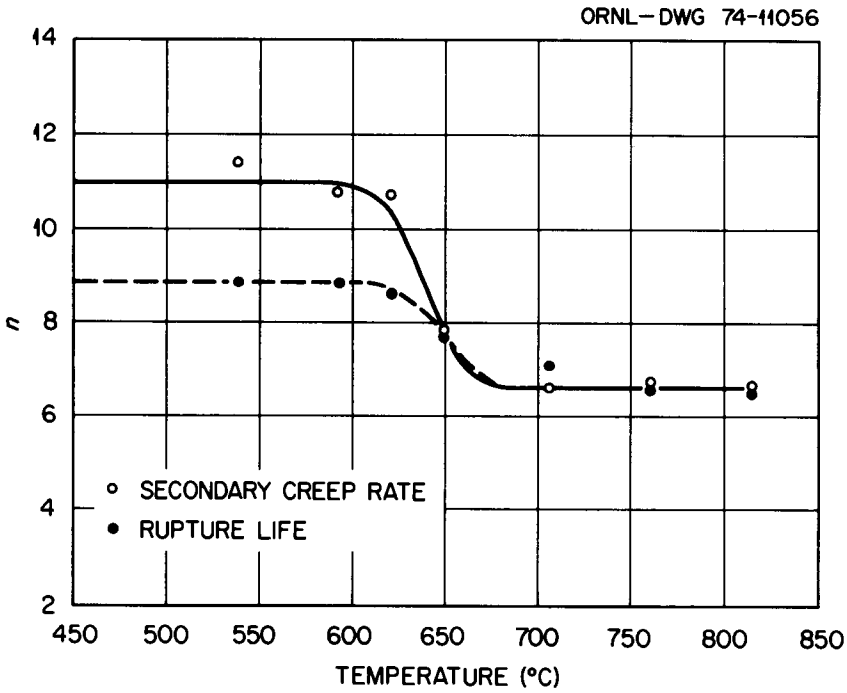

Fig. 5.92. Dependence of the Exponent n in the Power Law on Temperature for Type 304 Stainless Steel (25.4-mm Plate from Heat 9T2796).

Table 5.41. Values for the Constants Required to Describe the Temperature Dependence of the Power Law Model[a] of Creep Rate and Rupture Life of Type 304 Stainless Steel (Heat 9T2796)

Constant	Stress Unit	Value for Indicated Data	
		$\dot{\varepsilon}$, Creep Rate	t_R Rupture Life
A^c	ksi	121	133
	MPa	835	917
α		6.94×10^{-3}	5.77×10^{-3}
T^c		700	700
n^c		11.0	8.85
Δn		4.35	2.2
θ		2950	2867
β		20	20

[a] $\dot{\varepsilon} = (S/A)^n$, $(1/t_R) = (S/A)^n$, where $A = A^c \exp[-\alpha(T - T^c)]$; $n = n^c - \Delta n \{1 - 1/\exp[\theta(1/T^c - 1/T)]^\beta\}$.

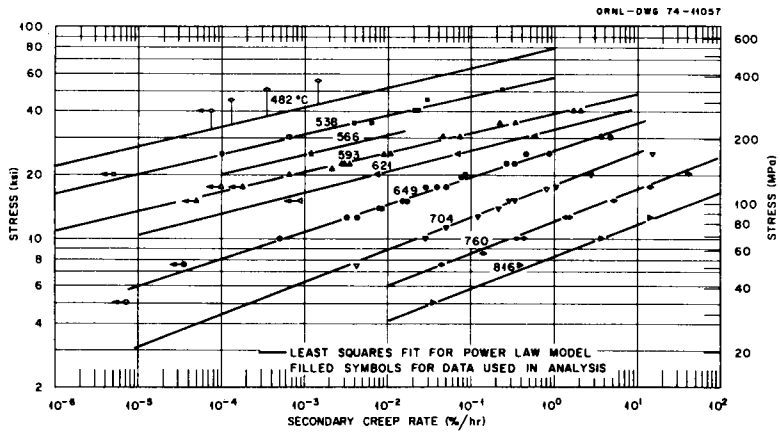

Fig. 5.93. Fit of the Power-Law Model to Secondary Creep Rate Data for Type 304 Stainless Steel (25.4-mm Plate from Heat 9T2796).

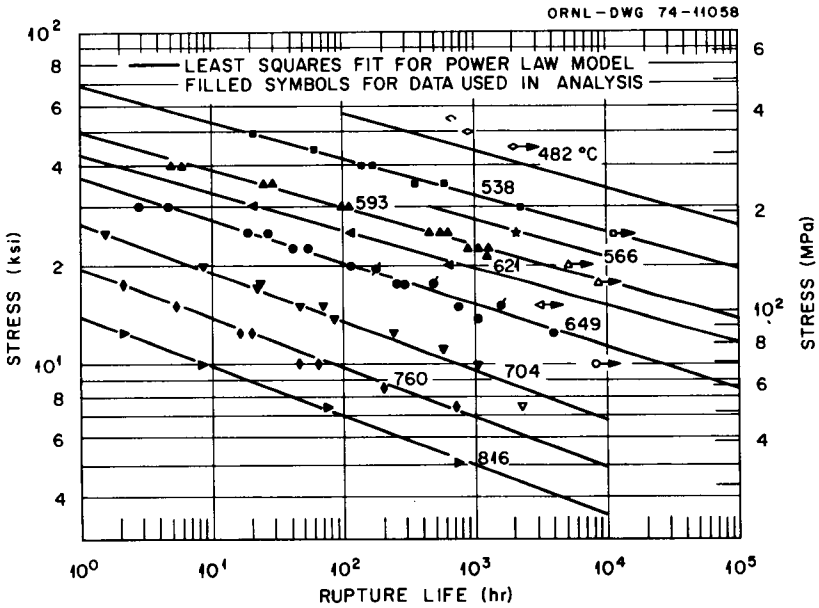

Fig. 5.94. Fit of the Power-Law Model to Rupture Life Data for Type 304 Stainlesss Steel (25.4-mm Plate from Heat 9T2796).

Table 5.42. Temperature Dependence of the Constants in the Power Law Representing Creep-Rupture of Type 304 Stainless Steel (Heat 9T2796) for Modulus-Compensated True Stresses

Temperature		Creep Rate		Rupture	
(°C)	(°F)	A	n	A	n
538	1000	3.16×10^{-3}	9.25	4.22×10^{-3}	7.03
593	1100	2.06×10^{-3}	9.16	2.84×10^{-3}	7.33
621	1150	1.68×10^{-3}	9.07	2.44×10^{-3}	7.14
649	1200	1.35×10^{-3}	7.31	1.97×10^{-3}	7.06
704	1300	9.32×10^{-4}	6.36	1.44×10^{-3}	6.97
760	1400	6.48×10^{-4}	6.65	1.08×10^{-3}	6.44
816	1500	4.88×10^{-4}	7.17	7.89×10^{-4}	6.98

Data for 482, 538, 566, and 593°C (900, 1000, 1050, and 1100°F) are shown in Figs. 5.95 through 5.98 and include several heats and heat treatments. The data base also includes information from monotonic straining as well as hold-time strain-cycling tests. These curves, or similar ones, have potential value in design situations that involve relaxation, since they are easier to use than isochronous stress-strain curves based on creep data. The relaxed stresses appear to increase with increasing starting stresses, but the effect becomes less pronounced as temperature or time increases. There is still some influence of starting stress on the relaxed stress, however, even at 704 and 760°C, when only short relaxation times are considered. Data showing the results of a series of relaxation tests on a specimen tested at 760°C are shown in Fig. 5.99. In this test series the specimen was repetitively loaded into the plastic flow region, given about 0.1% plastic strain, and then allowed to relax from different loads between the flow stress and near zero. The letters on the different curves designate the sequence of testing. Runs A, F, and H represent relaxation from the flow stress and are repetitive. Run C represents relaxations from about 75% of the flow stress and exhibits decreasing stresses with increasing times. Runs B, G, and E represent relaxations from less than 25% of the flow stress and show increasing rather than

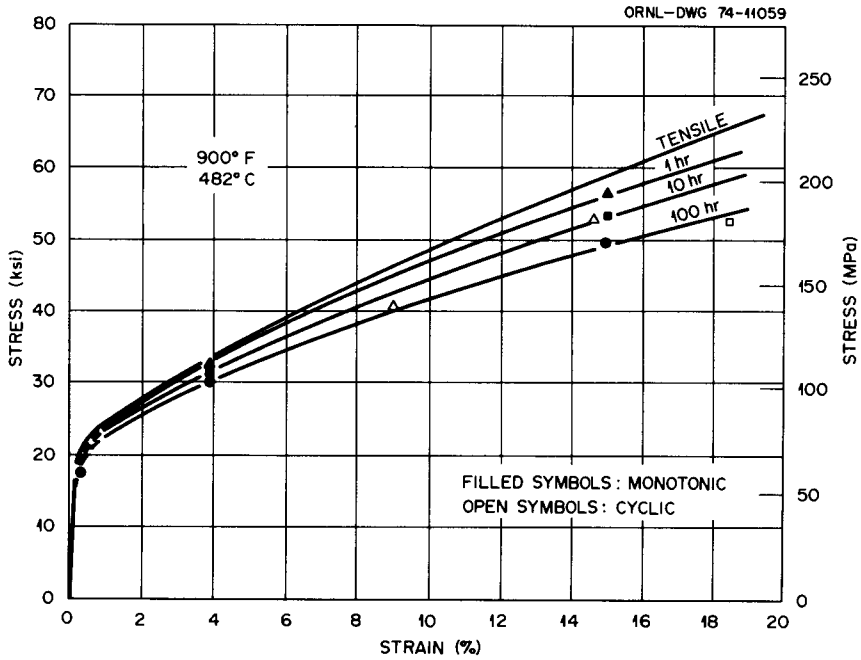

Fig. 5.95. Isochronous Relaxation Curves for Type 304 Stainless Steel at 482°C.

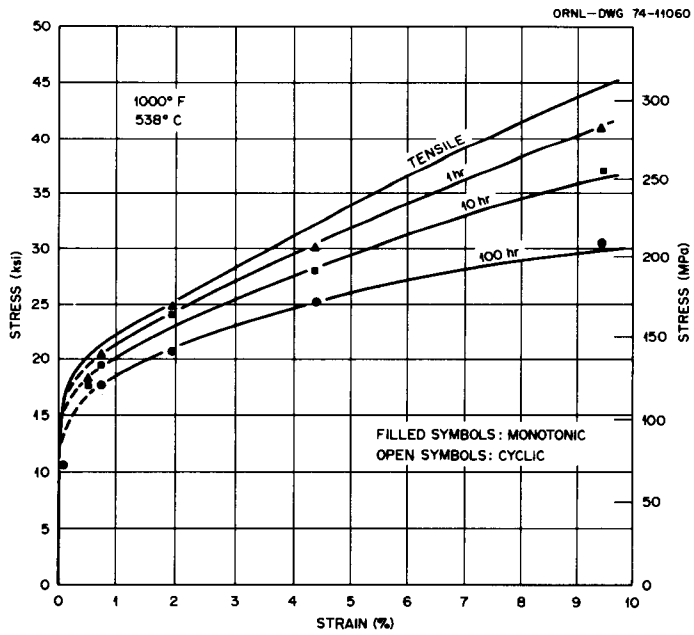

Fig. 5.96. Isochronous Relaxation Curves for Type 304 Stainless Steel at 538°C.

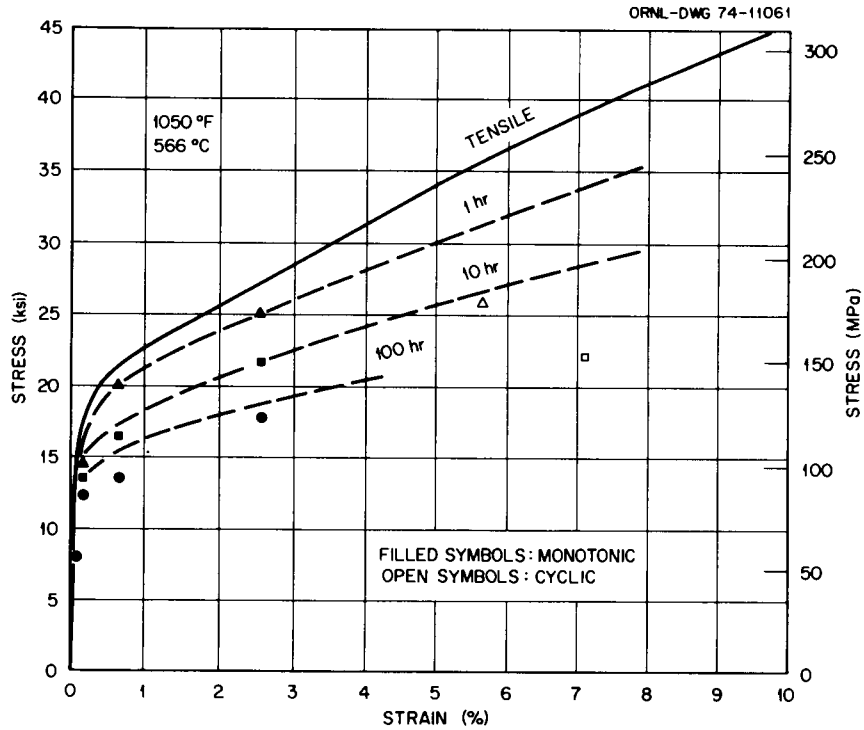

Fig. 5.97. Isochronous Relaxation Curves for Type 304 Stainless Steel at 566°C.

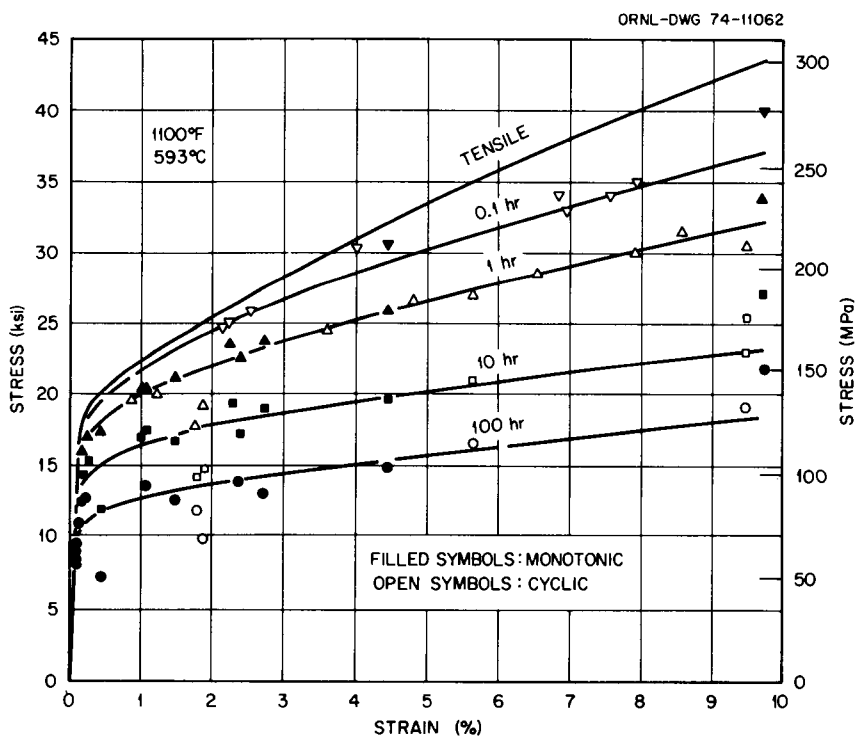

Fig. 5.98. Isochronous Relaxation Curves for Type 304 Stainless Steel at 593°C.

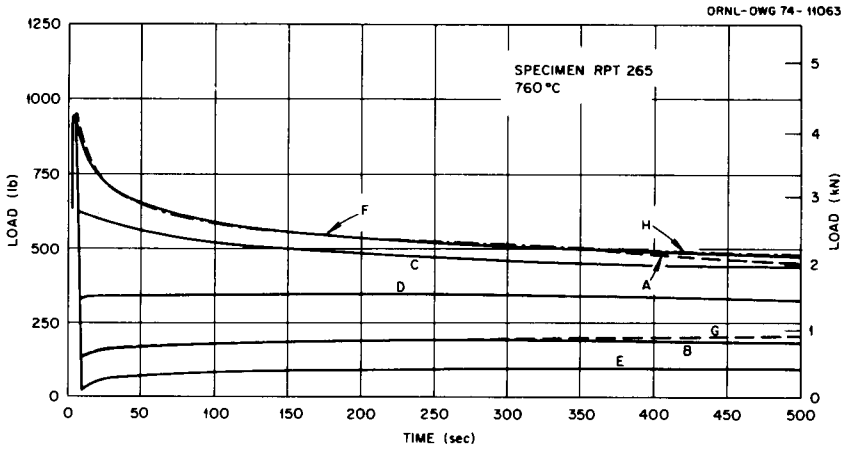

Fig. 5.99. Influence of Initial Load on Relaxation for Type 304 Stainless Steel at 760°C. Specimen was strained into the plastic region before each run. The letters specify the sequence of testing.

decreasing loads. We monitored the dimensional stability of the specimen at zero stress, without restraint, and observed contractions after introducing plastic deformation. We conclude from this that load increases are associated with recovery of inelastic strains developed during the flow process. In Fig. 5.100 we have plotted the load change in 750 sec, ΔP, against the starting load P for 649, 704, and 760°C (1200, 1300, and 1400°F).

5.5.1.3 Creep-Plasticity Studies — R. W. Swindeman and R. L. Klueh

As part of an effort to produce data helpful in the development of hardening rules for 2 1/4 Cr-1 Mo steel, exploratory creep-plasticity tests are under way. Figure 5.101 shows the hardening behavior for a specimen that was crept at 25 ksi (172 MPa) at 510°C (950°F) but cycled 20 times once per week at 0.4% strain range. The trend of the data suggests that creep exposure does not harden the material. The influence that the strain cycling exerts on the creep behavior is indicated by Fig. 5.102, which compares monotonic creep curves at 27.5, 25, and 22 ksi (190, 172, and 152 MPa) with the creep strain accumulated between the strain cycling periods. It appears that the strain cycling has a fairly small influence on the total creep curve.

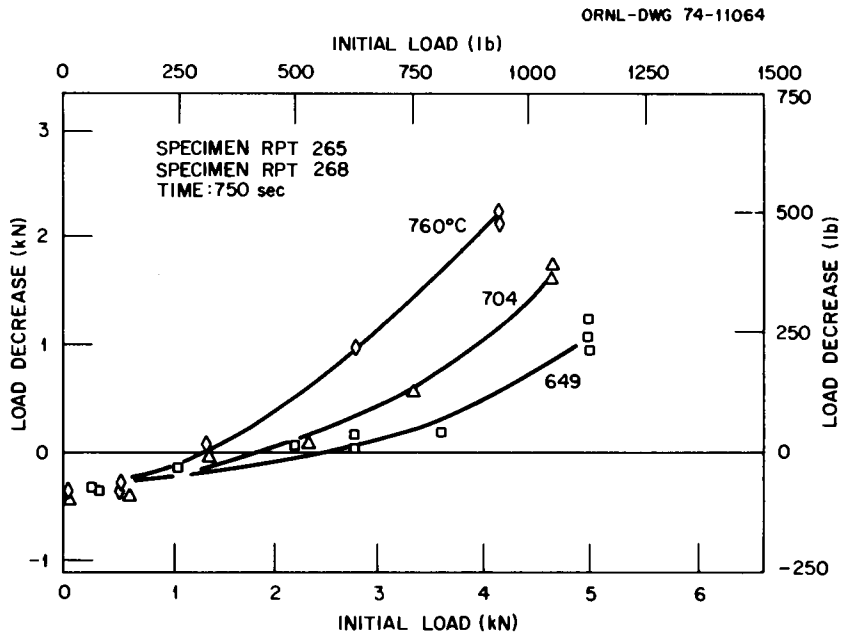

Fig. 5.100. Influence of Initial Load on the Load Decrease During Relaxation for Type 304 Stainless Steel. Specimens were strained into the plastic region before each run. The load decrease was monitored at 750 sec.

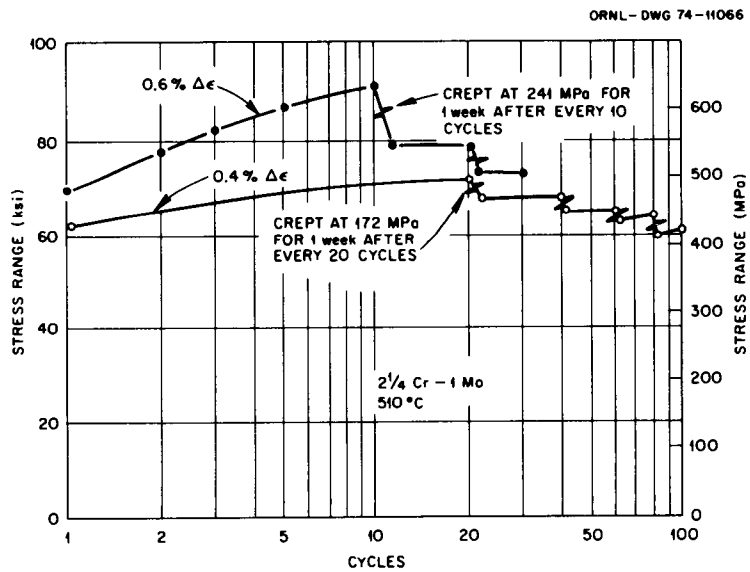

Fig. 5.101. Influence of Strain Cycling on the Creep Curve for 2 1/4 Cr-1 Mo Steel at 510°C (950°F).

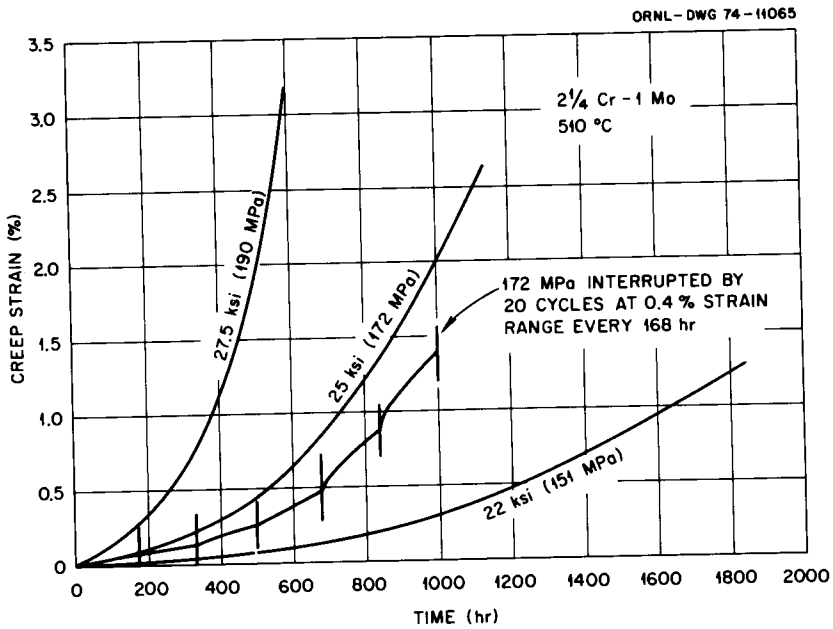

Fig. 5.102. Influence of Creep on the Cyclic Hardening Behavior for 2 1/4 Cr-1 Mo Steel at 510°C (950°F).

5.5.1.4 Strain Cycling

Strain cycling tests have been resumed on the reference heat of type 304 stainless steel (heat 9T2796), and evaluation of the cyclic hardening behavior is currently under way.

5.5.2 Investigations of Creep Failure Under Uniaxial and Multiaxial Conditions — C. C. Schultz, Babcock and Wilcox

The status of the constant-load uniaxial, step-load uniaxial, and interrupted uniaxial tests at the end of this report period is given in Tables 5.43 to 5.45, respectively. The only ruptures that occurred during this period were the step-load tests (BWLF-6, BWLF-9, and BWLF-10). Tests BWR-6 (19 ksi) and BWI-3 (19.5 ksi) are both well into tertiary creep. The creep strain vs time data for these last two tests are shown in Figs. 5.103 and 5.104.

During this reporting period, a major effort was directed toward investigating observed heterogeneous duplex grain structure (see Fig. 5.105). We previously reported[64] that the heterogeneous duplex grain structure significantly affected the time-to-rupture results at 28 ksi. We later speculated[65] that the significant variations observed in much of our

Table 5.43. Status of Uniaxial Constant-Load Rupture Tests — Type 304 Stainless Steel (Heat 9T2796), 593°C (1100°F)

Test No.	Specimen No.	Stress (ksi)	Total strain on loading[a] (%)	Time to secondary creep (hr)	Minimum creep rate (%/hr)	Time to tertiary creep[b] (hr)	Intercept creep strain[c] (%)	Test time[d] (hr)	Fracture elongation[e] (%)	Reduction in area (%)
BWC-1	7-15	30	4.7					187 R	19.0	30.5
BWR-1	7-1	30						138 R	21.5	32.9
BWC-2	2-22	28	5.8	40	0.016	195	0.50	227 R	13.0	20.4
BWR-2	2-1	28		40	0.022	230	0.65	368 R	16.5	29.0
BWR-13	7-13	28		60	0.023	215	0.88	276 R	16.5	18.9
BWC-9	7-25	28	3.8	85	0.021		1.16	415 R	18.3	25.2
BWC-3[f]	7-28	25	N.A.	80	0.0065	500	0.45	667 R	12.7	12.0
BWR-3	7-8	25		100	0.0079	585	0.71	948 R	17.0	23.2
BWC-4	2-28	22	3.7	175	0.0014	1400	0.60	2,130 R	10.7	13.7
BWR-4	7-7	22		160	0.0030	1170	0.72	2,026 R	12.5	16.6
BWC-5[g]	2-15	20						D		
BWC-5B	2-16	20	1.8	5000	0.000165	8700	1.84	9,584 R	10.5	12.0
BWR-5[h]	2-14	20						4,842 D		
BWR-6	7-14	19						16,700 I		
BWR-9	7-11	18						15,700 I		
BWR-11[i]	2-12	17						94 D		
BWR-11B	2-10	17						15,900 I		
BWR-7	2-4	16						16,400 I		
BWR-14	2-9	20	2.02	3200	0.00044	5800	1.88	6,868 R	8.5	13.1
BWC-10	7-18	20	1.52					4,850 I		

[a]All specimens were step loaded at 1.87-ksi increments, except test BWC-5B, which was step loaded at 1.49-ksi increments. Loading curves on BWR series include load train displacements (thus not reported).

[b]Time to tertiary creep based on the 0.2% offset from the minimum rate line.

[c]Intercept creep strain does not include the elastic and initial plastic components.

[d]R = rupture; D = discontinued; I = in test.

[e]Elongation over 3 in. in BWC series; over 2 in. in BWR series.

[f]Failure occurred near end of gage length.

[g]Temperature excursion to 704°C (1300°F) prior to loading; replaced by test BWC-5B.

[h]Temperature excursion to 749°C (1380°F) at 4842 hr; terminated.

[i]Temperature excursion to 704°C (1300°F) at 94 hr; replaced by test BWR-11B.

Table 5.44. Status of Uniaxial Step-Load Ruputure Tests — Type 304 Stainless Steel (Heat 9T2796), 593°C (1100°F)[a,b]

Test No.	Specimen No.	Stress (ksi)	Total strain on loading (%)	Time at load[a] (hr)	Life fraction (%)	Fracture elongation[b] (%)	Reduction in area (%)
BWC-6	2-17	16	0.42	3,871	6		
		25		136	17		
		20		9,251	123		
				13,258 R		9.0	16.0
BWR-10	2-11	16		3,871	6		
		25		136	17		
		20		5,655	75		
				9,662 R	98	11.5	17.8
BWC-7	2-18	17	0.76	3,699	11		
		25		136	17		
		20		5,066	68		
				8,901 R	96	12.0	20.6
BWR-8	2-5	17		3,703	11		
		25		136	17		
		20		8,901	110		
				12,740 R	147	11.0	13.8
BWLF-5	2-25	20	2.06	503	7		
		25		198	25		
		20		5,246	70		
				5,947 R	102	12.5	17.0
BWC-8	7-16	18	1.78	5,071	25		
		25		136	17		
		20		5,420	72		
				10,627 R	114	8.0	15.5
BWR-12	7-12	18		4,897	24		
		25		136	17		
		20		3,996	53		
				9,029 R	94	11.5	17.2
BWLF-5B	2-21	21	2.62	500	10		
		25		200	25		
		21		1,236	25		
				1,936 R	60	10.3	15.9
BWLF-7	2-26	21	2.25	750	15		
		25		136	17		
		21		2,003	40		
				2,889 R	72	12.3	20.5
BWLF-9	7-24	21	2.21	1,014	20		
		25		136	17		
		21		1,816	36		
				2,966 R	73	18.0	16.5
BWLF-10	7-27	21	2.47	1,006	20		
		25		136	17		
		21		2,286	45		
				3,428 R	82	16.0	18.2
BWLF-8	7-23	21		750	15		
		25		136	17		
		21		2,500 I	50		
BWLF-6	7-22	21	3.11	500	10		
		25		200	25		
		21		1,214	24		
				1,914 R	59	10.5	14.8

[a]R = rupture; D = discontinued; I = test.

[b]Elongation over 3 in. in BWC series; over 2 in. in BWR series.

Table 5.45. Status of Uniaxial Interrupted Tests — Type 304 Stainless Steel (Heat 9T2796), 593°C (1100°F), 19.5 ksi

Test No.	Specimen No.	Time at load (hr)
BWI-1	4-6	10,500
BWI-2	5-6	10,500
BWI-3	6-6	10,500
BWI-4	1-6	3,550
BWI-5	2-6	3,550
BWI-6	3-6	3,550

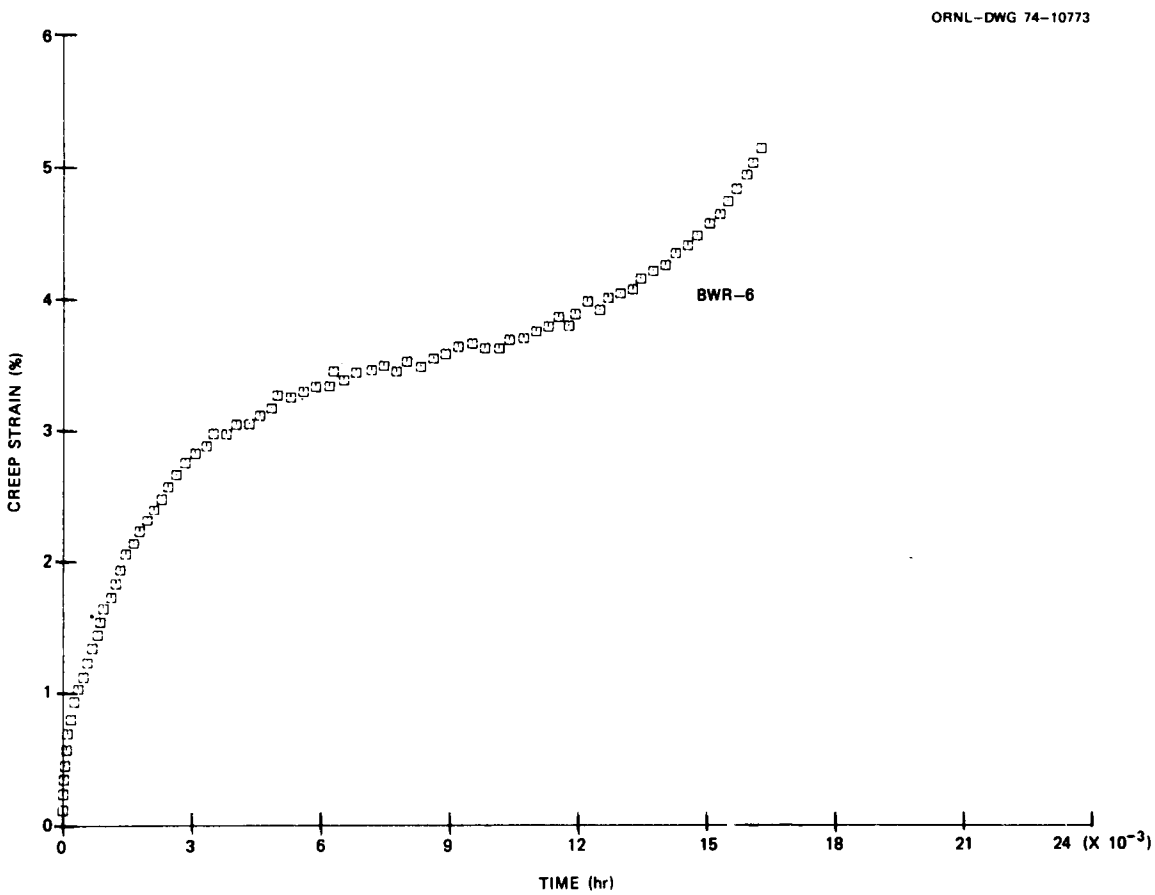

Fig. 5.103. Constant-Load Uniaxial Rupture Test (in Progress). Loaded at 19 ksi at 593°C (1100°F), type 304 stainless steel (heat 9T2796), 5/8-in. bar.

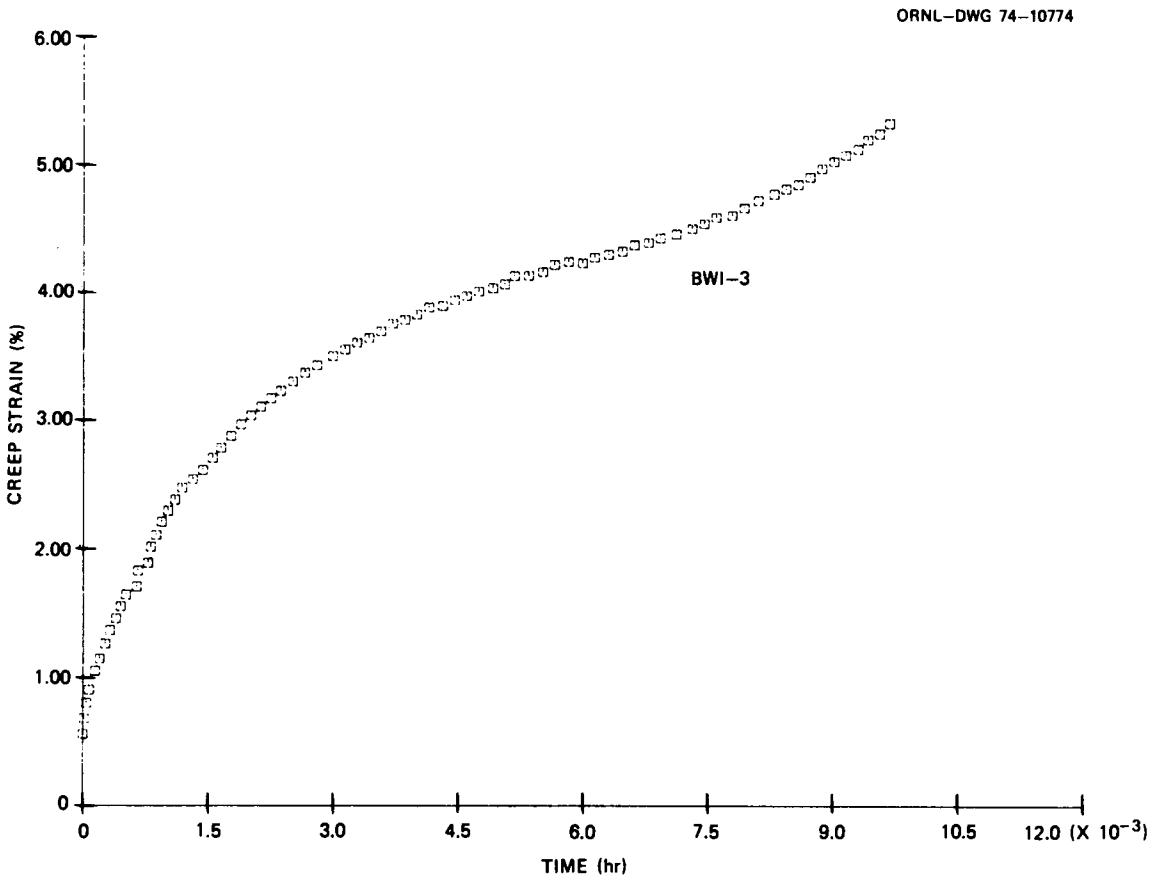

Fig. 5.104. Constant-Load Uniaxial Rupture Test (in Progress). Loaded at 19.5 ksi at 593°C (1100°F), type 304 stainless steel (heat 9T2796), 5/8-in. bar.

other time-to-rupture data (particularly evident in the step-load tests) were also resulting from grain size variations. Subsequently, we decided to postpone initiating any additional uniaxial tests until the extent and impact of the grain size problem were resolved.

The results of earlier work that first indicated the grain size problem are reviewed here for completeness. The initial effort concerned the four tests loaded at 28 ksi (BWR-2, BWC-2, BWR-13, and BWC-9); the creep strain vs time data for these are shown in Fig. 5.106. The stress-strain data during loading, available for only the BWC tests, are shown in Fig. 5.107. Figures 5.108 and 5.109 are photomicrographs of the longitudinal sections of the four specimens showing the diversity in

PHOTO 2771–74

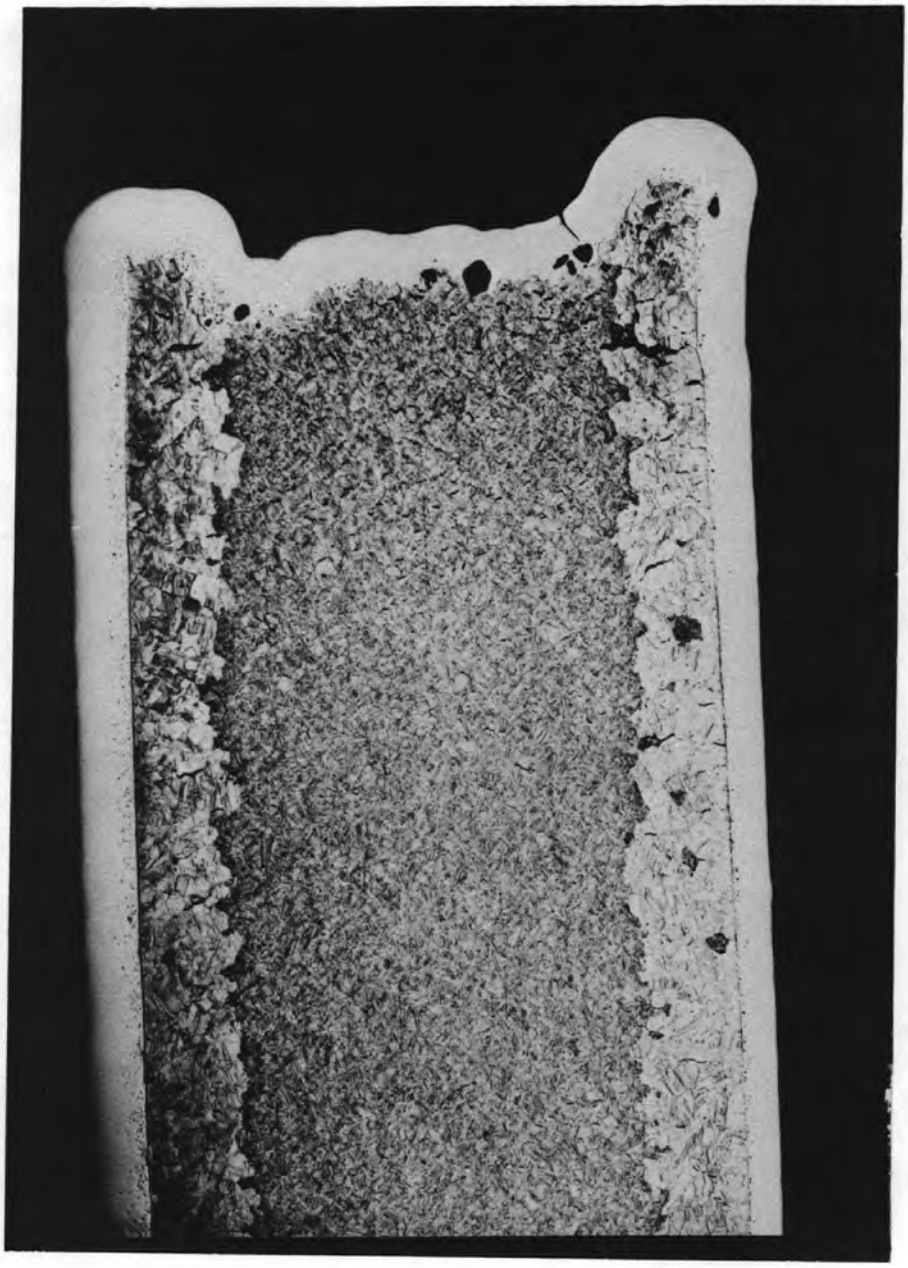

Fig. 5.105. Heterogeneous Duplex Grain Structure Observed in Uniaxial Test Specimens. Longitudinal section, type 304 stainless steel (heat 9T2796), 5/8-in. bar (10×).

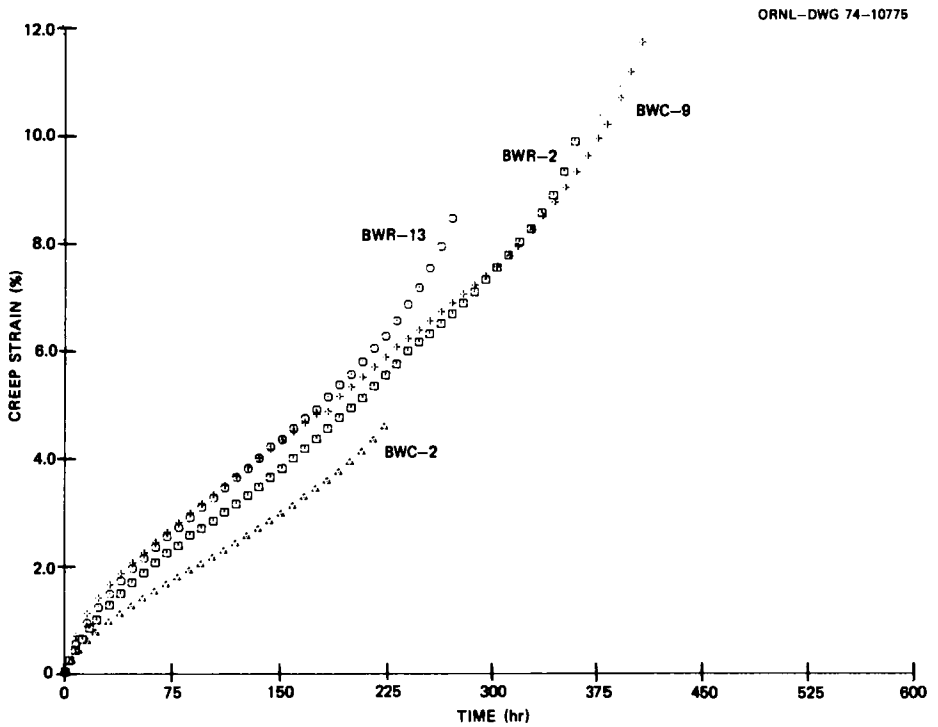

Fig. 5.106. Constant-Load Uniaxial Rupture Tests. Loaded at 28 ksi at 593°C (1100°F), type 304 stainless steel (heat 9T2796), 5/8-in. bar.

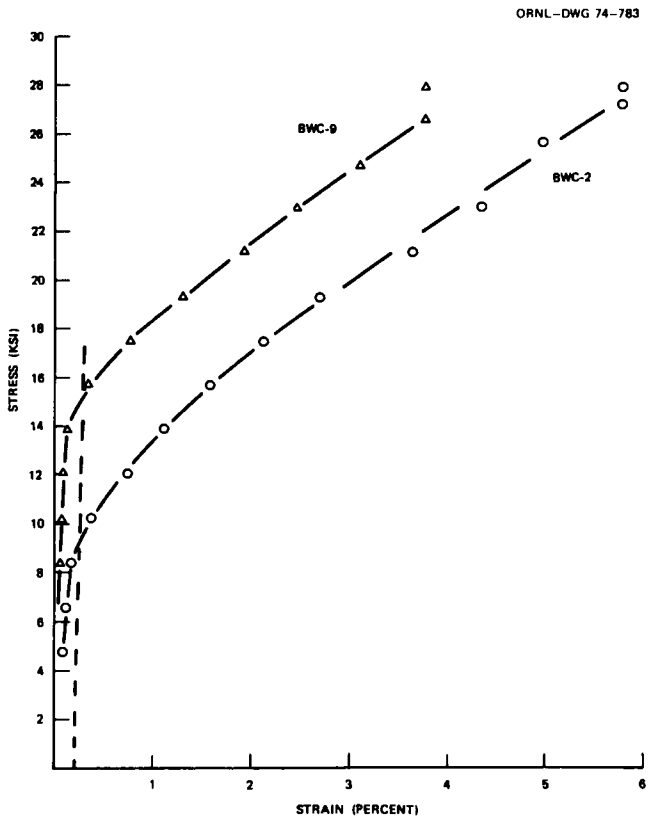

Fig. 5.107. Stress-Strain Behavior, on Loading, for Constant-Load Uniaxial Rupture Tests at 593°C (1100°F). Type 304 stainless steel (heat 9T2796), 5/8-in. rod.

PHOTO 2772-74

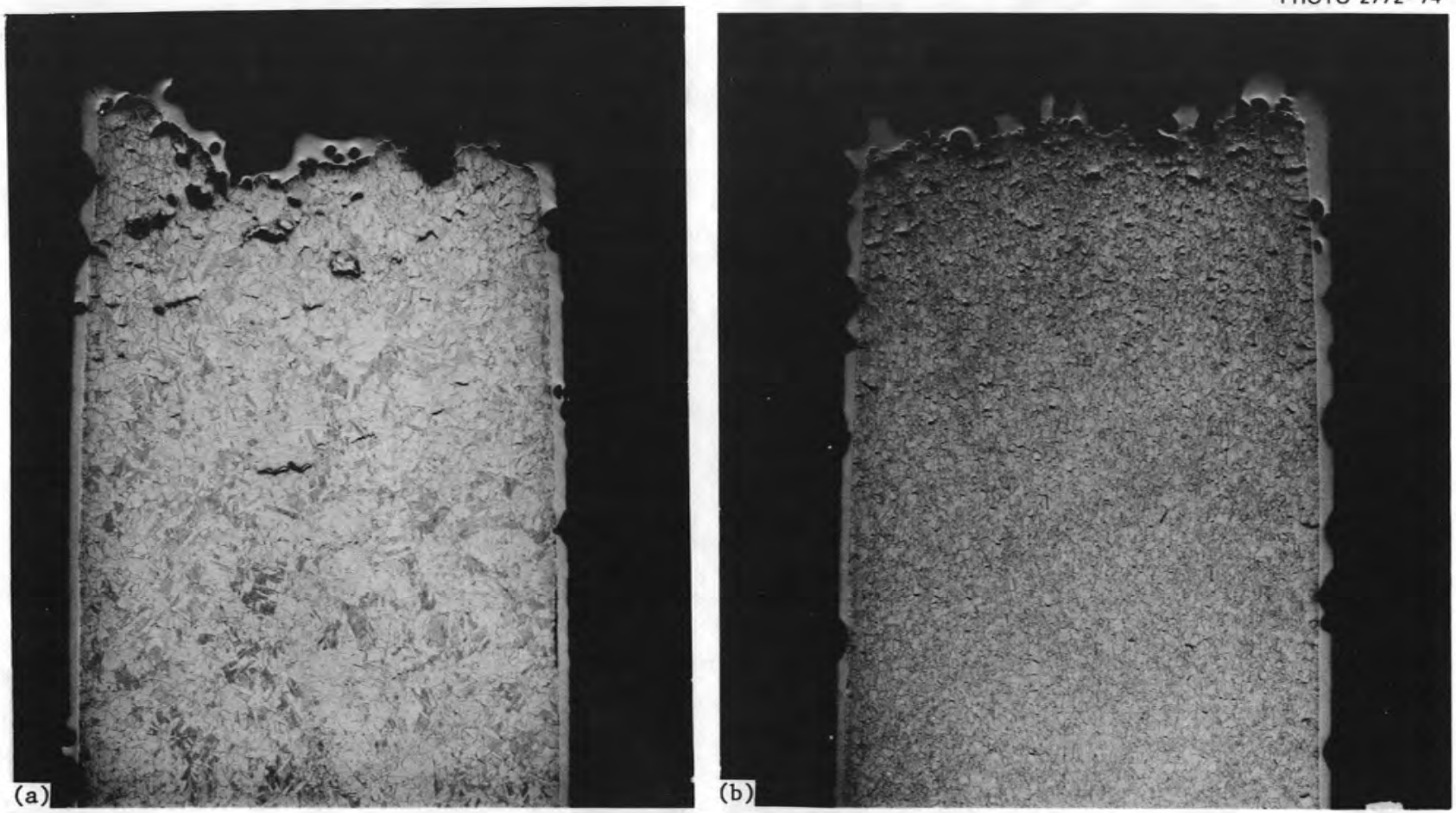

Fig. 5.108. Longitudinal Sections of Uniaxial Specimens Ruptured at 28 ksi at 593°C (1100°F). Type 304 stainless steel (heat 9T2796), 5/8-in. bar. (a) Test BWC-2, rupture life 227 hr (10×); (b) test BWC-9, rupture life 415 hr (10×).

PHOTO 2773-74

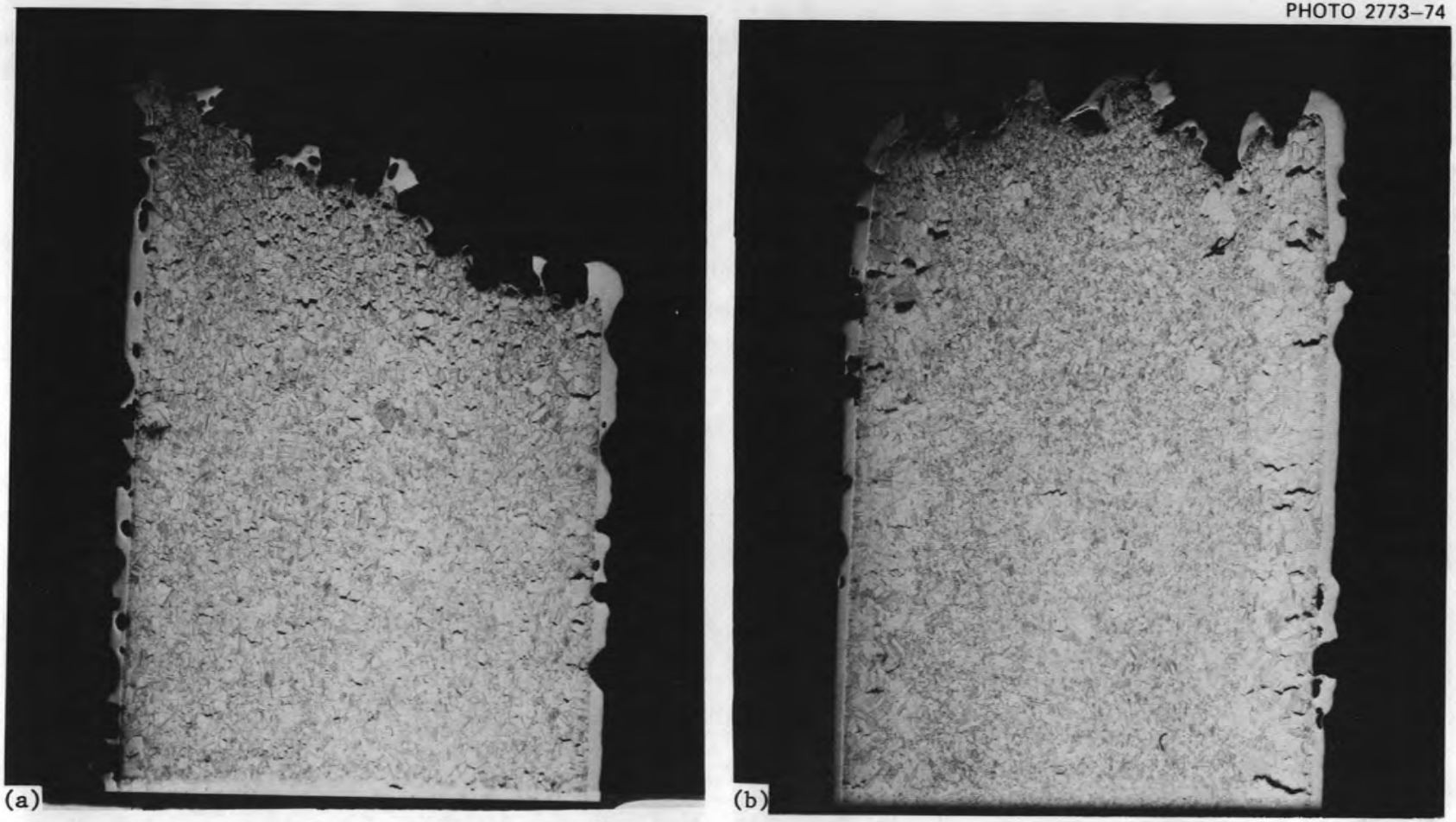

Fig. 5.109. Longitudinal Sections of Uniaxial Specimens Ruptured at 28 ksi at 593°C (1100°F). Type 304 stainless steel (heat 9T2796), 5/8-in. bar. (a) Test BWR-2, rupture life 368 hr (10×); (b) test BWR-13, rupture life 276 hr (10×).

grain size. Figure 5.110 compares the rupture time to a measure of grain size. Specifically, the measure of grain size is $d^{-1/2}$, where d is the mean linear intercept (including twin boundaries) in microns. In specimen 7-13 (test BWR-13), the grains were markedly duplex; thus some representation of an equivalent, or average, mean linear intercept was required. The average shown is weighted by the percentage of the specimen cross-sectional area occupied by each of the two predominant grain sizes. The trend shown in Fig. 5.110 is opposite to what is expected for normal creep rupture behavior but is not disturbing in view of the high stress and resulting short lives. The stress-strain data during loading shown in Fig. 5.107 are compatible with the grain size existing in those two specimens.

The following five specimens were selected next for grain size determination: 2-5 (BWR-8), 2-16 (BWC-5B), 2-18 (BWC-7), 2-21 (BWLF-5B), and 7-16 (BWC-8). Specimens 2-5 and 2-18 had been subjected to identical load-time histories yet yielded significantly different rupture lives.

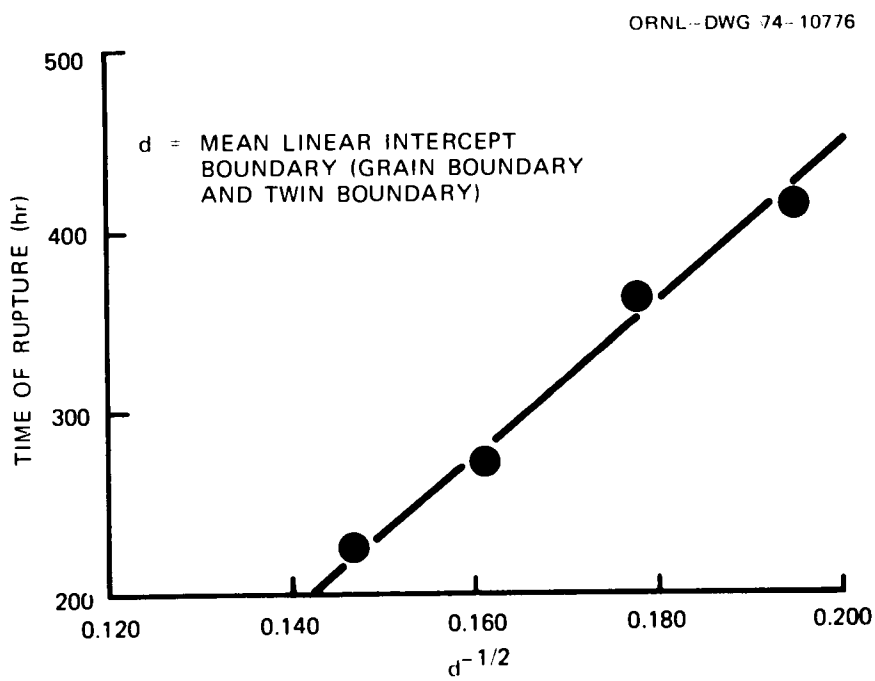

Fig. 5.110. Comparison of Rupture Time to Measure of Grain Size. Uniaxial tests at 28 ksi at 593°C (1100°F), type 304 stainless steel (heat 9T2796), 5/8-in. rod.

Specimen 2-18 (test BWC-7) had a rupture life of 8901 hr, and specimen 2-5 (test BWR-8) had a rupture life of 12,740 hr. The creep strain vs time data for these two tests are shown in Fig. 5.111. In addition, specimen 2-18, with a computed life fraction of 0.96, was, in the original bar, adjacent to specimen 2-17, which had a significantly higher life fraction (1.46). Figure 5.112 shows photomicrographs for specimens 2-5 and 2-18, and specimens 2-16 and 2-18, which were annealed in the same batch, are compared in Fig. 5.113. Specimen 2-21, in addition to yielding an exceptionally low life fraction (0.60), had, in the original bar, been adjacent to the previously examined specimen 2-22; these specimens are compared in Fig. 5.114. Specimens 7-16 and 2-22, annealed in the same batch, are compared in Fig. 5.115. No clear conclusions have been drawn from these comparisons other than the grain size variations are

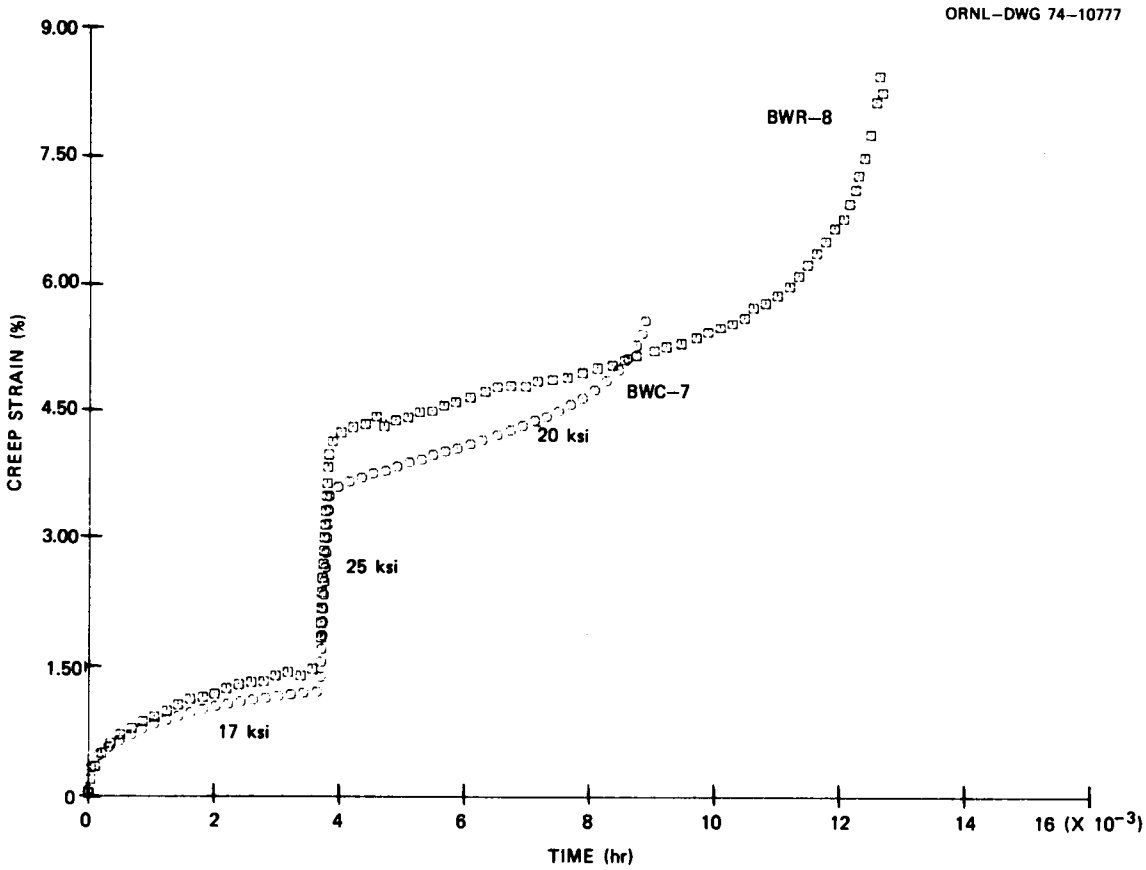

Fig. 5.111. Step-Load Uniaxial Rupture Tests with Same Load History at 593°C (1100°F). Type 304 stainless steel (heat 9T2796), 5/8-in. rod.

PHOTO 2774-74

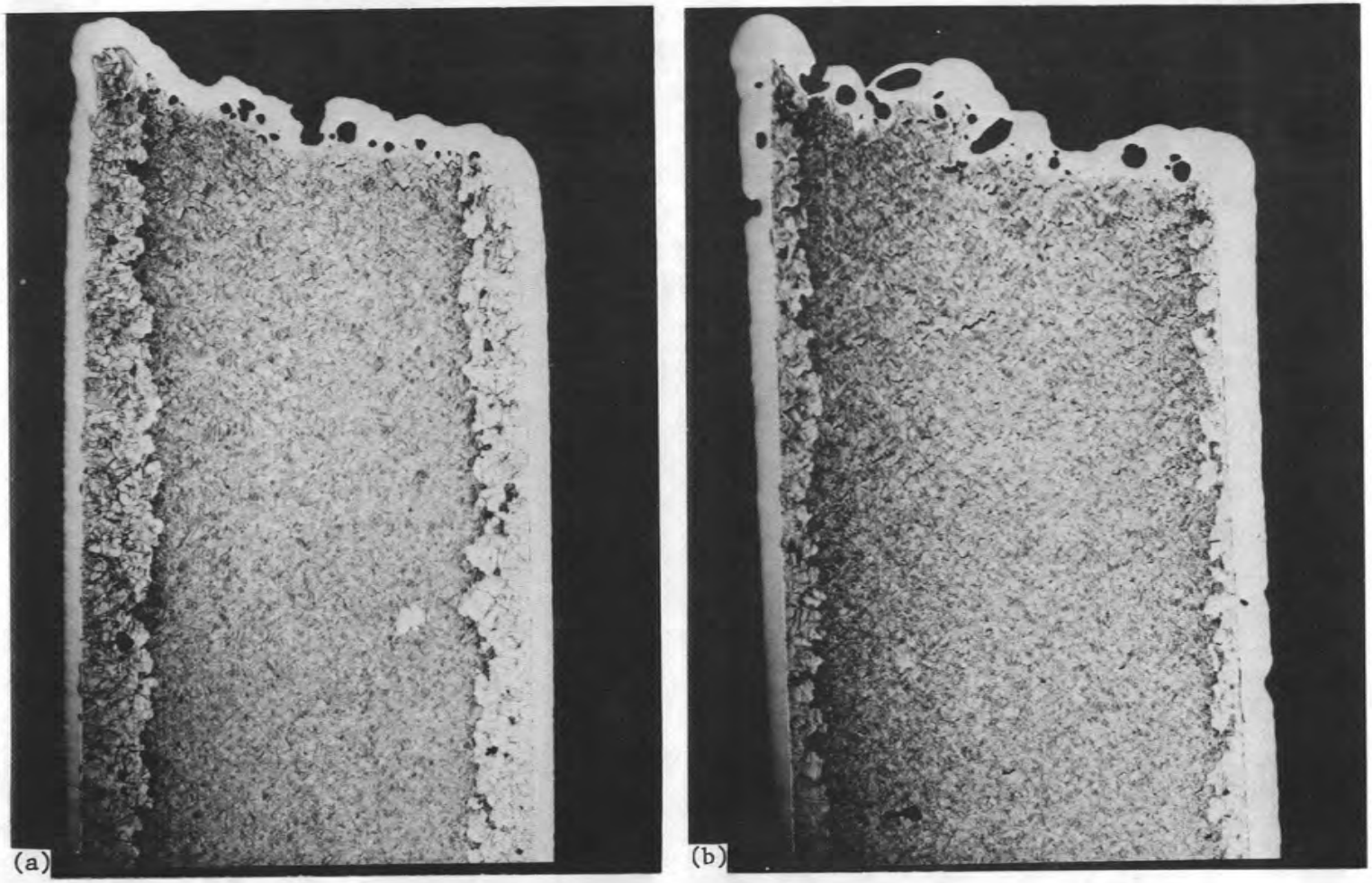

Fig. 5.112. Longitudinal Sections of Step-Loaded Uniaxial Rupture Specimens with Identical Load Histories (See Table 5.44). Tested at 1100°F, type 304 stainless steel (heat 9T2796), 5/8-in. rod. (a) Specimen 2-18, test BWC-7, rupture life 8901 hr, life fraction 0.96 (10×); (b) specimen 2-5, test BWR-8, rupture life 12,740 hr, life fraction 1.47 (10×).

PHOTO 2775-74

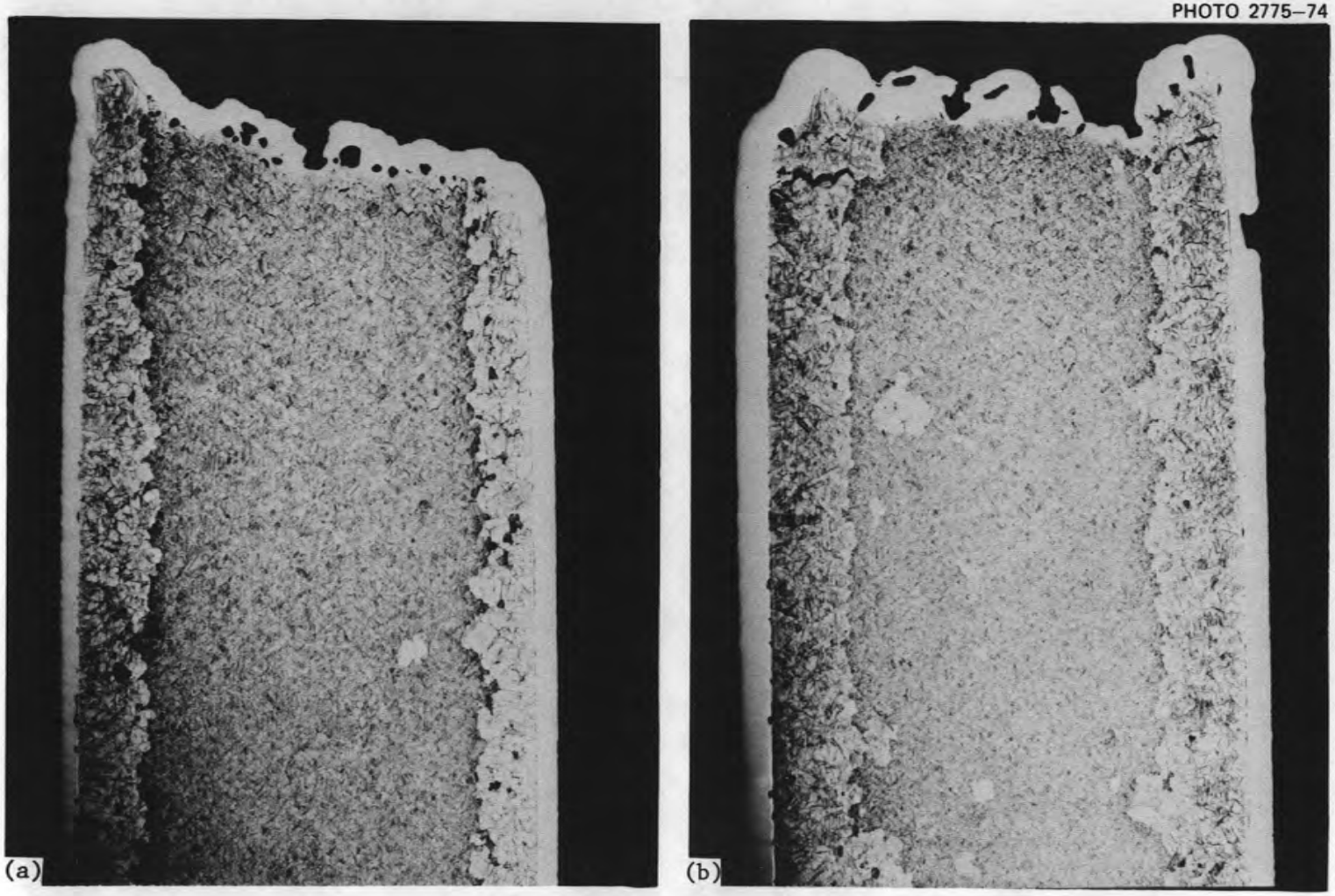

Fig. 5.113. Longitudinal Sections of Two Uniaxial Specimens Annealed in the Same Batch. Type 304 stainless steel (heat 9T2796), 5/8-in. rod. (a) Specimen 2-18, test BWC-7, step load at 17, 25, and 20 ksi (10×); (b) specimen 2-16, test BWC-5B, constant load at 20 ksi (10×).

PHOTO 2776–74

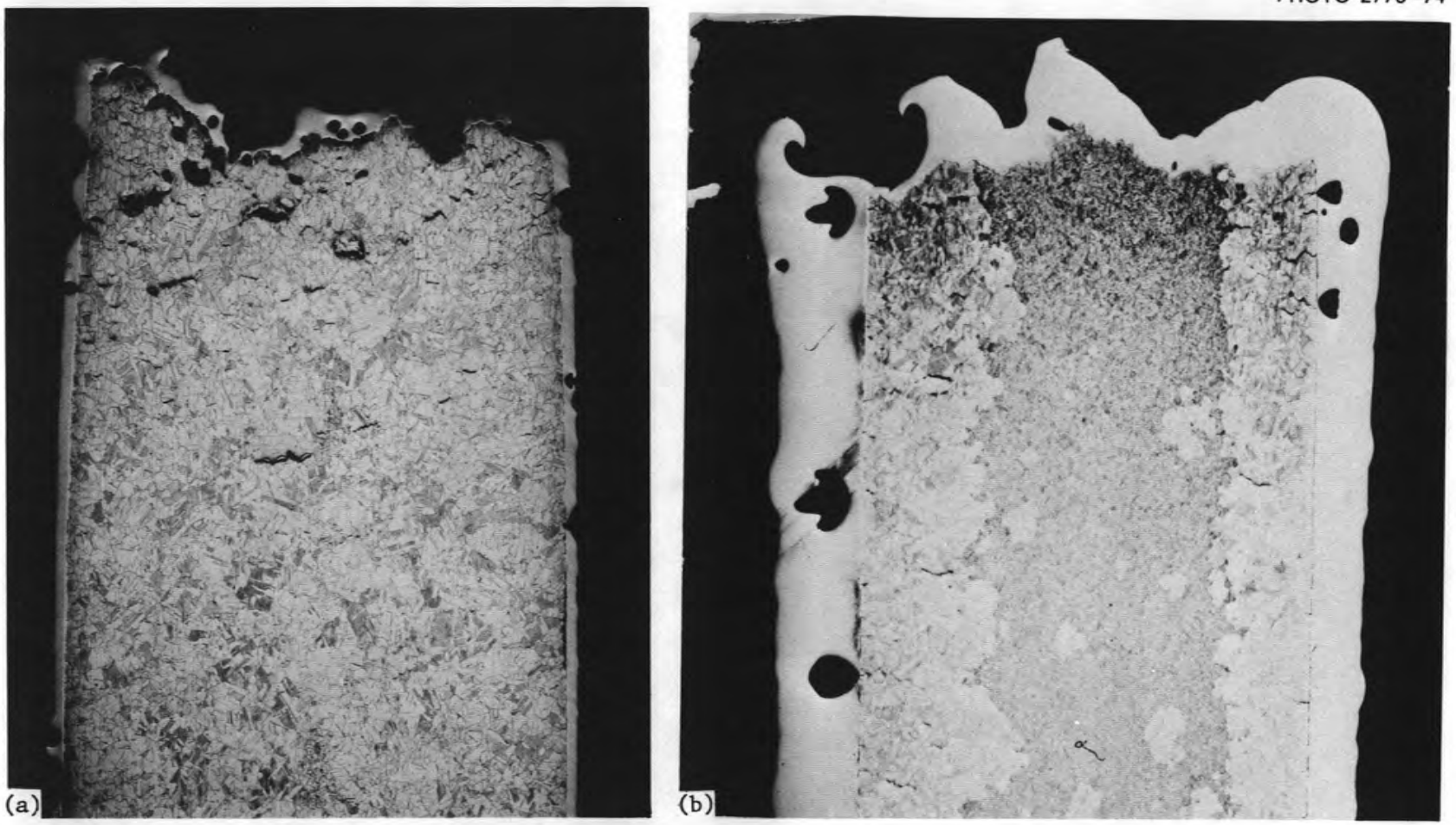

Fig. 5.114. Longitudinal Sections of Uniaxial Specimens Taken from Adjacent Locations in the As-Received Bar. Type 304 stainless steel (heat 9T2796), 5/8-in. rod. (a) Specimen 2-22, test BWC-2 (10×); (b) specimen 2-21, test BWLF-5B (10×).

PHOTO 2777-74

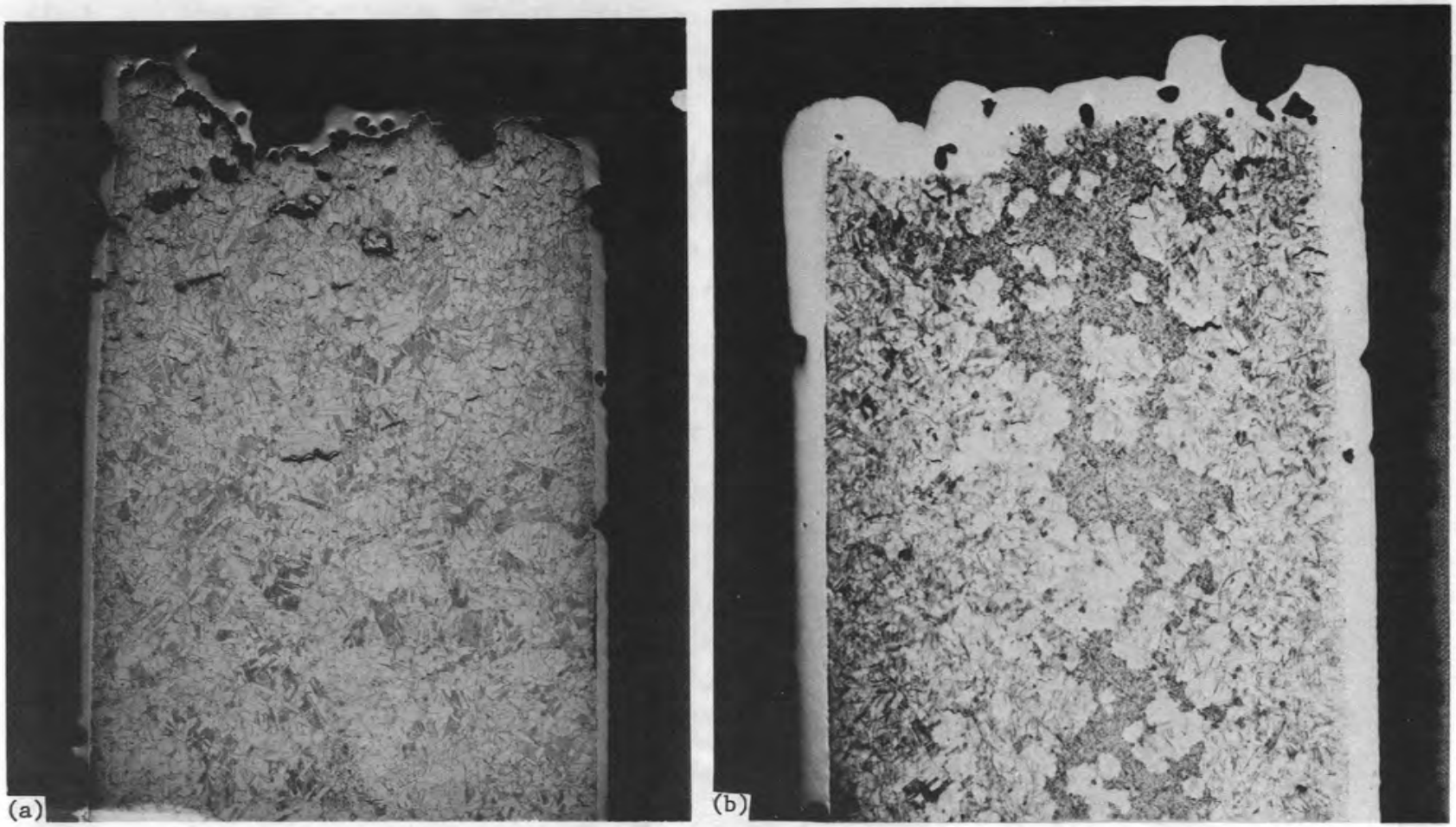

Fig. 5.115. Longitudinal Sections of Two Specimens Annealed in the Same Batch. Type 304 stainless steel (heat 9T2796), 5/8-in. rod. (a) Specimen 2-22, test BWC-2 (10×); (b) specimen 7-16, test BWC-8 (10×).

significant within individual specimens as well as among specimens. The mean linear intercept results for these specimens are included in Table 5.46. With the knowledge that the variations are significant, efforts have been undertaken to identify the source.

With the exception of those specimens for the BWI series tests, all specimens were machined from bars 2 and 7. Residual pieces of each of these two bars were longitudinally sectioned, with half of these remaining in the as-received conditions and the other undergoing the standard reanneal [1093°C (2000°F) for 30 min followed by rapid cooling]. Each bar responded similarly to the anneal, and no evidence of the heterogeneous duplex grain structure existed in these unmachined pieces. This indicates that specimen machining could introduce sufficient cold work to cause variations.

To determine the effect of a wide range of machining conditions, a 6-in. piece of bar 6, in the as-received condition, was machined as shown in Table 5.47. Following machining and the standard reanneal, the test piece was longitudinally sectioned for examination, and no variations were noted. With machining effects eliminated as a source of the variations, the final variable considered was the annealing temperature.

To examine the effect of annealing temperature, the test setup shown in Fig. 5.116 was used to obtain a thermal gradient along a 4-in. test piece. Two 4-in. pieces from bar 6 were tested, one in the as-received condition and the second following uniform machining identical to that of segment 11 in Table 5.47. Table 5.48 shows the time-temperature history for the test of the machined specimen and is typical of that for the as-received test piece. The grain size varies through the thickness in both test pieces, and this variation cannot be attributed to a radial thermal gradient. It is concluded that the through-the-thickness grain size variations result from through-the-thickness cold-work gradient and that this is the source of the grain size variations observed in the specimens machined from bars 2 and 7. A combination of variations in cold work (both axially and radially) and the reanneal time and temperature then contribute to the observed variations in grain sizes.

As an alternate to the specified reanneal, specimen 2-21 [shown in Fig. 5.117(a) subsequent to the original reanneal at 2000°F for 1/2 hr]

Table 5.46. Comparative Grain Sizes — Type 304 Stainless Steel (Heat 9T2796) Specimens from 5/8-in.-Diam Bar

Stress (ksi)	Test No.	Specimen No.	Center		Edge		Equivalent $d^{-1/2}$
			$d^{-1/2}$	Percent of cross-sectional area	$d^{-1/2}$	Percent of cross-sectional area	
30	BWC-1	7-15	0.222	74	0.156	26	0.205
30	BWR-1	7-1	0.184	52	0.121	48	0.154
25	BWC-3	7-28	0.214	43	0.142	57	0.173
25	BWR-3	7-8	0.184	75	0.144	25	0.174
22	BWC-4	2-28	0.130	47	0.135	53	0.133
22	BWR-4	7-7	0.175	51	0.122	49	0.149
20	BWC-5B	2-16	0.215	40	0.116	60	0.155
20	BWR-5	2-14	0.171	51	0.141	49	0.156
20	BWR-14	2-9	0.178	46	0.129	54	0.152
21,25,21	BWLF-5B	2-21	0.204	33	0.131	67	0.155
21,25,21	BWLF-7	2-26	0.162	42	0.122	58	0.139
21,25,21	BWLF-6	7-22	0.139	65	0.148	35	0.142
18,25,20	BWC-8	7-16	0.198	12	0.134	88	0.142
17,25,20	BWC-7	2-18	0.189	59	0.144	41	0.171
17,25,20	BWR-8	2-5	0.189	75	0.128	25	0.174

Table 5.47. Machining Variables to Determine Effect on Postanneal Grain Size

1	2	3	4	5	6	7	8	9	10	11	12
1/2"	Segment numbers									Headstock end of piece	

Segment No.	Spindle speed (rpm)	Feed (ipr)	Depth of cut (in.) off radius		
1	205	0.0075	0.050		
2	409	↓	↓		
3	205	0.0075	0.020	← Two cuts	These are only segments where more than one cut was taken on the segment
	409	0.0034	0.005	← One cut	
4	205	0.0075	0.020	← Two cuts	
5	205		0.020		
6	409				
7	205	0.0034			
8	409				
9	205	0.0075	0.005		
10	409				
11	205	0.0034			
12	409				

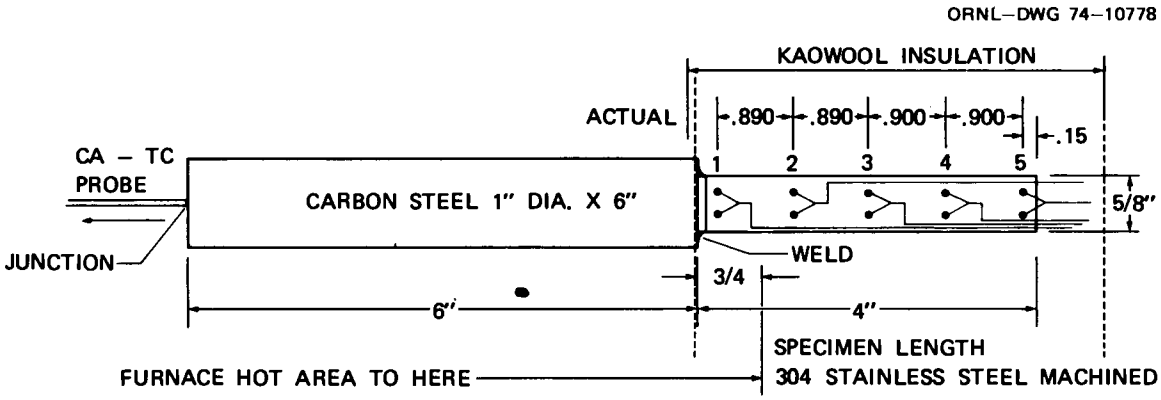

Fig. 5.116. Schematic of Test Setup Used to Obtain an Axial Thermal Gradient During a Test Anneal.

Table 5.48. Time-Temperature History During Test Anneal With Axial Thermal Gradient

Time (min)	Probe temperature [°C(°F)]	Specimen thermocouple readings (°F)				
		1	2	3	4	5
0	1177(2150)	Insert specimen				
2	1096(2005)	1130	660	320	170	125
8	1152(2105)	1650	1240	860	600	470
18	1171(2140)	1880	1630	1360	1180	1090
23	1177(2150)	1940	1745	1545	1385	1290
28	1182(2160)	1985	1825	1650	1505	1410
33	1188(2170)	2005	1855	1700	1570	1480
38	1190(2175)	2030	1900	1755	1630	1540
43	1190(2175)	2040	1915	1770	1645	1560
48	1193(2180)	2045	1925	1785	1670	1570
Begin hold time						
53	1193(2180)	2050	1935	1800	1680	1585
58	1193(2180)	2055	1935	1805	1685	1590
63	1193(2180)	2055	1940	1815	1690	1595
68	1193(2180)	2055	1940	1815	1695	1595
73	1193(2180)	2055	1945	1820	1690	1600
78	1193(2180)	2055	1945	1820	1700	1605
83	1193(2180)	2055	1945	1820	1700	1605
Remove and air cool						

PHOTO 2778–74

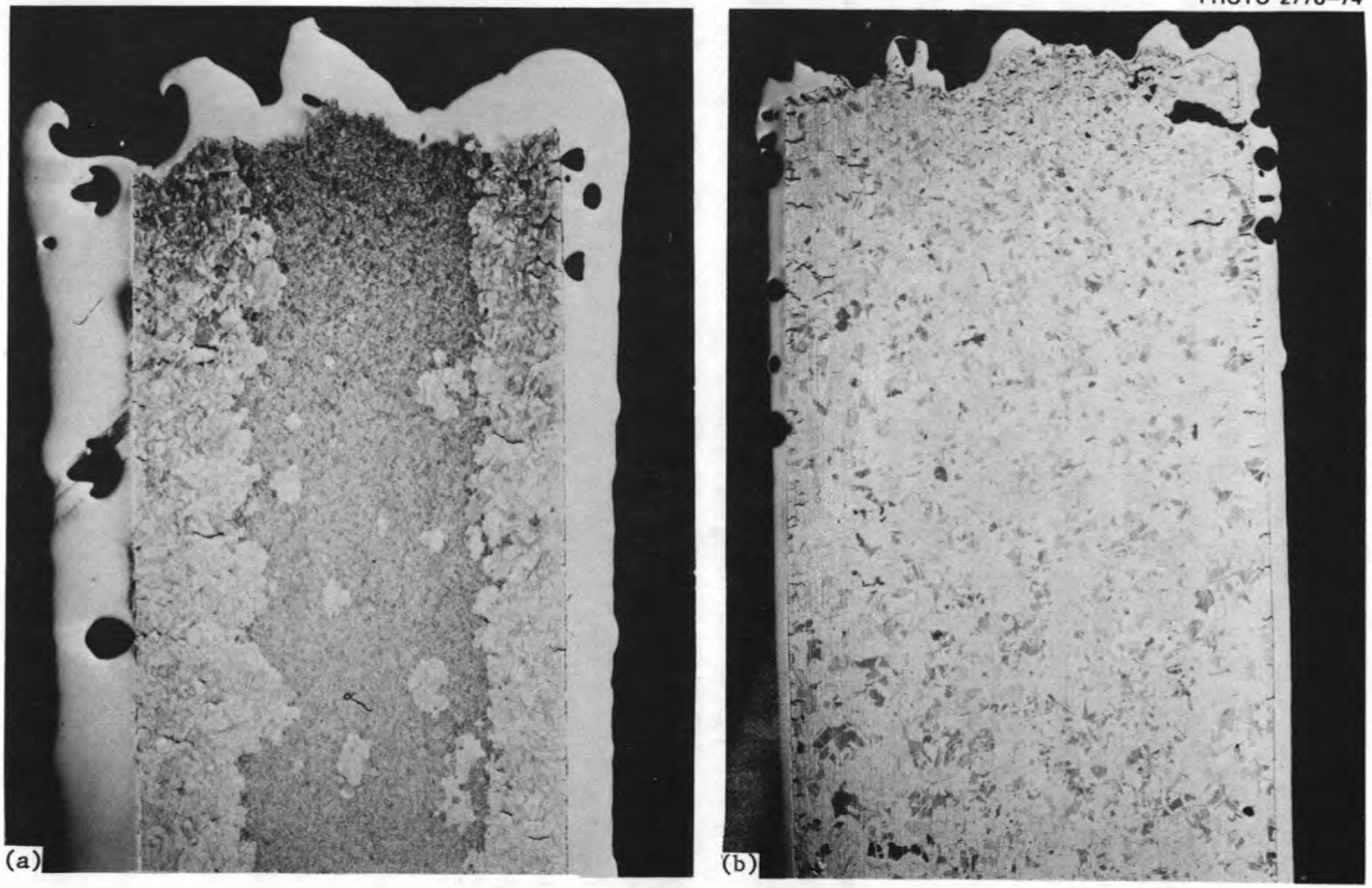

Fig. 5.117. Microstructure of Specimen 2-21 After Standard Reanneal (a) at 2000°F for 30 min and (b) After Reanneal at 2000°F for 90 min. Type 304 stainless steel (heat 9T2796), 5/8-in. rod (10×).

was again reannealed at 2000°F for an additional 1 hr. The resulting grain structure [Fig. 5.117(b)] indicates that the heterogeneous duplex grain structure was eliminated by this additional treatment.

At a meeting with ORNL on April 29 to discuss current results, the following activities were to be subsequently pursued.

1. Prepare and study additional photomicrographs, including those for all 5/8-in.-diam specimens tested at 20, 25, and 30 ksi at both Babcock and Wilcox and ORNL.

2. Examine the grain structure in two of the ruptured tubular specimens to assess the possible need of a further reanneal of the untested specimens. Heterogeneous duplex grains were not expected because of the relatively thin wall, although the possibility of smaller-than-desired grains might exist. These examinations have been completed, and the results show grain sizes of ASTM 3-4, which is acceptable. Figure 5.118 is typical of the results.

3. Examine initial specimens in the BWI series tests when either ruptured or terminated (per original schedule). In this test series, it is important that the grain size be consistent from specimen to specimen as well as within a specimen. This is because a single specimen at multiple points in time is assumed to be represented by multiple specimens at single points in time to investigate creep damage on a microstructural scale.

4. Reanneal future test specimens at 1093°C (2000°F) for 90 min. The 11 specimens shown in Table 5.49 were originally reannealed for 30 min and have been reannealed for an additional 60 min at 1093°C (2000°F). In the first batch, a portion of a previously examined specimen was included to again verify the effects of this additional anneal.

Investigations of apparent different strain-time responses seen in the two types of testing machines and specimens have continued. Test BWC-10 (20 ksi) was specifically to investigate the possible localization of strain prior to tertiary creep. As shown in Fig. 5.119, strain localization is not apparent and is hence eliminated as an explanation. However, this test will be continued to failure. In addition to the time to rupture, the progression of strain localization during tertiary

PHOTO 2779-74

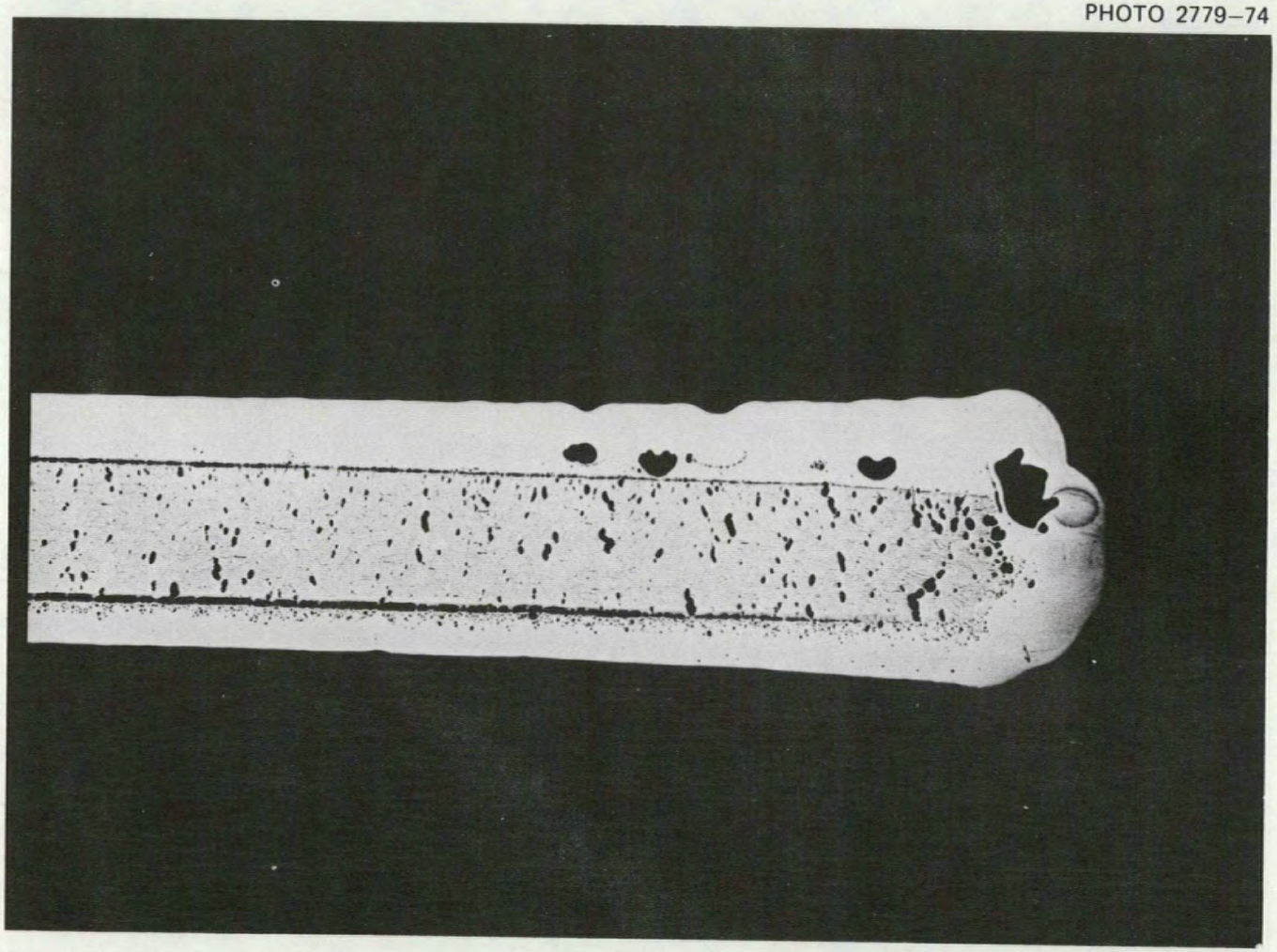

Fig. 5.118. Typical Microstructure in Longitudinal Section from Thin-Walled Tubular Specimen. Post failure; axial loading only; 1100°F; type 304 stainless steel (heat 9T2796), 5/8-in. rod (10×).

Table 5.49. Specimen Reanneal (90 min)[a] Identification

Reanneal batch	Specimen No.
1	2-3, 7-2, 7-3, 7-4, 7-5, 7-6
2	2-19, 7-19, 7-20, 7-26, 7-27

[a]Originally reannealed at 1093°C (2000°F) for 30 min; subsequently reannealed at 1093°C (2000°F) for an additional 60 min.

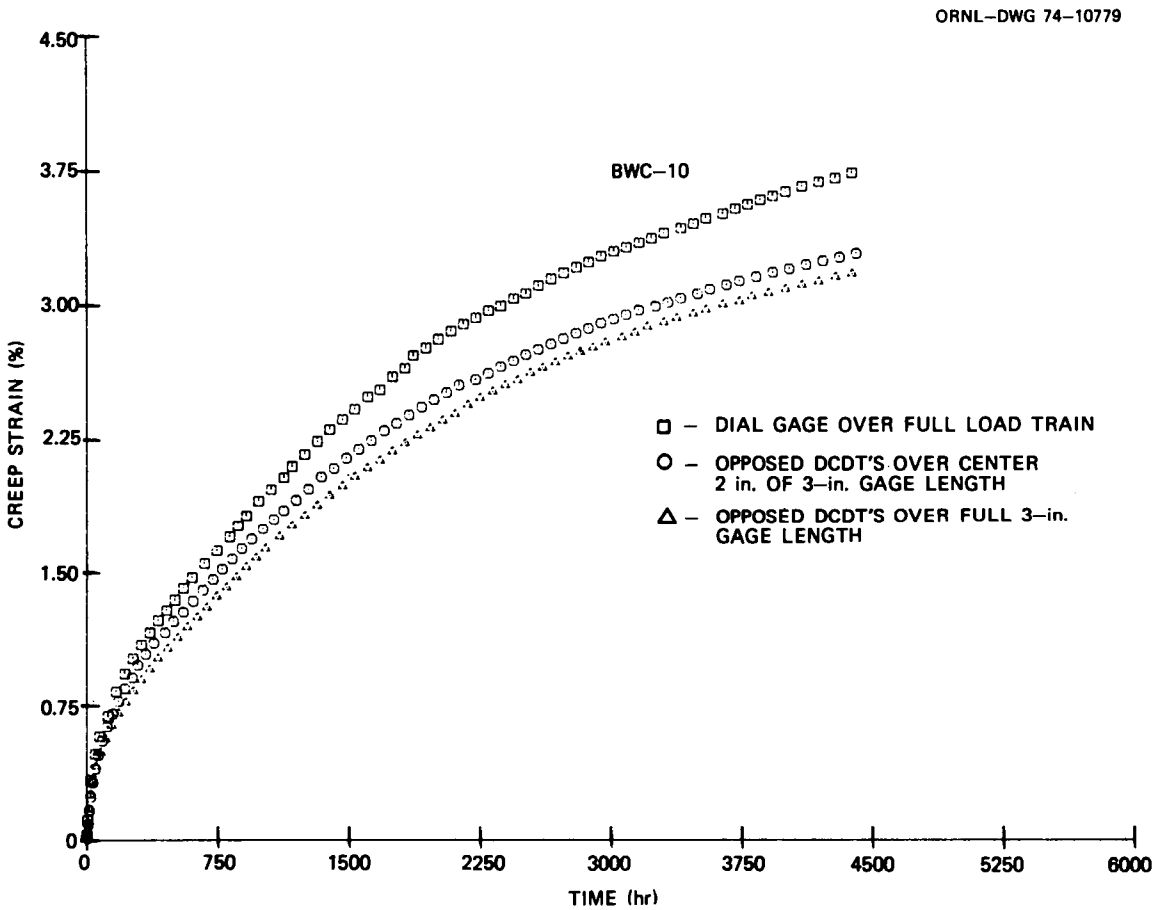

Fig. 5.119. Constant-Load Uniaxial Test to Evaluate Localization of Strain in 3-in. Buttonhead Creep Machine Specimen. Loaded at 20 ksi and 593°C (1100°F), type 304 stainless steel (heat 9T2796), 5/8-in. rod.

creep will be examined. Figure 5.120, which compares data from four tests at 20 ksi, indicates a definite difference in response for the two types of testing machines and specimens. Figure 5.121 compares the same four tests when all data are from full-load train displacement; some improvement is seen, but the difference is still significant. Investigations are continuing.

Five specimens were examined in an attempt to correlate the dependence of creep rate on grain size. Two of these specimens (2-28 and 7-7) were tested at 22 ksi, two (7-22 and 2-26) at 21 ksi, and one (2-21) at 20 ksi. Some of these specimens represent extremes of the scatter at the corresponding stress. These specimens are included in Table 5.46, but no simple correlation was apparent.

The first loading period of 100 hr was completed on the exploratory tubular specimen. The loading is equal biaxial tension of 21.85 ksi. Reference marks had been applied to this specimen to evaluate a procedure for strain determination by periodically interrupting the test for specimen measurement. The axial creep strain vs time results are shown in Fig. 5.122 (DCDT measurements over the center 5 in. of the 8-in. gage length). The discontinuity is the result of a temperature controller malfunction that allowed the temperature to locally approach 704°C (1300°F). The entire transient involved approximately 2 hr. The previous practice of attaching thermocouples by wire wrapping was discontinued because of the excessive radial restraint. The method used in this test was to spot weld 10-mil thermocouple wire directly to the specimen. The reference marks had been established by silver plating the entire test section and then masking at the desired location, followed by reversing the plating process to remove the excess silver. The initial loading period of 100 hr caused loss of the reference marks, probably by vaporization. New reference marks have now been established by spot welding (15 W-sec, 2 1/2-lb pressure) 5-mil type 304 stainless steel shim stock to the specimen and then pulling the shim stock off, leaving a small weld deposit. This process was tried on a previously tested (post-test) uniaxial specimen that was sectioned longitudinally through one such weld for microexamination. The photomicrograph of this section, shown in Fig. 5.123, illustrates approximately 3 mils penetration.

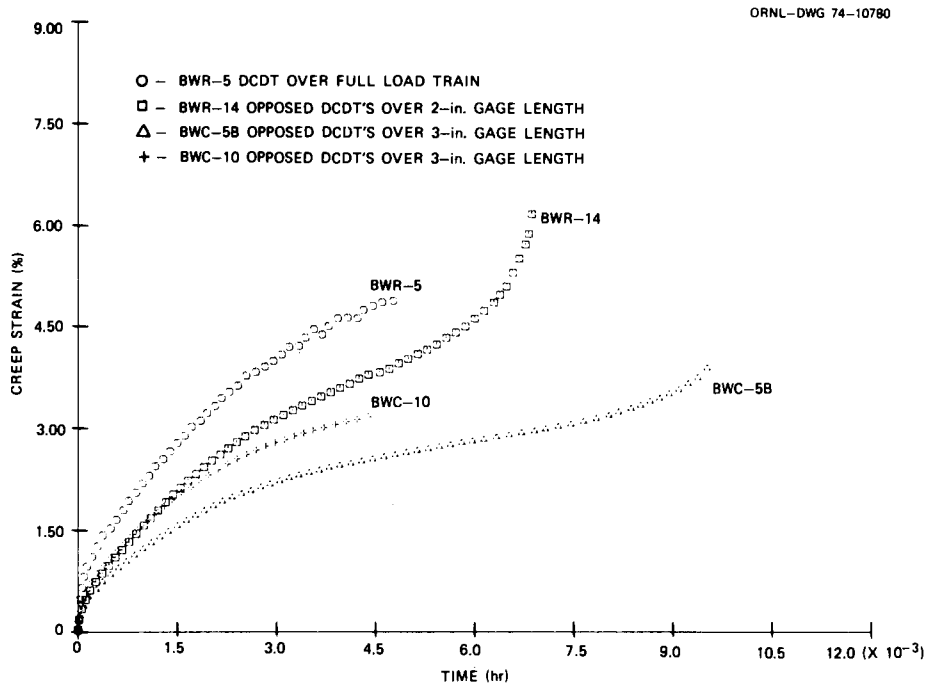

Fig. 5.120. Comparison of Uniaxial Tests All Loaded at 20 ksi and 593°C (1100°F). Type 304 stainless steel (heat 9T2796), 5/8-in. rod.

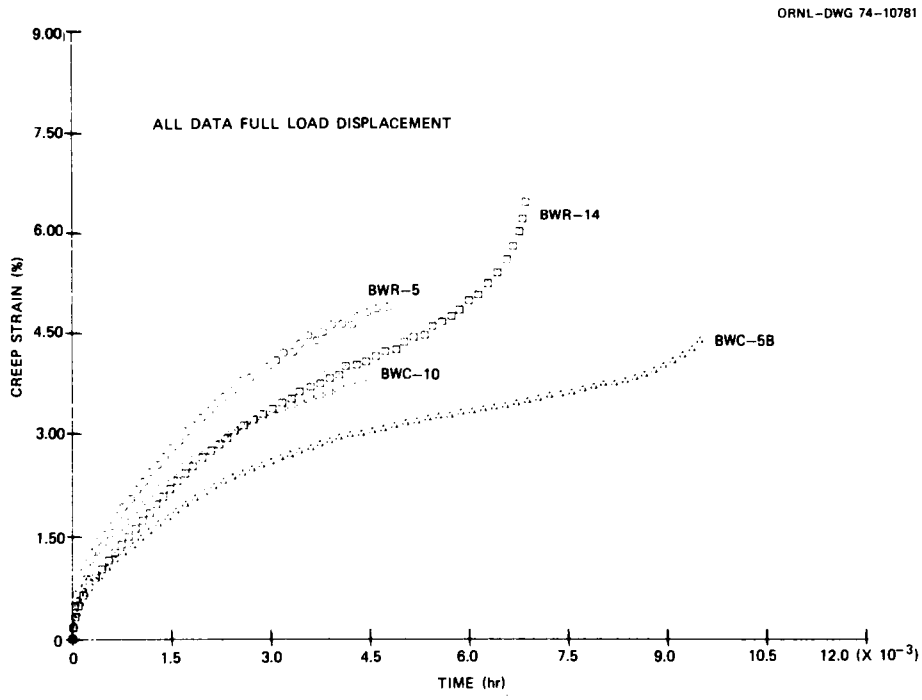

Fig. 5.121. Comparison of Uniaxial Tests All Loaded at 20 ksi and 593°C (1100°F). Type 304 stainless steel (heat 9T2796), 5/8-in. rod.

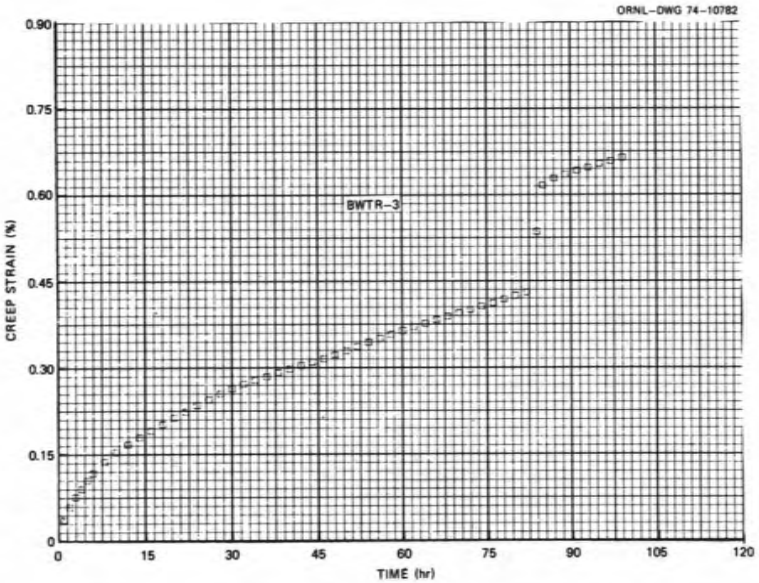

Fig. 5.122. Axial Creep Strain in Constant-Load Biaxial Rupture Test. Tubular specimen with internal pressure and additional axial load: equal biaxial tension of 21,850 psi; 593°C (1100°F); outside diameter of 1.50 in. and wall thickness of 0.075 in.; type 304 stainless steel (heat 9T2796); 5/8-in. rod.

PHOTO 2780–74

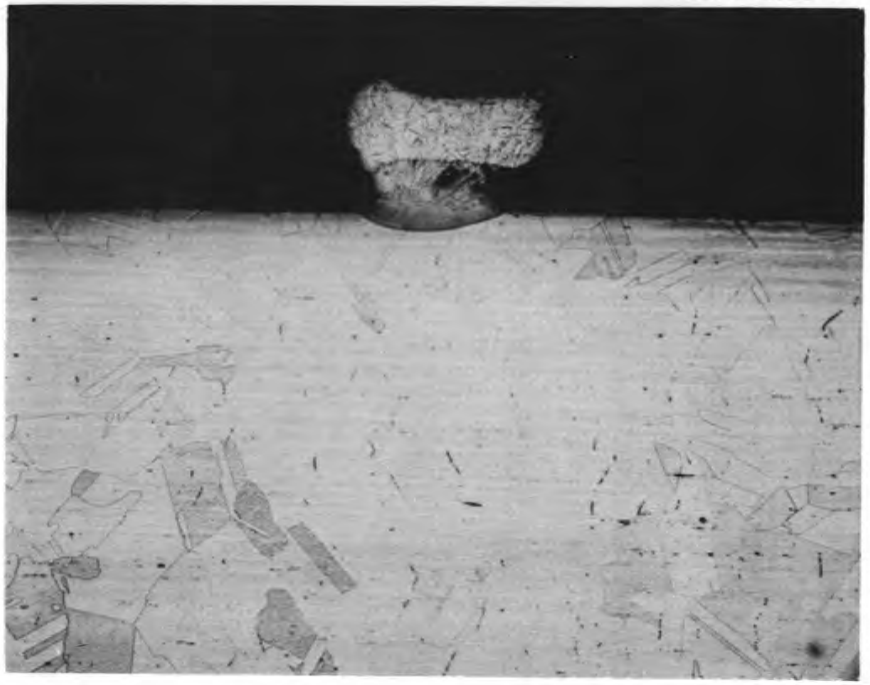

Fig. 5.123. Cross Section of Spot Weld Showing Depth of Penetration into Base Metal of Specimen. Typical of reference mark used on exploratory tubular test (75×).

5.6 MECHANICAL PROPERTIES OF HTGR STEAM GENERATOR AND PRIMARY CIRCUIT MATERIALS — P. L. Rittenhouse

The primary purpose of this program is to provide confirmation that the mechanical properties and behavior of HTGR structural alloys are not adversely affected by the thermal and chemical environment of the HTGR primary system. To this end, mechanical property tests (i.e., tensile, creep, low-cycle fatigue, and subcritical crack growth) are being conducted on a number of materials at temperatures consistent with their service in the HTGR. In most instances these tests are conducted in helium and steam atmospheres appropriate to HTGR operating conditions.

5.6.1 Materials

We currently have on hand all the materials needed for testing (i.e., low-carbon steel, 2 1/4 Cr-1 Mo steel, Incoloy 800, Hastelloy X, Hastelloy S, 9 Cr-1 Mo steel, and Inconel 617) except Incoloy 800 and the low-carbon steel. Quoted delivery dates for Incoloy 800 range from 15 to 18 months, but General Atomic Company has offered to supply several feet of bar stock within 2 to 3 months. Recent developments have indicated that both types 304 snd 316 stainless steel should be given consideration in our programs. These materials will be available from reference heats at ORNL. High-alloy ferritic steels (11—13% Cr) are also becoming of interest in HTGR technology, and such materials should become available from the LMFBR Steam Generator Advanced Materials Program.

5.6.2 Tensile Testing — W. R. Corwin and A. B. Boatwright*

Eighteen elevated-temperature tensile tests were performed on specimens of 9 Cr-1 Mo steel from G. O. Carlson heat 316381-1A. These were done to compare the tensile properties of the material reannealed at ORNL with those of the as-received material with a mill anneal. The ORNL heat treatment of the steel was an isothermal anneal [i.e., austenitized at 927°C (1700°F) and held for 2 hr at 704°C (1300°F), with controlled cooling rates, both from the austenitizing temperature to 704°C and to room temperature].

---

*Co-op student from Tuskegee Institute.

The differences in yield and ultimate strengths between the two sample lots were very small, nonsystematic, and within normal experimental error. The results of the tests on the reannealed material are given in Table 5.50.

Also, 54 elevated-temperature tests were performed on three lots of 2 1/4 Cr-1 Mo steel from Babcock and Wilcox, heats 72768, 36202, and X-6216. All lots were given the same isothermal anneal as specified for the 9 Cr-1 Mo steel. The results of most of the tests are listed in Table 5.51. The remainder are still being processed. When complete there will be four tests conducted on every heat at room temperature and two per heat at each elevated temperature.

5.6.3 Environmental Creep Testing. — W. R. Corwin

The FY 1975 creep rupture test matrix for HTGR structural materials in simulated HTGR primary coolant helium is shown in Table 5.52. The gas mixtures in which the materials will be tested will be within those specified in Table 5.53. According to D. I. Roberts of General Atomic Co. in San Diego, California, the helium impurity limits specified under "normal operation" represent the levels of impurity gases expected in an operating HTGR during normal operation without water leakage. These impurity levels are essentially those observed in steady-state operation at Peach Bottom. Similarly, the impurity limits specified under "worse case" represent the impurity levels that would be expected to prevail if the reactor were operated continuously with a very small water leak. The test matrix for FY 1975 for control tests in air of HTGR structural materials is shown in Table 5.54.

The testing facility that is committed to the above testing consists of ten environmental creep frames and six air creep frames. The gas for five frames will be supplied directly from bottles of gas premixed to the specifications for the test. Experiments conducted earlier this year showed test separation of gas species within the bottles due to gas settling or sticking to tank walls is negligible.

The other five frames will be supplied from a common source, which dynamically mixes the gas directly from its components before it is

Table 5.50. Elevated-Temperature Tensile Data for 9 Cr-1 Mo Steel

Test	Temperature		Tensile Strength			
			0.2% Yield		Ultimate	
	(°C)	(°F)	(ksi)	(MPa)	(ksi)	(MPa)
14130	25	77	38.6	266	76.0	524
14131	25	77	39.9	275	75.4	520
14132	25	77	38.7	267	75.5	521
14133	25	77	40.3	278	76.1	525
14134	260	500	29.6	204	66.4	458
14135	260	500	29.0	200	66.0	455
14136	316	600	28.0	193	63.9	441
14137	316	600	28.2	194	64.5	445
14138	371	700	27.1	187	63.8	440
14139	372	700	27.1	187	63.3	436
14140	427	800	27.8	192	59.8	412
14141	427	800	25.6	177	59.0	407
14142	482	900	24.7	170	52.3	361
14143	482	900	24.1	166	52.3	361
14144	538	1000	22.3	154	40.3	278
14145	538	1000	23.3	161	41.2	284
14146	593	1100	19.7	136	30.0	207
14147	593	1100	19.5	134	29.7	205

Table 5.51. Elevated Temperature Tensile Data for 2 1/4 Cr-1 Mo Steel

Test	Heat	Temperature		Tensile Strength			
				0.2% Yield		Ultimate	
		(°C)	(°F)	(ksi)	(MPa)	(ksi)	(MPa)
14152	72768[a]	260	500	25.9	179	56.3	388
14153	72768	260	500	25.8	178	55.5	383
14154	36202[b]	260	500	27.5	190	60.3	416
14155	36202	260	500	28.3	195	60.0	414
14151	X-6216[b]	260	500	28.6	197	61.6	425
14111	X-6216	260	500	28.1	194	58.5	403
14066	72768	315	600	25.0	172	57.1	394
14068	72768	315	600	22.4	154	56.9	392
14071	36202	315	600	27.8	192	61.3	423
14073	36202	315	600	27.6	190	61.7	425
14158	X-6216	315	600	27.0	186	59.8	412
14070	72768	371	700	26.4	182	66.3	457
14086	36202	371	700	25.9	179	64.6	445
14067	X-6216	371	700	26.3	181	63.3	436
14069	X-6216	371	700	27.2	188	62.8	433
14089	72768	427	800	23.9	165	57.9	399
14091	72768	427	800	20.7	143	57.6	397
14094	36202	427	800	29.4	203	62.0	427
14075	X-6216	427	800	26.1	180	60.2	415
14088	X-6216	427	800	27.7	191	56.7	391
14092	72768	482	900	23.5	162	52.5	362
14093	72768	482	900	26.7	184	52.5	362
14095	36202	482	900	19.1	132	56.6	390
14096	36202	482	900	18.7	129	56.5	390
14087	X-6216	482	900	23.3	161	54.5	376
14097	X-6216	482	900	25.5	176	55.3	381
14101	72768	538	1000	21.1	145	44.1	304
14104	72768	538	1000	19.2	132	44.2	305
14109	36202	538	1000	23.1	159	47.3	326
14098	X-6212	538	1000	23.6	163	48.2	332
14100	X-6212	538	1000	22.0	152	46.1	318
14102	72768	593	1100	16.8	116	34.7	239
14108	36202	593	1100	21.1	145	37.3	257
14097	X-6216	593	1100	19.7	136	36.2	250
14099	X-6216	593	1100	21.9	151	36.2	250

[a]Carbon content = 0.10%.

[b]Carbon content = 0.12%.

Table 5.52. Matrix for FY 1975 Creep-Rupture Testing of HTGR Structural Materials in Simulated HTGR Primary Coolant Helium

Material	Stress, ksi (MPa) Applied at Indicated Temperatures				
	427°C 800°F	482°C 900°F	538°C 1000°F	593°C 1100°F	704°C 1300°F
2 1/4 Cr-1 Mo steel	45(310)	25(172) 30(207)	15(103)	10(69)	
Incoloy 800			40(276) 45(310) 50(345)	25(172) 30(207)	
Hastelloy X				45(310)	20(138) 30(207)
1010/1020 steel	20(138)	10(69)			
9 Cr-1 Mo steel		25(172)	20(138)	10(69)	
Inconel 617				50(345)	
Hastelloy S					30(207)

Table 5.53. Helium Impurity Levels for Creep-Rupture Tests

Impurity	Content, μatm[a]	
	"Normal"	"Worse Case"
H_2O	<1	25
CH_4	20	25
CO	10	400
CO_2	<1	<1
H_2	200	1500

[a]Microatmospheres (i.e., 10^{-6} atm or 1 ppm at 1 atm).

Table 5.54. Matrix for FY 1975 Creep-Rupture Testing of HTGR Structural Materials — Control Tests in Air

Material	Stress, ksi(MPa) Applied at Indicated Temperatures				
	427°C 800°F	482°C 900°F	538°C 1000°F	593°C 1100°F	704°C 1300°F
2 1/4 Cr-1 Mo steel	45(310)	30(217)	15(103)		
Incoloy 800			50(345)	30(207)	
Hastelloy X				45(310)	30(207)
1010/1020 steel	20(138)				
9 Cr-1 Mo steel		25(172)	20(138)		
Inconel 617					40(276)
Hastelloy S					30(207)

introduced to the creep frames (see Fig. 5.124). This is a method presently in use at GAC in San Diego and seems to be highly acceptable there. In the completed gas supply system the actual composition of the gas can be monitored both before it enters the environmental chamber and after it leaves. An on-line Bendix series 2110 gas chromatograph will measure concentrations of all gas species except H_2O and concentrations of O_2 below 1 ppm. The H_2O level will be measured with an on-line Beckman model 340 trace moisture analyzer with a low-pressure sampling adapter rated at a sensitivity of 1 ppm. The low-level O_2 pressure will be measured with an on-line platinum loop oxygen potential meter such as is in current use at GAC, where oxygen pressures as low as 10^{-25} atm (10^{-20} Pa) have been monitored. At this writing, the installation of the above system is approximately 60% complete. The bottle portion of the system will be essentially complete by late October. In the interim, two of the environmental frames have been temporarily fully equipped and have been started. These tests are 2 1/4 Cr-1 Mo steel at 593°C (1100°F) under 10 ksi (69 MPa) and Hastelloy S at 704°C (1300°F) under 30 ksi (217 MPa). The gas chromatograph is presently tied into the temporary system and will be switched into the permanent system when

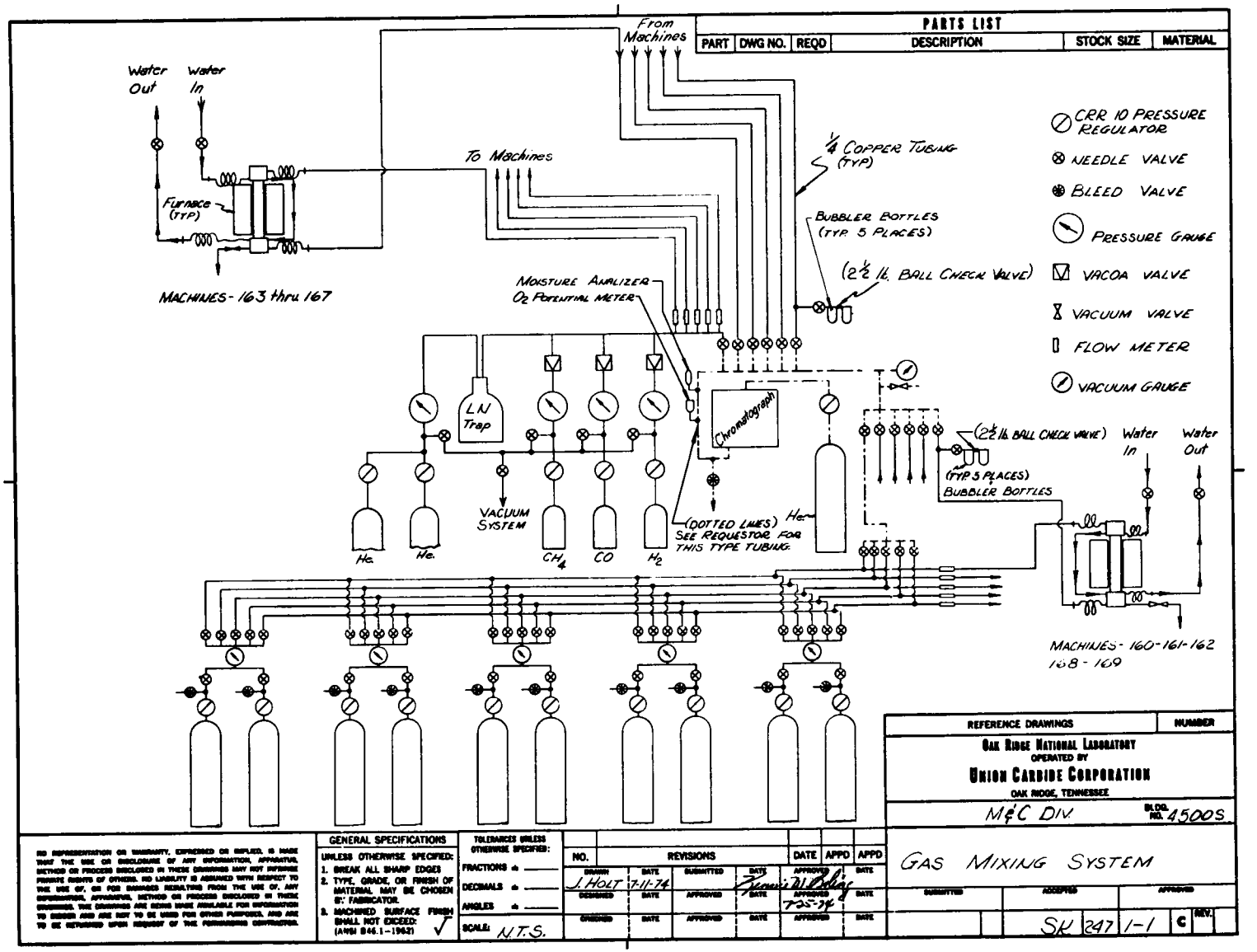

Fig. 5.124. Schematic of Gas Supply and Control System for Environmental Creep Tests.

completed. The remaining components for the moisture analyzer and the O_2 potential meter have just arrived, and their installation is under way. During the transition from the temporary system to the permanent one, test continuity can be maintained.

5.6.4 Environmental Fatigue Testing

5.6.4.1 Subcritical Crack Growth

The test matrix for FY 1975 subcritical crack growth tests in both steam and helium is shown in Table 5.55. The impurity levels in the helium will be similar to those for HTGR creep testing.

A schematic of the environmental supply and control system for testing in helium is shown in Fig. 5.125. Unfortunately, when the gas chromatograph underwent its initial setup and calibration earlier this month it did not perform to its factory specifications. A faulty detector unit seems to be the problem. At this point neither the full extent of the problem nor the timetable for its correction have been established. Work is presently under way to determine both. Also, alternate methods are being investigated for interim use until the above problem is corrected.

The Gilmore load frame in which the helium tests will be conducted has been aligned as has the internal load train of the environmental chamber. The remainder of the load train is being fabricated and should be completed in early October. With the exception of the gas chromatograph, whose status is presently unclear, the components for the gas supply and monitoring system have been ordered and most have arrived. The last to arrive should be the regulators, which are expected by mid-October. Installation is presently being scheduled.

The crack propagation tests in steam have begun. The first, which is now in progress, is 2 1/4 Cr-1 Mo steel WOL specimen in steam at 510°C (950°F). The steam production system is presently being automated to increase test machine productivity.

Table 5.55. Matrix for FY 1975 Subcritical Crack Growth Tests in Both Steam and Helium

Material	Temperature[a] (°C)	Temperature[a] (°F)	R[b]	Frequency[c] (cpm)	Hold
Incoloy 800	427	800	0.05	40	
Incoloy 800	538	1000	0.05	40	
Incoloy 800	649	1200	0.05	40	
Incoloy 800	760	1400	0.05	40	
Incoloy 800	871	1600	0.05	40	
Incoloy 800	427	800	0.05	400	
Incoloy 800	538	1000	0.05	400	
Incoloy 800	649	1200	0.05	400	
Incoloy 800	760	1400	0.05	400	
Incoloy 800	871	1600	0.05	400	
Incoloy 800	427	800	0.5	40	
Incoloy 800	538	1000	0.5	40	
Incoloy 800	649	1200	0.5	40	
Incoloy 800	760	1000	0.05	4	
Incoloy 800	871	1400	0.05	4	
Incoloy 800	760	1200	0.05	4	0.01-hr tensile
2 1/4 Cr-1 Mo	427	800	0.05	40	
2 1/4 Cr-1 Mo	510	950	0.05	40	
2 1/4 Cr-1 Mo	593	1100	0.05	40	
2 1/4 Cr-1 Mo	427	800	0.05	400	
2 1/4 Cr-1 Mo	510	950	0.05	400	
2 1/4 Cr-1 Mo	593	1100	0.05	400	
2 1/4 Cr-1 Mo	510	950	0.05	4	
2 1/4 Cr-1 Mo	593	1100	0.05	4	
2 1/4 Cr-1 Mo	510	950	0.5	40	
2 1/4 Cr-1 Mo	593	1100	0.5	40	
2 1/4 Cr-1 Mo	510	950	0.05	40	0.01-hr tensile
2 1/4 Cr-1 Mo	593	1100	0.05	40	0.01-hr tensile

[a]Upper temperatures for steam tests are furnace limited to about 650°C (1200°F).

[b]Ratio of minimum to maximum stress.

[c]Triangular wave form excluding hold time.

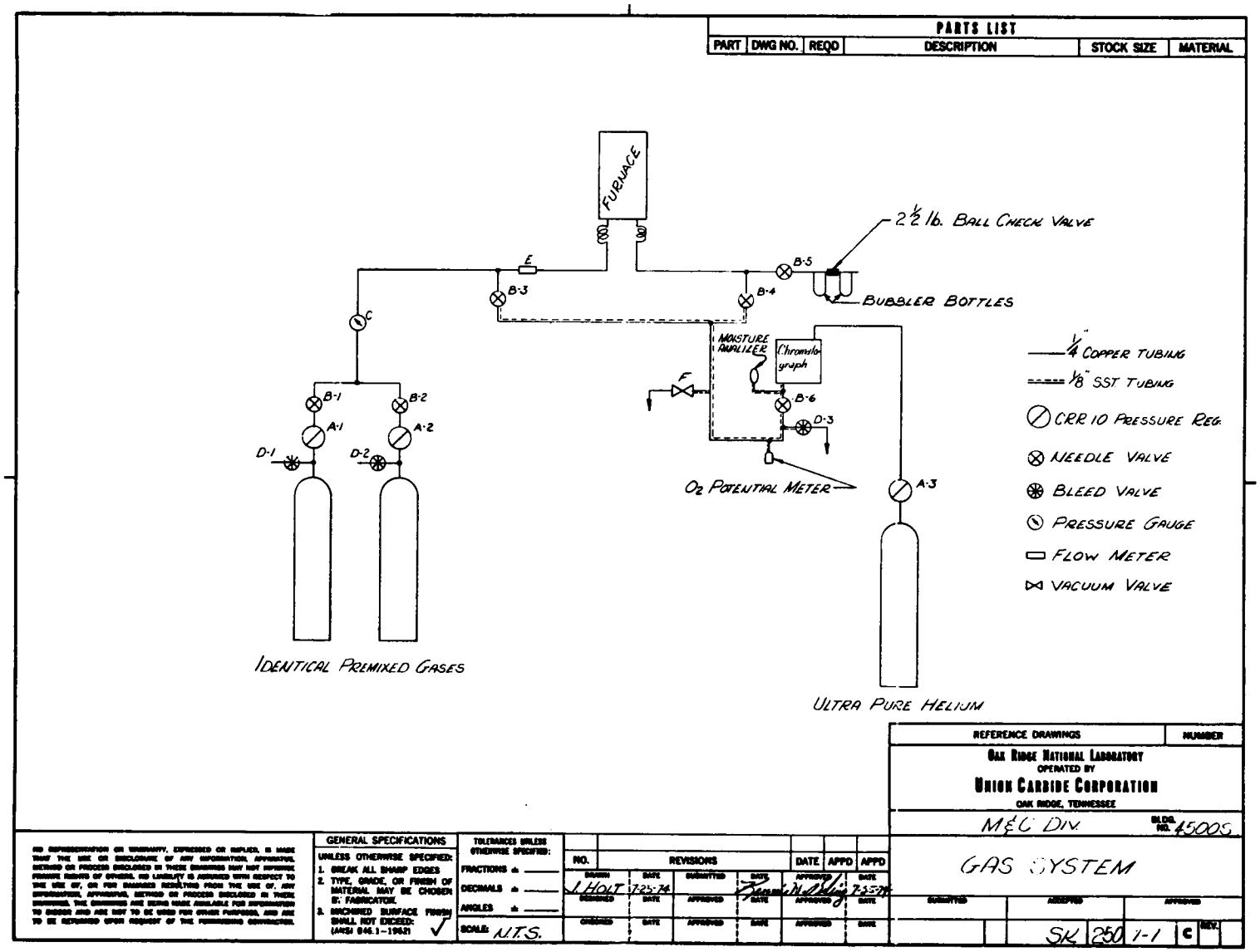

Fig. 5.125. Schematic of Gas Supply and Control System for Environmental Subcritical Crack Growth Tests.

5.6.4.2 Fatigue Life Testing

A 55,000-lb (245 KN) MTS system for use in environmental fatigue studies was delivered on Sept. 20, 1974. Its gas supply and monitoring system will be an integral part of the creep environmental control system. Installation and initial setup of the MTS will commence this period. Design work for the environmental chamber and control system is in progress.

5.7 REFERENCES

1. V. K. Sikka, *Mechanical Properties Test Data for Structural Materials Quart. Progr. Rep. July 31, 1974*, ORNL-4998, pp. 120–31.
2. L. D. Blackburn, Hanford Engineering Development Laboratory, private communication, November 1973.
3. A. Kirsch, paper 62, pp. 1-81–1-89, *Joint International Conference on Creep*, The Institute of Mechanical Engineers, London, 1963.
4. V. K. Sikka, *Mechanical Properties Test Data for Structural Materials Quart. Progr. Rep. Apr. 30, 1974*, ORNL-4963, pp. 84–103.
5. H. E. McCoy, *Mechanical Properties Test Data for Structural Materials Quart. Progr. Rep. Apr. 30, 1974*, ORNL-4963, pp. 108–9.
6. F. Garofalo et al., *Trans. AIME* 221: 310–19 (1961).
7. A. J. Lovell, L. D. Blackburn, and J. J. Holmes, *Quarterly Progress Report Irradiation Effects on Reactor Structure Materials, August, September, October 1970*, WHAN-FR-40-1, pp. 8.4–8.14.
8. F. Garofalo, *Fundamentals of Creep and Creep-Rupture in Metals*, Macmillan, New York, 1965, pp. 220–26.
9. C. R. Brinkman, *Mechanical Properties Test Data for Structural Materials Quart. Progr. Rep. Jan. 31, 1974*, ORNL-4948, pp. 221–26.
10. *Ibid., Apr. 30, 1974*, ORNL-4963, pp. 119–26.
11. R. M. Goldhoff, "A Method for Extrapolating Rupture Ductility," pp. 82–94 in *Elevated Temperature Testing Problem Areas, ASTM Spec. Tech. Publ.* 488, American Society for Testing and Materials, Philadelphia, 1971.
12. G. V. Smith, *Properties of Metals at Elevated Temperature*, McGraw-Hill, New York, 1950, p. 151.

13. R. K. Penny and D. L. Marriott, *Design for Creep*, McGraw-Hill Book Co. (UK) Limited, London, 1971, pp. 173–81.

14. V. K. Sikka, *Mechanical Properties Test Data for Structural Materials Quart. Progr. Rep. July 31, 1974*, ORNL-4998, pp. 122–31.

15. S. S. Manson, "Time-Temperature Parameters — A Re-Evaluation and Some New Approaches," pp. 1–113 in *Time-Temperature Parameters for Creep-Rupture Analysis, ASM Publ.* D8-100, American Society for Metals, Metals Park, Ohio, 1968.

16. J. B. Conway, *Stress-Rupture Parameters: Origin, Calculation, and Use*, Gordon and Breach, New York, 1969.

17. R. L. Orr, O. D. Sherby, and J. E. Dorn, "Correlations of Rupture Data for Metals at Elevated Temperatures," *Trans. Amer. Soc. Metals* 46: 113 (1954).

18. S. S. Manson and G. Succop, "Stress-Rupture Properties of Inconel 700 and Correlation on the Basis of Several Time-Temperature Parameters," pp. 40–46 in *Symposium on Metallic Materials for Service at Temperatures Above 1600°F, ASTM Spec. Tech. Publ.* 174, American Society for Testing and Materials, Philadelphia, 1956.

19. D. A. Woodford, "A Graphical Optimization Procedure for Time-Temperature Rupture Parameters," *Mater. Sci. Eng.* 15: 169–75 (1974).

20. B.L.P. Booker and M. K. Booker, "CREEP," unpublished computer program, 1974.

21. S. S. Manson and A. Mendelson, *Optimization of Parametric Constants for Creep-Rupture Data by Means of Least Squares*, NASA-Memo 3-10-59E (1959).

22. C. R. Ensign and S. S. Manson, "MEGA 6," unpublished computer program, 1974.

23. J. P. Hammond and M. W. Moyer, *Mechanical Properties Test Data for Structural Materials Quart. Progr. Rep. Apr. 30, 1974*, ORNL-4963, pp. 126–33.

24. H. E. McCoy, M. W. Moyer, and T. W. Dews, *Fuels and Materials Development Program Quart. Progr. Rep. Dec. 31, 1973*, ORNL-TM-4524, pp. 75–82.

25. J. A. Clinard and J. S. Crowell, *ORNL User's Manual for CREEP-PLAST Computer Program*, ORNL-TM-4062 (November 1973).

26. P. W. Bridgman, "The Stress Distribution at the Neck of a Tension Specimen," *Trans. Amer. Soc. Metals* 32: 553–74 (1944).

27. R. T. King, J. K. Alley, and B. McNabb, Jr., *Mechanical Properties Test Data for Structural Materials Quart. Progr. Rep. Oct. 31, 1973*, ORNL-4936, pp. 142–47.

28. R. T. King, J. K. Alley, and E. Bolling, *Fuels and Materials Development Program Quart. Rep. Mar. 31, 1973*, ORNL-TM-4250, pp. 139–51.

29. R. T. King, R. E. Adams, and G. M. Goodwin, *Fuels and Materials Development Program Quart. Progr. Rep. Mar. 31, 1972*, ORNL-TM-3797, pp. 210–20.

30. R. T. King and G. M. Goodwin, *Mechanical Properties Test Data for Structural Materials Quart. Progr. Rep. Oct. 31, 1973*, ORNL-4936, pp. 138–42.

31. R.G.D. Steel and J. H. Torrie, *Principles and Procedures of Statistics*, McGraw-Hill, New York, 1960.

32. R. T. King, J. O. Stiegler, and G. M. Goodwin, "Relation Between Mechanical Properties and Microstructure in CRE Type 308 Weldments," *Weld. J. (Miami)* 53: 307-s–313-s (1974).

33. R. T. King, *Fuels and Materials Development Program Quart. Progr. Rep. Dec. 31, 1973*, ORNL-TM-4524, pp. 146–62.

34. L. D. Blackburn, "Isochronous Stress-Strain Curves for Austenitic Stainless Steels," pp. 15–48 in *The Generation of Isochronous Stress-Strain Curves*, ed. by A. O. Schaefer, American Society of Mechanical Engineers, New York, 1972.

35. R. T. King and J. O. Stiegler, "Effect of Composition on Fracture Characteristics and Creep Ductility of Type 308 Stainless Steel Weld Metal," paper presented at the 1973 Annual Winter Meeting of ASME, Detroit, Michigan, November 1973, to be published.

36. R. L. Klueh, *Fuels and Materials Development Program Quart. Progr. Rep. Mar. 31, 1974*, ORNL-TM-4620, pp. 26–31.

37. J. H. Holloman, *Trans. AIME* 162: 268 (1945).

38. P. Ludwik, *Elemente der Technologischen Mechanik,* Springer, Berlin, 1909.

39. D. C. Ludwigson, *Met. Trans.* 2: 2825 (1971).

40. E. Voce, *J. Inst. Metals* 74: 537 (1948).

41. R. L. Klueh, *Mechanical Properties Test Data for Structural Materials Quart. Progr. Rep. July 31, 1974,* ORNL-4998, pp. 207–12.

42. K. F. Hale, pp. 650–58 in *Proc. 4th Intern. Conf. Electron Microscopy,* Vol. 1, Springer-Verlag, Berlin, 1960.

43. R. G. Baker and T. Nutting, *J. Iron Steel Inst.* 192: 257–68 (1957).

44. C. R. Brinkman and J. P. Strizak, *Mechanical Properties Test Data for Structural Materials Quart. Progr. Rep. July 31, 1974,* ORNL-4998, pp. 213–22.

45. Brookhaven National Laboratory, private communication.

46. M. K. Booker, *Mechanical Properties Test Data for Structural Materials Quart. Progr. Rep. July 31, 1974,* ORNL-4998, pp. 168–72.

7. J. Nunes, "Flow-Stress-Strain Relationships in Tension Tests of Steel," *Mater. Res. Stand.* 3(9): 719–22 (1963).

8. D. O. Hobson and T. L. Hebble, *Mechanical Properties Test Data for Structural Materials Quart. Progr. Rep. July 31, 1974,* ORNL-4998, pp. 221–25.

49. D. Tabor, *The Hardness of Metals,* The Clarendon Press, Oxford, 1951, p. 107.

50. H. O'Neill, *Hardness Measurement of Metals and Alloys,* Chapman and Hall, London, 1967, pp. 32–83.

51. R. L. Klueh, *Fuels and Materials Development Program Quart. Progr. Rep. Mar. 31, 1974,* ORNL-TM-4620, pp. 36–46.

52. R. L. Klueh, *Mechanical Properties Test Data for Structural Materials Quart. Progr. Rep. July 31, 1974,* ORNL-4998, pp. 225–31.

53. G. V. Smith, *An Evaluation of the Yield, Tensile, Creep, and Rupture Properties of Wrought 304, 316, 321, and 347 Stainless Steels at Elevated Temperatures, ASTM Data Ser. Publ.* DS 5-S2, American Society for Testing and Materials, Philadelphia, February 1969.

54. R. L. Klueh and D. A. Canonico, *Elevated-Temperature Tensile Strength and Microstructure of a Weld-Overlaid Type 304 Stainless Steel Forging*, ORNL-TM-4521 (March 1974); also pp. 113–40 in *Symp. on Elevated Temperature Properties of Austenitic Stainless Steel* (June 24–28, 1974, Miami Beach, Florida), The American Society of Mechanical Engineers, New York, 1974.

55. R. W. Swindeman, *Mechanical Properties Test Data for Structural Materials Quart. Progr. Rep. Apr. 30, 1974*, ORNL-4963, pp. 190–95.

56. F. R. Larson and J. Miller, "A Time-Temperature Relationship for Rupture and Creep Stresses," *Trans. ASME* 74: 765 (1952).

57. S. S. Manson and A. M. Haferd, *A Linear Time-Temperature Relation for Extrapolation of Creep and Stress-Rupture Data*, NASA-TN-2890 (1953).

58. R. Bhargava, C. Schmidt, and J. Moteff, *Mechanical Properties Test Data for Structural Materials Quart. Progr. Rep. Apr. 30, 1974*, ORNL-4963, pp. 242–49.

59. C. R. Barrett, A. J. Ardell, and O. D. Sherby, "Influence of Modulus on the Temperature Dependence of the Activation Energy for Creep at High Temperature," *Trans. Met. Soc. AIME*, 230: 200–204 (1964).

60. R. W. Weeks, D. R. Diercks, and C. F. Cheng, *ANL Low-Cycle Fatigue Studies — Program, Results, and Analysis*, ANL-8009 (November 1973).

61. M. J. Manjoine, "Stress Relaxation Characteristics of Type 304 Stainless Steel," paper presented at the International Conference on Creep and Fatigue in Elevated Temperature Applications, Philadelphia, September 1973 and Sheffield, UK, April 1974.

62. C. R. Brinkman and G. E. Korth, *Heat-to-Heat Variations in the Fatigue and Creep-Fatigue Behavior of AISI Type 304 Stainless Steel, and the Fatigue Behavior of Type 308 Stainless Steel Weld Material*, ANCR-1097 (May 1973).

63. R. W. Swindeman, unpublished data collected in support of the ORNL program on High-Temperature Structural Design Methods for LMFBR Components.

64. C. C. Schultz, "Investigations of Creep Failure under Uniaxial and Multiaxial Conditions," *High-Temperature Structural Design Methods for LMFBR Components Progr. Rep. Dec. 31, 1973*, ORNL-4947, pp. 75–103.

65. *Ibid., Mar. 31, 1974*, ORNL-4977, pp. 79–94.

6. WESTINGHOUSE ADVANCED REACTORS DIVISION

E. C. Bishop

6.1 INTRODUCTION

The program being performed at Westinghouse Advanced Reactors Division (ARD) is entitled "Validation of High Temperature Design Methods and Criteria" (189a No. 04165). Two of the tasks in this program are "Basic Specimen Testing" and "Tubular Specimen Testing." The objective of these tasks is to design and test specimens of increasing complexity to determine the inelastic behavior and strain tolerances of Types 304 and 316 stainless steel under complex stress distributions. This report covers the work performed during the period from June 1, 1974 to August 31, 1974.

6.2 BASIC SPECIMEN TESTING - N. J. Ettenson, M. Manjoine (Westinghouse Research Laboratories)

A variety of specimen designs have been selected for this task, as shown in Table 6.1 and Figure 6.1. Data obtained to date are presented in Table 6.2.

6.2.1 Uniaxially Loaded Specimen Models with Uniform Gage Section (304 SS, Heat 9T2796)

6.2.1.1 Test Piece Description

Types A, B, and G test piece designs, as shown in Table 6.1, are used for this part of the test program.

6.2.1.2 Current Results

A topical report is being prepared on the completed A-, B-, and G-type specimens. Preliminary comparisons indicate reasonable overall agreement between the predictive analysis with CREEP PLAST and the test data. Refinements being considered for future analyses are listed below:

Table 6-1. Model Types

Specimens From Base Material[a]

Code Designation	Description[b]
A.	Plane Stress Specimen 1/3 x 2/3 x 3 in. (8.5 x 17 x 76.2 mm) gage section.
B.	Plate Specimen 1/3 x 10/3 x 3 in. (8.5 x 85 x 76.2 mm) gage section.
C.	Plate Specimen with Central Hole of 1/3 in. (8.5 mm) Diameter, 1/3 x 10/3 x 3 inc. (8.5 x 85 x 76.2 mm) plate section.
D.	Round Circumferentially Notched Specimen, Major Diameter = 0.96 in. (24.4 mm), Minor Diameter = 0.64 in. (16.2 mm), K_t = 4, Root Radius = 0.018 in. (0.46 mm), Two nearly identical notches in specimen.
E.	Plate Specimen in bending and tension, 1/3 x 10/3 x 2 in. (8.5 x 85 x 50.8 mm) plates section, eccentric load
F.	Designation generally refers to failure or fracture; therefore, it is not used to identify a type of model.
G.	Plane Strain Specimen 1/3 x 10/3 x 1 in. (8.5 x 85 x 26 mm) gage section, Ends constrained in transverse direction
H.	Biaxially Loaded Notched Plates, Wedge-opening-loaded Plates with 1/3 in. (8.5 mm) Diameter Notch.

Specimen With Welds

BTW - B-type plate specimen with transverse weld at mid-length of gage section.

BAW - B-type plate specimen with axial weld at center of gage section.

CTW - C-type specimen with hole through transverse weld.

CAW - C-type specimen with hole through axial weld.

DTW - D-type specimen with notch root in transverse weld.

DZTW - D-type specimen with notch root at weld fusion line of heat affected zone.

GTW - G-type specimen with transverse weld at mid-gage length.

GAW - G-type specimen with axial weld at center of gage section.

(a) Type 304 SS (HT9T2796) annealed at 2000°F.

(b) Reference Figure 6-1.

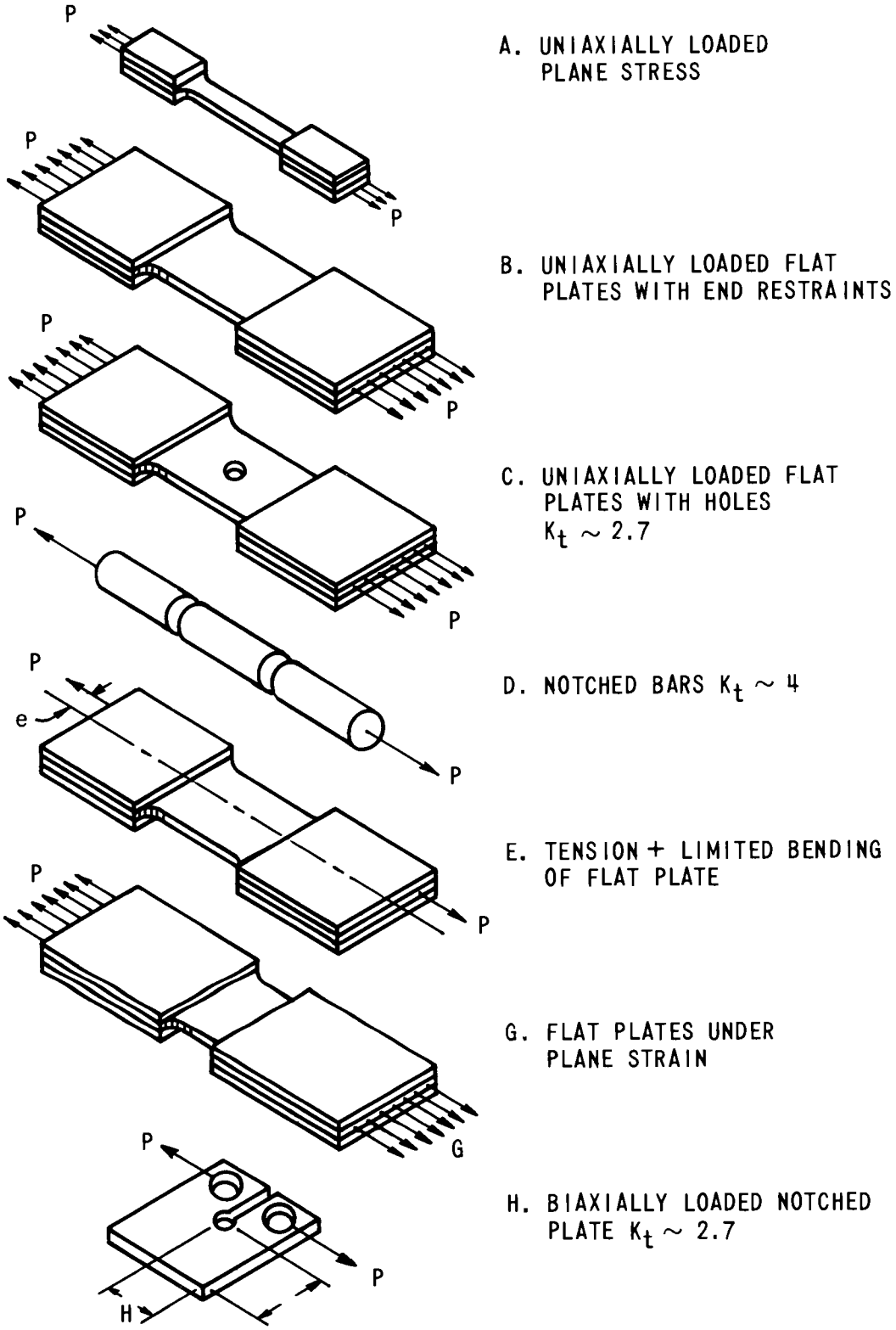

Figure 6-1 Basic Specimen Types

6593-15

Table 6-2 Summary of Creep Data, Type 304 Stainless Steel* at 1100°F (593°C)

Test No. (Gage Section)	Loading Data			Creep Data					
	Stress		Plastic Strain	Creep Rate	Increment		Accumulated		Permanent Strain
	(ksi)	(MPa)	(%)	(%/hr)	Strain (%)	Time (hr)	Strain (%)	Time (hr)	(%)
A1	21.0	144.8	4.66	2.2×10^{-3}	1.10	303	1.10	303[a]	5.76
(1/3x2/3x3 in)				2.2×10^{-3}	0.89	403	1.99	706[a]	6.65
(8.5x17x76.2mm)					1.48	544	3.47	1250[b]	8.13
					0.18	20	3.65	1270[c]	8.31
					3.69	556	7.34	1826	12.00[d]
A2	10.0	68.95	0.215	8.5×10^{-5}	0.228	2180	0.228	2180[a]	0.443
(1/3x2/3x3 in)				6.2×10^{-5}	0.028	405	0.256	2585[e]	0.471
(8.5x17x76.2mm)	11.0	75.84	0	8.6×10^{-5}	0.124	1349	0.380	3934[e]	0.595
	12.5	85.68	0	2.0×10^{-4}	0.213	1002	0.593	4936[e]	0.808
	15.0	103.4	0.014	2.5×10^{-4}	0.811	1848	1.404[a]	6784[e]	1.619
	21.0	144.8	0.646	4.5×10^{-3}	28.75	4266	30.15	11050[h]	31.0
B1	21.0	144.8	5.34	1.4×10^{-3}	1.76	666	1.76	666[a]	7.10
(1/3x10/3x3 in)				8.8×10^{-4}	1.03	1005	2.79	1671[a]	
(8.5x85x76.2mm)				1.7×10^{-3}				3000[c]	
					1.72	1587	4.51	3258[a]	9.85[g]
								3525[h]	
B2	10.0	68.95	0.273[i]	8.6×10^{-5}	0.31	1644	0.31	1644[a]	0.58
(1/3x10/3x3 in)	j			9.0×10^{-5}	0.14	1462	0.45	3106[e]	0.72
(8.5x85x76.2mm)	11.0	75.84	0	1.1×10^{-4}	0.16	1804	0.61	4910[e]	0.88
	12.5	85.68	0	2.0×10^{-4}	0.33	1364	0.94	6274[e]	1.21
	15.0	103.4	0.051	4.7×10^{-4}	1.00	1302[a]	1.93	7576[e]	1.98
	21.0	144.8	1.88	8.4×10^{-3}	16.47	1563	18.40	9139[h]	20.33

*HT 9T2796, annealed 2000F (1094C)

[a]Interrupted for photographic measurement

[b]Transition at 0.2% OFFSET

[c]Transition at double minimum rate

[d]Rupture, R

[e]Stress raised (step-loaded test)

[f]Test in progress

[g]Crack initiated

[h]Test terminated, crack tearing

[i]Strain gage average, bending noted

[j]Specimen rotated 180° to investigate bending

[k]Net Section Stress, Gross Section Stress = 0.9 N.S.S.

[l]Time at final strain

[m]Average overall strain

[p]Test in preparation

[q]Specimen to be sectioned to determine damage at 78% of estimated rupture life

[r]Deflection of notch, inches (25.4 mm)

[t]True strain = In(Ao/A)

[u]Test interrupted, 1/2 of specimen continued

Table 6-2 (Continued)

Test No. (Gage Section)	Loading Data			Creep Data					
	Stress		Plastic Strain	Creep Rate	Increment		Accumulated		Permanent Strain
	(ksi)	(MPa)	(%)	(%/hr)	Strain (%)	Time (hr)	Strain (%)	Time (hr)	(%)
C1	23.3[k]	160.6	8[n]		1.7[n]	100[c]			
(1/3x10/3x3in)							22.9[n]	138[d]	
(8.5x85x76.2mm)									
Central Hole									
1/3in(8.5mm)dia.									
C2	10.0[k]	68.95	0.14[n]		0.62[n]	2808[a]	0.62[n]	2808[e]	0.76[n]
Same as C1	11.0[k]	75.84	0		0.40[n]	1290	1.02[n]	4098	1.16[n]
	12.5[k]	85.68	0		0.50[n]	1300[a]	1.52[n]	5398	1.66[n]
	15.0[k]	103.4	0.28[n]		0.82[n]	1148	2.34[n]	6546	2.76[n]
	18.0[k]	124.1	0.06[n]		3.31[n]	1630[a]	5.65[n]	8176[g]	6.13[n]
					0.89[n]	791[a]	6.54[n]	8967	7.02[n]
					1.05[n]	944[a]	7.59[n]	9911	8.07[n]
					1.12[n]	1339[a]	8.71[n]	11250	9.19[n]
					1.60[n]	1468 6172[d]	10.30	12718[h]	10.79
C3	21.0[k]	144.8	4.4[n]		1.5[n]	325[c]			
Same as C1							4.1[n]	397[h]	8.5[n]
D1	30.0	206.8							
D=.96 in(24.4mm)									
d=.64 in(16.2mm),									
R=.19 in(0.46mm)									
D1-1	30.0	206.8	2.60[t]		0.30[t]	137	0.30[t]	137	2.90[t]
					0.20[t]	102	0.50[t]	239[g]	3.10[t]

[*] HT 9T2796, annealed 2000F (1094C)

[a] Interrupted for photographic measurement

[b] Transition at 0.2% OFFSET

[c] Transition at double minimum rate

[d] Rupture, R

[e] Stress raised (step-loaded test)

[f] Test in progress

[g] Crack initiated

[h] Test terminated, crack tearing

[i] Strain gage average, bending noted

[j] Specimen rotated 180° to investigate bending

[k] Net Section Stress, Gross Section Stress = 0.9 N.S.S.

[l] Time at final strain

[m] Average overall strain

[p] Test in preparation

[q] Specimen to be sectioned to determine damage at 78% of estimated rupture life

[r] Deflection of notch, inches (25.4 mm)

[t] True strain = In(Ao/A)

[u] Test interrupted, 1/2 of specimen continued

Table 6-2 (Continued)

Test No. (Gage Section)	Loading Data: Stress (ksi)	Stress (MPa)	Plastic Strain (%)	Creep Data: Creep Rate (%/hr.)	Increment Strain (%)	Increment Time (hr)	Accumulated Strain (%)	Accumulated Time (hr)	Permanent Strain (%)
G1	25.0	172.4	2.00[i]		0.88[i]	47[a]	0.88	47	2.47
				3.5×10^{-3}	1.12[i]	268[a]	2.00	315	4.00
				—	0.90[i]	170[a]	2.90[c]	485[g]	4.90
				—	0.65[i]	83	3.55	568[h]	5.60
G2	21.0	144.8	0.43	3.9×10^{-4}	1.34	1195[a]	1.34	1195	1.77
(1/3x10/3x1 in)			0	1.0×10^{-4}	0.83	5520[a]	2.17	6715[e]	2.60
(8.5x85x25mm)	25.0	172.4	0.01	2.3×10^{-3}	1.80	700	—	7415	—
				—	2.50	450[c]	4.67	7865	—
				—	4.43	283[a]	6.60	8148	—
				—	—	1827[l]	—	8552[d]	—
BAW-1	25.0	172.4	0.25	8.3×10^{-3}	4.35[n]	477[a]	4.35	477	4.60[g]
B Type Specimen				1.1×10^{-2}	8.32[n]	765[a]	12.67	1242	12.92
With Central Axial				1.5×10^{-2}	3.42[n]	216[a]	16.09	1458	16.34
Weld				—	2.35[n]	71	18.44	1529	18.69
				—	—	—	—	1532[d]	—
CAW-1	18.0	124.1	0.03	—	0.42	791	—	—	—
C Type Specimen					0.33		0.75	2998[f]	
With Central Axial									
Weld									
DTW-2	25.0	172.4						3546[b]	
GAW-1	23.0	158.6	0.10[n]	5.1×10^{-3}	1.56[n]	1882	1.56[n]	188	1.65[n]
G. Type Specimen				4.2×10^{-3}	1.93[n]	452[a]	3.59[n]	640	3.69[n]
With Axial				5.3×10^{-3}	1.64[n]	307[a]	5.13[n]	947	5.23[n]
Weld				5.3×10^{-3}	2.00[n]	379[a]	7.13[n]	13269	7.23[n]
				—	2.21[n]	456[a]	9.34[n]	1782	9.44[n]
					0.64[n]		9.90	1901[f]	
BTW-1	21.0	144.8	0.17[n]	3.2×10^{-3}	1.29[n]	339[a]	1.29[n]	339	1.47[n]
B Type Specimen			0.01	3.2×10^{-3}	2.35[n]	718[a]	3.64[n]	1057[g]	3.82[n]
With Transverse					1.25[n]	474[a]	4.89[n]	1531	5.07[n]
Weld							5.67[n]	1724	
								1734[d]	
GTW-1	25.0	172.4	0.09	4.7×10^{-3}	1.62[n]	240[a]	1.62	240	1.71
G Type Specimen				—	—	208	—	448[d]	—
With Transverse Weld									

[*] HT 9T2796, annealed 2000F (1094C)

[a] Interrupted for photographic measurement

[b] Transition at 0.2% OFFSET

[c] Transition at double minimum rate

[d] Rupture, R

[e] Stress raised (step-loaded test)

[f] Test in progress

[g] Crack initiated

[h] Test terminated, crack tearing

[i] Strain gage average, bending noted

[j] Specimen rotated 180° to investigate bending

[k] Net Section Stress, Gross Section Stress = 0.9 N.S.S.

[l] Time at final strain

[m] Average overall strain

[p] Test in preparation

[q] Specimen to be sectioned to determine damage at 78% of estimated rupture life

[r] Deflection of notch, inches (25.4 mm)

[t] True strain = In(Ao/A)

[u] Test interrupted, 1/2 of specimen continued

Table 6-2 (Continued)

Test No. (Gage Section)	Loading Data			Creep Data					
	Stress		Plastic Strain	Creep Rate	Increment		Accumulated		Permanent Strain
	(ksi)	(MPa)	(%)	(%/hr)	Strain (%)	Time (hr)	Strain (%)	Time (hr)	(%)
D1-2	30.0	206.8	2.20[t]		0.26[t]	137	0.26[t]	137	2.46[t]
					0.22[t]	113	0.48[t]	250[c]	2.68[t]
							10.92[t]	305[d]	13.12[t]
D2-1	25.0	172.4	0.009[r]				0.006[r]	1371	0.015[r]
								1371[g]	2.17[t]
D2-2	25.0	172.4	0.009[r]				0.006[r]	1240[c]	
								1371[d]	5.3[t]
D3	21.0	144.8	0.002[r]					5499[h]	
D4	10.0	68.95	0			406		406[e]	
	11.0	75.84	0			477		883[e]	
	12.5	85.68	0			434		1317[e]	
	15.0	103.40	0			404		1721[e]	
	21.0	144.80	0.001[r]		0.004[r]	433		2154[e]	
	25.0	172.40	0.003[r]		0.033[r]	1581[g]		3735[u]	
D4-1	One Notch of Specimen D4 to be Sectioned.								
D4-2	25.0	172.40				2904[h]		5058[h]	
D5	23.0	158.4				1681[g]		1681	
D5-1	One Notch of Specimen D5 to be Sectioned.								
D5-2	23.0	158.4				150		1831[d]	
D6	20.0	137.9			1.0[t]	4023[u]			

[*] HT 9T2796, annealed 2000F (1094C)

[a] Interrupted for photographic measurement

[b] Transition at 0.2% OFFSET

[c] Transition at double minimum rate

[d] Rupture, R

[e] Stress raised (step-loaded test)

[f] Test in progress

[g] Crack initiated

[h] Test terminated, crack tearing

[i] Strain gage average, bending noted

[j] Specimen rotated 180° to investigate bending

[k] Net Section Stress, Gross Section Stress = 0.9 N.S.S.

[l] Time at final strain

[m] Average overall strain

[p] Test in preparation

[q] Specimen to be sectioned to determine damage at 78% of estimated rupture life

[r] Deflection of notch, inches (25.4 mm)

[t] True strain = In(Ao/A)

[u] Test interrupted, 1/2 of specimen continued

Table 6-2 (Continued)

Test No. (Gage Section)	Loading Data			Creep Data					
	Stress		Plastic Strain	Creep Rate	Increment		Accumulated		Permanent Strain
	(ksi)	(MPa)	(%)	(%/hr)	Strain (%)	Time (hr)	Strain (%)	Time (hr)	(%)
D6-1	One Notch of Specimen D6 to be Sectioned.								
D6-2	20.0		137.9					1821	
E1	13.0[n]	89.6	9.1		3.6	90	3.6	90[a]	
					3.2	650	6.8	740[e]	
					0.8	170	7.6	910[e]	
					0.7	180	8.3	1090[e]	
						130	9.05	1220[e]	
						140	9.6	1360[a]	
						250	10.5	1610[e]	
						195	11.2	1805[e]	
						205	11.9	2010[e]	
						280	12.8	2290[e]	
						190	13.5	2480[e]	
						23	13.65	2503[b]	

*HT 9T2796, annealed 2000F (1094C)

[a]Interrupted for photographic measurement

[b]Transition at 0.2% OFFSET

[c]Transition at double minimum rate

[d]Rupture, R

[e]Stress raised (step-loaded test)

[f]Test in progress

[g]Crack initiated

[h]Test terminated, crack tearing

[i]Strain gage average, bending noted

[j]Specimen rotated 180° to investigate bending

[k]Net Section Stress, Gross Section Stress = 0.9 N.S.S.

[l]Time at final strain

[m]Average overall strain

[n]Nominal elastic bending stress.

[p]Test in preparation

[q]Specimen to be sectioned to determine damage at 78% of estimated rupture life

[r]Deflection of notch, inches (25.4 mm)

[s]Loaded and reload to determine retained bending

[t]True strain = In(Ao/A)

[u]Test interrupted, 1/2 of specimen continued

1. In the current analyses the specimens were allowed to creep under a constant load, whereas in the experiment the specimens were unloaded and reloaded a few times during the test duration. Furthermore, the specimen loading sometimes took a significant time and, at elevated temperature, may have caused additional creep strain which may have to be separated from time-independent plastic strain. Therefore, in all future nonlinear analyses, an attempt will be made to follow the actual load histogram.

2. The lateral restraint has considerable influence on the stress distribution in the fillet region of the specimen. Therefore, it may be necessary to model more realistically the actual lateral restraint experienced by the specimen.

3. Some of the test specimens show cracks near the fillet radius in the transition region. Further refinement of the analytical model might help in understanding the specimen behavior in the transition region. This region is complicated by the multiaxial stress state and high strain gradients; hence its behavior will be investigated in detail and may have to be differentiated from the overall inelastic behavior in the uniform section of the specimen, where stress distribution is not significantly affected by the boundary constraints.

4. The effect of higher order elements on the accuracy of the predicted results will be evaluated with respect to presently available analytical techniques.

5. If a better mathematical creep model is available, it will be incorporated in the analysis and its behavior compared with the single exponential creep equation.

6. The relative damage calculations, at various locations of the specimen, will be evaluated with state-of-the-art and/or hypothesized damage rules.

7. To evaluate the effect of the material property variation on the analytical prediction capability, a sensitivity study will be conducted on one of the basic specimens. The material properties that will be varied in the contemplated detailed inelastic anlayses are the yield stress, the work-hardening slope, and the creep equation constants.

6.2.2 Uniaxially Loaded Specimen Models with Nonuniform Gage Section

6.2.2.1 Test Piece Description

Types C, D, and E test piece designs, as shown in Table 6.1, are used for this part of the test program.

6.2.2.2 Current Results

The double-notch specimen D6, machined from one-inch diameter bar stock and annealed after finished machining, was tested for 4023 hours when an examination revealed cracks in both notches. The two notches were separated, and the test was continued on one of the notches. This phase of testing has continued for an additional 1821 hours.

When Specimen E1 was unloaded from 20 ksi at 94 hours, it was noted that an elastic bending stress was still evident. Therefore, the specimen was unloaded at 742 and 909 hours to measure the relaxation of the bending stress. At 1024 hours the creep strain on the higher stressed side was 8.1 percent while that on the other side was only 4.8 percent. The average creep rate is about 3.5×10^{-3} percent per hour, which is about 4 times that for simple tension under the same average stress. The effect of the eccentric loading at 1786 hours has diminished but is still evident after 9 percent average creep strain. The average creep rate is about three times that estimated for tension loading. The test is still in progress at 2503 hours.

6.2.3 Specimens with Welds (304 SS, Heat 9T2796)

6.2.3.1 Test Piece Description

The weld specimens are described in Table 6.1 and Figure 6.1.

6.2.3.2 Current Results

Specimen CAW-1 has been loaded at 18 ksi for 2998 hours, and the test is continuing.

Specimen DTW, at 25 ksi, is still in progress at 3546 hours. The base metal sample failed in about 1400 hours at these test conditions.

Thus, the weld metal has a notch strength higher than that of the base metal.

Specimen GAW-1 failed at 3096 hours. Cracks in the heat-affected zone were initiated at 1782 hours, which is about one-half of the expected life. Interruptions were made to photograph specimens at 188, 680, 947, 1326, 1782, 2358, and 2886 hours to determine initiation and propagation of cracks; grid strain photographs were also taken. Details of this test will be discussed and the data evaluated in future reports.

6.3 TUBULAR SPECIMEN TESTING - K. C. Thomas, P. C. S. Wu

6.3.1 Test Piece Description

The tubular test pieces used in this program are Type 304 SS, Heat 9T2796, of 1.8-inch OD, 1.6-inch ID, and 8.7-inch length. However, thinner wall (1.7-inch OD and 1.6-inch ID) test pieces are planned for use in future tests to reduce the stress variation through the wall thickness during multiaxial testing.

6.3.2 Test Results and Planning (304 SS, Heat 9T2796)

Current test results are shown in Table 6.3.

Four multiaxial creep tests (Nos. 6, 8, 9, and 12) were completed during the present report period. Multiaxial Test No. 6 was terminated after 808 hours due to sample burst. The specimen was tested under 2729 psi internal pressure and no axial load with an effective stress of 20,000 psi and stress ratio ($\sigma_{hoop}/\sigma_{axial}$) of 2.0. Tests No. 9 and No. 12 were terminated after 573 and 1096 hours, respectively. These specimens were tested under the same stress level as Test No. 6 and were already in the tertiary creep stage; therefore, these tests were terminated for safety reasons. Multiaxial Creep Test No. 8, tested under 1515 lbs. axial load and 2000 psi internal pressure (with nominal effective stress of 15,000 psi), has also been completed for its intended 2000-hour test. The creep-strain relationship obtained from these tests has not been completed finished and corrections have to be made before reporting. The final computer printouts obtained from the tests completed during this quarter will be reported during the next report period.

Table 6-3. 304 SS Tubular Test Results

Uniaxial Creep Test Results

Test No.	Nominal Test Temperature (°F)	Axial Stress (psi)	Test Hours Accumulated	Axial Loading Strain (%)	Axial Creep Strain (%)	Total Axial Strain (%)
1B	1100	25,000	241.5	0.7988	3.5572	4.3660
2A	1100	10,000	2016	0.0490	0.0697	0.1187
2B	1100	10,000	2000	0.0780	0.0880	0.1660
3A	1100	20,000	336	- - -	0.9591	- - -
3B	1100	20,000	1990	0.1783	2.7468	2.9251
3C	1100	7,700	2002	0.0461	0.0534	0.0995
3D	1100	5,000	1721.3	0.0253	0.0089	0.0342

Multiaxial Creep Test Results

Test No.	Nominal Test Temp. (°F)	Axial Load (lbs)	Nominal Internal Pressure (psi)	Nominal Effective Stress (psi)	Nominal Principal Stress Ratio (σ_θ/σ_z)	Test Time (hours)	Average[a] Loading Strain (%)		Nominal Average Creep Strain[a]			
							Axial	Hoop	Radial	Hoop	Axial	Effective
4A	1100	323.0	1209.5	10,000	2.0	1965.7	0.01048	0.02174	-0.12711	0.12466	0.00245	0.1453
5	1115	484.0	1814.3	15,000	2.0	1998.0	0.09208	0.08499	-0.57795	0.54670	0.03125	0.6499
6[c]	1100	0.0	2716.9	20,000	2.0	762.0	0.13321	2.71103	-2.12850	2.16000	-0.03150	2.4700
7A	1100	1211.0	1180.0	10,000	1.5	1648.0	0.04240	0.03521	-0.02101	0.01360	0.00741	0.0211
7[b]	1100	1211.0	1180.0	10,000	1.5							
8	1100	1515.0	2000.0	15,000	1.5	2009.3	0.19414	0.80047	-0.84800	0.71900	0.12900	0.9130
9[d]	1100	2018.6	2668.4	20,000	1.5	573.4	0.00541	0.02334	-3.74600	3.31000	0.43600	4.0900
10	1100	2670.0	1049.4	10,000	1.0	2033.8	0.04363	0.01994	-0.06130	0.03890	0.03330	0.0600
11	1100	4005.0	1574.0	15,000	1.0	2012.9	0.03288	0.07339	-0.48900	0.21100	0.27800	0.4720
12[d]	1100	5340.7	2353.0	20,000	1.0	1096.5	1.82117	0.99892	-2.82000	1.56000	1.26000	2.7900

(a) The axial loading strain is the average of two readings.
The loop strain is the average of three readings.

(b) Test terminated due to instability of the strain measuring system.

(c) Sample rupture after 808 hours under the test condition.

(d) Test terminated because the sample has already reached tertiary creep stage.

A preliminary and two interim reports were issued on the unusual occurrence in which Multiaxial Creep Test No. 6 was terminated due to tear 5-1/2 inches long and visual examination of the specimen revealed that longitudinal cracking and bulging preceded the rupture. Metallographic examination of the burst sample was conducted to reveal structural information which is pertinent to understanding the material behavior under the test condition. The morphology of the bursting and the locations where specimens were taken for microstructural analysis are shown in Figure 6.2. Eleven specimens were examined and the observations were consistent. In general, cracks were initiated at both outside and inside surfaces; however, they initiate predominantly from the outside surface and penetrate toward the inside surface, as shown in Figures 6.3 and 6.4. Crack initiation from the outside results from the fact that the sample was tested in air while internally pressurized with argon. Therefore oxidation, particularly along grain boundaries, apparently contributes to crack initiation and propagation.

The penetration depth of the cracks was deeper in the middle than at the ends of the sample. In most cases the depth of penetration was more than halfway through the wall thickness. At one point, the crack seemed to penetrate the total wall and led to a pinhole which might have caused the loss of test pressure. The microstructure of the fractured surface at Locations 1 and 2 is shown in Figure 6.5. It was noted that severe grain boundary separation occurred. In some cases, the whole grain fell out during polishing and left a hole behind. The grain size distribution of the sample at the fractured interface is shown in Figure 6.6. Again, severe oxidation at the fractured interface and grain boundary separation within the matrix was observed. The grain size of the test sample ranges from ASTM grain size No. 1 to No. 5; however, the fracture seems to occur along the boundaries of predominantly large grains. In addition, the direction of the crack propagation is found to be normal to the hoop stress. This is consistent with the fact that the hoop stress is twice as much as the axial stress for the specimen.

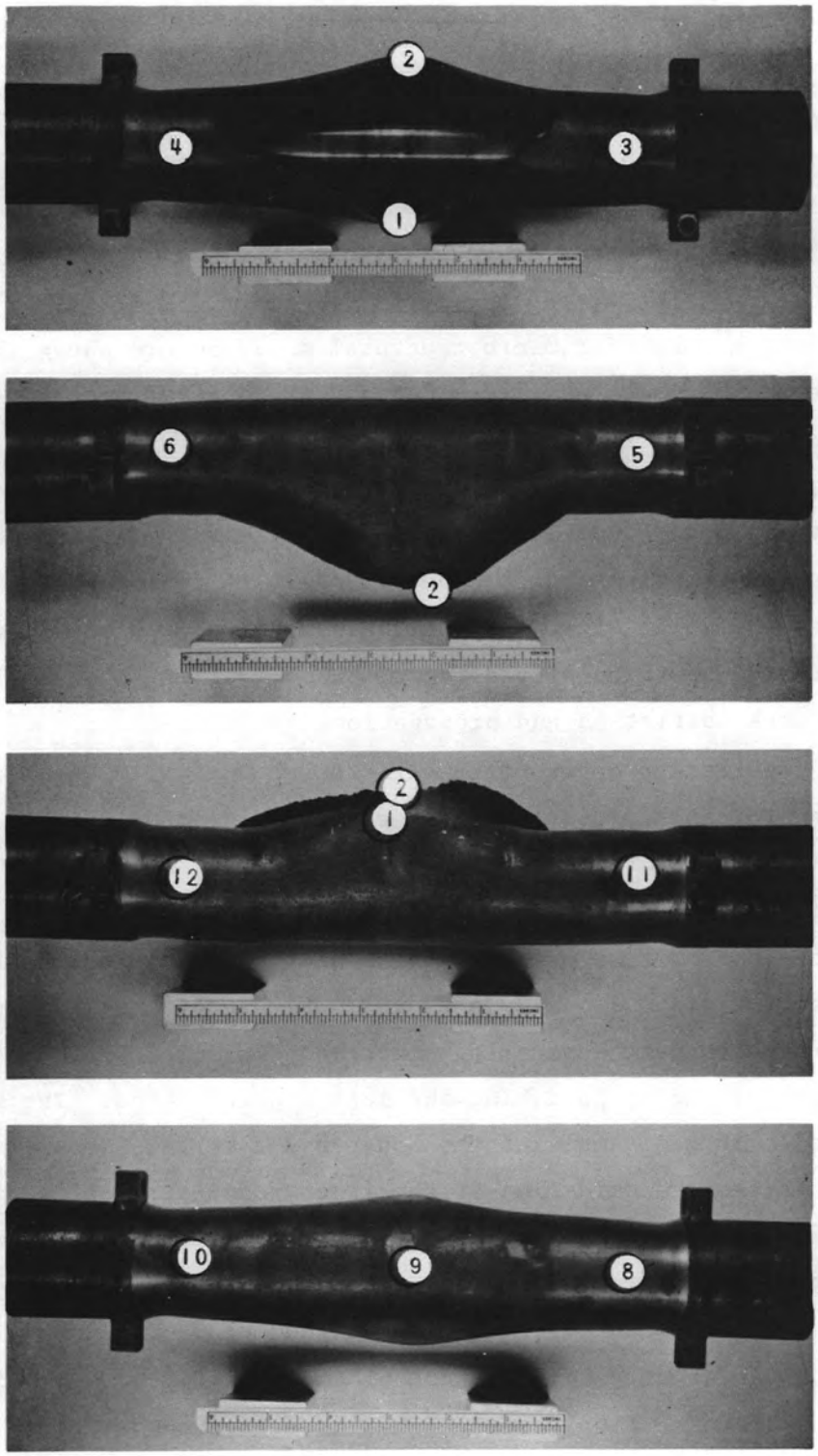

Figure 6-2 Burst Morphology and the Locations Where Specimens Where Taken for Microstructural Analysis

6619-6

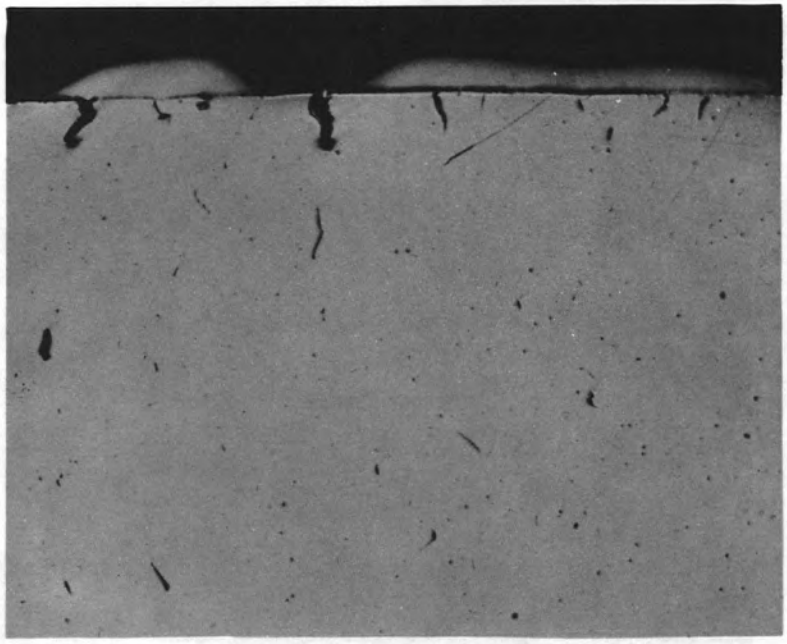

OUTSIDE SURFACE 50X

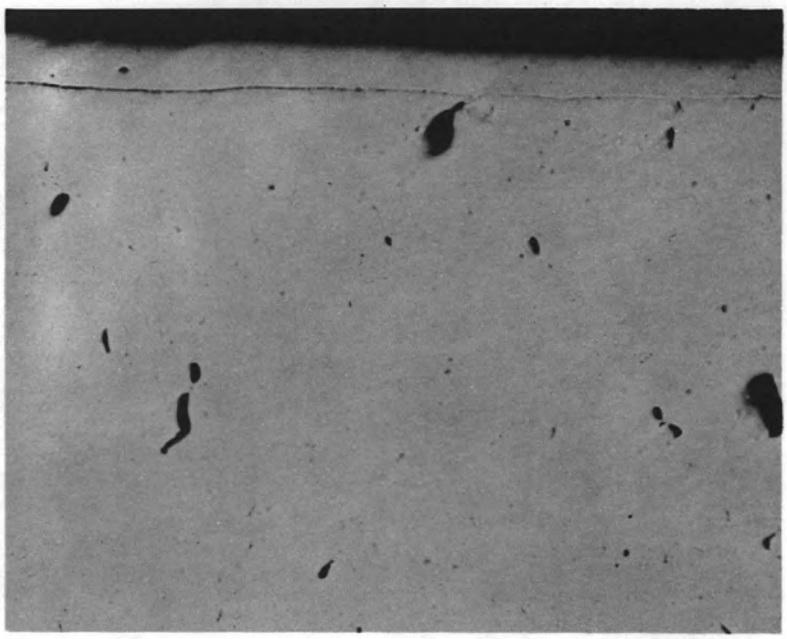

INSIDE SURFACE 50X

Figure 6-3 Surface Condition of the Specimen Taken at Location 1 Shown in Figure 6-2

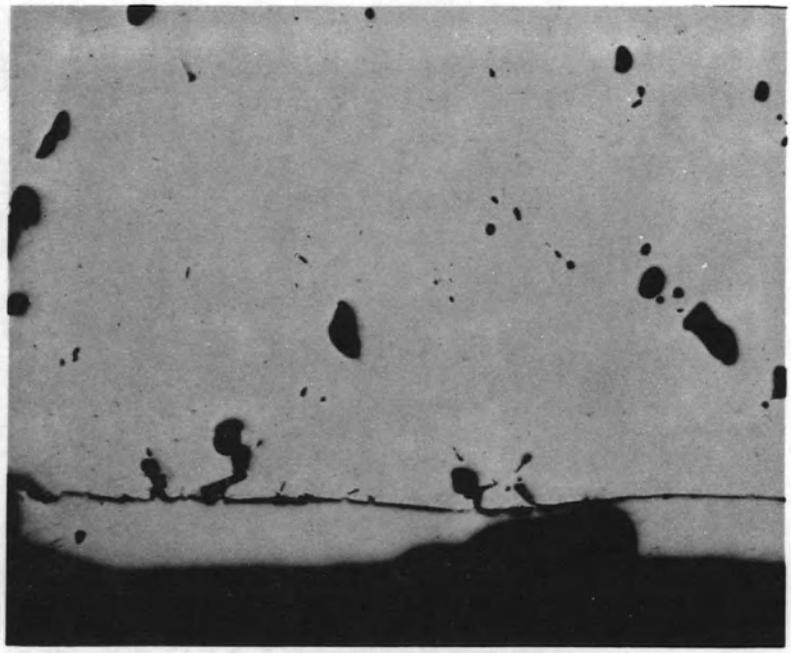

OUTSIDE SURFACE 50X

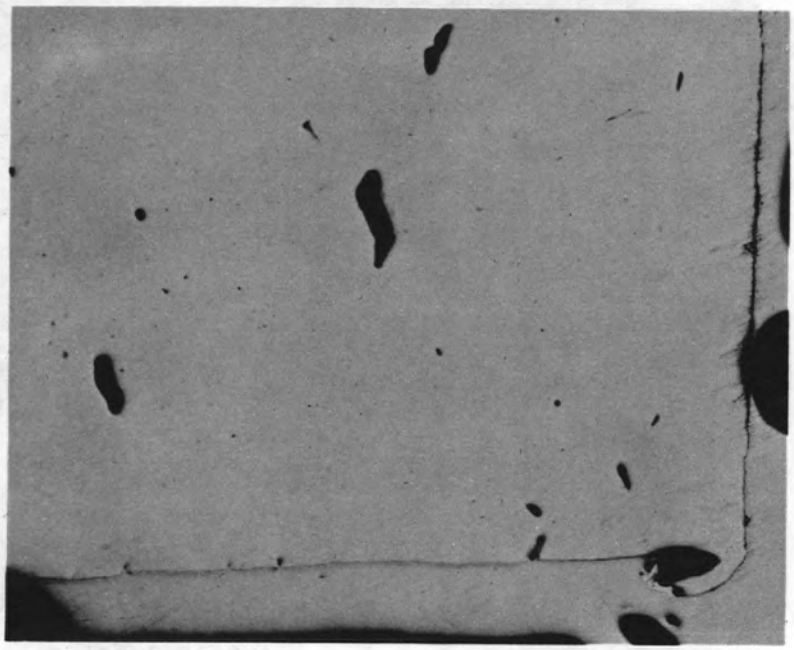

INSIDE SURFACE 50X

Figure 6-4 Surface Condition of the Specimen Taken at Location 2 Shown in Figure 6-2

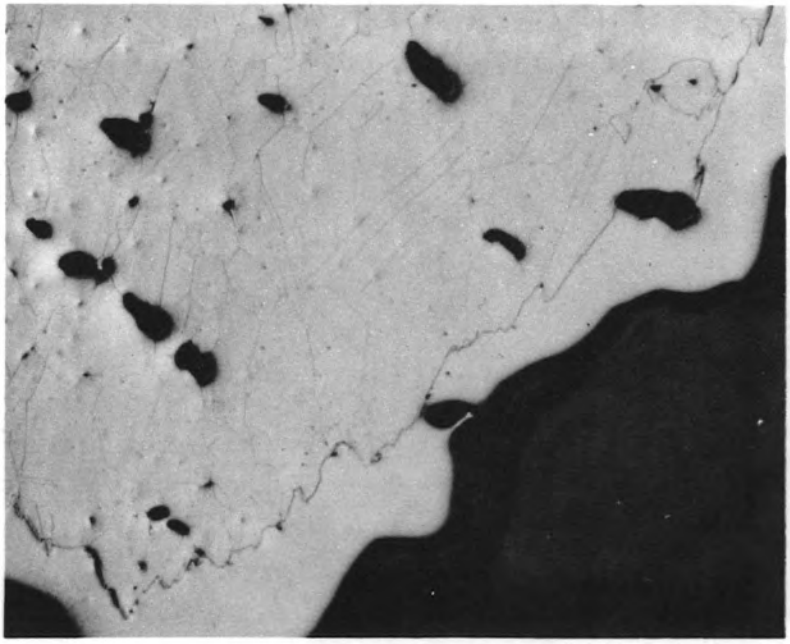

LOCATION 1 200X

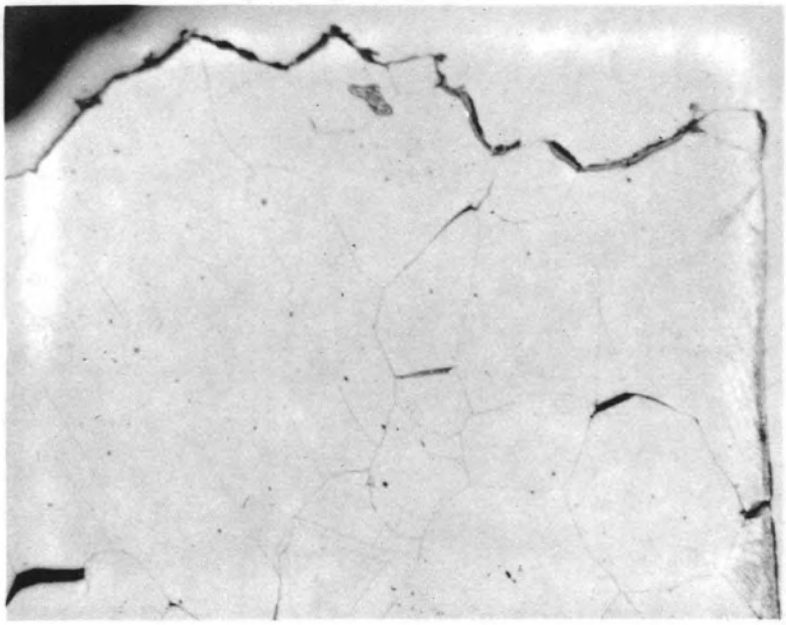

LOCATION 2 200X

Figure 6-5 Microstructure of the Fractured Surface Type 304 SS (Heat 9T2796), Gly.HCl-HNO_3 etch

6619-2

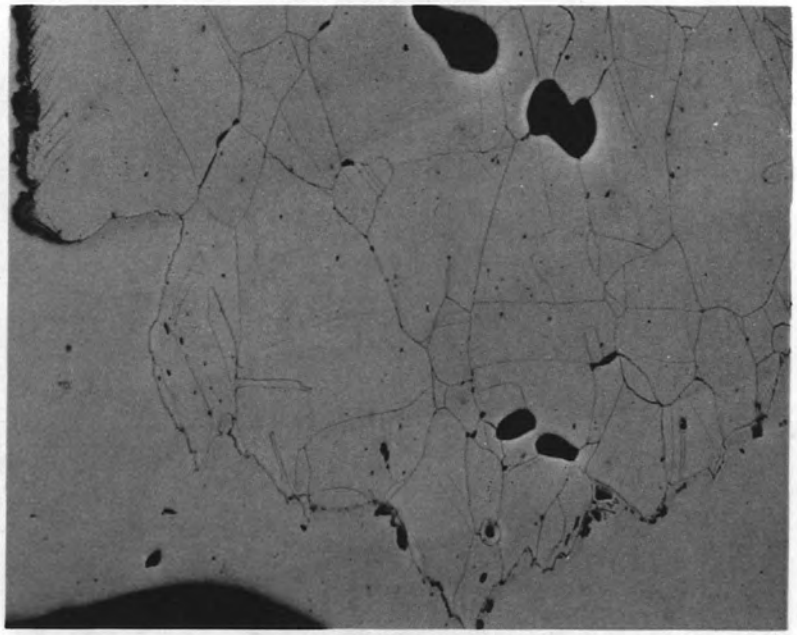

LOCATION 1 100X GRAIN SIZE 1 TO 5

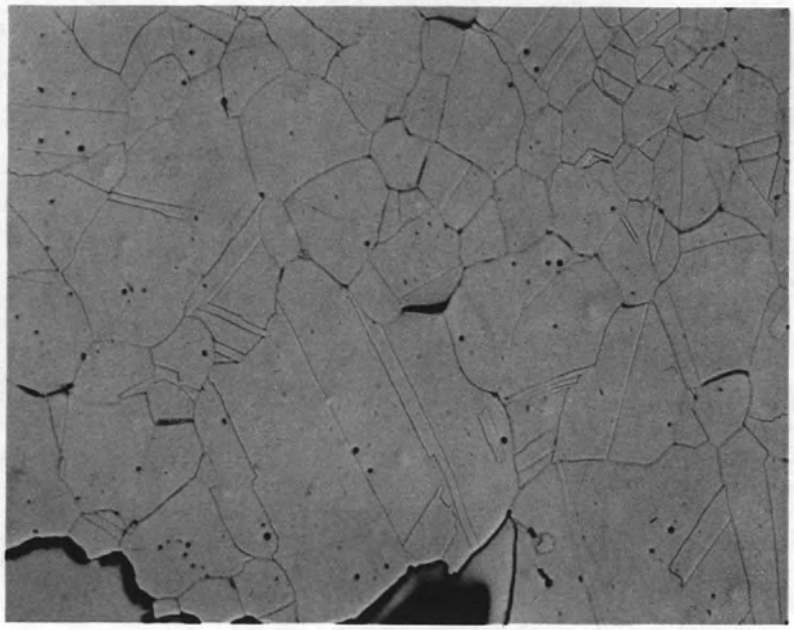

LOCATION 2 100X GRAIN SIZE 1 TO 3

Figure 6-6 Grain Size Distribution of Test Sample Type 304SS (Heat 9T2796), Gly. HCL-HNO_3 etch

6619-1

Available literature on creep-rupture of tubular specimens was surveyed to evaluate test condition selection. It was concluded that stress-to-rupture correlates better with the "maximum stress" as opposed to "effective stress" criterion. Future test planning will use the "maximum stress" criterion and modified thin cylinder formula based on the equilibrium tube model[1]. Additional proposals are as follows:

1. Correlate multiaxial stress data to uniaxial initiation of tertiary creep (0.2 percent offset) data instead of the uniaxial creep to rupture data.

2. In future tests planned to study secondary creep rate, the creep stress rupture level, based on the uniaxial tertiary creep initiation data, will be conservatively reduced by 20 percent to avoid creep rupture.

3. To investigate the variation in the material properties in the axial and the circumferential directions, tests will be conducted on flat uniaxial specimens of the same geometry and fabricated from the reference heat (9T2796) 304 SS tube. These tests will establish the instantaneous stress-strain curve as well as the creep rupture life for the two orientations of the test samples. The tubular specimen rupture life will then be re-evaluated based upon the results obtained from the uniaxial tests.

6.3.3 316 SS Tubular Testing

Initiation of effort on this task is pending receipt of reference heat material from ORNL; currently scheduled for November 1974.

6.4 REFERENCES

1. Westinghouse Advanced Reactors Division, *Validation of High Temperature Design Methods and Criteria, Quarterly Progress Report for Period Ending February 28, 1974*, WARD-HT-3045-5.

7. UNIVERSITIES

7.1 UNIVERSITY OF CINCINNATI — J. Moteff

7.1.1 Introduction

The objective of this program is to (a) evaluate the time, temperature and stress dependent properties of several austenitic stainless steels, (b) determine the relation of these properties to the microstructure and (c) show the contribution of grain boundary microcracking to the plastic deformation behavior at high temperature. Special consideration has been given to operating conditions typical of nuclear reactor applications, including the knowledge that the radiation environment can influence the substructure of these metals, a circumstance which can lead to significant changes in the mechanical property behavior. Related substructure studies on other metals and alloys are also being investigated.

7.1.2 Experimental Program

Transmission electron microscopy has been used to study the deformation substructure resulting from fatigue, tensile and creep deformation at elevated temperatures. Grain boundary behavior in specimens which have been plastically deformed at elevated temperature is being investigated. Special studies have been initiated on Incoloy 800 including the comparison of the substructure developed following both a push-pull and a bend fatigue testing mode. Work started on the evaluation of the substructure developed in 304 stainless steel tested in a

creep-fatigue (hold-time) mode is now undergoing analysis. Creep and tensile data from ORNL (Heat Number 9T2796) was evaluated through regression analysis in preparation for the correlation of the macroscopic deformation properties with the substructure results.

The work in progress will be presented according to the separate mini-research programs for convenience. A general description and a brief discussion will be given on several of the programs that are presently active.

7.1.2.1 Characterization of the Creep and Tensile Substructure of 304 Stainless Steel, Reference Heat 9T2796 — R. Bhargava

The characterization of the substructure of specimens fabricated from Reference Heat 9T2796 of AISI 304 stainless steel tested in the creep and tensile mode was initiated and the results from three specimens were reported before.[1] In the period of this progress report, the substructure evaluation of six additional specimens was completed. Figure 7.1 shows the substructure developed in three tensile tested specimens at temperatures of 538, 593, and 704°C. These specimens were tested at a strain rate of 8.33×10^{-5} sec^{-1}. At 538°C the substructure consisted of cells which are elongated and not so well formed as compared to those formed at 593°C. The increased mobility of dislocations at 593°C makes the cell structure a little more defined. At 704°C the recovery processes tend to develop thin cell walls into better defined boundaries and resulting substructure consisting of subgrains is formed.

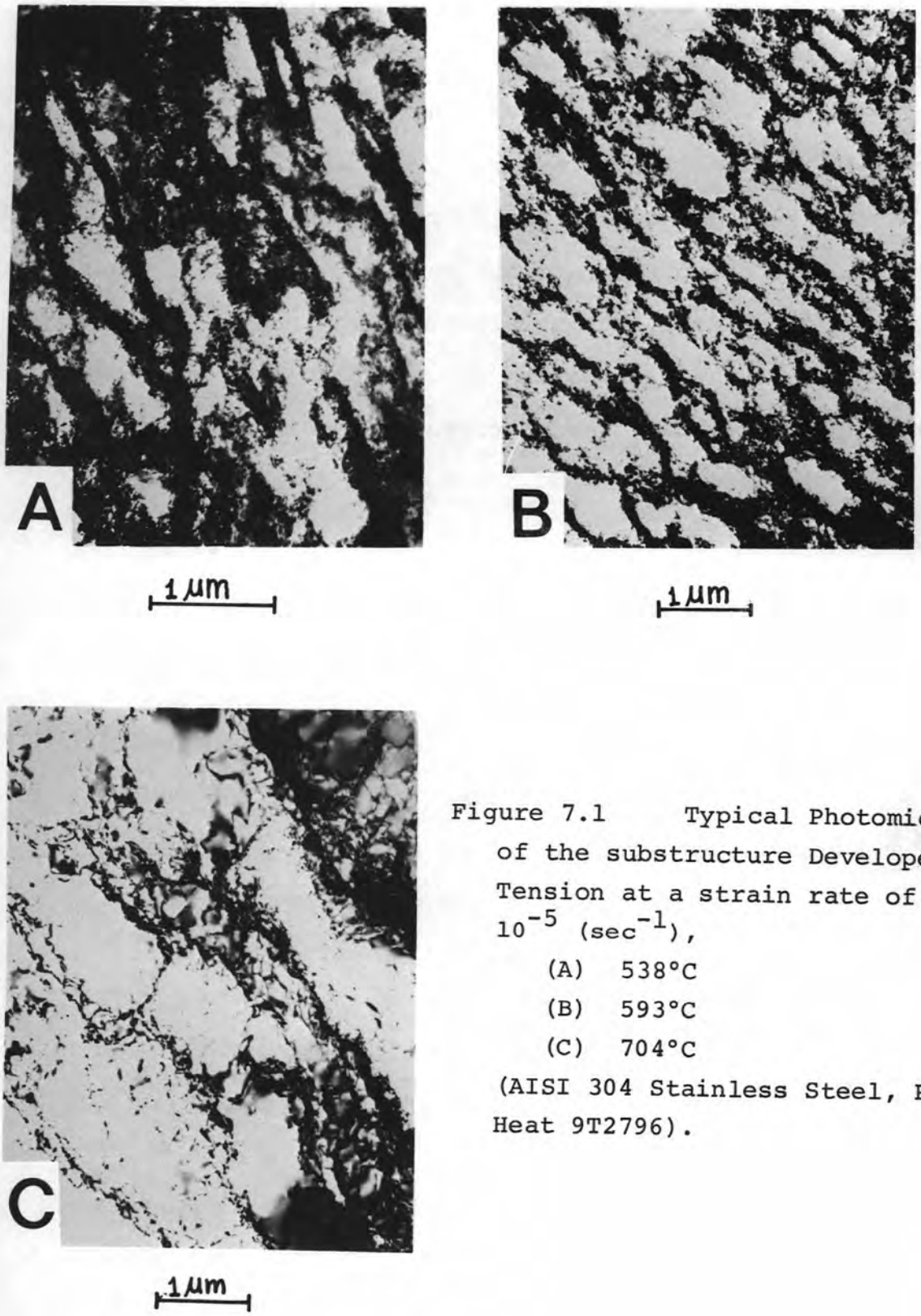

Figure 7.1 Typical Photomicrographs of the substructure Developed in Tension at a strain rate of 8.33 x 10^{-5} (sec^{-1}),

(A) 538°C

(B) 593°C

(C) 704°C

(AISI 304 Stainless Steel, Reference Heat 9T2796).

Figure 7.2 shows substructure representative of three specimens which are creep tested at 649°C. The applied stress levels were 25,000, 20,000 and 15,000 psi. The corresponding minimum creep rates were 4.6×10^{-3}, 8.7×10^{-4} and 1.5×10^{-4} sec^{-1}. The subgrain boundaries formed in the specimen tested at the fastest creep rate are not well defined and the subgrains are elongated. But at slower creep rates, the recovery processes allow the dislocation structure to form into well defined subboundaries. The specimen tested at 15,000 psi showed carbide precipitation. From the diffraction pattern analysis the precipitate is found of the nature $M_{23}C_6$. The cell or subgrain intercept for these specimens are plotted in Figure 7.3 versus a modulus compensated true stress parameter, σ/G. The solid line represents the relationship based on work published previously (See Figure 7.2 in Reference 1). More work is being done in characterization of the substructure and will be reported in future reports. The dislocation density measurements as well as the misorientation angle between various subgrains is also being determined and will be reported later.

7.1.2.2 Analysis of Relationships of Deformation Rate, Stress and Temperature for 304 Stainless Steel — R. Bhargava

Some results on the analysis of the creep data to determine the relationship between the steady state creep rate, temperature and stress for AISI 304 stainless steel (Reference Heat 9T2796) were presented in previous reports.[2,3] In or-

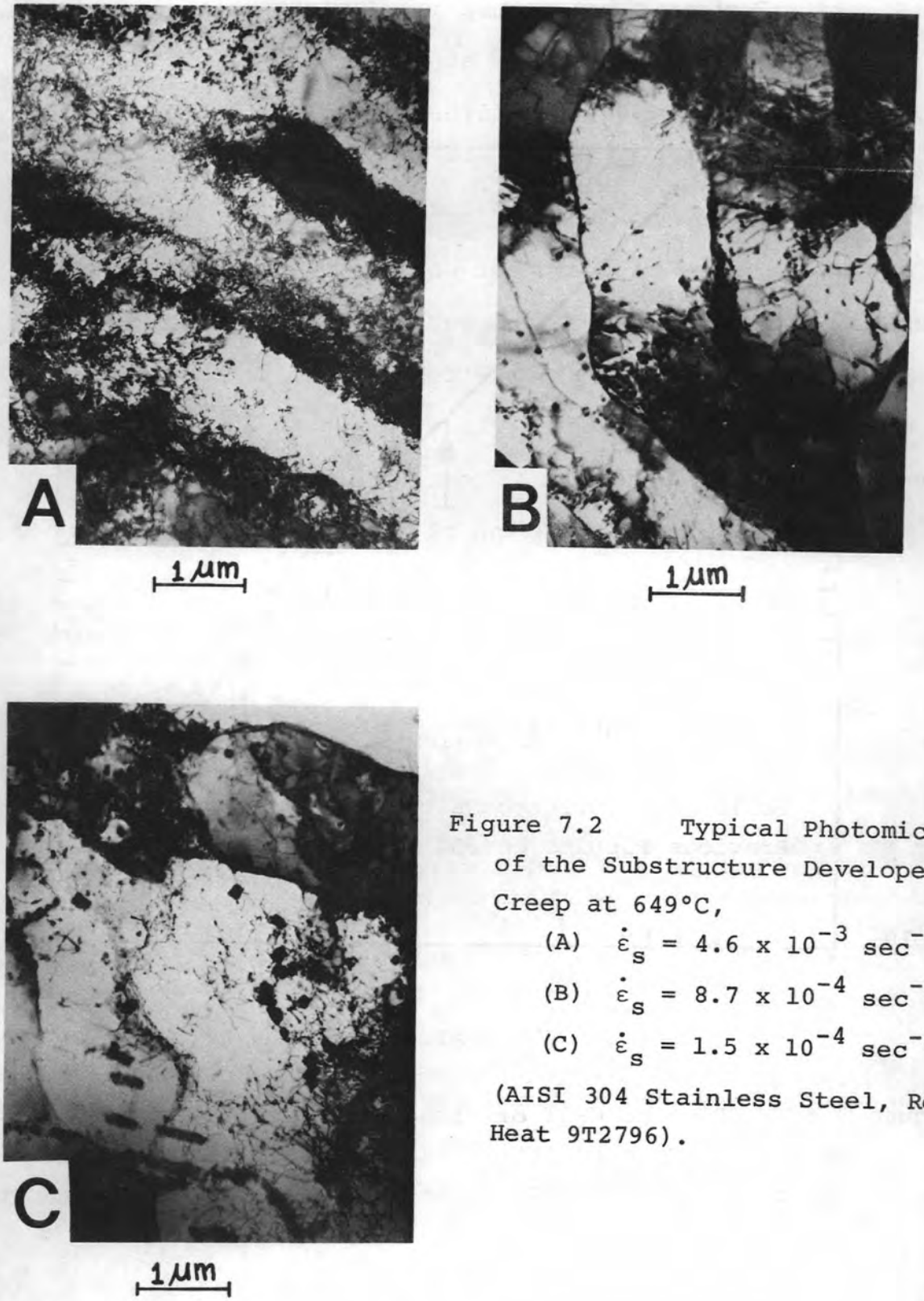

Figure 7.2 Typical Photomicrographs of the Substructure Developed in Creep at 649°C,

(A) $\dot{\varepsilon}_s = 4.6 \times 10^{-3}\ sec^{-1}$

(B) $\dot{\varepsilon}_s = 8.7 \times 10^{-4}\ sec^{-1}$

(C) $\dot{\varepsilon}_s = 1.5 \times 10^{-4}\ sec^{-1}$

(AISI 304 Stainless Steel, Reference Heat 9T2796).

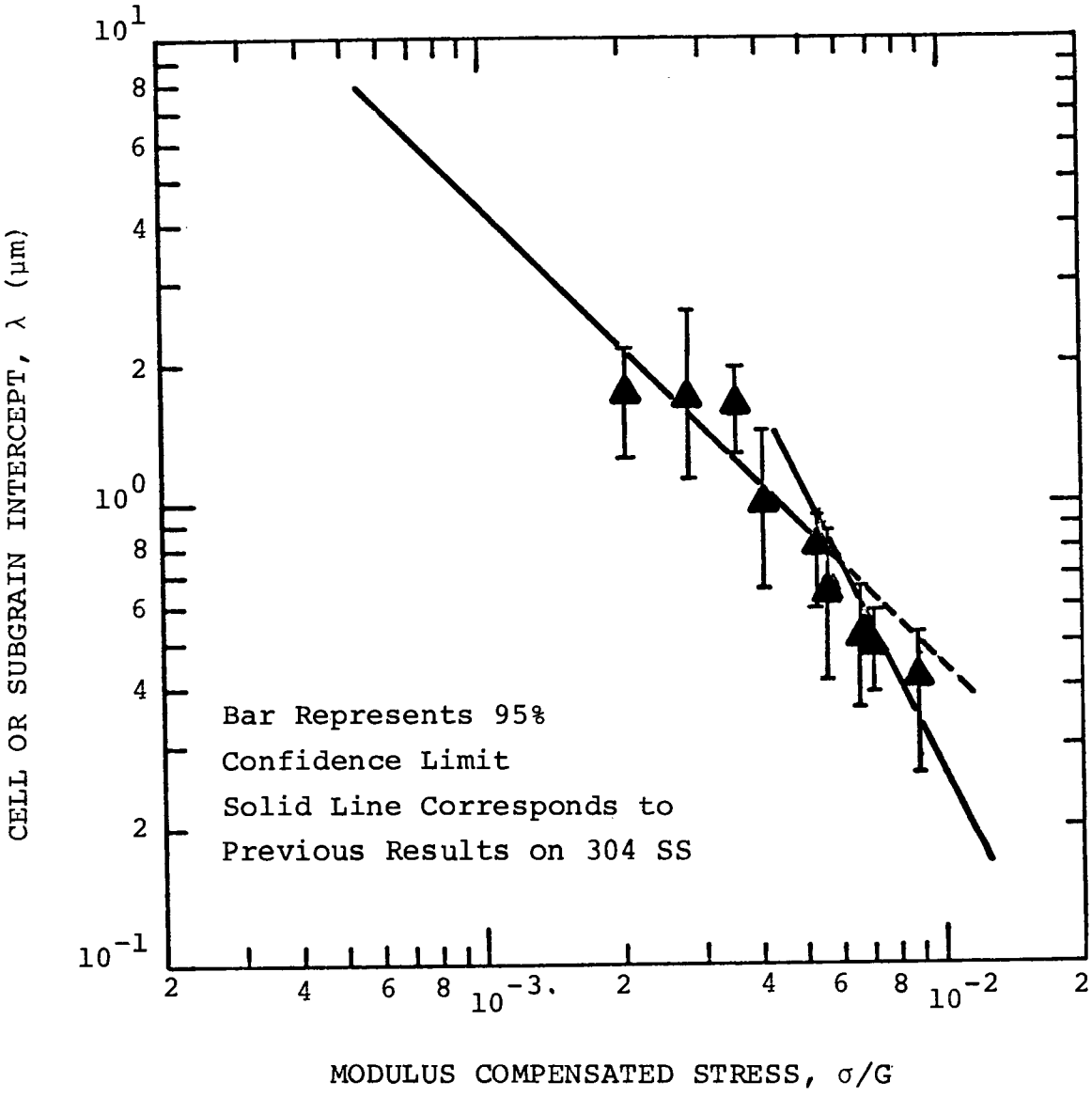

Figure 7.3 Plot of Cell or Subgrain Intercept versus Modulus Compensated Stress. (AISI 304 Stainless Steel) Reference Heat No. 9T2796.

der to further carry out this analysis over wider ranges of strain rates and stress levels the data obtained during tensile tests[4] have also been included in the analysis. As compared to the effective true stress determined for the creep tests, a similar true stress was obtained by using true ultimate tensile strength according to the following equation:

$$\sigma \text{ (True UTS)} = \sigma_{UTS} (1 + e_{UL}) \qquad [1]$$

where σ_{UTS} is the ultimate tensile strength and e_{UL} is the uniform elongation. The parameter σ/E (modulus compensated true stress)* was also evaluated in order to separate the effect of temperature on the stress levels. E is the Young's Modulus at the given test temperatures. The strain rates obtained from the tensile tests and the minimum creep rates from the creep tests are converted into a Zener Hollomon type parameter, Z, according to the following equation:

$$Z = \dot{\varepsilon} \exp (Q_c/RT) \qquad [2]$$

where Q_c is the apparent activation energy for creep and RT has its usual meaning. For the present comparison, the value of Q_c was set equal to 85,000 Cals/mole. The temeprature compensated deformation rate, Z, has been plotted in Figures 7.4-7.6 versus the modulus compensated true stress, σ/E.

At slower strain rates and lower stress levels a power law of the form

---

*The values of σ/G used previously and σ/E will normally differ by a constant. The shear modulus G generally is used in the correlation of strength with the dislocation substructure.

$$Z = A\ (\sigma/E)^n \qquad [3]$$

describes the data very well with the value of $n \sim 7.0$. A straight line (slope = 7.0) can be drawn through the data on log Z vs. log (σ/E) plot as shown in Figure 7.4. As the stress increases, the deformation rate increases at a much faster rate than predicted by Equation [3]. At higher stress levels, the deformation rate is described by the relation

$$Z = A'\ e^{\beta\sigma/E} \qquad [4]$$

The plot (Figure 7.5) of log Z vs. σ/E shows a linear relationship as predicted by Equation [4]. Again at lower stresses the deformation rate decreases much faster than predicted by Equation [4].

Garofalo[5] proposed an empirical relation of the form

$$\dot{\varepsilon} = K\ (\mathrm{Sinh}\ B\sigma)^n \qquad [5]$$

for the creep rate $\dot{\varepsilon}$ and stress σ. K, B and n are empirical constants. A similar analysis performed on the data shows that the temperature compensated deformation rate Z can be expressed as

$$Z = \mathrm{Constant}\ (\mathrm{Sinh}\ \alpha\ \sigma/E)^n \qquad [6]$$

with Z varying from $\sim 10^{11}$ to $\sim 10^{21}$ (sec^{-1}). As predicted by Equation [6], a straight line can be drawn in the plot (Figure 7.6) of log Z versus log Sinh ($\alpha\ \sigma$/E).

Further work is under way to determine functional relationships of the creep behavior which include explicit structural terms in the equations. This is consistent with the

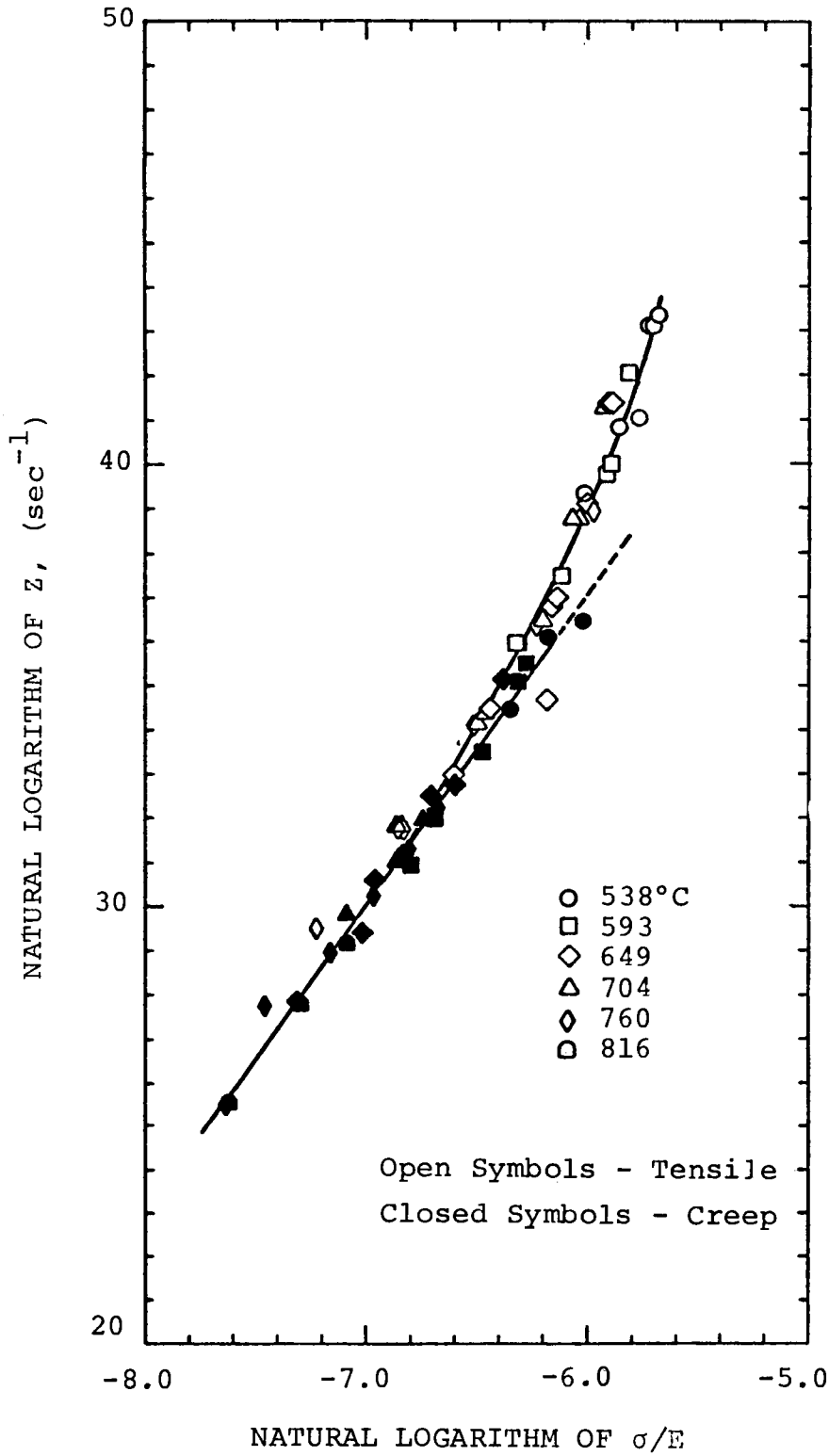

Figure 7.4 Plot of the Temperature Compensated Deformation Rate, Z, versus the Modulus Compensated Stress, σ/E, on a ℓn-ℓn Scale.

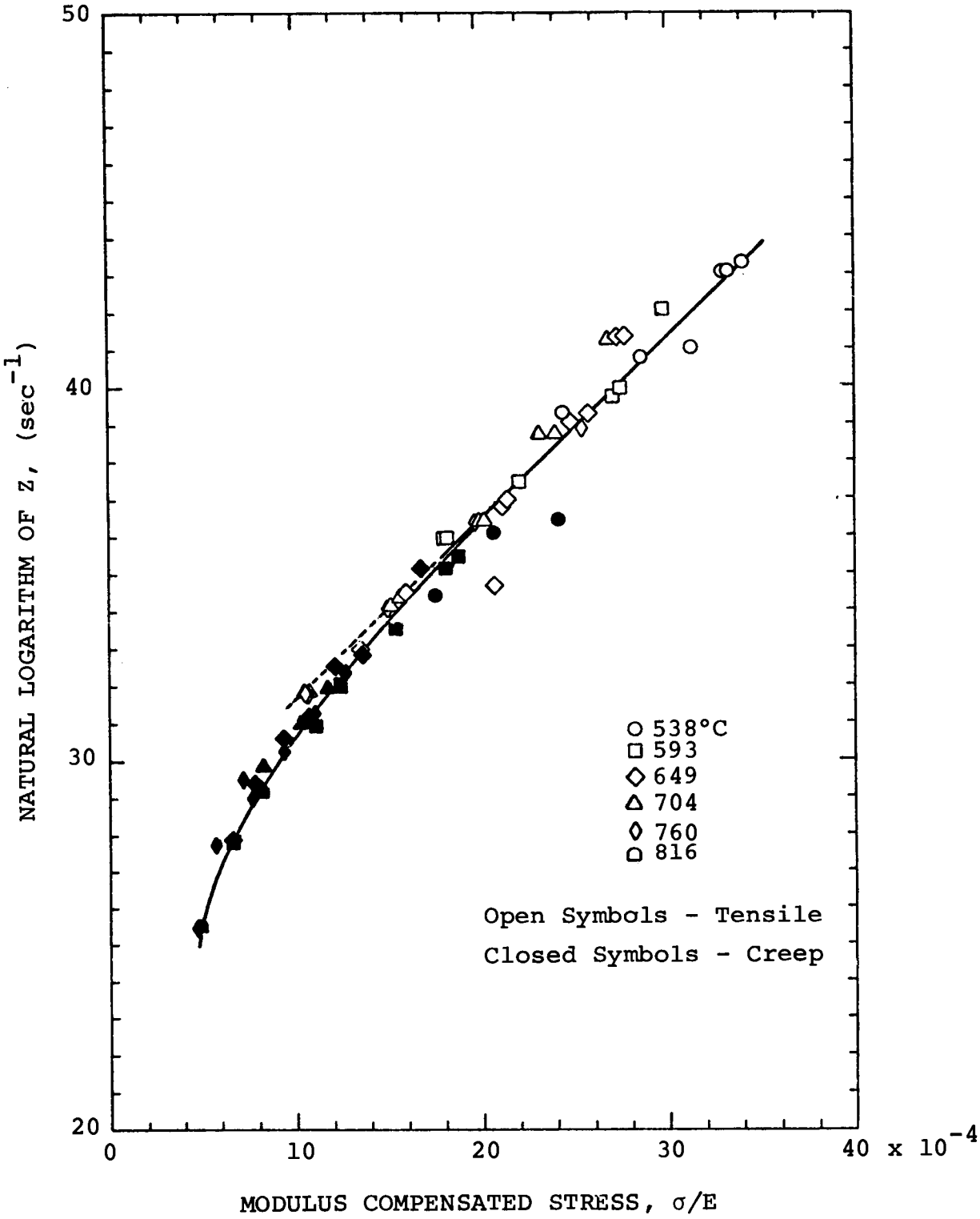

Figure 7.5 Plot of the ℓn Temperature compensated Deformation Rate, Z, versus the Modulus Compensated stress, σ/E.

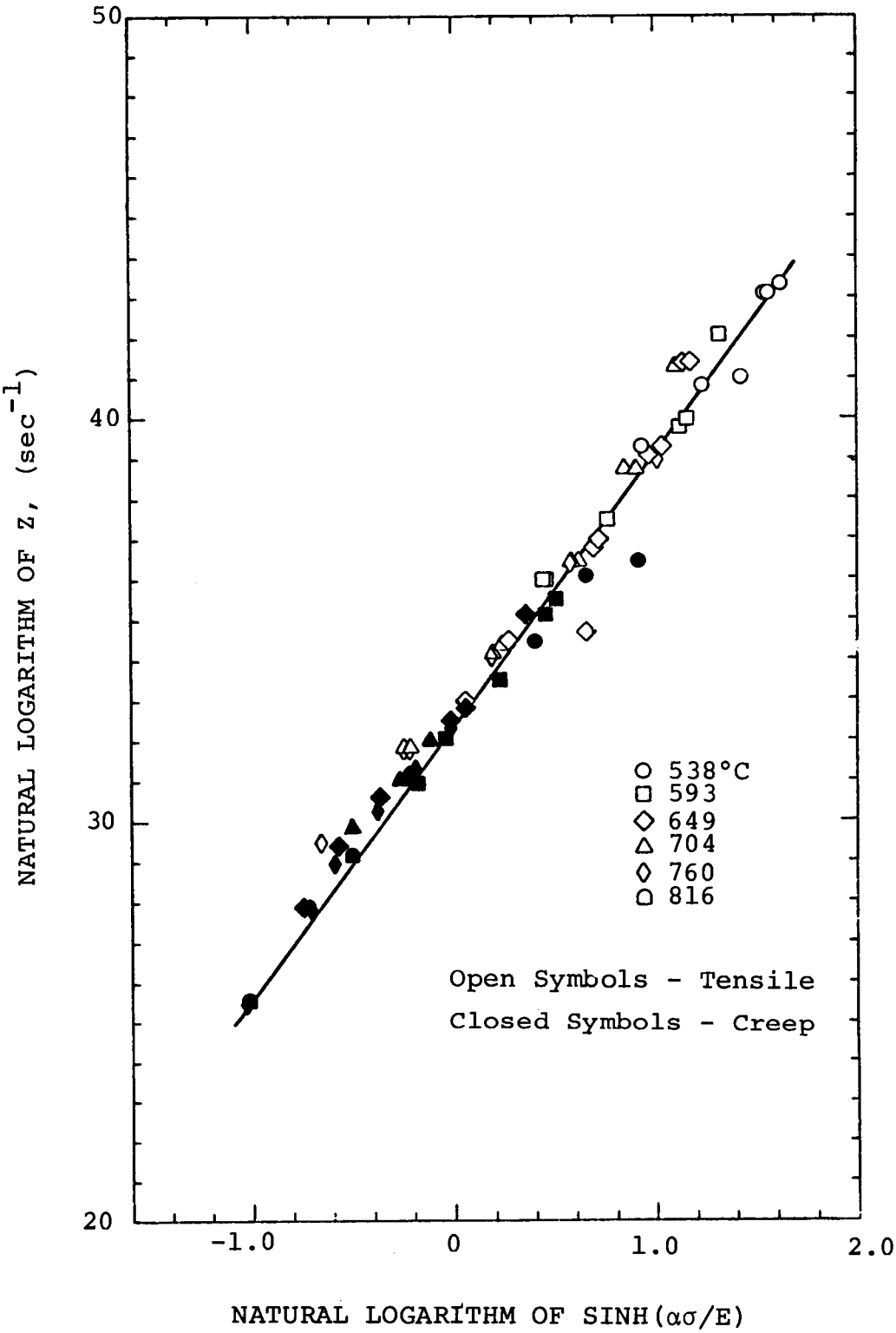

Figure 7.6 Plot of the Temperature Compensated Deformation Rate, Z, versus the Hyperbolic SINE function of (ασ/E) on a ℓn-ℓn scale.

central purpose of this work which is to correlate the macroscopic deformation properties with the corresponding microstructure.

7.1.2.3 Intragranular Deformation Behavior of AISI 304 Stainless Steel at Elevated Temperature — H. Nahm

The effect of grain size on creep properties of metals and alloys has been studied by many investigators. Theoretical and empirical relationships have been proposed to attempt to explain the role of grain size on the complex high temperature deformation process. For example, based on the concept of different mobile dislocation densities which may be present in the various grains of different sizes, Garofalo[6] proposed the equation:

$$\dot{\varepsilon}_s = \frac{A_1}{d} + A_2 d^2 \qquad [7]$$

where $\dot{\varepsilon}_s$ is the secondary creep rate, d is the grain size and A_1 and A_2 are constants. Barrett, Lytton and Sherby[7] suggested an equation of the type:

$$\dot{\varepsilon}_s = k(\lambda/d)\ \dot{\varepsilon}_{gb} + [1-k(\lambda/d)]\ \dot{\varepsilon}_i \qquad [8]$$

where $\dot{\varepsilon}_s$ is the secondary creep rate, k is a constant, λ is the subgrain size, d is the grain size, $\dot{\varepsilon}_{gb}$ is the grain boundary sliding rate and $\dot{\varepsilon}_i$ is the intragranular deformation rate. Equation [8] was obtained from the considerations that the deformation is more significant near the grain boundary than inside the grain, and the total grain boundary area per unit volume of the specimen becomes larger as the grain size becomes smaller.

Recently Gifkins[8] developed a theoretical expression for the creep rate, $\dot{\varepsilon}_s$, given as follows:

$$\dot{\varepsilon}_s = \dot{\varepsilon}_i + \dot{\varepsilon}_i (2Kw\ \lambda/d^2) \qquad [9]$$

where $\dot{\varepsilon}_i$ is the intragranular deformation rate, K and w are the stress concentration factor and the width of the fold at the triple point respectively, λ is the subgrain size and d is the grain size. This was derived by considering the climb-controlled accommodation of grain boundary sliding due to the triple point fold formation, together with the climb-controlled intragranular deformation.

Most studies on the effect of grain size, including the preceding three equations, are based on the assumption that the metals or alloys considered have a uniform distribution of the grains with a constant given diameter. It should be realized, however, that there will be a distribution in grain sizes and one usually reports only the average size of the grains.

It is, therefore, quite informative to find how the individual grains behave and contribute to the overall deformation at elevated temperature. The purpose of this section is to report the preliminary results from the study on the deformation behavior of the individual grains by grain shape analysis.

The modified grain shape analysis by Hensler and Gifkins[9] was used on the six specimens of 304 stainless steel (9T2796) which were tested in tension and creep-rupture modes at 650°C. The deformation rates covered were between 8.33×10^{-4} sec^{-1}

and 4.16×10^{-8} sec^{-1}, which correspond the stress range from 42 ksi to 15 ksi. The chemistry and the testing results are available elsewhere.[10] The grain intercept of six specimens was 180±5μm. This was obtained from the measurement of more than 500 intercepts of the shoulder portion of each specimen.

Intragranular elongation, $\dot{\varepsilon}_i$, was obtained from the equation:

$$\dot{\varepsilon}_i = (l/w)^{2/3} - 1 \qquad [10]$$

where l is the average length of the grain and w is the average width of the grain, with respect to the stress axis. More than 800 grains were measured individually in terms of the length (l) and the width (w) for each specimen. The grain intercept was determined from

$$d = \frac{l+w}{2} \qquad [11]$$

and the intragranular elongation was calculated for the grains with 50μm intervals such as d is from 0∿50μm, 50∿100μm, 100μm∿150μm, etc.

The distribution of grain intercepts with intervals of 50μm as a function of relative frequencies measured is given in Figure 7.7. This was obtained from the underformed section (button-head) of a tensile specimen ($\dot{\varepsilon} = 8.33 \times 10^{-4}$ sec^{-1}) with more than 1300 grains measured. As can be shown in Figure 7.7, even in the same specimen with the average grain intercept dimension of ∿ 180μm, there is a wide range of distribution of different grain sizes. The distribution shows the positive skewness, i.e. there are more small grains than large grains.

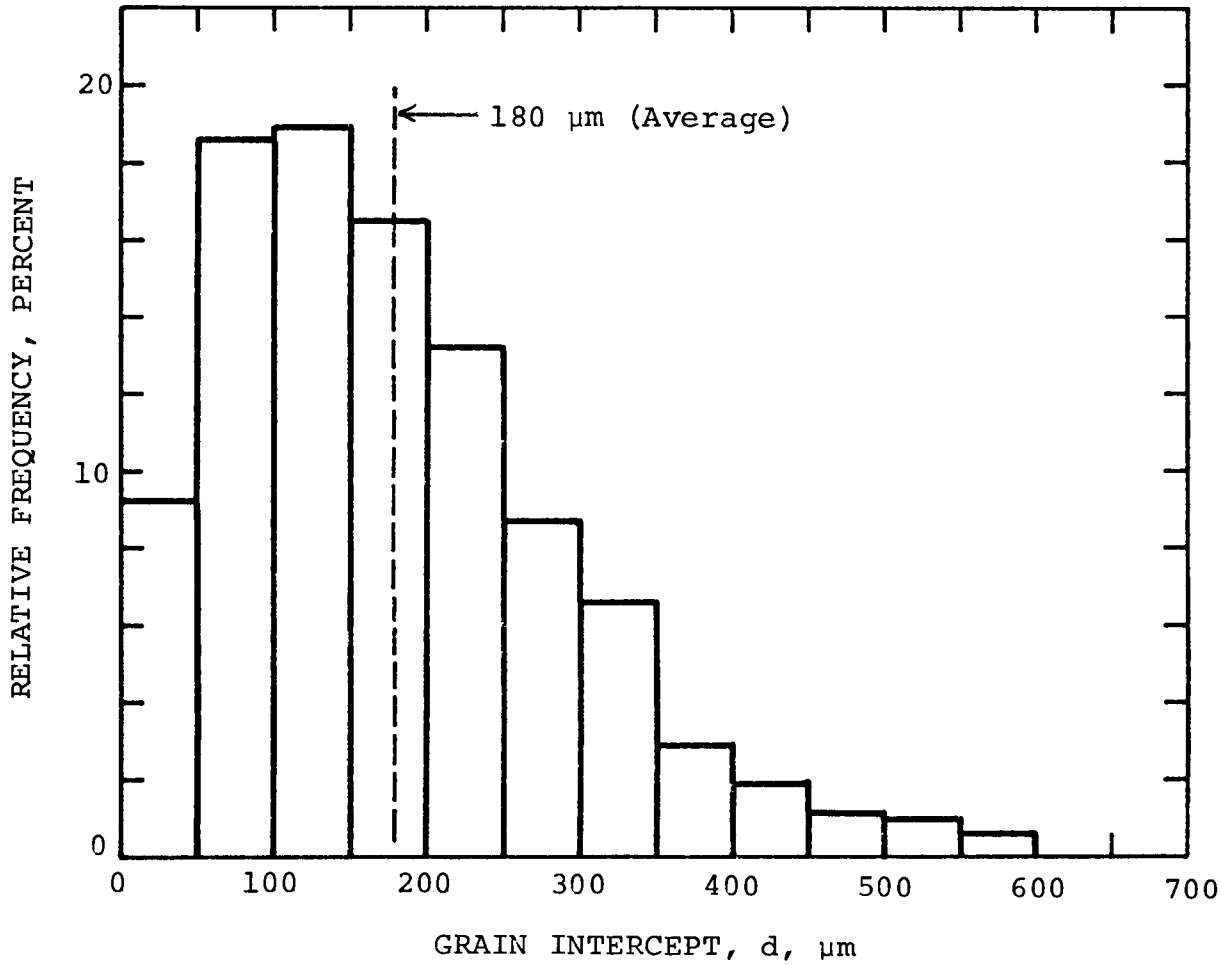

Figure 7.7 Distribution of Grain Intercepts in the Undeformed Region of a Tensile Tested Specimen ($\dot{\varepsilon}_t$=8.33 x 10^{-4} sec^{-1}) of AISI 304 (9T2796).

Figure 7.8 shows the intragranular elongations as a function of grain intercept intervals of 50μm from the deformed regions of the respective specimens. Several important observations can be noted. The intragranular deformation is a strong function of the grain size and it becomes more significant as the strain rate increases. In other words, the influence of grain size diminishes as the deformation rate decreases. For example, no appreciable change in the intragranular deformation can be noted for the case where the grain intercept, d, is larger than 100μm at the 4.16×10^{-8} sec^{-1} deformation rate, while at the 8.33×10^{-4} sec^{-1} the intragranular deformation increases as the grain size increases to values up to more than 400μm. One more result can be drawn from the data presented in this figure and that is that grain boundary sliding becomes important as the deformation rate decreases as noted by comparing the total elongation and the intragranular elongation. This observation is consistent in the studies of McLean, Garofalo, etc.,and with the previous results on microcracking behavior on these identical specimens[10] in the sense that microcracking increases as the deformation rates is decreased.

The present result as shown in Figure 7.7 is undoubtedly complex and not easily explained. However, it appears that the different deformation mechanisms might be operative in this wide range of strain rates, considering the previous microcracking behavior on these specimens.[10,11,12] At higher strain rates the grain size strengthening appears to be impor-

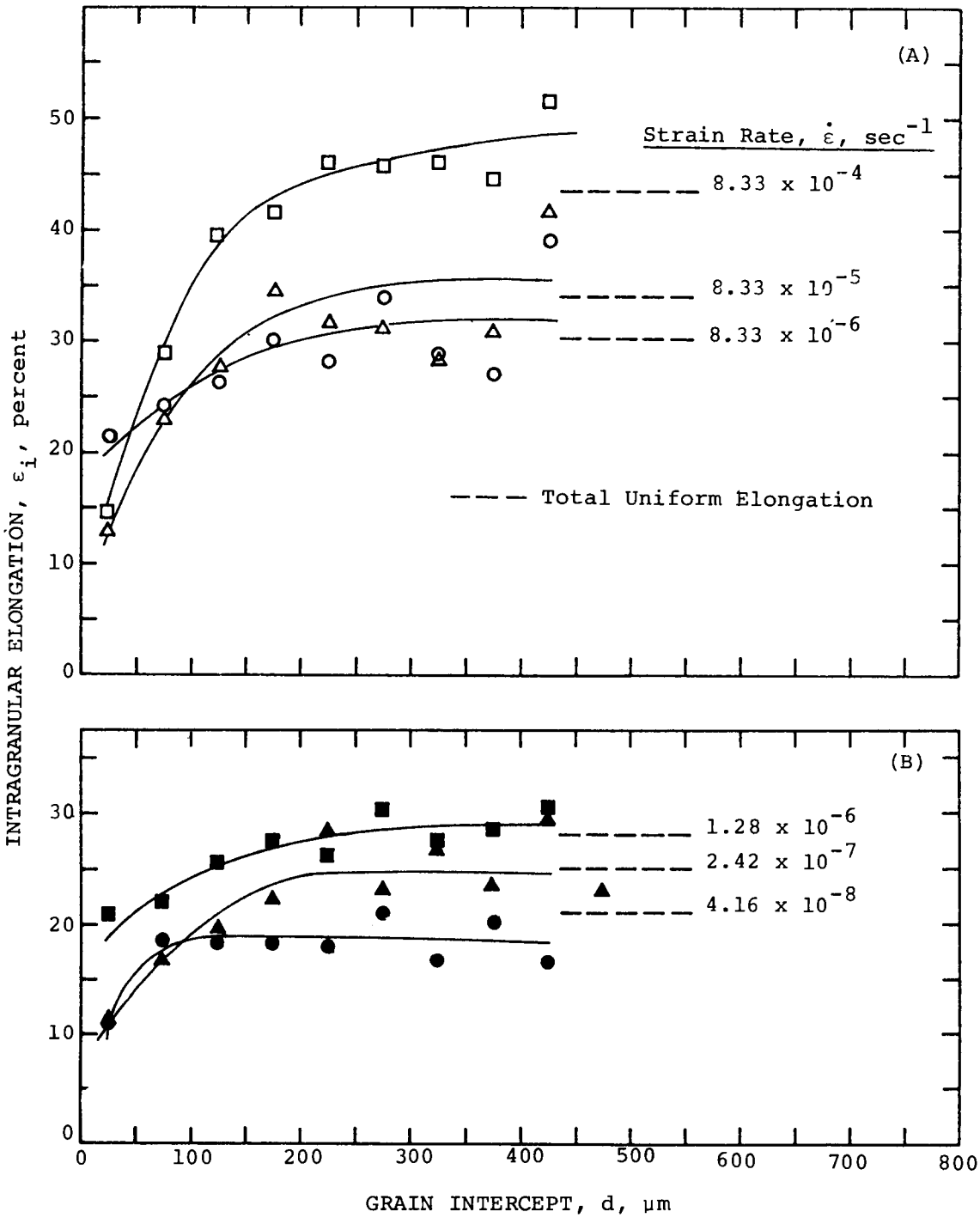

Figure 7.8 Intragranular Elongation as a Function of Grain Intercept for the Family of Tensile (A) and Creep (B) Tested Specimens of AISI 304 (9T2796) at 650°C.

tant, similar to the case of the grain size effect on the room temperature property. As the strain rate decreases, the grain boundary sliding becomes more important and the reasonings contained in Equations [8] and [9] or the interpretation by Matlock and Nix[13] could be applied. This phenomena becomes even more important in the evaluation of the embrittlement observed in irradiated stainless steels, a case where the matrix of the grain is hardened and grain boundary sliding is significantly reduced. Detailed analysis comprising the sub-grain dimension on these observations is still underway at this laboratory.

7.1.2.4 Deformation Substructure of Austenitic Stainless Steel from Low Cycle Fatigue at Elevated Temperature — H. Nahm, T. Kenfield,* and D. Porter

As an ongoing program at the University of Cincinnati, more data has been generated to further the knowledge of the influence of substructure on the elevated temperature low-cycle fatigue properties of the austenitic stainless steels. Push-pull and bend fatigue modes in Incoloy 800 has been studied in terms of the dislocation structure. Work has been completed on the influence of hold-time on the low cycle fatigue behavior of 304 stainless steel. The microstructural analysis was performed on the identical specimens which were used by Berling and Conway[14] in their classic hold-time experiments and as

*Now at the General Electric Company, San Jose, California

reported later by Coffin[15] and Manson[16]. Work is now also being initiated on the hold-time microstructure effects in 316 stainless steel. The influence of the substructure, especially the subgrain size on the hardening behavior of 304 stainless steel is being investigated through room temperature hardness measurements of samples having different subgrain sizes. Particular attention will be placed on the thermal stability of this hardening mode by annealing the samples at elevated temperature for given periods of time.

7.1.2.5 Deformation Behavior and Substructure Characteristics of Several Nickel Based Alloys — C. Schmidt and G. Stroble

A program is being initiated to study the creep behavior and the resulting substructure of three alloys* having the following chemical composition:

Alloy	Nominal Compositions		
	Fe	Cr	Ni
E19	66	15	19
E23	40	15	45
E36	--	15	85

Procedures for thinning various types of nickel based alloys for TEM evaluations and the generation of typical microstructures has been initiated. The alloys being investigated include the following:

*Material furnished by HEDL.

Alloy	Chromium Content,%	Type
Incoloy 903	0	γ' - fcc hardened
Inconel 600	15-20	solid solution hardened
Incoloy 801	15-20	γ' - fcc hardened
Inconel 625	15-20	γ' - bct hardened
Incoloy 802	15-20	$M_{23}C_6$ carbide hardened
Inconel MA754	15-20	dispension plus γ'-fcc hardened
Inconel 671	50	solid solution hardened

7.1.3 References

1. ORNL-4998, "Mechanical Properties Test Data for Structural Materials" quarterly prcgress report for period ending July 31, 1974, p. 307-310.

2. ORNL-4963, "Mechanical Properties Test Data for Structural Materials" quarterly progress report for period ending April 30, 1974, p. 242.

3. ORNL-4998, "Mechanical Properties Test Data for Structural Materials" quarterly progress report for period ending July 31, 1974, p. 310.

4. R.W. Swindeman, ORNL-4998, "Mechanical Properties Test Data for Structural Materials" quarterly progress report for period ending January 31, 1974, p. 280-283.

5. F. Garofalo, Trans. AIME, 227, (1963) p. 351.

6. F. Garofalo, Et Al., Trans. AIME, 230 (1964) p. 1460.

7. C.R. Barrett, J.L. Lytton and O.D. Sherby, Trans. AIME, 239 (1967) 170.

8. Gifkins, J. Aust. Inst. Met., 18 (1973) 137.

9. J. H. Hensler and R.C. Gifkins, J. Inst. Met., 92, (1963-1964) 340.

10. H. Nahm, D.J. Michel, and J. Moteff, J. Mat. Sci., 8 (1973) p. 104.

11. D.J. Michel, H. Nahm and J. Moteff, Mat. Sci. and Eng., 11 (1973) 97-102.

12. Submitted for publication.

13. D.K. Matlock and W.D. Nix, Met. Trans., 5 (1974) 961.

14. J.T. Berling and J.B. Coffin, 1st International Conference on Pressure Vessel Technology, Delft, 1969.

15. L.F. Coffin, Jr., Fatigue at High Temperature, Fatigue at Elevated Temperatures, Editors, A.E. Carden, A.J. McEvily and C.H. Wells, ASTM STP 520, 1973, p. 18.

16. S.S. Manson, The Challenge to Unity Treatment of High Temperature Fatigue - A Partisan Proposal Based on Strain-range Partitionings, ibid., p. 760.

7.2 UNIVERSITY OF CALIFORNIA, LOS ANGELES — K. Ono, A. J. Ardel, and A. S. Tetelman

7.2.1 Microstructure and High Temperature Deformation of Cr-Mo Steels for LMFBR Heat Exchanger — P. A. Chalco, K. Ono, S. Y. Hsu, and S. L. Wang

7.2.2 Introduction

We have examined microstructural variations as a function of time and temperature, and the concomitant effects on mechanical behavior in 2-1/4Cr-1Mo steels of different carbon content. The microstructural variation in Alloys L (0.009%C), I(0.03%C) and H(0.12%C) has been reported previously.[1,2] In this report, the creep behavior of these alloys is presented. In addition to the three alloys, which were originally prepared at the Bureau of Mines and were received from Oak Ridge National Laboratory (ORNL) we have received a piece of low carbon 2-1/4Cr-1Mo steel (0.03%C) plate (1" x 10" x 10") also from ORNL. Some creep data on this material, to be referred to as alloy M,are included in this presentation. It is planned to examine

the strain burst phenomenon during stress changes in this material as well as in decarburized specimens.

During this report period, P.A. Chalco has completed his dissertation entitled "Microstructure and Mechanical Properties of Cr-Mo steels" and has been awarded the Ph.D. degree from University of California.

7.2.3 Creep Properties of 2 1/4 Cr-1 Mo Steels

The creep behavior of Alloys L, I, and H was investigated as a function of temperature and stress. The materials tested were in the normalized and tempered condition and long-term-tempered condition. The latter were tempered at 1050°F for 12 months. Most creep curves exhibited a stage of primary creep right after the stress was increased, as shown by curves A and C of Fig. 1. However, in the case of Alloys L and I, very often an increment of stress was accompanied by a strain burst, after which a primary creep stage was observed. This type of creep behavior is represented by curve B in Fig. 1. We will discuss further these strain bursts later in this section.

One of the main objectives in the present creep testing was to obtain steady state creep rates as a function of stress and temperature. The results are presented in the form of creep stress vs. strain rate plots in Figs. 2 through 7. In order to present these data clearly, individual curves have been plotted for a given material tested at various temperatures. The observed values of the stress exponent, n, are tabulated in Table I. In the case when n is reported as 4, higher values of n (up to 6) can be obtained if the data points at

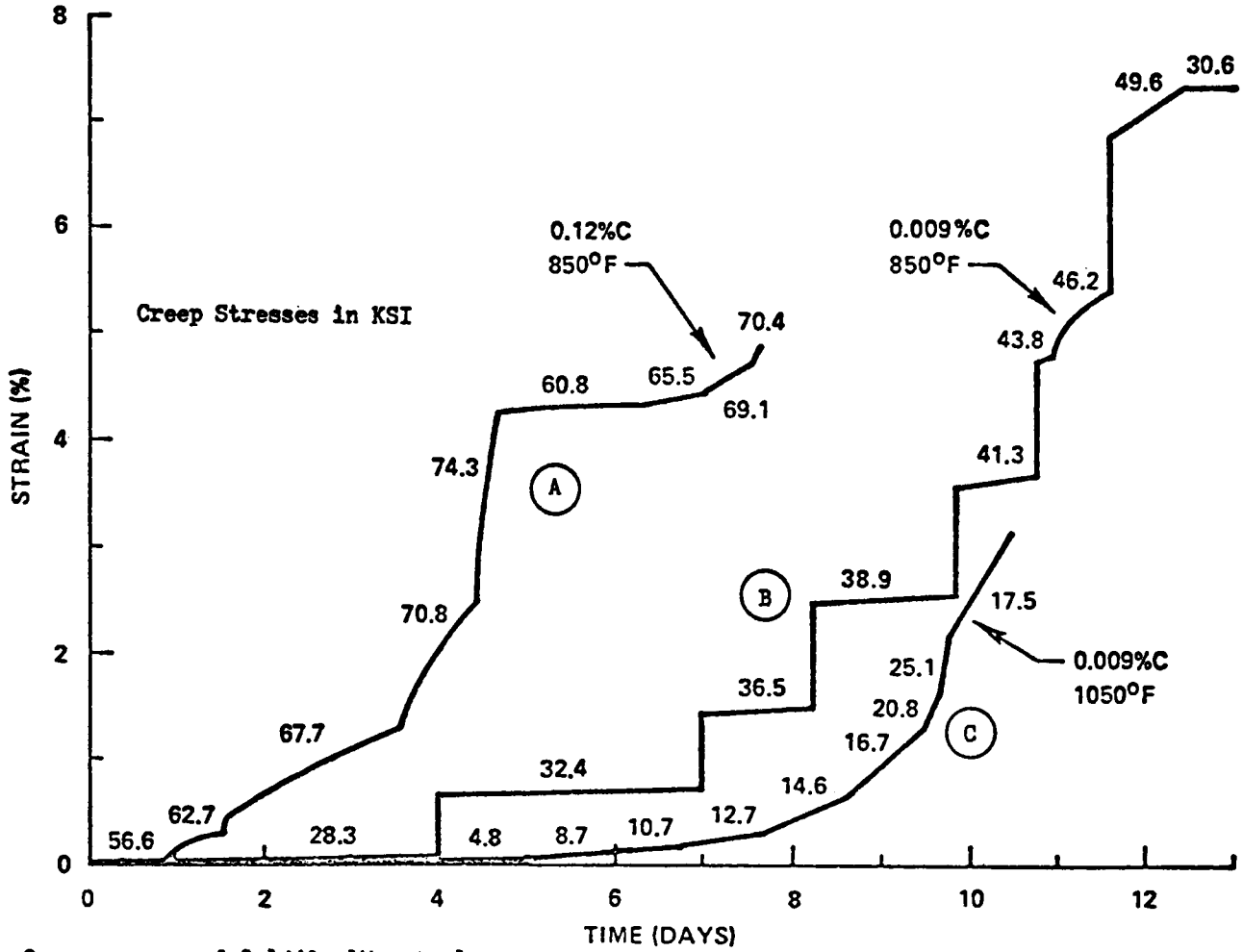

Figure 1 Creep curves of 2-1/4Cr-1Mo steels

TABLE I

Approximate Values of n

Alloy	Condition	Temp. (°F)	n	Stress range (KSI)
L	N&T	850	12	30-50
		1050	10	14-30
			4	5-14
	N&T&T*	850	14	22-33
			4	10-22
		1050	9	9-22
			4	3-9
I	N&T	850	14	50-54
			(2)	32-50
			10	29-32
		950	7	23-35
		1050	16	22-28
			6	11-22
			4	5-11
	NT&T*	850	22	29-41
			14	22-29
		1050	9	11-22
			4	4-11
H	N&T	850	44	66-74
			16	57-66
		890	41	53-63
			16	48-53
		930	10	30-51
			4	25-30
		970	10	26-54
			4	20-26
		1010	10	22-44
			4	11-22
		1050	10	18-38
			4	4-18

TABLE I (Cont'd)

Alloy	Condition	Temp. (°F)	n	Stress range (KSI)
H	NT&T*	850	18	35-50
			4	15-30
		1050	11	19-32
			4	7-19
			< 4	2.5-7
	N&T	850	17	45-60
			7	27-45
		900	21	33-45
			8	23-33

*Long-term-tempered at 1050°F for 12 months.

higher $\dot{\epsilon}_s$ are also included; however, a value of n = 4 was chosen because this value is predicted by the Ansell-Weertman theory for dispersion hardened materials. The reported values of n, other than 4 were accurate to about ± 1.

7.2.3.1 Alloy H (High Carbon)

Fig. 2 shows the stress dependence of the steady state creep rate at 850, 890, 930, 970, 1010 and 1050°F in Alloy H normalized and tempered (N&T) at 1300°F for one hour. In this figure, it can be easily recognized that the obtained curves follow a different pattern at 850 and 890°F from those obtained at higher temperatures. At 850 and 890°F, the stress exponent n (d log $\dot{\epsilon}_s$/d log σ) is about 42 and 16. At 930, 970, 1010, and 1050°F two different but much lower values of n were obtained. At higher stresses, n is around 10 and at lower stresses it is about 4.

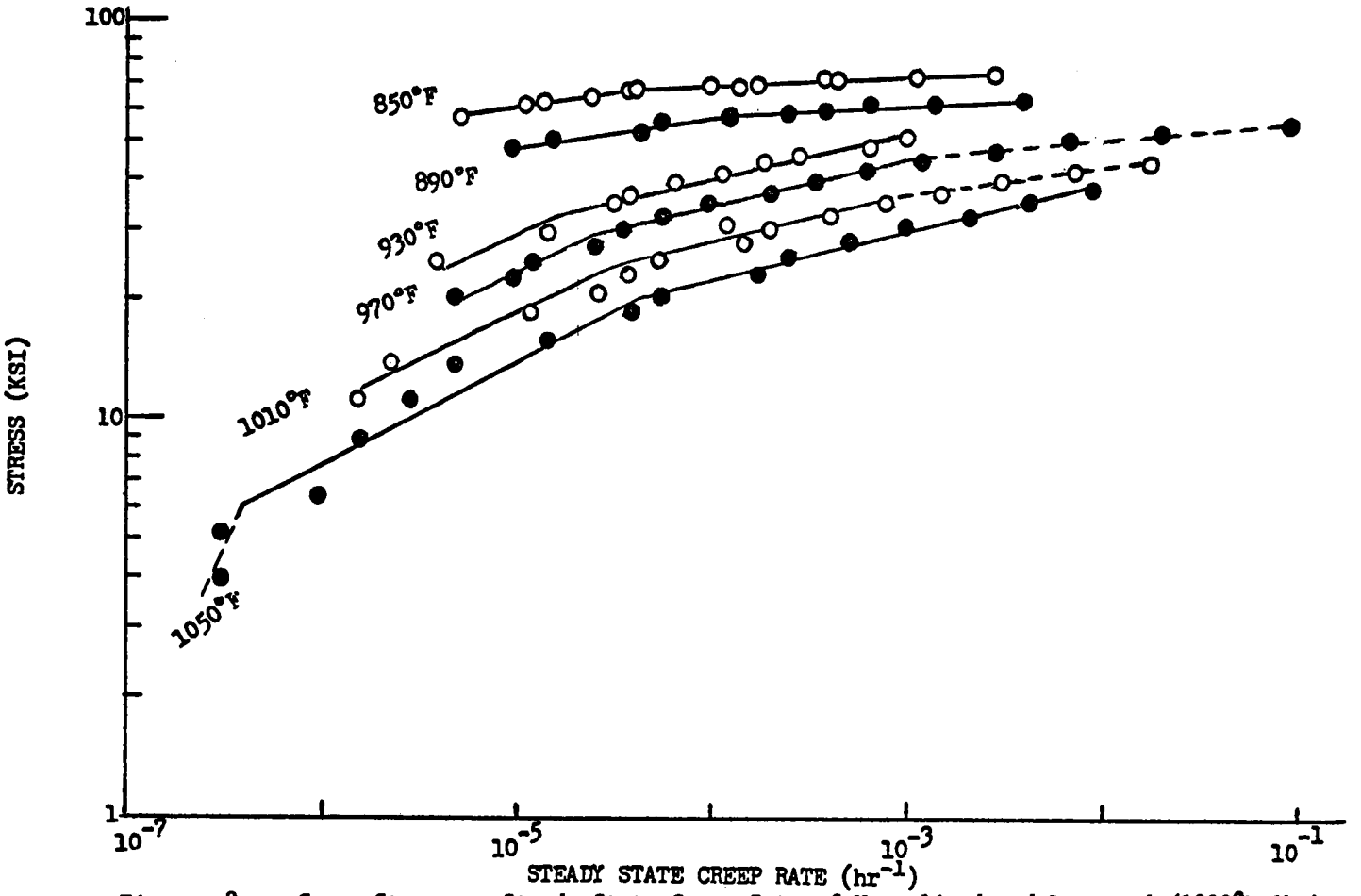

Figure 2 Creep Stress vs Steady State Creep Rate of Normalized and Tempered (1300°F 1hr) Alloy H (0.12% C)

Fig. 3 shows two log $\dot{\epsilon}_s$ vs. log σ curves for alloy H in the N&T condition, tempered at 1050°F for 12 months and tested at 850 and 1050°F. In addition, Fig. 4 also shows, for comparison purposes, similar curves for materials in the N&T condition (Fig. 2) tested at 850 and 1050°F. It can be seen that the long tempering has shifted the curves to lower stresses, this being more accentuated at 850°F than at 1050°F. Also, at 850°F, the two corresponding curves for Alloy H are not as close to being parallel as they are at 1050°F. The values of n in Fig. 3 are approximately 18 and 4 at 850°F, and 11, 4, and < 4 at 1050°F.

7.2.3.2 Alloy I (Intermediate Carbon)

Figs. 4 and 5 show log $\dot{\epsilon}_s$ vs. log σ curves obtained for Alloy I in the N&T (Fig. 4) and long-term-tempered (Fig. 5) conditions. In the N&T condition, Alloy I showed a very unusual behavior when tested at 850 and 950°F. As mentioned before, an increment in stress of about 2 Ksi triggered a strain burst ($\sim$1%) throughout the entire range of creep stresses used in these materials. The first burst occurred during loading from 29.5 to 32 Ksi at 850°F and from 23 to 24 Ksi at 950°F. Below these stresses no creep tests were performed, but no strain bursts occurred during loading. In the case of the long-term-tempered material, tested at 850°F, no strain burst occurred until the stress was increased from 36.4 to 40.9 Ksi which corresponds to the highest stress used at this temperature. This particular strain burst had a magnitude of about 5%.

An examination of Fig. 4 shows a region of discontinuity in the curve obtained at 850°F. In this region, n is of the order of 2,

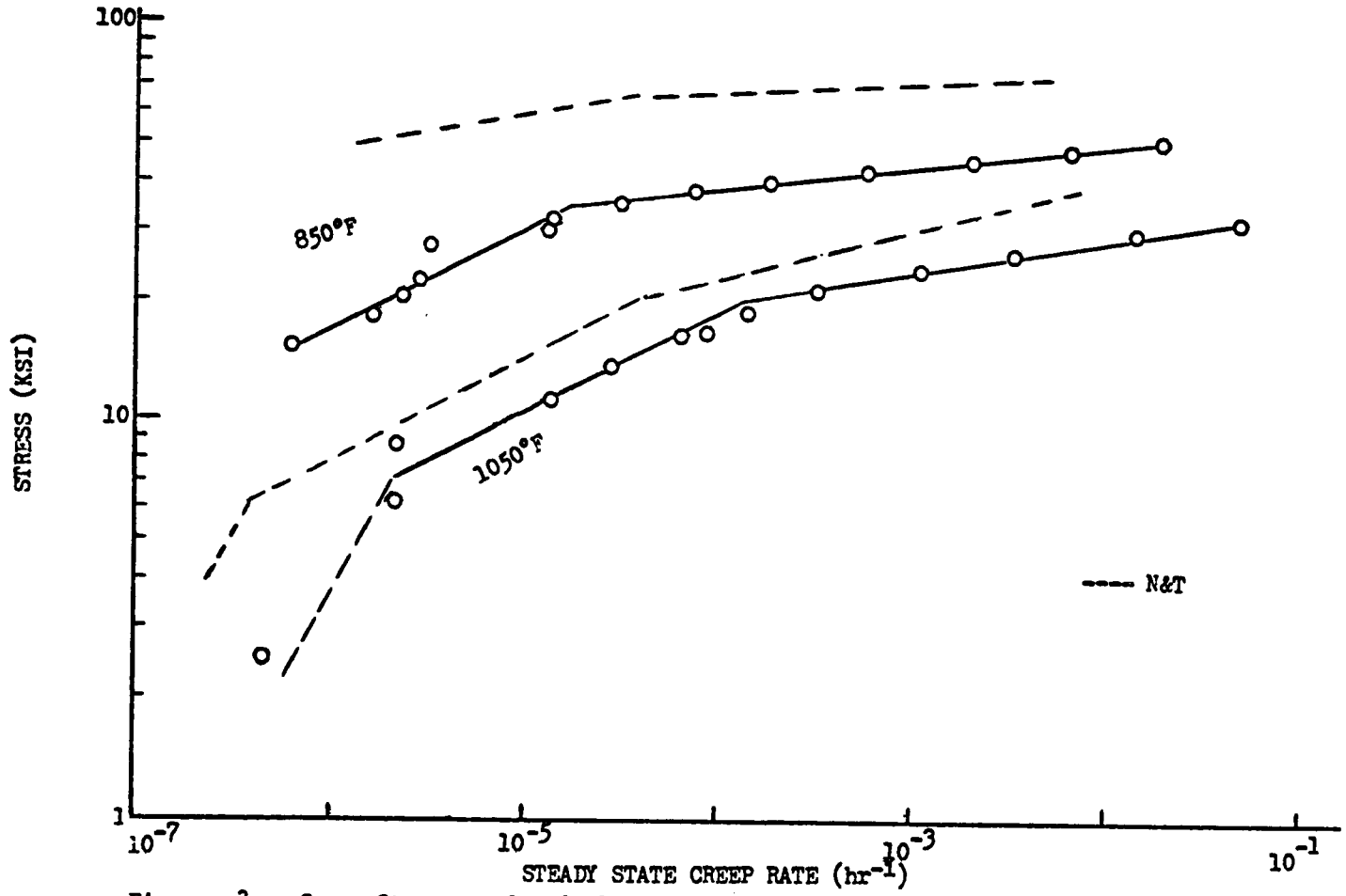

Figure 3 Creep Stress vs Steady State Creep Rate of Normalized and Tempered (1300°F,1hr) Alloy H (0.12% C), Tempered at 1050°F for 12 Months

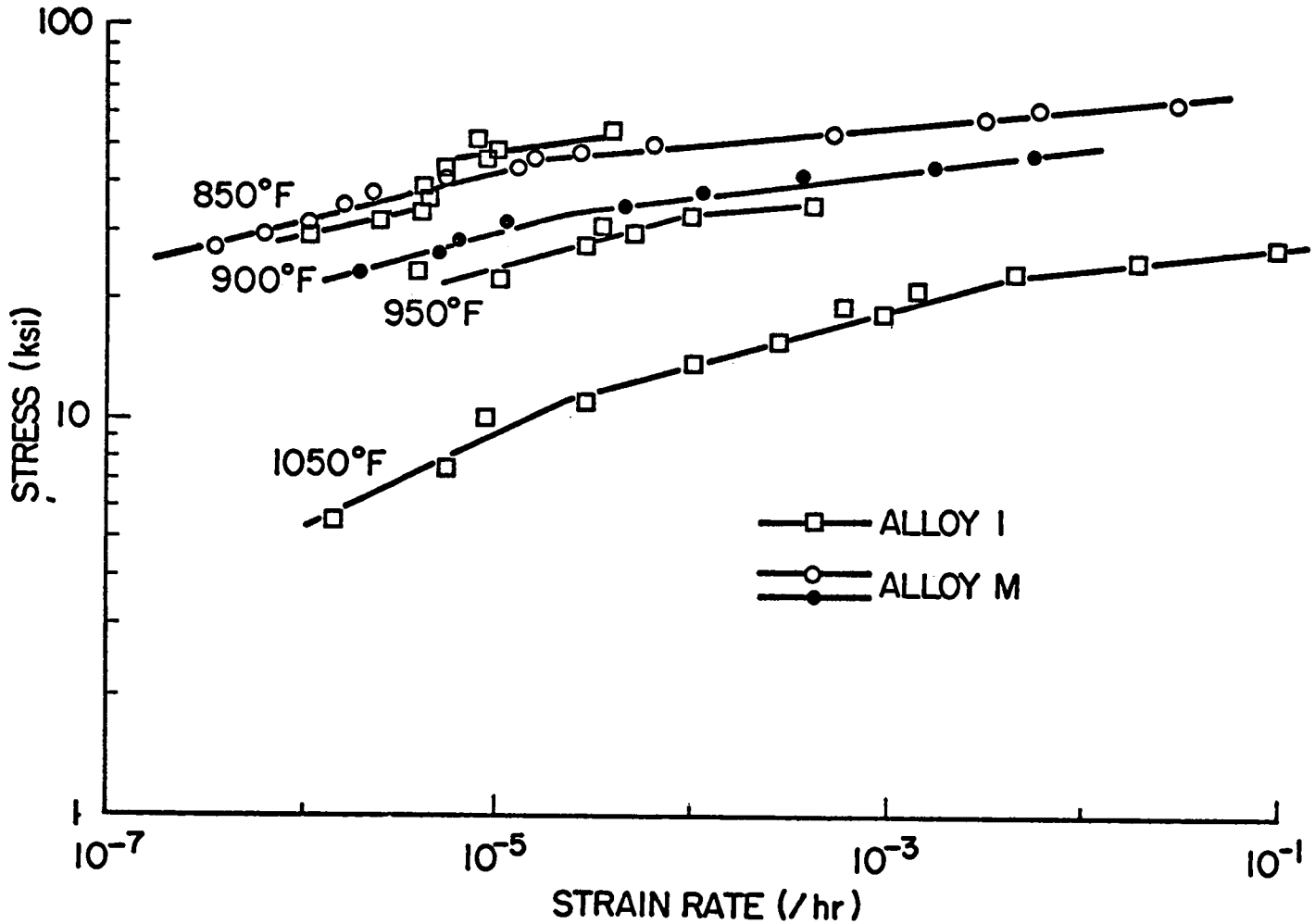

Figure 4 Creep stress vs. Steady State Creep Rate Normalized and Tempered (1300°F, 1 hr.) Alloy I (0.03%C) and Alloy M (0.03%C).

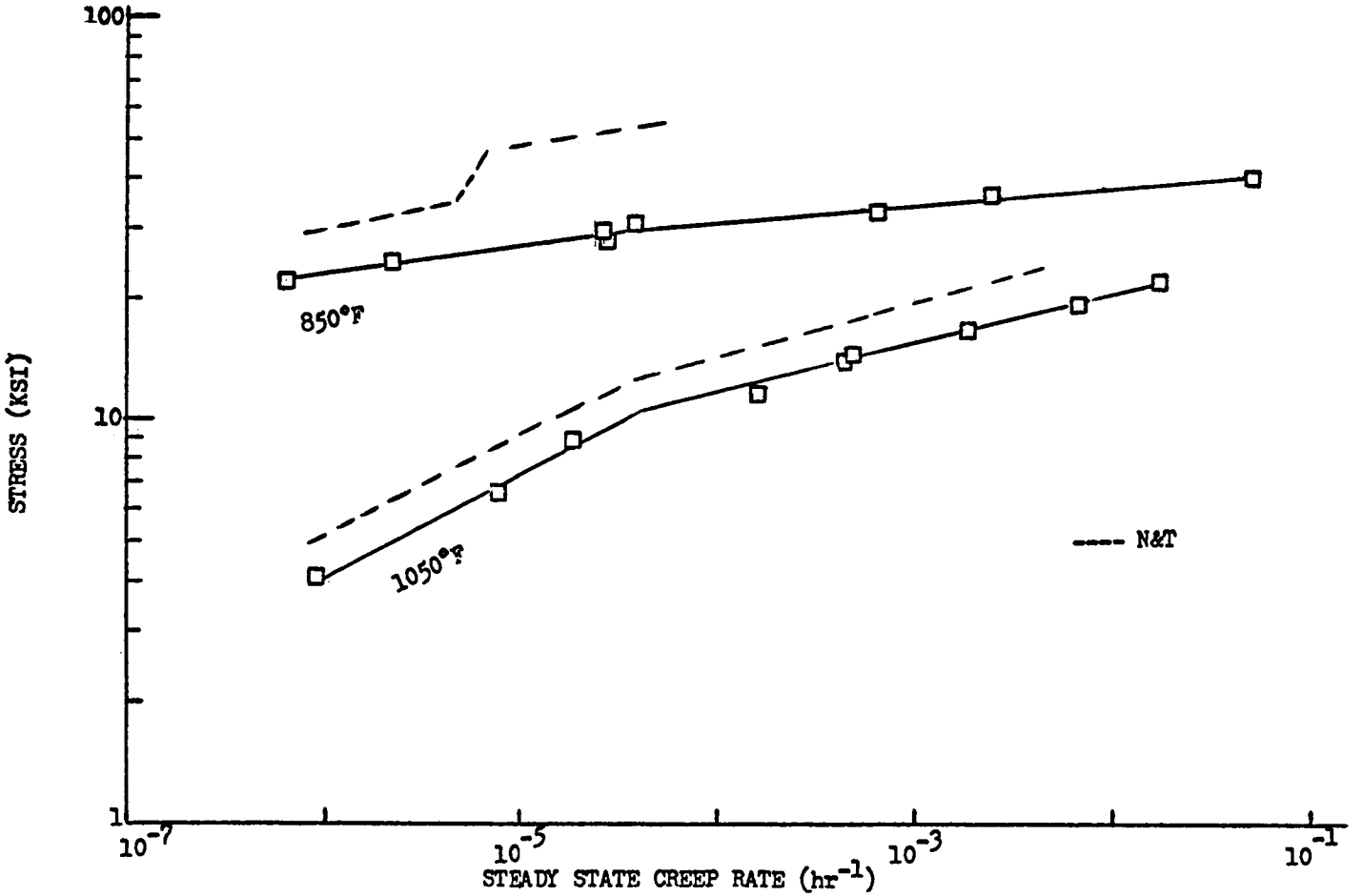

Figure 5 Creep Stress vs Steady State Creep Rate of Normalized and Tempered (1300°F, 1hr) Alloy I (0.03% C), Tempered at 1050°F for 12 Months

while above and below this region, n was 14 and 10, respectively. For this same material condition (N&T) tested at 950°F, n was equal to 7, but no discontinuity can be readily observed as in the previous case. In the case of the long-term-tempered material (Fig. 5) tested at 850°F, n was equal to 22 and 14. At 1050°F, no strain bursts were observed during creep testing of either N&T or long-term-tempered materials. For a given creep rate, the long-term-tempered material deformed at lower stresses than the N&T material did. n values were found to be 16, 6, and 4 for the N&T material, and 9 and 4 for the long-term-tempered materials.

7.2.3.3 Alloy L (Low Carbon)

Alloy L also showed strain bursts during stress increments at 850°F. At this temperature, the first burst occurred when the stress was increased from 28 to 32 Ksi and from 27 to 30 Ksi in the N&T and long-term-tempered materials, respectively. In both of these material conditions, strain bursts were consistently observed upon further stress increments, up to the highest stress used in these tests.

At 850°F, the log $\dot{\epsilon}_s$ vs. log σ curve for the N&T material (Fig. 6) was approximately straight having n = 12. No clear discontinuities can be observed as in the intermediate carbon (N&T) material tested at 850°F. In the case of the long-term-tempered material, tested at 850°F, two different values of n were obtained; these are 14 and 4 (Fig. 7). Compared to the N&T materials, the long-term-tempered materials deformed at lower stress for a given creep rate. This was also the case at 1050°F for creep rates above

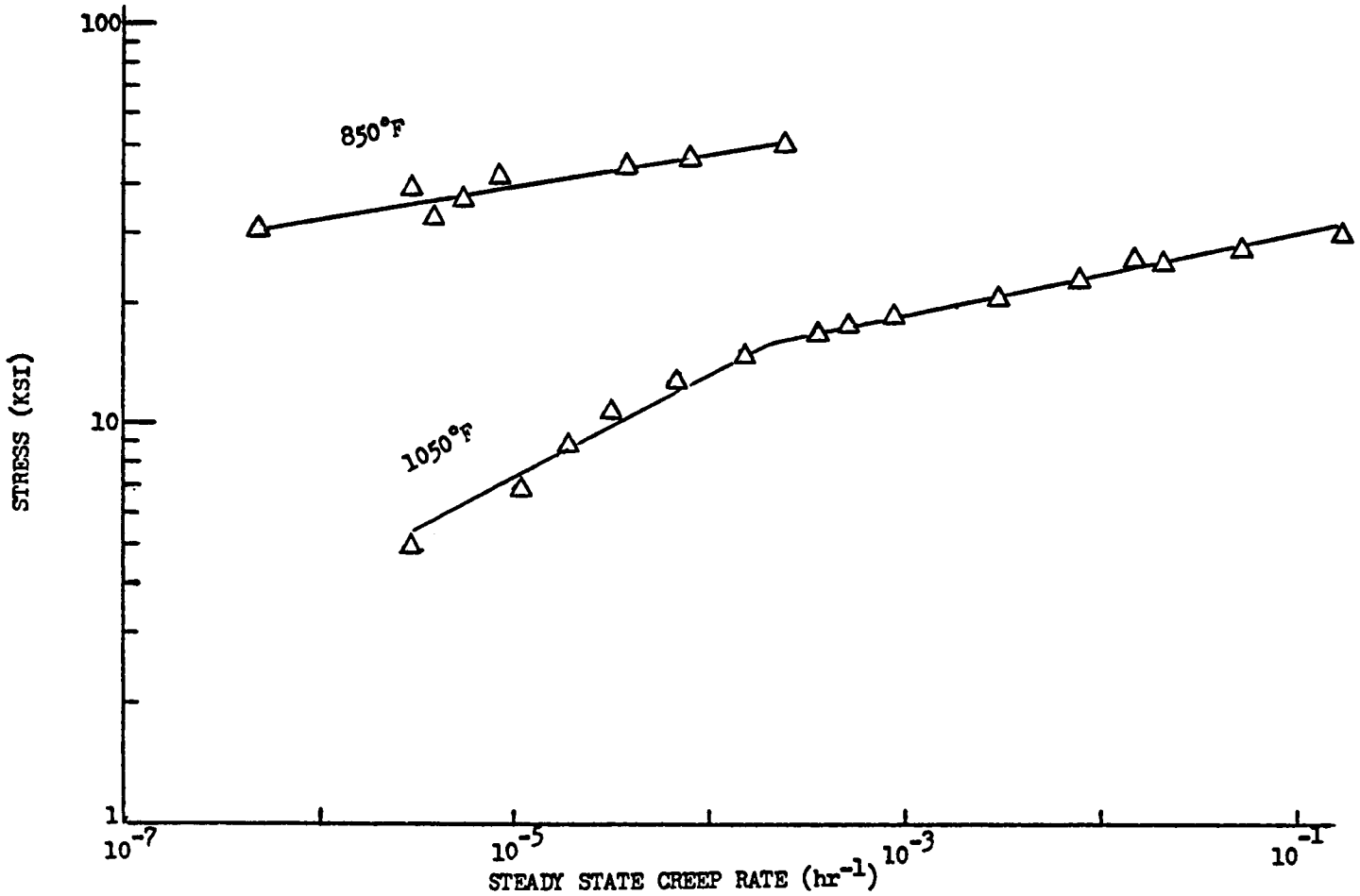

Figure 6 Creep Stress vs Steady State Creep Rate of Normalized and Tempered (1300°F. 1hr.) Alloy L (0.009% C)

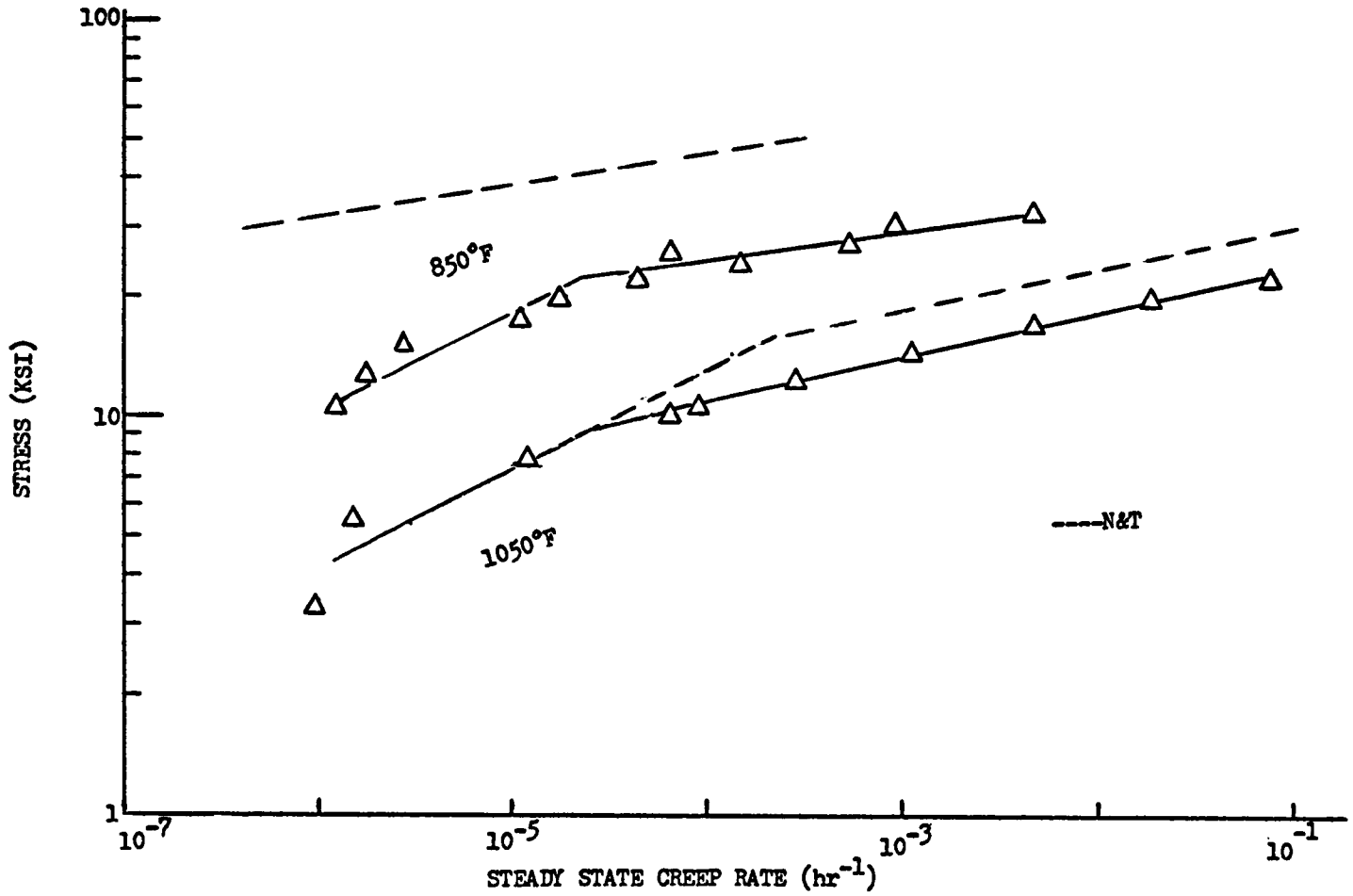

Figure 7 Creep Stress vs Steady State Creep Rate of Normalized and Tempered (1300°F 1hr.) Alloy L (0.009% C), Tempered at 1050°F for 12 Months

$2 \times 10^{-5}/hr^{-1}$, but the opposite was true below this value of creep rate. Also at 1050°F, n was around 10 and 4 for both the N&T and long-term-tempered materials.

7.2.3.4 Alloy M (Medium Carbon)

Creep tests on the N&T condition of the alloy were initiated to establish $\dot{\epsilon}_s$ - σ relation and the range of σ where the strain burst phenomenon may exist. Two tests have been completed and the results are shown in Fig. 4. At 850°F, creep rates were comparable to those observed in Alloy I, but the unusual $\dot{\epsilon}_s$ - σ behavior in the latter was absent in Alloy M. At 900°F, observed creep rates were about 5 times lower than those of Alloy I at 950°F, which is reasonable. In all instances of stress increases (kept to ~3 Ksi), no strain burst was found during creep tests of Alloy M. At present, reason for the failure to observe strain bursts is not known. The values of n were greater than 7 (cf. Table I).

Further tests at 950°F, 1000°F and 1050°F are in progress. Other heat-treatment conditions of this alloy will also be creep tested.

7.2.4 Creep Studies in Lightly Cold-Worked Stainless Steels — O. Ajaja and A. J. Ardell

In this research program, the influence of small amounts of cold work (0-10%) on the elevated temperature creep kinetics of austenitic stainless steels (types 316 and 304) is being studied. Previous experiments on 316 have shown that an optimum level of cold work exists for which the creep rutpure life is maximized, and suggested that there exists a much lower level of cold work (in the range 0-10%

for our present test conditions) for which the rupture life is a minimum. This latter observation has provided the impetus for the present experiments, in which the effect of small amounts of cold work on the creep characteristics of types 304 and 316 will be investigated for various temperatures and stresses.

A constant stress creep apparatus has been built and calibrated. The following test conditions have been selected for initial testing. Some of these tests are in progress.

Test temperatures	:	1100, 1200, and 1300°F
Prestrain (%)	:	0, 2, 4, 6, 8 and 10
Stress levels	:	35, 37.5, 40 ksi at 1100°F
		25, 27.5, 30 ksi at 1200°F
		15, 17.5, 20 ksi at 1300°F

These stress levels were selected to correspond to the rupture life of up to 1000 hr.

7.2.5 The Effect of Case Carburization Fracture Mode of Type 316 Stainless Steel — P. L. Jones and A. S. Tetelman

7.2.5.1 Introduction

Austenitic stainless normally fracture in a ductile transgranular mode when tensile-tested over the entire temperature range of austenite stability.[3] Failure occurs by initiation and coalescence of microvoids and, in several, is ductile due to the intensive slip required to produce microvoids. There are instances, however, in which brittle behavior has been observed.[4,5] An important consideration in determining the behavior of material failing by ductile

fracture is the volume fraction of microvoids formed, and their distribution. If microvoids form at inclusions or precipitates before gross deformation occurs, the fracture stress in the region containing no voids can be reached before general yielding can occur, resulting in brittle failure. Two studies[6,7] conducted on the effect of inclusions on ductile fracture have yielded similar semi-quantitative results. In both cases, the fracture strain was found to be primarily dependent on the volume fraction of second phase particles.

Although austenitic stainless steels usually fail in a transgranular mode, there are special cases on which fracture follows an intergranular pattern. The additions of carbon to stainless steel not only has a pronounced effect on tensile ductility, but also fracture mode. It has generally been found that increasing the carbon content of stainless steel either by case hardening or alloying, leads to a transition from a transgranular to an intergranular fracture mode.[8-12] However, a satisfactory explanation of this transition has not been proposed, so far as the author is aware. The research discussed in this report is an attempt to characterize the effects of case carburization on the observed fracture mode of type 316 stainless steel.

7.2.5.2 Experimental Procedures/Fractography

In order to determine the fracture mode as a function of volume fraction of recarbon case, all fracture surfaces were examined using a Cambridge Stereoscan electron microscope. Fracture surfaces were cleaned several times with acetate replicating material to remove the thin scale that had formed on the fracture surface during elevated

temperature tensile testing. Specimens were then ultrasonically cleaned and mounted for viewing.

7.2.6 Results

7.2.6.1 Mechanical Properties

The effects of case carburization on the mechanical properties of type 316 stainless steel have been discussed in a previous report.[13] The most significant finding was the sharp decrease in ductility that occurred when the volume fraction of case was increased from 0.121 to 0.246. This ductility drop was explained on the basis of a change in the fracture controlling process.

7.2.6.2 Fracture Mode

Fig. 8 graphically displays tensile ductility and observed fracture mode as a function of volume fraction. There is an obvious relationship between tensile ductility and fracture mode. Specimens exhibiting a relatively large tensile ductility failed transgranularly, while specimens failing at intermediate and low strains displayed a mixed or entirely intergranular fracture mode. There are several possible explanations for this observed transition in fracture mode as the case depth increased: 1) increase in matrix hardness, 2) chromium depletion in regions adjacent to grain boundaries, 3) increased tri-axiality of stress acting on the matrix when the case fails, and 4) an increased strain rate acting on the matrix when the case fails by unstable, brittle fracture.

An increase in matrix hardness due to carbide precipitation could strengthen the core to such an extent that an intergranular

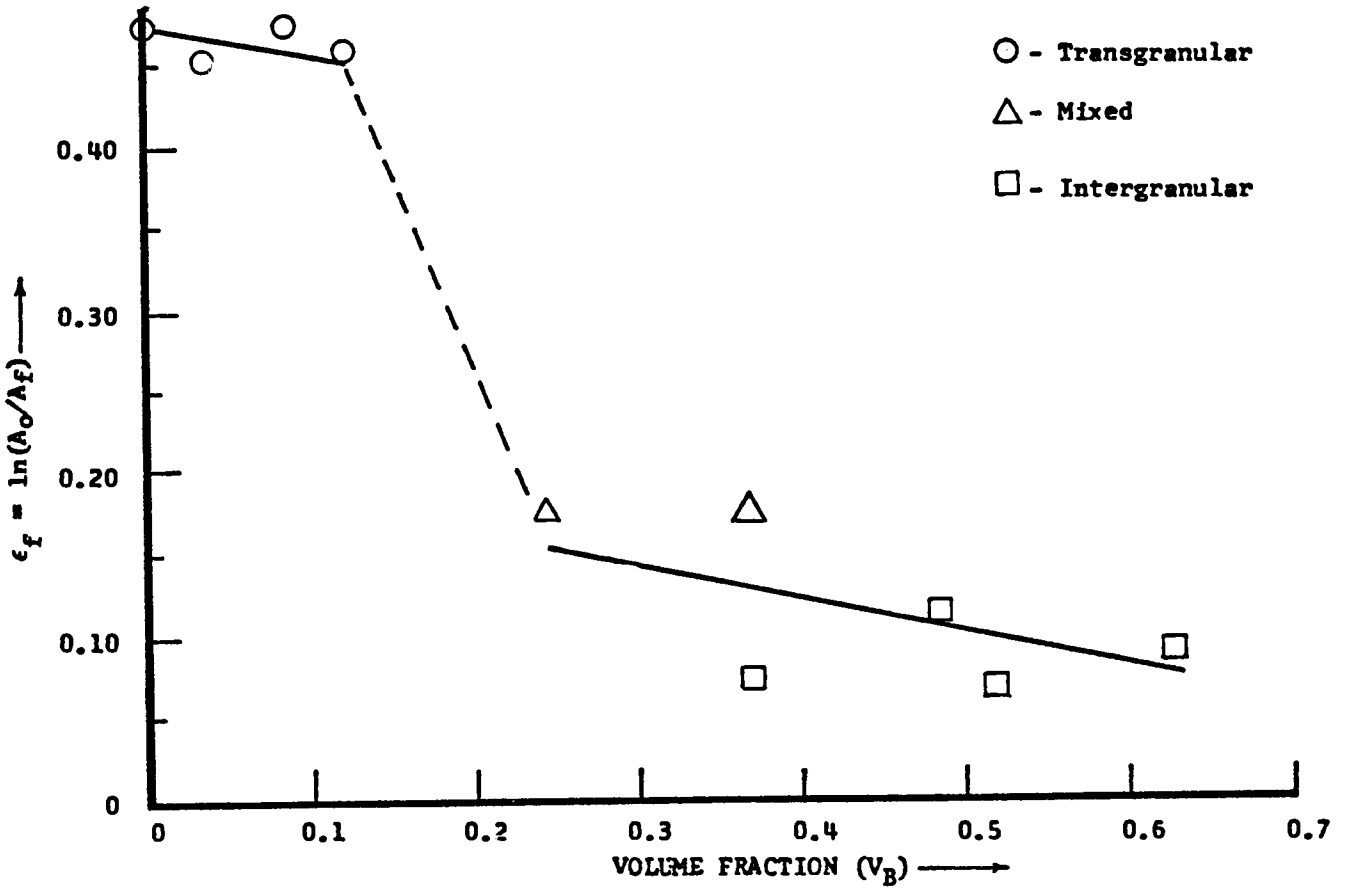

Figure 8 Tensile Ductility Compared to Volume Fraction and Fracture Mode

fracture mode would occur preceeding (i.e., at a lower stress level) a transgranular mode. Knoop hardness numbers were obtained for the matrix region of each carburized specimen. The results are shown in Fig. 9. A slight, but insignificant, increase in matrix hardness occurred as the case depth was increased. If increased matrix hardness was responsible for the transition in fracture mode, a much larger (and discontinuous) increase would be expected as the case depth was increased.

Sensitization due to chromium depletion in regions adjacent to grain boundaries can lead to intergranular failure, as discussed by Plateau, et al.[14] Electron microprobe studies were conducted on specimens case carburized to a depth of 0, 0.00387 and 0.0063 inches. It was determined that grain boundary regions become more distinct on the chromium X-ray micrographs as the case depth increases. This implies that chromium depletion has occurred in these areas. To check if this chromium depletion is sufficient to induce a change from transgranular to intergranular fracture, several specimens were case carburized and the case removed by surface grinding before tensile testing at 760°C. All specimens failed in a transgranular mode, regardless of the original case depth. This result rules out the possibility of the fracture mode transition being caused by sensitization.

Another potential explanation of the observed transition in fracture mode is the introduction of a triaxial stress state in the matrix at the tip of a crack in the carbon case. Brittle fracture occurs at a critical tensile stress ϵ_f, while transgranular dimpled fracture occurs at a critical plastic strain ϵ_f.[15] If the triaxial

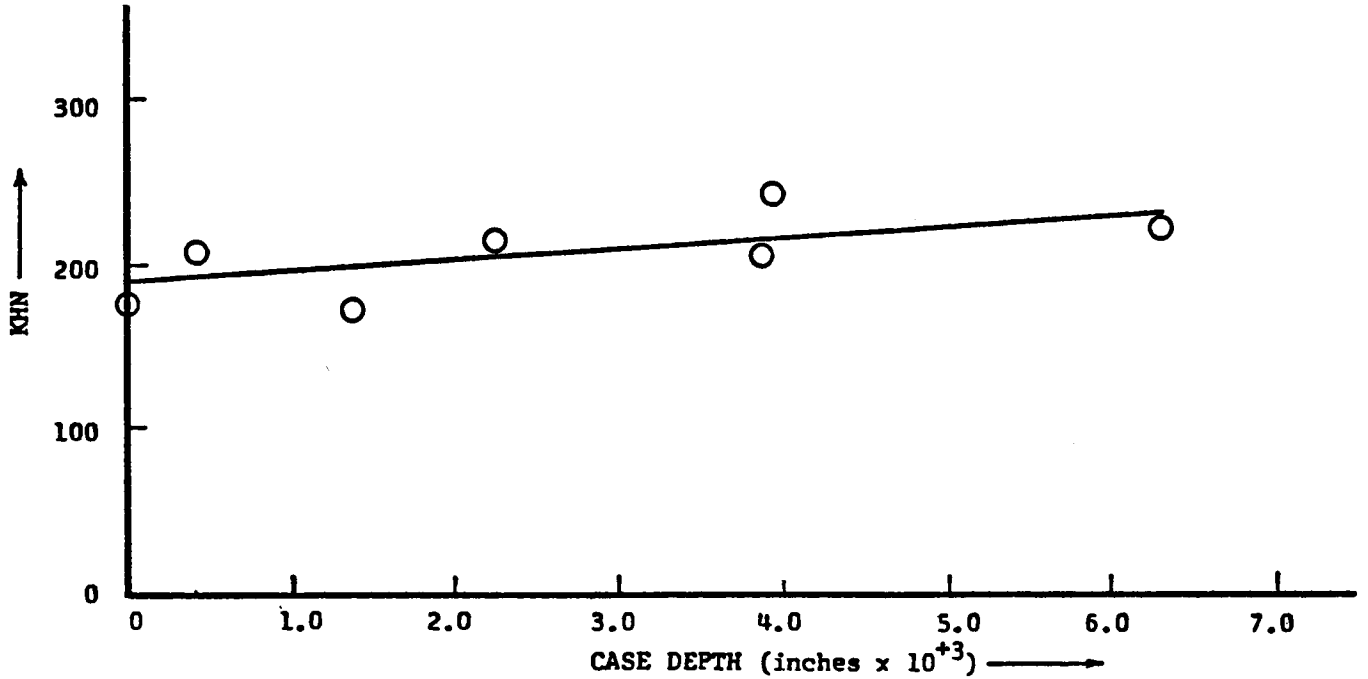

Figure 9 Knoop Hardness of Core Material versus Case Depth

constraint induced by a deep crack in the carbon case increased the longitudinal stress, $\sigma_{yy} = \sigma_{flow}$, acting on the matrix to such an extent that the critical stress for intergranular failure, $\sigma_{f(crit)}$, was achieved before the strain ϵ reached the critical strain, $\epsilon_{f(crit)}$, required for ductile fracture, the fracture mode would change from transgranular to intergranular. This phenomenon is shown schematically in Fig. 10. A similar effect could occur under high strain rate, uniaxial loading if the flow stress were raised sufficiently by the high strain rate (Fig. 11).

To determine the effects of triaxiality on the fracture behavior of type 316 stainless steel at 760°C, tensile tests were conducted on uncarburized, single edge notched specimens, and the results compared with data obtained using double edge notched specimens. Net area tensile ductility and net area yield strength are compared in Figs. 12 and 13, respectively. The effect of triaxiality is reflected in the lower ductility and larger net section yield strength recorded for doubly notched specimens at a given notch depth. Although the ductility of doubly notched specimens closely parallels the case carburized material, there is no transition from transgranular to grain boundary failure as the notch depth was increased (Fig. 14). Thus, the transition in fracture mode in case hardened material is not caused by increased triaxiality due to failure of the carbon case. Although the triaxial constraint in notched specimens is not sufficient to change the fracture mode from transgranular to intergranular, it still contributes to the ductility loss associated with singly and doubly notched specimens (Fig. 12).

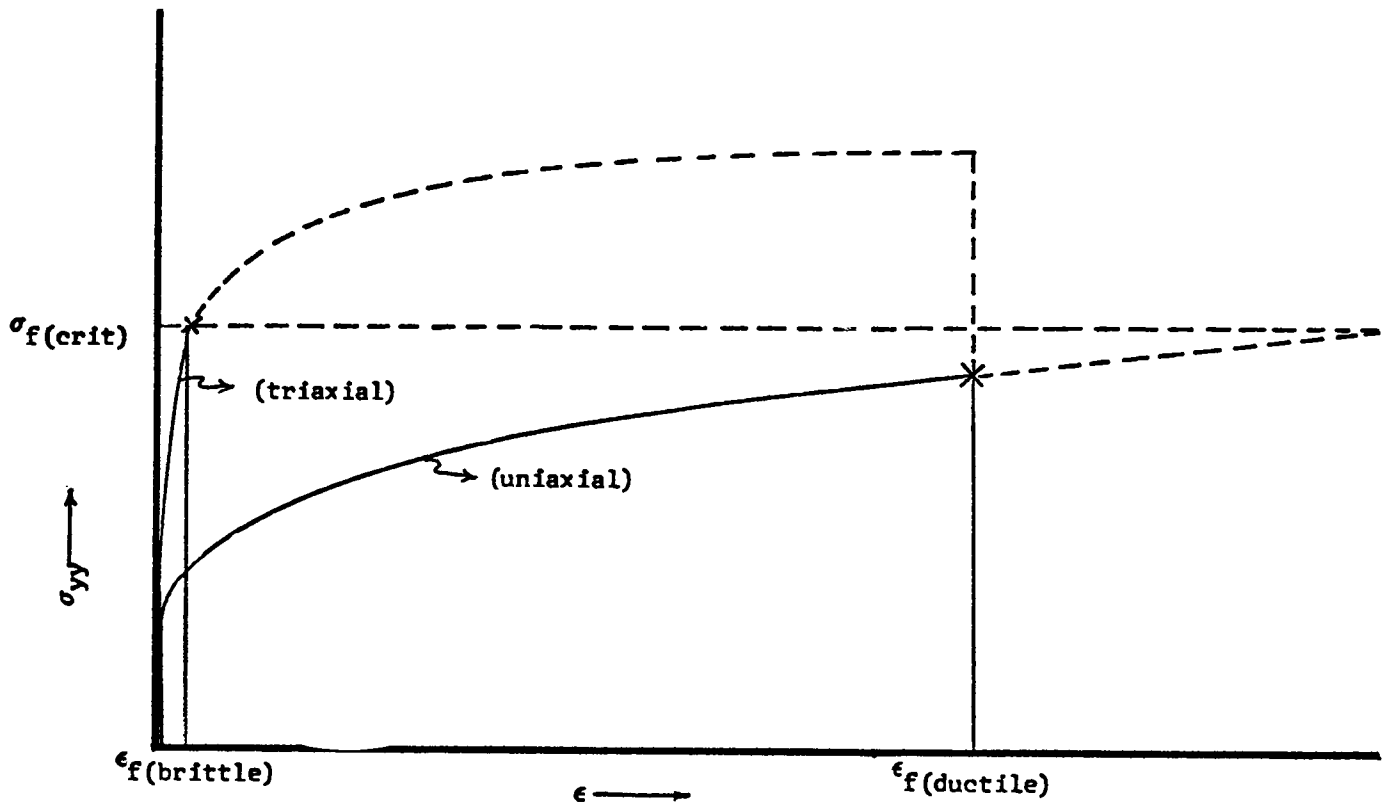

Figure 10 Schematic Stress-Strain Diagram Showing the Effect of an Imposed Triaxial Stress State

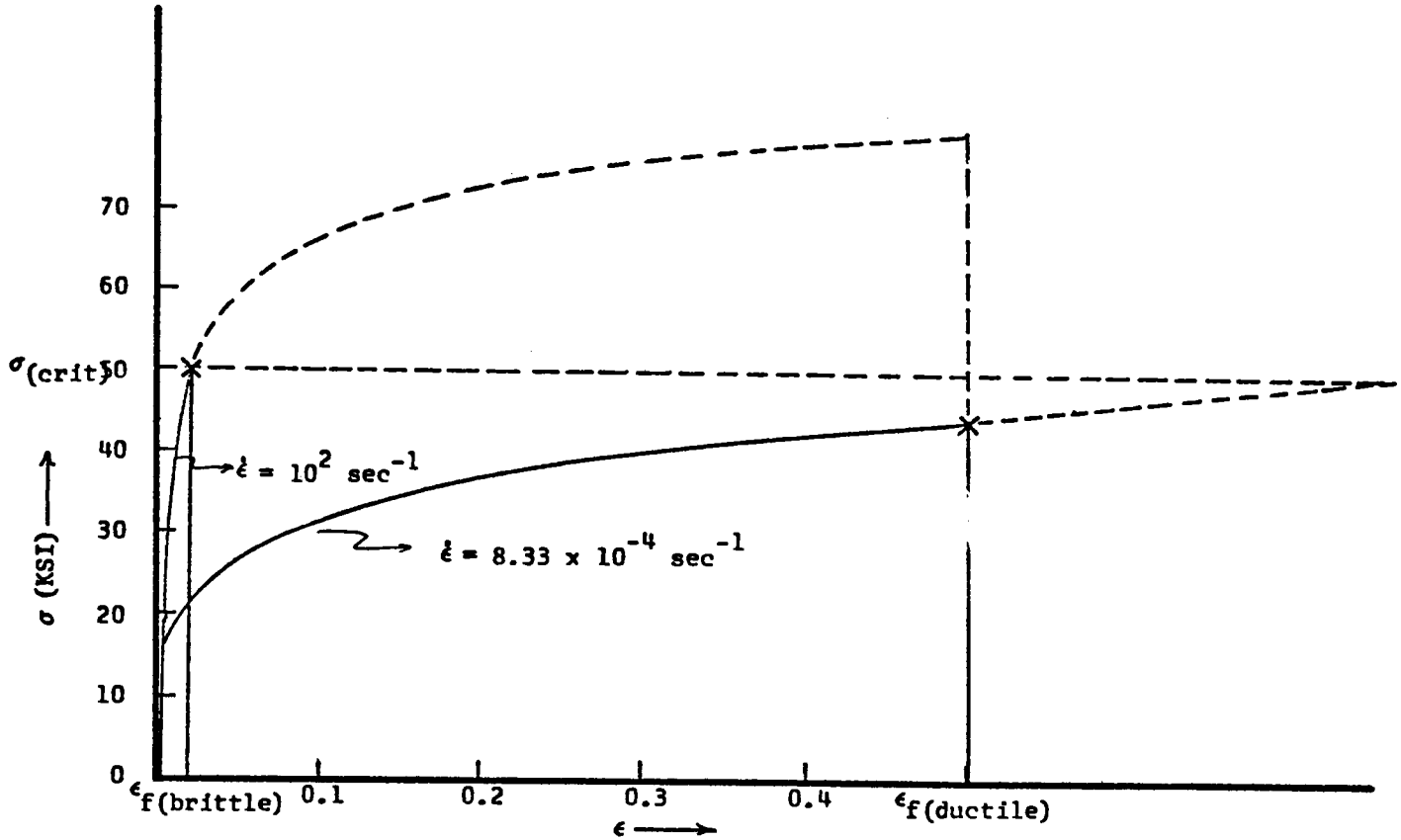

Figure 11 Stress-Strain Curves for Austenitic Stainless Steel Tested at Two Strain Rates.

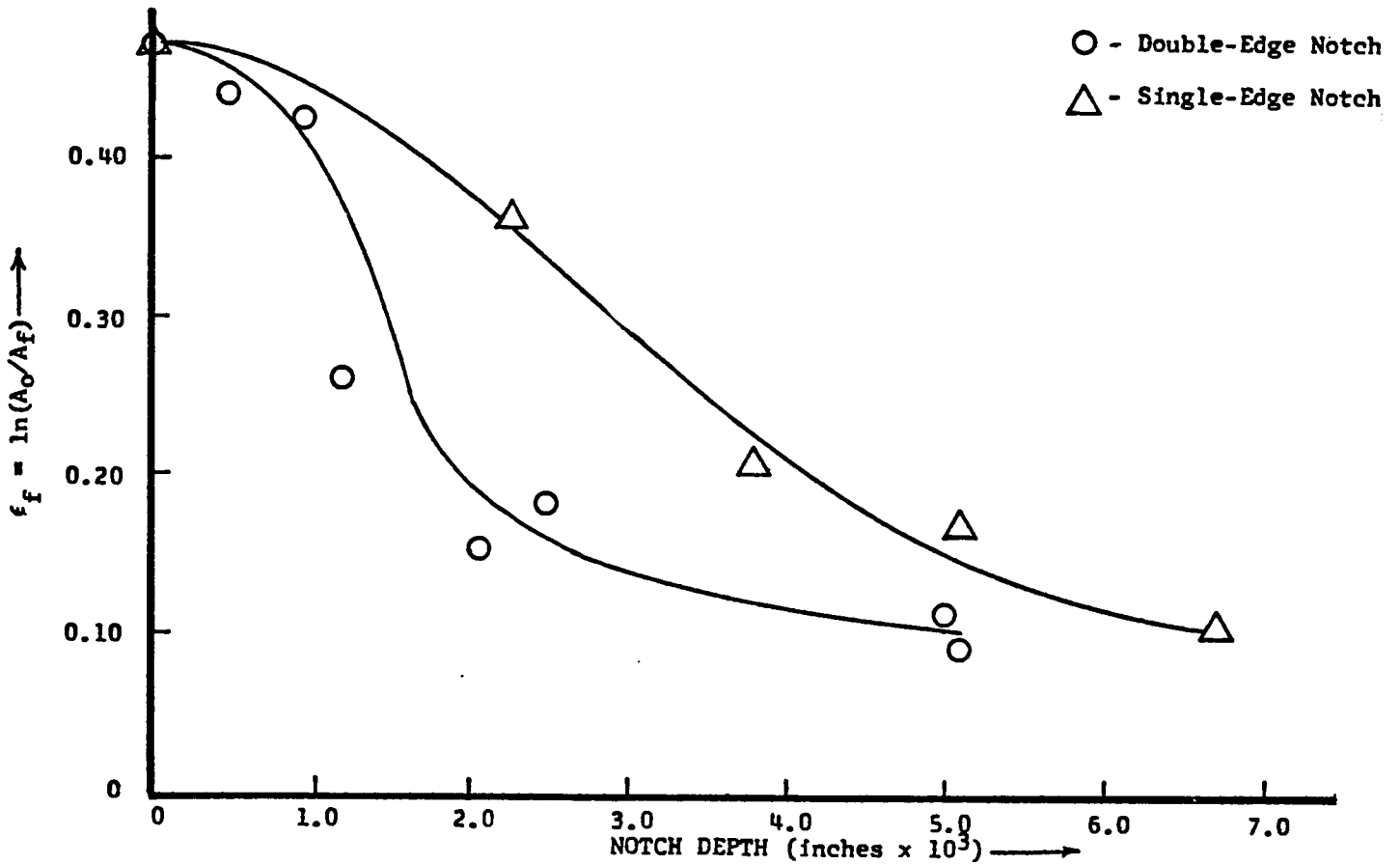

Figure 12 Net Area Tensile Ductility of Single and Double-Edge Notched Tensile Specimens versus Notch Depth

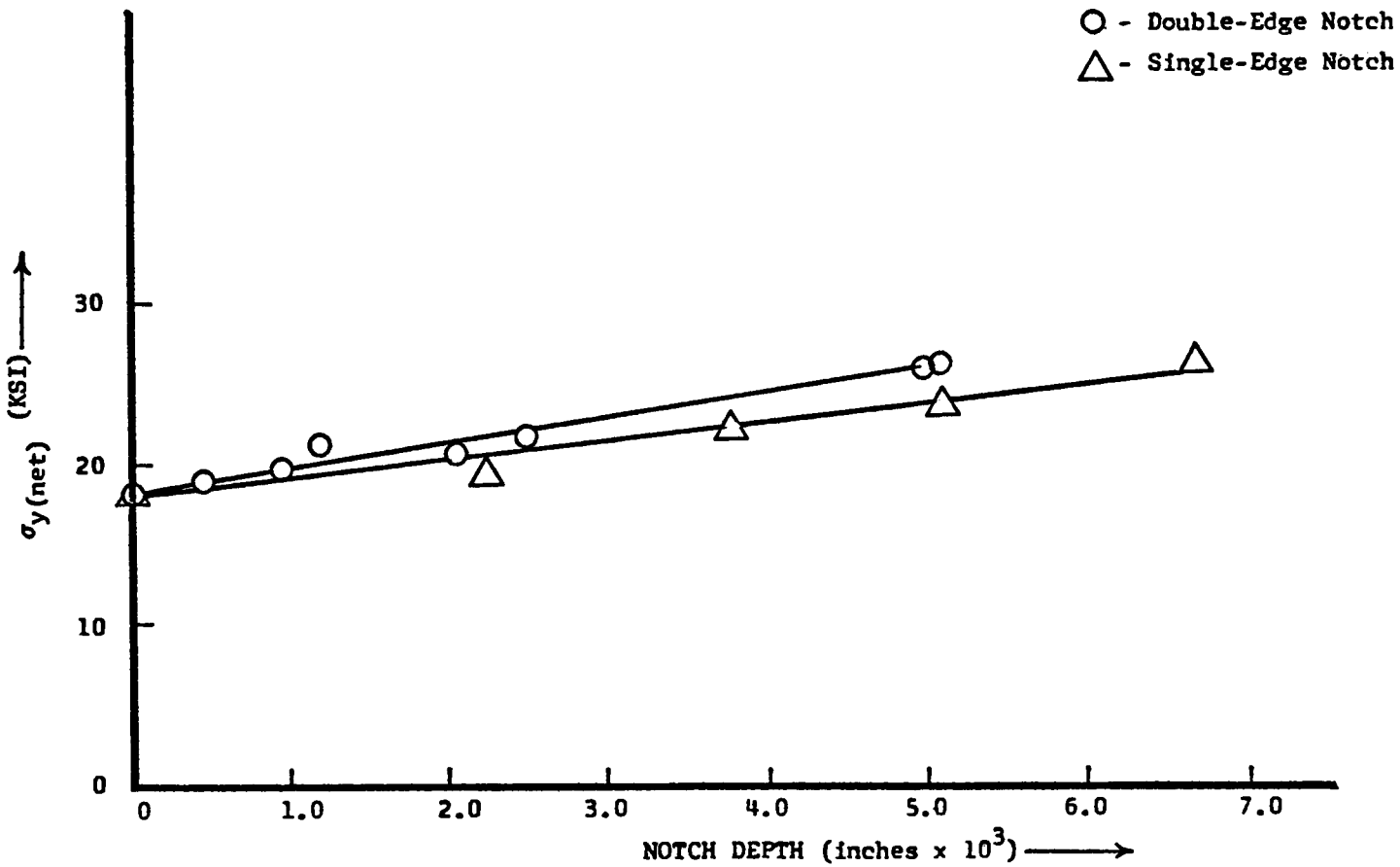

Figure 13 Net Area Yield Strength for Single and Double Edge Notched Tensile Specimens

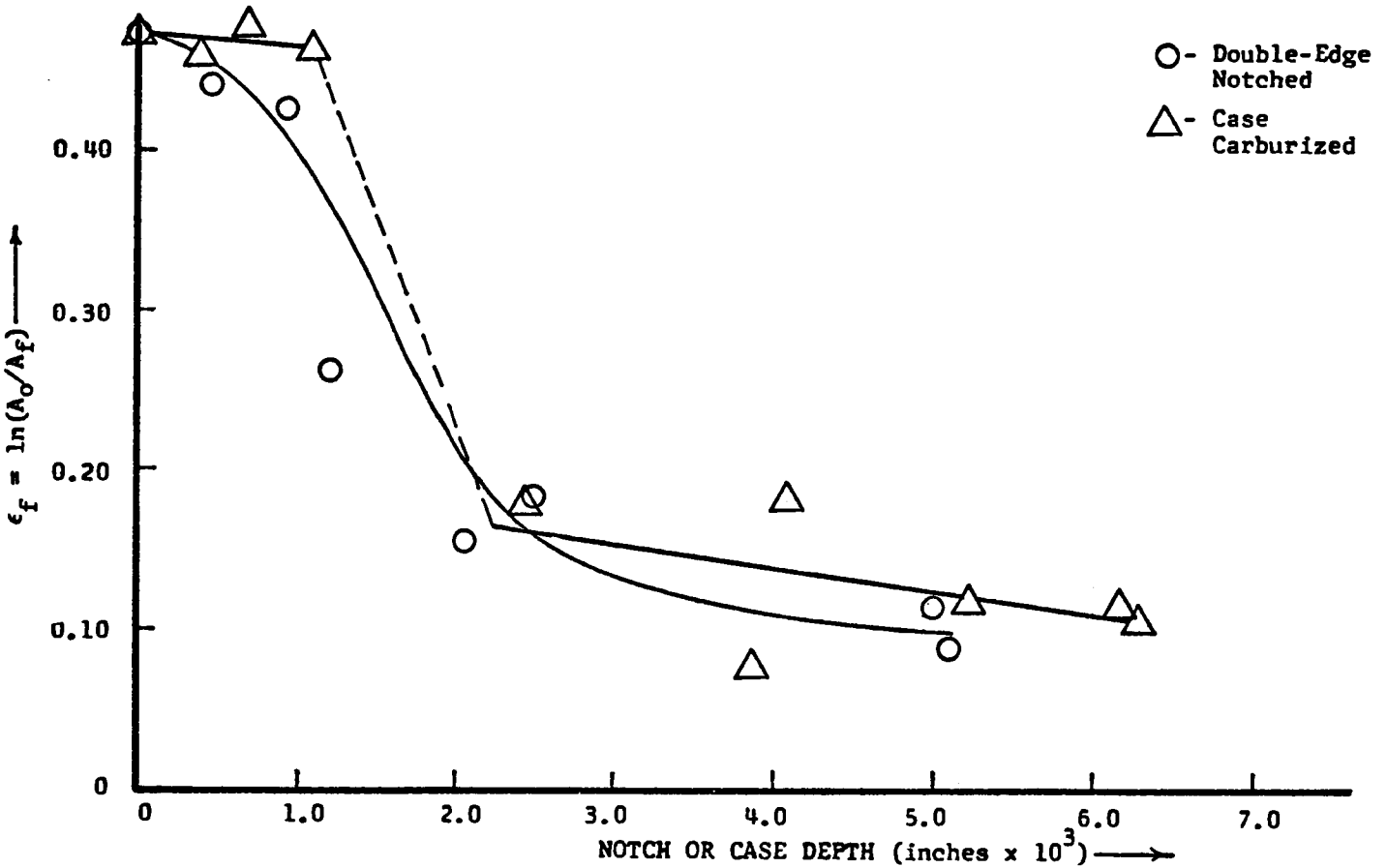

Figure 14 Tensile Ductility versus Notch or Case Depth

As mentioned in a previous report,[13] cracking of the carbon case is the first step involved in the fracture of case carburized type 316 stainless steel. Upon fracture of the case, the matrix will either absorb the load and fail in a ductile mode, or immediately fail by overload. The local strain rate imposed on the matrix material is much higher when the entire load carried by the case is immediately transferred to the core at the tip of a crack in the case (when the case suddenly fails) than when the core material is loaded in tension at a nominal loading rate. For a given applied loading rate, there is a higher local strain rate, $\dot{\epsilon}$, (strain concentration) at the crack tip.[16] Steichen and Knecht[17] have used a modified Ludwik relation of the form

$$\sigma = K\,\epsilon^{n} + \exp(K' + n'\epsilon)$$

to describe the effect of strain rate on the flow behavior of austenitic stainless steels. Parameters obtained at 760°C by Steichen and Knecht were used to develop the two stress-strain curves shown in Fig. 11. As can be seen, the effect of increasing the strain rate from 8.33×10^{-4} sec^{-1} (which is comparable to the strain rate used in this study), to 10^{2} sec^{-1} (reasonable for the rate imposed by case cracking) is quite dramatic. To determine whether the increased local strain rate acting on the matrix when the case fails is sufficient to produce brittle intergranular fracture, case carburized specimens were tensile tested with the case removed using crosshead speeds of 0.05 and 2.0 inches/min. All specimens loaded at 0.05 inches/min. failed in a transgranular mode. However, when the case carburized specimens were tensile tested with the case removed at a crosshead

speed of 2 inches/min., the fracture mode becomes primarily intergranular. Thus, it appears justifiable to attribute the primary case of the observed transition in fracture mode to the increase in the local strain rate acting on the matrix at the tip of case cracks when failure of the carbon case is the controlling step in the fracture process. It should be pointed out that although the local strain rate effect is primarily responsible for the fracture mode transition, there are other contributing factors. Sensitization due to chromium depletion and the imposition of a triaxial stress state due to case cracks will both facilitate the transition, although taken alone, neither phenomena is sufficient.

7.2.7 References

1. Ono, K. et al, UCLA-34P177-21, June 1974.
2. Chalco, P.A. and Ono, K., ORNL-4963, June 1974, pp. 261-282.
3. Tetelman, A.S. and McEvily, A.J. (Jr.), Fracture of Structural Materials, Wiley, 1967, p. 660.
4. Irwin, G., "Fracture Dynamics," Fracture of Metals, ASM, 1948, p. 147.
5. Wells, A.A., British Welding Research Association Report RB 12a, 1955.
6. Gurland, J. and Plateau, J., Trans. Quarterly ASM, 56 (1969) 318-326.
7. Broek, D., "Some Contributions of Electron Fractography to the Theory of Fracture," NLR TR 72029U, 1972, 51-69.
8. Yoshia, H., Yoda, R., Koike, K. and Matuo, K., Tetsu-to-Hogane 56 (1970) 311-330.

9. Pearlman, H., Trans. Am. Nuc. Soc. 11 (1968) 126-127.

10. Natesan, K. and Kassner, T.F., ANL 7646, Argonne, December 1969, p. 28.

11. Bauer, A.A. and Conner, J.G., BMI 1901, Battelle, January 1970, p. 140.

12. Andrews, R.C., MSAR-65-194, December 1965, p. 135.

13. Ono, K., et al. ORNL-4998, September 1974, p. 329.

14. Plateau, J.G., Henry, G. and Coussard, C., Precipitation Processes in Steels, Percy Lund and Humphries, London, 1957, p. 157.

15. Tetelman, A.S., Robinson, J.R., Mohamed, S.A. and Ensha, S., UCLA-ENG-7290, University of California, September 1972.

16. Rau, C.A. (Jr.), SU-DMS Report No. 67-12, Stanford University, Palo Alto, April 1967, p. 9.

17. Steichen, J.M. and Knecht, R.L., HEDL-TME-72-105, August 1972, pp. 21-29.

8. GENERAL ELECTRIC COMPANY

(Will report next quarter.)

INDEX

Test	Material	Page
Chemical Analysis		
	type 316 SS	139
Creep Test Data		
Base-Line Data		
	type 304 SS	260
	type 304 SS plate	109, 241, 303–12
	type 304 SS welded bar	312
	type 304 SS welded plate	312–13
	overlaid type 304 SS forging . .	236
	type 304 SS tube	313–21
	type 316 SS tube	321
	type 316 SS, 20% cold worked . .	60–88
	type 16-8-2 SS weld metal	203, 347
Correlations		
	2 1/4 Cr-1 Mo	233, 234
	type 304 SS	148, 241, 326
	type 316 SS, 20% cold worked . .	89–97
Effect of Aging		
	type 304 SS	126
	type 316 SS	137
Effect of Strain Cycling		
	type 304 SS	258
Heat-to-Heat Variation		
	type 304 SS	119, 122
	type 316 SS	137
Intergranular Cracking		
	type 304 SS	334
Interrupted Tests		
	type 304 SS	260
Step-Load Tests		
	type 304 SS	260
	2 1/4 Cr-1 Mo	344, 349, 353

Test	Material	Page
Creep Test Data (Continued)		
Strain Limits		
	type 304 SS	148
Elastic Properties		
	type 304 SS	164
Fatigue-Creep Interaction		
	type 304 SS	101–5
Fatigue Test Data		
Cyclic Fatigue Test Data		
	Inconel 718	41–44
	2 1/4 Cr-1 Mo	220
Effect of Hold Time		
	types 304 and 308 SS	1–6
	type 316 SS, 20% cold worked . .	47–59
Effect of Rising Mean Strain		
	type 304 SS	7–12
Effect of Sodium Environment		
	types 304 and 316 SS	13–17
Load-Controlled Tests		
	2 1/4 Cr-1 Mo	220
Strain-Controlled Tests		
	2 1/4 Cr-1 Mo	220
	Inconel 718	12–14
Crack Growth Rate Data		
Effect of 25% Cold Work		
	type 304 SS	102–5
Effect of Hold Time		
	type 304 SS	102–5
Effect of Stress Intensity Factor		
	Inconel 718	45–46
Effect of Thermal Aging		
	type 316 SS, 20% cold worked . .	51
	type 304 SS	101–5

Test	Material	Page
Hardness Correlation		
	2 1/4 Cr-1 Mo	234
Microstructure		
	2 1/4 Cr-1 Mo	219
	type 304 SS	260, 324
	type 316 SS	137
Relaxation		
	type 304 SS	250
Tensile Test Data		
Base-Line Data		
	types 308/308L, 308 CRE, and 16-8-2	22
	tungsten, TZM	33—36
	2 1/4 Cr-1 Mo	220, 286
	9 Cr-1 Mo	286
Correlations		
	types 308/308L, 308 CRE, and 16-8-2	23—32
	tungsten, TZM	37—41
	2 1/4 Cr-1 Mo	207, 232
	type 304 SS welded plate	175
Effect of Carbon		
	type 316 SS	359
Effect of Prior Creep		
	type 304 SS	116
Effect of Triaxiality		
	type 316 SS	363
Heat-to-Heat Variations		
	type 316 SS	137
Thermal Properties		
	type 308 SS weld metal	183

ORNL-5103
UC-79b, -h, -k
(Liquid Metal Fast
Breeder Reactors)

INTERNAL DISTRIBUTION

(3) Central Research Library
ORNL — Y-12 Technical Library
Document Reference Section
(10) Laboratory Records Department
Laboratory Records, ORNL RC
ORNL Patent Office
R. J. Beaver
M. Bender
R. G. Berggren
J. J. Blass
M. K. Booker
C. R. Brinkman
D. A. Canonico
J. Corum
W. R. Corwin
F. L. Culler
J. E. Cunningham
J. H. DeVan
D. P. Edmonds
G. Fee
M. H. Fontana
W. R. Gall
B. L. Greenstreet
J. C. Griess, Jr.
J. P. Hammond
W. O. Harms
R. L. Heestand
(5) M. R. Hill
D. O. Hobson
F. J. Homan
H. Inouye
P. R. Kasten
J. F. King
R. T. King
R. L. Klueh
K. C. Liu
C. T. Liu
A. L. Lotts
(20) W. R. Martin
W. J. McAfee
H. E. McCoy
H. C. McCurdy
C. J. McHargue
J. Merkle
P. Patriarca
S. Peterson
H. Postma
C. E. Pugh
P. L. Rittenhouse
D. N. Robinson
T. Roche
J. L. Scott
Myrtleen Sheldon
V. K. Sikka
G. M. Slaughter
W. J. Stelzman
J. P. Strizak
R. W. Swindeman
D. B. Trauger
T. N. Washburn
J. R. Weir, Jr.
G. D. Whitman
T. Yahr
Walter Kohn (consultant)
W. C. Leslie (consultant)
John Moteff (consultant)
J. A. Pask (consultant)
J. W. Prados (consultant)
G. V. Smith (consultant)

EXTERNAL DISTRIBUTION

USAEC DIVISION OF REACTOR RESEARCH AND DEVELOPMENT, Washington, DC 20545

(2) Director

USAEC OAK RIDGE OPERATIONS OFFICE, P.O. Box E, Oak Ridge, TN 37830

Research and Technical Support Division
Director, Reactor Division

USAEC TECHNICAL INFORMATION CENTER, Office of Information Services, P.O. Box 62, Oak Ridge, TN 37830

For distribution as shown in TID-4500 Distribution Category, UC-79b (Fuels and Materials Engineering Development); UC-79h (Structural Materials and Design Engineering); UC-79k (Components)

☆U. S. GOVERNMENT PRINTING OFFICE: 1974-748-189/107